Activated Carbons Derived from Victorian Brown Coal as Adsorbents for CO_2 Capture

A thesis submitted for the degree of

Doctor of Philosophy (PhD)

Lachlan Alexander Ciddor

School of Chemistry, Monash University

Clayton, Victoria, Australia

August 2016

This PhD project was undertaken with funding from Brown Coal Innovation Australia (BCIA) in association with the Cooperative Research Centre for Greenhouse Gas Technologies (CO2CRC), and was done under the supervision of

Prof. Alan L. Chaffee, Monash University, School of Chemistry, Faculty of Science

Prof. Sankar Bhattacharya, Monash University, Faculty of Engineering

Prof. Paul Webley, Melbourne University, Faculty of Chemical and Molecular Engineering

I certify that I have made all reasonable efforts to secure copyright permissions for third-party content included in this thesis and have not knowingly added copyright content to my work without the owner's permission.

This work is dedicated to my late grandfather

Alexander Keppoch MacDonald

Declaration

To the best of my knowledge and belief this thesis contains no material which has been accepted for the award of any degree or diploma in any university, nor any material previously published or written by any other person except where due reference is made in the text.

Lachlan Alexander Ciddor

Acknowledgments

First and foremost, I would like to express my gratitude to Professor Alan Chaffee for providing me with the opportunity to complete my PhD in the School of Chemistry at Monash University. He has been a wealth of knowledge, a source of guidance and an invaluable support.

Secondly I would like to thank my co-supervisor Associate Professor Sankar Bhattacharya for his assistance, enthusiasm and support, particularly in respect to the fixed bed gasification rig.

A major thank you also must go out to Dr. Gregory Knowles, for being there to bounce ideas off and just in general being there to answer questions and help me with ideas on all aspects of my project. Greg you're an absolute dude and I probably wouldn't have made it through my PhD if not for you (and your sense of humour).

I'd also like to thank all my friends and family for their support throughout my candidature. Shah and Neat your warped senses of humour, so close to my own and your borderline insanity helped keep me sane and lift my spirits even when things weren't going my way, sharing an office with you both was a privilege. Tom and Pete, you have both put up with so much, or so little due to my constant absenteeism, when we did manage to see each other you always helped me put things into perspective and help me forget about work even if only for a little while. You're the best mates anyone could ever ask for, I cherish our friendship greatly and hope to for the remainder of my years. Mum and Dad, thanks for your support over the years and obviously for making me. Rivka and Rhian you're awesome sisters thanks for everything and just for being there. Nanna and Poppa you helped raise me and shape the man I have become, there are no words to express how much you've both meant to me.

Dr. Michael Schwartz, well what can I say, I probably wouldn't be here if it wasn't for you, thanks for making me believe in myself and playing a large part in turning me into a functional member of society (I use the word functional loosely).

Ruben Urban, you're probably the only reason I made it through high school, you encouraged me towards this (so I know who to blame if it goes tits up) and were truly the best teacher I've ever had in my life, I can never repay the enthusiasm for science that you instilled in me, nor understand how you could have such unlimited patience with me.

Dr. Francois Malherbe, you took a chance on me as an undergrad and took me on as your research assistant. Throughout your mentorship I developed my love of material science, in addition to a friendship that I am sure will last a lifetime.

To my animals, Angus (Gus the bus), Iona, Squee, Stark and the late Onslow you are the best and most loyal study buddies, always keeping me company and helping me work late into the night (or acting as a welcome distraction). I love you all, my dysfunctional little monkeys.

Finally I must thank my wonderful wife Priscilla. Pree you were my rock. As a fellow PhD student I truly believe that only you truly knew what it took and what I was going through. Thank you for your patience, your assistance (driving me into the lab at 2 am to put on TGA runs), for kicking my ass when it needed kicking and mostly for your love and friendship.

Abstract

Atmospheric levels of CO_2 have increased from 275-285 ppm prior to the industrial revolution, to 400 ppm in 2013. CO_2 and other greenhouse gases (GHGs) have been implicated in global warming, and climate change. Due to increasing environmental, social and economic pressures, the release of anthropogenic CO_2 must be minimised. The work described in this thesis focuses on the development of solid carbon adsorbents and adsorbent supports for the post-combustion capture of CO_2 from coal fired power plants. One of the major hurdles for the implementation of adsorbent-based carbon capture technology is the cost of the adsorbent. With this in mind, the objective of this research was to investigate the potential to convert inexpensive and readily available Victorian brown coal (VBC) into activated carbons (AC) for application as CO_2 adsorbents.

Three series of microporous ACs (miACs) were produced from VBC and VBC-derived chars by either chemical or physical activation at 1073 K in a fixed-bed reactor. Physically activated miACs were produced using mild steam gasification conditions for extended time periods to encourage the development of micropores. Chemical activation was undertaken using KOH as the activating agent at doping levels < 10 wt%, followed by carbonisation. A further two series of mesoporous ACs (meACs) were prepared by catalysed steam activation using lanthanoid oxide catalysts of the form Ln_xO_y (where Ln was Ce or La), to produce materials with larger pore diameters amenable for subsequent amine-modification. Several of the most promising ACs were further investigated as supports for polyethylene imine (PEI).

All the materials prepared using these methods were thoroughly characterised in terms of their chemical composition, surface chemistry, physicochemical structure and surface morphology using a combination of analytical techniques, including x-ray photoelectron spectroscopy (XPS), near edge x-ray adsorption fine structure (NEXAFS) spectroscopy, Raman spectroscopy, powder x-ray diffraction (P-XRD), gas physisorption and transmission electron microscopy (TEM). The gas separation behaviour of the carbon adsorbents was evaluated using a thermogravimetric analyser equipped with a gas dosing manifold to simulate the partial pressure conditions that would occur in a vacuum swing adsorption (VSA) process. The measurements were undertaken using gas mixtures of Ar and CO_2, in a procedure that is referred to as partial pressure swing adsorption (PPSA).

Several promising miACs were identified through the PPSA studies. Two of the miACs in particular (AC-90 and AC-K10), outperformed a leading commercial carbon (AC-N) for CO_2 adsorption at all temperature and CO_2 partial pressure conditions investigated, despite having smaller pore volumes. Intensive surface chemistry studies using XPS and NEXAFS spectroscopy revealed that the surface of AC-90 and AC-K10 possessed much higher concentrations of hydroxyl and carboxylic acid species than AC-N, which increased the affinity of the surfaces of these ACs for CO_2. This clearly highlighted the importance that AC surface chemistry can play in adsorption processes, a fact that is often overlooked. Importantly, PPSA studies performed in the presence of H_2O, revealed very little competitive adsorption over AC-90, whilst AC-K10 exhibited significant competitive adsorption with H_2O. The results for AC-90 were interesting, as ACs that adsorb appreciable amounts of CO_2 also adsorb significant amounts of H_2O. This may make the VBC derived carbons attractive for industrial scale CO_2 separation, on account of their relatively high CO_2 adsorption capacity and low cost.

In an attempt to further develop the mesoporosity of the ACs, Ln_xO_y was used to catalyse partial oxidation reactions during the gasification of VBC. However, this approach was not as successful as had been desired. Through the development of protocol to post-synthetically remove the Ln_xO_y using H_2SO_4, it was found that much of the mesoporosity of similar materials presented in the literature was actually due to the porosity inherent to the Ln_xO_y itself. From the PPSA studies, the Ln-meACs exhibited lower CO_2 adsorption relative to the miACs. This was not surprising on account of the differences in surface chemistry and pore structure existed between the miACs and meACs. Selected carbons were used as supports for polyethylene imine (PEI). All of the PEI-AC composites exhibited higher CO_2 capacities than their corresponding support materials. However, post-synthetic vacuum treatment of the PEI-AC composites reduced the CO_2 adsorption capacity, possibly by drawing the PEI deeper into the carbon pores, leading to stronger interactions between the PEI and the carbon such that the PEI mobility is restricted.

The ACs presented in this thesis were produced from VBC which is a readily available, easily accessible and inexpensive starting material. Several promising carbon adsorbents for CO_2 were identified and found to outperform a leading commercial carbon. Moreover, many of the ACs that showed high CO_2 adsorption capacity did not undergo competitive adsorption with H_2O which may indicate their potential for industrial scale CO_2 capture. The viability of these materials should be investigated further in bench scale studies. It is likely that further improvements to both the development of the pore structure and the surface chemistry of the ACs could be achieved through adjustments to the activation process, such as gasification rate.

Abbreviations

AC	Activated carbon
AC-N	Commercially available Norit R230CO2 activated carbon
AS	Australian Synchrotron
BET	Brunauer, Emmett, Teller
BJH	Barrett, Joyner, Halenda
CCS	Carbon capture and storage
CH	Char
CHLR	Run of production char produced using a Lurgi Retort
CHRK	Char produced using a Rotary Kiln
CMS	Carbon molecular sieves
CO_2	Carbon dioxide
DETA	Diethylenetriamine
DFT	Density functional theory
DR	Dubinin-Radushkevich
EDX	Electron dispersive X-ray
ESA	Electrical swing adsorption
EtOH	Ethanol
GHE	Greenhouse effect
GHG	Greenhouse gas
GHGs	Greenhouse gases
HAADF	High angular annular dark field
HMS	Hexagonal mesoporous silica

HP	High precision
HRTEM	High resolution transmission electron microscopy
IEA	International Energy Agency
IR	Infrared
IR	Infrared
IUPAC	International Union of Pure and Applied Chemistry
KIT-6	Korean Advanced Institute for Science and Technology mesoporous silica
Ln	Lanthanide, La or Ce
Ln-meAC	Lanthanide catalysed physically activated mesoporous carbon
LPH	Low pressure hysteresis
MCEM	Monash Centre for Electron Microscopy
MCF	Mesocellular Siliceous Foam
MCP	Microchannel plate
MCM-41	Mobil Composition of Matter No. 41, mesoporous silica
MCM-48	Mobil Composition of Matter No. 48, mesoporous silica
MEA	Monoethanolamine
meAC	Mesoporous activated carbon
MeOH	Methanol
miAC	Microporous activated carbon
MOF	Metal organic framework
NEXAFS	Near edge X-ray absorption fine structure
NMR	Nuclear magnetic resonance
NO_x	Nitrogen oxides (NO or NO_2)
P/P_o	Relative pressure
PEHA	Pentaethylenehexamine
PEI	Polyethyleneimine
PEY	Partial electron yield

PPSA	Partial pressure swing adsorption
PSA	Pressure swing adsorption
PSD	Pore size distribution
P-XRD	Powder X-ray diffraction
SBA-15	Santa Barbara Amorphous type material No.15, mesoporous silica
SBA-16	Santa Barbara Amorphous type material No.16, mesoporous silica
STEM	Scanning transmission electron microscopy
STP	Standard temperature and pressure
SXR	Soft X-ray
TEM	Transmission electron microscopy
TFY	Total fluorescence yield
TGA	Thermogravimetric analysis
TO_3	Silica or aluminosilicates
TSA	Temperature swing adsorption
v/v	Volume for volume
VBC	Victorian brown coal
VBCB	Victorian brown coal briquette
VSA	Vacuum swing adsorption
W	Micropore width
wt%	Weight percent
XAS	X-Ray absorption spectroscopy
XPS	X-ray photoelectron spectroscopy

Table of Contents

1 Introduction

1.1 General Introduction

The objective of this project was to develop solid carbon adsorbents and adsorbent supports for the post-combustion capture of CO_2 for carbon capture and storage (CCS). Possibly the greatest hurdle in the implementation of CCS utilising solid adsorbents has been adsorbent cost. Compared to many other adsorbents carbons can be made in a very inexpensive manner from waste materials. From the standpoint of local resource utilisation, brown coal in Victoria (Australia) is cheap and readily available, and as will become clear throughout this thesis can be used to produce high quality carbon adsorbents for CCS.

1.2 Climate Change

Over the last 200 years since the beginning of the industrial revolution anthropogenic CO_2 has been released into the Earth's atmosphere at ever increasing amounts. Atmospheric levels of CO_2 have increased from 275-285 ppm prior to the industrial revolution, to 400 ppm in 2013 [1].

The first indications of the greenhouse effect (GHE) were noted by French mathematician Joseph Fourier in 1827 [2]. There he noted that the Earth was warmer than expected due to the radiation from the Sun alone, though he did not attempt to give a reason a why this might be.

In the 1850s an Irish physicist by the name of John Tyndall [3] wrote a series of papers on the absorption of infrared (IR) radiation by water vapour, CO_2 and other gases; now collectively referred to as greenhouse gases (GHGs). He also noted that these gases were predominately transparent to the ultraviolet radiation from the Sun, and that these two phenomena could cause increases in the Earth's temperature. Tyndall is generally accepted as being the first person to propose the concept of the GHE, shown in ***Figure 1-1***. In the late 1890s Svante

Arrhenius published further work on the GHE elaborating on the work of Tyndall and on the potential effects the GHE would have on the overall climate of the planet [4]. A great deal more work was also carried out by numerous scientists in a multitude of fields throughout the 1900s [5-14], most of which; like those of the 1800s were generally ignored and indeed forgotten about. Thus the GHE and human involvement, leading to global warming is by no means a new concept.

It is for this reason that the release of GHGs must be brought under control. Of the proposed CO_2 mitigation strategies that will be discussed herein the capture aspects of carbon capture and storage (CCS) will be the primary focus. The storage aspects will be discussed only in passing as they are of no particular relevance to this proposal.

There is much conjecture over whether or not climate change is caused by human action or merely a naturally occurring cycle of the planet. The purpose of the work entailed herein is not to convince anyone that the present climate changes being observed are in fact human caused, it will simply treat climate change as a matter of fact. Where reference is made to increases in atmospheric CO_2 or other GHGs throughout this document, unless otherwise stated are with respect to anthropogenic increases only and not those due to natural phenomena.

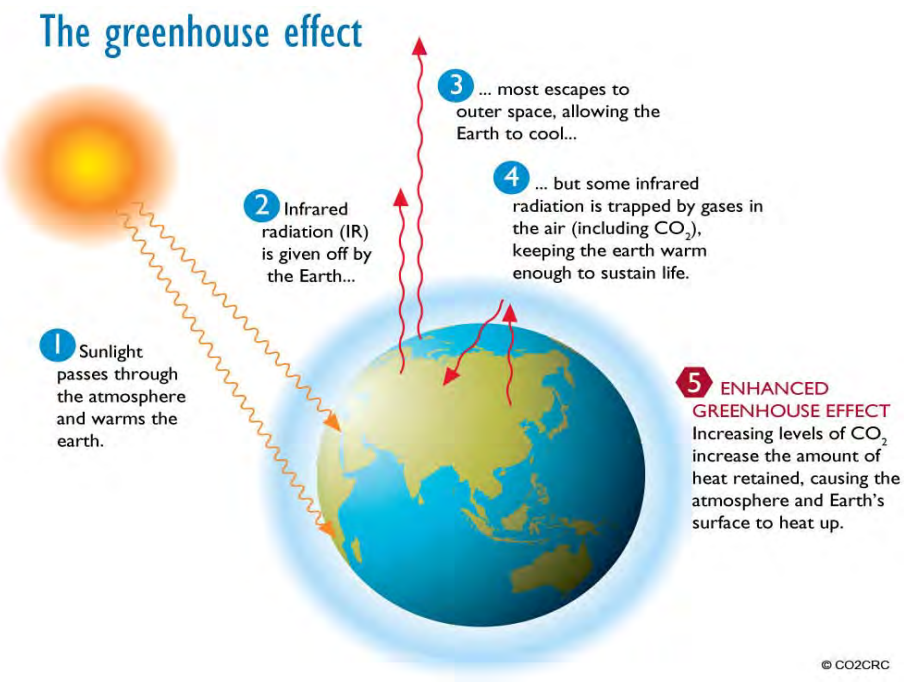

Figure 1-1 *~ The Greenhouse Effect*

(Reproduced with permission from the CO2CRC Ltd)

1.3 CO_2 Mitigation Strategies

There are many strategies for the mitigation of anthropogenic CO_2, these being as varied as the situations in which they are to be applied. Such strategies fall into one of three categories as outlined below:

1. ***Alternative Fuels*** – the use of fuels with a low or neutral carbon footprint. Nuclear fission itself produces little CO_2 itself, but does produce some in ancillary processes such as fuel and waste transport [15]. Renewable fuels are fuels with biomass feedstock's, that are processed via many different means to obtain the final fuel, such as gasification for H_2 production [16], pyrolysis for oil production [17, 18]. Through the production of the biomass (plant growth, CO_2 negative) and processing (i.e. fermentation, CO_2 negative) a fuel can be prepared for use with conventional technologies, producing CO_2 as has been done since the industrial revolution, but with a low carbon footprint.

2. ***Process Engineering*** – Through the use of alterations to already existing industrial processes, reduction in anthropogenic CO_2 can be achieved [19, 20]. This can be achieved, for example, through the use of heat integration [21] and, waste stream recycling [21] to improve the efficiency of energy recovery [19].

3. ***Carbon Capture and Storage*** – Carbon capture and storage (CCS) is a group of technologies used for the separation and sequestration of CO_2 produced by industrial processes [22-27]. Carbon capture is the primary focus of this thesis and will be elaborated on in the following section. The sequestration of CO_2 is proposed to be undertaken in empty gas wells), marine aquifers and abandoned oil wells or those in the end-stages of use (enhanced oil recovery, EOR) [28].

As mentioned, of the three categories mentioned above, carbon capture and storage is the primary focus of this thesis and as such the following discussion will cover this is more detail.

1.4 Carbon Capture & Storage (CCS)

Carbon capture and storage (CCS) is presently thought to be a suitable means to mitigate anthropogenic CO_2 emissions from point sources. Rather than a single technology, CCS is composed of a number of technologies that must be integrated to facilitate the capture, transport and storage of CO_2. A diagram that clearly illustrates how these technologies can fit together is shown in ***Figure 1-2***. As this project has been aimed at capture, storage will not be discussed, as it is beyond the scope of this thesis.

As indicated in ***Figure 1-2***, CCS processes focus on the capture of CO_2 from point sources such as power plants. In Victoria (Australia), coal-fired power plants are the major source of electricity generation. Flue gases generated from the combustion of coal contain between 15-16% CO_2 and are a major contributor to greenhouse gas emissions in the State. There are four main groups of technologies that show potential for CO_2 capture are:

1. Cryogenic Separation [26, 27, 29]
2. Solvent Absorption [26, 27, 29-34]
3. Solid Adsorption [26, 27, 29, 35-37]
4. Membrane Separation [26, 27, 29, 36, 38]

The work contained herein focuses on the adsorption of CO_2 by solid adsorbents. However absorption by solvents will also be discussed briefly, as the chemical reactions between CO_2 and amine-based solvents are relevant to understanding the CO_2 capture properties of certain amine-modified adsorbents (discussed later).

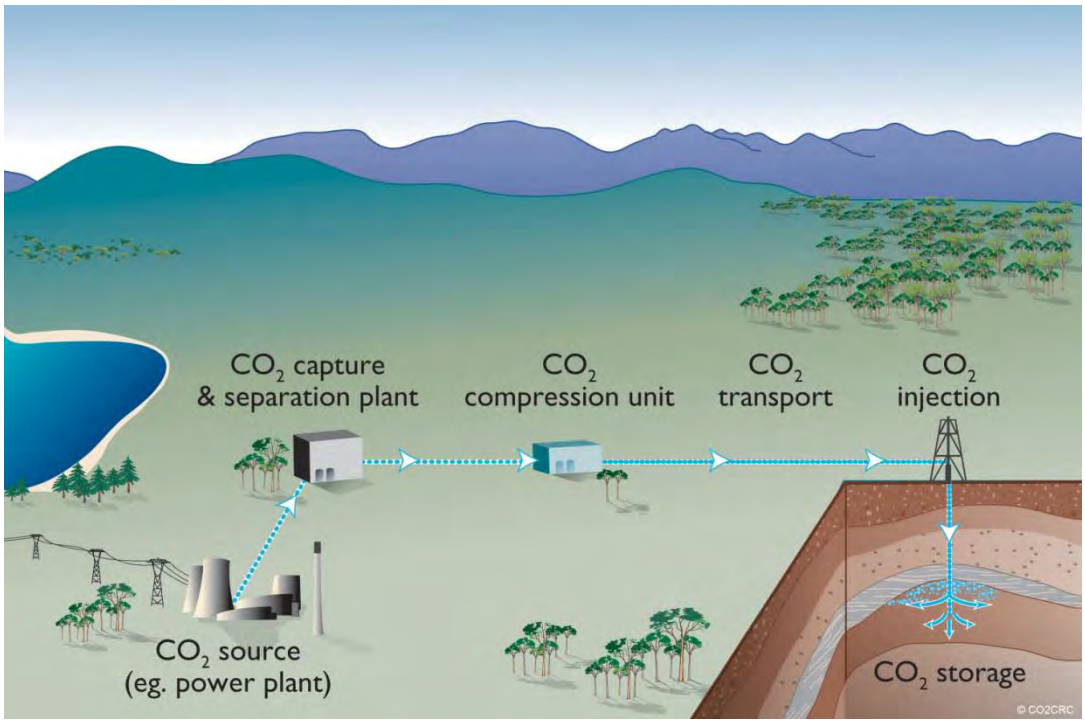

Figure 1-2 ~ *General Process of Carbon Capture and Storage (CCS)*

(Reproduced with permission from the CO2CRC Ltd)

1.5 Gas Adsorption and Separation

Adsorption from solution has been known since ancient Egyptian times, but it was not until the late 1700's that a scientific understanding of adsorption began to be developed [39]. Although a scientific understanding had started to be developed it was not until 1918 that Irving Langmuir published his groundbreaking work on monolayer adsorption [40]. This was the first time a fully realised theory had been developed that was able to unify experimental observations with theoretical predictions. For this and other works in surface chemistry Langmuir was awarded the 1932 Nobel Prize in chemistry [39]. Over the subsequent decades a great deal of development in both the theoretical and practical aspects of adsorption was achieved [41, 42]. Brunauer, Emmett and Teller developed the first mathematical model to explain pore condensation, allowing for the first accurate determination of surface area using the now famous and widely used BET equation (***section 6.6.3.2.1***, ***equation 6-1***)[43]. The BET equation and the subsequent models developed to explain adsorption phenomena have allowed for the determination and quantification of characteristics important in adsorbent development and deployment. Textural characteristics such as the pore volume, shape and diameter that are important in predicting adsorption behaviour; are important in part due to the development of such theories. An integral part of the theoretical understanding of adsorption is grounded in the thermodynamic quantities used to explain the adsorption phenomena, such as the heat of adsorption (ΔH_{Ads}). The most prominent thermodynamic description being given by the Gibbs [44, 45] free energy equation (***equation 1-1***) shown below:

$$\Delta G = \Delta H - T\Delta S \qquad \textbf{1-1}$$

where ΔG is the change in free energy, ΔH is the change in enthalpy or heat (in this case the heat of adsorption), T is the absolute temperature (K), and ΔS is the change in entropy.

The Gibbs free energy equation describes how the free energy of a system relates to the entropy, enthalpy and temperature [44]. For a process to be thermodynamically favourable, the change in the free energy of the system must be negative. When using ***equation 1-1*** to describe an adsorption process at constant temperature, it tells us that there is a decrease in entropy. As the gas molecules in the gas phase possess three degrees of freedom, upon adsorption they lose a degree of freedom, hence the decrease in entropy. This makes sense as the change in enthalpy is negative and for adsorption to occur the free energy changes must also be negative [46].

1.5.1 Adsorption: *physisorption vs. chemisorption*

The two major types of adsorption process that can occur are physisorption and chemisorption. As they names imply physisorption is an entirely physical process, that is no chemical reaction occurs; whilst for chemisorption a chemical reaction is taking place between a component of the gas/vapour phase and the surface of the adsorbent [47, 48]. That is to say that in chemisorption there is a sharing of electrons between the adsorbent and adsorbate, however, for physisorption no such sharing of electrons takes place [47]. The two processes often occur concurrently and can be differentiated by the heat of adsorption (ΔH_{Ads}), with the ΔH_{Ads} of a physisorption process being between 20-40 kJ/mol and that of a chemisorption process being in the range 40-400 kJ/mol [49]. The energies involved in a chemisorption process are clearly much higher than that of physisorption, but this arises from the highly specific process occurring. As such the selectivity of chemisorption towards a particular adsorbate or type of adsorbate is high [47, 48]. It is for this reason that chemisorbants have received a great deal of attention in recent years, as shall be elaborated on later when amine functionalised adsorbents is discussed (***section 1.7.3***).

1.5.2 Gas Separation Mechanisms

Separation by adsorbents is achieved via one of three mechanisms, equilibrium, kinetic and steric separation [50, 51].

Steric separation is a process involving the separation of gases according to their molecular size and is a property intricately associated with the size of the adsorbent pores. Steric separation has been demonstrated using zeolites, carbon molecular sieves (CMSs) and some other adsorbents with molecular sieving properties [50].

Kinetic separation is achieved on the basis of differences in the rate of diffusion of the different components of the gas mixture. Few industrially significant processes rely on kinetic over equilibrium separation, however one that is well known is air separation [50, 51].

Equilibrium separation is based on an adsorbent surface affinity for different adsorbates in a mixture. This strongly relies on interaction between the adsorbent and adsorbate such as electrostatic interactions [50]. For example in the separation of an N_2/CH_4 mixture over a zeolite, the zeolite will have a higher affinity for N_2 compared to CH_4, as N_2 has a small quadrupole moment that will allow it to have a higher affinity for the charged zeolite surface through its cation. Similarly for an AC that the surface functional groups will play a significant role in the interaction of the activated carbons (ACs) with the adsorbates [52, 53].

1.6 Carbon Capture Technologies

1.6.1 CO_2 Capture by Absorption

The solvents used in CO_2 capture are commonly amine based due to the basic nature of the amine groups reacting with the acidic nature of CO_2 gas. The mechanism of CO_2 capture is via absorption rather than adsorption, as with adsorbent and membrane capture technologies. With respect to CO_2 capture from a power plant, flue gas passes through a column (absorber) containing the solvent (***Figure 1-3***). The pressure in the absorber is generally atmospheric, and typically the working temperatures are in the range 263-353 K depending on both the separation being undertaken and the solvent being used [27]. The CO_2 rich solution then flows into a subsequent column (desorber) where the solvent is regenerated at increased temperatures (up to 393 K), causing the release of the CO_2 from the solution [27]. The mechanism of solvent regeneration is via increasing the temperature of the regenerator column, whilst decreasing the pressure [26]. The most traditional solvent used has been monoethanolamine (MEA) having been used in the chemical industry for over 60 years for CO_2 removal from natural gas [54]. Furthermore, due to its long period of use the mechanisms process issues for solvent based absorption are understood to a greater extent than for other CO_2 capture technologies.

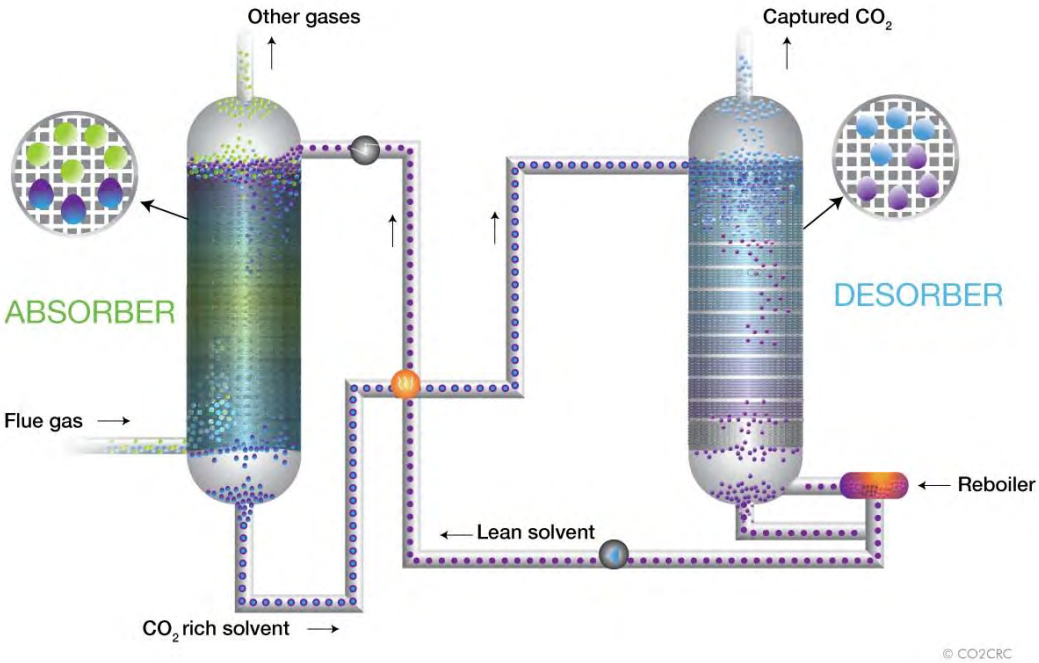

Figure 1-3 *~ Process of CO_2 capture via solvent absorption*

(Reproduced with permission from the CO2CRC Ltd)

Aqueous ammonia has also shown promise in several investigations for separation of CO_2 from flue gas [34, 55-58]. The products of the reaction between CO_2 and ammonia are either ammonium mono- or bicarbonate. The ammonium bicarbonate is the preferred product for the Chinese fertiliser industry [56]. This unique method of fertiliser production was developed in the 1950s by Dr. Dapong He, and uses coal steam gasification as a source of CO_2 [56].

Bai and Yeh (1997) investigated the potential of using ammonia scrubbing, already in place for NO_x removal from flue gas as a potential method for CO_2 removal [57]. For the 28% (w/w) ammonia solution the CO_2 capacity was 0.9 Kg CO_2/g solution, which was well above the upper limit of MEA of 0.36 kg CO_2/kg solution (20% w/w MEA solution) [55, 59, 60].

Li *et al* (2003) investigated the use of aqueous ammonia not for absorption based capture of CO_2, but as a novel method for fertilizer production [61]. Instead of regenerating the ammonia solution, the ammonia bicarbonate precipitate was removed from the ammonia solution. The emphasis of this work was on the solid material obtained, and much less on the CO_2 absorbed. The best result obtained was ~50% capture from the CO_2 in the gas stream [61].

In a subsequent investigation Yeh *et al* (2005) showed that CO_2 absorption using aqueous ammonia of 7, 10.5 and 14% (w/w) resulted in CO_2 capacities (0.40, 0.53 and 0.68 kg CO_2/kg solution) comparable to those of MEA (0.36 kg CO_2/kg solution, 20 vol.% MEA solution [55, 59, 60]). The heat of regeneration for aqueous ammonia has been shown to be 45% that of MEA. However, the heat of formation for aqueous ammonia is much higher than that of MEA, so recovery of the aqueous ammonia vapour is more energy intensive than it is for MEA [55].

However, alkanolamines and ammonia do not only react with the CO_2 is solution, but also other acid gases. It has been shown particularly in the case of MEA that acidic gases (e.g. SO_x) must be kept at levels below 10 ppm, as they form stable salts with the amine solvents [26].

1.6.2 CO_2 Capture by Adsorbents

Unlike absorption based capture by solvents the adsorption based capture of CO_2 by solid adsorbents involves the physical adsorption of CO_2 onto the material. The identification of the most desirable properties for such a material has been the subject of many investigations. These are most commonly considered to be high surface area materials with a high degree of porosity. Material porosity is divided into three classes, on the basis of pore diameter. The guidelines generally accepted worldwide are those of the International Union of Pure and Applied Chemistry (IUPAC). In the IUPAC Compendium of Chemical Terminology [62] the three classes of porous material are microporous (<2 nm), mesoporous (2-50 nm) and macroporous (≥50 nm).

1.6.2.1 Mechanisms of Separation using Adsorbents

The mechanisms involved in adsorbent-based CO_2 capture are usually either temperature or pressure driven, or a combination of these. These are referred to as "swing adsorption" processes, on account of the temperature or pressure swing (abrupt change) which drives the adsorption/desorption of the component of interest from the gas stream. There are other variables that affect the adsorption/desorption of components of a mixed gas, but these are functions of the material itself, such as pore size and structure, as well as diffusion through the material, and are not covered here [42].

1.6.2.1.1 Pressure Swing Adsorption (PSA)

One of the first studies involving PSA as a form of carbon capture for CCS applications was performed by the International Energy Agency (IEA, SR2 report, 1994)[63]. There it was found that pressure swing adsorption (PSA) was not economically viable due to the high costs of gas compression. This report was a major setback to PSA as a potential technology for CCS [42, 63, 64]. As stated one of the main drawback to the economic use of PSA is the cost of gas compression, this is where VSA has shown to be superior to PSA, from a cost perspective [65]. In PSA the gas being compressed is diluted by the components of the gas from which it must be separated [42, 64, 65].

With respect to CO_2 capture either the zeolite 13X [66-73] or activated carbon [66, 74-79] have been the most commonly used adsorbents for PSA. With respect to equilibrium separation (opposed to kinetic), it has been shown that zeolite 13X is a better sorbent than activated carbon for CO_2 sorption [67].

In PSA the adsorption is carried out at greater than atmospheric pressure, the subsequent desorption step is then carried out at atmospheric pressure. The pressure change being the driving force for the separation of the components of the gas. The first and simplest example of the industrial use of a PSA process was invented by Skarstrom in 1960, and later patented by Exxon. This method was aimed primarily at the separation of N_2 from air [80]. A typical PSA cycle for the separation of CO_2 from flue gas consists of four main steps:

1. Pressurization
2. Adsorption
3. Depressurization/Blowdown
4. Desorption/Regeneration/Purge

The PSA process is further outlined in ***Figure 1-4A***. This is however far more advanced than the simple two bed method of Skarstrom, but is commonly used as an example in order to allow clarity of the steps in the PSA process.

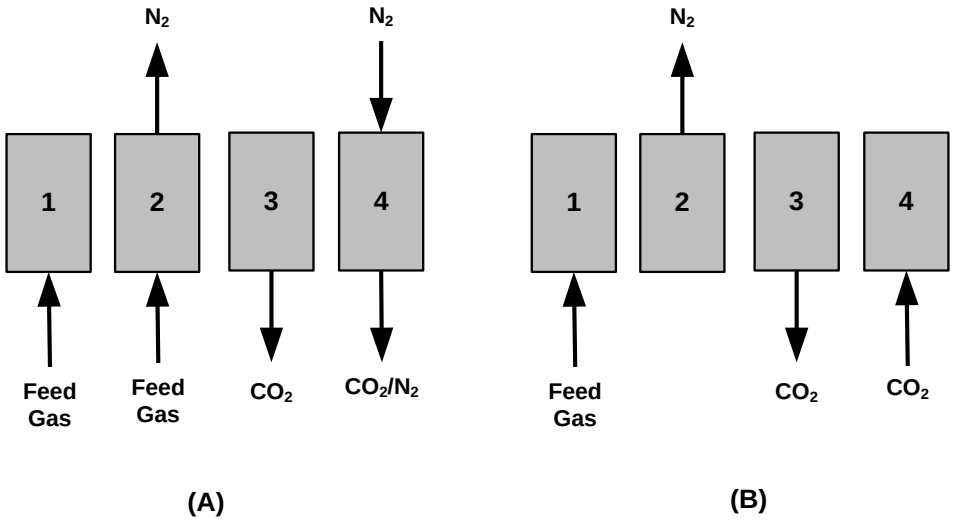

Figure 1-4 ~ *Schematic Representation of the PSA & VSA Processes.* ***(A)*** *PSA Process, (1) Feed gas flows onto column, (2) CO_2 is retained, N_2 product flows through and out of the column, (3) CO_2 product is recovered from the, (4) N_2 purge helps remove remaining CO_2 from column.* ***(B)*** *VSA Process, (1) Flue gas feeds onto the column, (2) N_2 product flows through and out of the column, (3) CO_2 is recovered from the column, (4) Column repressurisation (with CO_2).*

PSA that utilises the sorbent material in the form of packed beds of pellets or beads can suffer from pressure drops across the column and are subject to substantial heat and mass transfer limitations [81, 82]. By using monoliths the pressure drops associated with packed beds can be avoided. In a comparison of gas separation by packed beds and monoliths in a PSA system, Mosca *et al* (2008) compared zeolite 13X loaded onto the surface of a monolith and found the CO_2 capacity was 23 times less than that of the pure 13X beads [81]. Thus in order to equal the capacity of the beads, one would require 67 fold more material to obtain a comparable result, this would easily counteract the economic losses from pressure drop across a packed bed column. One way around this issue proposed by the author was to produce films 67 times thicker, or by making the cycle time 39 fold less [81].

1.6.2.1.2 Vacuum Swing Adsorption (VSA)

Vacuum swing adsorption (VSA) is generally referred to as a subset of PSA. Like PSA, the driving force of separation in VSA is pressure based. The major difference between PSA and VSA is that instead of pressurizing in order to drive the adsorption of the desired compound, adsorption is

carried out at atmospheric pressure or slightly above atmospheric pressure. The desorption of CO_2 is carried out at sub-atmospheric pressures. However in some cases, in order to adsorb the compound of interest the adsorption pressure is increased, such that it is above atmospheric pressure. The VSA process is outlined briefly in ***Figure 1-4B*** along with the PSA process (***Figure 1-4A***). Depending on whether the column is initially pressurized, there are two desorption steps, one down to atmospheric pressure, and another to sub-atmospheric pressure [37, 83, 84]. For CO_2 capture utilizing the VSA process the most commonly used adsorbent material has been zeolite 13X [67, 70, 71, 73, 84-88]. Chou *et al* (2004) undertook CO_2 separation from a CO_2/N_2 mixture (20% CO_2, 80% N_2) using VSA over zeolite 13X, resulting in a CO_2 recovery of 87% and CO_2 purity of 48%, for a 6 step cycle.

Li *et al* (2008) investigated the effect of the presence of water during CO_2 capture via VSA using zeolite 13X. They found that the presence of water greatly inhibited CO_2 adsorption, decreasing the amount of CO_2 captured by 99% [87]. Cyclic VSA experiments were undertaken utilizing the same conditions with dry flue gas, resulting in CO_2 recovery of 78.5% and CO_2 purity of 69%, a substantial improvement on earlier work, such as that by Chou *et al* (2004)[88].

Since the pressure shift in VSA is achieved by evacuation of the column to sub-atmospheric pressure once the unbound gases have passed through the column, the work done is only on the desired product. Therefore, as less work is required in VSA it is more economical to run as compared to PSA, where the work is undertaken on the entire influent gas stream [42].

1.6.2.1.3 Temperature Swing Adsorption (TSA)

Another method of swing adsorption is temperature swing adsorption (TSA, also referred to as thermal swing adsorption). In TSA, the adsorption step is carried out at a particular temperature suitable to the system in question (as low as is possible). In order to desorb the desired compound from the adsorbent, the temperature is increased. The temperature shifts in TSA are controlled by heating the influent gas [42]. Due to its energy intensive requirements, TSA is less likely to be used as a standalone method for CO_2 capture. There have been several investigations into pressure-temperature based swing adsorption methods for CO_2 capture, as well as separation of other gases [83, 89, 90].

Over the last decade an alternate form of TSA has been developed, for which the temperature shifts are controlled by electrical heating of the adsorbent itself, rather than by hot or cold gas [91]. This method adds a further requirement on the adsorbent material, that it must be electrically conductive. For this reason activated carbon is commonly used, as it can act as a semi-conductor [92, 93]. This method of swing adsorption is known as electrical or electrothermal swing adsorption (ESA) [91]. The adsorbent material is fabricated into a

monolith, to which electrodes are attached at either end; usually copper plates are used as an intermediate between monolith and electrodes [91, 94]. Above all, ESA is a more energy efficient and rapid method for heating in comparison to traditional TSA, potentially reducing both cost and cycle time [91].

1.7 Adsorbents for CO_2 Capture

Adsorption based capture of CO_2 by solid adsorbents involves the physical adsorption of CO_2 onto the material. The identification of the most desirable properties for such a material has been the subject of many investigations. These are most commonly considered to be high surface area materials with a high degree of porosity [95].

As the focus of this project is on the preparation of ACs this will be discussed in more detail than zeolites, furthermore the focus will be on the preparation from coal as the main precursor. There are several other classes of adsorbents that show great potential in CO_2 capture, such as hydrotalcites, metal organic frameworks (MOFs) and metal oxide supported materials. A detailed discussion of all prospective adsorbents is beyond the scope of this work, for further information regarding these materials, the reader is referred to the recent reviews by Davidson [36], Choi [35], Samanta [22], Wang [96] or Lee [97].

1.7.1 Zeolites

Zeolites are highly porous crystalline aluminosilicates, for which the repetitive unit is TO_2 (where T is Si or Al) [98]. They belong to the family of materials known as molecular sieves, and are commonly used in gas separation [36]. They are mostly composed of silica, and the presence of alumina causes negative framework charges, as it is in the form of AlO_2 [99]. These negative framework charges are compensated for by exchangeable cations in the pores, rendering the materials highly polar [41, 98]. A number of zeolites are naturally occurring aluminosilicate mineral; however additional types have also been synthesized, allowing them to be tailored for specific purposes [98]. CO_2 adsorption on zeolites is usually a reversible physisorption process, though some chemisorption does take place to a limited degree [36, 98, 100, 101]. The level of CO_2 adsorption is directly related to the level of alumina and thus the level of exchangeable cations present, as well as the degree of porosity within the material [35, 102]. Furthermore the CO_2 capacity of zeolites has been shown to be greatly affected by the type of exchangeable cation present, as well as the type of zeolite [98, 103]. In general zeolites preferentially bind water

over CO_2; as such their use for CO_2 capture from flue gas streams is greatly limited unless water can be removed from the flue gas.

Siriwardane *et al* (2005) investigated CO_2 capture on zeolite 13X at 393 K in the presence of water [85]. For this particular zeolite the presence of water had a significant effect between cycles 1 and 2. Thermal regeneration studies were undertaken, and it was found that complete CO_2 desorption was observed at 393 K, however complete water desorption did not occur until 623 K. Four further cycles were carried out after thermal regeneration at 623 K, in the absence of water and no capacity loss was observed. This led to the conclusion that water selectively adsorbed and preferentially occupied the CO_2 adsorption sites [85].

1.7.2 Activated Carbon (AC)

Activated carbons (ACs) are carbonaceous materials comprised of an interconnected carbon matrix that are derived from a high carbon content parent material. In general ACs have a very high surface area, however the degree to which this is true is highly dependent on the precursor material used. This holds true for all physical properties of activated carbons, as the distribution of carbon in the parent material will reflect the porosity and strength of the resulting carbon matrix formed. The most common parent material for the preparation of ACs is coal. However, ACs can be prepared from many materials. A list of common AC precursors organised into the three main classes based on source:

1. **Coal**
    - Anthracite [104-107]
    - Bituminous Coal [105, 108-113]
    - Lignite [105, 107, 109, 114-120]
2. **Industrial by-products**
    - Polymers/Resins [121-123]
    - Fly Ash [124-127]
    - Pitch [128-133]
    - Used Tires [134, 135]
3. **Biomass**
    - Coconut Shells [136-140]
    - Wood [141, 142]
    - Fruit Stones [107, 143-145]
    - Almond Shells [144, 146, 147]
    - Olive Stones [147, 148]
    - Peat [149, 150]

Any material of high carbon content can be used to prepare ACs; however, as the main factor is general availability and price, coal remains the most popular AC precursor worldwide. For further information on the different AC precursors, the reader is advised to the work of Pollard *et al* [151]. When activated carbons are produced most of the carbonous matter is removed via either carbonization or gasification. Activation is generally classified as one of the following types:

1. Physical Activation
    a. Unassisted Physical Activation (just referred to as "physical activation")
    b. Catalytic Physical Activation
2. Chemical Activation

For physical activation the parent material is carbonised (pyrolysed) under an inert atmosphere, leaving only the carbon matrix in its wake (char). The char is then activated at high temperature (873-1273 K) under a flow of H_2O or CO_2 gas [136, 143, 152-154] (***Table 1-1***).

Table 1-1 *~ Chemical Reactions Occurring During Steam Gasification of Carbon Materials*

Type of Reaction	Reaction	$\Delta H_{298\,K}$ (KJ mol^{-1})
Combustion	$C + O_2 = CO_2$	-394
Partial Oxidation	$C + ½O_2 = CO$	-111
Steam Gasification	$C + H_2O = CO + H_2$	+130
Boudouard	$C + CO_2 = 2CO$	+171
Hydrogasification	$C + 2H_2 = CH_4$	-75
Water-gas Shift	$CO + 2H_2 = CO_2 + H_2$	-40
Methanation	$CO + 3H_2 = CH_4 + H_2O$	-260

In chemical activation, the parent material is impregnated with an activating agent (e.g. KOH, NaOH or $ZnCl_2$) at moderate temperature (293-343 K) and is then carbonised at high temperature (873-1273 K) under an inert gas flow [152, 155, 156]. The resulting AC is then washed (acid followed by water) to remove any residual activating agent. The precise mechanism of chemical activation is a source of some conjecture amongst researchers [155, 156]. However, one of the two most prominent theories claims that the dehydrating action of KOH causes swelling of the coal particles upon wet impregnation, which also inhibits shrinkage

of the coal particles during the initial stages of carbonisation allowing for greater development of the porosity [155]. The second theory, which has gained momentum over the last decade, is that KOH reacts with gaseous CO and CO_2 (produced during carbonisation) to form K_2CO_3 that further reduces to metallic K [155, 157, 158]. As such, KOH acts as an oxygen carrier and promotes gasification. Unlike in physical activation, chemical activation occurs predominantly within the pore structure of the parent material, rather than acting from the outer surface, inwards. The interested reader is referred to a number of reports for further details on other proposed chemical activation mechanisms that are considered outside the scope of this review [152, 155, 156, 159-163].

Regardless of the precise mechanism of chemical activation, two things are widely agreed upon. Firstly, the volatile matter is dehydrogenated by KOH, leading to less tar being produced in the carbonisation step. This occurs because the amount of "pyrolytic decomposition" of heavier components of the volatile matter is reduced, thus allowing them to be carbonised, instead of removed as tar [105, 155]. Secondly, it is widely accepted that the action of KOH is localised to areas between the graphene sheets of the parent carbon [155, 157].

As previously noted the physical properties of an AC are highly dependent on the parent material. As such the type (rank) of coal used must be considered in the production of AC materials. ACs can be readily tailored in particular with regard to the size and structure of their pores. Depending on the parent material and the treatments and processing of the material, both microporous and mesoporous materials can be prepared. However, in the case of ACs derived from coal, reproducibility of structure development can be difficult to achieve. In general ACs have short range, not long range order, making them reasonably amorphous materials. There have been numerous investigations into the preparation of activated carbon molecular sieves (CMSs), with micropore widths (W) ≤ 0.37 nm [137, 164-167]. This point of reference has been chosen by many researchers due to the fact that the molecular diameter of CO_2 is 0.33 nm, whereas CH_4 is 0.38 nm [168]. Therefore such materials (0.37 nm ≤ W ≥ 0.33 nm) would be able to adsorb CO_2 in its micropores preferentially over CH_4 [168].

One of the most important characteristics of ACs that make them better candidate CO_2 adsorbents for post-combustion capture is that ACs are more tolerant to the effects of water than other common adsorbents, such as zeolites and MOFs. However, like in the case of zeolites, water is still preferentially adsorbed over CO_2. The presence of water is a major issue for zeolites and MOFs, since water molecules can competitively adsorb with CO_2 and cause material degradation, respectively [35, 42].

1.7.2.1 Activated Carbons for CO_2 Capture

The adsorption of gases by ACs is controlled by two major characteristics of the AC, namely the pore structure and the surface chemistry [52, 169]. Of these two characteristics, pore structure (particularly pore volume) is historically considered the major controlling factor in gas adsorption, and it is often assumed that gas adsorption on an AC surface is rarely affected by the surface chemistry. As will be shown throughout this project, the surface chemistry can in fact play a major role in gas adsorption. Due to the highly flexible nature of ACs the surface chemistry can easily be tailored to increase the affinity of the AC surface for certain adsorbates. The main functionality on an AC surface that affects the adsorption of polar gases such as CO_2, are the oxygenated or nitrogenated groups. Certain oxygenated moieties such as hydroxyl and carboxylic groups are able to form hydrogen bonds with CO_2 [52]. Whilst others such as anhydrides, carbonyls and ethers interact via weak electrostatic forces [52].

Table 1-2 includes selected literature examples of activated carbons that have been investigated for their CO_2 adsorption properties. For reference, key features/properties of the materials are shown (such as precursor material, preparation conditions, surface area, CO_2 uptake and CO_2 adsorption conditions). From ***Table 1-2*** it is apparent that the synthetic method used to prepare activated carbons for CO_2 capture applications can be classified into four main methods: pyrolysis, gasification, steam activation and chemical activation.

The CO_2 adsorption capacity of activated carbons is generally associated with the surface area and pore size distribution (PSD) of the material, with high surface area materials tending to possess large numbers of small pores and greater CO_2 uptakes [170]. Often, only BET surface areas are quoted (***Table 1-2***). However, ACs are unique in that they have very wide PSDs, which requires the use of more than one adsorbate to probe the surface morphological features. Typically N_2 is used to measure surface area as it is considered to be a "universal" adsorbate. However, the kinetic and steric hindrances of N_2 at its boiling point make it unsuitable for use in determining the surface area of many microporous materials [170]. Instead, CO_2 adsorption at 273 K (usually determined volumetrically) can be used, particularly for carbon materials and coals to determine the surface area and pore volumes [170].

The CO_2 adsorption capacity of activated carbons at temperature of interest for CCS is typically assessed experimentally using thermogravimetric analysis (TGA). This technique relies on measuring changes in the sample mass when it is placed in a CO_2 atmosphere.

Table 1-2 ~ Selected examples of activated carbons used for CO_2 capture

Parent Material	Activation Process	Activating Agent	Activation Temp. (K)	Surface area (m^2/g)	CO_2 uptake (mmol/g)	Adsorption conditions	Ref.
Anthracite	Gasification	H_2O	1073	540	65.7 mg CO_2/g	TGA, 303 K	[171]
Phenolic resin	Gasification	CO_2	1273	308	87.8 mg CO_2/g	TGA, R.T.	[123]
Phenolic resin	Pyrolysis	-	1273	2.40	59.2 mg CO_2/g	TGA, R.T.	[123]
Almond shells	Gasification	CO_2	1073	822	9.7 wt.%	TGA, 298 K	[172]
Olive stones	Gasification	CO_2	1073	1079	10.7 wt.%	TGA, 298 K	[173]
Fly ash	Gasification	H_2O	1323	88	0.4 wt.%	TGA, 348 K	[127]
Lignite and copolymer	Gasification	CO_2	1073	566	3.7 cm^3/g	278 K, 3.8 torr	[174]
Sawdust	Chemical Activation	KOH	873	1260	4.8 mmol/g	TGA, 298 K	[175]
PVDC-methyl acrylate copolymer	Pyrolysis	-	1073	1135	4.2 mmol/g	298 K, 1 atm	[176]
Urea formaldehyde resin	Chemical Activation	K_2CO_3	773	365	8.19 wt.%	298 K, 1 atm	[177]

1.7.3 Amine Modified Adsorbents

It has been found over the course of investigations aimed at improving the CO_2 capacity and selectivity of many adsorbents, that this can be achieved with the use of amine functionalisation [35, 36, 62, 150, 171, 178-195]. Physisorption still occurs on amine functionalized adsorbents to some degree; however CO_2 chemisorption through carbamate and carbonate formation dominates, as shown in ***Figure 1-5***. The mechanism via which this is achieved is the same as that employed for amine-based solvent absorption. The degree of physisorption is dependent on the surface coverage, and thus the amine loading and the non-functionalised surface of the adsorbent free to interact with CO_2.

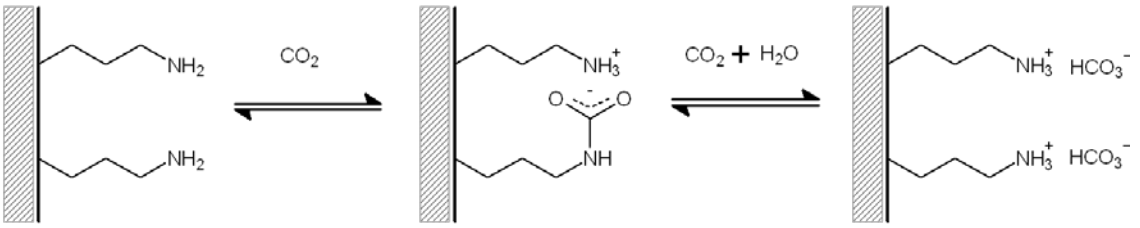

Figure 1-5 *~ Reaction of surface amine groups with CO_2 and H_2O to form surface bicarbonates*

1.7.3.1 Amine Functionalised Silica Adsorbents

Many silica materials have similar structures to those of zeolites, most commonly those zeolites with the lowest alumina content. Therefore like zeolites these materials have been popular due to their flexibility and ability to be easily tailored to a specific purpose [196-198]. The amines used in the functionalisation of silica adsorbents differ greatly from those used on ACs, in that most groups already contain some type of silica functionality. This is however entirely dependent on the method used for functionalisation.

In some of the earliest work on CO_2 capture by amine functionalised silica's, Leal *et al* (1995), showed that the mechanism of capture involved the formation of carbamate species. Furthermore in the presence of water the capacity of the material effectively doubles due to the formation of bicarbonate species (***Figure 1-5***)[199]. This observation was later supported in several other investigations [187, 193].

Knowles *et al* (2005, [190]), investigated the effect that tethering of aminopropyl- and aminoethylaminopropyl- groups to hexagonal mesoporous silica (HMS) would have on its CO_2 capture capacity. There they looked at not only the two different kinds of tethers, but also the tether density on the HMS surface. They found that at high amine loadings that the capture mechanism did indeed switch predominately from physisorption to chemisorption, whereas at low amine loading physisorption was predominate [190].

Recently there has been a shift away from the use of aminopropyl groups for functionalisation, towards the use of alkanolamines, with more complex branching [35, 36, 186, 192, 193, 200]. Over the last decade in particular, a great deal of work has also focussed on the impregnation (as opposed to grafting) of amine rich, branched polymers such as polyethyleneimine (PEI), into the pore structure of mesoporous silicas [192, 194, 201-206].

Son *et al* (2008, [192]) used a range of mesoporous silicas (e.g. MCM-41, MCM-48, SBA-15, SBA-16 and KIT-6) as PEI supports in order to probe the effects that different pore structures had on the CO_2 adsorption properties of the PEI-SiO_2 composites. Comparing the different silicas at 50

wt% PEI loading, Son *et al* found that the highest CO_2 adsorption results were obtained when SBA and KIT type materials with open ended channel pores were used.[192]

Elaborating on the work of Son *et al* [192], Yan *et al* (2011, [206]) investigated the effects that modification of SBA-15 textural properties had on the CO_2 adsorption performance of PEI/SBA-15 materials. By changing the duration of the hydrothermal treatment step during the SBA-15 synthesis, the authors were able to tailor the diameter of the mesopores. It was found that there was a strong relationship between the diameter of the mesopores of the support and the CO_2 adsorption capacity of the PEI impregnated SBA-15 materials; with the CO_2 adsorption capacity increasing with the pore diameter of the support.

Much of the work that has been undertaken on mesoporous silica supported PEI materials has focused on isothermal adsorption studies, which are more applicable to PSA or VSA type separation processes. Drage and co-workers [203] also investigated the use of PEI-SiO_2 composites for CO_2 separation by TSA processes. In this work, Drage highlighted several thermal stability issues associated with these materials (notably the volatility of PEI and it's susceptibility to form urea compounds at high temperatures) which would limit the application of PEI-SiO_2 materials in TSA.[203]

Recently, Knowles *et al* [201] developed a method to pelletise PEI-SiO_2 materials (which is a required format for large scale separation processes). The mesoporous silica used in this study was mesocellular siliceous form (MCF), and was impregnated with PEI at 80, 85 and 90 % on a pore loading basis. Attempts to directly pelletise PEI-MCF were unsuccessful, and resulted in extrusion of the material by the press despite significant post-synthetic treatments under N_2 and vacuum to remove volatile PEI. However, the authors found that carbonation of PEI within the PEI-MCF materials enabled good quality pellets to be produced, that retained much of the CO_2 adsorption capacity of the powdered PEI-MCF.

1.7.3.2 Amine Functionalised Carbon Adsorbents

Table 1-3 summarises selected literature examples of amine modified activated carbons that have been investigated for their CO_2 adsorption properties. For ease of reference, the amine modification strategy, BET surface area and CO_2 uptake and adsorption conditions are listed.

Carbon adsorbents for CO_2 capture have generally been microporous carbons or CMSs. As such the different amine containing compounds that can be incorporated is limited due to the high potential for pore blockage. This has been shown to be a major limiting factor with functionalising microporous carbons [38, 180, 181, 207-213]. This was an extremely important part of the investigation of Pevida *et al* [180]. They showed that the introduction of amine

functionality via two different reactions with ammonia. In both cases substantial reduction in the pore size distribution were observed. These changes were found to be due to the treatment method used [180]. When the treatment was carried out at 1073 K or higher, some of the porosity of the original material was able to be recovered. This was however shown later to be due to partial gasification of the AC itself. Furthermore, for both materials the CO_2 capacity was greatly increased, this being most predominate when the ammonia treatment was carried out at >1073 K [180].

Bimer *et al* (1998), investigated the effect of amine incorporation into the two coal precursors (bituminous coal & lignite, ***Table 1-3***) of activated carbon [214]. The compounds used to introduce amine functionality were ammonia, ammonium carbonate, urea, hydrazine and hydroxylamine. They showed that regardless of the amine used, the level of amine incorporation was directly related to the level of carboxyl groups present in the precursor [214].

Starck *et al* (2006), investigated the effect of demineralization on the incorporation of amine functionality into lignite samples prior to activation (***Table 1-3***)[215]. The surface properties of the demineralised lignite proved to be acidic, compared to the basic surface of the untreated lignites. This was shown to be the case regardless of the demineralization protocol used. More importantly, the basicity introduced via ammoxidation, is much greater once the mineral matter has been removed. Thus it appears that the mineral matter hinders the introduction of nitrogen-groups, due to changes in the nature of the surface groups present, which could react with ammonia.

Plazza *et al* (2007), investigated the effect of incorporating different amino groups (polyethyleneimine (PEI), diethylentriamine (DETA) and pentaethylenehexamine (PEHA)) into a commercial AC [181]. An overall decrease in the micropore volume of all the treated ACs was observed (***Table 1-3***), in turn resulting in a decrease in the CO_2 capture capacity of the materials compared to the non-modified commercial AC (at 293 K).

It is clear from the above works that incorporation of amine functional groups of such size will not work for microporous carbon; however the effects on mesoporous carbon may yield excellent results, and will be a major focus in the second part of this thesis.

Table 1-3 ~ *Selected examples of amine modified carbons for application to CO_2 capture. Parent material (PM), modified material (mod.)*

Precursor material	Modification method (Conditions)	Surface area (m^2/g)	CO_2 uptake (mmol/g)	Adsorption conditions	Ref.
CWZ-35	Direct ammination	1,323 (PM) n.s. (Mod.)	0.06-0.0767 mg CO^2/mg C	309.15 K, 1 bar	[216]
Norit CGP Super	Ammoxidation	1,361 (PM) 964 (Mod.)	6.5 wt% 1.9 wt.%	298 K, 1 bar 373 K, 1 bar	[150]
Norit R2030 CO2	Ammoxidation	942 (PM) 950 (Mod.)	9.2 wt.% 2.7 wt.%	298 K, 1 bar 373 K, 1 bar	[150]
Olive stones	Ammoxidation	43 (PM) 120 (Mod.)	6.8 wt.% 1.9 wt.%	298 K, 1 bar 373 K, 1 bar	[150]
Norit CGP Super	Impregnation (DETA MW 103)	1,762 (PM) 157 (Mod.)	4.0 wt.%	298 K, 1 bar	[181]
Norit CGP Super	Impregnation (PEHA MW 232)	1,762 (PM) 170 (Mod.)	4.8 wt.%	298 K, 1 bar	[181]
Norit CGP Super	Impregnation (PEI MW 423)	1,762 (PM) 90 (Mod.)	4.9 wt.%	298 K, 1 bar	[181]
Soybean	In-situ N from proteins in precursor	811 (Mod.)	41.0 mg/g 22.4 mg/g	303 K, 1 bar 348 K, 1 bar	[184]
Commercial Palm shell	Direct ammination	768 (PM) 858 (400°C) 889 (800°C)	50.0 mg/g 45.0 mg/g 67.0 mg/g	303 K, 1 bar	[217]
Palm shell	Direct ammination	768 (PM) 723 (400°C) 826 (800°C)	50.0 mg/g 62.0 mg/g 73.5 mg/g	303 K, 1 bar	[217]
VulcanXC72R (Cabot)	Grafting (paraphenylenediamine)	221 (PM) 113 (Mod.)	0.34 (PM) 0.24 (Mod.)	313 K, 1 bar	[218]
VulcanXC72R (Cabot)	Grafted (aminobenzylaniline)	221 (PM) 104 (Mod.)	0.34 (PM) 0.24 (Mod.)	313 K, 1 bar	[218]
VulcanXC72R (Cabot)	Grafting (aminoethylaniline)	221 (PM) 102 (Mod.)	0.34 (PM) 0.24 (Mod.)	313 K, 1 bar	[218]
PAN Fibres (MW 250,000)	Inherent Nitrogen	2,366	2.70	323 K, 1 atm	[219]
Carboxyl-rich polymer from glucose and acrylic acid	Grafted (TEPA)	1,109 (PM) 639 (Mod.)	3.2 2.4 1.7	298 K, 1 bar 323 K, 1 bar 348 K, 1 bar	[220]
Olive stones	Direct ammination	n.s. (PM) 390 (Mod.)	3.16. (PM) 5.29 (Mod.)	303 K, 100% CO_2	[221]
Almond shells	Direct ammination	n.s. (PM) 588 (Mod.)	3.10 (PM) 7.10 (Mod.)	303 K, 100% CO_2	[221]
Coal	Impregnation (50 wt.% PEI, MW 423)	1,486 (PM) 37 (Mod.)	135 mg/g (Mod.)	298 K, 100% CO_2, 1 bar	[222]

1.8 Victorian Brown Coal

As has been mentioned brown coal has commonly been used as the parent material for ACs. In particular Victorian brown coal (VBC) has shown to be an excellent parent material, for several reasons. Firstly, VBC has a low ash, nitrogen and sulphur content as compared to other brown coals around the world [223]. The result of which is a cleaner product (and cleaner waste gas) with a low ash content, which is advantageous as a higher yield of the AC can be obtained [223]. Due to the high water content of VBC [224], a great deal of work has been done over the years on dry VBC [225]. As such dry compressed products are easily accessible locally, such as those used in this study[1]. During the drying processes commonly employed, some of the volatile matter is also lost. As will become clear throughout this thesis, the presence of some water and volatile matter in the parent material for AC production is actually a requirement, as controlling its removal during pore development is important in tailoring the pore structure.

Furthermore, the coal-to-overburden ratio is low, making VBC not only readily accessible, but also readily obtainable [226]. In addition to this, the coal industry and ancillary infrastructure (e.g. transport, storage) in Victoria are well established [226], further making this an industrially viable option for the production of large quantities of inexpensive carbon adsorbents.

1.9 Characterisation of Carbon Materials

The characterisation of carbon materials (e.g. coal, char and activated carbons) is notoriously difficult by typical methods of materials characterisation, more specifically spectroscopic techniques. This is primarily due to the excellent ability of carbon materials to act as blackbodies, with respect to the absorption of electro-magnetic waves. This has only been a major issue for investigating the surface chemistry of carbon materials, whereas bulk composition, morphology and structural characterisation are undertaken using typical methods of materials characterisation. Further details regarding the characterisation techniques described below can be found in ***section 6.6*** of ***Chapter 6***.

[1] The EnergyBrix factory at Morwell closed after this project was started

1.9.1 Chemical Composition

Bulk chemical analysis is achievable by methods such as elemental analysis commonly used across the entire spectrum of chemical sciences. Proximate analysis, more commonly used in the coal sciences is also common to the bulk analysis of carbon materials.

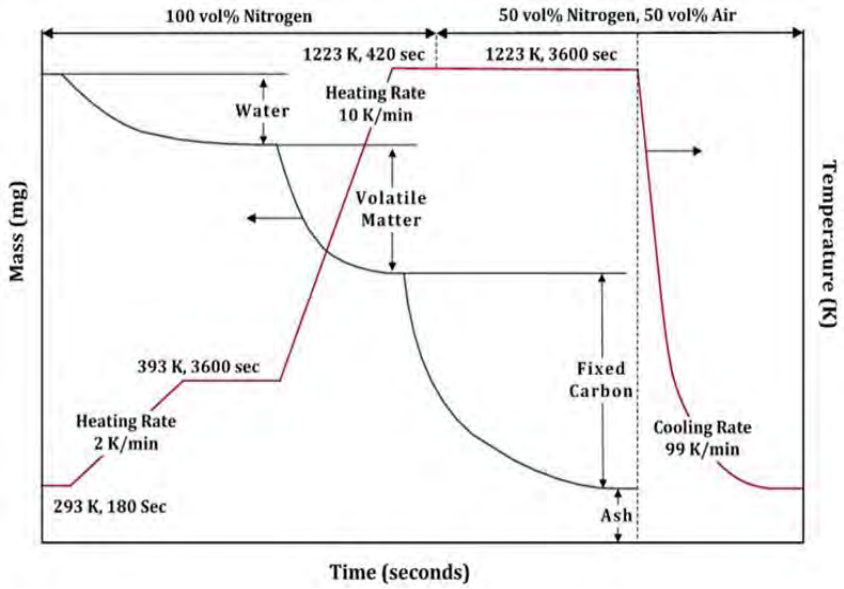

Figure 1-6 ~ *Proximate Analysis via Thermogravimetric Analysis (TGA)*

The analysis of the elemental composition of carbon materials can take on one of two forms, organic or inorganic elemental analysis. Analysis of organic elements in a carbon material is achieved through carbon, hydrogen, nitrogen (CHN) analyser via combustion of the carbon material followed by analysis of the resulting gases, usually via an infrared (IR) detector. Many current instruments are also able to analyse sulphur as well, with oxygen being determined via difference.

The analysis of the inorganic components of a carbon material (if important) is done via the analysis of the ash [227-230]. This usually involved combustion of the large portion of the sample, with the incombustible inorganic remanent being subjects to analysis by x-ray fluorescence (XRF), inductively coupled plasma mass spectrometry (ICP-MS) or a similar technique (i.e. ICP-OES) [231, 232].

The analysis of groups of components in carbon materials such as ash (incombustible inorganics), fixed carbon (non-volatile carbon) and volatile matter by proximate analysis has been in wide use for determining the quality of solid fuels (i.e. coals, bio-mass) [59, 230, 233]. This can be achieved by thermal treatment of the carbon material under different atmospheres

(i.e. N_2 or air), as is outlined in ***Figure 1-6***. This has historically been undertaken using separate furnaces under different atmospheres for the determination of each fraction [233], but it is becoming more common for this to be carried out in a thermogravimetric analyser (TGA) [230, 234]. Furthermore, due to the increased use of CHN analysis; a well developed a rapid automated method of elemental analysis, proximate analysis is being used much less, with only the ash and moisture content being commonly reported along with the elemental composition.

1.9.2 Surface Chemistry

It has only been in more recent years that electron spectroscopy (such as XPS or NEXAFS spectroscopy) has been able to be used to investigate the surface chemistry of carbons. Chemical methods have been more commonly used up until the last decade or so [235-237]. Wet chemical methods such as the Bohem titration method, a potentiometric titration method, that though widely used, had several short-comings. The primary issue with the Bohem titration and similar potentiometric titration methods is in the reproducibility of results that can arise from CO_2 dissolved in the reagents used. This can result in over-estimation of the acid sites on the carbon surface [237, 238]. It has become more common in recent years to use x-ray photoelectron spectroscopy (XPS) or near edge x-ray absorption fine structure (NEXAFS) spectroscopy [215, 239-250].

1.9.2.1 The Photoelectric Effect

The photoelectric effect describes the excitation and ejection of electrons from atoms by electromagnetic waves. The ejection of core electrons leaves holes that must be filled by electrons from higher energy orbital's [251, 252] As this occurs electromagnetic wave of characteristic energy is emitted, both the energy of the ejected electron and the wavelength of the emitted light can be used to determine the chemical state of the atom from which the ejection or emission occurred (***Figure 1-7***). This phenomenon was first discovered by Heinrich Hertz in 1887, but he was unable to fully explain it. Further experimental evidence was obtained by J.J. Thomson on electron ejections from metal plates inside vacuum tubes, from irradiation with ultraviolet light. It was this experimental evidence that Albert Einstein used to develop his theory on the photoelectric effect, which he publish in 1905 and subsequently received the Nobel prize for physics in 1921 [251, 253].

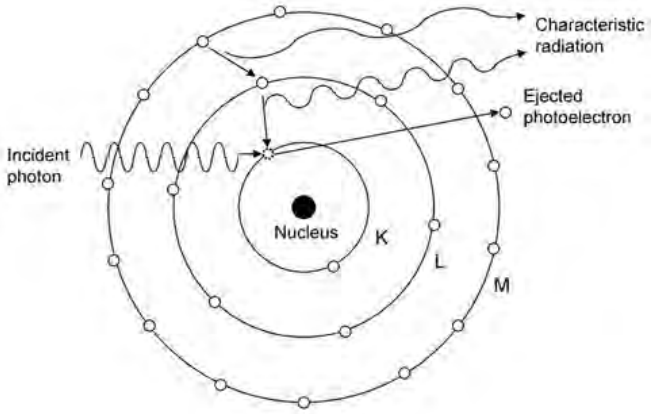

Figure 1-7 ~ *The Photoelectric Effect (modified from [254])*

Einstein's theory predicted that the energy of the ejected electrons increases linearly with the frequency of the incident light used. Even though the initial publication on the photoelectric effect was published in 1905, it was not until 1914 that this was experimentally confirmed by Robert Miliken [251].

1.9.2.2 X-ray Photoelectron Spectroscopy

The premise of x-ray photoelectron spectroscopy (XPS) is based on the photoelectric effect previously discussed. Monochromatic x-rays are produced by bombarding either an aluminium or magnesium anode with a beam of high energy electrons producing Al K_α (λ = 1486.7 nm) or Mg K_α (λ = 1253.0 nm) x-rays, respectively. The resulting x-rays are used to illuminate the sample (***Figure 1-8***), exciting the core shell electrons, ejecting them from the sample. The ejected photoelectrons then travel through to the electron energy analyser (usually hemispherical), being composed of two charged plates used to smooth out the signal of the electrons with different energy, and a channeltron electron multiplier for detection [252, 255]. As electrons can only travel freely in a vacuum, as such the majority of the XPS apparatus is operated under ultra high vacuum conditions (UHV, $\leq 10^{-3}$ torr).

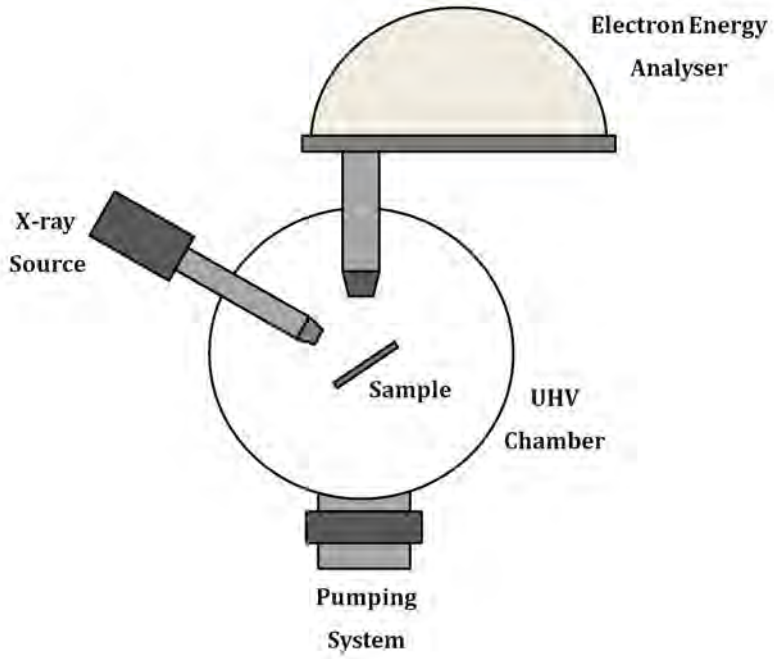

Figure 1-8 ~ *Schematic Diagram of an X-ray Photoelectron Spectrometer*

The use of XPS to characterise the surface of activated carbons has become commonplace over the last decade [239-242, 244, 256, 257]. The XPS spectra are peak fitted against peak positions known from the literature from pure compounds or spectra where well resolved peaks of single functional groups are present [239-242, 244, 256, 257].

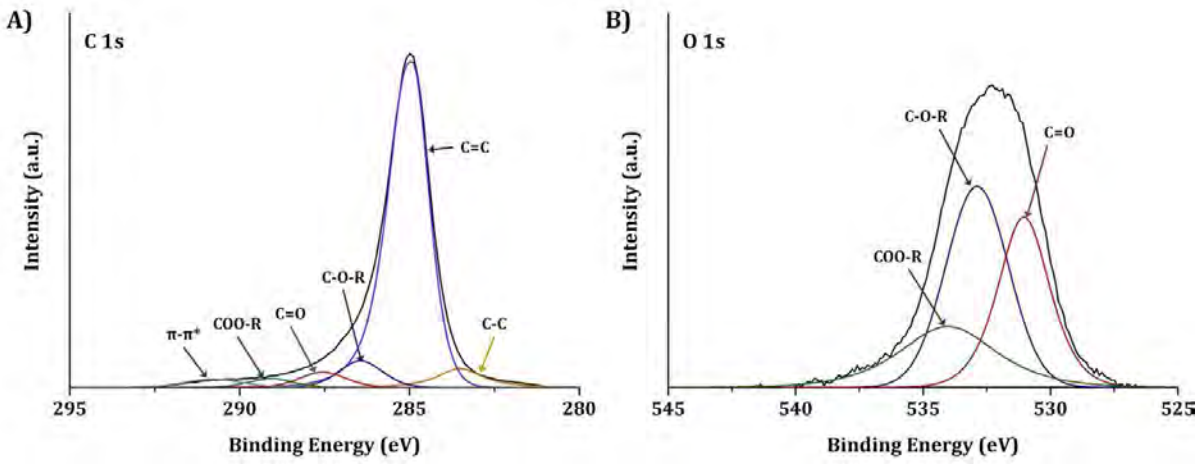

Figure 1-9 ~ *Peak Fitting of C 1s and O 1s XPS Spectra. Shown are* ***A)*** *Peak Fitted C 1s XPS Spectra, and* ***B)*** *Peak Fitted O 1s XPS Spectra*

For carbon materials the identification and quantification of different functional groups can also be achieved via comparison of the high resolution spectra of different elements (***Figure 1-9***)[80, 241, 243, 258-260]

1.9.2.3 Near Edge X-ray Absorption Fine Structure (NEXAFS) Spectroscopy

Near edge x-ray absorption fine structure (NEXAFS) spectroscopy is one of several types of x-ray absorption spectroscopy (XAS), that focuses on the absorption edge, where as extended x-ray absorption fine structure (EXAFS) spectroscopy focuses on the post-edge region (***Figure 1-10A***). Unlike in XPS the wavelength of the incident energy used in NEXAFS spectroscopy (and all XAS) is varied. However, even though the wavelength is varied, the energy is monochromatic. In this way the electrons ejected at each incident wavelength can be studied.

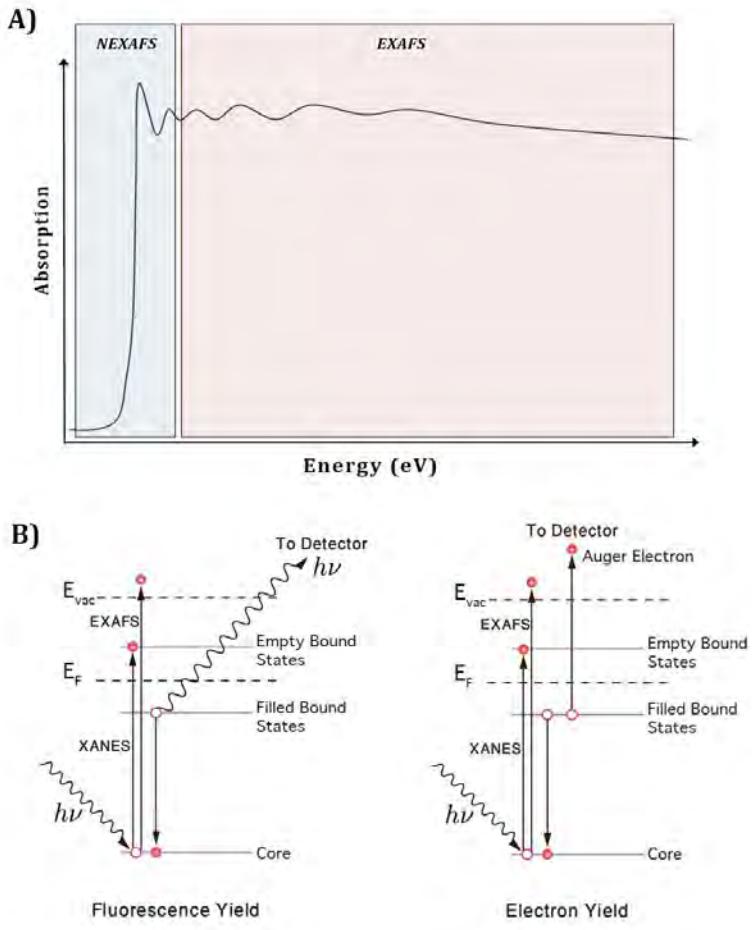

Figure 1-10 *~ X-ray Absorption Spectroscopy (XAS), showing* ***A)*** *The distinction between NEXAFS and EXAFS on the basis of the energy range (modified from [261]), and* ***B)*** *The different electron transition occurring during fluorescence and electron yield measurements [262]*

The apparatus used for NEXAFS spectroscopy is very similar in many respects to that used for XPS, however, the light source used must be much more powerful. As such synchrotron radiation must be used, and it is this part of the apparatus that differs greatly from XPS [252, 263]. The mounting of the sample in NEXAFS spectroscopy is on a gold plate, through which a constant charge of electrons is passed. When electrons are discharged from the sample, the change in electron density due to the emitted electrons can be determined, known as the drain current [263, 264].

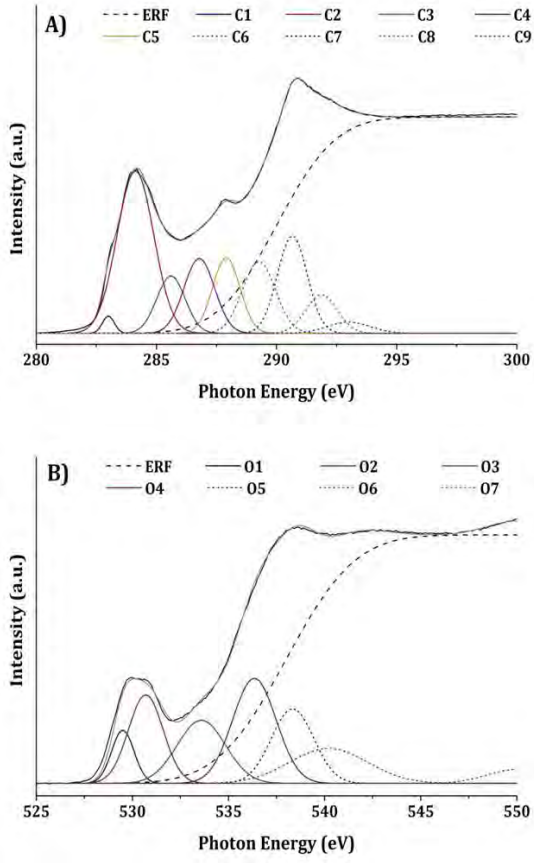

K Edge	Name	Group	Assignment
C 1s	C1	C=O	Carbonyl substituted aromatic carbon (quinone)
	C2	C-C C=C	Aromatic carbon, or substituted aromatic carbon
	C3	C-OH C=O	Phenolic or ketonic carbon
	C4	C-OH COOH COO C=O	Carboxylic acid or lactone carbon
	C5	C-O-C	Cyclic ether carbon
	C6	C-OH C=O	Aldhyde or hydroxyl substituted aliphatic carbon
	C7	C-OH COOH COO C=O	Carboxylic acid or lactone carbon
	C8	C-O-C	Cyclic ether carbon
	C9	C-C C=C	Aromatic carbon (long range order)
O 1s	O1	C=O	Aliphatic (linear or cyclic) aldehyde oxygen
	O2	C=O	Carbonyl oxygen (ketonic or carboxylic acid)
	O3	C-O-C	Aliphatic cyclic ether
	O4	C-OH	Hydroxyl oxygen (alcohol)
	O5	C-OH C=O	Hydroxyl or carbonyl oxygen of carboxylic acid
	O6	C-O-C	Aromatic cyclic ether
	O7	C-OH	Phenolic oxygen

Figure 1-11 *~ Peak Fitting for NEXAFS Spectroscopy. Shown are* ***A)*** *Fitting of Peaks for a C 1s NEXAFS Spectra, and* ***B)*** *Fitting of Peaks for an O 1s NEXAFS spectra*

As can be seen from ***Figure 1-7*** and ***Figure 1-10***, as core electrons are ejected as photoelectrons leave a hole that must be filled by electrons at a higher energy orbital. As the electron from the higher energy orbital has a greater energy than is required by the orbital of the ejected photoelectron, energy must be released. This is done via fluorescence, the wavelength of which will be characteristic of the orbital transition occurring, and thus the nature of the chemical environment of the atom in question. As such, this emitted light can be used to gain further information about the atoms under investigation (***Figure 1-10B***). Unlike XPS, NEXAFS

spectroscopy is semi-quantifiable at best, and is generally used in conjunction with XPS to further identify functional groups already identified and quantified by XPS.

The peak fitting of a NEXAFS spectra is done against the peak positions of known compounds from the literature [245, 246, 248-250, 265-271]. The absorption edge possesses an edge step, which is the energy jump between the pre- and post-edge, as is also been observed in the survey spectra in XPS (***Figure 1-11***). The absorption edge data for the element of interest must first be processed prior to any fitting procedure, which is done using an inverse tangent or an error function (***section 6.6.2.2***).

1.9.3 Structural Characterisation

The long and short range structure of a material have great bearing on the adsorption properties the material will possess. For example the size, shape and interconnectivity of the mesopores within each particle of a material will have a significant effect on the rate with which mass-transport through particles of the material can occur, whilst the overall surface area that each particle possesses, will affect its overall capacity. A wide range of characterisation techniques exist in order to achieve full characterisation of these aspects of a material, the most important and widely used is gas physisorption. However, finer structural features can be determined using electron microscopy and the diffraction or scattering of electromagnetic waves (Raman spectroscopy and x-ray diffraction).

1.9.3.1 Chemical Structure of Carbons

1.9.3.1.1 Raman Spectroscopy

Raman spectroscopy is a type of vibrational spectroscopy based on Raman scattering. The Raman scattering phenomena discovered in 1928 by Sir Chandrasekhara Venkata Raman [251]. For this discovery Raman received the 1930 Nobel Prize for physics. ***Figure 1-12*** outlines the mechanisms involved in both infrared (IR) and Raman spectroscopies.

From ***Figure 1-12A*** it can be seen that in IR spectroscopy that some of the incident light has been absorbed. The incident light in an IR spectrometer is actually monochromatic, but the wavelength is varied (scanning) over the range of wavelengths of interest using an interferometer. Conversely, in Raman spectroscopy (***Figure 1-12B***) no absorption of light occurs, but it is instead scattered. The light used in Raman spectroscopy is in the form of a laser of monochromatic light and it is the frequency that changes as the light interacts with the molecular bonds of the sample [251, 252, 255].

In the case of using Raman spectroscopy as a means to characterise activated carbons, it is necessary to deconvolute the resultant Raman spectra, relative to known peaks from previous investigations (***Table 1-4*** and ***Figure 1-13***) [272-277]. The focus of the deconvolution is on the so-called "**G**" and "**D**" bands of peaks, standing for graphitic and diamond, respectively. The **D** band is a band of peaks resulting from scattering of photons by disordered graphitic lattices, that is to say the scattering of photons is done by interactions with the bonds of the graphene layer edges of disordered carbons (**S**, **D** and **A** peaks). The **G** band peaks arise from the scattering of photons by the bonds of the graphene layer edges of highly ordered carbon (**G** peak).

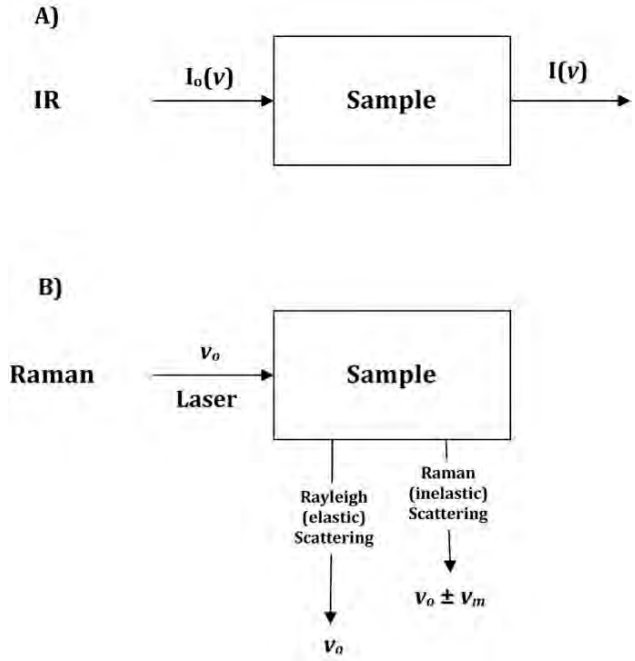

Figure 1-12 *~ Infrared (IR) vs Raman. Shown are the mechanism for* ***A)*** *Infrared spectroscopy. Where I_o is the intensity of the incident electromagnetic waves and I is the intensity of the electromagnetic waves minus those absorbed by the sample, and* ***B)*** *Raman spectroscopy. Where V_o is the frequency of the laser and the Rayleigh (elastically) scattered electromagnetic waves, V_m is the vibrational frequency of the molecule under investigation.*

Table 1-4 *~ Raman Peak Assignment Table*

Peak Name	Peak Assignment	Raman Shift (cm^{-1})
S	Disordered Graphitic Lattice*	1150-1250
D	Disordered Graphitic Lattice†	1275-1350
A	Amorphous Carbon	1475-1525
G	Ideal Graphitic Lattice	1575-1625

* *Hetro-atoms Bond to Graphene Layer Edges*

† *Graphene Layer Edges*

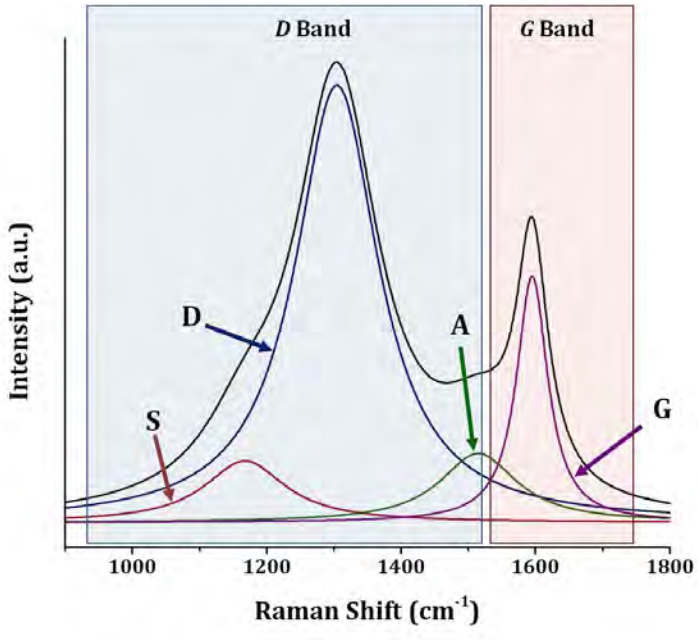

Figure 1-13 *~ Example of Peak Fitting and Assignments for Raman Spectra of Activated Carbons*

1.9.3.1.2 X-ray Diffraction (XRD)

The diffraction of x-rays by a solid material as a means of identifying the crystalline phases from the lattice parameters as well as the particle (crystallite) size. The diffraction of x-rays occurs via elastic scattering and can be described mathematically according to Bragg's Law (***Figure 1-14A***) [255]. The diffraction pattern is produced by constructive interference of the scattered x-rays, resulting in a pattern of "lines". The diffraction pattern produced in reality is not actually composed of well defined lines, but instead peaks. In powder XRD (PXRD) this is due in part to the effects of interparticulate distances varying. Moreover, the degree of line/peak broadening

is greatly affected by the degree of crystallinity, being sharper for more crystalline phases and broadens for more amorphous phases.

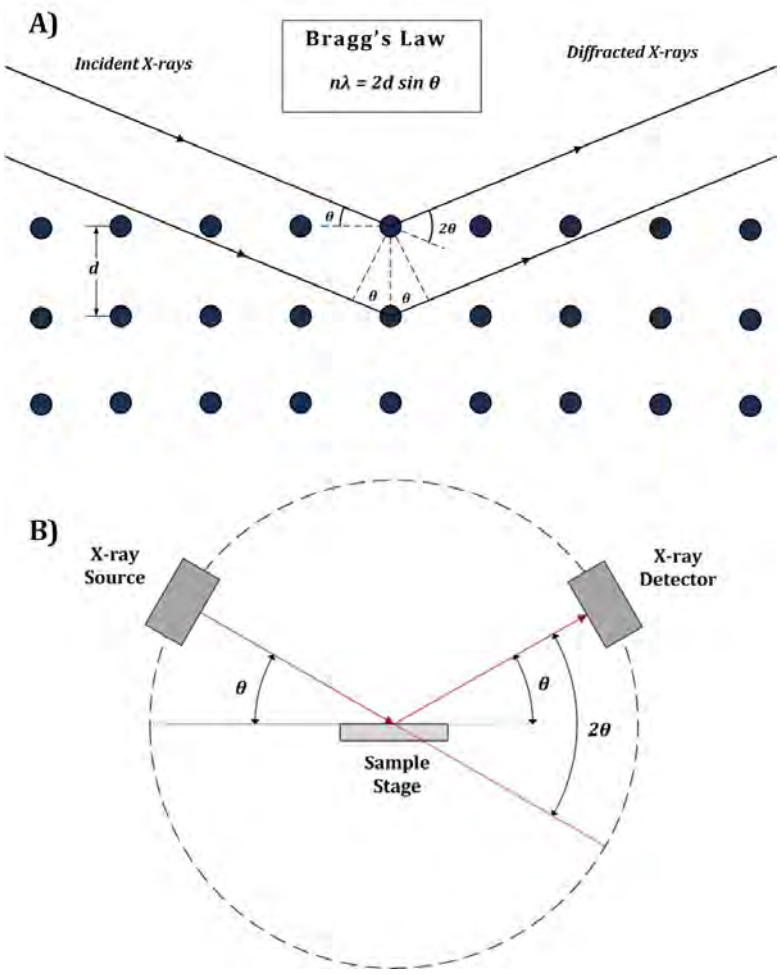

Figure 1-14 *~ The Process of Powder X-ray Diffraction (modified from [278]). Shown are* ***A)*** *The XRD process as it occurs at the atomic level and how Bragg's Law is derived from this process. Where λ is the wavelength of the x-rays, d is the distance between lattice planes, θ is the angle of diffraction normal to the lattice plane, and n is an integer known as the order of the reflection; and* ***B)*** *Schematic diagram of a typical x-ray diffractometer.*

For amorphous carbons such as those produced throughout this work, only 2 very broad peaks were generally observed. These two peaks are the reflection in the **002** plane, resulting in a peak observed at 24° 2θ, and a reflection in the **100/101** plane giving rise to the peak at 43° 2θ [279, 280]. Furthermore, for many AC a peak is observed around 26° 2θ, that is attributed to amorphous metal oxides (**MO**) from ash (e.g. SiO_2, K_2O, Na_2O or Al_2O_3) [279]. Amorphous carbons produced from parent carbons such as brown coal (a non-graphatisable coal) rarely

possess sharp graphitic peaks. In order to produce an amorphous carbon with a significant amount of graphitic carbon would require carbonisation temperatures upwards of 1400 K.

1.9.3.2 Physical Structure of Carbons

1.9.3.2.1 Gas physisorption

A great deal of information can be determined from the shape of an adsorption isotherm and the type and shape (if any) of the hysteresis loop, such as pore shape and structure. The most prominent interpretation of adsorption isotherms were publish by Sing *et al* (1985) [281] (***Figure 1-15***), still commonly referred to, to this day.

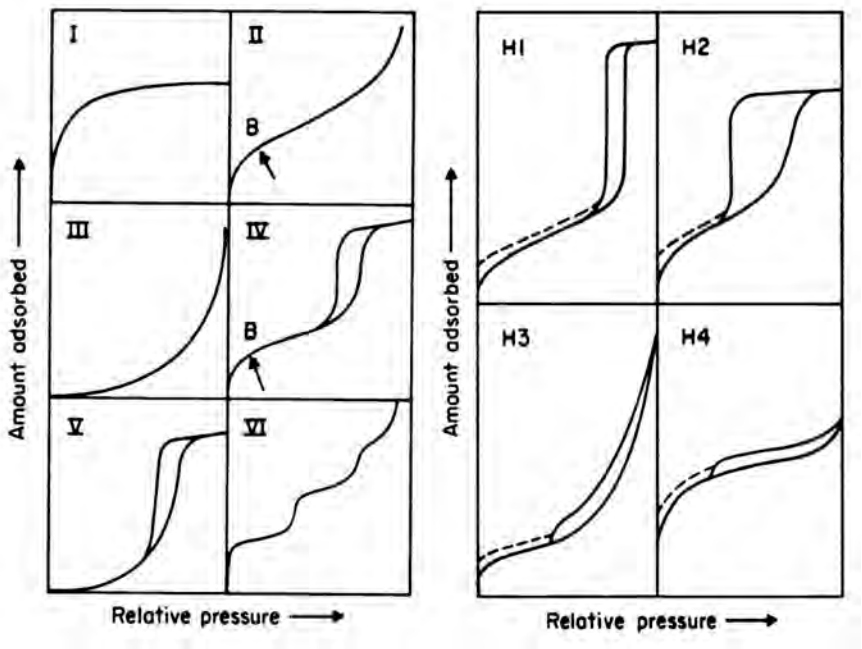

Figure 1-15 ~ *Gas Adsorption Isotherms and Hysteresis Types (Modified from Sing et al, 1985 [281])*

Regarding carbon materials, the type of isotherm produced will depend greatly on the adsorbate used. For instance, the use of CO_2 at either 195 or 273 K will result in a ***type I*** isotherm (***Figure 1-15***), assuming the adsorbent possesses micropores. This occurs as with CO_2 only a monolayer can be formed, as no pore condensation can occur due to the fact that CO_2 is a non-condensable adsorbate [42, 170, 282]. Conversely if N_2 or Ar are used as the adsorbate at temperature close to their boiling point (usually 77 or 87 K), condensation of the gas into the liquid form can occur. When gas condensation into a liquid occurs in pores a very different type

of adsorption behaviour is observed [42, 170, 282]. For instance, upon desorption hysteresis (***type H1-4***, ***Figure 1-15***) will occur in materials that possess mesopores (***type IV*** and ***V***, ***Figure 1-15***). In materials that possess no micropores or micropores too small to allow certain adsorbates access, no micropore region can be observed (***type III*** and ***V***, ***Figure 1-15***) [282, 283].

As carbon materials commonly possess a wide distribution of pore sizes (referred to as a pore size distribution, PSD), the use of more than one type of adsorbate is ideally required to produce a full picture of the pore morphology of the material. Physisorption of CO_2 at 273 K and N_2 at 77 K are the most commonly applied, although Ar physisorption at 77 K or 87 K has also become relatively commonplace [284]. One of the advantages to using Ar physisorption at 87 K is that, Ar is a monatomic gas and possesses a smaller cross-sectional area (14.2 $Å_2$) than N_2 (16.2 $Å_2$), which enables higher resolution of the pore structure. The use of CO_2 is confined to the investigation of the micropore structure, as it is a non-condensable gas and, as such, only forms a monolayer: this only allows for information of the micropores to be obtained. Furthermore, due to the higher temperature of the analysis, the CO_2 can more easily access the innermost pore structure of micropores, which N_2 (at 77K) is incapable of doing for extremely small micropores. N_2 is able to be condensed into a liquid within the pores unlike CO_2 and so is well suited for investigating the structure and volume of mesopores. Although Ar physisorption is preferred to N_2 physisorption the expense of using Ar gas for such experiments makes it unsuitable for wide-scale use.".

By applying one of the many commonly used equations to describe these phenomena, such as the BET [43] or BJH theories [284], important values such as the surface area, micro- or mesopore volume can be determined, which is elaborated on in greater detail in ***section 6.6.3.2.1***.

1.9.3.2.2 Electron Microscopy

Electron microscopy involves the use of electrons instead of photons in order to create an image of the fine structures of incredible small objects. This is possible due in large part to the work on wave-particle duality by Louise de Broglie, for which he received the 1929 Nobel prize in physics [251]. From the theory on wave-particle duality it is possible to treat electrons as waves, possessing wavelengths dependant on their velocity. As such in electron microscopy a beam of high velocity electrons, possessing the same velocity can be used to create a beam of electrons that are essentially monochromatic with respect to their wavelength, for example electrons with energy of 100 keV having a wavelength less than 1 Å. With electrons of such

small wavelengths, structure at the nano, molecular and even atomic scale is able to be resolved [251, 255].

Unlike in conventional optical microscopy, electron microscopes do not possess tangible optical lenses, but instead utilise magnetic and electric fields to focus and direct the electron beam onto the sample, referred to as the primary electron beam. There are many ways in which the primary electron beam can interact with the sample as outlined in ***Figure 1-16A***, giving rise to several types of electron microscopy and detection [255].

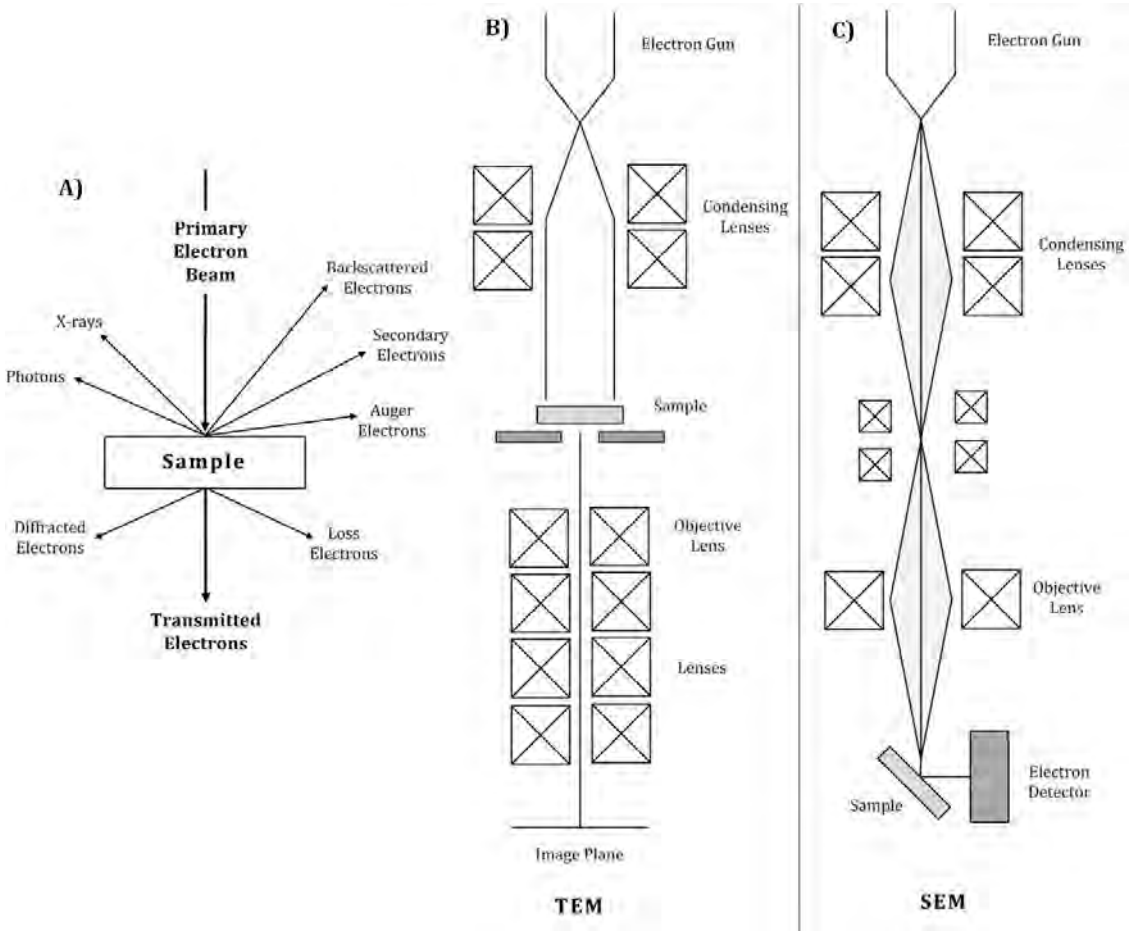

Figure 1-16 ~ *Electron Microscopy and its Underlying Principles (Modified from [255]). Shown are* ***A)*** *The Interaction of Electrons with Matter,* ***B)*** *Diagram of a TEM Instrument, and* ***C)*** *Diagram of an SEM Instrument*

In the case of transmission electron microscopy (TEM) (***Figure 1-16B***) it is the transmitted electrons and x-rays that arise from interaction of the primary electron beam with the sample that are used to produce a 2D image of the sample. The transmitted electrons pass through the sample and are detected by a fluorescent screen, producing what is known as the bright field image. Conversely the backscattered and primary electrons are used to produce what is known

as the dark field image. Conversely in scanning electron microscopy (SEM) it is the back scattered electrons that are used to produce an image, as outlined in ***Figure 1-16C***.

The use of TEM to characterise carbon materials allows a great deal of structural detail to be obtained, especially regarding the alignment of the graphene layer edges as well as other structural features. Elemental mapping is also possible through the use of energy dispersive x-ray (EDX) spectroscopy, which is of great use in characterising carbon materials.

1.10 Project Outline and Perspective

As has already been stated, a major hurdle for the implementation of adsorbent-based CO_2 capture is reduction in the adsorbent cost. With this in mind, the use of VBC has been investigated in this thesis as a means by which to produced inexpensive carbon adsorbents and supports. In particular, this project aimed to use Victorian brown coal:

1. To produce carbon adsorbents that are predominately microporous

2. To produce carbon adsorbents that are predominately mesoporous

3. To modify those carbons that possess suitable pore structure with basic nitrogen functionality in order to increase both the CO_2 capacity and selectivity

As such the structure of this thesis is broken down into two major parts, one focussing on microporous carbon adsorbents, while the second part focuses on mesoporous and amine modified carbon adsorbents. The section on microporous carbons is split into two chapters, one on the synthesis and characterisation of these materials (***Chapter* 2**), and the other on the gas separation properties of them (***Chapter* 3**). Similarly the section on mesoporous and amine modified carbons is split into a synthesis and characterisation chapter (***Chapter 4***) and a gas separation chapter (***Chapter* 5**). ***Chapter 6*** contains the full experimental details concerning the preparation of chars, activated carbons and amine modified materials for CO_2 capture, as well as the analytical protocols used throughout the project. The final chapter, (***Chapter 7***) draws the conclusions of the research and suggests potential avenues for future research.

1.11 References

1. Monastersky, R., *Global carbon dioxide levels near worrisome milestone.* Nature, 2013. **497**(7447): p. 13-14.
2. Fourier, J.-B.J., *On the Temperatures of the Terrestrial Sphere and Interplanetary Space.* M´emoires d l'Acad´emie Royale des Sciences de l'Institute de France, 1827. **II**: p. 570-604.
3. Tyndall, J., *"On the Adsorption and Radiation of Heat by Gases and Vapours, and on the Physical Connexion of Radiation, Adsorption and Conduction".* Royal Irish Academy, 1861.
4. Arrhenius, S., *On the Influence of Carbonic Acid in the Air upon the Temperature of the Ground.* Philosophical Magazine and Journal of Science, 1896. **41**(5): p. 237-276.
5. Ruddiman, W.F. and A. McIntyre, *Time-transgressive deglacial retreat of polar waters from the North Atlantic.* Quaternary Research, 1973. **3**(1): p. 117-130.
6. Idso, S.B., *Climatic effects of increased industrial activity upon the world's established agro-ecosystems.* Agro-Ecosystems, 1974. **1**(C): p. 7-17.
7. Broecker, W.S., *Climatic change: Are we on the brink of a pronounced global warming?* Science, 1975. **189**(4201): p. 460-463.
8. Kellogg, W.W. and S.H. Schneider, *Global air pollution and climate change.* IEEE TRANS. GEOSCI. ELECTRON., 1978. **GE-16**(1): p. 44-50.
9. Wigley, T.M.L., P.D. Jones, and P.M. Kelly, *Scenario for a warm, high- CO2 world.* Nature, 1979. **282**(5742): p. 17-21.
10. Wigley, T.M.L., P.D. Jones, and P.M. Kelly, *Global warming?* Nature, 1981. **291**(5813): p. 285.
11. Etkins, R. and E.S. Epstein, *The rise of global mean sea level as an indication of climate change.* Science, 1982. **215**(4530): p. 287-289.
12. Raper, S.C.B., et al., *Recent temperature changes in the Arctic and Antarctic.* Nature, 1983. **306**(5942): p. 458-459.
13. Peters, R.L. and J.D.S. Darling, *The greenhouse effect and nature reserves. Global warming would diminish biological diversity by causing extinctions among reserve species.* BioScience, 1985. **35**(11): p. 707-717.
14. Wigley, T.M.L. and M.E. Schlesinger, *Analytical solution for the effect of increasing CO2 on global mean temperature.* Nature, 1985. **315**(6021): p. 649-652.
15. Turkenburg, W.C., *Sustainable development, climate change, and carbon dioxide removal (CDR).* Energy Conversion and Management, 1997. **38**(SUPPL. 1).
16. Lickrastina, A., et al., *Gasification of pelletized renewable fuel for clean energy production.* Fuel, 2011. **90**(11): p. 3352-3358.
17. Halim, R., M.K. Danquah, and P.A. Webley, *Extraction of oil from microalgae for biodiesel production: A review.* Biotechnology Advances, 2012. **30**(3): p. 709-732.
18. Bridgwater, A.V., *Review of fast pyrolysis of biomass and product upgrading.* Biomass and Bioenergy, 2012. **38**(0): p. 68-94.
19. Harkin, T., A. Hoadley, and B. Hooper, *Optimisation of power stations with carbon capture plants – the trade-off between costs and net power.* Journal of Cleaner Production, 2012. **34**(0): p. 98-109.
20. Chakma, A., *CO_2 capture processes - Opportunities for improved energy efficiencies.* Energy Conversion and Management, 1997. **38**(Supplement 1): p. S51-S56.
21. Harkin, T., A. Hoadley, and B. Hooper, *Process integration analysis of a brown coal-fired power station with CO2 capture and storage and lignite drying.* Energy Procedia, 2009. **1**(1): p. 3817-3825.
22. Samanta, A., et al., *Post-Combustion CO2 Capture Using Solid Sorbents: A Review.* Industrial & Engineering Chemistry Research, 2011. **51**(4): p. 1438-1463.
23. Yang, H., et al., *Progress in carbon dioxide separation and capture: A review.* Journal of Environmental Sciences, 2008. **20**(1): p. 14-27.

24. Cottrell, A.J., et al. *Post-combustion capture R&D and pilot plant operation in Australia*. 2009. Washington DC.
25. Stangeland, A., *A model for the CO_2 capture potential.* International Journal of Greenhouse Gas Control, 2007. **1**(4): p. 418-429.
26. Gibbins, J. and H. Chalmers, *Carbon capture and storage.* Energy Policy, 2008. **36**(12): p. 4317-4322.
27. Kerr, T., *CO_2 Capture and Storage - A Key Carbon Abatement Option*, T. Kerr, Editor 2008, IEA: Paris.
28. Shukla, R., et al., *A review of studies on CO_2 sequestration and caprock integrity.* Fuel, 2010. **89**(10): p. 2651-2664.
29. Meisen, A. and X. Shuai, *Research and development issues in CO_2 capture.* Energy Conversion and Management, 1997. **38**(Supplement 1): p. S37-S42.
30. Erga, O., O. Juliussen, and H. Lidal, *Carbon dioxide recovery by means of aqueous amines.* Energy Conversion and Management, 1995. **36**(6-9): p. 387-392.
31. Hatch Jr, T.F. and R.L. Pigford, *Simultaneous absorption of carbon dioxide and ammonia in water.* Industrial and Engineering Chemistry Fundamentals, 1962. **1**(3): p. 209-214.
32. Shen, K.P. and M.H. Li, *Solubility of carbon dioxide in aqueous mixtures of monoethanolamine with methyldiethanolamine.* Journal of Chemical and Engineering Data, 1992. **37**(1): p. 96-100.
33. Yeh, J.T., H.W. Pennline, and K.P. Resnik, *Study of CO_2 absorption and desorption in a packed column.* Energy and Fuels, 2001. **15**(2): p. 274-278.
34. Jilvero, H., et al., *The Rate of CO2 Absorption in Ammonia—Implications on Absorber Design.* Industrial & Engineering Chemistry Research, 2014. **53**(16): p. 6750-6758.
35. Choi, S., J.H. Drese, and C.W. Jones, *Adsorbent materials for carbon dioxide capture from large anthropogenic point sources.* ChemSusChem, 2009. **2**(9): p. 796-854.
36. Davidson, R.M., *Post-Combustion Carbon Capture - Solid Sorbents and Membranes*, 2009, IEA Clean Coal Centre: Cheltenham, UK.
37. Krishnamurthy, S., et al., *CO2 capture from dry flue gas by vacuum swing adsorption: A pilot plant study.* AIChE Journal, 2014. **60**(5): p. 1830-1842.
38. Chew, T.-L., A.L. Ahmad, and S. Bhatia, *Ordered mesoporous silica (OMS) as an adsorbent and membrane for separation of carbon dioxide (CO2).* Advances in Colloid and Interface Science, 2010. **153**(1-2): p. 43-57.
39. Dabrowski, A., *Adsorption - From theory to practice.* Advances in Colloid and Interface Science, 2001. **93**(1-3): p. 135-224.
40. Larsen, J.W., *Sorption of Carbon Dioxide by Coals.* ACS Division of Fuel Chemistry, Preprints, 2003. **48**(1): p. 112-113.
41. Thomas, W.J. and B. Crittenden, *Adsorbents*, in *Adsorption Technology & Design*1998, Butterworth-Heinemann: Oxford. p. 8-30.
42. Yang, R.T., *Gas Separation by Adsorption Processes*. 2nd ed. Series on Chemical Engineering, ed. R.T. Yang. Vol. 1. 1987, London: Imperial Collage Press.
43. Brunauer, S., P.H. Emmett, and E. Teller, *Adsorption of gases in multimolecular layers.* Journal of the American Chemical Society, 1938. **60**(2): p. 309-319.
44. Gibbs, J.W., *On the equilibrium of heterogeneous substances* American Journal of Science, 1878. **16**: p. 441-458.
45. Moore, W.J., *Physical Chemistry*. 4th ed1963, London: Longmans Green and Co LTD.
46. Do, D.D., *Adsorption Analysis: Equilibria and Kinetics*. Series on Chemical Engineering. Vol. 2. 2008, London: Imperial College Press. p.17.
47. Yang, R.T., *Gas Separation by Adsorption Processes*, in *Series on Chemical Engineering*, R.T. Yang, Editor 1987, Imperial Collage Press: London. p. 26.
48. Ruthven, D.M., *Principles of Adsorption and Adsorption Processes*, D.M. Ruthven, Editor 1984, John Wiley and Sons: New Jersey. p. 29.
49. Bansal, R.C. and M. Goyle, *Activated Carbon Adsorption*, 2005, Taylor & Francis Group: Florida. p. 68.

50. Yang, R.T., *Adsorbents: Fundamentals and Applications*, R.T. Yang, Editor 2003, John Wiley & Sons: New Jersey. p. 3.
51. Ruthven, D.M., *Principles of Adsorption and Adsorption Processes*, D.M. Ruthven, Editor 1984, John Wiley and Sons: New Jersey. p. 3.
52. Yang, R.T., *Adsorbents: Fundamentals and Applications*, R.T. Yang, Editor 2003, John Wiley & Sons: New Jersey. p. 79-130.
53. Bansal, R.C. and M. Goyle, *Activated Carbon Adsorption*, 2005, Taylor & Francis Group: Florida. p. 8.
54. Anderson, S. and R. Newell, 2004. p. 109-142.
55. Crowley, T.J., *Causes of climate change over the past 1000 years.* Science, 2000. **289**(5477): p. 270-277.
56. Vitha, M. and P.W. Carr, *The chemical interpretation and practice of linear solvation energy relationships in chromatography.* Journal of Chromatography A, 2006. **1126**(1-2): p. 143-194.
57. Khan, M.R., *Significance of char active surface area for appraising the reactivity of low- and high-temperature chars.* Fuel, 1987. **66**(12): p. 1626-1634.
58. Shakerian, F., et al., *A comparative review between amines and ammonia as sorptive media for post-combustion CO2 capture.* Applied Energy, 2015. **148**(0): p. 10-22.
59. Karatepe, N. and S. Küçükbayrak, *Proximate analysis of some Turkish lignites by thermogravimetry.* Thermochimica Acta, 1993. **213**: p. 147-150.
60. Rodriguez, N.M. and H. Marsh, *Structure of coals studied by iodine and water adsorption.* Fuel, 1987. **66**(12): p. 1727-1732.
61. Li, X., et al., *Removal of carbon dioxide from flue gas by ammonia carbonation in the gas phase.* Energy and Fuels, 2003. **17**(1): p. 69-74.
62. Dantas, T.L.P., et al., *Adsorption of carbon dioxide onto activated carbon and nitrogen-enriched activated carbon: Surface changes, equilibrium, and modeling of fixed-bed adsorption.* Separation Science and Technology, 2010. **45**(1): p. 73-84.
63. Reiner, P., H. Audus, and A.R. Smith, *Carbon Dioxide Capture from Fossil Fuel Power Plants*, in *Report SR2*1994, IEA Greenhouse Gas R&D Programme: Cheltenham, U.K.
64. Ho, M.T., G.W. Allinson, and D.E. Wiley, *Reducing the cost of CO_2 capture from flue gases using pressure swing adsorption.* Industrial and Engineering Chemistry Research, 2008. **47**(14): p. 4883-4890.
65. Radosz, M., et al., *Flue-gas carbon capture on carbonaceous sorbents: Toward a low-cost multifunctional carbon filter for "green" energy producers.* Industrial and Engineering Chemistry Research, 2008. **47**(10): p. 3783-3794.
66. Lee, J.S., et al., *Adsorption equilibria of CO_2 on zeolite 13X and zeolite X/activated carbon composite.* Journal of Chemical and Engineering Data, 2002. **47**(5): p. 1237-1242.
67. Chue, K.T., et al., *Comparison of activated carbon and zeolite 13X for CO_2 recovery from flue gas by pressure swing adsorption.* Industrial and Engineering Chemistry Research, 1995. **34**(2): p. 591-598.
68. Diagne, D., M. Goto, and T. Hirose, *Parametric studies on CO2 separation and recovery by a dual reflux PSA process consisting of both rectifying and stripping sections.* Industrial and Engineering Chemistry Research, 1995. **34**(9): p. 3083-3089.
69. Ko, D., R. Siriwardane, and L.T. Biegler, *Optimization of a pressure-swing adsorption process using zeolite 13X for CO_2 sequestration.* Industrial and Engineering Chemistry Research, 2003. **42**(2): p. 339-348.
70. Harlick, P.J.E. and F.H. Tezel, *An experimental adsorbent screening study for CO_2 removal from N_2.* Microporous and Mesoporous Materials, 2004. **76**(1-3): p. 71-79.
71. Choi, W.K., et al., *Optimal Operation of the Pressure Swing Adsorption (PSA) Process for CO_2 Recovery.* Korean Journal of Chemical Engineering, 2003. **20**(4): p. 617-623.
72. Zhang, J., R. Singh, and P.A. Webley, *Alkali and alkaline-earth cation exchanged chabazite zeolites for adsorption based CO_2 capture.* Microporous and Mesoporous Materials, 2008. **111**(1-3): p. 478-487.

73. Hu, X., et al., *Diffusion mechanism of CO2 in 13X zeolite beads.* Adsorption, 2014. **20**(1): p. 121-135.
74. Kikkinides, E.S., R.T. Yang, and S.H. Cho, *Concentration and recovery of CO_2 from flue gas by pressure swing adsorption.* Industrial and Engineering Chemistry Research, 1993. **32**(11): p. 2714-2720.
75. Gomes, V.G. and K.W.K. Yee, *Pressure swing adsorption for carbon dioxide sequestration from exhaust gases.* Separation and Purification Technology, 2002. **28**(2): p. 161-171.
76. Siriwardane, R.V., et al., *Adsorption of CO_2 on molecular sieves and activated carbon.* Energy and Fuels, 2001. **15**(2): p. 279-284.
77. Na, B.K., et al., *CO_2 Recovery from Flue Gas by PSA Process using Activated Carbon.* Korean Journal of Chemical Engineering, 2001. **18**(2): p. 220-227.
78. Ribeiro, R.P., et al., *Adsorption of CO_2, CH_4, and N_2 in activated carbon honeycomb monolith.* Journal of Chemical and Engineering Data, 2008. **53**(10): p. 2311-2317.
79. Gil, M.V., et al., *Carbon adsorbents for CO2 capture from bio-hydrogen and biogas streams: Breakthrough adsorption study.* Chemical Engineering Journal, 2015. **269**(0): p. 148-158.
80. Jansen, R.J.J. and H. van Bekkum, *XPS of nitrogen-containing functional groups on activated carbon.* Carbon, 1995. **33**(8): p. 1021-1027.
81. Mosca, A., et al., *Optimization of synthesis procedures for structured PSA adsorbents.* Adsorption, 2008. **14**(4-5): p. 687-693.
82. Yates, M., et al., *Vapour adsorption capacity of controlled porosity honeycomb monoliths.* Microporous and Mesoporous Materials, 2003. **65**(2-3): p. 219-231.
83. Tlili, N., G. Grévillot, and C. Vallières, *Carbon dioxide capture and recovery by means of TSA and/or VSA.* International Journal of Greenhouse Gas Control, 2009. **3**(5): p. 519-527.
84. Xiao, P., et al., *Capture of CO_2 from flue gas streams with zeolite 13X by vacuum-pressure swing adsorption.* Adsorption, 2008. **14**(4-5): p. 575-582.
85. Siriwardane, R.V., et al., *Adsorption of CO_2 on zeolites at moderate temperatures.* Energy and Fuels, 2005. **19**(3): p. 1153-1159.
86. Rezaei, F., et al., *Comparison of traditional and structured adsorbents for CO_2 separation by vacuum-swing adsorption.* Industrial and Engineering Chemistry Research, 2010. **49**(10): p. 4832-4841.
87. Li, G., et al., *Capture of CO_2 from high humidity flue gas by vacuum swing adsorption with zeolite 13X.* Adsorption, 2008. **14**(2-3): p. 415-422.
88. Chou, C.T. and C.Y. Chen, *Carbon dioxide recovery by vacuum swing adsorption.* Separation and Purification Technology, 2004. **39**(1-2 SPEC. ISS.): p. 51-65.
89. Nastaj, J.F., B. Ambrozek, and J. Rudnicka, *Simulation studies of a vacuum and temperature swing adsorption process for the removal of VOC from waste air streams.* International Communications in Heat and Mass Transfer, 2006. **33**(1): p. 80-86.
90. Boger, T., A. Salden, and G. Eigenberger, *A combined vacuum and temperature swing adsorption process for the recovery of amine from foundry air.* Chemical Engineering and Processing: Process Intensification, 1997. **36**(3): p. 231-241.
91. An, H., B. Feng, and S. Su, *CO_2 capture by electrothermal swing adsorption with activated carbon fibre materials.* International Journal of Greenhouse Gas Control, 2010.
92. Grande, C.A. and A.E. Rodrigues, *Electric Swing Adsorption for CO_2 removal from flue gases.* International Journal of Greenhouse Gas Control, 2008. **2**(2): p. 194-202.
93. Moon, S.H. and J.W. Shim, *A novel process for CO_2/CH_4 gas separation on activated carbon fibers-electric swing adsorption.* Journal of Colloid and Interface Science, 2006. **298**(2): p. 523-528.
94. Delaney, S.W., G.P. Knowles, and A.L. Chaffee. *Electrically regenerable mesoporous carbon for CO_2 capture*. 2006. Atlanta, GA.
95. Yang, R.T., *Adsorbents: Fundamentals and Applications*, R.T. Yang, Editor 2003, John Wiley & Sons: New Jersey. p. 17-53.
96. Wang, J., et al., *Recent advances in solid sorbents for CO2 capture and new development trends.* Energy & Environmental Science, 2014. **7**(11): p. 3478-3518.

97. Lee, S.-Y. and S.-J. Park, *A review on solid adsorbents for carbon dioxide capture.* Journal of Industrial and Engineering Chemistry, 2015. **23**: p. 1-11.
98. Das, U., et al., *Electron-spin echoes and saturation in coal.* Fuel, 1983. **62**(3): p. 285-288.
99. Weitkamp, J., *Zeolites and catalysis.* Solid State Ionics, 2000. **131**(1): p. 175-188.
100. Samaras, P., X. Dabou, and G.P. Sakellaropoulos, *Production, characterization and applications of carbon molecular sieves from a high ash Greek lignite* Studies in Surface Science and Catalysis, 1999. **120 A**: p. 425-457.
101. Li, Z., W. Yan, and S. Dai, *Surface functionalization of ordered mesoporous carbons - A comparative study.* Langmuir, 2005. **21**(25): p. 11999-12006.
102. Delgado, J.A., et al., *Adsorption equilibrium of carbon dioxide, methane and nitrogen onto Na- and H-mordenite at high pressures.* Separation and Purification Technology, 2006. **48**(3): p. 223-228.
103. Reucroft, P.J., P.B. Rao, and G.B. Freeman, *Binary vapor adsorption by activated carbon.* Carbon, 1983. **21**(3): p. 171-176.
104. Daulan, C., et al., *Influence of anthracite pretreatment in the preparation of activated carbons.* Fuel, 1998. **77**(6): p. 495-502.
105. Illán-Gómez, M.J., et al., *Activated carbons from Spanish coals. 2. Chemical activation.* Energy and Fuels, 1996. **10**(5): p. 1108-1114.
106. Lillo-Ródenas, M.A., et al., *Preparation of activated carbons from Spanish anthracite: II. Activation by NaOH.* Carbon, 2001. **39**(5): p. 751-759.
107. Razvigorova, M., et al., *Purification of water by activated carbons from apricot stones, lignites and anthracite.* Water Research, 1998. **32**(7): p. 2135-2139.
108. Ahmadpour, A., B.A. King, and D.D. Do, *Comparison of Equilibria and Kinetics of High Surface Area Activated Carbon Produced from Different Precursors and by Different Chemical Treatments.* Industrial and Engineering Chemistry Research, 1998. **37**(4): p. 1329-1334.
109. Chen, G., B.W. Dussert, and I.H. Suffet, *Evaluation of granular activated carbons for removal of methylisoborneol to below odor threshold concentration in drinking water.* Water Research, 1997. **31**(5): p. 1155-1163.
110. El Qada, E.N., S.J. Allen, and G.M. Walker, *Adsorption of Methylene Blue onto activated carbon produced from steam activated bituminous coal: A study of equilibrium adsorption isotherm.* Chemical Engineering Journal, 2006. **124**(1-3): p. 103-110.
111. Hippo, E.J., W.S. O'Brien, and J. Sun, *Production of activated carbons from Illinois coals.* ACS Division of Fuel Chemistry, Preprints, 1996. **41**(1): p. 241-243.
112. Hsu, L.-Y. and H. Teng, *Influence of different chemical reagents on the preparation of activated carbons from bituminous coal.* Fuel Processing Technology, 2000. **64**(1-3): p. 155-166.
113. Jagtoyen, M., J. Groppo, and F. Derbyshire, *Activated carbons from bituminous coals by reaction with H_3PO_4: The influence of coal cleaning.* Fuel Processing Technology, 1993. **34**(2): p. 85-96.
114. Cetinkaya, S., B. Sakintuna, and Y. Yürüm, *Formation of crystal structures during activated carbon production from Turkish Elbistan lignite.* ACS Division of Fuel Chemistry, Preprints, 2003. **48**(1): p. 67-69.
115. Chattopadhyaya, G., et al., *Preparation and characterization of chars and activated carbons from Saskatchewan lignite.* Fuel Processing Technology, 2006. **87**(11): p. 997-1006.
116. Durie, R.A. and H.N.S. Schafer, *The production of active carbon from brown coal in high yields.* Fuel, 1979. **58**(6): p. 472-476.
117. Ohtsuka, Y., et al., *Nitrogen removal during atmospheric-pressure pyrolysis of brown coal with iron.* Fuel, 1994. **73**(7): p. 1093-1097.
118. Önal, Y., et al., *Adsorption kinetics of malachite green onto activated carbon prepared from Tunçbilek lignite.* Journal of Hazardous Materials, 2006. **128**(2-3): p. 150-157.

119. Pietrzak, R., et al., *Preparation of modified active carbon from brown coal by ammoxidation.* Fuel Processing Technology, 2007. **88**(4): p. 409-415.
120. Pokonova, Y.V., *Production of carbon adsorbents from brown coal.* Carbon, 1996. **34**(3): p. 411-415.
121. Nakagawa, K., et al., *Mesoporous Activated Carbons from Phenolic Resins.* Chemical Engineering Research and Design, 2007. **85**(9): p. 1331-1337.
122. Huang, M.C. and H. Teng, *Urea impregnation to enhance porosity development of carbons prepared from phenol-formaldehyde resins.* Carbon, 2002. **40**(6): p. 955-958.
123. Przepiórski, J., B. Tryba, and A.W. Morawski, *Adsorption of carbon dioxide on phenolic resin-based carbon spheres.* Applied Surface Science, 2002. **196**(1-4): p. 296-300.
124. Zhang, Y., M.M. Maroto-Valer, and Z. Tang, *Microporous Activated Carbons Produced from Unburned Fly Ash and their Application for CO_2 Capture.* ACS Division of Fuel Chemistry, Preprints, 2004. **49**(1): p. 304-305.
125. Zhang, Y., et al., *Development of Microporous Activated Carbons from Unburned Carbon in Fly Ash.* ACS Division of Fuel Chemistry, Preprints, 2003. **48**(1): p. 65-66.
126. Gray, M.L., et al., *CO_2 capture by amine-enriched fly ash carbon sorbents.* Separation and Purification Technology, 2004. **35**(1): p. 31-36.
127. Arenillas, A., et al., *CO_2 capture using some fly ash-derived carbon materials.* Fuel, 2005. **84**(17): p. 2204-2210.
128. Alcaniz-Monge, J., et al., *The influence of iron chloride addition to the precursor pitch on the formation of activated carbon fibers.* Microporous and Mesoporous Materials, 2007. **100**(1-3): p. 202-209.
129. Boudou, J.P., et al., *Effect of $MoCl_5$ addition on the carbonization and the subsequent steam activation of pitch and coking coals.* Carbon, 2000. **38**(4): p. 525-534.
130. Daguerre, E., A. Guillot, and X. Py, *Microporosity of activated carbons produced from heat-treated and fractionated pitches.* Carbon, 2000. **38**(1): p. 59-64.
131. Gañán-Gómez, J., et al., *Preparation and characterization of activated carbons from impregnation pitch by $ZnCl_2$.* Applied Surface Science, 2006. **252**(17): p. 5976-5979.
132. Tamai, H., et al., *Characteristics and catalytic activity of carbons obtained from pitch containing noble metal complexes.* Carbon, 2000. **38**(6): p. 899-906.
133. Yanagisawa, K. and T. Suzuki, *Carbonization of oxidized mesophase pitches originating from petroleum and coal tar.* Fuel, 1993. **72**(1): p. 25-30.
134. Hamadi, N.K., et al., *Adsorption kinetics for the removal of chromium(VI) from aqueous solution by adsorbents derived from used tyres and sawdust.* Chemical Engineering Journal, 2001. **84**(2): p. 95-105.
135. Aranda, A., et al., *Steam activation of tyre pyrolytic carbon black: Kinetic study in a thermobalance.* Chemical Engineering Journal, 2007. **126**(2-3): p. 79-85.
136. Cagnon, B., et al., *The effect of the carbonization/activation procedure on the microporous texture of the subsequent chars and active carbons.* Microporous and Mesoporous Materials, 2003. **57**(3): p. 273-282.
137. Vyas, S.N., et al., *Adsorption of Gases on Carbon Molecular Sieves.* Journal of Colloid and Interface Science, 1994. **168**(2): p. 275-280.
138. Julien, F., M. Baudu, and M. Mazet, *Relationship between chemical and physical surface properties of activated carbon.* Water Research, 1998. **32**(11): p. 3414-3424.
139. Hu, Z., M.P. Srinivasan, and Y. Ni, *Novel activation process for preparing highly microporous and mesoporous activated carbons.* Carbon, 2001. **39**(6): p. 877-886.
140. Azevedo, D.C.S., et al., *Microporous activated carbon prepared from coconut shells using chemical activation with zinc chloride.* Microporous and Mesoporous Materials, 2007. **100**(1-3): p. 361-364.
141. Budinova, T., et al., *Characterization and application of activated carbon produced by H_3PO_4 and water vapor activation.* Fuel Processing Technology, 2006. **87**(10): p. 899-905.

142. Maroto-Valer, M.M., Y. Zhang, and B. Miller, *Development of activated carbons from coal and biomass combustion and gasification chars.* ACS Division of Fuel Chemistry, Preprints, 2004. **49**(2): p. 690-691.
143. Gergova, K. and S. Eser, *Effects of activation method on the pore structure of activated carbons from apricot stones.* Carbon, 1996. **34**(7): p. 879-888.
144. Gergova, K., N. Petrov, and S. Eser, *Adsorption properties and microstructure of activated carbons produced from agricultural by-products by steam pyrolysis.* Carbon, 1994. **32**(4): p. 693-702.
145. Hall, W.A., D.E. Bellamy, and S.S. Walse, *Activated Carbons from End-Products of Tree Nut and Tree Fruit Production as Sorbents for Removing Methyl Bromide in Ventilation Effluent Following Postharvest Chamber Fumigation.* Journal of Agricultural and Food Chemistry, 2015. **63**(12): p. 3094-3103.
146. Toles, C.A., et al., *Steam- or carbon dioxide-activated carbons from almond shells: physical, chemical and adsorptive properties and estimated cost of production.* Bioresource Technology, 2000. **75**(3): p. 197-203.
147. Rivera-Utrilla, J., et al., *Comparison of activated carbons prepared from agricultural raw materials and spanish lignites when removing chlorophenols from aqueous solutions.* Carbon, 1991. **29**(4-5): p. 613-619.
148. Pereira, M., et al., *Chromium adsorption in olive stone activated carbon.* Adsorption, 2006. **12**(2): p. 155-162.
149. Chiang, Y.C., P.C. Chiang, and C.P. Huang, *Effects of pore structure and temperature on VOC adsorption on activated carbon.* Carbon, 2001. **39**(4): p. 523-534.
150. Plaza, M.G., et al., *Ammoxidation of carbon materials for CO_2 capture.* Applied Surface Science, 2008. **In Press, Accepted Manuscript**.
151. Pollard, S.J.T., et al., *Low-cost adsorbents for waste and wastewater treatment: A review.* Science of the Total Environment, 1992. **116**(1-2): p. 31-52.
152. Ahmadpour, A. and D.D. Do, *The preparation of active carbons from coal by chemical and physical activation.* Carbon, 1996. **34**(4): p. 471-479.
153. Prauchner, M.J. and F. Rodríguez-Reinoso, *Chemical versus physical activation of coconut shell: A comparative study.* Microporous and Mesoporous Materials, 2012. **152**(0): p. 163-171.
154. Marsh, H. and F. Rodríguez-Reinoso, *Chapter 5 - Activation Processes (Thermal or Physical)*, in *Activated Carbon*, H.M. Rodríguez-Reinoso, Editor 2006, Elsevier Science Ltd: Oxford. p. 243-321.
155. Marsh, H. and F. Rodríguez-Reinoso, *Chapter 6 - Activation Processes (Chemical)*, in *Activated Carbon*, H.M. Rodríguez-Reinoso, Editor 2006, Elsevier Science Ltd: Oxford. p. 322-365.
156. Alcañiz-Monge, J. and M.J. Illán-Gómez, *Insight into hydroxides-activated coals: Chemical or physical activation?* Journal of Colloid and Interface Science, 2008. **318**(1): p. 35-41.
157. Lillo-Ródenas, M.A., D. Cazorla-Amorós, and A. Linares-Solano, *Understanding chemical reactions between carbons and NaOH and KOH: An insight into the chemical activation mechanism.* Carbon, 2003. **41**(2): p. 267-275.
158. Ehrburger, P., et al., *Carbonization of coals in the presence of alkaline hydroxides and carbonates: Formation of activated carbons.* Fuel, 1986. **65**(10): p. 1447-1449.
159. Cazorla-Amorós, D., et al., *Carbon Activation by Alkaline Hydroxides*, in *Chemistry & Physics of Carbon*2007, CRC Press. p. 1-62.
160. Molina-Sabio, M. and F. Rodríguez-Reinoso, *Role of chemical activation in the development of carbon porosity.* Colloids and Surfaces A: Physicochemical and Engineering Aspects, 2004. **241**(1-3): p. 15-25.
161. Teng, H. and L.Y. Hsu, *High-porosity carbons prepared from bituminous coal with potassium hydroxide activation.* Industrial and Engineering Chemistry Research, 1999. **38**(8): p. 2947-2953.

162. Zhao, W., et al., *Impact of synthesis conditions of KOH activated carbons on their hydrogen storage capacities.* International Journal of Hydrogen Energy, (0).
163. Yoshizawa, N., et al., *XRD evaluation of KOH activation process and influence of coal rank.* Fuel, 2002. **81**(13): p. 1717-1722.
164. Belmabkhout, Y., G. De Weireld, and M. Frère, *High-pressure adsorption isotherms of N_2, CH_4, O_2 and Ar on different carbonaceous adsorbents.* Journal of Chemical and Engineering Data, 2004. **49**(5): p. 1379-1391.
165. Chagger, H.K., et al., *Kinetics of adsorption and diffusional characteristics of carbon molecular sieves.* Carbon, 1995. **33**(10): p. 1405-1411.
166. Das, M., J.D. Perry, and W.J. Koros, *Effect of processing on carbon molecular sieve structure and performance.* Carbon, 2010.
167. Huang, Q. and M. Eić, *Commercial adsorbents as benchmark materials for separation of carbon dioxide and nitrogen by vacuum swing adsorption process.* Separation and Purification Technology, 2013. **103**(0): p. 203-215.
168. Kyotani, T., *Control of pore structure in carbon.* Carbon, 2000. **38**(2): p. 269-286.
169. Burg, P., M.H. Abraham, and D. Cagniant, *Methods of determining polar and non-polar sites on carbonaceous adsorbents. The contribution of the linear solvation energy relationship approach.* Carbon, 2003. **41**(5): p. 867-879.
170. Lowell, S., et al., *Characterization of Porous Solids and Powders: Surface Area, Pore Size and Density*, B. Scarlett, Editor 2004, Springer: Dordrecht. p. p. 15-55.
171. Maroto-Valer, M.M., Z. Tang, and Y. Zhang, *CO_2 capture by activated and impregnated anthracites.* Fuel Processing Technology, 2005. **86**(14-15): p. 1487-1502.
172. Plaza, M.G., et al., *A comparison of two methods for producing CO_2 capture adsorbents.* Energy Procedia, 2009. **1**(1): p. 1107-1113.
173. Plaza, M.G., et al., *Development of low-cost biomass-based adsorbents for postcombustion CO_2 capture.* Fuel, 2009. **88**(12): p. 2442-2447.
174. Walker Jr, P.L. and M. Shelef, *Carbon dioxide sorption on carbon molecular sieves.* Carbon, 1967. **5**(1): p. 7-11.
175. Sevilla, M. and A.B. Fuertes, *Sustainable porous carbons with a superior performance for CO2 capture.* Energy & Environmental Science, 2011. **4**(5): p. 1765-1771.
176. Donald Carruthers, J., et al., *Molecular sieve carbons for CO2 capture.* Microporous and Mesoporous Materials, 2011(0).
177. Drage, T.C., et al., *Preparation of carbon dioxide adsorbents from the chemical activation of urea–formaldehyde and melamine–formaldehyde resins.* Fuel, 2007. **86**(1–2): p. 22-31.
178. Fifield, L.S., et al., *Carbon dioxide capture using amine-based molecular anchors on multi wall carbon nanotubes.* ACS Division of Fuel Chemistry, Preprints, 2004. **49**(1): p. 296-297.
179. Gray, M.L., et al., *CO_2 capture by amine-enriched fly ash carbon sorbents.* Separation and Purification Technology, 2004. **35**(1): p. 31-36.
180. Pevida, C., et al., *Surface modification of activated carbons for CO_2 capture.* Applied Surface Science, 2008. **254**(22): p. 7165-7172.
181. Plaza, M.G., et al., *CO_2 capture by adsorption with nitrogen enriched carbons.* Fuel, 2007. **86**(14): p. 2204-2212.
182. Sayari, A. and Y. Belmabkhout, *Stabilization of amine-containing CO_2 adsorbents: Dramatic effect of water vapor.* Journal of the American Chemical Society, 2010. **132**(18): p. 6312-6314.
183. Snape, C.E., et al., *Comparison of two different approaches for enhancement of CO_2 removal by adsorption on carbons.* ACS Division of Fuel Chemistry, Preprints, 2004. **49**(2): p. 685-686.
184. Thote, J.A., et al., *In situ nitrogen enriched carbon for carbon dioxide capture.* Carbon, 2010. **48**(2): p. 396-402.
185. Chaffee, A.L., et al., *CO_2 capture by adsorption: Materials and process development.* International Journal of Greenhouse Gas Control, 2007. **1**(1): p. 11-18.

186. Chatti, R., et al., *Amine loaded zeolites for carbon dioxide capture: Amine loading and adsorption studies.* Microporous and Mesoporous Materials, 2009. **121**(1-3): p. 84-89.
187. Franchi, R.S., P.J.E. Harlick, and A. Sayari, *Applications of pore-expanded mesoporous silica. 2. Development of a high-capacity, water-tolerant adsorbent for CO_2.* Industrial and Engineering Chemistry Research, 2005. **44**(21): p. 8007-8013.
188. Jadhav, P.D., et al., *Monoethanol amine modified zeolite 13X for CO_2 adsorption at different temperatures.* Energy and Fuels, 2007. **21**(6): p. 3555-3559.
189. Knowles, G.P., S.W. Delaney, and A.L. Chaffee, *Diethylenetriamine[propyl(silyl)]-functionalized (DT) mesoporous silicas as CO_2 adsorbents.* Industrial and Engineering Chemistry Research, 2006. **45**(8): p. 2626-2633.
190. Knowles, G.P., et al., *Amine-functionalised mesoporous silicas as CO_2 adsorbents*, in *Studies in Surface Science and Catalysis*2005, Elsevier. p. 887-896.
191. Schladt, M.J., T.P. Filburn, and J.J. Helble, *Supported amine sorbents under temperature swing absorption for CO_2 and moisture capture.* Industrial and Engineering Chemistry Research, 2007. **46**(5): p. 1590-1597.
192. Son, W.-J., J.-S. Choi, and W.-S. Ahn, *Adsorptive removal of carbon dioxide using polyethyleneimine-loaded mesoporous silica materials.* Microporous and Mesoporous Materials, 2008. **113**(1-3): p. 31-40.
193. Su, F., et al., *Adsorption of CO_2 on amine-functionalized y-type zeolites.* Energy and Fuels, 2010. **24**(2): p. 1441-1448.
194. Xu, X., et al., *Novel polyethylenimine-modified mesoporous molecular sieve of MCM-41 type as high-capacity adsorbent for CO_2 capture.* Energy and Fuels, 2002. **16**(6): p. 1463-1469.
195. Zukal, A., et al., *Functionalization of delaminated zeolite ITQ-6 for the adsorption of carbon dioxide.* Langmuir, 2009. **25**(17): p. 10314-10321.
196. Walcarius, A., M. Etienne, and J. Bessière, *Rate of access to the binding sites in organically modified silicates. 1. Amorphous silica gels grafted with amine or thiol groups.* Chemistry of Materials, 2002. **14**(6): p. 2757-2766.
197. Subagyono, D.J.N., et al., *CO2 adsorption by amine modified siliceous mesostructured cellular foam (MCF) in humidified gas.* Microporous and Mesoporous Materials, 2014. **186**(0): p. 84-93.
198. Knowles, G.P., et al., *Aminopropyl-functionalized mesoporous silicas as CO_2 adsorbents.* Fuel Processing Technology, 2005. **86**(14-15): p. 1435-1448.
199. Leal, O., et al., *Reversible adsorption of carbon dioxide on amine surface-bonded silica gel.* Inorganica Chimica Acta, 1995. **240**(1-2): p. 183-189.
200. Yue, M.B., et al., *Promoting the CO_2 adsorption in the amine-containing SBA-15 by hydroxyl group.* Microporous and Mesoporous Materials, 2008. **114**(1-3): p. 74-81.
201. Knowles, G.P., Z. Liang, and A.L. Chaffee, *Shaped polyethyleneimine sorbents for CO2 capture.* Microporous and Mesoporous Materials.
202. Sanz, R., et al., *CO2 adsorption on branched polyethyleneimine-impregnated mesoporous silica SBA-15.* Applied Surface Science, 2010. **256**(17): p. 5323-5328.
203. Drage, T.C., et al., *Thermal stability of polyethylenimine based carbon dioxide adsorbents and its influence on selection of regeneration strategies.* Microporous and Mesoporous Materials, 2008. **116**(1–3): p. 504-512.
204. Gargiulo, N., et al., *Preparation and characterization of polyethylenimine-modified mesoporous silicas as CO_2 sorbents*, in *Studies in Surface Science and Catalysis*2007, Elsevier. p. 1938-1943.
205. Subagyono, D.J.N., et al., *CO2 adsorption by amine modified siliceous mesostructured cellular foam (MCF) in humidified gas.* Microporous and Mesoporous Materials, 2014. **186**: p. 84-93.
206. Yan, X., et al., *Amine-modified SBA-15: Effect of pore structure on the performance for CO2 capture.* Industrial and Engineering Chemistry Research, 2011. **50**(6): p. 3220-3226.

207. Tamai, H., et al., *Surface functionalization of mesoporous and microporous activated carbons by immobilization of diamine.* Journal of Colloid and Interface Science, 2006. **295**(1): p. 299-302.
208. Abe, M., et al., *Amination of activated carbon and adsorption characteristics of its aminated surface.* Langmuir, 2000. **16**(11): p. 5059-5063.
209. Cagniant, D., et al., *Structural characterization of nitrogen-enriched coals.* Energy and Fuels, 1998. **12**(4): p. 672-681.
210. Nowicki, P., R. Pietrzak, and H. Wachowska, *Comparison of physicochemical properties of nitrogen-enriched activated carbons prepared by physical and chemical activation of brown coal.* Energy and Fuels, 2008. **22**(6): p. 4133-4138.
211. Gibson, J.A.A., et al., *The effect of pore structure on the CO2 adsorption efficiency of polyamine impregnated porous carbons.* Microporous and Mesoporous Materials, 2015. **208**(0): p. 129-139.
212. Zhang, C., et al., *CO2 Capture with Activated Carbon Grafted by Nitrogenous Functional Groups.* Energy & Fuels, 2013. **27**(8): p. 4818-4823.
213. Wang, J., et al., *Carbon dioxide capture using polyethylenimine-loaded mesoporous carbons.* Journal of Environmental Sciences, 2013. **25**(1): p. 124-132.
214. Bimer, J., et al., *Modified active carbons from precursors enriched with nitrogen functions: Sulfur removal capabilities.* Fuel, 1998. **77**(6): p. 519-525.
215. Starck, J., et al., *The influence of demineralisation and ammoxidation on the adsorption properties of an activated carbon prepared from a Polish lignite.* Carbon, 2006. **44**(12): p. 2549-2557.
216. Przepiórski, J., M. Skrodzewicz, and A.W. Morawski, *High temperature ammonia treatment of activated carbon for enhancement of CO_2 adsorption.* Applied Surface Science, 2004. **225**(1-4): p. 235-242.
217. Shafeeyan, M.S., et al., *Ammonia modification of activated carbon to enhance carbon dioxide adsorption: Effect of pre-oxidation.* Applied Surface Science, 2011. **257**(9): p. 3936-3942.
218. Grondein, A. and D. Bélanger, *Chemical modification of carbon powders with aminophenyl and aryl-aliphatic amine groups by reduction of in situ generated diazonium cations: Applicability of the grafted powder towards CO2 capture.* Fuel, 2011. **90**(8): p. 2684-2693.
219. Hsiao, H.-Y., et al., *Preparation of high-surface-area PAN-based activated carbon by solution-blowing process for CO2 adsorption.* Separation and Purification Technology, 2011. **82**(0): p. 19-27.
220. Yang, H., Y. Yuan, and S.C.E. Tsang, *Nitrogen-enriched carbonaceous materials with hierarchical micro-mesopore structures for efficient CO2 capture.* Chemical Engineering Journal, 2012. **185–186**(0): p. 374-379.
221. Plaza, M.G., et al., *Evaluation of ammonia modified and conventionally activated biomass based carbons as CO2 adsorbents in postcombustion conditions.* Separation and Purification Technology, 2011. **80**(1): p. 96-104.
222. Wang, D., et al., *Development of Carbon-Based "Molecular Basket" Sorbent for CO2 Capture.* Industrial & Engineering Chemistry Research, 2012.
223. Durie, R.A., *The Science of Victorian Brown Coal: Structure, Properties and Consequences for Utilization*1991, Oxford, Great Britan: Butterworth-Heinemann Ltd. p. 703-738.
224. Durie, R.A., *The Science of Victorian Brown Coal: Structure, Properties and Consequences for Utilization*1991, Oxford, Great Britan: Butterworth-Heinemann Ltd. p. 105.
225. Durie, R.A., *The Science of Victorian Brown Coal: Structure, Properties and Consequences for Utilization*1991, Oxford, Great Britan: Butterworth-Heinemann Ltd. p. 103-150.
226. Barton, C.M., C.S. Gloe, and G.R. Holdgate, *Latrobe Valley, Victoria, Australia: A world class brown coal deposit.* International Journal of Coal Geology, 1993. **23**(1-4): p. 193-213.
227. Tahmasebi, A., et al., *Thermogravimetric study of the combustion of Tetraselmis suecica microalgae and its blend with a Victorian brown coal in O2/N2 and O2/CO2 atmospheres.* Bioresource Technology, 2013. **150**: p. 15-27.

228. Bowling, K.M. and P.L. Waters, *Fluidized-bed char from Australian coals.* Fuel, 1970. **49**(2): p. 146-164.
229. Allardice, D.J., et al., *The characterisation of different forms of water in low rank coals and some hydrothermally dried products[small star, filled].* Fuel, 2003. **82**(6): p. 661-667.
230. Sadek, F.S. and A.Y. Herrell, *Methods of proximate analysis by thermogravimetry.* Thermochimica Acta, 1984. **81**: p. 297-303.
231. Lu, Z., M.M. Maroto-Valer, and H.H. Schobert, *Catalytic effects of inorganic compounds on the development of surface areas of fly ash carbon during steam activation.* Fuel, 2010. **89**(11): p. 3436-3441.
232. Vogt, C., *Speciation of the inorganic components in brown coal.* Fresenius' Journal of Analytical Chemistry, 1994. **350**(1): p. 89-92.
233. Baten, W.D. and C.C. DeWitt, *Use of Discriminant Function in Comparison of Proximate Coal Analyses.* Industrial & Engineering Chemistry Analytical Edition, 1944. **16**(1): p. 32-34.
234. Mayoral, M.C., et al., *Different approaches to proximate analysis by thermogravimetry analysis.* Thermochimica Acta, 2001. **370**(1-2): p. 91-97.
235. Boehm, H.P., et al., *Surface Oxides of Carbon.* Angewandte Chemie International Edition in English, 1964. **3**(10): p. 669-677.
236. Boehm, H.P., *Some aspects of the surface chemistry of carbon blacks and other carbons.* Carbon, 1994. **32**(5): p. 759-769.
237. Oickle, A.M., et al., *Standardization of the Boehm titration: Part II. Method of agitation, effect of filtering and dilute titrant.* Carbon, 2010. **48**(12): p. 3313-3322.
238. Kim, Y.S., et al., *Effects of carbon dioxide and acidic carbon compounds on the analysis of Boehm titration curves.* Carbon, 2012. **50**(4): p. 1510-1516.
239. Gong, H., et al., *Simple quantification of surface carboxylic acids on chemically oxidized multi-walled carbon nanotubes.* Applied Surface Science, 2013. **266**: p. 219-224.
240. Biniak, S., et al., *The characterization of activated carbons with oxygen and nitrogen surface groups.* Carbon, 1997. **35**(12): p. 1799-1810.
241. Burg, P., et al., *The characterization of nitrogen-enriched activated carbons by IR, XPS and LSER methods.* Carbon, 2002. **40**(9): p. 1521-1531.
242. Burke, G.M., et al., *Surface Characterization of Activated Charcoal by X-Ray Photoelectron Spectroscopy (XPS): Correlation with Phenobarbital Adsorption Data.* Pharmaceutical Research, 1992. **9**(1): p. 126-130.
243. Desimoni, E., et al., *XPS determination of oxygen-containing functional groups on carbon-fibre surfaces and the cleaning of these surfaces.* Surface and Interface Analysis, 1990. **15**(10): p. 627-634.
244. Nowicki, P., R. Pietrzak, and H. Wachowska, *X-ray photoelectron spectroscopy study of nitrogen-enriched active carbons obtained by ammoxidation and chemical activation of brown and bituminous coals.* Energy and Fuels, 2010. **24**(2): p. 1197-1206.
245. Heymann, K., et al., *C 1s K-edge near edge X-ray absorption fine structure (NEXAFS) spectroscopy for characterizing functional group chemistry of black carbon.* Organic Geochemistry, 2011. **42**(9): p. 1055-1064.
246. Singh, B., et al., *NEXAFS and XPS characterisation of carbon functional groups of fresh and aged biochars.* Organic Geochemistry, 2014. **77**(0): p. 1-10.
247. Turner, J.A., K.M. Thomas, and A.E. Russell, *The identification of oxygen functional groups in carbonaceous materials by oxygen K-edge XANES.* Carbon, 1997. **35**(7): p. 983-992.
248. Lee, V., et al., *Soft X-ray Absorption Spectroscopy Studies of the Electronic Structure Recovery of Graphene Oxide upon Chemical Defunctionalization.* The Journal of Physical Chemistry C, 2012. **116**(38): p. 20591-20599.
249. Takashiro, J.I., et al., *Heat treatment effect on the electronic and magnetic structures of nanographene sheets investigated through electron spectroscopy and conductance measurements.* Physical Chemistry Chemical Physics, 2014. **16**(16): p. 7280-7289.

250. Ramm, M., et al., *Studies of amorphous carbon using X-ray photoelectron spectroscopy, near-edge X-ray-absorption fine structure and Raman spectroscopy.* Thin Solid Films, 1999. **354**(1–2): p. 106-110.
251. Gribbin, J., *Q is for Quantum: Particle Physics from A to Z*1999, London: Phoenix Giant.
252. Hollas, J.M., *Modern Spectroscopy*. 4th ed2003: Wiley.
253. Einstein, A., *Über einen die Erzeugung und Verwandlung des Lichtes betreffenden heuristischen Gesichtspunkt.* Annalen der Physik, 1905. **322**(6): p. 132-148.
254. BushBerg, J.T., et al., *The Essential Physics of Medical Imaging*. 2nd ed2002, Philadelphia, USA: Lippincott, Willilams & Wilkins.
255. Chorkendorff, I. and J.W. Niemantsverdriet, *Catalyst Characterization*, in *Concepts of Modern Catalysis and Kinetics*2005, Wiley-VCH Verlag GmbH & Co. KGaA. p. 129-166.
256. Puziy, A.M., et al., *XPS and NMR studies of phosphoric acid activated carbons.* Carbon, 2008. **46**(15): p. 2113-2123.
257. Thommes, M., et al., *Assessing surface chemistry and pore structure of active carbons by a combination of physisorption (H₂O, Ar, N₂, CO₂), XPS and TPD-MS.* Adsorption, 2011. **17**(3): p. 653-661.
258. Gong, B., P.J. Pigram, and R.N. Lamb, *Identification of inorganic nitrogen in an Australian bituminous coal using x-ray photoelectron spectroscopy (XPS) and time-of-flight secondary ion mass spectrometry (TOFSIMS).* International Journal of Coal Geology, 1997. **34**(1-2): p. 53-68.
259. Grzybek, T., R. Pietrzak, and H. Wachowska, *X-ray photoelectron spectroscopy study of oxidized coals with different sulphur content.* Fuel Processing Technology, 2002. **77-78**: p. 1-7.
260. Pels, J.R., et al., *Evolution of nitrogen functionalities in carbonaceous materials during pyrolysis.* Carbon, 1995. **33**(11): p. 1641-1653.
261. Newville, M., *Fundamentals of XAFS*, in *Reviews in Mineralogy and Geochemistry*2014. p. 33-74.
262. Davis, U. *XANES: Theory*. Available from: http://chemwiki.ucdavis.edu/@api/deki/files/9775/FY_EY_mechanism.png.
263. Calvin, S., *XAFS for Everyone*2012: CRC Press.
264. Stohr, J., *NEXAFS Spectroscopy*. Spinger Series in Surface Sciences, ed. R. Gomer1996, Berlin: Springer.
265. Keiluweit, M., et al., *Dynamic Molecular Structure of Plant Biomass-Derived Black Carbon (Biochar).* Environmental Science & Technology, 2010. **44**(4): p. 1247-1253.
266. Lee, D.W., et al., *The Structure of Graphite Oxide: Investigation of Its Surface Chemical Groups.* The Journal of Physical Chemistry B, 2010. **114**(17): p. 5723-5728.
267. Lehmann, J., et al., *Near-edge X-ray absorption fine structure (NEXAFS) spectroscopy for mapping nano-scale distribution of organic carbon forms in soil: Application to black carbon particles.* Global Biogeochemical Cycles, 2005. **19**(1): p. 1-12.
268. Ganguly, A., et al., *Probing the Thermal Deoxygenation of Graphene Oxide Using High-Resolution In Situ X-ray-Based Spectroscopies.* The Journal of Physical Chemistry C, 2011. **115**(34): p. 17009-17019.
269. De Jesus, L.R., et al., *Inside and Outside: X-ray Absorption Spectroscopy Mapping of Chemical Domains in Graphene Oxide.* The Journal of Physical Chemistry Letters, 2013. **4**(18): p. 3144-3151.
270. Kuznetsova, A., et al., *Oxygen-Containing Functional Groups on Single-Wall Carbon Nanotubes: NEXAFS and Vibrational Spectroscopic Studies.* Journal of the American Chemical Society, 2001. **123**(43): p. 10699-10704.
271. Schultz, B.J., et al., *X-ray absorption spectroscopy studies of electronic structure recovery and nitrogen local structure upon thermal reduction of graphene oxide in an ammonia environment.* RSC Advances, 2014. **4**(2): p. 634-644.
272. Sadezky, A., et al., *Raman microspectroscopy of soot and related carbonaceous materials: Spectral analysis and structural information.* Carbon, 2005. **43**(8): p. 1731-1742.

273. Shimodaira, N. and A. Masui, *Raman spectroscopic investigations of activated carbon materials.* Journal of Applied Physics, 2002. **92**(2): p. 902-909.
274. Li, X., J.-i. Hayashi, and C.-Z. Li, *Volatilisation and catalytic effects of alkali and alkaline earth metallic species during the pyrolysis and gasification of Victorian brown coal. Part VII. Raman spectroscopic study on the changes in char structure during the catalytic gasification in air.* Fuel, 2006. **85**(10–11): p. 1509-1517.
275. Wesełucha-Birczyńska, A., K. Babeł, and K. Jurewicz, *Carbonaceous materials for hydrogen storage investigated by 2D Raman correlation spectroscopy.* Vibrational Spectroscopy, 2012. **60**(0): p. 206-211.
276. Zhang, S., et al., *Effects of volatile-char interactions on the evolution of char structure during the gasification of Victorian brown coal in steam.* Fuel, 2011. **90**(4): p. 1529-1535.
277. Bratek, W., et al., *Characteristics of activated carbon prepared from waste PET by carbon dioxide activation.* Journal of Analytical and Applied Pyrolysis, 2013. **100**(0): p. 192-198.
278. Chorkendorff, I. and J.W. Niemantsverdriet, *Catalyst Characterization*, in *Concepts of Modern Catalysis and Kinetics*2005, Wiley-VCH Verlag GmbH & Co. KGaA. p. 132.
279. Nabais, J.M.V., et al., *Production of activated carbons from almond shell.* Fuel Processing Technology, 2011. **92**(2): p. 234-240.
280. Shen, W., et al., *Preparation of mesoporous carbon from commercial activated carbon with steam activation in the presence of cerium oxide.* Journal of Colloid and Interface Science, 2003. **264**(2): p. 467-473.
281. Sing, K.S.W., *REPORTING PHYSISORPTION DATA FOR GAS/SOLID SYSTEMS.* Pure and Applied Chemistry, 1984. **58**(4): p. 567-583.
282. Ruthven, D.M., *Principles of Adsorption and Adsorption Processes*, D.M. Ruthven, Editor 1984, John Wiley and Sons: New Jersey. p. 29-61.
283. Lowell, S., et al., *Characterization of Porous Solids and Powders: Surface Area, Pore Size and Density*, B. Scarlett, Editor 2004, Springer: Dordrecht. p. p. 13.
284. Barrett, E.P., L.G. Joyner, and P.P. Halenda, *The Determination of Pore Volume and Area Distributions in Porous Substances. I. Computations from Nitrogen Isotherms.* Journal of the American Chemical Society, 1951. **73**(1): p. 373-380.

2 Synthesis and Characterisation of Microporous Carbons

2.1 Introduction

Microporous activated carbons (miACs) possess large pore volumes which make them attractive candidate materials for adsorption applications [1]. Although microporous carbons have been prepared from a variety of starting materials, very little research has focussed on the preparation of microporous carbons from Victorian Brown Coal (VBC) [2-4]. The objective of the research presented in this chapter was to develop procedures for the synthesis of microporous carbons from VBC or VBC derived chars, and to characterise the physical properties of the new materials.

In this section of the project, miACs were prepared from VBC using either chemical activation or physical activation (for details refer to ***section 6.4***). In the physical activation method, VBC or a VBC char was carbonised at 1073 K in a fixed-bed reactor, and H_2O was used to partially oxidise (gasify) the parent material. In the chemical activation method, KOH-doped VBC was carbonised at 1073 K under an inert atmosphere.

2.1.1 Chapter Outline

This chapter is separated into three distinct sections, on the basis of the method and parent material used to produce the series of carbon materials:

1. Physically activated VBC derived miACs
2. Physically activated VBC char derived miACs
3. Chemically activated (KOH) VBC derived miACs

The characterisation of each series of miACs was separated into a further three sections on the basis of the characteristic of the material being investigated. The three main sections investigate

the bulk composition, surface chemistry and structural characteristics of each series of materials, an example of which is shown below for coal derived carbons:

2.3 Physically Activated Coal Derived Carbons

2.3.1 Composition of Coal Derived Carbons

2.3.2 Surface Chemistry of Coal Derived Carbons

2.3.3 Structure of Coal Derived Carbons

2.3.3.1 Chemical Structure of Coal Derived Carbons

2.3.3.2 Physical Structure of Coal Derived Carbons

The section investigating the bulk composition of each series of materials, involved the use of elemental and ash analysis. The VBC used was a mixture of two low ash brown coals (refer to ***section 6.4.1*** for details), however, as up to 50% of the mass of the parent material can be expected to be lost as a result of the carbonisation process, keeping track of the ash content is very important. Understanding the changes in the carbon, oxygen and nitrogen content as a result of the activation processes is of great importance, as oxygen and nitrogen functional groups can influence the adsorption behaviour of the resulting carbon materials.

The surface chemistry section concerns the use of two different types of x-ray absorption spectroscopy (XAS). These were x-ray photoelectron spectroscopy (XPS) and near edge x-ray absorption fine structure (NEXAFS) spectroscopy. Both XPS and NEXAFS spectroscopy allow for different aspects of the functional group composition on the carbon surface to be investigated. XPS allows the major oxygenated functional groups (C=O, C-O-R and COO-R) to be determined and quantified. Due to the complex nature of the surface of amorphous carbon materials, it is often necessary to fully identify the groups on the carbon surface, as this can affect the properties of the AC. This is where NEXAFS spectroscopy is an incredibly powerful tool, as it allows for further identification of functional groups unable to be resolved using XPS. However, unlike XPS, NEXAFS does not allow quantification, and as such the two techniques are complimentary.

The section on structure addresses both the physical and chemical structural aspects of the carbons. The chemical structure was investigated using powder x-ray diffraction (XRD) and Raman spectroscopy, both involving the scattering (or diffraction) of electromagnetic waves by the material, resulting in important information regarding the alignment of atoms and molecules within the carbon material. The investigation of the physical structure uses gas physisorption and transmission electron microscopy (TEM). Gas physisorption allows for the

shape and size of pore within the materials to be determined. This further allows for the internal surface area to be determined, which is crucial when investigating an adsorbent system. TEM is of great importance in confirming observations from characterisation techniques such as Raman spectroscopy, as well as uncovering structural information in its own right relating to the types of morphology throughout particles of an AC.

2.2 Production of Physically Activated Microporous Carbons

Physically activated carbons were prepared from VBC briquettes (composed of an 80%/20% mixture of field coals from Loy Yang and Yallourn East, respectively) and two industrially produced VBC-derived chars (supplied by AusChar), according to the flow diagram in ***Figure 2-1***. The first supplied VBC-derived char was prepared in a Lurgi retort (CHLR) at 1173 K using the flue gas generated from the combustion of tars evolved during the charring process. The second supplied VBC-derived char (CHRK) was prepared in a rotary kiln at 973 K.

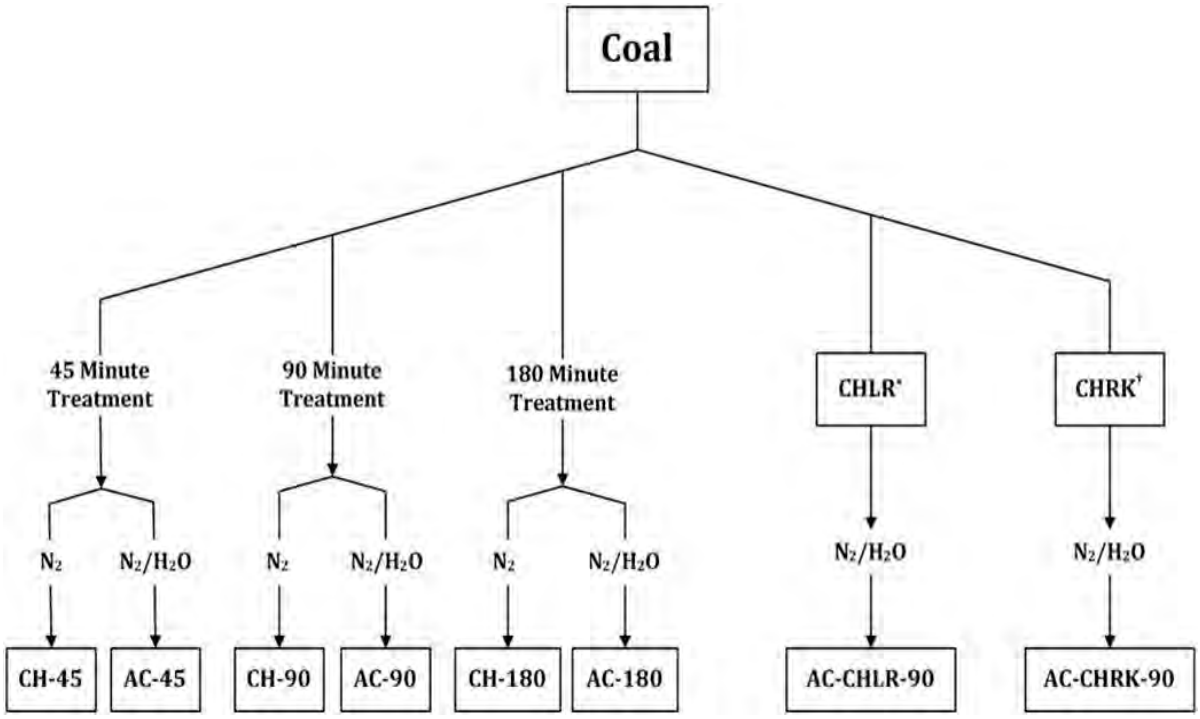

Figure 2-1 *~ Flow Diagram for the Physical Activation of VBC and VBC Derived Chars. * Produced by AusChar – Lurgi Retort, Run of Production, † Produced by AusChar – Rotary Kiln, Test Run (Product Development)*

Previous studies using VBC indicated that the optimal temperature used for steam activation was in the range of 1073-1123 K [5-7]. For physical activation experiments in this research, approximately 10 g of the homogenised VBC was carbonised in a fixed-bed reactor at 1073 K under a stream of N_2 (3 dm^3/min). Steam was then passed over the materials for a period of 45, 90 or 180 min using a liquid water flow rate of 0.25 cm^3/min diluted in the N_2 stream (3 dm^3/min, ***Figure 2-1***). The VBC derived chars were produced under identical conditions as the steam activated miACs, but in the absence of steam (i.e. carbonisation not gasification). A similar process was used in the production of steam activated miACs derived from the two industrial chars, with the char being used in place of VBC. Herein, the activated carbons produced using the steam activation procedure are assigned codes containing the prefix, AC; whereas the analogous chars were assigned the prefix, CH. In doing so, the AC and CH materials could be directly compared, and the influence of steam activation on the properties of the resulting materials could be differentiated from that associated with prolonged heat treatment at 1073 K. The sample codes also include the length of the gasification time (in min).

A commercially available activated carbon, Norit R2030 CO2 (referred to as AC-N), was used as a benchmark material throughout this thesis, as it is marketed as having an extremely high CO_2 capacity [8, 9].

2.3 Physically Activated Coal Derived Carbons

The VBC derived carbons were produced either by carbonisation under an N_2 flow at 1073 K for 45, 90, and 180 min to produce chars, or by activation under a flow of H_2O/N_2 at 1073 K for 45, 90 or 180 min to produce miACs.

2.3.1 Composition of Coal Derived Carbons

The yields and chemical composition of the homogenised VBC, thermally activated chars and steam activated miACs are presented in ***Table 2-1***. Ash analysis was performed thermogravimetrically (Mettler Toledo, TGA/DSC 1, Star* System) and elemental compositions were determined by dry combustion (Vario MICRO cube, Elementar), the details of which can be found in ***section 6.6.1***.

From ***Table 2-1***, it can be seen that the overall yield of ACs decreased as a function of increased gasification time (obtained yields were 45.0, 43.4, 39.9%, respectively). This was expected

since, in addition to pyrolysis, steam gasification converted the carbon groups at the surface of the parent material to CO_2(g) [1]. Varying only the pyrolysis time in the production of the CH series of materials, resulted in less variation in the mass of recovered material (44.8-46.6%), due to the fact that the carbonisation process only acted to remove the volatile matter present in the starting VBC [10]. As such, the char yields appear to be subject to minor variations in volatile matter within the coal sample used. Despite efforts to homogenise the starting coal briquettes by grinding (refer ***Section 6.4.1***), VBC is an inherently heterogeneous material.

Table 2-1 *~ Elemental and Ash Analysis of Coal Derived Physically Activated Carbons*

Sample	Reaction Time (min)	Yield (wt%)	Elemental Analysis (wt%, daf)				H/C Ratio	Ash (wt%)
			C	H	N	O_{diff}		
AC-N	-	-	76.3	0.8	1.0	21.9	0.12	10.9
VBC	-	-	61.4	4.4	0.6	33.5	0.86	0.4
CH-45	45	44.8	91.7	1.4	0.9	6.0	0.18	3.2
AC-45		45.0	90.5	1.3	0.9	7.4	0.17	5.3
CH-90	90	46.6	89.9	1.1	0.5	8.4	0.15	3.8
AC-90		43.4	82.2	1.3	0.7	15.7	0.19	6.4
CH-180	180	44.9	94.0	1.2	1.0	3.7	0.16	3.0
AC-180		39.9	89.6	1.2	0.9	8.4	0.16	7.3

VBC is known to have a low ash content [11]. The two coals used in the VBC briquettes blend both have a low ash content (***Appendix 1 – Parent Material Data Sheets***), and the blended sample was found to contain an ash content of 0.4 wt% (***Table 2-1***). All the carbons produced from the briquetted VBC contained ash contents less that 7.5 wt%, which was lower than that of the AC-N reference material (*Ash* = 10.9 wt%).

As expected, carbonisation or gasification of the starting VBC resulted in carbon enrichment of the materials (***Table 2-1***). ***Table 2-1*** also shows a large decrease in the oxygen content of the chars and ACs (O_{bulk} = 5-20 wt%) in comparison to the starting VBC (O_{bulk} = 33.5 wt%), due to the high oxygen content of the volatile matter removed during both of these processes. Furthermore, in comparing AC-45, AC-90 and AC-180 with their respective carbons from the CH series (CH-45, CH-90 and CH-180), it can be seen that there is a significant degree of O enrichment brought about by steam gasification (e.g. *O%* for AC-90 15.7 wt% vs. *O%* for CH-90 8.4 wt%). This was expected, since the gasification process is a partial oxidation process [12].

The composition of AC-N shows several quite distinct differences from VBC or any of the CH or miAC series. This is a result of having been produced from an entirely different carbon precursor, peat [13]. The bulk C and H content of AC-N is somewhat lower than the VBC derived carbon materials, but the most prominent difference that can be observed is the significantly higher bulk O content of AC-N. This has been attributed to the higher bulk O content of the peat used to produced AC-N, as it has previously been shown that under certain activation conditions peat based carbon materials with high bulk O are able to be obtained [13]. However, the precise details of how AC-N was produced are not available and as such this cannot be confirmed.

2.3.2 Surface Chemistry of Coal Derived Carbons

The determination of the surface chemistry of carbon materials is notoriously difficult; no one method alone is able to be used. Instead, results from multiple spectroscopic and wet chemical analyses are typically used. Due to the inherent difficulties of the wet chemical methods [14-16] that are often employed, here x-ray absorption spectroscopic methods (i.e. XPS, NEXAFS) were applied in order to determine the nature and identity of the functional groups at the AC surface.

2.3.2.1 X-ray Photoelectron Spectroscopy (XPS)

X-ray photoelectron spectroscopy (XPS) analysis allows the identification and quantification of functional groups present at the AC surface, through excitation of core level electrons. Photoelectrons from a carbon or oxygen atom in a particular functional group have a characteristic energy, which can also be quantified in order to determine its abundance at the AC surface. The XPS measurements were taken on a Kratos Axis HSi X-ray photoelectron spectrometer, as outlined in ***section 6.6.2.1***. The C 1s and O 1s XPS spectra obtained for the reference material, AC-N, are presented in ***Figure 2-2A-B***. The C 1s and O 1s XPS spectra of the thermally activated VBC derived chars (CH-45, CH-90 and CH-180) are presented in ***Figure 2-3A-F***, whilst those for the steam activated miACs (AC-45, AC-90 and AC-180) are shown in ***Figure 2-4A-F,*** with the results of the peak fitting reported in for all carbons presented in ***Table 2-2***. The peak fittings and assignments for both the C 1s and O 1s spectra were undertaken using methods reported in the literature [17-21], further details of which can be found in ***section 6.6.2.1***.

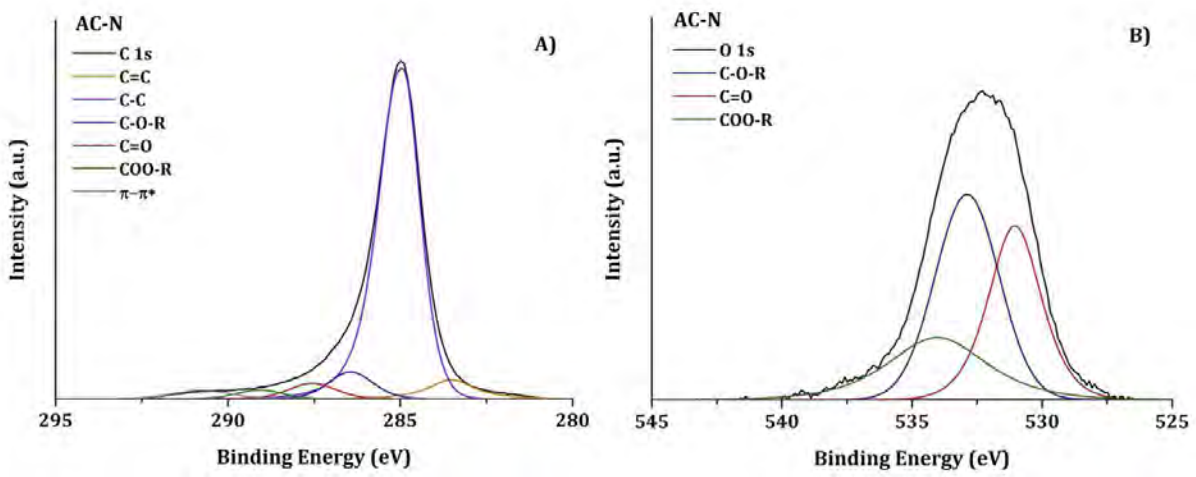

Figure 2-2 ~ *High Resolution XPS Spectra of C 1s & O 1s for AC-N. Shown are* ***A)*** *C 1s Spectra of AC-N,* ***B)*** *O 1s Spectra of AC-N*

Comparing the XPS results within the VBC derived CH (CH-45, CH-90 and CH-180) series and within the miAC (AC-45, AC-90 and AC-180) series, no regular pattern emerges as to the effect of carbonisation time or activation time on the surface concentration of C or O. However, for the same treatment time, the steam activated samples (AC-45, AC-90 and AC-180) always possessed lower surface O and higher surface C, relative to the analogous sample in the CH series. The bulk composition of the CH and miAC series mirrored this result (***Table 2-1***).

Overall the concentration of C=O and COO-R groups decrease as a result of steam activation, whilst the concentration of C-O-R groups increase (except for the CH-180/AC-180 pair). Interestingly, the ratio of C 1s to O 1s peak areas of the C-O-R peak for both CH-45 and AC-45 ***(Table 2-2***) were approximately 2:1. This strongly indicates that the C-O-R peak can mostly be attributed to ether functional groups, rather than hydroxyl groups as is more commonly associated with an AC surface [1]. Hydroxyl groups have lower hydrothermal stability above 973 K than ethers, and as such a decrease in hydroxyl groups is expected from the steam activation (performed at an activation temperature 1073 K). The concentrations of C=O and COO-R decrease as a result of steam activation (AC-45) relative to CH-45. This is with the expectation that the C=O and COO-R groups are not as hydrothermally stable as C-O-R groups. Moreover, the nitrogen content determined from the N 1s peak showed no change for AC-45, relative to CH-45.

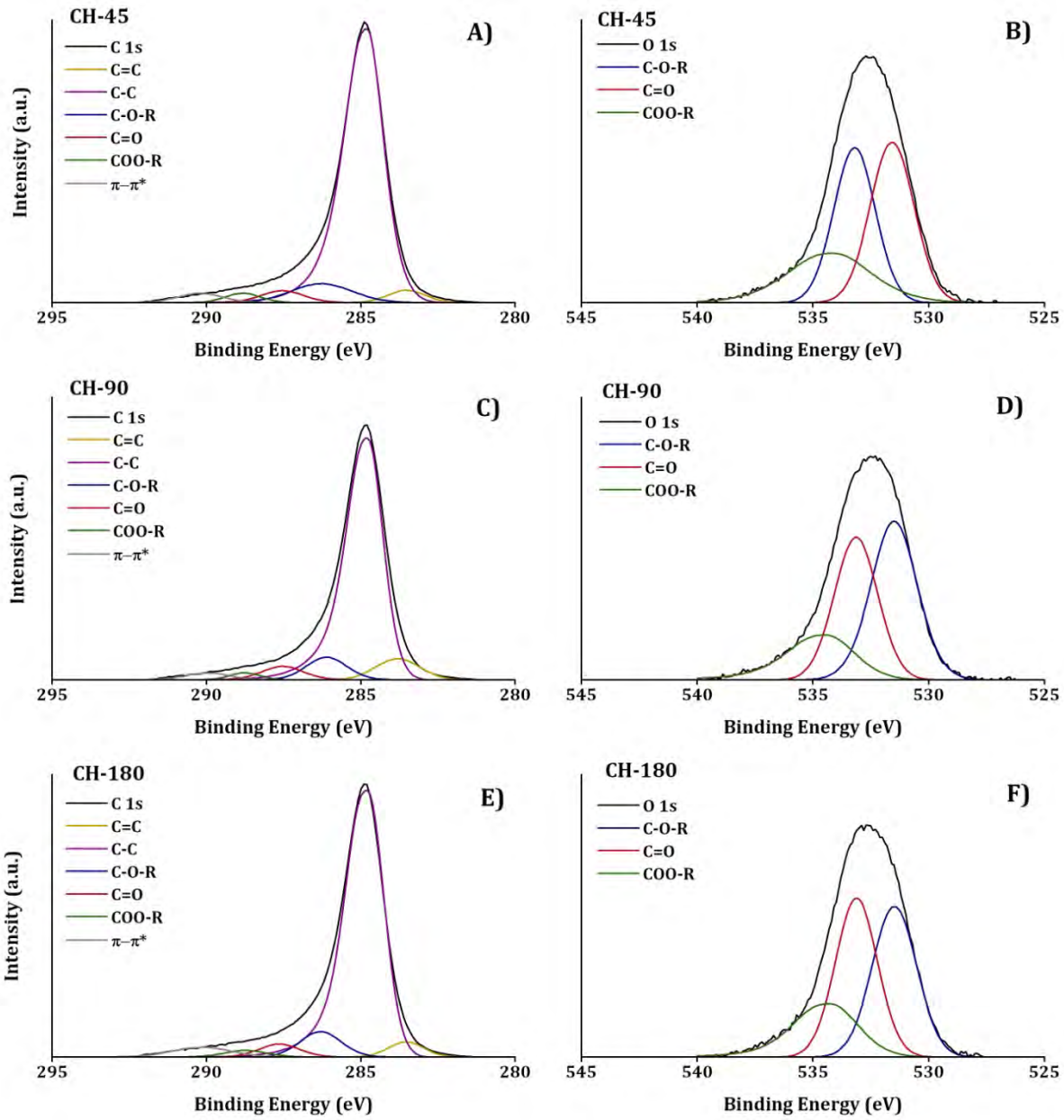

Figure 2-3 ~ *High Resolution XPS Spectra of C 1s and O 1s for CH-45, CH-90 and CH-180. Shown are* ***A)*** *C 1s Spectra of CH-45,* ***B)*** *O 1s Spectra of CH-45,* ***C)*** *C 1s Spectra of CH-90,* ***D)*** *O 1s Spectra of CH-90,* ***E)*** *C 1s Spectra of CH-180, and* ***B)*** *O 1s Spectra of CH-180*

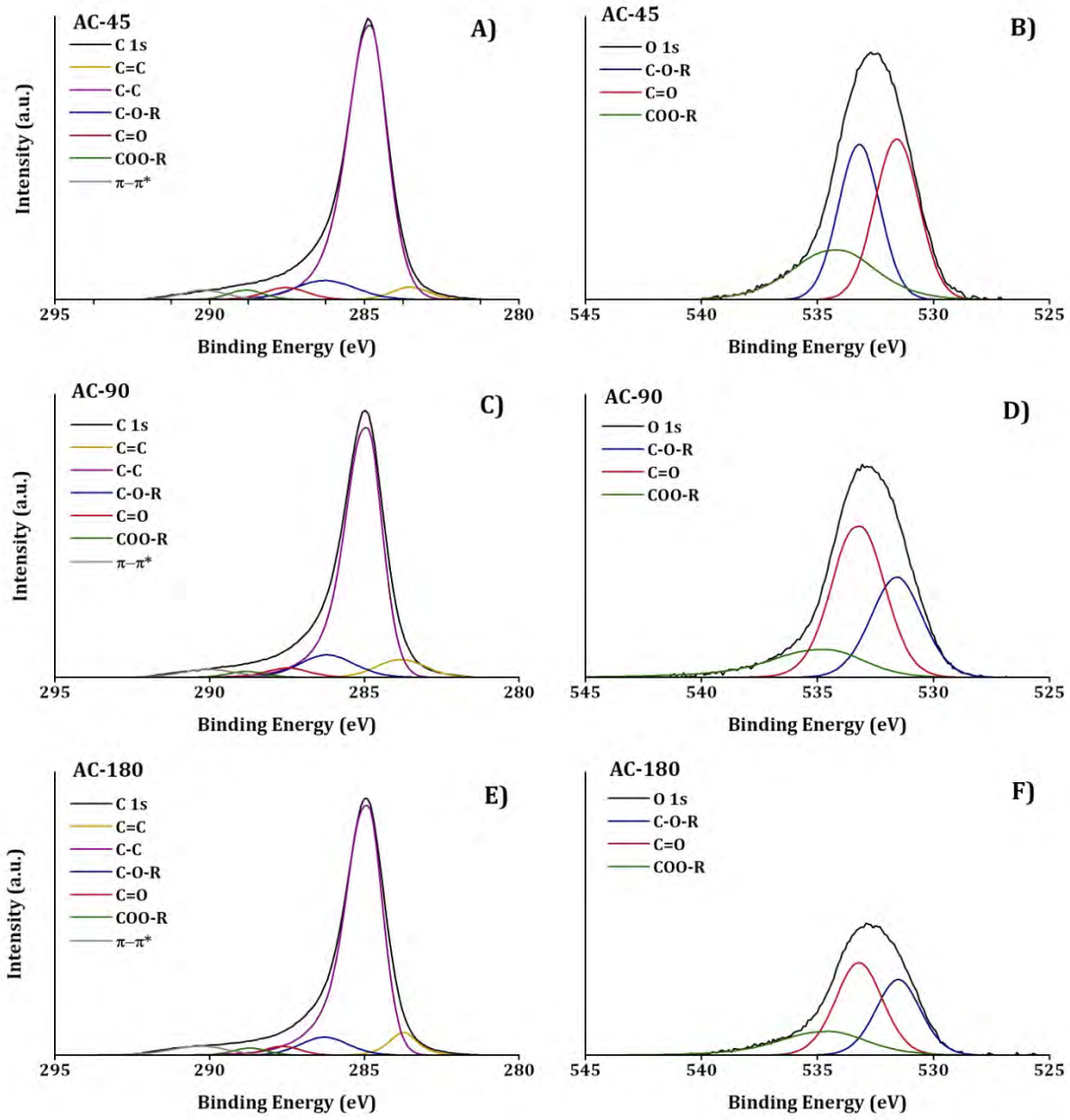

Figure 2-4 ~ *High Resolution XPS Spectra of C 1s and O 1s for AC-45, AC-90 and AC-180. Shown are* ***A)*** *C 1s Spectra of AC-45,* ***B)*** *O 1s Spectra of AC-45,* ***C)*** *C 1s Spectra of AC-90,* ***D)*** *O 1s Spectra of AC-90,* ***E)*** *C 1s Spectra of AC-180, and* ***F)*** *O 1s Spectra of AC-180*

Table 2-2 *~ XPS Peak Fitting for CH-45, AC-45, CH-90, AC-90, CH-180 and AC-180*

Peak Assignment	Binding Energy (eV)	Surface Concentration (at%)						
		AC-N	CH-45	AC-45	CH-90	AC-90	CH-180	AC-180
C 1s	284.9	91.95	90.12	91.21	90.11	90.16	90.80	92.49
C=C	283.8	5.08	2.93	4.45	6.70	6.04	3.54	5.07
C-C	284.8	72.91	72.00	73.10	68.69	68.28	71.07	72.95
C-O-R	286.1	6.01	7.22	7.38	6.66	8.48	6.90	6.37
C=O	287.5	3.60	3.23	2.70	4.15	2.80	3.50	2.36
COO-R	288.8	1.97	2.09	1.53	1.61	1.56	1.92	1.82
π–π^*	289.9	2.38	2.66	2.05	2.29	3.00	3.87	3.92
O 1s	531.9	7.83	9.37	8.28	9.42	9.16	8.88	6.71
C=O	531.5	3.50	3.71	2.67	4.14	2.96	3.50	2.30
C-O-R	533.1	2.58	3.40	4.05	3.47	4.60	3.49	2.94
COO-R	534.4	1.75	2.26	1.55	1.80	1.59	1.89	1.47
N 1s	400.9	0.22	0.51	0.51	0.47	0.68	0.32	0.80

Comparing the 90 min thermal versus steam activation (resulting in CH-90 and AC-90, respectively), a decrease is observed in both the C=O and COO-R peaks (***Figure 2-3D*** and ***Figure 2-4D***), as a result of steam activation. The C=O peak decreased by 29%, with a simultaneous increase of 25% in the C-O-R peak. Overall, only very minor increases were observed in the surface N and surface C concentrations for CH-90 and AC-90, as determined from the N 1s and C 1s XPS.

For the CH-180/AC-180 pair (***Figure 2-3F*** and ***Figure 2-4F***) similar decreases in the peak areas corresponding to C=O and COO-R groups were observed as a result of the steam activation (***Table 2-2***). However, for the CH-45/AC-45 and CH-90/AC-90 pairs there was an associated increase in the concentration of C-O-R groups, which was not observed for the CH-180/AC-180 pair (***Table 2-2***). Instead, there was a decrease in C-O-R groups, indicating that the increased carbonisation/activation time resulted in the removal of the C-O-R groups. Furthermore, for the CH-180/AC-180 pair there was an increase in surface nitrogen of approximately 0.5 at% as a result of steam activation.

Relative to most of the steam activated miACs and their analogues from the CH series; AC-N has a lower surface oxygen content. Such a low surface oxygen content is expected to impact the CO_2 adsorption capacity of AC-N compared to the steam activated miACs, as this will also result in a decrease in oxygenated functional groups with a high affinity for CO_2 [1]. The distribution of

oxygenated functional groups on the surface of AC-N reveals that it possesses lower C-O-R groups than the miACs. Whether the C-O-R groups are due to ether or hydroxyl groups is expected to have an impact on the CO_2 adsorption behaviour of AC-N, since hydroxyl groups have a higher affinity for CO_2 over any other oxygenated functional group type [1].

Some indications of the identities of the unknown groups are implied by the ratio of peak areas for C 1s to O 1s, for the peaks assigned to these groups. For example, the C 1s to O 1s ratio for the C-O-R peaks is 2:1, suggesting that there is twice as much surface C bound to these groups, than surface O. This implies that the identity of the R group in this case is a C atom of an ether group. To more definitively assign these surface functional groups, near edge x-ray absorption fine structure (NEXAFS) spectroscopy was used.

2.3.2.2 Near Edge X-ray Absorption Fine Structure (NEXAFS) Spectroscopy

Near edge X-ray absorption fine structure (NEXAFS) spectroscopy is an incredibly powerful tool for determining the identity of the functional groups at a carbon surface, with greater resolution than XPS. This is achieved by irradiating the sample with a range of energies close to those of the K edge in the case here. This results in better resolution of the different energies of the photoelectrons and in turn more information about the different types of bonds to the element being investigated. The carbon and oxygen K-edge NEXAFS spectra were obtained using the soft X-ray (SXR) beamline at the Australian Synchrotron. The C 1s and O 1s K-edge NEXAFS spectra for AC-N are reported in ***Figure 2-5***, with the results of the peak fitting presented in ***Table 2-3***. The NEXAFS spectra obtained for the steam activated VBC derived miACs and chars CH-45, AC-45, CH-90, AC-90, CH-180 and AC-180 are presented in ***Figure 2-6***, with the peak fitting shown in ***Table 2-3***. The complete fitting for both the C 1s and O 1s spectra can be found in ***Appendix 2 – NEXAFS Spectroscopy Peak Fitting***, for all of the carbon materials investigated. The main purpose of the NEXAFS investigation was to gain further information pertaining to the identity of functional groups that could not be properly resolved by XPS alone, such as the distinction between ethers and hydroxyls or ketones and aldehydes.

As was noted in ***section 1.9.2.3*** and ***section 6.6.2.2*** NEXAFS spectroscopy is only a semi-quantifiable technique. As such, the results of the peak fitting are presented as percent peak area. XPS and NEXAFS are complimentary techniques, however owing to the complexity of the surface chemistry of carbonaceous materials; it can be difficult to directly correlate the observations made. This is due to the differences in the depth of x-ray penetration into the carbon materials. For XPS this is commonly in the vicinity of 10 nm and for NEXAFS spectroscopy this can be upwards of 100 nm.

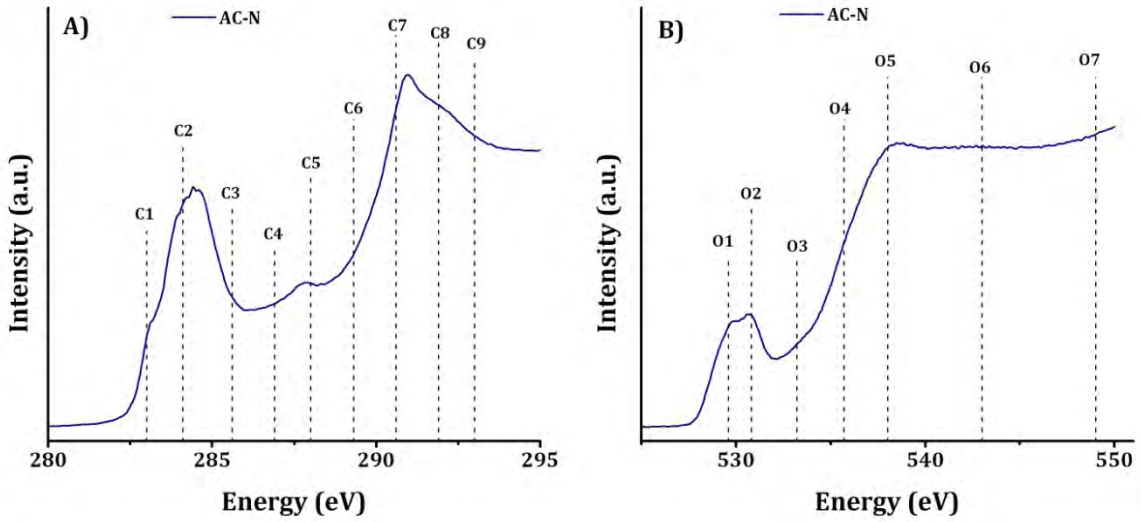

Figure 2-5 *~ C 1s and O 1s NEXAFS Spectra of AC-N. Shown are* ***A)*** *C 1s spectra, and* ***B)*** *O 1s spectra*

The C 1s and O 1s NEXAFS spectra for CH-45 and AC-45 (***Figure 2-6A-B*** and ***Table 2-3***) indicate minor variation in the surface chemistry between these two carbons, a fact also supported by the XPS analysis of these carbon materials (***Figure 2-3A-B***, ***Figure 2-4A-B*** and ***Table 2-2***). One difference that was observed was in both the C 1s and O 1s peaks assigned to aldehyde groups (***C6*** and ***O1***). This was expressed as a ~ 2.5% decrease in both the ***C6*** and ***O1*** peaks of AC-45 ($C6_{AC\text{-}45}$=14.4%, $O1_{AC\text{-}45}$=10.0%) compared to CH-45 ($C6_{CH\text{-}45}$=16.9%, $O1_{CH\text{-}45}$=12.4%). Interestingly, the decrease in aldehyde groups was not accompanied by any significant change in either ketone (***C3*** or ***O2***) or ether (***C5***, ***C8***, ***O3*** or ***O8***) groups. This is a strong indication that the changes in aldehyde groups between AC-45 and CH-45 did not result in the formation of another functional group, but were merely the result of fewer aldehyde groups forming during the 45 min steam activation. Moreover, the exact groups that give rise to the C-O-R peaks in the C 1s and O 1s spectra from the XPS of both AC-45 and CH-45 was able to be confirmed to be due to the presence of both ether (***C5***, ***C8***, ***O3*** and ***O6***) and hydroxyl (***C3***, ***C6***, ***O4*** and ***O7***) groups.

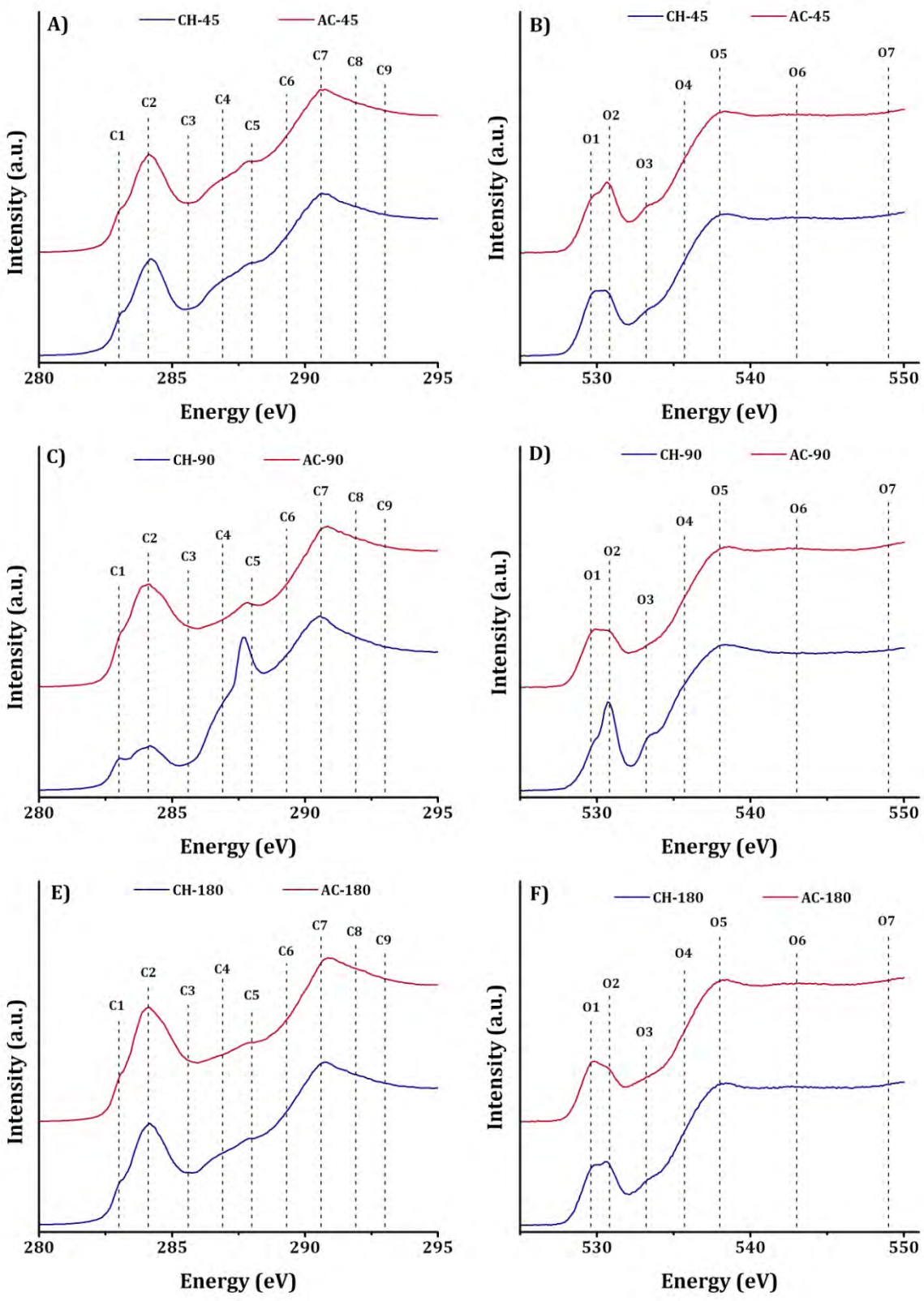

Figure 2-6 *~ C 1s & O 1s K edge NEXAFS Spectra CH-45, AC-45, CH-90, AC-90, CH-180 & AC-180. Shown are* ***A)*** *C 1s K Edge NEXAFS Spectra of CH-45 & AC-45,* ***B)*** *O 1s K Edge NEXAFS Spectra of CH-45 & AC-45,* ***C)*** *C 1s K Edge NEXAFS Spectra of CH-90 & AC-90,* ***D)*** *O 1s K Edge NEXAFS Spectra of CH-90 & AC-90,* ***E)*** *C 1s K Edge NEXAFS Spectra of CH-180 & AC-180, and* ***F)*** *O 1s K Edge NEXAFS Spectra of CH-180 & AC-180*

Table 2-3 ~ *C 1s & O 1s K Edge NEXAFS Peak Fitting of CH-45, AC-45, CH-90, AC-90, CH-180 & AC-180*

K Edge	Name	Group		Assignment	Photon Energy (eV)	Peak Area %						
						AC-N	CH-45	AC-45	CH-90	AC-90	CH-180	AC-180
C 1s	C1	C=O	π*	Carbonyl substituted aromatic carbon (quinone)	283.0	12.5	2.0	1.6	1.0	1.1	0.7	0.5
	C2	C-C C=C	π*	Aromatic carbon, or aliphatic substituted aromatic carbon	284.1	32.7	23.4	24.9	13.9	31.3	28.9	32.6
	C3	C-OH C=O	π*	Phenolic or ketonic carbon	285.6	6.8	6.7	7.8	7.6	8.5	5.8	8.1
	C4	COOH COO	π*	Carboxylic acid or lactone carbon	286.9	9.3	13.8	13.5	8.4	11.2	13.5	12.0
	C5	C-O-C	π*	Cyclic ether carbon	288.0	7.5	12.3	11.6	7.7	13.3	10.7	9.4
	C6	C-OH C=O	π*	Aldhyde or hydroxyl substituted aliphatic carbon	289.3	7.4	16.9	14.4	18.2	10.5	15.4	12.0
	C7	COOH COO	σ*	Carboxylic acid or lactone carbon	290.6	11.5	15.8	16.6	31.1	15.2	15.8	15.3
	C8	C-O-C	σ*	Cyclic ether carbon	291.9	11.2	5.7	6.0	7.4	6.4	6.2	7.1
	C9	C-C C=C	σ*	Aromatic carbon (long range order)	293.0	1.2	3.3	3.5	4.6	2.5	3.1	3.1
O 1s	O1	C=O	π*	Aliphatic (linear or cyclic) aldehyde oxygen	529.6	11.2	12.4	10.0	5.8	6.4	11.4	13.1
	O2	C=O	π*	Carbonyl oxygen (ketonic or carboxylic acid)	530.8	8.1	10.0	12.3	13.9	16.5	10.6	7.3
	O3	C-O-C	π*	Aliphatic cyclic ether	532.7	11.9	14.3	14.9	21.3	16.4	14.1	15.7
	O4	C-OH	π*	Hydroxyl oxygen (alcohol)	535.7	33.0	31.7	32.1	20.2	24.6	31.3	31.3
	O5	C-OH C=O	σ*	Hydroxyl or carbonyl oxygen of carboxylic acid	538.0	20.5	21.8	21.1	28.8	17.0	22.4	21.7
	O6	C-O-C	σ*	Aromatic cyclic ether	543.0	2.8	6.0	6.2	5.5	14.7	6.6	6.6
	O7	C-OH	σ*	Phenolic oxygen	549.8	12.3	3.8	3.5	4.5	4.5	3.6	4.3

From the NEXAFS investigation of the surface chemistry of the CH-90/AC-90 pair (***Figure 2-6A-B*** and ***Table 2-3***), a greater degree of variation in the percentage peak area of several groups was observed. Compared to the other chars (CH-45 and CH-180) the surface distribution of aromatic carbon (***C2***) was low for CH-90. Moreover, the ***C6*** peak assigned to aldehydes/hydroxyls of AC-90 (10.5%) was almost half that of CH-90 (18.2%), without any apparent change in the ***O1*** peak, assigned to aldehydes alone. This is evidence that the hydroxyl (not aldehyde) content has diminished. However, the picture becomes somewhat complicated at this point, as there is no change in the ***O4*** peak, assigned to hydroxyl groups. However, a decrease in the ***O5*** peak (assigned to hydroxyl or carbonyl oxygen of carboxylic acids) is

observed for AC-90, relative to CH-90. The decrease in the ***O5*** peak is accompanied by a decrease in the ***C7***, but not ***C4*** peak, which are both assigned to different resonant forms of carboxylic acids. The proposed explanation for these results is that the carboxylic acid groups, undergo dehydroxylation to carbonyl groups (ketones or aldehydes). It appears therefore that AC-90 and CH-90 are very different materials and, under the different sets of reaction conditions, two very different distributions of surface chemical functionality are formed. To more fully understand what is at play here would require the use of an *in situ* XAS (most likely NEXAFS) investigation so that the evolution of surface chemical species could be studied throughout the activation process. The increase in the aromatic ***C2*** peak of AC-90 compared to CH-90 was more than twofold, yet no significant increase the aromatic ***C9*** peak of AC-90 was observed relative to CH-90. This would suggest that, while the proportion of aromatic carbon has increased, there has been no increase in the long rang order such as the significant development of distinct graphitic domains. The C 1s NEXAFS spectra obtained for AC-90 also showed an overall increase in the distribution of cyclic ethers (***C5***) compared to CH-90, which can be understood in more detail by analysis of the O 1s spectra. A significant increase in aromatic cyclic ethers (***O6***) was accompanied by a decrease in aliphatic cyclic ethers (***O3***), which implied that the steam activation process resulted in higher quantities of hydrothermally stable aromatic ethers. Thus the hydroxyl and ether groups that give rise to the C-O-R peak in the XPS are able to be clearly identified by NEXAFS spectroscopy.

The changes in the distribution of functional groups of CH-180 compared to AC-180, are much less pronounced than those of the CH-90/AC-90 pair, but more so than the CH-45/AC-45 pair. An increase in the percentage peak area of the ***O1*** and ***O2*** peaks (assigned to aldehydes and ketones, respectively) is observed for AC-180 relative to CH-180. There is an increase in the ***C2*** peak of 1.7%, with a decrease in the ***C1*** peak of 3.3%. Interestingly a decrease in the ***C6*** peak allocated to aldehydes/hydroxyls of 3.4% is observed, with a decrease in the ***C3*** peak of ketone/phenols of 2.3% is observed. However, although some ambiguities remain regarding the differences observed between the C 1s and O 1s spectra for the CH-180/AC-180 pair, both hydroxyl and ether groups (C-O-R peaks from XPS, ***Table 2-2***) were able to be confirmed as being present on the surface of both CH-180 and AC-180.

NEXAFS spectroscopy was successfully used to further identify several functional groups of interest from the XPS (C=O, C-O-R and COO-R) investigation of the surface chemistry of the CH series and the miAC series. The most important identification was of the groups responsible for the C-O-R peak in XPS, as this group was found to be present in the highest concentrations at the carbon surface. The two groups to which the C-O-R peak was attributed were to hydroxyl (C-O-H) and ether (C-O-C) groups. From NEXAFS spectroscopy it was also possible to determine that

the C=O peaks from XPS was due to both ketone and aldehyde groups. It was also shown that for treatment times of 45 and 90 min, there was a slightly higher proportion of aldehydes, whilst for treatment times of 180 min seemed to favour ketones. Furthermore, the COO-R peak from XPS was able to be confirmed as being due to carboxylic acid groups, as is common on the surface of ACs.

2.3.3 Structure of Coal Derived Carbons

Gas physisorption methods were primarily employed in order to determine the structure of the physically activated miACs; however, electron microscopy methods were also employed in addition to laser and X-ray diffraction methods.

2.3.3.1 Chemical Structure of Coal Derived Carbons

2.3.3.1.1 Raman Spectroscopy

Important information about the chemical structure of a material can be obtained from the interaction of the chemical bonds with electromagnetic waves from the inelastic (Raman) scattering of laser light. Such information can be vital for the characterisation of carbon materials since it provides information on the extent of order/disorder, amount of graphite-like lattice structures (***section 1.9.3.1.1***). The Raman spectra obtained for the ACs that were physically activated were taken on a confocal micro-Raman system (Renshaw), the details of which are given in ***Section 6.6.3.1.1***. The Raman spectrum obtained for AC-N is shown below in ***Figure 2-7***, while the spectra obtained for the ACs derived directly from VBC are presented with their corresponding chars in ***Figure 2-8***. All spectra were normalised, baseline corrected and deconvoluted. The subsequent peak fitting was undertaken in a manner similar to Sadezky *et al* [22] and Shimodaira *et al* [23] (***Table 1-4***). The results of the peak fitting for the carbons presented in both ***Figure 2-7*** and ***Figure 2-8*** are reported in ***Table 2-4***.

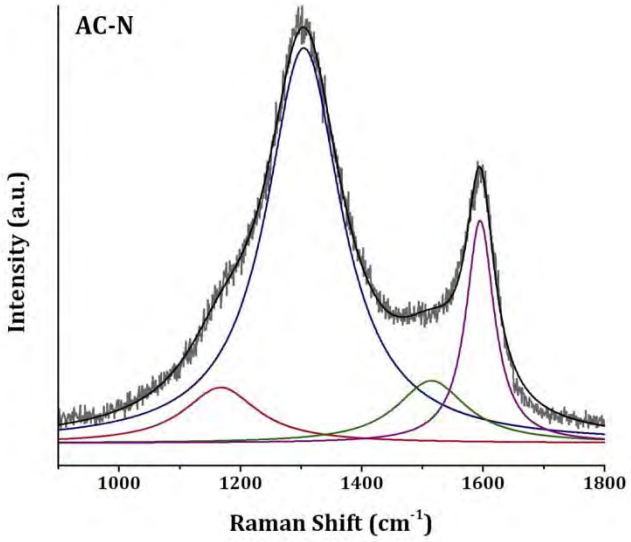

Figure 2-7 *~ Deconvoluted Raman Spectra of AC-N. Shown are the peaks for the (—) Normalised Data, (—) Sum of Deconvoluted Peaks, (—) S peak, (—) D peak, (—) A peak, (—)*

The most prominent feature of all the Raman spectra shown in both ***Figure 2-7*** and ***Figure 2-8*** is the ***D*** peak, assigned to disordered graphitic carbon, as such it is clear that carbon of this type makes up the bulk phase of such carbon materials. It can be seen that for a treatment time of 45 min, the presence or absence of steam does not influence the amount of non-heteroatom containing disordered graphitic lattices, since the ***D*** peak areas are similar for the steam activated (AC-45) and carbonised (CH-45) materials. On the other hand, the amount of disordered graphitic lattices containing heteroatoms decreased for AC-45 relative to CH-45, as characterised by a decrease in the ***S*** peak area. The ***S*** peak has been attributed to the presence aromatic ethers by Li *et al* [24], and in general the heteroatoms bound to the graphene layer edges are considered to be oxygen. Furthermore, increases were observed in the areas of both the ***A*** and ***G*** peaks. This indicates that the presence of steam during the activation process (AC-45) results in carbons with a higher degree of amorphous (***A***) and graphitic carbon (ideal graphitic lattices, ***G***) compared to CH-45, which possesses a higher degree of moderately ordered carbon (characterised by the presence of disordered graphitic lattices, ***S*** and ***D***).

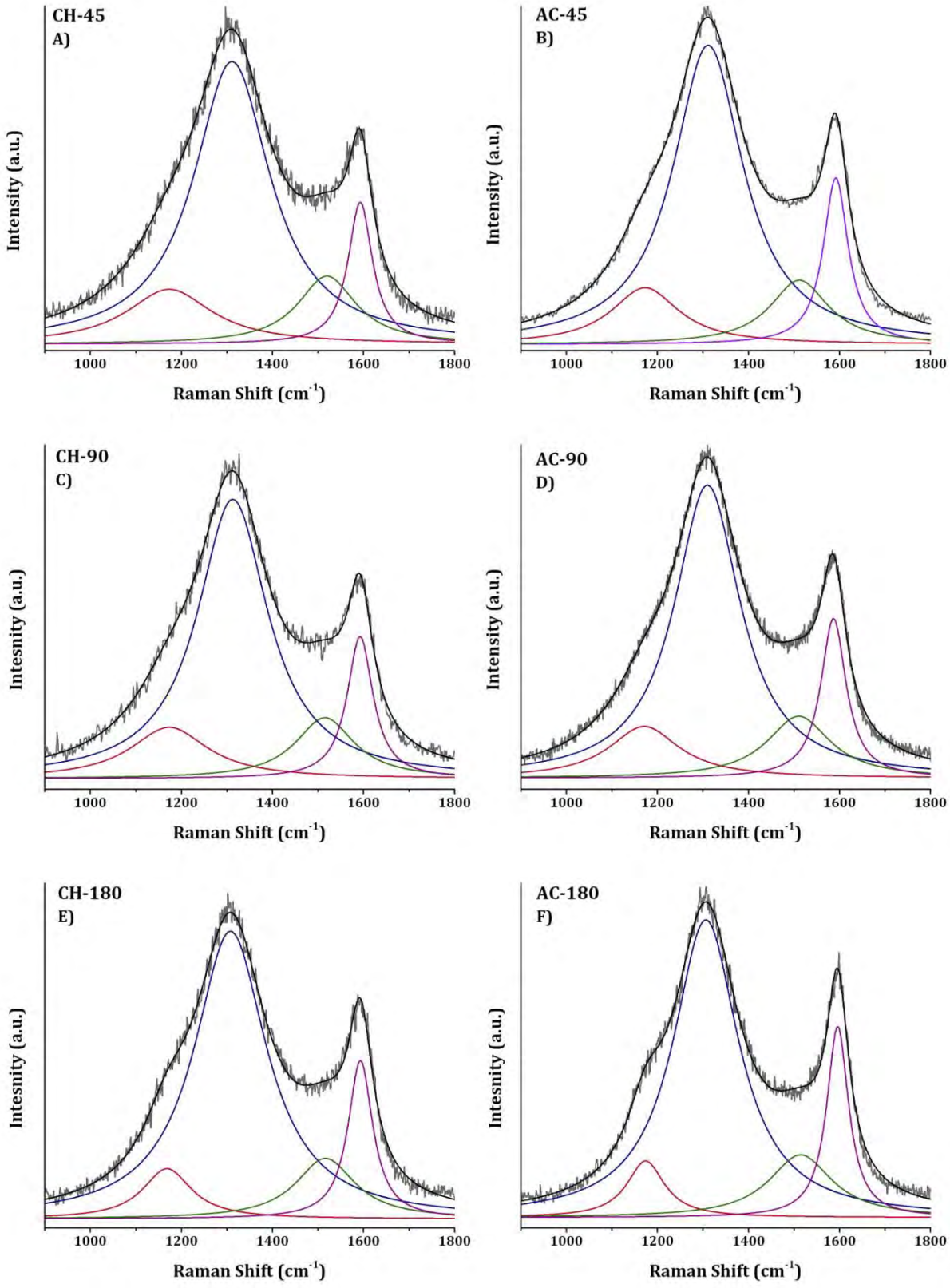

Figure 2-8 ~ *Deconvoluted Raman Spectra of CH-45, AC-45, CH-90, AC-90, CH-180 & AC-180. Shown are the peaks for the (—) Normalised Data, (—) Sum of Deconvoluted Peaks, (—) S peak, (—) D peak, (—) A peak, (—) G peak* ***A)*** *CH-45,* ***B)*** *AC-45,* ***C)*** *CH-90,* ***D)*** *AC-90,* ***E)*** *CH-180, and* ***F)*** *AC-180*

Table 2-4 *~ Raman Peak Fitting Tables for the VBC derived steam activated miACs*

Sample Name	Peak Area			
	S Disordered Graphitic Lattice*	**D** Disordered Graphitic Lattice†	**A** Amorphous Carbon	**G** Ideal Graphitic Lattice
AC-N	9.2	66.7	9.8	14.1
CH-45	13.9	64.0	11.7	10.3
AC-45	11.7	64.0	12.6	11.5
CH-90	12.9	63.6	11.6	11.8
AC-90	11.7	62.4	12.7	13.0
CH-180	8.0	67.6	11.7	12.7
AC-180	7.1	65.3	13.3	14.0

* *Heteroatoms Bound to Graphene Layer Edges*

† *Graphene Layer Edges*

A similar overall result was observed for the CH-90/AC-90 pair, as can be seen from ***Table 2-4***. However, the decrease in the area of the ***S*** peak of AC-90 relative to CH-90 is larger than AC-45/CH-45, and is accompanied by a decrease in the area of the ***D*** peak. This indicates a more substantial decrease in heteroatoms bound to graphene layer edges as well as an overall decrease in graphene layer edges. Interestingly, there are only very minor changes in the amount of amorphous carbon (***A*** peak) present within the carbons as a result of increasing the carbonisation time or activation time from 45 to 90 min. Furthermore, the amount of ideal graphitic lattice edges (***G*** peak) increased as a function of increasing carbonisation or activation time, and through the utilisation of steam during activation. Collectively, the decreases in the areas of the ***S*** and ***D*** peaks, and increases in the ***G*** peak of AC-90 relative to CH-90 (and also the CH-45/AC-45 pair) indicate that the overall structural order of the resulting materials was enhanced when the carbonisation/activation time was increased from 45 to 90 min and when steam was used during the activation.

The differences in the chemical structure determined by Raman spectroscopy for materials prepared using carbonisation/activation times of 45 and 90 min were less significant than when the carbonisation/activation time was extended further to 180 min (***Table 2-4***). In ***Figure 2-8E-F*** (CH-180/AC-180), the ***S*** peak became sharper which indicated an increase in the orientation of some of the disordered graphitic lattices. An increase in the ***G*** peak was also observed, and

was attributed to an increase in the ordered graphitic phase. Together the changes in the ***S*** and ***G*** peaks are the result of an overall increase in the ordered graphitic lattices, whilst showing a decrease in the disordered ones, thus the graphitic lattices of the carbons are reorienting/aligning to become more ordered. Moreover, the area of the ***S*** peak of the CH-180/AC-180 pair, decreased by approximately a third, with an increase of similar magnitude in the ***D*** peak. This suggests that in addition to the reorienting of the disordered graphitic lattices (change in ***S*** peak shape), there has been an overall decrease in the amount of heteroatoms bound to graphene layer edges, while the overall amount of graphene layer edges remains constant (***S*** and ***D*** peak areas combined).

The area of the ***S*** peak in the spectrum obtained for AC-N is significantly smaller than the miACs and CH series carbons reacted for 45 or 90 min. This may suggest a lower degree of heteroatoms bound to graphene layer edges, but from the increased area of the ***D*** peaks it can be seen that there is a higher overall amount of graphene layer edges, relative to the ACs and chars reacted for 45 and 90 min. Furthermore, the ***A*** peak of AC-N is lower than any of the steam activated miACs and chars, indicating that AC-N is a less amorphous carbon than those produced here from VBC.

In summation, with the overall increases in the areas of the ***G*** and ***A*** peaks as a result of both carbonisation/activation time and the presence of steam during activation, and decreases in the area of the ***S*** and ***D*** peaks with increasing carbonisation/activation time and the presence of steam; it can be seen that increasing the carbonisation/activation time or by using steam during activation results in an overall increase in the level of order present within the resulting carbons (***Table 2-4***).

2.3.3.1.2 Powder X-ray Diffraction (PXRD)

X-ray diffraction (XRD) like Raman spectroscopy allows for greater insight into the chemical structure of ACs. However, in Raman spectroscopy the electromagnetic waves interact with the bonds of the material, where is in XRD they interact with the atoms themselves. The XRD of the physically activated coal and char carbons are presented below in ***Figure 2-21A-D***. From the spectra in ***Figure 2-21***, it is clear that there is no extensive crystallinity in any of the samples. The plots are typical of amorphous carbons [25-27].

The XRD patterns of the steam activated miACs presented three minor, but distinct peaks, all common to highly amorphous carbons [28]. The most predominant of these peaks was centred at 24° 2θ, and is attributed to the reflection of the ***002*** plane [28]. The second major peak to present in the XRD patterns of the steam activated miACs was centred at 43° 2θ, and can be

attributed to the ***100*** and ***101*** reflections that overlap [25, 28]. The third peak to be observed from the XRD patterns presented in ***Figure 2-21*** was the very sharp peak centred at 26° 2θ, and is often hidden under the ***002*** peak at 24° 2θ. This third peak is exhibited more often in amorphous carbons derived from coal or bio-mass sources, and is attributed to amorphous metal oxides (***MO***) (e.g. SiO_2, K_2O, Na_2O or Al_2O_3), most commonly aluminosilicates [29]. The observations of the ***002***, ***100*** and ***101*** peaks are typical of the diffraction pattern of amorphous carbons [25, 27-32]. The ***002*** reflection is the result of the diffraction by the atoms of parallel graphitic domains. These well defined graphitic domains are also a strong indication of the presence of micropores, which in ACs is known to be present between parallel graphene sheets [25]. The presence of the ***100*** and ***101*** peaks are indicative of an increase in the lateral order within the graphitic domains [30, 32]. However, no significant changes in the intensity of either the ***002*** or ***10*** peaks are clearly apparent, indicating that there have been no significant changes in the long range order of the CH or miAC series that can be distinguished by XRD.

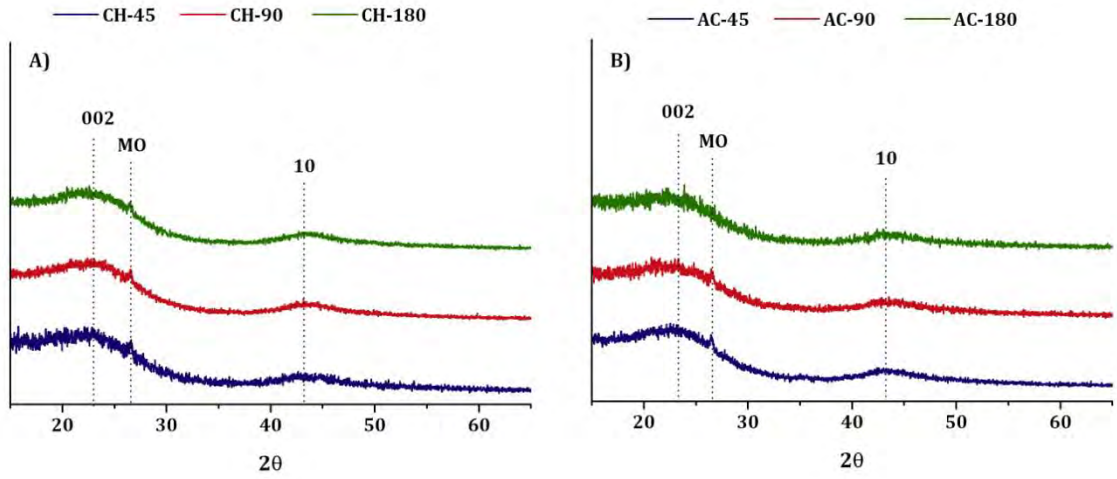

Figure 2-9 *~ X-ray Diffraction of Steam Activated miACs and Chars Derived from VBC. Shown are the XRD Patterns for* ***A)*** *CH-45, CH-90 and CH-180, and* ***B)*** *AC-45, AC-90 and AC-180*

2.3.3.2 Physical Structure of Coal Derived Carbons

2.3.3.2.1 Gas physisorption and displacement

The adsorption of gas at or near their boiling point allows for gas condensation within the pores of porous materials. The way in which this occurs can be studied and the information obtained allows for a great deal of information pertaining to the diameter and shape of the pores to be determined (ref to ***section 6.6.3.2.1*** for more information). The surface area and porosity of each AC was determined from the adsorption isotherms of N_2 and CO_2 at 77 and 273 K, and the

BET surface area, DR surface area, DR micropore volumes and BHJ mesopore volumes are presented in ***Table 2-11***. The details of these calculations can be found in ***section 6.6.3.2.1***.

Table 2-5 ~ *Surface Area, Pore Volume & True Density of VBC Steam Activated miACs*

Sample Name	Surface Area (m^2/g)		Pore Volume (cm^3/g)				True Density (g/cm^3)
	CO_2	N_2	CO_2	N_2			
	DR	BET	V_{micro}	V_{micro}	V_{meso}	V_{total}	
VBC	148	-	0.05	-	-	-	1.40
AC-N	799	645	0.26	0.36	0.12	0.38	1.48
CH-45	620	263	0.20	0.14	0.04	0.17	1.84
AC-45	690	358	0.22	0.19	0.08	0.23	1.88
CH-90	640	282	0.21	0.16	0.06	0.18	1.85
AC-90	696	397	0.23	0.20	0.13	0.24	1.90
CH-180	626	304	0.21	0.16	0.06	0.20	1.84
AC-180	758	486	0.25	0.25	0.21	0.35	1.82

CO_2 Physisorption

The CO_2 adsorption isotherms were measured on a TriStar II 3020 (Micromeritics) at 273 K using an ice bath to maintain the temperature. Measurements were made on a relative pressure basis, over a P/P_0 range of 0.00-0.03. The CO_2 isotherms for the miACs produced directly from VBC are presented in ***Figure 2-10***, those for the miACs produced from the supplied VBC-derived chars are presented in ***Figure 2-22***, and the surface area and limiting micropore volumes (determined using the DR equation) are presented in ***Table 2-11***.

Referring to ***Figure 2-10***, the CO_2 isotherms for the carbons produced directly from VBC displayed typical type ***I*** isotherms (Langmuir-like) – with higher CO_2 uptake at higher relative pressures**.** By comparing the CO_2 uptakes of the carbons produced, compared with the CO_2 uptake of the parent VBC sample, it can be seen that there is an obvious increase in uptake due to the removal of the volatile matter in the coal (CH series) and subsequent gasification (AC series) of the carbon surface. The effect of the presence of steam in the gas stream, on the development of microporosity can be seen in ***Figure 2-10*** from the increased adsorption at

higher relative pressures (P/P_0 0.015-0.030), indicating there is an increase in the volume of larger micropores.

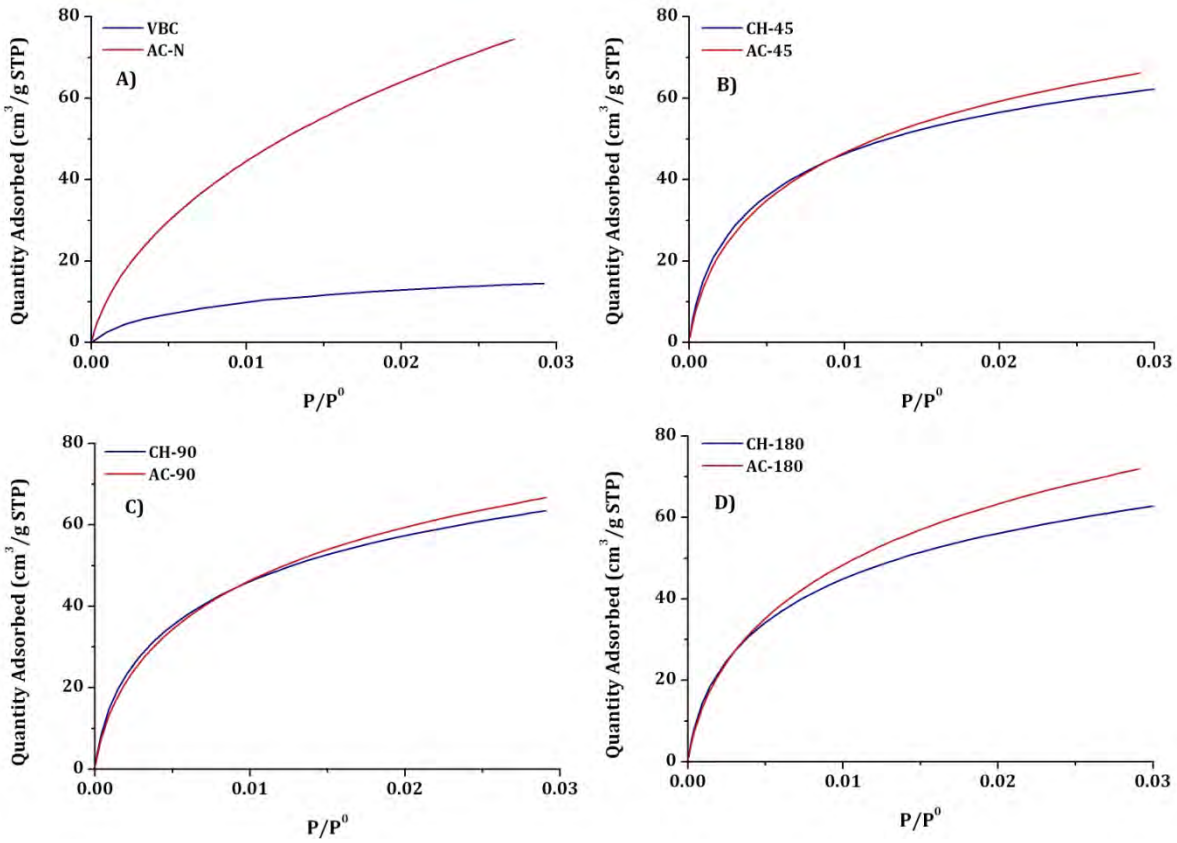

Figure 2-10 *~ CO_2 Adsorption Isotherms at 273 K of Carbonised and Steam Activated VBC. Shown are the CO_2 Isotherms of* ***A)*** *VBC and AC-N,* ***B)*** *CH-45 and AC-45,* ***C)*** *CH-90 and AC-90,* ***D)*** *CH-180 and AC-180*

N_2 Physisorption

Physisorption of N_2 was undertaken in a TriStar II 3020 (Micromeritics) at 77 K using a Dewar of liquid nitrogen to maintain the temperature. Measurements were made over a P/P_0 range of 0.050-0.995. N_2 Isotherms and PSDs measured for the carbons derived directly from VBC, are presented in ***Figure 2-12A-F*** for the carbons treated for 45, 90 and 180 min respectively. Furthermore, the N_2 adsorption isotherm and PSD for the AC-N benchmark carbon is presented in ***Figure 2-11A-B***.

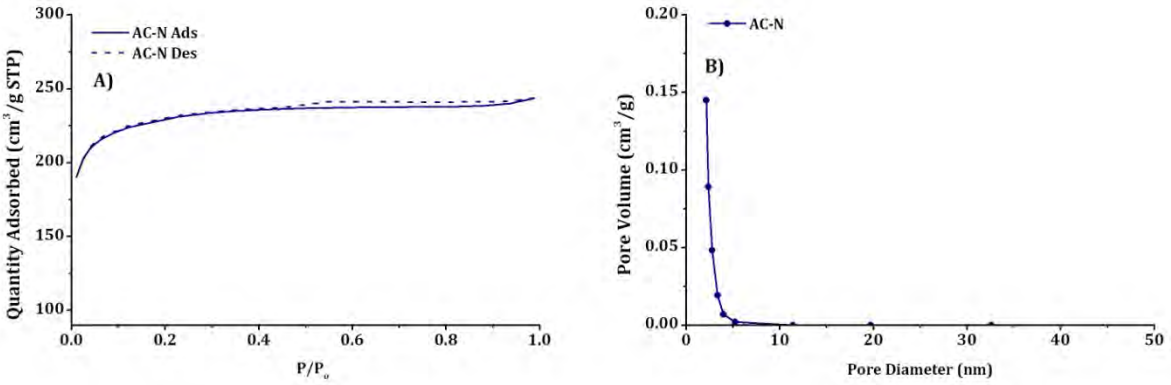

Figure 2-11 *~ N_2 Adsorption-Desorption Isotherm and PSD taken at 77 K for AC-N. Shown are* ***A)*** *N_2 Adsorption Isotherm for AC-N, and* ***B)*** *N_2 PSD for AC-N*

Referring to ***Figure 2-12***, all carbons displayed typical type ***II*** isotherms [33], with type ***H4*** hysteresis loops [34]. Collectively, these results indicate that the materials possess both micro- and mesopores with slit-shaped pore morphologies. From ***Figure 2-12***, it can be observed that the hysteresis loops of the CH series do not fully close, whereas those of the ACs do close at relative pressures close to P/P_o= 0.45. This type of behaviour has been previously reported in the literature and described as low pressure hysteresis (LPH) [35-37]. The underlying phenomena that gives rise to LPH in ACs has been thoroughly discussed for example by Silverstre-Albero *et al* (2012) [35], and is attributed to one of two main causes. The first cause is from swelling of non-ridged pores, however, this is not a common occurrence in ACs. The second and more likely cause of LPH in the cases observed here is due to equilibrium within the micropores having not been initially achieved. This can arise from either the pore opening being close in diameter to that of the adsorbate, or from He entrapment. The only option to counteract such behaviour is to submit the sample to a second round of degassing once the He free space measurement has been completed, or by using longer equilibration times, or both (as has been done for selected ACs in the following section in order to obtain high resolution isotherms). The condensation of gas occurs via addition of multiple layers of N_2, eventually resulting in a bulk liquid phase. Removal of the condensed gas is via evaporation from a hemispherical meniscus [38]. The evaporation in this way will be significantly hindered in materials that possess slit shaped pore, as the very last part of the meniscus is very slow to be removed. The removal of non-condensed N_2 from the micropores cannot be removed until this remaining N_2 from the bottom of the meniscus has been removed. As such for complete removal of the entrapped N_2 to be achieved, either a stronger vacuum will have been required than was available on the instrument used, or a longer equilibration period employed.

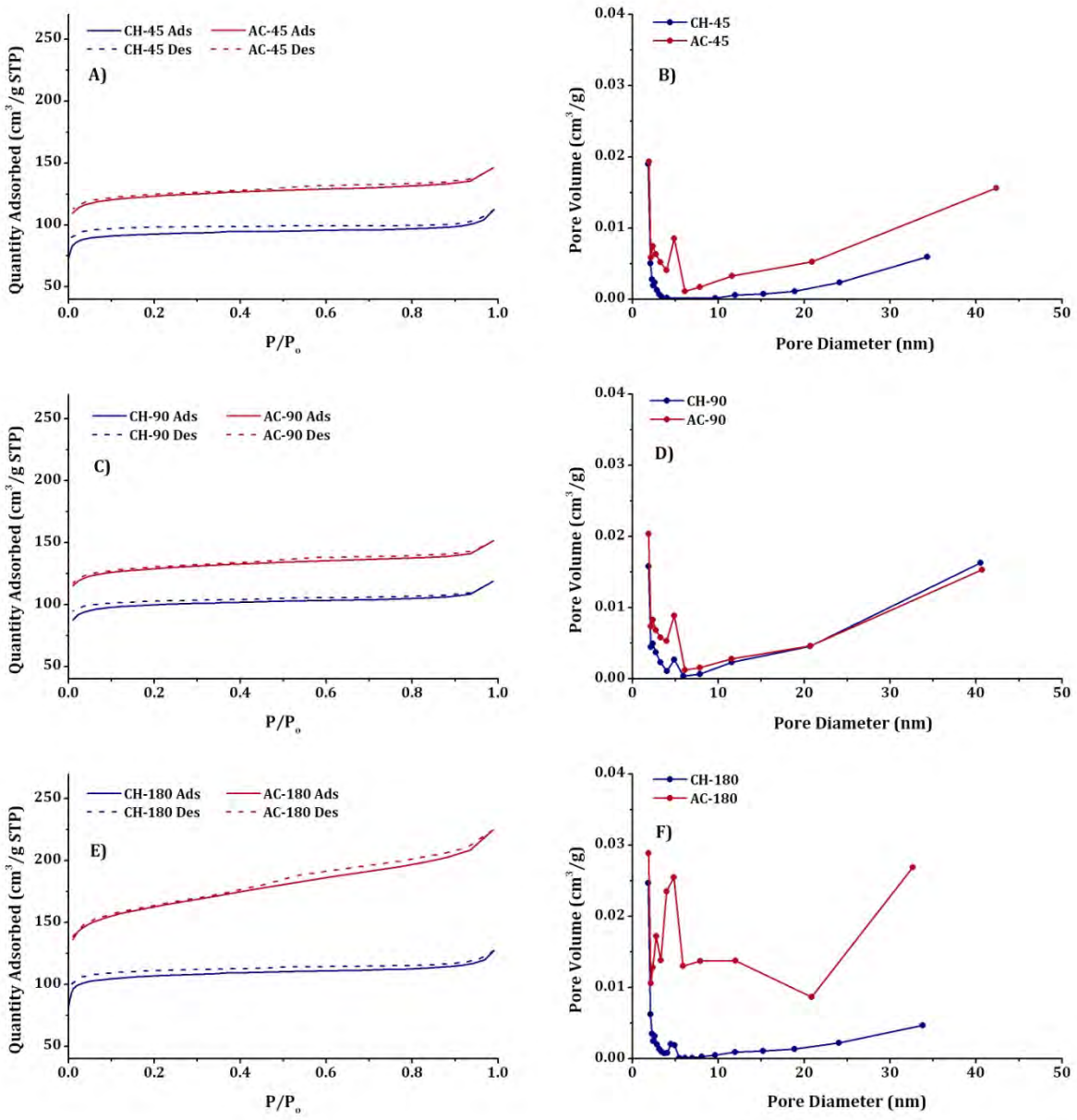

Figure 2-12 *~ N_2 Adsorption Isotherms and Pore Size Distributions at 77 K of Carbonised and Steam Activated VBC. Shown are* ***A)*** *N_2 Isotherms for CH-45 and AC-45,* ***B)*** *N_2 PSDs for CH-45 and AC-45,* ***C)*** *N_2 Isotherms for CH-90 and AC-90,* ***D)*** *N_2 PSDs for CH-90 and AC-90,* ***E)*** *N_2 Isotherms for CH-180 and AC-180, and* ***F)*** *N_2 PSDs for CH-180 and AC-180*

Furthermore, **Figure 2-12*B*** and ***Figure 2-12D*** shows a small spike in pore diameter at around 5 nm in the chars compared with a significantly greater volume present in the ACs at this pore diameter. In ***Figure 2-12B***, the PSD of the CH-45 char shows no such increase in pore volume at a 5 nm pore diameter demonstrating the low mesoporosity of the material.

For the AC-180 carbon, there is a significant increase in mesoporosity compared with the AC-45 and AC-90 samples. This can be observed by the overall increase in adsorption, shown in

Figure 2-12C, and is accompanied by a notable increase in the contribution of pore volume for pores with >2 nm diameter (***Figure 2-12F***). This would indicate that a gasification time somewhere between 90-180 min, results in a tipping point where the conversion of micropores to mesopores overtakes the development of new micropores. As the pore volume significantly decreases below 5 nm there are substantial increases in the micropore volume, which cannot be characterised by N_2 or Ar physisorption. Furthermore, as the pore volume significantly increases beyond 5 nm the pore volume again increases, as due to the mesopores with larger pore diameters, and the presence of macropores.

Overall, the use of steam in order to further develop both the micro- and mesopore volume in the ACs relative to those of their respective chars was successful. For all three activation times the presence of steam increased the surface area and pore volume for pores in both the micro- and mesopore regions, as compared to the chars that were carbonised under N_2 alone (***Table 2-5***). Furthermore, even with the use of steam as an activating agent, ACs with both micro- and mesopore volumes equal to the industrial benchmark AC-N, were unable to be achieved.

The magnitude of the difference between the micropore volumes determined by CO_2 and N_2 physisorption can be strongly correlated with the mesopore volume of the miAC (***Table 2-5***). For miACs that possessed substantial mesopore volumes, there was on minor difference between the micropore volumes determined regardless of the adsorbate. However, for miACs that did not possess a significant mesoporosity, the micropore volumes determined from the N_2 physisorption data were significantly lower than those calculated from the CO_2 physisorption data.

High Resolution N_2 and Ar Physisorption

The physisorption of N_2 at 77 K in the previous section only allowed for a small amount of information to be determined about the micropore region, on an ASAP 2020 HP instrument. By using an instrument with higher resolution at lower relative pressures (i.e. a 0.1 torr pressure transducer, opposed to a 1 torr), more complete adsorption isotherms for N_2 were able to be measured, and in turn more information about the micropores was able to be elucidated. The using of Ar gas adsorption at 87 K allowed for additional information about both micro- and mesopore distributions to be determined, owing to the smaller kinetic diameter of Ar, relative to N_2. Furthermore, as the ASAP 2020 instrument was operated with its cryostat system (refer to ***section 6.6.3.2.1*** for further details), it was possible to heat the sample to 300 K after the He free space measurement, allowing for He entrapment to be completely avoided, allowing for more accurate measurements. Due to the adsorption behaviour of AC-90 towards CO_2

(presented in ***Chapter 3***), more information regarding the pore structure was warranted. The high resolution adsorption isotherms were for both N_2 at 77 K and Ar at 87 K are presented in ***Figure 2-13***. From the isotherms values for the surface area and pore volume of AC-90 were calculated using the BJH and HK methods, and compared to values for AC-N (***Table 2-6***). Furthermore, PSDs were constructed using the BJH and HK methods for each adsorbate. These are presented in ***Figure 2-13C-F***. With the HK equation being able to resolve pores down to diameters of 0.7 nm, where as the BJH method only allows accurate determination of pores with diameters down to 2 nm.

With the exception of the low relative pressure points able to be taken for AC-90 and AC-N, the high resolution N_2 isotherms shown in ***Figure 2-13A-B*** show only small differences to the N_2 isotherms already presented in ***Figure 2-11*** and ***Figure 2-12***. For the latter cases, increases in adsorption occur at higher relative pressures. This is ascribed the 15 sec difference in equilibration times used on the two instruments (30 sec for the TriStar II 3020, and 45 sec for the ASAP 2020 HP). The low pressure hysteresis (LPH) of the Ar isotherms is much more pronounced than that observed in the N_2 isotherms. This was interesting, since it was expected that LPH would be reduced upon minimisation of He entrapment (refer to ***section 6.6.3.2.1*** for details). As such, the LPH observed here can only be attributed to residual condensed gas being removed from the mesopores concurrently with the desorption of non-condensed N_2 or Ar from the micropores. This is actually quite conceivable considering the slit shaped pores with wide mouths. As the meniscus of the condensed gas lowers towards the bottom of the mesopore, the gaseous adsorbate can desorb from within the micropores stemming from the walls of the mesopores.

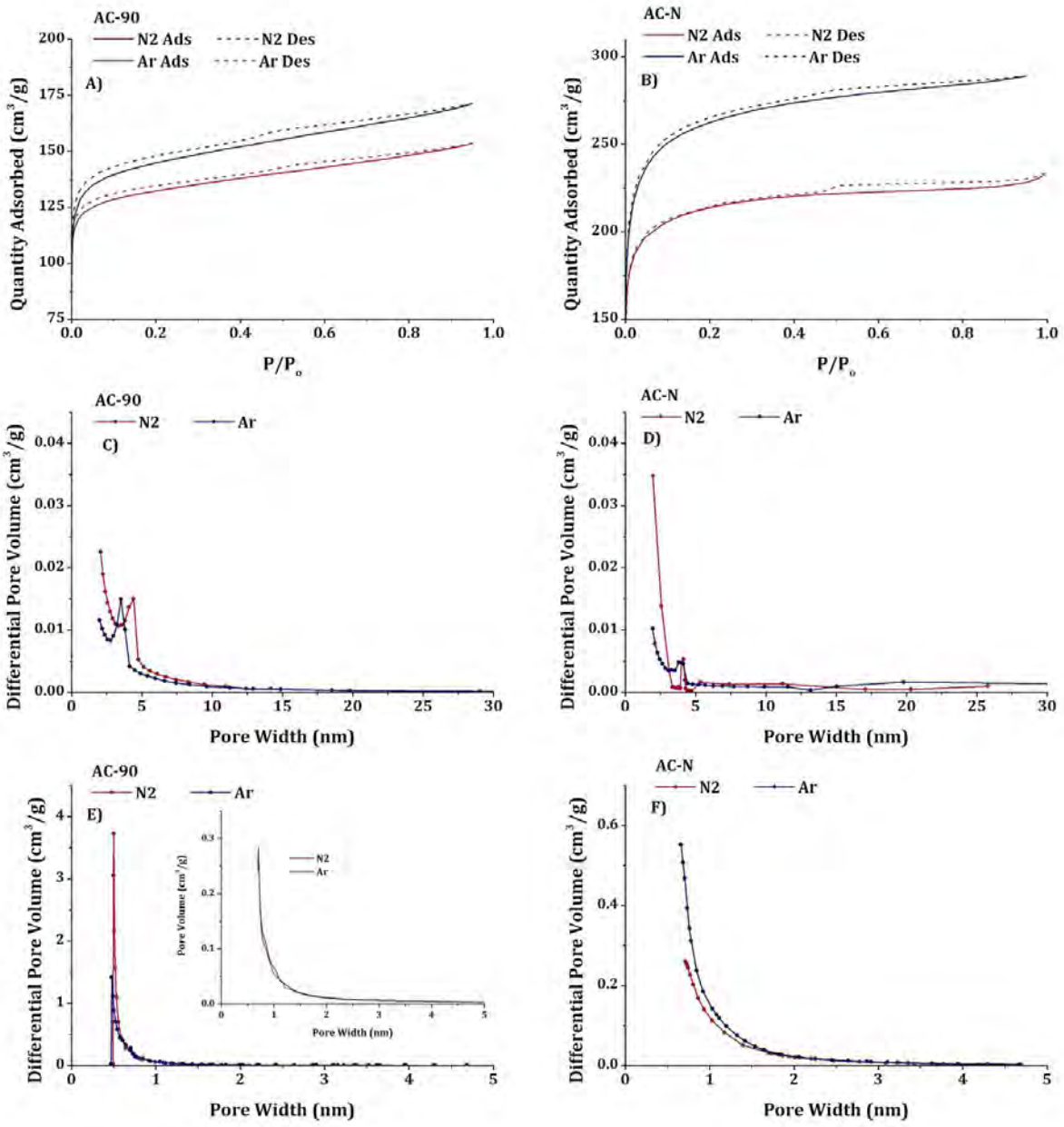

Figure 2-13 *~ Adsorption Isotherms and PSDs for N_2 and Ar at 77 K and 87 K for AC-90 and AC-N. Shown are* ***A)*** *N_2 and Ar Isotherms for AC-90,* ***B)*** *N_2 and Ar Isotherms for AC-N,* ***C)****The N_2 and Ar BJH PSD for AC-90,* ***D)****The N_2 and Ar BJH PSD for AC-N,* ***E)****The N_2 and Ar HK PSD for AC-90, and* ***F)****The N_2 and Ar HK PSD for AC-N*

Table 2-6 ~ *Surface Areas and Pore Volumes Calculated using the BET, DR, BJH and HK Methods from High Resolution CO_2, N_2 and Ar Physisorption at 273, 77 and 87 K for AC-90 and AC-N*

Sample Name	Surface Area (m^2/g)			Pore Volume (cm^3/g)				
				V_{micro}			V_{meso}	
	DR_{CO2}	BET_{N2}	BET_{Ar}	DR_{CO2}	HK_{N2}	HK_{Ar}	BJH_{N2}	BJH_{Ar}
AC-N	902	637	695	0.29	0.32	0.33	0.50	0.46
AC-90	646	397	382	0.21	0.20	0.18	0.19	0.11

The PSDs obtained from the relative pressure data revealed important information pertaining to the micropores, that was unable to be obtained from the N_2 isotherm shown in ***Figure 2-12C***. From ***Figure 2-13C*** and ***Figure 2-13E*** there are important comparisons between the PSDs for AC-90 calculated using the BJH and HK methods, with the former used to determine the PSD for the mesopore region and the latter used the determine the PSD for the micropore region. Importantly it can be seen from ***Table 2-6*** for both carbons that the large micropore volumes calculated by applying the DR equation to the CO_2 adsorption isotherms from ***Figure 2-10*** are very similar to those obtained by applying the HK equation to the high resolution N_2 isotherm of both AC-N and AC-90 (***Figure 2-13***). Similar micropore volumes are also obtained by applying the HK equation to the high resolution Ar isotherms.

Due to the higher resolution of the instrument, micropore volumes were able to be determined from both the N_2 and Ar physisorption data that are in good agreement with those calculated from the CO_2 physisorption data using the DR equation. However, even though greater resolution was achieved for both ACs, the low partial pressure data obtained for AC-N from both N_2 and Ar physisorption was limited to pores with diameters of >0.7 nm, whereas for AC-90 pores with diameters as small as 0.5 nm were able to be resolved. This does not mean that pores with diameters smaller than 0.7 nm were absent in AC-N, just that they were unable to be resolved by the instrument. The insert in ***Figure 2-13E*** clearly shows that AC-90 actually adsorbed smaller quantities of N_2 and Ar than AC-N (***Figure 2-13F***) when pore volumes arising from pores with diameters >0.7 nm are considered.

High resolution physisorption using N_2 and Ar over AC-90 and AC-N further supported the results obtained from the moderately resolved isotherms in the previous section. This in itself, resulted in a greater understanding of the pore structure of both AC-90 and AC-N.

He Pycnometry

The true density of all physically ACs and their precursor carbon materials were determined using gas displacement via He displacement in a gas pycnometer (Micromeritics, Accupyc 1340). Density values are important parameters to measure as they are used in volumetric calculations such as void and pore space, and provide an indication of the amount of volatile matter removed. The measured true densities of the materials are presented (along with the surface areas and pore volumes measured by gas physisorption) in ***Table 2-5***.

Referring to ***Table 2-5***, the measured densities of all the produced materials are greater than the true density measured for the parent VBC. This can be attributed to the removal of volatile matter leaving the condensed carbon matrix. The measured values for true density of the VBC derived ACs suggest that a maxima is reached after 90 min gasification time, which sharply drops upon further increase of the gasification time to give a true density value lower than that of AC-45. This is proposed to be due to the significant increase in the level of microporosity present in the AC-180 carbon compared with that of AC-45 and AC-90.

2.3.3.2.2 Transmission Electron Microscopy (TEM)

Transmission electron microscopy (TEM) was used to investigate the structural domains for the steam activated miACs. Imaging of several particles within each sample was undertaken, with the most representative shown here. In addition to investigating observable domains by TEM, confirmatory information was also obtained for the observations made by Raman spectroscopy and XRD. The electron micrographs of AC-45, AC-90, AC-180 and CH-90, are presented in ***Figure 2-14***, ***Figure 2-15***, ***Figure 2-16*** and ***Figure 2-17***, respectively. In each figure the graphitic domains have been highlighted, along with any other domains or structures of interest.

From the region indicated with a red circle in the electron micrograph of AC-45 (***Figure 2-14***), a great deal of alignment of the graphene sheets (graphitic domains) can be observed. Moreover, the carbon surrounding the structured domains appears largely amorphous in character. This is in good agreement with the XRD results of AC-45 (***Figure 2-9B***), in that there is short range (indicating structural domains), but not long range order within the carbon structure (repetitive structural units).

The electron micrograph of AC-90, presented in ***Figure 2-15*** shows more ordered graphitic domains dispersed amongst the bulk amorphous carbon relative to AC-45 (***Figure 2-14***). This is particularly evident in ***Figure 2-15B*** where there is a higher proportion of well defined graphitic domains with visible lattice fringes. Furthermore, in ***Figure 2-15B*** clearly discernible graphitic domains can be observed in which aromatic rings were both perpendicular (*circled*

red) and parallel (*circled green*) to the electron beam. The carbon surrounding these domains still appears to possess a highly amorphous character. The TEM results for AC-90 are in good agreement with the XRD results (***Figure 2-9B***), again confirming short range order, but no long range order. Furthermore, the observations from the micrographs in ***Figure 2-15*** support the Raman data obtained for AC-90 (***Figure 2-8***), where there was a decrease in the ***D*** peak; associated with a decrease in graphene layer edge at the surface of AC-90 (relative to AC-45), whilst an increase in the ***G*** peak was also observed (associated with the structured graphitic phase).

The electron micrograph of AC-180 (***Figure 2-16***) revealed a number of small graphitic-like domains that were not observed in the micrographs obtained for the materials activated for 45 or 90 min. This indicates that prolonged activation for 180 min led to the carbon becoming more structured. Although one well defined graphitic domain was observed in the micrograph of AC-180 (red circle, ***Figure 2-16B***) most of the order within the carbon structure arose from the alignment of graphene layer edges rather than well defined graphitic domains (***Figure 2-16B***, see green circles). Similar observations were made in the Raman spectra of AC-180 (***Figure 2-8D***), in that only a relatively minor increase in the ordered carbon (***G*** peak) was observed relative to the Raman spectra of AC-90 (***Figure 2-8B***).

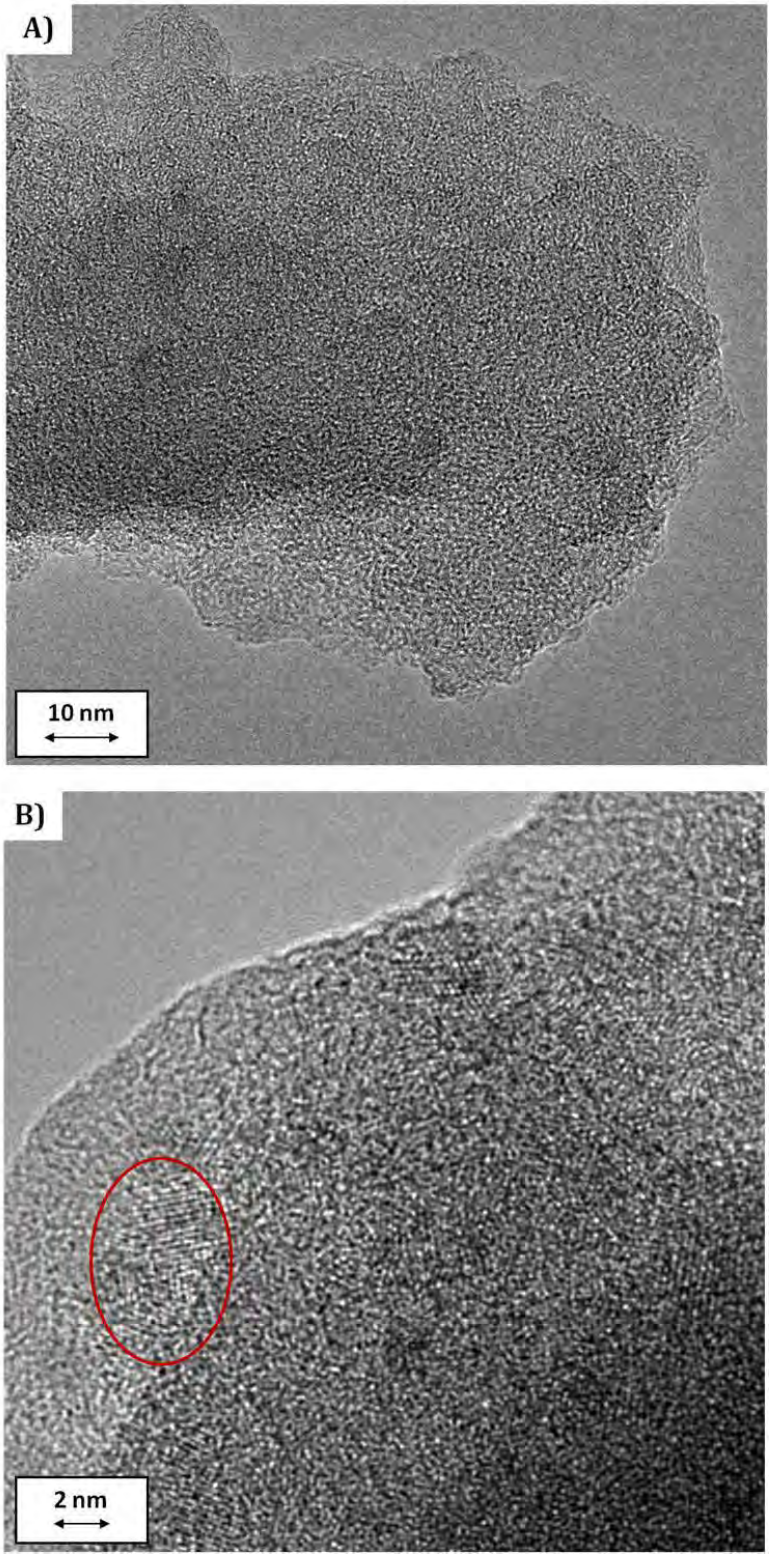

Figure 2-14 *~ Transmission Electron Micrograph of Activated Carbon Derived from Victorian Brown Coal after 45 min Steam Gasification (AC-45). Shown is* ***A)*** *Medium-High magnification of AC-45,* ***B)*** *High magnification of AC-45; lattice fringes of graphitic domain circled (○)*

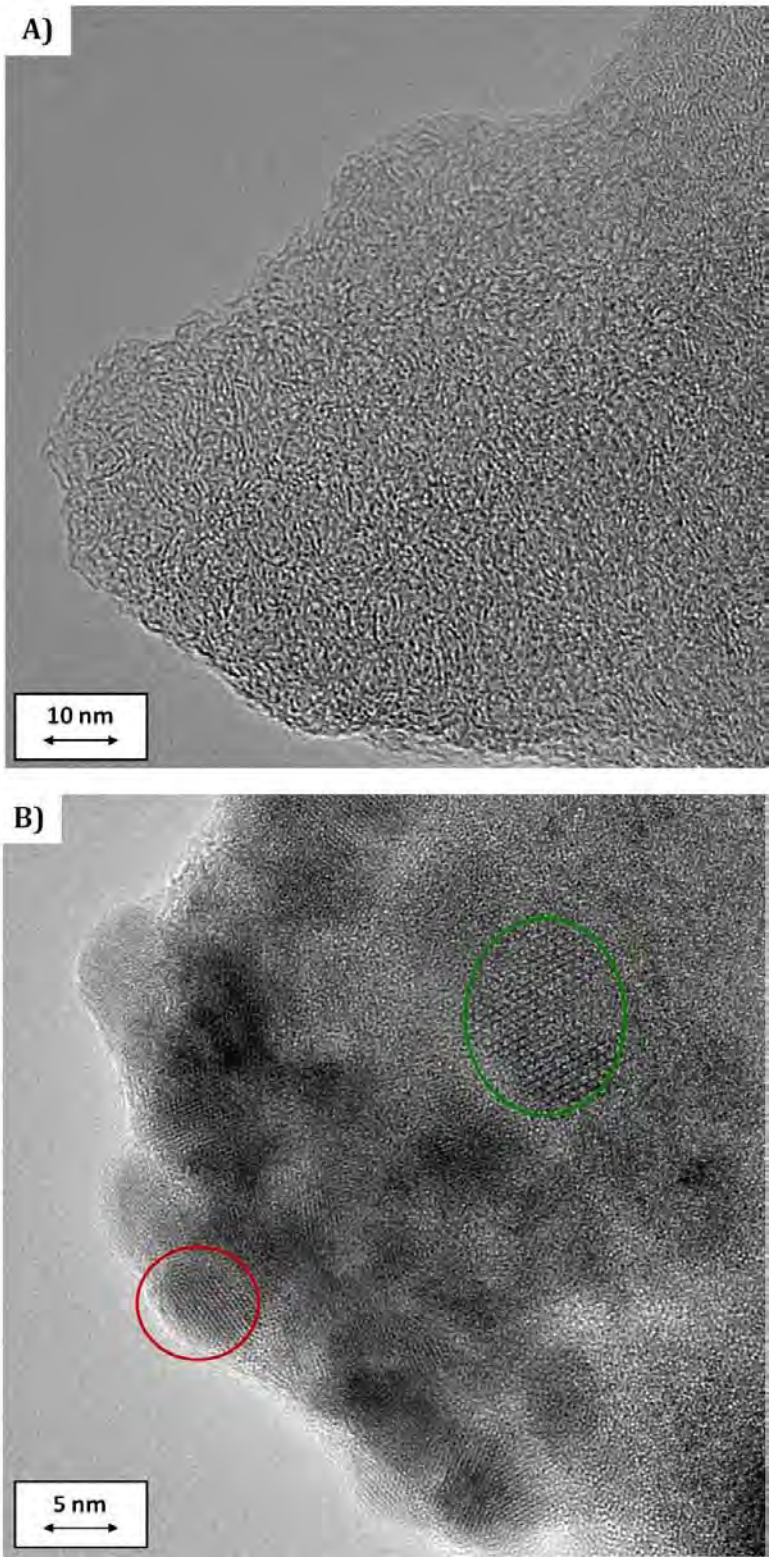

Figure 2-15 ~ *Transmission Electron Micrograph of Activated Carbon Derived from Victorian Brown Coal after 90 min Steam Gasification (AC-90). Shown is* ***A)*** *Medium-High magnification of AC-90,* ***B)*** *High magnification of AC-90; lattice fringes of graphitic domain circled (◯), edge of graphene sheet circled (◯)*

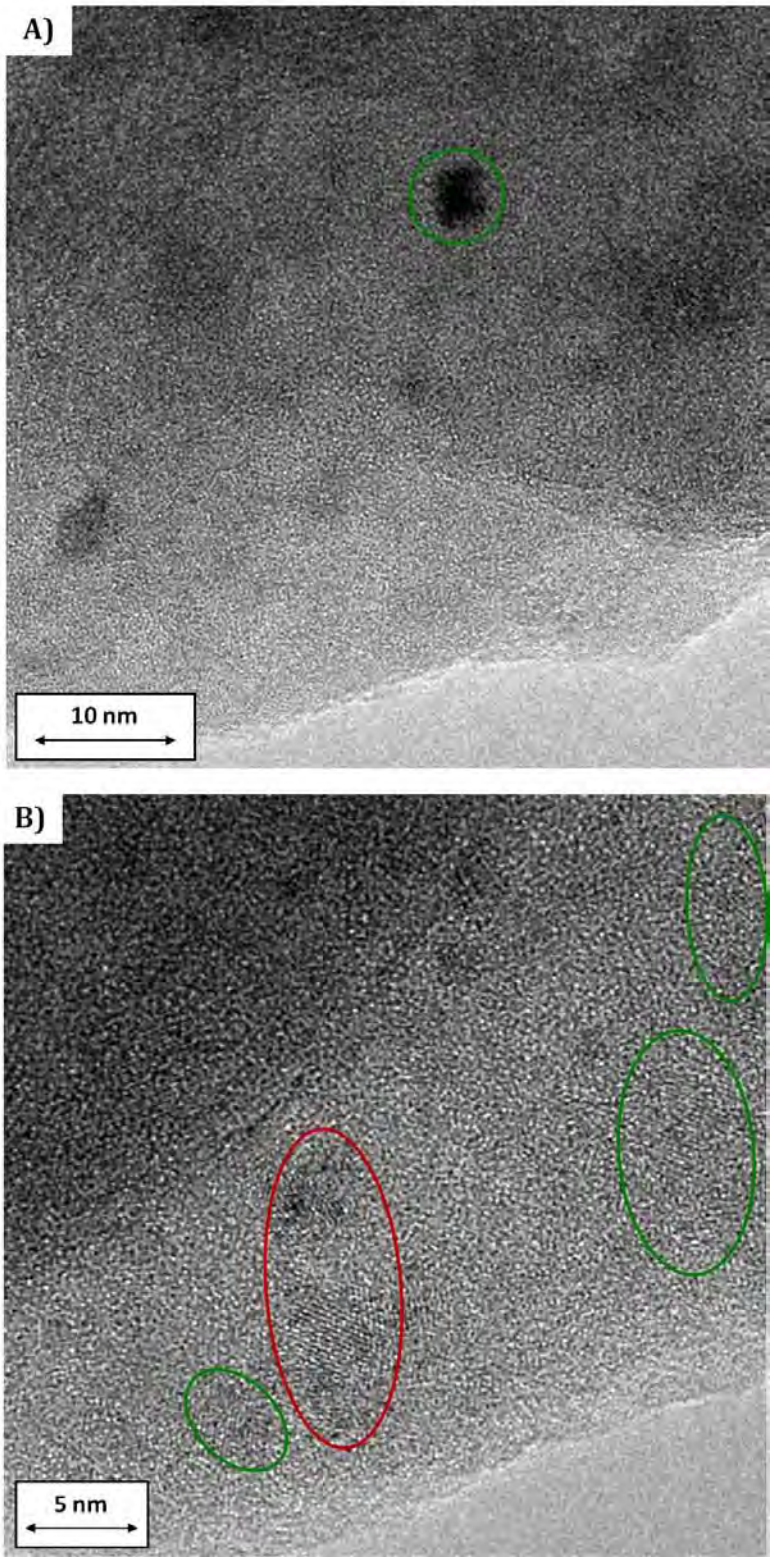

Figure 2-16 *~ Transmission Electron Micrograph of Activated Carbon Derived from Victorian Brown Coal after 180 min Steam Gasification (AC-180). Shown is* ***A)*** *Medium-High magnification of AC-180; ash particle circled (◯), **B)** High magnification of AC-180; lattice fringes of graphitic domain circled (◯) graphite-like domain circled (◯)*

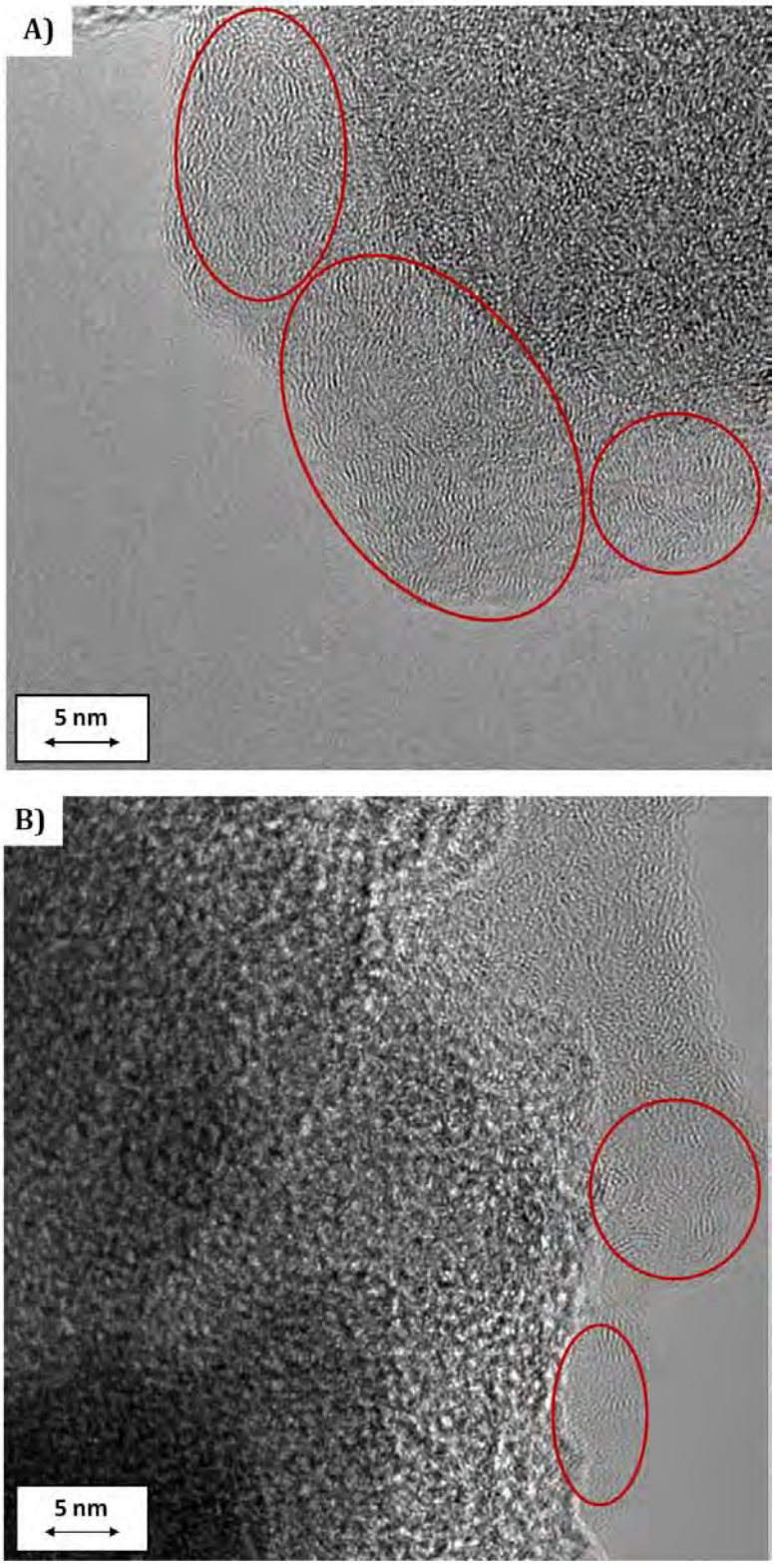

Figure 2-17 ~ *Transmission Electron Micrograph of Victorian Brown Coal Char, 90 min Pyrolysis (CH-90). Shown is* ***A)*** *Medium-High magnification of CH-90,* ***B)*** *Medium-High magnification of CH-90*

The electron micrographs of CH-90, shown in ***Figure 2-17,*** exhibited a small amount of ordered carbon. No well defined graphitic domains were observed in any of the imaged particles, although some developing structural alignments is apparent (shown by the red circles in ***Figure 2-17***). This was an interesting result, since the XRD (***Figure 2-9***) show no significant structural differences between CH-90 and AC-90. Whereas the results of the Raman spectroscopy (***Table 2-4***) showed CH-90 to possess a lower the proportion of ordered graphitic carbon and higher proportion of disordered graphitic carbon than AC-90, which is reasonably with the TEM results. Some alignment of graphene layer edges was observed around the outside of the CH-90 particle shown, but these structures are not well defined graphitic domains.

The TEM of the steam activated miACs were with the observations made by Raman spectroscopy, XRD and gas physisorption. That is that there is no significant long range structure to the carbons in the CH and miAC series, but well defined structural domains were observed.

2.3.4 Summary

For the CH series (CH-45, CH-90 and CH-180) as the carbonisation time was increased and more and more volatile matter was removed from VBC, a significant increase in bulk C content of ~ 30 wt%, occurred together with a decrease in bulk H content of ~ 3 wt%, and a decrease in the bulk O content by 25-30 wt%. Furthermore, the initial carbonisation of VBC for 45 min resulted in an almost four-fold increase in micropore volume (ΔV_{micro} = 0.13 cm^3/g, ***Table 2-5***). An extension of carbonisation time from 45 to 90 min caused an increase in micropore volume of only 0.01 cm^3/g, with an increase in mesopore volume of 0.02 cm^3/g. These differences in pore volume were barely outside the error range of the measurements (±0.005 cm^3/g) and as such were of little consequence. This is presumably due to near complete removal of volatile matter from the inner pore structure at the lower carbonisation time. Furthermore, no changes outside the limits of error were observed upon extending the carbonisation from 90 to 180 min. It can be seen that there was not any significant development of pore volume in the CH series, beyond the initial 45 min carbonisation of VBC (***Table 2-5***). There was also no clear pattern in the changes in the bulk composition of the CH series as a function of carbonisation time, due to significant variation across the series of samples examined (***Table 2-1***).

Compared to one another the bulk composition of the miACs (AC-45, AC-90 and AC-180) showed a similar pattern to their respective material in the CH series as a function of reaction time. That is a decrease in bulk C, with an associated increase in bulk O, between 45-90 min activation; with the opposite being true between 90-180 min activation. The results of gas

physisorption showed that the use of steam during activation proved to increase the micropore volume, and also that the duration of time under steam gasification conditions resulted in increased mesopore volume (***Table 2-5***). Furthermore, both the presence and duration of steam activation had an effect of the development of mesopores, due in large part to the mechanism of pore development occurring under steam gasification conditions. Results are with a view that steam gasification develops pores from the outside of the carbon particles, working its way inwards. It is for this reason that mesopores and pores with wider mouths are developed at the expense of micropores; however, both are still developed, just at different rates. From the Raman spectroscopy it can be seen that between 45-90 min steam activation there is a decrease in the ***D*** peak, with an associated increase in the ***G*** peak. This would suggest structural development of amorphous carbon into more ordered graphene sheet structures (***Table 2-4***). A similar pattern of progressive change was observed for the Raman spectra of AC-180, but there was also an observed decrease in the ***S*** peak (as was also observed for CH-180). This suggests a decrease in the number of heteroatoms bound to graphene layer edges by increasing the reaction time from 90 to 180 min. An increase in the number of well structured graphitic domains was also observed in the TEM investigation (***Figure 2-14-Figure 2-16***). Despite the changes in physical structure apparent from Raman spectroscopy and TEM, no such changes were observed from the XRD patterns of the steam activated VBC derived miACs (***Figure 2-9B***).

The XPS results showed no clear pattern in the variation the surface concentrations of C, O or N with increasing carbonisation/activation time (***Table 2-2***). Moreover, there was no clear relationship between the distribution of the main functional groups (C=O, C-O-R and COO-R) or types of carbon (C-C or C=C) at the surface as a function of carbonisation/activation time.

However, clear patterns did emerge from the XPS data for pairs of materials generated by direct carbonisation versus those prepared by steam activation. The use of steam resulted in a decrease in both C=O and COO-R groups, whilst significant increases were observed for the C-O-R groups, despite an overall decrease in the surface O content of the miACs as compared to their respective chars. NEXAFS spectroscopy (***Table 2-3***) was used to further probe the identify the C=O, COO-R and C-O-R groups detected by XPS. The C=O groups identified by XPS were found to result from both ketone and aldehyde groups, in relatively equal proportions, whilst the COO-R groups were confirmed as carboxylic acids groups. The most notable identification being made for the C-O-R groups, which were attributed to both hydroxyls and ethers, with the former being present in higher proportions. Hydroxyl groups are known to possess the highest affinity for CO_2 of all the functional groups commonly found on AC surfaces, thus indicating that the use of steam activation not only allows for greater pore development, but also more desirable surface chemistry for CO_2 adsorption [1].

The bulk O content of AC-N was determined to be more than twice that of any of the VBC derived chars or steam activated miACs, whilst the surface O content of AC-N was significantly lower than any of these carbons. The higher bulk O content is attributed is attributed to the higher bulk O content of the peat from which it was derived [13]. There was a substantial difference in the distribution of oxygenated functional groups on the surface of AC-N relative to the VBC derived chars and miACs. The most prominent difference was observed for the C-O-R groups, shown from NEXAFS spectroscopy to be due predominately to hydroxyl groups. As hydroxyl groups have shown to have a greater effect on the affinity of an AC surface for CO_2 the lower concentration of hydroxyl groups on the surface of AC-N might lead to a lower affinity of its surface for CO_2.

In closing, the steam activated VBC derived miACs were shown to possess increased pore development and ordered chemical structure, as opposed to their carbonised counterparts. Despite the increases in both the micro- and mesopore volume of the steam activated miACs relative to their analogues from the CH series, the pore volumes were still smaller than those of AC-N. The surface chemistry of almost all the VBC derived carbon materials possessed a higher surface O content than AC-N, which might have lead to these carbon materials with surfaces that possessed a higher affinity for CO_2, than AC-N. As both surface chemistry and pore volume are important factors in determining the gas adsorption properties of carbon materials, their affect on the adsorption properties of the VBC derived carbon materials and AC-N, will be the focus of the gas separation studies for these carbons, reported in ***Chapter 3***.

2.4 Physically Activated Char Derived Carbons

The char derived miACs were produced using two industrially produced chars, made using the same VBC source as was used to produce the coal derived miACs presented in ***section 2.3***. The two chars were milled and homogenised in the same manner at the VBC used in ***section 2.3***, as outlined in ***section 6.3.2*** of ***Chapter 6***. The two industrial chars were obtained from Australian Char LTD PTY (AusChar), one of which was produced in a Lurgi-style retort at 1173 K (CHLR), and the other in a rotary kiln at 973 K (CHRK). The VBC chars were reacted for 90 min at 1073 K, under a flow of H_2O/N_2, in the same manner as AC-90 (for details refer to ***section 6.4.2***).

2.4.1 Composition of Char Derived Carbons

The yields and chemical composition of the starting materials and prepared carbons are presented in ***Table 2-7***. Ash analyses were performed thermogravimetrically (Mettler Toledo, TGA/DSC 1, Star* System) and elemental compositions were determined by dry combustion (Vario MICRO cube, Elementar).

The ACs produced from the two industrial chars (***Table 2-7***) show small decreases in the oxygen content upon steam gasification (e.g. O% for CHLR 24.3 wt% vs. O% for AC-CHLR-90 22.8 wt%). The elemental composition from chars to ACs in these cases shows little change in composition, due to the relatively non-reactive nature of the two industrial chars. This is not too surprising since the CHLR char was produced industrially at 1173 K, whereas the activation process considered here was performed at 1073 K. Therefore, any components that would have been reactive at the 1073 K have already experienced greater temperatures during the production of the char. Further consequences of their non-reactive nature will become apparent later, with respect to both their pore development and CO_2 capacities.

The ash content of both industrial chars was much higher than that observed for any of the steam activated VBC miACs. Of interest however, is that upon steam activation of CHRK that a decrease in ash content was observed to actually decrease, the only occurrence of this throughout this work. This observation can be put down to heterogeneity inherent in the sample. Furthermore, other than the fact that CHRK was derived from VBC and produced in a rotary kiln at 973 K, little is known about the treatment of the sample.

Table 2-7 *~ Elemental and Ash Analysis of Physically Activated Char Derived Carbons*

Sample	Reaction Time (min)	Yield (wt%)	Elemental Analysis (wt%, daf)				H/C Ratio	Ash (wt%)
			C	H	N	O_{diff}		
AC-N	-	-	76.3	0.8	1.0	21.9	0.12	10.9
VBC	-	-	61.4	4.4	0.6	33.5	0.86	0.4
CH-90	90	46.6	89.9	1.1	0.5	8.4	0.15	3.8
AC-90		43.4	82.2	1.3	0.7	15.7	0.19	6.4
CHLR	-	-	74.0	1.1	0.6	24.3	0.18	6.0
AC-CHLR-90	90	74.3	75.6	1.0	0.6	22.8	0.16	5.2
CHRK	-	-	76.6	1.7	0.8	20.9	0.27	6.9
AC-CHRK-90	90	81.0	78.6	1.0	0.5	19.6	0.15	7.4

2.4.2 Surface Chemistry of Char Derived Carbons

A combination of XPS and NEXAFS spectroscopy's were used in order to indentify and quantify the functional groups on the surface of the two industrial chars and the miACs derived from them, with specific focus on the oxygenated functional groups that effect the adsorption properties of the ACs.

2.4.2.1 X-ray Photoelectron Spectroscopy (XPS)

The fitting of the high resolution C 1s and O 1s XPS spectra obtained for CHLR, AC-CHLR-90, CHRK and AC-CHRK-90 are given in ***Figure 2-18A-H***. The XPS measurements were taken on a Kratos Axis HSi X-ray photoelectron spectrometer, as outlined in ***section 6.6.2.1***. The tabulated results of the peak fitting for these carbons are report in ***Table 2-8***. For reference and comparison the peak fitting results obtained for AC-N and AC-90 are reported in ***Table 2-8***, with the corresponding C 1s and O 1s XPS spectra presented in ***section 2.3.2.1***.

The XPS analysis of CHLR, CHRK and the miACs derived from them (AC-CHLR-90 and AC-CHRK-90, respectively) showed significant differences between the two industrial chars, as well as after steam activation of each char. For the CHLR/AC-CHLR-90 pair steam activation resulted in increases in the surface C and N content (ΔC_{surf} = 3.2 at% and ΔN_{surf} = 0.2 at%), but a decrease to the surface O content (ΔO_{surf} = 3.4 at%). The observed decrease in surface O of AC-CHLR-90 relative to CHLR manifested as substantial decreases in all three oxygenated functional groups (C=O, C-O-R and COO-R, ***Table 2-8***). Thus, it might be expected that a reduction in surface C-O-R groups will result in a decrease in the affinity for the surface of AC-CHLR-90 for CO_2, compared to that of CHLR [1]. On a side note, it is also import to keep in mind that in the production of CHLR, oxygen deficient gas was used during the carbonisation of VBC to produced CHLR. This oxygen deficient gas was the result of the combustion of tars produced during the carbonisation of CHLR itself, and as such the gas will have inevitably possessed CO and CO_2 in addition to N_2. This might account for the very high surface O concentration of CHLR.

The opposite relationship was observed upon steam activation of CHRK in order to produce AC-CHRK-90. AC-CHRK-90 displayed an increase in surface O (ΔO_{surf} = 4.3 at%) and decrease in surface C and N (ΔC_{surf} = 3.9 at% and ΔN_{surf} = 0.4 at%), relative to CHRK. The increase in surface O of CHRK/AC-CHRK-90 was much more substantial than the decrease in surface O was observed for AC-CHLR-90 with respect to CHRK. Of the 4.3 at% increase in surface O for the CHRK/AC-CHRK-90 pair, 2.4 at% were due to C-O-R groups alone.

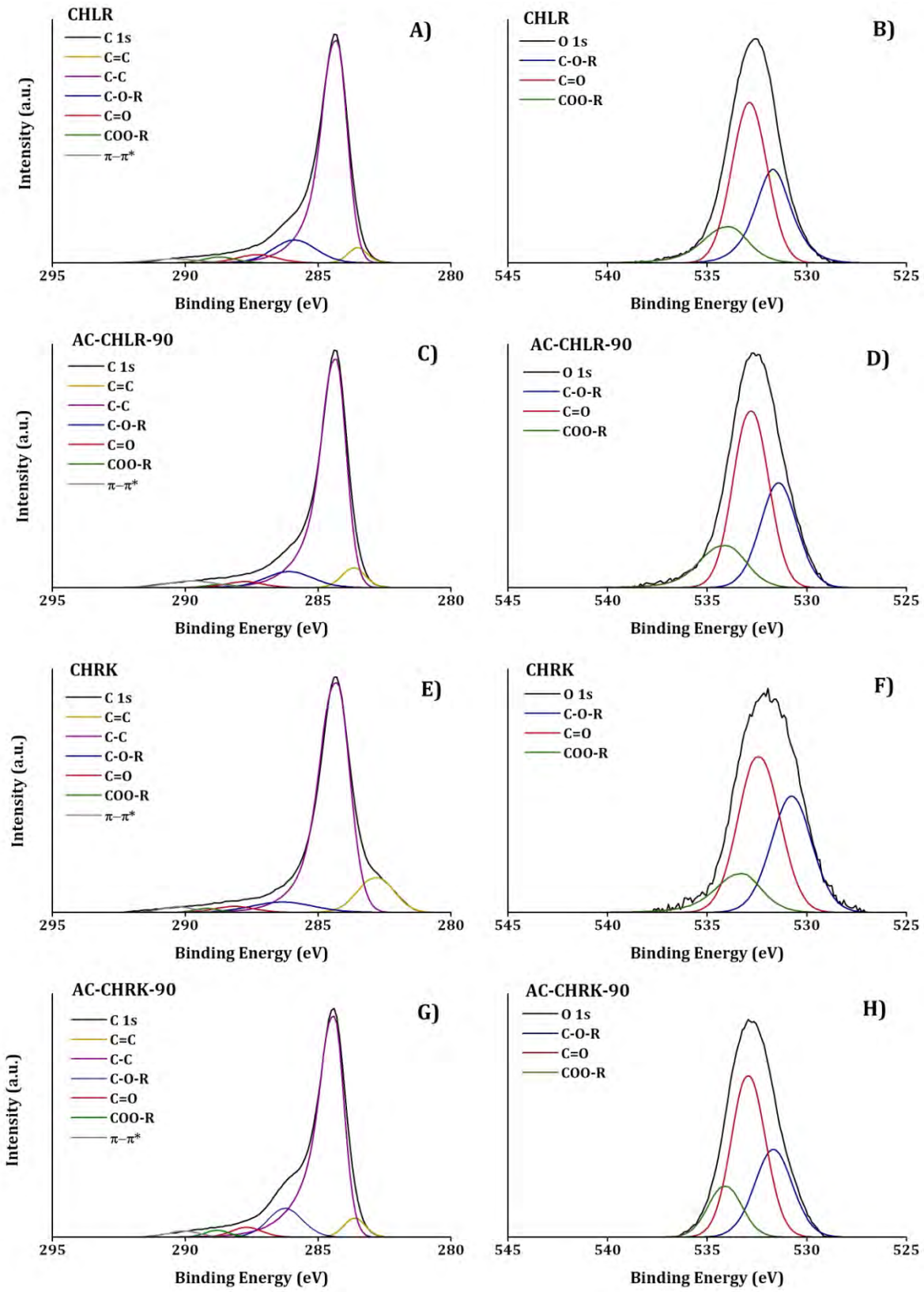

Figure 2-18 ~ *C 1s and O 1s XPS Spectra for CHLR, AC-ACLR-90, CHRK and AC-CHRK-90. Shown are* ***A)*** *C 1s Spectra of CHLR,* ***B)*** *O 1s Spectra of CHLR,* ***C)*** *C 1s Spectra of AC-CHLR-90,* ***D)*** *O 1s Spectra of AC-CHLR-90,* ***E)*** *C 1s Spectra of CHRK,* ***F)*** *O 1s Spectra of CHRK* ***G)*** *C 1s Spectra of AC-CHRK-90, and* ***H)*** *O 1s Spectra of AC-CHRK-90*

Table 2-8 *~ XPS Peak Fitting for CHLR, AC-CHLR-90, CHRK, AC-CHRK-90, AC-90 and AC-N*

Peak Assignment	Binding Energy (eV)	Surface Concentration (at%)					
		AC-N	AC-90	CHLR	AC-CHLR-90	CHRK	AC-CHRK-90
C 1s	284.9	91.95	90.16	87.81	91.02	92.72	88.85
C=C	283.8	5.08	6.04	3.13	5.03	11.65	4.20
C-C	284.8	72.91	68.28	66.71	70.54	70.15	67.58
C-O-R	286.1	6.01	8.48	10.38	8.22	5.98	10.12
C=O	287.5	3.60	2.80	3.49	2.47	2.30	3.15
COO-R	288.8	1.97	1.56	2.05	1.06	0.94	1.74
π–π^*	289.9	2.38	3.00	2.06	3.70	1.71	2.06
O 1s	531.9	7.83	9.16	11.33	7.93	6.31	10.57
C=O	531.5	3.50	2.96	3.68	2.51	2.29	3.32
C-O-R	533.1	2.58	4.60	5.84	4.08	3.11	5.52
COO-R	534.4	1.75	1.59	1.80	1.34	0.91	1.73
N 1s	400.9	0.22	0.68	0.86	1.05	0.97	0.58

Compared to AC-90 the surface O content (and by extension, the concentration of C=O, C-O-R and COO-R groups) of AC-CHLR-90 is much lower. This is be expected to cause a decrease in the affinity of the AC-CHLR-90 surface for CO_2 and thus a decrease in adsorption of CO_2 relative to AC-90 [1]. Conversely for AC-CHRK-90, the surface O content and that of all three major functional groups (C=O, C-O-R and COO-R) are much higher than observed for AC-90; particularly with respect to the concentration of C-O-R groups (***Table 2-8***).

Upon comparison of the surface chemistry of AC-N to the char derived miACs (AC-CHLR-90 and AC-CHRK-90), both AC-CHLR-90 and AC-CHRK-90 possessed substantially higher surface O (C=O, C-O-R and COO-R) than AC-N. Based on the surface chemistry results presented above for AC-CHLR-90 and AC-CHRK-90, relative to AC-N, it is predicted that the surface of both miACs might possess a higher affinity for CO_2 than the surface of AC-N[1].

As previously mentioned, the C 1s to O 1s ratio assigned to a given functional group (e.g. C=O, C-O-R or COO-R) can permit the identification of a functional group. For example, if the C 1s to O 1s ratio of the C-O-R peak was 2, this could be assigned to an ether; whereas a C 1s to O 1s ratio of 1, would more likely indicate hydroxyls. Although this is important information that can be ascertained from XPS, further evidence is required in order to more definitively confirm the identity of the functional groups. It is for this reason that NEXAFS spectroscopy was employed, as it is a powerful and complimentary technique to XPS and is ideally suited for this purpose.

To summarise, quite significant differences were observed in the surface chemistry of the two industrial chars. Importantly, shifts in the surface composition upon activation of the two

industrial chars were quite different from that observed for the carbon materials presented in ***section 2.3.2.1***, a fact also supported by the bulk compositional analysis of these carbons.

2.4.2.2 Near Edge X-ray Adsorption Fine Structure (NEXAFS) Spectroscopy

The carbon and oxygen K-edge NEXAFS spectra were taken on the soft x-ray (SXR) beamline at the Australian Synchrotron. The C and O K-edge NEXAFS spectra for AC-N are reported in ***section 2.3.2.2***, with the results of the peak fitting reproduced in ***Table 2-9*** for ease of comparison. For the industrial chars and their steam activated counterparts the C 1s and O 1s NEXAFS spectra are shown in ***Figure 2-19***, with the spectral fitting given in ***Table 2-9***. The complete fitting for both the C 1s and O 1s spectra can be found in ***Appendix 2 – NEXAFS Spectroscopy Peak Fitting***, for all of the carbon materials investigated.

It is important to note that for AC-CHLR-90 (***Figure 2-19A-B*** and ***Table 2-9***) a decrease (2.5-8%) in three (***C5***, ***O3*** and ***O6***) of the four (***C5***, ***C8***, ***O3*** and ***O6***) ether peaks are observed, relative to CHLR. A decrease in the C-O-R peak from the XPS comparison of the two carbons revealed a decrease in the C-O-R peak (assigned to hydroxyl and/or ether groups)(***Table 2-8***). The observed decrease in the C-O-R peak from the XPS of AC-CHLR-90, relative to CHLR is interesting, as a quite significant increase (7%) was observed in the area of the hydroxyl peak (***O4***) in the O 1s NEXAFS spectrum obtained for AC-CHLR-90. For an overall decrease to have been observed in the C-O-R peak from XPS, the increase in hydroxyl groups indicated by NEXAFS spectroscopy must have been of lesser magnitude than the decrease in ether content.

Interestingly there is a notable decrease in the ***C4*** carboxylic acid/lactone peak of AC-CHLR-90 relative to CHLR (***ΔC4*** = 1.9 %), which is in agreement with the observed changes in the COO-R peak from the XPS of AC-CHLR-90 relative to CHLR (***Table 2-8***). Whereas, the ***C7*** carboxylic acid/lactone peak of AC-CHLR-90 only exhibited relatively a comparably minor decrease. Furthermore, the peak area of the ***O5*** carboxylic acid/lactone peak from the O 1s NEXAFS spectra was somewhat larger for AC-CHLR-90 than for CHLR, which seems to contradict the C 1s NEXAFS data.

The increase in surface aromatic carbon (***C2***) of the CHLR/AC-CHLR-90 pair as a result of steam activation, is similar to other analogous comparisons presented thus far. Whilst the increase in the area of the ***C2*** peak for AC-CHLR-90 was significant relative to CHLR, the decrease in the ***C9*** peak was quite minor. This suggests that steam activation of CHLR has increased the amount of surface aromatic carbon, with no significant change in the long range order of the carbon material.

Similarly, for the CHRK/AC-CHRK-90 pair (***Figure 2-19c-d*** and ***Table 2-9***) an increase in the area of the ***C2*** aromatic peak was observed as a result of steam activation. The magnitude of the change in the ***C2*** peak (12.4%) was greater than observed for the CHLR/AC-CHLR-90 pair, but still smaller than for the CH-90/AC-90 (17.4%) pair. Likewise, only a relatively minor decrease in ***C9*** accompanied the change in the area of ***C2***, indicating that no change of any consequence in the long range order had occurred as a result of steam activation of CHRK.

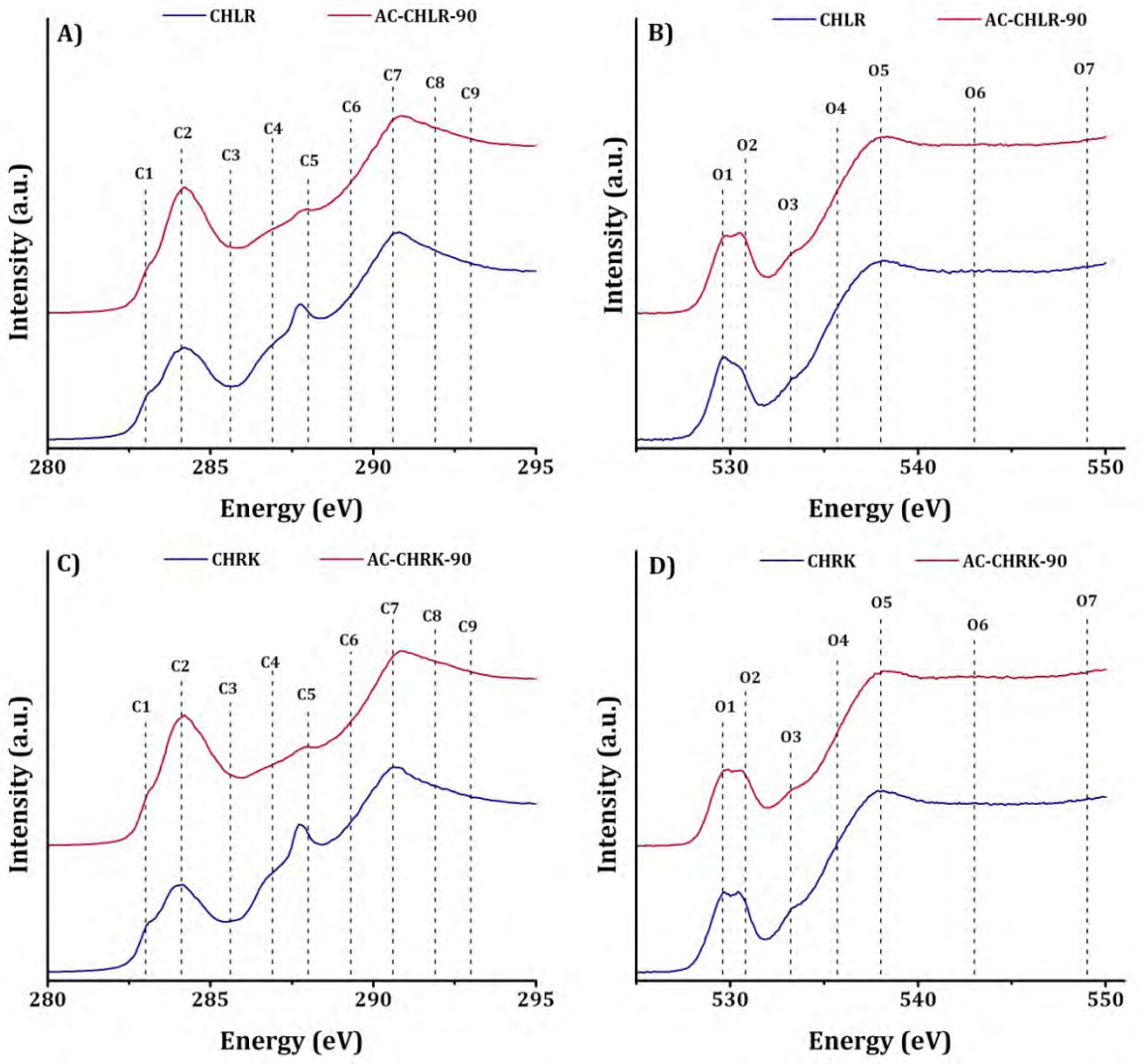

Figure 2-19 *~ C 1s & O 1s K edge NEXAFS Spectra CHLR, AC-CHLR-90, CHRK & AC-CHRK-90. Shown are* ***A)*** *C 1s K Edge NEXAFS Spectra of CHLR & AC-CHLR-90,* ***B)*** *O 1s K Edge NEXAFS Spectra of CHLR & AC-CHLR-90,* ***C)*** *C 1s K Edge NEXAFS Spectra of CHRK & AC-CHRK-90,* ***D)*** *O 1s K Edge NEXAFS Spectra of CHRK & AC-CHRK-90*

A decrease in the ***C5*** and ***O3*** ($\pi^*_{C\text{-}O\text{-}C}$) ether peaks of ~4% was observed for AC-CHRK-90, relative to CHRK. Interestingly this is not accompanied by a change in either the ***C8*** or ***O6*** ($\sigma^*_{C\text{-}O\text{-}}$

c) ether peaks. Furthermore, a substantial decrease in the ***C6*** aldehyde/hydroxyl peak is observed, along with an increase in the ***O4*** hydroxyl peak. These changes in oxygenated functional groups as observed by NEXAFS spectroscopy appear contradictory to the XPS results and make interpretation difficult. However, these inconsistencies might be explained by the differences in the X-ray penetration depth of NEXAFS spectroscopy compared to XPS (~ 100 nm versus ~ 10 nm, for NEXAFS and XPS respectively). Additionally as NEXAFS spectroscopy speaks only to the distribution of groups and not to their actual quantification, the data must be treated cautiously.

Table 2-9~ *C 1s & O 1s K Edge NEXAFS Peak Fitting of CHLR, AC-CHLR-90, CHRK and AC-CHRK-90, in Addition to CH-90, AC-90 and AC-N for Comparison*

K Edge	Name	Group		Assignment	Photon Energy (eV)	Peak Area %						
						AC-N	CH-90	AC-90	CHLR	AC-CHLR-90	CHRK	AC-CHRK-90
C 1s	C1	C=O	π*	Carbonyl substituted aromatic carbon (quinone)	283.0	12.5	1.0	1.1	1.5	1.4	1.7	1.0
	C2	C-C C=C	π*	Aromatic carbon, or aliphatic substituted aromatic carbon	284.1	32.7	13.9	31.3	19.1	27.4	18.7	31.1
	C3	C-OH C=O	π*	Phenolic or ketonic carbon	285.6	6.8	7.6	8.5	7.4	9.0	8.0	9.6
	C4	COOH COO	π*	Carboxylic acid or lactone carbon	286.9	9.3	8.4	11.2	11.2	9.3	9.8	10.8
	C5	C-O-C	π*	Cyclic ether carbon	288.0	7.5	7.7	13.3	14.6	12.1	13.7	9.5
	C6	C-OH C=O	π*	Aldhyde or hydroxyl substituted aliphatic carbon	289.3	7.4	18.2	10.5	18.1	14.4	21.8	12.4
	C7	COOH COO	σ*	Carboxylic acid or lactone carbon	290.6	11.5	31.1	15.2	17.4	16.9	16.9	15.6
	C8	C-O-C	σ*	Cyclic ether carbon	291.9	11.2	7.4	6.4	6.6	6.5	5.9	6.6
	C9	C-C C=C	σ*	Aromatic carbon (long range order)	293.0	1.2	4.6	2.5	3.9	3.1	3.5	3.3
O 1s	O1	C=O	π*	Aliphatic (linear or cyclic) aldehyde oxygen	529.6	11.2	5.8	6.4	13.4	11.0	11.3	11.7
	O2	C=O	π*	Carbonyl oxygen (ketonic or carboxylic acid)	530.8	8.1	13.9	16.5	5.9	11.4	9.7	10.7
	O3	C-O-C	π*	Aliphatic cyclic ether	532.7	11.9	21.3	16.4	17.1	9.2	11.6	7.8
	O4	C-OH	π*	Hydroxyl oxygen (alcohol)	535.7	33.0	20.2	24.6	33.2	40.3	36.7	41.4
	O5	C-OH C=O	σ*	Hydroxyl or carbonyl oxygen of carboxylic acid	538.0	20.5	28.8	17.0	19.5	21.8	25.1	21.9
	O6	C-O-C	σ*	Aromatic cyclic ether	543.0	2.8	5.5	14.7	7.1	2.4	2.1	2.2
	O7	C-OH	σ*	Phenolic oxygen	549.8	12.3	4.5	4.5	3.8	3.9	3.5	4.3

Similarly to the VBC derived steam activated miACs (***section 2.3.2.2***), no regular patterns emerged from the NEXAFS spectroscopy concerning the effect of steam activation of the two industrial chars. This is due in part to the substantial differences that exist between to two industrial chars as a result of the methods used in order to produce them (e.g. temperature, type of reactor, etc).

2.4.3 Structure of Char Derived Carbons

As was the case in ***section 2.3.3***, the structural characterisation of the char derived miACs was divided into two sections, the characterisation of the chemical and physical structure. Raman spectroscopy and XRD were used to characterise the chemical structure of the char derived miACs, whilst gas physisorption alone was used to characterise their physical structure.

2.4.3.1 Chemical Structure of Char Derived Carbons

2.4.3.1.1 Raman Spectroscopy

A confocal micro-Raman system (Renshaw) was used to take all Raman spectroscopy measurements for the industrial chars (CHLR and CHRK) and their miACs (AC-CHLR-90 and AC-CHRK-90, respectively). The normalised, deconvoluted and peak fitted Raman spectra are shown in ***Figure 2-7A-D***, with the results of the peak fitting reported in ***Table 2-10,*** along with those of AC-N, CH-90 and AC-90. As was reported in ***section 2.3.3.1.1***, the peak fitting and peak assignments were performed in-line with those reported by Sadezky *et al* [22] (***Table 1-4***).

As was the case for the carbon materials presented in ***section 2.3.3.1.1***, the most prominent feature of the Raman spectra obtained for the two industrial chars and their respective miACs (***Figure 2-20***), was the large ***D*** peak. This implies that like the carbon materials presented in ***section 2.3.3.1.1***, the chemical structure of the industrial chars is dominated by a disordered graphitic carbon, which is with previous findings for amorphous carbons [22, 39]. As the area of the ***A*** peak (assigned to amorphous carbon) remains relatively unchanged in the spectra obtained for these industrial chars and their miACs (***Table 2-10***), it appears that steam activation does not affect the relative proportion of this fraction.

The area of the ***G*** peak for the CHLR/AC-CHLR-90 pair exhibited very little change as a result of steam activation (***Table 2-10***), suggesting that the proportion of ordered graphitic carbon was unaffected by the conditions employed during steam activation (refer to ***section 6.4.2*** for details). A minor increase was observed in disordered graphitic carbon for AC-CHLR-90 relative to CHLR, which comprised a slight increase in the ***S*** peak and a corresponding decrease to the ***D***

peak of the same magnitude. This suggests a minor increase in the amount of graphene layer edges containing bound heteroatoms, but no overall change in the amount of disordered graphitic carbon within the CHLR/AC-CHLR-90 pair. Since no obvious changes were detected in the proportions of amorphous and ordered graphitic carbon, and only minor changes were found in the proportion of disordered graphitic carbon, it is clear that the chemical structure of AC-CHLR-90 relative to CHLR was relatively unchanged in these respects. This can be attributed to the non-reactive nature of CHLR, which was produced at 1173 K (100 K higher than the temperature used for steam activation).

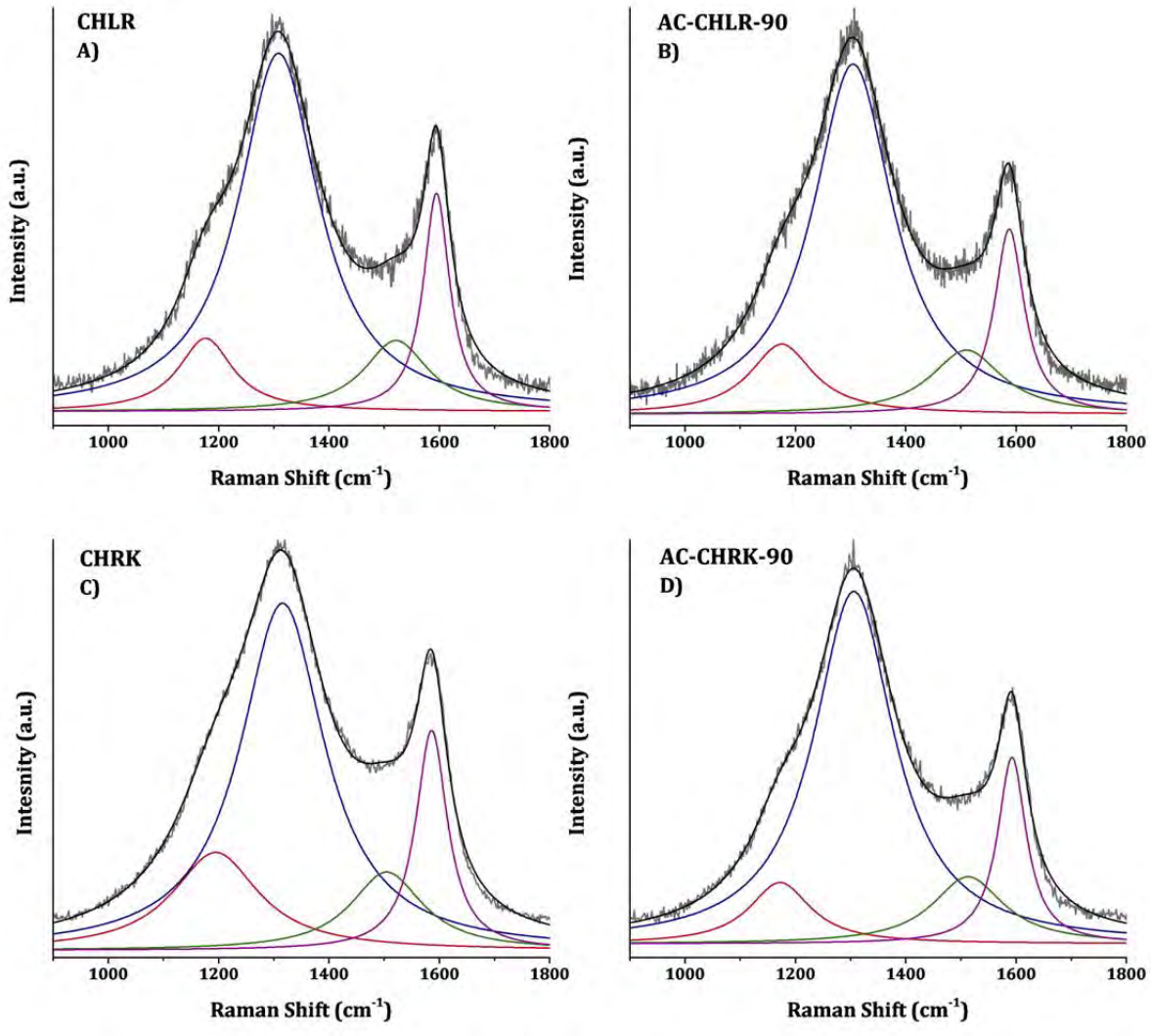

Figure 2-20 *~ Deconvoluted Raman Spectra of CHLR, AC-CHLR-90, CHRK & AC-CHRK-90. Shown are the peaks for the (—) Normalised Data, (—) Sum of Deconvoluted Peaks, (—) S peak, (—) D peak, (—) A peak, (—) G peak,* ***A)*** *CHLR,* ***B)*** *AC-CHLR-90,* ***C)*** *CHRK, and* ***D)*** *AC-CHRK-90*

It can be seen that CHRK underwent more change than CHLR as a result of steam activation, which is not unexpected as its carbonisation temperature (973 K) was 100 K lower than that employed during steam activation (1073 K). There was a relatively minor difference in the amount of amorphous carbon (***A*** peak) between CHRK or CHLR, but this did not change as a result of steam activation of either material.

Table 2-10 *~ Raman Peak Fitting Tables for the Char derived steam activated miACs*

Sample Name	Peak Area			
	S Disordered Graphitic Lattice*	**D** Disordered Graphitic Lattice†	**A** Amorphous Carbon	**G** Ideal Graphitic Lattice
AC-N	9.2	66.7	9.8	14.1
CH-90	12.9	63.6	11.6	11.8
AC-90	11.7	62.4	12.7	13.0
CHLR	9.3	66.5	10.7	13.4
AC-CHLR-90	10.5	65.5	10.8	13.1
CHRK	16.8	58.0	11.2	13.9
AC-CHRK-90	8.9	66.9	11.3	12.7

* *Heteroatoms Bound to Graphene Layer Edges*

† *Graphene Layer Edges*

For the CHRK/AC-CHRK-90 pair, there was a slight decrease in the amount of ordered graphitic carbon (***G*** peak) as a result of steam activation of CHRK (***Table 2-10***). Like CHLR, the amorphous and ordered graphitic carbon within CHRK was essentially unaffected by the conditions used for the steam activation process. Conversely, the disordered graphitic phases of CHRK (***S*** and ***D*** peaks) were more vulnerable to the effects of steam activation (AC-CHRK-90). The relative proportion of disordered graphitic lattices with bound heteroatoms decreased quite significantly upon steam activation, as characterised by a decrease in the area of the ***S*** peak of AC-CHRK-90 compared to CHRK. In fact the area of the ***S*** peak in the spectrum of CHRK was the highest measured for any carbon material presented in this thesis. Moreover, the decrease in the area of the ***S*** peak, equated to a nearly equivalent increase in the area of the ***D*** peak of AC-CHRK-90 relative to CHRK. While there was no overall change in the amount of disordered graphitic carbon within the CHRK/AC-CHRK-90 pair, the proportion of graphitic

lattice edges with bound heteroatoms reduced. Again, this was not surprising considering that the temperature of CHRK carbonisation was 100 K lower than the carbon materials presented in ***section 2.3.3.1.1*** and 200 K lower than CHLR.

Interestingly, the chemical structure of AC-CHRK-90 and the CHLR/AC-CHLR-90 pair possessed a great deal more in common with AC-N than they did with any of the carbon materials produced directly from VBC (***section 2.3.3.1.1***). One might attribute these findings to the materials having undergone industrial scale processing. In particular, the carbonisation temperature of CHLR is closer to that of AC-N (ΔT = 50 K) than to the VBC derived carbon materials presented in ***section 2.3.3.1.1***. Further information regarding the conditions used to produce AC-N might enable a more thorough comparison to be made.

Overall, the differences in chemical structure observed between CHLR and AC-CHLR-90 were insignificant. However, the changes observed for CHRK and AC-CHRK-90 were quite significant, indicating changes in the structural order of the carbon as a result of steam activation. For both chars the changes observed were found to be strongly tied to the temperature at which the char was initially produced.

2.4.3.1.2 Powder X-ray Diffraction (PXRD)

The x-ray diffraction (XRD) patterns of the industrial chars and the miACs derived from them are presented below in ***Figure 2-21A-B***. From the diffraction pattern in ***Figure 2-21***, it is clear that carbon structure possesses a low degree of structural order, typical of amorphous carbons [25-27].

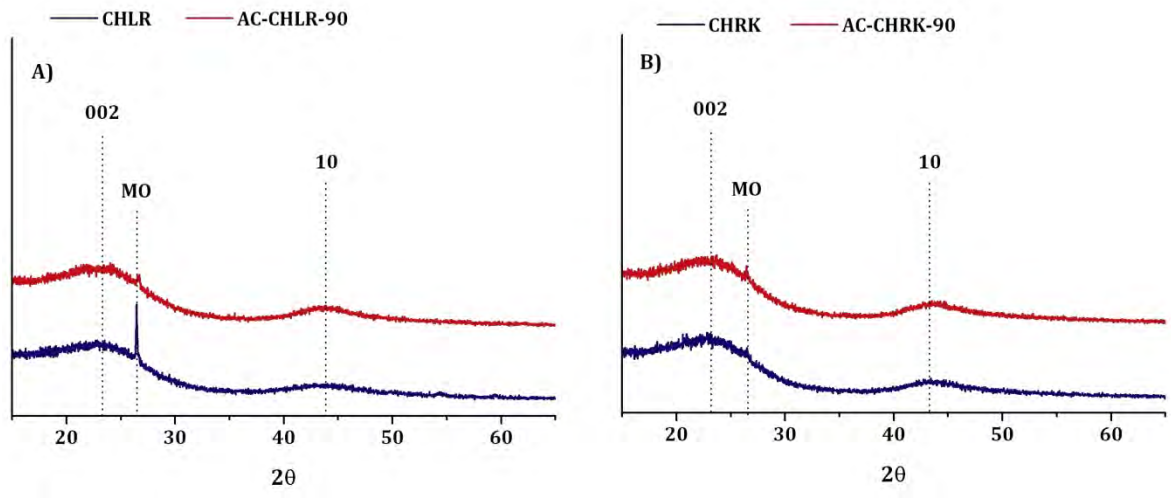

Figure 2-21 ~ *X-ray Diffraction of Steam Activated Industrial Chars. Shown are the XRD Patterns of* ***A)*** *CHLR and AC-CHLR-90, and* ***B)*** *CHRK and AC-CHRK-90*

Like the coal derived miACs two main diffraction peaks were observed for the char derived miACs, a peak at 24° 2θ due to the ***002*** reflection and another at 43° 2θ due to the ***10*** reflection. As was noted in ***section 2.3.3.1.2*** the ***10*** reflection is a combination of the ***100*** and ***101*** reflections, overlapping each other, and as such is just commonly referred to as the ***10*** peak. The ***10*** peak is known to arise from lateral order within the graphitic domains, with increases in intensity indicating an increase in lateral order [25]. The ***002*** reflection is known to result from the diffraction by atoms in parallel graphene sheets, with an increase in this peak indicating well defined graphitic domains [25]. For neither of the industrial chars, nor their steam activated miACs was there an observed change in the intensity of either the ***002*** or ***10*** peaks in the, indicating that no major changes in chemical structure of the graphitic phases has taken place (***Figure 2-21***).

Furthermore, another peak observed in ***section 2.3.3.1.2*** centred at 26° 2θ was also present, having been attributed to diffraction by amorphous metal oxides within the ash (***MO***) within the sample [29]. This peak is most pronounced for CHLR out of all the carbon materials presented in this thesis, due in large part to the high ash content of this char (ash_{CHLR} = 24.3 wt%), owing in part to the high temperature at which it was produced (1223 K).

In summation, the observations from the XRD study of the industrial chars and the miACs derived from them produced XRD patterns typical of amorphous carbons.

2.4.3.2 Physical Structure of Char Derived Carbons

2.4.3.2.1 Gas physisorption and displacement

In order to determine the surface area, pore volume and pore shape of both the micropores and mesopores within the ACs it was necessary to employ both CO_2 and N_2 adsorbates for the physisorption measurements (at 273 K and 77 K, respectively). The resultant BET and DR surface areas, along with the micropore and mesopore volumes together with the true density values for the industrial chars and their miACs are presented in ***Table 2-11***. Additionally the respective values for AC-N, VBC, CH-90 and AC-90 are also reported in ***Table 2-11*** to facilitate comparison.

CO_2 Physisorption

The CO_2 adsorption isotherms were measured on a TriStar II 3020 (Micromeritics) at 273 K using an ice bath to maintain constant temperature. Measurements were taken over a P/P_0

range of 0.00-0.03. The CO_2 isotherms for the two industrial chars and the miACs from their steam activation are presented in ***Figure 2-22A-B***, with the micropore surface area and limiting micropore volumes reported in ***Table 2-11***.

Table 2-11 ~ *Surface Area, Pore Volume & True Density of Char Derived Steam Activated miACs*

Sample Name	Surface Area (m^2/g)		Pore Volume (cm^3/g)				True Density (g/cm^3)
	CO_2	N_2	CO_2	N_2			
	DR	BET	V_{micro}	V_{micro}	V_{meso}	V_{total}	
VBC	148	-	0.05	-	-	-	1.40
AC-N	799	645	0.26	0.36	0.12	0.38	1.48
CH-90	640	282	0.21	0.16	0.06	0.18	1.85
AC-90	696	397	0.23	0.20	0.13	0.24	1.90
CHLR	609	384	0.20	0.22	0.02	0.29	1.83
AC-CHLR-90	623	351	0.20	0.23	0.05	0.27	1.88
CHRK	578	98	0.19	0.06	0.00	0.09	1.64
AC-CHRK-90	696	409	0.23	0.22	0.04	0.26	1.91

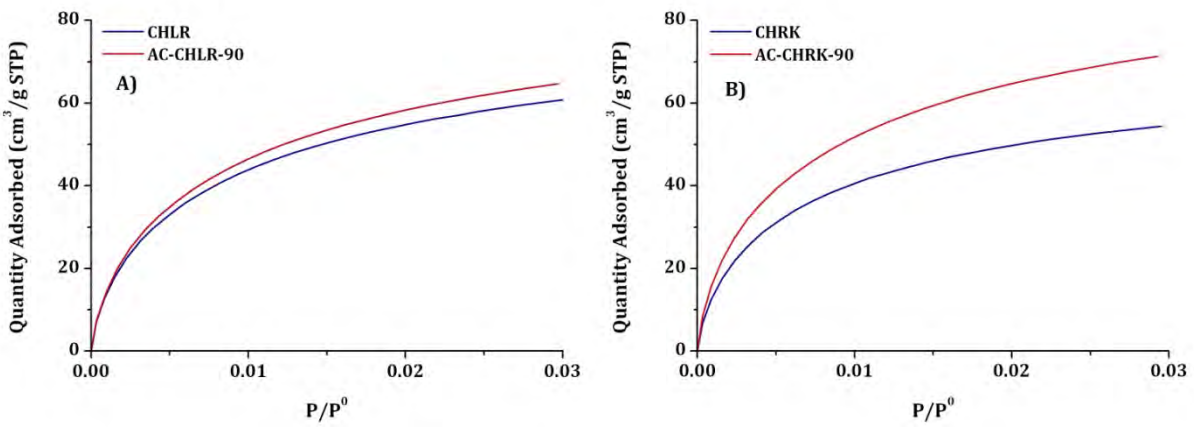

Figure 2-22 ~ *CO_2 Adsorption Isotherms at 273 K of Steam Activated Industrial Chars. Shown are the CO_2 Isotherms for **A)** CHLR and AC-CHLR-90, and **B)** CHRK and AC-CHRK-90*

Figure 2-22 shows the difference in CO_2 uptake of the commercial chars and their corresponding activated carbons. The magnitude of the difference between the CHLR char and AC-CHLR-90 is similar to that of the carbons produced directly from VBC and their respective

chars (***Figure 2-10***); whereas the magnitude of the difference between the CHRK and AC-CHRK-90 pair is greater, owing to the fact that the CHRK char exhibited a much lower CO_2 uptake compared to any of the other chars reported here. This was also reflected in the significant increase in DR surface area and micropore volume observed for AC-CHRK-90, relative to CHRK (***Table 2-11***). It is proposed that this is due to a higher content of volatile matter remaining in the char prior to activation, compared with that of any of the other chars reported here. Thus allowing for the control of the pore development in a similar manner to that of the carbons produced directly from VBC. Were this not the case, the magnitude of the difference between the CHRK and AC-CHRK-90 would be similar to that observed for the other carbon materials presented in ***section 2.3.3.2***.

N_2 Physisorption

The N_2 physisorption measurements for the two industrial chars and their miACs were carried out at 77 K over a P/P_0 range of 0.050-0.995 using a TriStar II 1320 (Micromeritics). From the N_2 adsorption isotherms, the BET surface area was calculated using ***equation 6-3***. The mesopore volume was calculated from the desorption arm of the isotherm using the BJH method (***section 6.6.3.2.1***). The N_2 adsorption isotherms and BJH PSDs of the industrial chars and the miACs derived from them are presented in ***Figure 2-23A-D***, with the BET surface area and mesopore volumes being reported in ***Table 2-11***.

In the N_2 adsorption isotherms (type ***II***) obtained for the industrial chars and their respective miACs (***Figure 2-23***), the hysteresis loops (type ***H4***) do not close. This has been attributed to low pressure hysteresis (LPH) [35-37], as was the case in ***section 2.3.3.2.1***, which was attributed to equilibrium not being achieved for the adsorption branch of the isotherm. For the two industrial chars, which lack any significant mesoporosity, closure of the hysteresis loops due to LPH was much more pronounced. For the two steam activated chars (AC-CHLR-90 and AC-CHRK-90, ***Figure 2-23B*** and ***Figure 2-23D***, respectively) closure of the hysteresis loop was more obvious, but by no means complete; which was attributed to the increases in the mesopore volume of these carbon materials relative to the chars from which they were derived (***Table 2-11***).

The N_2 physisorption showed that the steam activation of the CHLR (resulting in AC-CHLR-90) had little overall effect on the development of either micro- or mesopores (***Table 2-11***), especially when compared to the pore development observed for the steam activated coal derived miACs (***section 2.3.3.2.1***). These observations can be attributed to the temperature at

which CHLR had previously been carbonised, resulting in carbon that was less reactive under the steam gasification conditions.

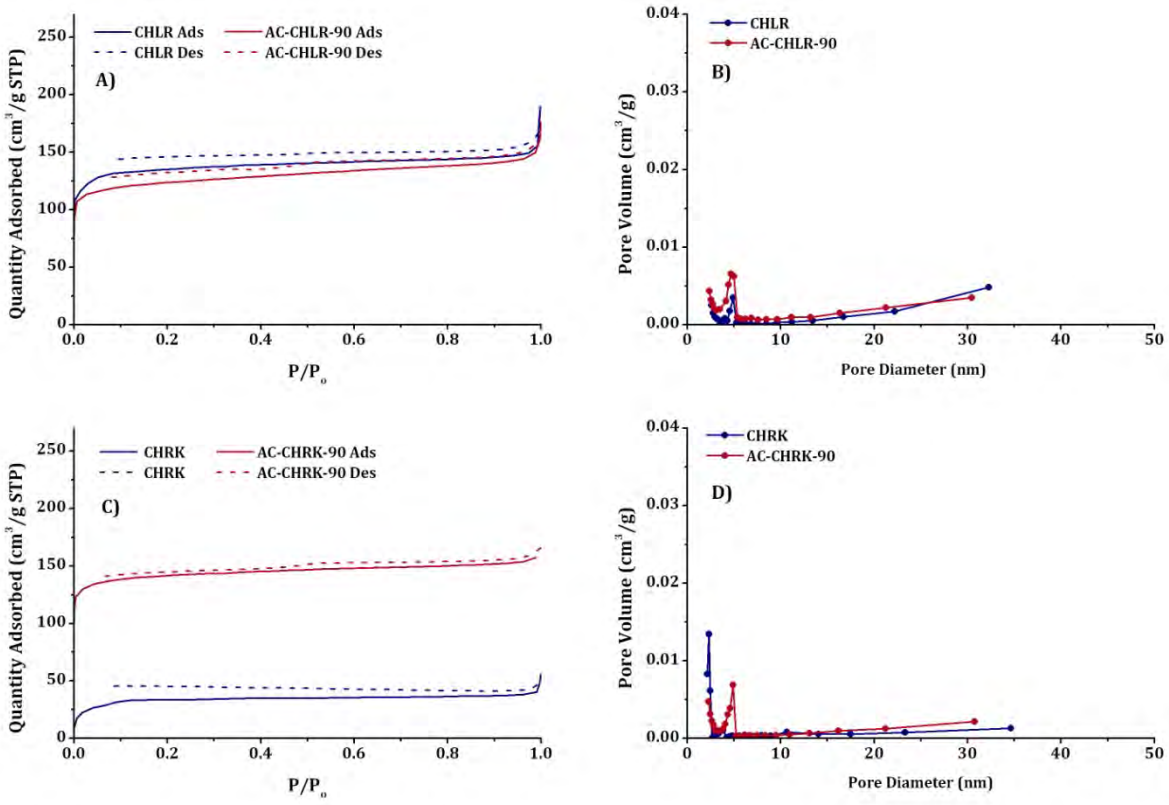

Figure 2-23 *~ N_2 Adsorption Isotherms and Pore Size Distribution at 77 K of Steam Activated Industrial Chars. Shown are* ***A)*** *N_2 Isotherms of CHLR and AC-CHLR-90,* ***B)*** *N_2 PSDs of CHLR and AC-CHLR-90,* ***C)*** *N_2 Isotherms of CHRK and AC-CHRK-90, and* ***D)*** *N_2 PSDs of CHRK and AC-CHRK-90*

The effect of steam activation on the pore development of CHRK was similarly retarded by the effects of having been previously carbonised at high temperature (973 K). However, as the carbonisation temperature of CHRK was lower than the steam activation temperature (1073 K) it possessed more carbon that was reactive under the steam activation conditions than was observed for CHLR. As such, much more substantial development of the pore structure was observed relative to CHLR, but this was predominantly isolated to the development of microporosity (and DR surface area, ΔS_{DR} = 311 m²/g). This can be observed from the significant increase in the adsorption of N_2 at P/P_o < 0.1 for AC-CHRK-90 relative to CHRK (***Figure 2-23C-D***), being due solely to the increased micropore volume of the steam activated AC-CHRK-90 (***Table 2-11***). This is not to say that there was no change in the mesopore volume of AC-CHRK-90 relative to CHRK, in fact the increase in mesopore volume was comparable to the increase in mesopore volume (***Table 2-11***).

In ***section 2.3.3.2.1*** it was noted that significant differences were observed in micropore volumes determined from the CO_2 and N_2 physisorption data, only when the miAC in question possessed a small mesopore volume. Although this did support the data presented in ***section 2.3.3.2.1*** (***Table 2-5***) it does not hold up for the CHLR char (***Table 2-11***), which possesses a smaller mesopore volume any of the VCB derived chars presented in ***section 2.3.3.2.1***. Conversely, the CHRK char exhibited no detectable mesopore volume, but followed the same trend of the VBC derived chars (***Table 2-11***). The N_2 micropore volume could be a single aberrant result, or more likely, it possessed numerous shallow micropores that allowed for the easier pore filling to take place; thus negating the need for significant mesoporosity. Furthermore, both AC-CHLR-90 and AC-CHRK-90 exhibited very similar CO_2 and N_2 micropore volumes, with both possessing greater mesopore volumes than their starting materials. The mesopore volumes for the AC-CHLR-90 and AC-CHRK-90 were however of the same magnitude as the VBC derived chars (***Table 2-11***).

He Pycnometry

For the industrial chars and the miACs derived from them, the true densities were determined by He displacement in a gas pycnometer (Micromeritics, Accupyc 1340). The measured true densities of the materials are presented (along with the surface areas and pore volumes measured by gas physisorption) in ***Table 2-11***. Referring to ***Table 2-11***, the measured densities of the char derived miACs are greater than the true density measured for the parent char. This can be attributed to the removal of volatile matter leaving the condensed carbon matrix.

2.4.4 Summary

Unlike the steam activated VBC derived miACs, no pattern was to be expected from the characterisation of the two industrial chars and their respective miACs. This is due to the vast differences that exist between the two methods by which the chars were produced.

For CHLR, which had previously been carbonised at 1173 K, steam activation resulted in only a minor increase in the bulk C content of AC-CHLR-90 (ΔC_{bulk} = 1.6 wt%), as CHLR was found to be highly non-reactive. Interestingly the bulk O and ash content actually decreased upon steam activation, the only instance of this occurring out of all the steam activated miACs. Although the decrease in ash content is a strange result, the XRD peak assigned to amorphous metal oxides in the ash (***MO***) that was so prominent in the XRD pattern of CHLR was significantly reduced in the XRD pattern of AC-CHLR-90. The strongest evidence as to the non-reactive nature of CHLR can be observed from the yield of AC-CHLR-90 (74.5 wt%), close to 30 wt% higher than the

difference between char and AC for the steam activated VBC derived miACs presented in ***section 2.2***. Moreover, for CHLR there was not any effective development in micro- or mesopore volume, under steam activation conditions at 1073 K. Other than the observation made of the decrease in the MO peak in the XRD of the CHLR/AC-CHLR-90 pair, no structural differences of significance were apparent.

Even though CHRK was produced at a lower temperature (973 K) than CHLR (1173 K), the yield of AC-CHRK-90 was ~ 6 wt% higher than AC-CHLR-90. Relative to CHRK, AC-CHRK-90 possessed a slight increase in bulk C content (ΔC_{bulk} = 2.0 wt%), with an almost negligible change in bulk O or ash. Despite the insignificant change in bulk O with steam activation, the XPS analysis of the CHRK/AC-CHRK-90 pair showed an increase in the surface O content (ΔO_{surf} = 4.3 at%), with an associated decrease in surface C content (ΔC_{surf} = 3.9 at%). As this occurred both micro- and mesopores were further developed as can be seen from both the CO_2 and N_2 gas physisorption data (***Figure 2-22*** and ***Figure 2-23***, respectively). However, even though the mesopore volume of AC-CHRK-90 (V_{meso} = 0.05 cm^3/g) was larger than CHRK (V_{meso} = 0.02 cm^3/g) as a result of steam activation, the total mesopore volume is still quite a bit lower than that of AC-90 (V_{meso} = 0.13 cm^3/g). Taking into account the minor changes in bulk composition, pore volume and surface chemistry, it is clear that due to the temperature at which CHRK was produced (973 K), that there has been little change in the bulk carbon structure, with the reaction occurring predominately at the surface of CHRK, as was also the case for the CHLR/AC-CHLR-90 pair. Similarly there was little change regarding these aspects of the structure as probed by XRD.

The main change in the surface chemistry (XPS) from the steam activation of CHRK was observed as an increase in the surface O content of ~ 4 at%, which was expressed as increases in all oxygenated surface functional groups (C=O, C-O-R, and COO-R). The most significant change was for the C-O-R group ($O_{C\text{-}O\text{-}R}$ = 5.5 at%) that, upon further investigation using NEXAFS spectroscopy, was found that hydroxyl groups present in a higher proportion to ethers. The implications this holds from a perspective of CO_2 adsorption is that, hydroxyl groups are likely to increase the affinity of the AC surface for CO_2 and that this change in surface chemistry should be favourable.

Overall, both the industrial chars were shown to be reasonably non-reactive under steam gasification conditions. As such only minor improvements in mesopore volume were achieved through steam activation. For the CHLR/AC-CHLR-90 pair the changes in both bulk composition and chemical structure as a result of steam activation were relatively insignificant, whereas quite substantial changes in the surface chemistry were observed. This indicated that steam activation primarily acted on the CHLR surface rather than the bulk structure of the carbon. On

the other hand, the CHRK/AC-CHRK-90 pair exhibited significant changes to both the structural order of the carbon as well as the carbon surface, as a result of steam activation. The differences in the reactivity of the two industrial chars was attributed to the different temperatures at which they were produced, with CHLR being produced 100 K higher than the steam activation temperature (1073 K), and CHRK produced 100 K lower.

2.5 Production of Chemically Activated Microporous Carbons

Chemical activation with the intent of producing ACs with PSDs shifted towards the micropore region, is best achieved using a chemically activating agent such as KOH or NaOH. This is not steam activated, but carbonised. The action of alkali metal hydroxides is the source of a great deal on conjecture amongst researchers, with several theories as to the exact mechanism of activation, all of which are scientifically sound (***section 1.7.2***) [40-42]. Regardless of the exact mechanism of action, KOH allows for the heavier components of the volatile matter of the AC precursor to be retained. The retained heavy components of the volatile matter are then carbonised, forming a complex interconnected matrix within the already small pores present. For this project only KOH was investigated, due to the large amount of studies done previously using it as an activating agent [2, 31, 41-46].

KOH was used as an agent for the chemical activation of the VBC precursor. Furthermore due to the high reactivity of potassium metal with water, the activation was done in the absence of steam, and as such, the samples were carbonised only, not gasified. In these experiments, the activation time was maintained at 60 min, but the amount of KOH was varied. This was achieved by wet impregnating the coal particles with KOH, followed by removal of the solvent, and subjecting the samples to a 60 min carbonisation treatment (1073 K in a N_2 atmosphere, in a fixed bed reactor).

2.5.1 Composition of Chemically Activated Carbons

The composition of the KOH activated miACs, VBC starting material and reference materials were investigated using elemental (Vario MICRO cube, Elementar) and ash analysis (Mettler Toledo, TGA/DSC 1, Star* System), the results of which are presented in ***Table 2-12***.

The elemental analysis of AC-K0 relative to VBC shows a substantial decrease in O and H content, with a major increase in C and ash content (ΔAsh = 3.2 wt%, ***Table 2-12***). This is what one would expect to observe from carbonisation alone, with a similar result obtained for CH-45

relative to VBC (***Table 2-1***). The KOH activated miACs (AC-K5, AC-K7.5 and AC-K10) did possess higher ash contents that the physically activated carbon materials presented in ***section 2.3*** and ***section 2.4***. The KOH active miACs were acid washed in order to remove excess K remaining from the activation process. This will also have acted to remove some of the inherent ash within VBC that would have been present; as such the ash content of the KOH activation miACs are lower than would be expected relative to the "as produced" carbons. For full compositional analysis to have been able to be carried out on the ash of the KOH activated miACs, several large batches would have been required to be produced solely for this purpose, as this type of analysis requires a minimum of 1 g of ash. This was deemed to be not feasible and as such was not undertaken. Furthermore, as it is well known than KOH exerts its action as a chemically activating agent predominately between graphene sheets, complete removal of K will be technically impossible.

Table 2-12 ~ *Elemental Analysis & Ash Determination of KOH Activated Carbon*

Sample Name	Yield (wt%)	Ultimate Analysis (wt%, daf)				H/C Ratio	Ash (wt%)
		C	H	N	O_{diff}		
AC-N	-	76.3	0.8	1.0	21.9	0.12	10.9
VBC	-	61.4	4.4	0.6	33.5	0.86	0.4
AC-K0	47.2	86.5	1.4	0.8	11.3	0.19	3.6
AC-K5	49.2	83.5	1.2	1.1	14.1	0.17	6.2
AC-K7.5	49.7	82.8	1.1	1.3	14.9	0.15	8.5
AC-K10	51.2	79.2	1.1	1.2	18.4	0.17	10.1

When KOH was introduced into the activation process (AC-K5), there were only minor changes to the N and H content, relative to AC-K0. However, there was a 3 wt% decrease in the C content, with a consequent increase of 2.8 wt% in both O and ash content. By increasing to KOH content further to 7.5 wt%, a small decrease of 0.7 wt% was observed was the C content of AC-K7.5, relative to AC-K5, with an increase of 2.3 wt% in ash. Relative to AC-K5, the O content of AC-K7.5 only increased by 0.8 wt%. It was not until at a KOH loading of 10 wt%, further changes occurred giving a C content 3.5 wt% lower, with an O content 3.5 wt% higher.

Moreover, all of the KOH activated miACs possessed an O content several percent lower (ΔO_{bulk} = 3-8 wt%) than the AC-N benchmark carbon. The C content of the KOH activated miACs were

between 3-7.5 wt% higher than that of AC-N, with the composition of AC-K10 possessing the closest similarity to AC-N of any AC presented in this thesis.

To summarise, the overall variation in composition as a function of KOH loading was relatively minor, especially when compared to the steam activated miACs. The composition of the KOH activated miACs is much more similar to that of AC-N, another KOH activated miAC, produced industrially.

2.5.2 Surface Chemistry of Chemically Activated Carbons

As previously stated regarding the steam activated carbons, both the standard spectroscopic methods for determining the surface chemistry (e.g. FT-IR) and issues with the reproducibility of wet chemical analysis, have left x-ray absorption spectroscopy (XAS) as the most reliable and reproducible method for determining the surface chemistry of carbon materials. The types of XAS used to investigate the surface chemistry of the KOH activated miACs was NEXAFS spectroscopy and XPS, as was the case with the steam activated miACs. The focus was to investigate the oxygenated functional groups at the AC surface, as these are known to have a more influential effect on the adsorption properties of the ACs.

2.5.2.1 X-ray Photoelectron Spectroscopy (XPS)

The high resolution C 1s and O 1s XPS spectra for the KOH miACs AC-K0, AC-K5, AC-K7.5 and AC-K10 are presented in ***Figure 2-24A-H***, with the peak fitting results shown in ***Table 2-13***. The XPS measurements were taken on a Kratos Axis HSi X-ray photoelectron spectrometer, as outlined in ***section 6.6.2.1***. The C 1s and O 1s XPS spectra obtained for the reference material, AC-N, are presented in ***Figure 2-2A-B.*** The peak fittings for both the C 1s and O 1s spectra were done according to standard practices employed by Biniak *et al* (1997)[17] and Puziy *et al* (2008)[18], including the assignment of each peak in the fitting [17-21].

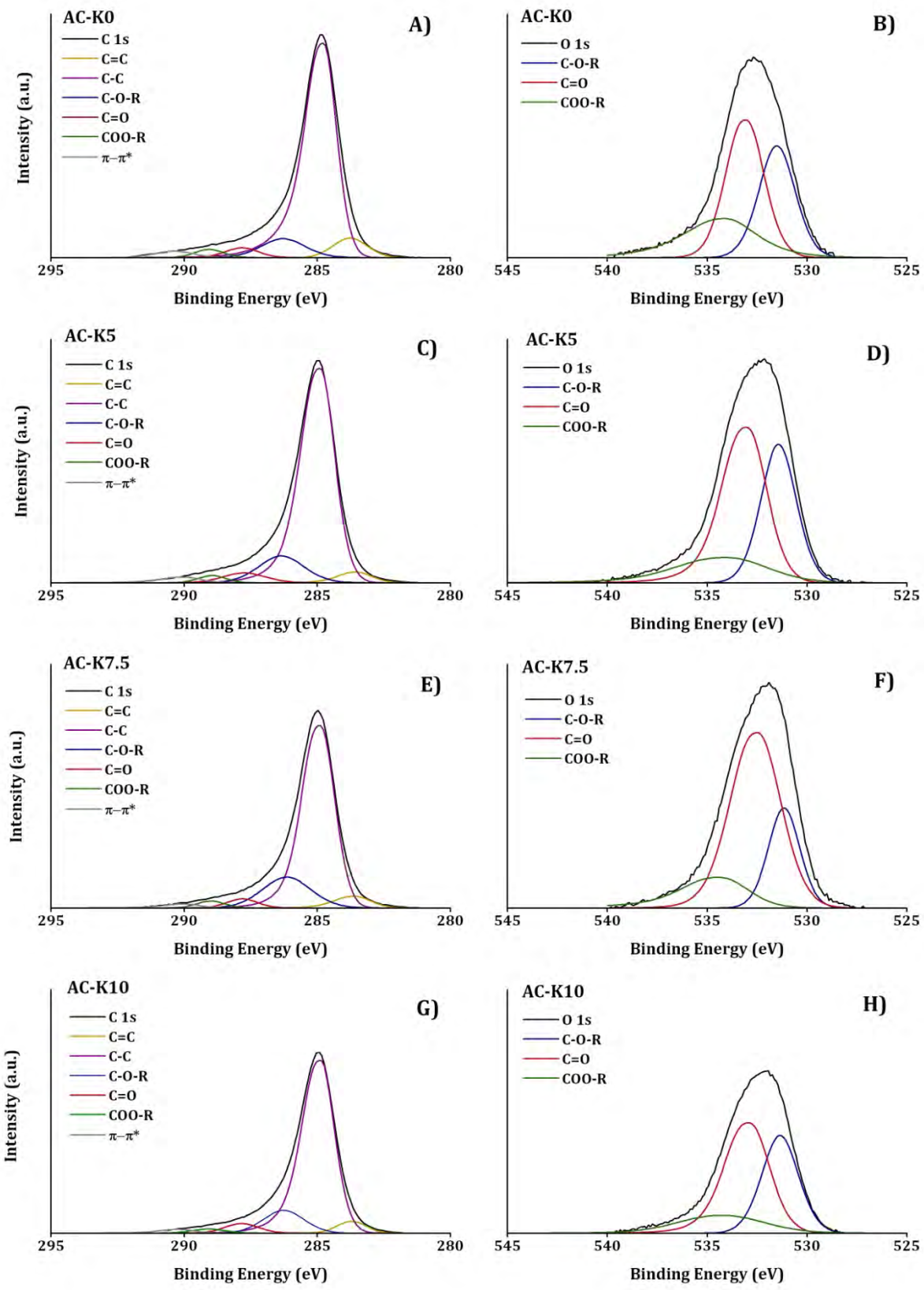

Figure 2-24 *~ High Resolution XPS Spectra of C 1s and O 1s for AC-K0, AC-K5, AC-K7.5 and AC-K10. Shown are* ***A)*** *C 1s Spectra of AC-K0,* ***B)*** *O 1s Spectra of AC-K0,* ***C)*** *C 1s Spectra of AC-K5,* ***D)*** *O 1s Spectra of AC-K5,* ***E)*** *C 1s Spectra of AC-K7.5,* ***F)*** *O 1s Spectra of AC-K7.5,* ***G)*** *C 1s Spectra of AC-K10, and* ***H)*** *O 1s Spectra of AC-K10*

Table 2-13 *~ XPS Peak Fitting for AC-K0, AC-K5, AC-K7.5 and AC-K10*

Peak Assignment	Binding Energy (eV)	Surface Concentration (at%)				
		AC-N	AC-K0	AC-K5	AC-K7.5	AC-K10
C 1s	284.9	91.95	90.22	87.28	85.43	87.47
C=C	283.5	5.08	6.15	3.33	4.41	3.87
C-C	285.0	72.91	68.65	65.66	60.13	66.24
C-O-R	286.3	6.01	7.75	10.59	14.58	10.38
C=O	287.5	3.60	3.05	3.69	2.80	3.72
COO-R	289.1	1.97	2.25	1.79	1.94	1.59
π–π^*	290.3	2.38	2.37	2.23	1.57	1.66
O 1s	532.1	7.83	9.48	11.41	12.76	10.68
C=O	531.6	3.50	3.10	3.86	2.81	3.74
C-O-R	533.4	2.58	4.04	5.67	7.97	5.33
COO-R	535.7	1.75	2.34	1.88	1.98	1.61
N 1s	400.9	0.22	0.30	0.79	1.01	0.98
K 2p	293.9	-	-	0.52	0.80	0.87

Compared to the coal derived miACs and their respective analogues in the CH series (e.g. CH-45, AC-45, CH-90, AC-90, CH-180 and AC-180), AC-K0 (***Figure 2-24B***) has a significantly higher surface O content. This is an important finding, as the major differences between the production methods used for AC-K0 and CH-45/CH-90 were the times of carbonisation (intermediate to CH-45 and CH-90) and, the secondary reactor used for activation. For CH-45 and CH-90 the secondary reactor was composed of steel mesh that allowed unhindered diffusion of N_2 through the walls and base of the steel mesh. Conversely, for AC-K0 and all the KOH activated miACs a quartz secondary reactor was used, comprising of a quartz tube with a sintered quartz frit at the base (porosity grade 1, refer ***section 6.4.2***). This reactor appears to have hindered the flow of gas, only permitting the downward flow of gas from the top through to the base. Due to the small porosity of the frit, flow through the frit was reduced. As such, a much higher amount of N_2 will have flown around the quartz reactor rather than through it, relative to the flow through the steel mesh reactor. This will likely have greatly affected the rate of removal of volatile and gaseous compounds from the carbon during activation. This probably helps to account for many of the differences in AC characteristics observed for the KOH activated miACs, and is important when trying to compare the miACs produced using the two different activation methods. The C=C bonds present on the surface of AC-K0 are several percent higher than observed for the miACs produced in the presence of KOH.

The surface oxygen content of AC-K5 (***Figure 2-24C-D***) was ~ 2 at% higher than AC-K0. This was expressed as an increase in the concentration of C-O-R ($\Delta O_{C\text{-}O\text{-}R}$ = 1.6 at%) and C=O ($\Delta O_{C=O}$ = 0.8 at%) groups, for AC-K5 relative to AC-K0. Conversely AC-K5 exhibited a decrease in COO-R groups relative to AC-K0, indicating that the use of KOH as an activating agent favoured the formation of C-O-R and other C=O groups over COO-R groups. Furthermore, a 2.5 fold increase in the surface nitrogen content was observed on AC-K5 (0.8 at%), compared to that of AC-K0 (0.3 at%) as a result of the introduction of KOH.

Increasing the amount of KOH from 5-7.5 wt% resulted in an increase in the surface oxygen content of 1.3 at% (***Table 2-13***). This increase in the surface oxygen concentration was mostly attributable to an increase in C-O-R groups of 3.9 at%. Although this was accompanied by a significant reduction in C=O groups (***Table 2-13***). Thus the XPS analysis of AC-K5 showed that the use of KOH at a loading of 5 wt% favoured the formation of C-O-R and C=O groups. The results for AC-K7.5 (***Figure 2-24E-F*** and ***Table 2-13***) showed that increasing the KOH loading to 7.5 wt% promoted the formation of C-O-R groups over C=O groups. The nitrogen surface content, also increased (ΔN_{surf} = 0.2 at%) with KOH loading.

For AC-K10 (***Figure 2-24G-H*** and ***Table 2-13***) a decrease in the surface oxygen content was observed as a result of increasing to KOH loading to 10 wt%. Moreover, the distribution of surface functional groups also changed significantly, such that there was no regular pattern in their variation as a function of KOH loading (***Table 2-13***). Interestingly, virtually no change in the nitrogen surface content was observed for AC-K10 compared to AC-K7.5.

It has already been noted that the ratio of C 1s to O 1s (C:O ratio) for a particular group from XPS can allow for greater insight into the identity of the group or groups responsible. This has shown to be of great importance in particular for the C-O-R peak. For the KOH activated miACs, as was the case for all the other miACs presented in this chapter, the C:O ratio of the C-O-R peak was ~ 2, implying the presence of ether groups.

Lastly, it is important to note that all the KOH activated miACs possessed low surface K concentrations. This was expected because the materials were subjected to rigorous acid washing protocols to dissolve and remove residual components of the activating agent.

2.5.2.2 Near Edge X-ray Absorption Fine Structure (NEXAFS) Spectroscopy

Carbon and oxygen K-edge NEXAFS spectra of all chemically activated miACs were taken on the SXR beamline at the Australian Synchrotron. The collection and processing details can be found in ***section 6.6.2.2***. The spectra are presented in ***Figure 2-25A-F***, with the fitting shown in ***Table***

2-14. The complete fitting for both the C 1s and O 1s spectra can be found in ***Appendix 2 – NEXAFS Spectroscopy Peak Fitting***, for all of the carbon materials investigated.

From the NEXAFS analysis of the KOH miACs (***Figure 2-25***), the changes in the percentage peak area of virtually all functional groups as a function of KOH loading are minor. There was some variation across the series of KOH miACs with respect to the area of the ***C2*** peak, with no regular pattern in the variation as a function of KOH loading. Similarly, the very minor variation in the ***C9*** peak area showed no clear pattern as a function of KOH loading. From this it can be inferred, that KOH had no significant effect on either the long range order, or the amount of surface aromatic carbon, as determined by NEXAFS spectroscopy. Furthermore, the NEXAFS data for the ***C2*** and ***C9*** peaks, are in agreement with the observed variation from the XPS for the C-C and C=C peaks (***Table 2-13***). A further point of interest was the observed decrease in the $\pi^*_{C\text{-}O\text{-}C}$ ether peaks (***C5*** and ***O3***) observed in both the C 1s and O 1s NEXAFS spectra with increasing KOH loading, but not for the $\sigma^*_{C\text{-}O\text{-}C}$ peaks (***C8*** and ***O6***), which indicates that the formation of aromatic ethers are more favourable with increasing KOH loading.

The ***C3*** peak, which is assigned to ketones/phenols, initially increases as KOH is introduced, but after a KOH loading of 5 wt% decreases marginally. This is accompanied by a clear increase in phenols, evident from increases in the ***O7*** peak area (assigned solely to phenolic oxygen) at KOH loadings above 5 wt%. While it is possible that the ketone content changed slightly, it is most likely that changes in ***C3*** and ***O7*** arise principally from increased phenolic content. Moreover, the overall ratio of ***O1*** to ***O2*** peaks did not differ greatly, which is further evidence that the distribution of ketones and aldehydes did not vary significantly as a function of KOH loading.

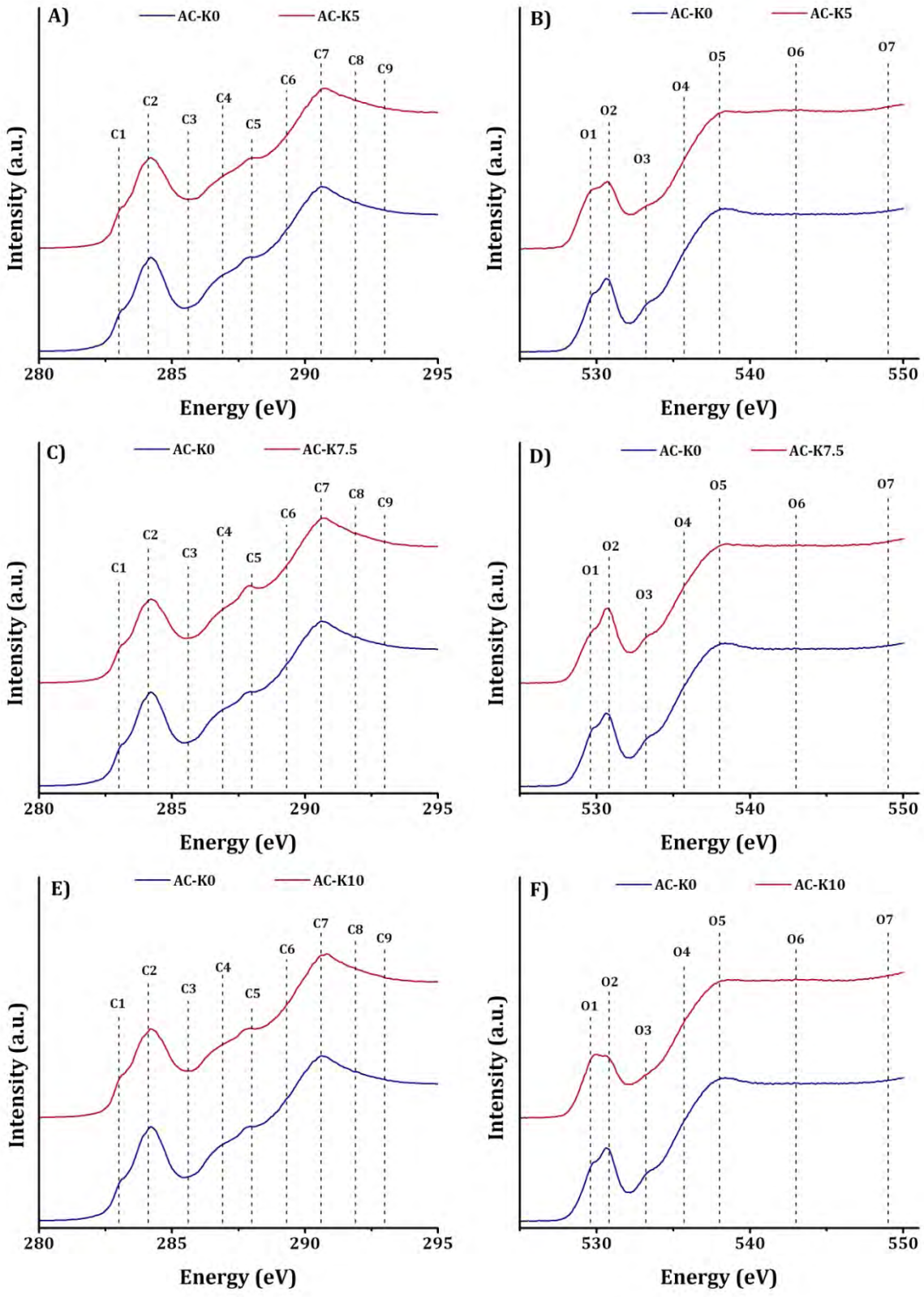

Figure 2-25 *~ C 1s and O 1s K-edge NEXAFS Spectra of AC-K0, AC-K5, AC-K7.5 & AC-K10. Shown are* ***A)*** *C 1s K Edge NEXAFS Spectra of AC-K0 & AC-K5,* ***B)*** *O 1s K Edge NEXAFS Spectra of AC-K0 & AC-K5,* ***C)*** *C 1s K Edge NEXAFS Spectra of AC-K0 & AC-K7.5,* ***D)*** *O 1s K Edge NEXAFS Spectra of AC-K0 & AC-K7.5,* ***E)*** *C 1s K Edge NEXAFS Spectra of AC-K0 & AC-K10, and* ***F)*** *O 1s K Edge NEXAFS Spectra of AC-K0 & AC-K10*

Table 2-14 *~ C 1s & O 1s K Edge NEXAFS Peak Fitting AC-K0, AC-K5, AC-K7.5, AC-K10 and AC-N*

K Edge	Name	Group		Assignment	Photon Energy (eV)	Peak Area %				
						AC-N	AC-K0	AC-K5	AC-K7.5	AC-K10
C 1s	C1	C=O	π*	Carbonyl substituted aromatic carbon (quinone)	283.0	12.5	2.0	1.4	1.3	1.6
	C2	C-C C=C	π*	Aromatic carbon, or aliphatic substituted aromatic carbon	284.1	32.7	22.4	25.1	23.0	24.7
	C3	C-OH C=O	π*	Phenolic or ketonic carbon	285.6	6.8	7.2	7.8	6.6	6.5
	C4	COOH COO	π*	Carboxylic acid or lactone carbon	286.9	9.3	13.8	13.1	13.9	15.3
	C5	C-O-C	π*	Cyclic ether carbon	288.0	7.5	12.1	11.9	11.4	9.8
	C6	C-OH C=O	π*	Aldhyde or hydroxyl substituted aliphatic carbon	289.3	7.4	16.4	15.3	17.2	15.8
	C7	COOH COO	σ*	Carboxylic acid or lactone carbon	290.6	11.5	17.2	16.5	17.1	17.2
	C8	C-O-C	σ*	Cyclic ether carbon	291.9	11.2	5.5	6.0	6.5	6.5
	C9	C-C C=C	σ*	Aromatic carbon (long range order)	293.0	1.2	3.4	2.8	2.8	2.5
O 1s	O1	C=O	π*	Aliphatic (linear or cyclic) aldehyde oxygen	529.6	11.2	9.3	12.8	9.5	10.5
	O2	C=O	π*	Carbonyl oxygen (ketonic or carboxylic acid)	530.8	8.1	12.4	12.0	11.3	11.5
	O3	C-O-C	π*	Aliphatic cyclic ether	532.7	11.9	11.8	10.6	9.9	9.4
	O4	C-OH	π*	Hydroxyl oxygen (alcohol)	535.7	33.0	36.0	36.2	35.8	37.6
	O5	C-OH C=O	σ*	Hydroxyl or carbonyl oxygen of carboxylic acid	538.0	20.5	24.6	21.6	18.1	19.2
	O6	C-O-C	σ*	Aromatic cyclic ether	543.0	2.8	2.3	2.7	2.7	2.6
	O7	C-OH	σ*	Phenolic oxygen	549.8	12.3	3.5	4.2	12.7	9.2

With the increase in C-O-R groups observed from the XPS analysis, NEXAFS reveals that the distribution of surface ether and hydroxyl groups is shifted slightly towards more hydroxyl groups as the KOH loading increased to 7.5 wt%. By further increasing the KOH loading to 10 wt%, a significant decrease in the C-O-R group content was observed by XPS, whilst the NEXAFS is conflicting on the exact distribution of hydroxyl and ether groups. Relative to AC-K7.5, AC-K10 showed a decrease in the area of the ***C6*** hydroxyl peak, but an increase in the ***O4*** hydroxyl peak. It would therefore seem that in general increasing the KOH loading to a point, favours the development of an AC surface with more hydroxyl groups and a presumably higher affinity for CO_2 [1].

Although discerning clear patterns in the changing surface chemistry from the NEXAFS spectroscopy was difficult, a better picture has been obtained as to the identity of certain functional groups, such as ethers, hydroxyl, ketones and aldehydes, that comprise the vast majority of oxygenated functional groups on the KOH miACs surface.

2.5.3 Structure of Chemically Activated Carbons

For the steam activated miACs the structural investigations were separated into two sections, that focusing on the chemical structure, whilst the other focused on the physical structure of the miACs. This separation of structural attributes was also applicable to the KOH activated miACs, with the chemical structure being characterised by Raman spectroscopy and XRD and the physical structure being characterised using gas physisorption and TEM.

2.5.3.1 Chemical Structure of Chemically Activated Carbons

2.5.3.1.1 Raman Spectroscopy

The results of the Raman spectroscopy for the KOH ACs were carried out on a confocal micro-Raman system (Renshaw). The normalised and deconvoluted spectra were peak fitted and are presented below in ***Figure 2-26***, with the results of the peak fitting being given in ***Table 2-15***, in accordance with the peak assignments outline in ***Table 1-4***.

The structural order of the KOH activated miACs (***Table 2-15***) varied gradually with increasing KOH loading. Upon the introduction of 5 wt% KOH into the system as an activating agent (to produce AC-K5), an increase in the amorphous carbon content was observed relative to AC-K0, which was accompanied by a decrease in the amount of ordered graphitic carbon. These observations were characterised by a decrease in the area of the ***A*** peak and an increase in the area of the ***G*** peak of AC-K5 relative to AC-K0. Interestingly, increasing the KOH loading beyond 5 wt% resulted in no further increase to the relative proportion of amorphous carbon within the KOH activated miACs. Other than an initial decrease in the amount of ordered graphitic carbon of AC-K5 relative to AC-K0 (***G*** peak), further increases to the KOH loading resulted in only minor decreases in the ordered graphitic carbon content of the materials (***Table 2-15***).

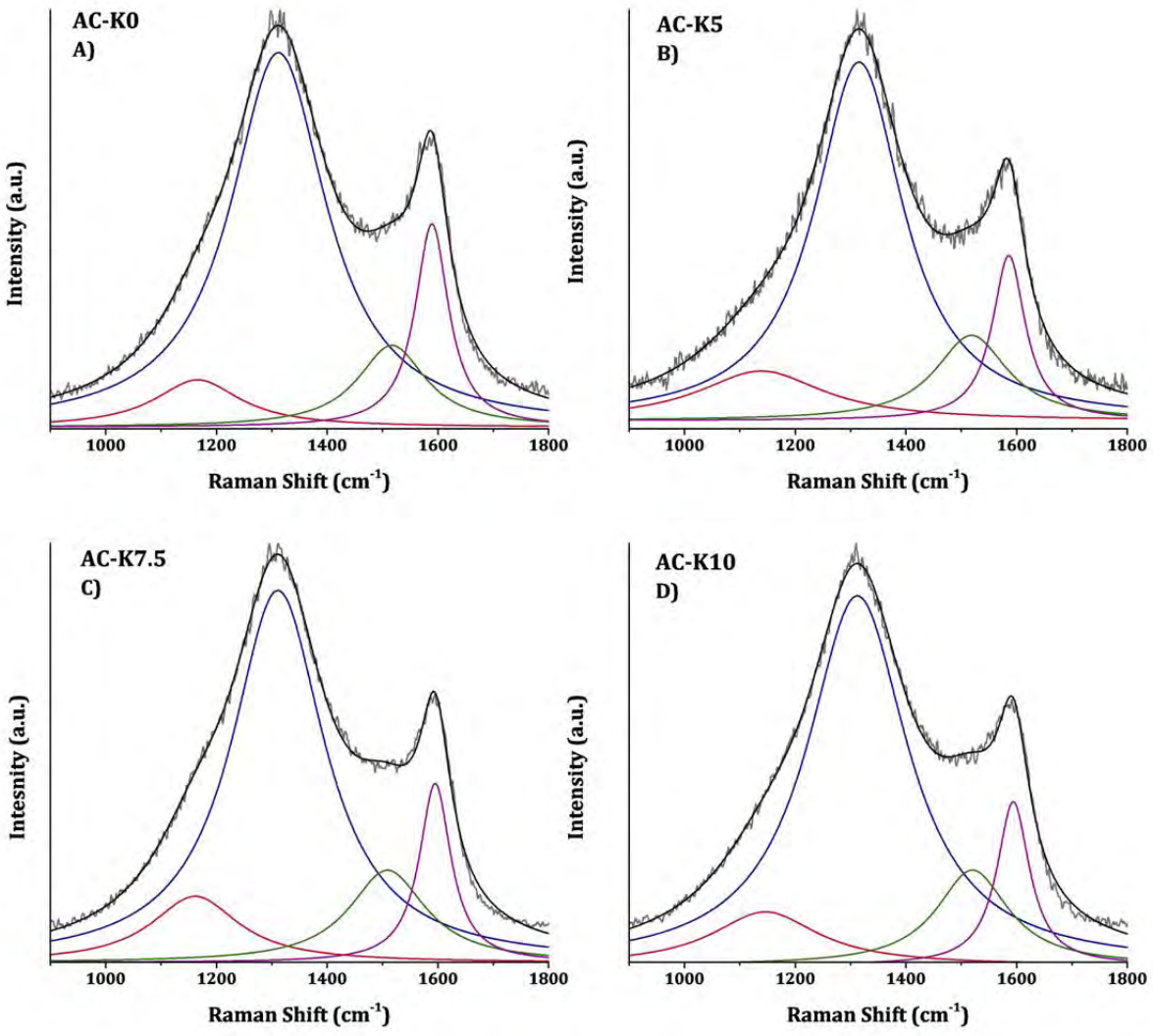

Figure 2-26 *~ Deconvoluted Raman Spectra of AC-K0, AC-K5, AC-K7.5 & AC-K10. Shown are the peaks for the (—) Normalised Data, (—) Sum of the fitted Peaks, (—) S peak, (—) D peak, (—) A peak, (—) G peak,* ***A)*** *CH-K0,* ***B)*** *AC-K5,* ***C)*** *AC-K7.5,* ***D)*** *AC-K10*

The introduction of KOH during activation had no effect on the overall amount of disordered graphitic carbon (***S*** plus ***D*** peaks), but it did shift the proportion of heteroatoms within this phase, as indicated by changes in the area of the ***S*** peak. These changes manifested not only as changes in the area of the ***S*** peak across the series, but also as well defined changes in the shape of the ***S*** peak. This was expressed initially as broadening of the ***S*** peak at a KOH loading of 5 wt%, which then sharpened and increased in intensity as the KOH loading was increased from 5 to 10 wt%. With gradual increases in the KOH loading beyond 5 wt%, successive decreases in the amount of heteroatoms present in the disordered graphitic phase were observed, along with increases in the proportion of disordered graphene layer edges without heteroatoms bound (***D*** peak). It is generally considered that the microporosity of ACs arises from the spaces between

graphene sheets [47], particularly for miACs produced using alkali metal hydroxides (e.g. NaOH, KOH). As the ***D*** peak is associated with the edges of the graphene sheets, an increase in the ***D*** peak, implies an increase in the number of graphene layer edges and thus an increase in microporosity [31]. This was indeed the relationship observed for AC-K10, with the increase in the ***D*** peak coinciding with a significant increase in micropore volume (***Table 2-16***).

Table 2-15 ~ *Raman Peak Fitting Results for KOH miACs*

Sample Name	Peak Area			
	S Disordered Graphitic Lattice*	**D** Disordered Graphitic Lattice†	**A** Amorphous Carbon	**G** Ideal Graphitic Lattice
AC-N	9.2	66.7	9.8	14.1
AC-K0	7.8	68.5	10.7	13.0
AC-K5	12.5	63.9	12.5	10.9
AC-K7.5	11.0	64.9	13.3	10.6
AC-K10	10.4	67.4	12.5	9.7

* *Heteroatoms Bound to Graphene Layer Edges*

† *Graphene Layer Edges*

The structural order of AC-N showed a great degree of similarity to that of AC-K0, but not to the KOH activated miACs. The KOH activated miACs possessed a much higher proportion of amorphous carbon than AC-N and had a lower proportion of ordered graphitic carbon, as can be observed from the increase in the area of the ***A*** peak and the decrease in the area of the ***G*** peak. However, the proportion of the disordered graphitic carbon (***S*** and ***D*** peaks) was similar for AC-N and the KOH activated miACs, while the amount of heteroatoms bound to graphene layer edges (***S*** peaks) was higher in the KOH activated miACs.

Although variation was observed in the chemical structure of the KOH activated miACs as a function of KOH loading, the changes across the series were much less pronounced than those observed in the carbon materials presented in ***sections 2.3.3.1.1*** and ***2.4.3.1.1***. The use of KOH during activation appeared to predominantly effect the distribution of heteroatoms bound within the disordered graphitic phases, which decreased with increasing KOH loading (***S*** peak). In addition, increasing the KOH loading resulted in a gradual decrease to the proportion of the ordered graphitic phases (***G*** peak), and hence an overall decrease in the level of structural order.

While the amount of amorphous carbon (***A*** peak) varied within the KOH activated miACs, it did not appear to change in a regular fashion with increased KOH loading.

2.5.3.1.2 Powder X-ray Diffraction (PXRD)

The powder x-ray diffraction spectra for the KOH activated carbons and the standard char for this series are shown in ***Figure 2-27***. In comparison to the XRD plots of the steam ACs (***Figure 2-21***), the graphitic peak at 24° 2θ was not present to any disenable degree, indicating even less short range order than the steam ACs. The XRD plots of the KOH ACs, are however, very indicative of highly amorphous ACs.

From the XRD patterns of the KOH activated miACs (***Figure 2-27***) no peaks arising from K were observed, which is of little surprise due to the post-synthetic acid washing that was undertaken on all miACs for which KOH was used in the activation process (AC-K5, AC-K7.5 and AC-K10). Moreover, for the steam activated miACs a small peak was observed at 26° 2θ, having been attributed to the amorphous ash (***MO***) within the samples [29]. For AC-K5, AC-K7.5 and AC-K10, which were acid washed, the ash content is significantly lower than any of the steam activated miACs or their respective chars. It is for this reason why the only AC in this series with even minor peak identifiable at is AC-K0, which was not acid washed.

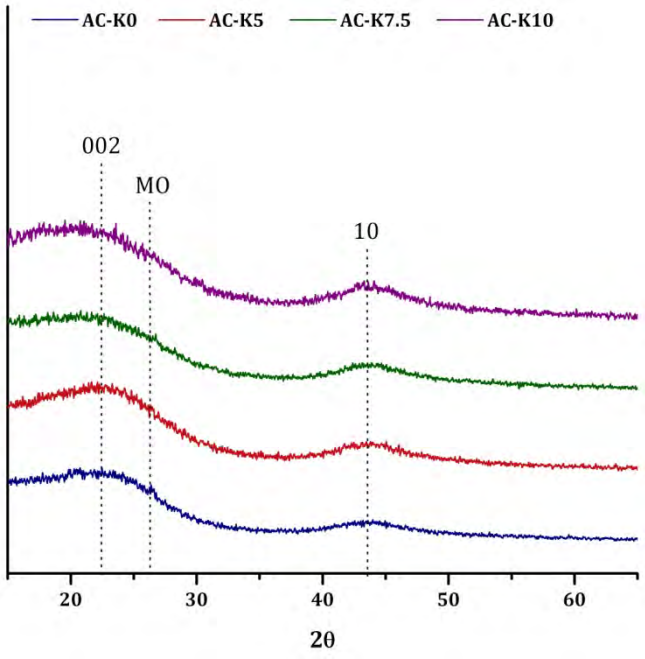

Figure 2-27 ~ *Powder X-ray diffraction Spectra of KOH Activated Carbons at Different KOH Loadings. Shown are the Peaks for the 002 Reflection and the 10 Reflection, Typical of Amorphous Carbon.*

Similarly to the steam activated miACs (***Figure 2-9*** and ***Figure 2-21***), two major peaks were observed, being attributed to the ***002*** and ***10*** reflection (24° and 43° 2θ, respectively). The ***002*** reflection indicating well structured graphitic domains, with the ***10*** peak (***100*** and ***101*** overlapping peaks) due to lateral order within the graphitic domains [25]. Interestingly, as the KOH concentration was increased the intensity of the ***10*** peak increased, indicating that with increasing KOH the lateral order of the graphitic phases increased.

Overall, with the exception of the observations made regarding the increases in the lateral order of the graphitic phase with increasing KOH loading, the observations made from the XRD investigation of the KOH activated miACs were consistent with those previously for the carbon materials presented in ***sections 2.3.3.1.2*** and ***2.4.3.1.2*** and were typical of what one would expect to see from amorphous carbons.

2.5.3.2 Physical Structure of Chemically Activated Carbons

2.5.3.2.1 Gas Physisorption

The major difference between the gas physisorption of the physically and chemically ACs was that, due to the small pore diameter of the KOH ACs, the diffusion of N_2 was greatly restricted. As such, N_2 physisorption was performed only on selected carbons. The surface area and porosity of each AC was determined from the adsorption isotherms of N_2 and CO_2 at 77 and 273 K respectively. The details outlining the analysis conditions used to obtain the isotherms by the adsorption of the aforementioned gases onto the chemically activated miACs can be found in ***section 6.6.3.2.1***, in addition to the models and equations used for data analysis.

Table 2-16 ~ *Surface Areas and Pore Volumes Calculated using the BET, DR, BJH and HK Methods from High Resolution CO_2, N_2 and Ar Physisorption at 273, 77 and 87 K for the KOH Activated miACs*

Sample Name	Surface Area (m^2/g)			Pore Volume (cm^3/g)						True Density (g/cm^3)
				V_{micro}			V_{meso}		V_{total*}	
	DR_{CO2}	BET_{N2}	BET_{Ar}	DR_{CO2}	HK_{N2}	HK_{Ar}	BJH_{N2}	BJH_{Ar}		
VBC	148	-	-	0.048	-	-	-	-	-	1.40
AC-N	799	645	695	0.256	0.32	0.33	0.50	0.46	0.38	1.48
AC-K0	646	-	-	0.210	-	-	-	-	-	1.35
AC-K5	643	16	-	0.209	0.01	-	0.02	-	0.03	1.33
AC-K7.5	638	-	-	0.207	-	-	-	-	-	1.35
AC-K10	735	56	36	0.238	0.03	0.02	0.03	0.02	0.05	1.38

* Determined from N_2 adsorption at P/P_o of 0.995

CO_2 Physisorption

The CO_2 adsorption isotherms taken at 273 K for the KOH miACs are presented in ***Figure 2-28***. The micropore volume and surface areas were determined from the data in ***Figure 2-28*** using the DR equation (***equation 6-1***), with the calculated values presented in ***Table 2-16***.

The CO_2 isotherms for the KOH miACs shown in ***Figure 2-28***, are type ***I*** isotherms typical of microporous carbons. There is little overall change in the amount of CO_2 uptake as a function of KOH loading, until 10 wt%. Furthermore, the largest increase in gas adsorption at 273 K occurring between the AC-K0 and VBC and can be attributed to the pyrolysis alone. The increases in the CO_2 uptake of the AC-K10 occur from the start of the isotherm (i.e. $P/P_0 = 0$), the increase is not only in the quantity adsorbed, but in the rate of the adsorption.

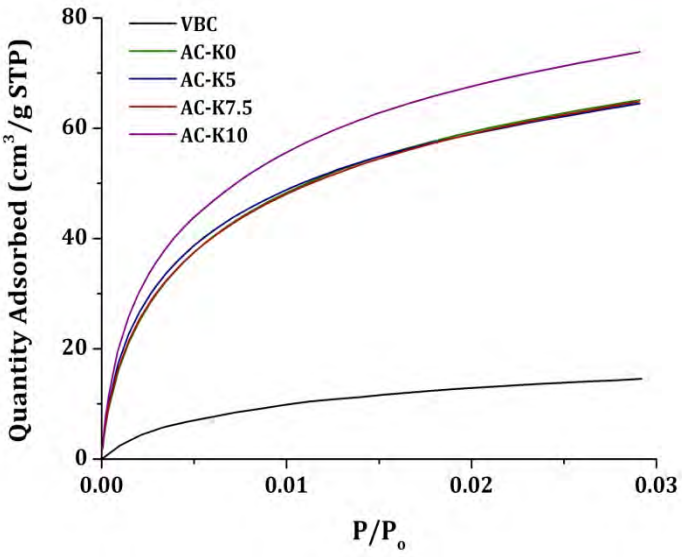

Figure 2-28 ~ *CO_2 Physisorption at 273 K over KOH ACs. Shown are the isotherms for VBC, AC-K0, AC-K5, AC-K7.5 & AC-K10*

N_2 and Ar Physisorption

The high resolution N_2 physisorption at 77 K of the KOH miACs were only carried out on two miACs, namely, AC-K5 and AC-K10. Furthermore, Ar physisorption was undertaken on AC-K10 at 87 K to investigate the effect of adsorbate on the resolution of micropores. Difficulties undertaking measurements were encountered for both the AC-K0 and AC-K7.5, due to entrapped He resulting from the free space measurements required prior to analysis. Furthermore, due to the similarity in the results from both AC-K5 and AC-K10 in the mesopore information obtainable, further study using this method was not attempted. The N_2 adsorption isotherms for AC-K5 and N_2 and Ar isotherms for AC-K10 are shown in ***Figure 2-29A*** and ***Figure 2-29B***, respectively. The PSDs for AC-K5 calculated using the BJH and HK methods are reported in ***Figure 2-29C*** and ***Figure 2-29E***, with the BJH and HK PSDs for AC-K10 are shown in ***Figure 2-29D*** and ***Figure 2-29F***.

From the N_2 isotherm of AC-K5 (***Figure 2-29A***) and the N_2 and Ar isotherms of AC-K10 (***Figure 2-29B***) incomplete closure of the hysteresis loops are observed. In all cases for all adsorbates the hysteresis loops observed were of type ***H4***.

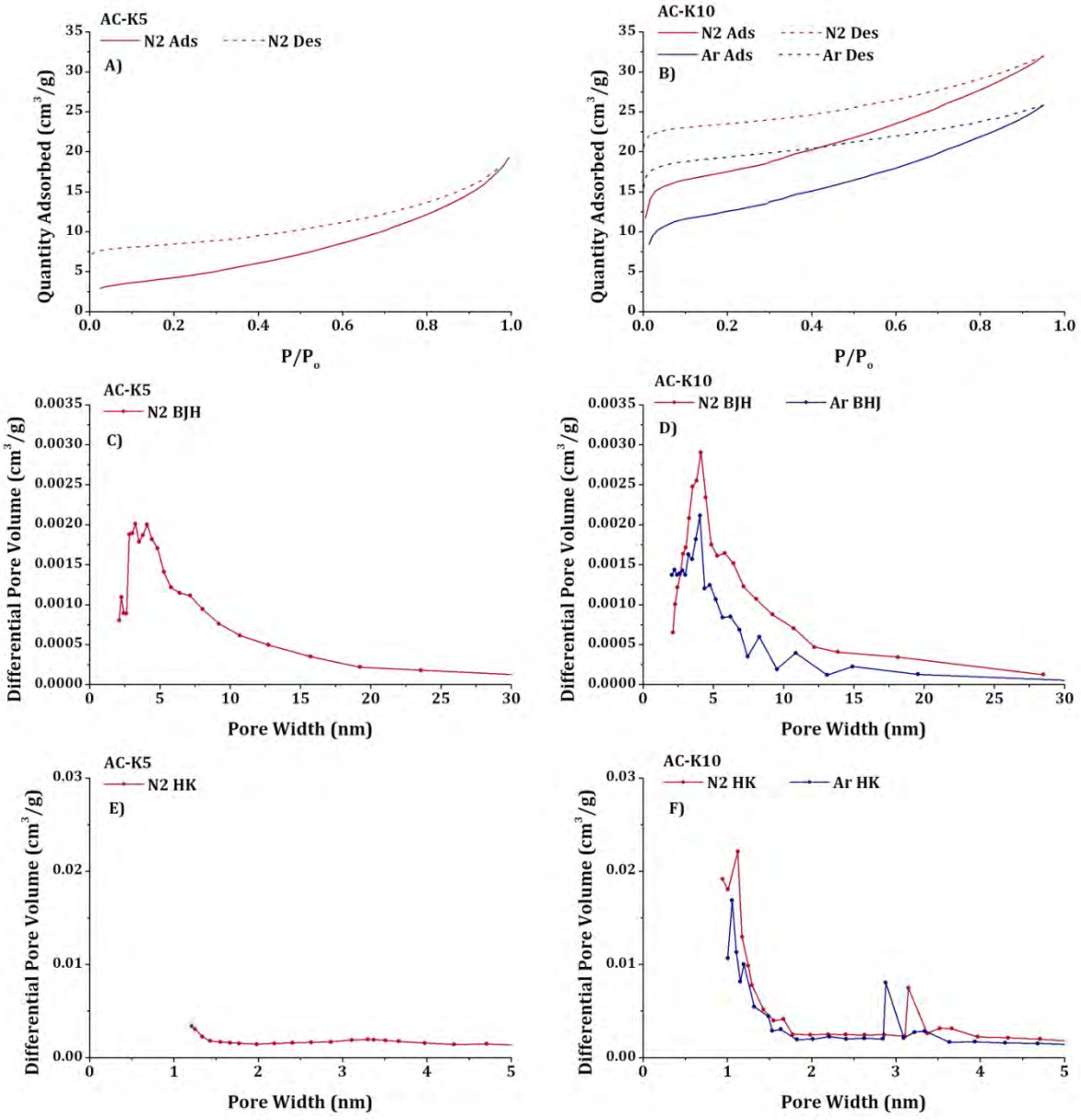

Figure 2-29 *~ Adsorption Isotherms and PSDs for N_2 and Ar at 77 K and 87 K for AC-K5 and AC-K10. Shown are* ***A)*** *N_2 Isotherms for AC-K5,* ***B)*** *N_2 and Ar Isotherms for AC-K10,* ***C)****N_2 BJH PSD for AC-K5,* ***D)*** *N_2 and Ar BJH PSD for AC-K10,* ***E)*** *N_2 HK PSD for AC-K5, and* ***F)*** *N_2 and Ar HK PSD for AC-K10*

It can be seen from ***Figure 2-29A***, that even with the high resolution achievable with the 0.1 torr pressure transducer of the ASAP 2020, that only very limited data pertaining to the micropores of AC-K5 was possible (***Figure 2-29A, Figure 2-29C*** and ***Figure 2-29E***). This has been attributed to the inability of the N_2 to permeate into the narrow diameter micropores of AC-K5 at 77 K, and can be seen more clearly from the HK PSD in ***Figure 2-29E***, in that only pores with diameters as small as 1.5 nm can be resolved. Furthermore, the micropore volume (V_{micro} = 0.01

cm^3/g) able to be calculated by applying the HK method (***equation 6-5***) is only a small fraction that obtained from the DR calculations from the CO_2 adsorption isotherm (V_{micro} = 0.18 cm^3/g). However, despite the limitations in the N_2 isotherm data at obtaining any insight into the micropore structure of AC-K5, it has still allowed for important mesopore information to be derived using the BJH method. As would be expected from a predominately microporous carbon, that the mesopore volumes are very low (V_{meso} = 0.02 cm^3/g).

From the high resolution adsorption isotherms for both N_2 and Ar over AC-K10 (***Figure 2-29B***) are very similar to that of the N_2 isotherm of AC-K5 (***Figure 2-29A***) in both shape and magnitude. The BJH and HK PSDs derived from the isotherms of both N_2 and Ar (***Figure 2-29B***) are shown in ***Figure 2-29C*** and ***Figure 2-29E***, respectively. Interestingly the resolution of the micropores for AC-K10 was such that micropores with diameters as low as 1 nm could be resolved, whereas the smallest pores that were able to be resolved for AC-K5 had diameters of 1.5 nm. As there are more micropores with slightly larger diameters for AC-K10 relative to AC-K5, more N_2 and Ar were able to permeate into the AC-K10 pore structure as compared to AC-K5. Moreover, the majority of the mesopores of AC-K10 with diameters centred around 5 nm that are the predominate feature of the BJH PSD (***Figure 2-29D***) are also clearly resolved in the HK PSD shown in ***Figure 2-29F***.

As was the case for the steam activated miACs and their respective chars presented in ***section 2.3.3.2.1*** and ***section 2.4.3.2.1***, the inability of the hysteresis loops of the KOH activated miACs to close, is attributed to low pressure hysteresis (LPH) [35-37]. The LPH behaviour observed over the KOH activated miACs is accentuated as it was for the two industrial chars (***Figure 2-23***) on account of a lack of any substantial mesoporosity. The small mesopore volume has slowed the diffusion of N_2 and/or Ar gas into the inner depths of the micropores in the time allocated for equilibrium to be achieved (45 sec). Thus it is thought that the adsorption branch of the isotherms have not reached true equilibrium, whilst the desorption branch probably has, as previously been noted (***section 2.3.3.2.1*** and ***section 2.4.3.2.1***). Were greater mesoporosity present or significantly longer equilibration time used for the analysis then complete diffusion into the micropores should be able to be achieved, along with true gas equilibrium. However, the analysis time that would be required in order to fully achieve this goal would not be an economical use of time, as the analysis took two days under the current analysis conditions. As the these analyses were undertaken was in two stages, any effects that might arise from He entrapment are able to be discounted. Using the cryostat attachment for the ASAP 2020, with a fully closed system, complete degassing was undertaken prior to the adsorption isotherm, once the He free space analysis had been completed.

In summation, the gas physisorption of the KOH activated miACs showed them to possess large micropore volumes, with almost negligible mesopore volumes. Physisorption using N_2/Ar gas was only undertaken on two of the KOH activated miACs (AC-K5 and AC-K10), resulting in limited information being obtained regarding the mesopore volume and structure. This was due to the extended time required for analysis and the usefulness of the information obtained.

2.5.3.2.2 Transmission Electron Microscopy (TEM)

Transmission electron microscopy (TEM) was used in order to visually verify the observations made from Raman spectroscopy, XRD and gas physisorption investigations. The TEMs and elemental mapping for C, O and K for AC-K0, AC-K5, AC-K7.5 and AC-K10 are presented in ***Figure 2-30***, ***Figure 2-31***, ***Figure 2-32***, and ***Figure 2-33*** respectively.

Figure 2-30A shows the electron micrograph of AC-K0, from which it can been seen that there are no clearly observable structural features, but some alignment of the carbon structure (*red circles*). With respect to the elemental mapping for K (***Figure 2-30E***) it is interesting to note that K is clearly present in the bulk, but was not found to be present at the surface at a level detectable by XPS analysis (***Table 2-13***).

From the electron micrograph of AC-K5 (***Figure 2-31A***) some alignment of the carbon structure can be observed throughout the sample (*red circles*), however, this is not expressed in the form of well defined graphitic domains (i.e. no layer edges). This would indicate that a 5% loading of KOH was insufficient to cause any extensive structural changes to the carbon. In fact the Raman spectra of AC-K5 (***Figure 2-26B***) showed a decrease in the structural order (***G*** peak) of AC-K5, relative to AC-K0 (***Figure 2-26A***). Compared to the elemental mapping for K from AC-K0 (***Figure 2-30E***) there is a significant increase in the intensity of the EDX signal for K of AC-K5 (***Figure 2-31E***). Furthermore, from the bright field image shown in ***Figure 2-31B***, the bright spots observed have been determined to be due to ash particles.

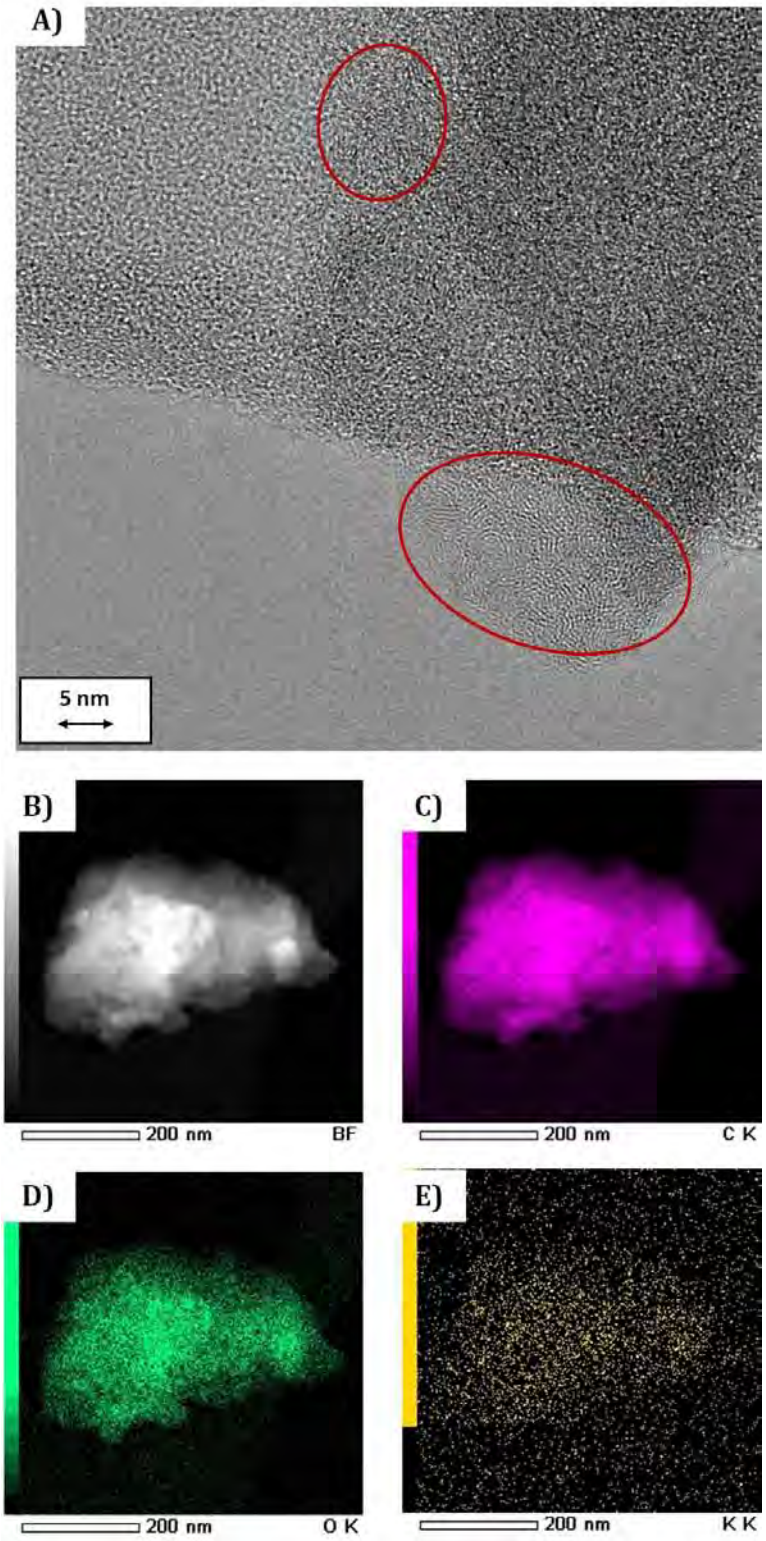

Figure 2-30 *~ Transmission Electron Micrograph and Elemental Mapping of KOH Activated miAC AC-K0. Shown is* ***A)*** *High Magnification Electron Micrograph,* ***B)*** *Bright Field Image of Mapped Particle,* ***C)*** *EDX Mapping of the C K-edge,* ***D)*** *EDX Mapping of the O K-edge,* ***E)*** *EDX Mapping of the K K-edge*

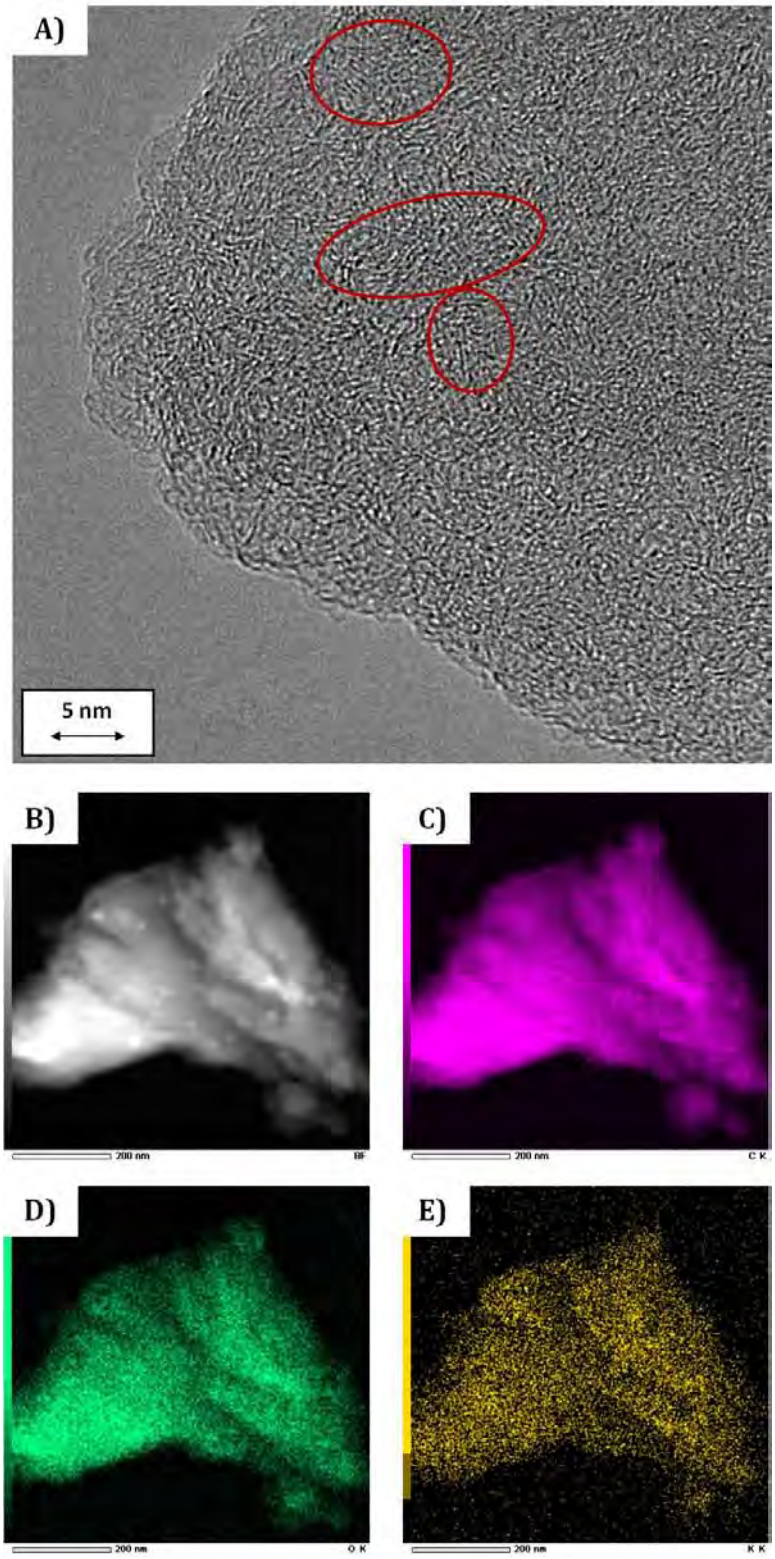

Figure 2-31 *~ Transmission Electron Micrograph and Elemental Mapping of KOH Activated miAC AC-K5. Shown is* ***A)*** *High Magnification Electron Micrograph,* ***B)*** *Bright Field Image of Mapped Particle,* ***C)*** *EDX Mapping of the C K-edge,* ***D)*** *EDX Mapping of the O K-edge,* ***E)*** *EDX Mapping of the K K-edge*

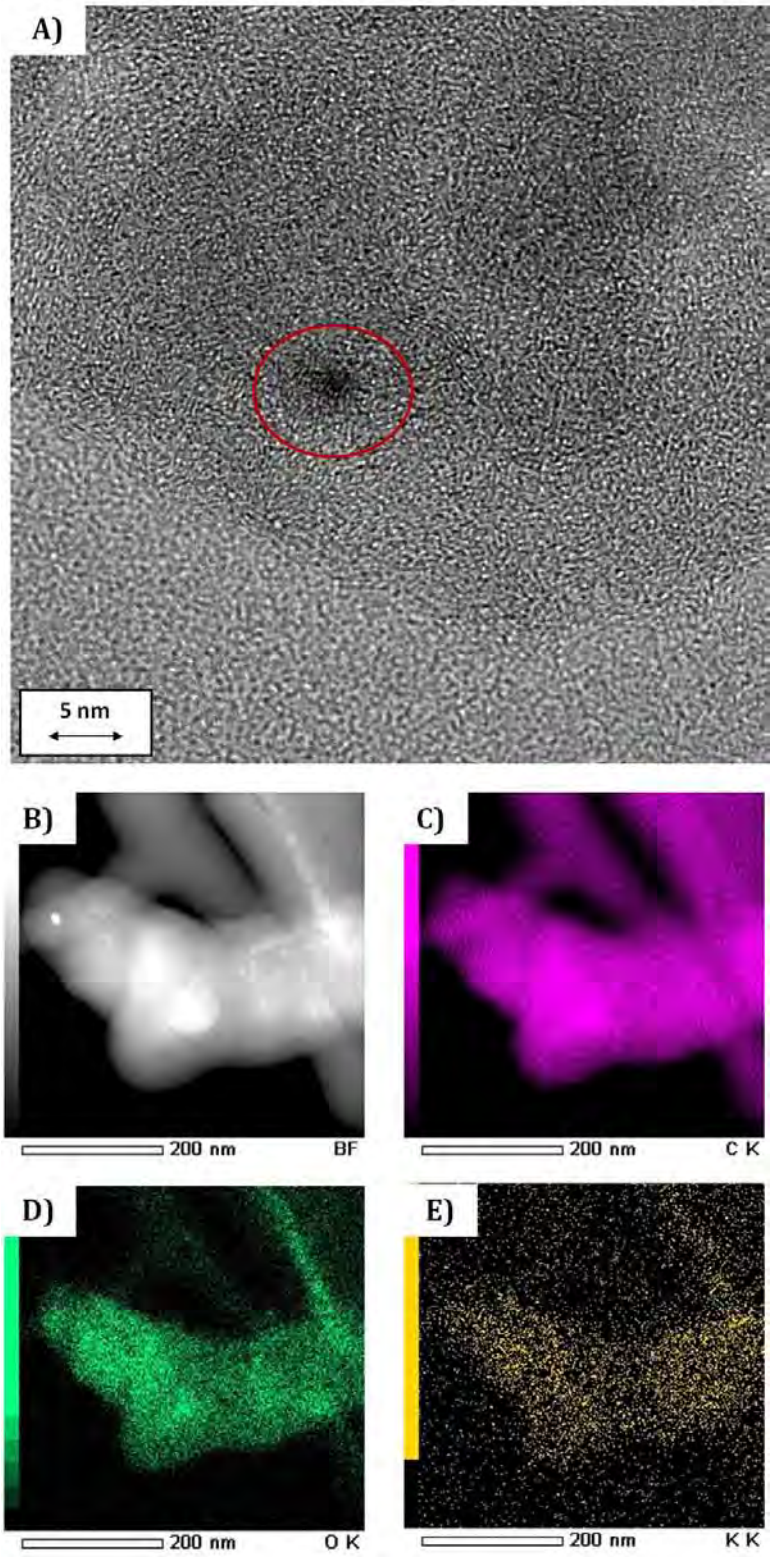

Figure 2-32 ~ *Transmission Electron Micrograph and Elemental Mapping of KOH Activated miAC AC-K7.5. Shown is* ***A)*** *High Magnification Electron Micrograph,* ***B)*** *Bright Field Image of Mapped Particle,* ***C)*** *EDX Mapping of the C K-edge,* ***D)*** *EDX Mapping of the O K-edge,* ***E)*** *EDX Mapping of the K K-edge*

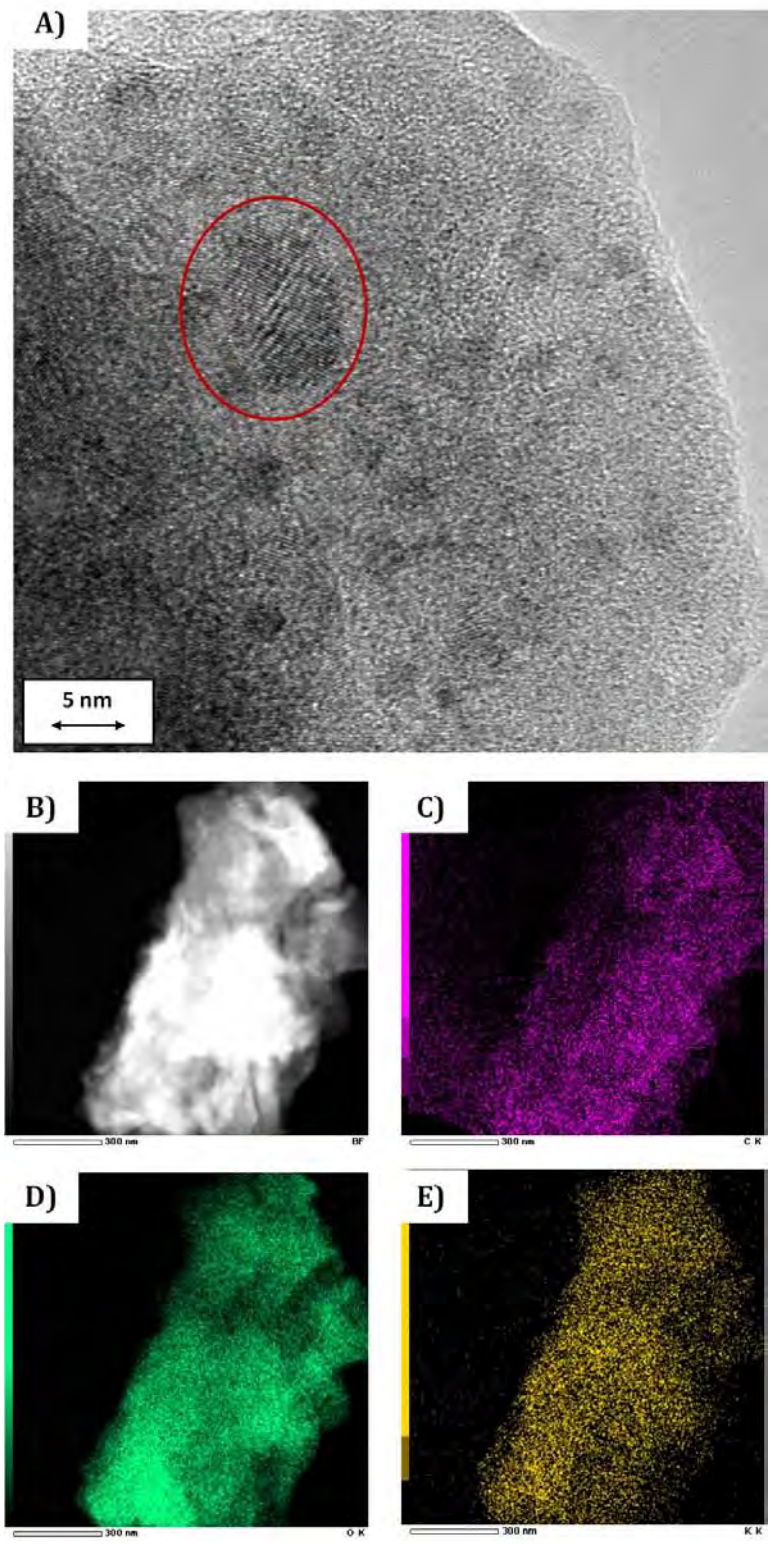

Figure 2-33 ~ *Transmission Electron Micrograph and Elemental Mapping of KOH Activated miAC AC-K10. Shown is* ***A)*** *High Magnification Electron Micrograph,* ***B)*** *Bright Field Image of Mapped Particle,* ***C)*** *EDX Mapping of the C K-edge,* ***D)*** *EDX Mapping of the O K-edge,* ***E)*** *EDX Mapping of the K K-edge*

The electron micrograph of AC-K7.5 presented in ***Figure 2-32A***, shows a fair increase in the order of the carbon structure relative to AC-K5. This is specifically highlighted in ***Figure 2-32A***, with a red circle encompassing a well defined graphitic domain, possessing clearly visible graphene layer edges. This further increase in the ordered carbon structure was also evident from the Raman spectroscopy results for AC-K7.5 relative to AC-K5 (***Figure 2-26C*** and ***Table 2-16***). There is an observable decrease in the amount of K present from the EDX elemental mapping (***Figure 2-32E***) relative to the K EDX signal obtain for either AC-K0 or AC-K5. This is however, the amount of K present within the bulk of the particle presented in ***Figure 2-32***, whereas there was an overall increase in the surface concentration of K relative to AC-K5 (as per the XPS results in ***Table 2-13***)

The strong relationship between increasing of ordered carbon with KOH loading was further evidenced in the electron micrographs of AC-K10 (***Figure 2-33***). Well defined graphitic domains are clearly evident, and are in fact the predominant feature of the micrographs, highlighted in the micrograph by red circles. The observable features are in good agreement with both the Raman spectroscopy and gas physisorption results for AC-K10 (***Figure 2-26D*** and ***Table 2-16*** respectively). From the Raman spectra of AC-K10 (***Figure 2-26D***) an increase in the ***D*** peak was observed relative to the other KOH miACs, indicating that the most prominent feature of the surface of AC-K10 is the graphene layer edges. This would furthermore account for the significantly increased microporosity of AC-K10 relative to the other KOH miACs, from the electron micrographs of AC-K10 (***Figure 2-33E***) this is however able to be visualised. A slight increase in the K signal from the EDX mapping relative to all other KOH miACs, but barely discernible from that observed for AC-K5 in ***Figure 2-31E***.

Not only are well defined graphitic domains visible from the electron micrographs of AC-K10, but the carbon surrounding the domains possesses a great deal of structure. This was true for all the KOH miACs compared to the steam activated miACs, but for AC-K10, this was much more pronounced.

2.5.4 Summary

Very clear patterns emerged between many of the characteristics of KOH activated miACs on the basis of KOH loading. For example a very strong relationship was found to exist between the KOH loading and bulk composition of the KOH activated miACs (***Table 2-12***). As the loading was increased from 0-10 wt% there was a gradual increase in the yield of the KOH activated miACs, along with a consequent increase in bulk O and ash content. The higher ash content of the KOH activated miACs is proposed to be in part due to the presence of K that was unable to be

removed via the washing protocols. However, without elemental analysis of the ash, further cannot be said on the exact proportion of K within the ash. Furthermore, as KOH was introduced into the system there was an initial decrease in micropore volume. Upon further increasing the KOH loading, significant increases in the micropore volume were observed with no consequent increase in mesopore volume.

From the XRD patterns on the KOH activated miACs (***Figure 2-27***) there is a clear increase in the intensity of the ***10*** peak, indicating the lateral growth of the graphitic phase. As was the case with the micropore volume the ***D*** peak from the Raman spectroscopy of the KOH activated miACs (***Table 2-15***) showed an initial decrease upon introduction of KOH to the system, and showed a steady increase with increasing KOH. Associated with the increase in the ***D*** peak with increasing KOH loading, was a decrease in the ***S*** and ***G*** peaks. This would suggest that both a decrease in graphene layer edges with heteroatoms bound and a decrease in the more ordered graphitic carbon is occurring, whilst there is an increase in the disordered graphitic carbon that does not possess heteroatoms (indicated by the increase in the ***D*** peak). Furthermore, both the observations from XRD and Raman spectroscopy are confirmed by the visual observations made from TEM investigation of the KOH activated miACs (***Figure 2-30-Figure 2-33***).

The results of the gas physisorption, XRD, Raman spectroscopy and TEM paint a very different picture of the development of the pore structure for the KOH activated miACs, than was observed for the steam activated miACs. For the KOH activated miACs, KOH dual roles, the first was to dehydrogenate the heavier components of the volatile matter, reducing the formation of tars and thus allowing for the heavier components of the volatile matter to be retained and carbonised [48]. The second role was as an oxygen source for the oxidation of the coal surface [40, 49] (***section 1.7.2***).

Therefore, the use of KOH as a chemical activating agent was highly successful in producing miACs with a narrow distribution of pore sizes. This should endow the KOH activated miACs with molecular sieving properties, that may also result in limitations of mass transport, which will be part of the gas separation investigations to be covered in the next chapter (***Chapter 3***).

2.6 Chapter Summary and Closing Remarks

Microporous activated carbons (miACs) were successfully produced using both chemical and physical activation methods, with the effect of precursor carbon material also being investigated for the physical activation method. A table summarising the major characterisation of all the carbon materials in this chapter are shown in ***Table 2-17***. These two classes of miACs

(chemically and physically activated) were vastly different from one another with respect to composition, surface chemistry and structure (***Table 2-17***). This being a direct result of the vast differences that exist between the underlying mechanisms for the two modes of activation, especially with respect to pore development.

Table 2-17 ~ *Overview of the Characterisation the Steam and KOH Activated miACs*

Sample	Bulk Composition						Surface Composition			Structural Morphology						
	Elemental Analysis (wt%, daf)				H/C Ratio	Ash (wt%)	Contentration (at%)			Surface Area (m^2/g)		Pore Volume (cm^3/g)				True Density (g/cm^3)
	C	H	N	O_{diff}			C	O	N	DR	BET	V_{micro} CO_2	V_{micro} N_2	V_{meso}	V_{total}	
AC-N	76.3	0.8	1.0	21.9	0.12	10.9	91.5	7.8	0.2	799	645	0.26	0.36	0.12	0.38	1.48
VCB	61.4	4.4	0.6	33.5	0.86	0.4	-	-	-	148	-	0.05		-	-	1.40
CH-45	91.7	1.4	0.9	6.0	0.18	3.2	90.1	9.4	0.5	620	263	0.20	0.14	0.04	0.17	1.84
AC-45	90.5	1.3	0.9	7.4	0.17	5.3	91.2	8.3	0.5	690	358	0.22	0.19	0.08	0.23	1.88
CH-90	89.9	1.1	0.5	8.4	0.15	3.8	90.1	9.4	0.5	640	282	0.21	0.16	0.06	0.18	1.85
AC-90	82.2	1.3	0.7	15.7	0.19	6.4	90.2	9.2	0.7	696	397	0.23	0.20	0.13	0.24	1.90
CH-180	94.0	1.2	1.0	3.7	0.16	3.0	90.8	8.9	0.3	626	304	0.21	0.16	0.06	0.20	1.84
AC-180	89.6	1.2	0.9	8.4	0.16	7.3	92.5	6.7	0.8	758	486	0.25	0.25	0.21	0.35	1.82
CHLR	74.0	1.1	0.6	24.3	0.18	6.0	87.8	11.3	0.9	609	384	0.20	0.22	0.02	0.29	1.83
AC-CHLR-90	75.6	1.0	0.6	22.8	0.16	5.2	91.0	7.9	1.1	623	351	0.20	0.23	0.05	0.27	1.88
CHRK	76.6	1.7	0.8	20.9	0.27	6.9	92.7	6.3	1.0	578	98	0.19	0.06	0.00	0.09	1.64
AC-CHRK-90	78.6	1.0	0.5	19.6	0.15	7.4	88.9	10.6	0.6	696	409	0.23	0.22	0.04	0.26	1.91
AC-K0	86.5	1.4	0.8	11.3	0.19	3.6	90.2	9.5	0.3	579	-	0.19		-	-	1.35
AC-K5	83.5	1.2	1.1	14.1	0.17	6.2	87.3	11.4	0.8	551	16	0.18		0.02	0.03	1.33
AC-K7.5	82.8	1.1	1.3	14.9	0.15	8.5	85.4	12.8	1.0	572	-	0.19		-	-	1.35
AC-K10	79.2	1.1	1.2	18.4	0.17	10.1	87.5	10.7	1.0	639	56	0.21		0.02	0.05	1.36

The micropore volumes of the VBC derived carbon materials (0.05-0.23 cm^3/g) were much lower than that of AC-N (0.29 cm^3/g, ***Table 2-17***). A general rule for carbon materials, is that the majority their pore volume resides in the micropores. For this reason it is this characteristic that is used as the best preliminary predictor of the potential capacity for gas adsorption applications [50]. On this basis alone, AC-N would be proposed as the best AC for CO_2 capture, of the carbon materials presented here. For the steam activated miACs from both VBC and industrial char precursors the development of pores by steam gasification slowly acted on the carbon particles from the outside, resulting in pores with wide mouths. The degree of variation

in the development of pores via steam gasification was also shown to be dependent on carbon precursor used. For example for the VBC derived miACs, steam had a profound effect on the development of both micro- and mesopores. Due to the presence of volatile matter within the VBC sample, that can easily react with the steam during the activation process. Whereas for the char derived miACs very little pore development was observed overall, owing to the non-reactive nature of the parent carbons, for which most of the volatile matter has been removed during the carbonisation process for producing the chars.

For the KOH activated miACs the KOH previously impregnated into the deepest regions of the VBC pore structure, allowed for retainment of the heavier components of the volatile matter [40, 48]. The retained components of the volatile matter could then be carbonised resulting in the development of micropores at the expense of mesopores, and ACs with narrow PSDs.

Interestingly there was a clear overall relationship observed between the degree of pore development and the bulk C content of the miACs and chars produced by both chemical and physical activation. For example the VBC derived steam activated miACs possessed the highest degree of development of both micro- and mesopores as well as the highest bulk C content of any of the miAC series presented here (***Table 2-17***). Moreover, the bulk O and ash content of the VBC derived steam activated miACs were the lowest as a series of any miAC series. Conversely the char derived steam activated miACs exhibited the smallest degree of pore development of any miAC series, as well as possessing the lowest bulk C, and highest bulk O of any miAC series. The KOH activated miACs possessed similar micropore volumes to the steam activated miACs, with substantially smaller mesopore volumes (***Table 2-17***). The bulk C content of the KOH activated miACs was higher overall than the char derived steam activated miACs despite possessing smaller mesopore volume; whilst the bulk C content is still smaller than the VBC derived steam activated miACs, which possess the most well developed pore structure of all the miACs. The KOH activated miACs also possess the highest bulk ash content of all the miACs, but not the highest bulk O content. This is the result of two major differences that exist between the KOH and steam activated miACs. The first is due to an expected reduced K phase, as the KOH was reduced by the carbon precursor during the reaction process, with KOH acting as an oxygen carrier. The second and probably more significant difference was in the post-synthetic treatment of the KOH activated miACs as compared to the steam activated miACs, in that the KOH activated miACs were acid washed (***section 6.4.4.2.1***) in order to remove excess inorganics from the surface allowing the AC surface to be free for adsorption. As was outlined in ***section 1.7.2***, the exact mechanism of action for KOH is the source of some conjecture. However, it is known that KOH exerts it action as an activating agent predominately between graphene sheets. This will have made complete removal of the reduced K phase incredibly difficult.

The changes in chemical structure that were observed across the series of steam activated VBC derived miACs and their analogues in the CH series took on the form of increases in the level of order of the carbon structure. This was most clearly observed by the increases in the ***G*** peak from the Raman spectroscopy of these carbons, which was visually confirmed by TEM, with no such changes being identifiable in the XRD patterns of the carbons. The Raman spectra of the VBC derived steam activated miACs and their analogues in the CH series showed a marked decrease in the ***S*** peak, with no associated change in the ***D*** peak. This would suggest that the manner in which heteroatoms bound to the graphene layer edges were removed was destructive to the graphene layer edges themselves. If the heteroatoms had been removed in a non-destructive manner, this would leave the layer edges intact, which would be indicated by an increase in the area of the ***D*** peak. Interestingly from the XRD patterns of the VBC derived steam activated miACs and their analogues in the CH series, there was no increase in intensity of the ***MO*** peak with increasing bulk ash content. Despite there being no observed changes in the chemical structure of the VBC derived steam activated miACs and their analogues in the CH series, an overall increase in the order of the chemical structure was observed from the increase in the ***G*** peak from the Raman spectroscopy, which was confirmed by the appearance of well defined graphitic domains by TEM.

No such significant changes in the chemical structure were observed for the CHLR/AC-CHLR-90 pair, other than a decrease in the ***MO*** peak from the XRD patterns of the two materials (***Figure 2-9A***). The lack of observable changes in the chemical structure added credence to the previous assertions pertaining to the non-reactive nature of CHLR from both the compositional analysis and gas physisorption studies (***Table 2-17***).

On the other hand the CHRK/AC-CHRK-90 pair did show some variation in chemical structure as a result of the steam activation process. As was the case with all other steam activated miACs, there were no noticeable differences in the ***002***, ***10*** or ***MO*** peaks of the XRD pattern of CHRK and AC-CHRK-90 (***Figure 2-9B***). However, decreases in the ***S*** peak with an associated increase in the ***D*** peak were observed in comparing the Raman spectra of AC-CHRK-90 to CHRK (***Table 2-10***). As noted previously such changes would suggest non-destructive removal of heteroatoms from graphene layer edges, during steam activation.

The most profound changes in chemical structure were observed for the KOH activated miACs. The Raman spectroscopy of the KOH activated miACs showed increases in the ***D*** peak with increasing KOH loading (***Table 2-15***). This indicates that increasing the KOH loading resulted in a increase in the number of graphene layer edges. Similarly from the XRD patterns on the KOH activated miACs (***Figure 2-27***) an increase in the size of the graphitic domains was observed by an increase in the intensity of the ***10*** peak. This observation from the XRD patterns is thus in

good agreement with the observations pertaining to the chemical structure of the KOH activated miACs made by Raman spectroscopy. Further confirmation to this end was visually observed from the TEM investigation of the KOH activated miACs (***Figure 2-30-Figure 2-33***), by increases in the number and size of size of graphitic domains with increasing KOH loading.

Finally, as the compositional and structural aspects of the carbon materials have been discussed the other major aspect that can affect their ability to adsorb CO_2 is their surface chemistry (***section 1.9.2***). As has been noted several times throughout this chapter, the change in the surface chemistry with the widest reaching implications for CO_2 capture were for the C-O-R peak observed by XPS. Upon further investigation by NEXAFS spectroscopy the C-O-R groups were found to be predominately hydroxyl groups, known to have the highest affinity for CO_2 of all commonly occurring functional groups on an AC surface [1]. Overall, steam activation resulted in increases in the concentration of C-O-R groups, whilst generally also resulting in an overall decrease in the surface O concentration.

In general, steam activation resulted in a decrease in the surface concentration of C=O groups as determined by XPS. The sole exception to this was observed for the CHRK/AC-CHRK-90 pair, where an increase in C=O groups was observed as a result of steam activation (***Table 2-8***). For the C=O groups on the surface of the KOH activated miACs, no regular pattern was observed in the variation as a function of KOH loading (***Table 2-13***). NEXAFS spectroscopy was used to further identify the C=O group detected by XPS, as a reasonably even distribution of ketones and aldehydes, found to be the major contributors to this peak, with a very minor contribution, in most cases, from quinones. The effect of the C=O groups on the affinity of the AC surface for CO_2 is relatively minimal, as compared to hydroxyl, ether and carboxylic acid groups [1].

From the XPS analysis of the surface concentration of COO-R groups, it was found that for all miACs and chars produced here that these groups were present in the lowest amount of any of the oxygenated surface functional groups. Moreover, further identification of the COO-R using NEXAFS spectroscopy resulted in confirmation that the COO-R groups were predominately due to carboxylic acids (COO-H), as had been predicted. It is of little surprise that carboxylic acids were present in such low concentrations at the AC surface, due to their low thermal stability and high chemical reactivity, especially under oxidising conditions. Under the activation conditions employed in the production of miACs (both chemical and physical activation), carboxylic acids either fail to form or are likely to react with either the steam or reactive components of the parent material, resulting in the formation of ethers, lactones, ketones and/or aldehydes.

In closing, steam activated miACs were successfully produced from both VBC and VBC chars (CHLR and CHRK). From the comparison of the physicochemical properties it was clear that the miACs produced directly from VBC (a single stage process) possessed more desirable

characteristics than the miACs produced from the industrial VBC chars (a two stage process). This was due to the higher level of volatile matter present in the parent carbon (VBC) allowing for the development of the pore structure and the surface chemistry to be directed to a much higher degree. The ability to tailor pore development is of the utmost importance as the right balance between micro- and mesoporosity much be achieved in order to maximise the capacity of the material for gas adsorption, whilst also not limiting mass transport.

The use of KOH as an activating agent in the chemical activation of VBC was also highly successful, producing miACs with high micropore volumes and narrow PSDs. Furthermore the KOH activated miACs possessed the highest surface O content of any of the series of miACs. As noted above, the PSDs were very narrow, with the KOH activated miACs possessing almost negligible mesopore volumes, which is expected to impart molecular sieving properties to the miACs, and may result in limited mass transport through the materials.

In the following chapter the gas separation properties of the miACs will be investigated using partial pressure swing adsorption (PPSA) as a means to simulate the partial pressure conditions of a vacuum swing adsorption (VSA) system.

2.7 References

1. Yang, R.T., *Adsorbents: Fundamentals and Applications*, R.T. Yang, Editor 2003, John Wiley & Sons: New Jersey. p. 79-130.
2. Amarasekera, G., M.J. Scarlett, and D.E. Mainwaring, *Development of microporosity in carbons derived from alkali digested coal.* Carbon, 1998. **36**(7-8): p. 1071-1078.
3. Durie, R.A. and H.N.S. Schafer, *The production of active carbon from brown coal in high yields.* Fuel, 1979. **58**(6): p. 472-476.
4. Chaffee, A.L. and A.G. Pandolfo. *Coal Derived Carbons for Methane Storage*. in *Proceedings - 4th Australia Coal Science Conference, Brisbane*. 1990.
5. Ahmadpour, A. and D.D. Do, *The preparation of active carbons from coal by chemical and physical activation.* Carbon, 1996. **34**(4): p. 471-479.
6. Azargohar, R. and A.K. Dalai, *Steam and KOH activation of biochar: Experimental and modeling studies.* Microporous and Mesoporous Materials, 2008. **110**(2-3): p. 413-421.
7. Chattopadhyaya, G., et al., *Preparation and characterization of chars and activated carbons from Saskatchewan lignite.* Fuel Processing Technology, 2006. **87**(11): p. 997-1006.
8. Dantas, T.L.P., et al., *Adsorption of carbon dioxide onto activated carbon and nitrogen-enriched activated carbon: Surface changes, equilibrium, and modeling of fixed-bed adsorption.* Separation Science and Technology, 2010. **45**(1): p. 73-84.
9. Dantas, T.L.P., et al., *Carbon dioxide–nitrogen separation through adsorption on activated carbon in a fixed bed.* Chemical Engineering Journal, 2011. **169**(1–3): p. 11-19.
10. Durie, R.A., *The Science of Victorian Brown Coal: Structure, Properties and Consequences for Utilization*1991, Oxford, Great Britan: Butterworth-Heinemann Ltd. p. 667.
11. Durie, R.A., *The Science of Victorian Brown Coal: Structure, Properties and Consequences for Utilization*1991, Oxford, Great Britan: Butterworth-Heinemann Ltd. p. 726.
12. Tomita, A. and Y. Ohtsuka, *Advances in the Science of Victorian Brown Coal*, C.-Z. Li, Editor 2004, Elsevier Science: Amsterdam. p. 224.
13. Sjoestroem, K. and G. Chen, *Properties of char produced by rapid pressurized pyrolysis of peat.* Industrial & Engineering Chemistry Research, 1990. **29**(5): p. 892-895.
14. Kim, Y.S., et al., *Effects of carbon dioxide and acidic carbon compounds on the analysis of Boehm titration curves.* Carbon, 2012. **50**(4): p. 1510-1516.
15. Goertzen, S.L., et al., *Standardization of the Boehm titration. Part I. CO2 expulsion and endpoint determination.* Carbon, 2010. **48**(4): p. 1252-1261.
16. Oickle, A.M., et al., *Standardization of the Boehm titration: Part II. Method of agitation, effect of filtering and dilute titrant.* Carbon, 2010. **48**(12): p. 3313-3322.
17. Biniak, S., et al., *The characterization of activated carbons with oxygen and nitrogen surface groups.* Carbon, 1997. **35**(12): p. 1799-1810.
18. Puziy, A.M., et al., *XPS and NMR studies of phosphoric acid activated carbons.* Carbon, 2008. **46**(15): p. 2113-2123.
19. Nowicki, P., R. Pietrzak, and H. Wachowska, *X-ray photoelectron spectroscopy study of nitrogen-enriched active carbons obtained by ammoxidation and chemical activation of brown and bituminous coals.* Energy and Fuels, 2010. **24**(2): p. 1197-1206.
20. Starck, J., et al., *The influence of demineralisation and ammoxidation on the adsorption properties of an activated carbon prepared from a Polish lignite.* Carbon, 2006. **44**(12): p. 2549-2557.
21. Boehm, H.P., *Surface oxides on carbon and their analysis: a critical assessment.* Carbon, 2002. **40**(2): p. 145-149.
22. Sadezky, A., et al., *Raman microspectroscopy of soot and related carbonaceous materials: Spectral analysis and structural information.* Carbon, 2005. **43**(8): p. 1731-1742.
23. Shimodaira, N. and A. Masui, *Raman spectroscopic investigations of activated carbon materials.* Journal of Applied Physics, 2002. **92**(2): p. 902-909.

24. Li, X., J.-i. Hayashi, and C.-Z. Li, *FT-Raman spectroscopic study of the evolution of char structure during the pyrolysis of a Victorian brown coal.* Fuel, 2006. **85**(12–13): p. 1700-1707.
25. Bratek, W., et al., *Characteristics of activated carbon prepared from waste PET by carbon dioxide activation.* Journal of Analytical and Applied Pyrolysis, 2013. **100**(0): p. 192-198.
26. Shen, W., et al., *Preparation of mesoporous activated carbon fiber by steam activation in the presence of cerium oxide and its adsorption of congo red and vitamin B12 from solution.* Journal of Materials Science, 2004. **39**(14): p. 4693-4696.
27. Liu, L., et al., *Effect of preparation conditions on the properties of a coal-derived activated carbon honeycomb monolith.* Carbon, 2007. **45**(14): p. 2836-2842.
28. Shen, W., et al., *Preparation of mesoporous carbon from commercial activated carbon with steam activation in the presence of cerium oxide.* Journal of Colloid and Interface Science, 2003. **264**(2): p. 467-473.
29. Skodras, G., et al., *Production of special activated carbon from lignite for environmental purposes.* Fuel Processing Technology, 2002. **77-78**: p. 75-87.
30. Li, Z.Q., et al., *X-ray diffraction patterns of graphite and turbostratic carbon.* Carbon, 2007. **45**(8): p. 1686-1695.
31. Yoshizawa, N., et al., *XRD evaluation of KOH activation process and influence of coal rank.* Fuel, 2002. **81**(13): p. 1717-1722.
32. Byrne, C.E. and D.C. Nagle, *Carbonized wood monoliths—Characterization.* Carbon, 1997. **35**(2): p. 267-273.
33. Lowell, S., et al., *Characterization of Porous Solids and Powders: Surface Area, Pore Size and Density*, B. Scarlett, Editor 2004, Springer: Dordrecht. p. p. 13.
34. Lowell, S., et al., *Characterization of Porous Solids and Powders: Surface Area, Pore Size and Density*, B. Scarlett, Editor 2004, Springer: Dordrecht. p. p. 44.
35. Silvestre-Albero, A.M., et al., *Low-Pressure Hysteresis in Adsorption: An Artifact?* The Journal of Physical Chemistry C, 2012. **116**(31): p. 16652-16655.
36. Silvestre-Albero, J., et al., *High-Resolution N2 Adsorption Isotherms at 77.4 K: Critical Effect of the He Used During Calibration.* The Journal of Physical Chemistry C, 2013. **117**(33): p. 16885-16889.
37. Silvestre-Albero, J., et al., *Physical characterization of activated carbons with narrow microporosity by nitrogen (77.4 K), carbon dioxide (273 K) and argon (87.3 K) adsorption in combination with immersion calorimetry.* Carbon, 2012. **50**(9): p. 3128-3133.
38. Lowell, S., et al., *Characterization of Porous Solids and Powders: Surface Area, Pore Size and Density*, B. Scarlett, Editor 2004, Springer: Dordrecht. p. p. 15-55.
39. Wesełucha-Birczyńska, A., K. Babeł, and K. Jurewicz, *Carbonaceous materials for hydrogen storage investigated by 2D Raman correlation spectroscopy.* Vibrational Spectroscopy, 2012. **60**(0): p. 206-211.
40. Marsh, H. and F. Rodríguez-Reinoso, *Chapter 6 - Activation Processes (Chemical)*, in *Activated Carbon*, H.M. Rodríguez-Reinoso, Editor 2006, Elsevier Science Ltd: Oxford. p. 322-365.
41. Alcañiz-Monge, J. and M.J. Illán-Gómez, *Insight into hydroxides-activated coals: Chemical or physical activation?* Journal of Colloid and Interface Science, 2008. **318**(1): p. 35-41.
42. Lillo-Ródenas, M.A., D. Cazorla-Amorós, and A. Linares-Solano, *Understanding chemical reactions between carbons and NaOH and KOH: An insight into the chemical activation mechanism.* Carbon, 2003. **41**(2): p. 267-275.
43. Gong, G.-z., et al., *Regulation of pore size distribution in coal-based activated carbon.* New Carbon Materials, 2009. **24**(2): p. 141-146.
44. Wu, F.-C., R.-L. Tseng, and C.-C. Hu, *Comparisons of pore properties and adsorption performance of KOH-activated and steam-activated carbons.* Microporous and Mesoporous Materials, 2005. **80**(1-3): p. 95-106.
45. Elmouwahidi, A., et al., *Activated carbons from KOH-activation of argan (Argania spinosa) seed shells as supercapacitor electrodes.* Bioresource Technology, 2012. **111**(0): p. 185-190.

46. Hsu, L.-Y. and H. Teng, *Influence of different chemical reagents on the preparation of activated carbons from bituminous coal.* Fuel Processing Technology, 2000. **64**(1-3): p. 155-166.
47. Marsh, H. and F. Rodríguez-Reinoso, *Chapter 2 - Activated Carbon (Origins)*, in *Activated Carbon*, H.M. Rodríguez-Reinoso, Editor 2006, Elsevier Science Ltd: Oxford. p. 13-86.
48. Illán-Gómez, M.J., et al., *Activated carbons from Spanish coals. 2. Chemical activation.* Energy and Fuels, 1996. **10**(5): p. 1108-1114.
49. Ehrburger, P., et al., *Carbonization of coals in the presence of alkaline hydroxides and carbonates: Formation of activated carbons.* Fuel, 1986. **65**(10): p. 1447-1449.
50. Yang, R.T., *Adsorbents: Fundamentals and Applications*, R.T. Yang, Editor 2003, John Wiley & Sons: New Jersey. p. 17-53.

3 Gas Separation by Microporous Carbons

3.1 Introduction

The previous chapter described the preparation and spectroscopic characterisation of carbon materials produced by direct carbonisation, steam activation or chemical activation. In the current chapter, the gas separation properties of these materials are studied using thermogravimetric analysis (TGA) and their CO_2 adsorption behaviours are compared.

In the TGA studies, CO_2 adsorption pseudo-isotherms and simulations of VSA were undertaken at a reference temperature of 293, 333 and 363 K, using partial pressure swing adsorption (PPSA), whereby the concentration of CO_2 in an argon gas stream is changed, thus changing the CO_2 partial pressure; this is discussed in more detail in the follow section (for details refer to ***section 6.6.4***).

3.1.1 Partial Pressure Swing Adsorption (PPSA)

In this chapter (and ***chapter 5***), partial pressure swing adsorption (PPSA) was used to study the gravimetric adsorption-desorption of CO_2 gas on ACs using a thermogravimetric analyser (TGA). As a direct vacuum couldn't be applied to the sample using the TGA instrument, the VSA process was instead simulated on a partial-pressure basis. In this research, three different approaches were applied (details in ***Section 6.6.4***). The first of these, known as the differential-step method, involved the incremental dosing of CO_2 over the AC. After each dose, 20 min was allowed for equilibration to be achieved. By following the mass changes of the AC sample after the introduction or removal of CO_2 from the analysis chamber, the CO_2 adsorption pseudo-isotherms could be constructed. The second method, known as the multi-cyclic method, was used to simulate VSA CO_2 partial pressure conditions, similar to those proposed for use in VSA

(P_{CO2} = 5-15 kPa), thereby enabling the determination of the working capacity of the ACs (***equation 6-11***).

The assessment of competitive adsorption between CO_2 and H_2O was undertaken only on select miACs, generally those which showed promise as CO_2 adsorbents. The competitive wet gas adsorption was done over the same CO_2 partial pressure range as the multi-cyclic measurements, however, only a single VSA cycle was simulated. Furthermore, the temperature range used for the measurements was 363-378 K, as a temperature close to the boiling point of H_2O was required to adequately investigate interactions at the gas-solid interface.

3.2 Physically Activated Carbons

The CO_2 adsorption studies over the steam activated miACs have been separated on the basis of the AC precursor (VBC, CHLR, CHRK), the characterisation of which was presented previously in ***section 2.2***. In order to compare the performance of the newly prepared carbons, each material was benchmarked against the commercial standard AC-N in differential-step and multi-cyclic adsorption measurements.

3.3 Physically Activated Coal Derived Activated Carbons

3.3.1 Differential-step CO_2 Adsorption

The CO_2 adsorption pseudo-isotherms for the VBC derived miACs (AC-45, AC-90 and AC-180) and their analogues from the CH series (CH-45, CH-90 and CH-180) obtained from thermogravimetric PPSA analysis at 293, 333 and 363 K are shown in ***Figure 3-2A-F*** for CH-45, AC-45, CH-90, AC-90, CH-180 and AC-180, respectively.

As one would expect from a physisorbent, the adsorption of gas increases with decreases in temperature [1-3]. As such the differences in adsorption become much more apparent at lower temperatures (***Figure 3-2***). Referring to ***Figure 3-1***, it is clear that the CO_2 adsorption behaviour of VBC was very poor, as one would expect from the low micropore volume and undetectable mesopore volume it possessed (***Table 2-5***).

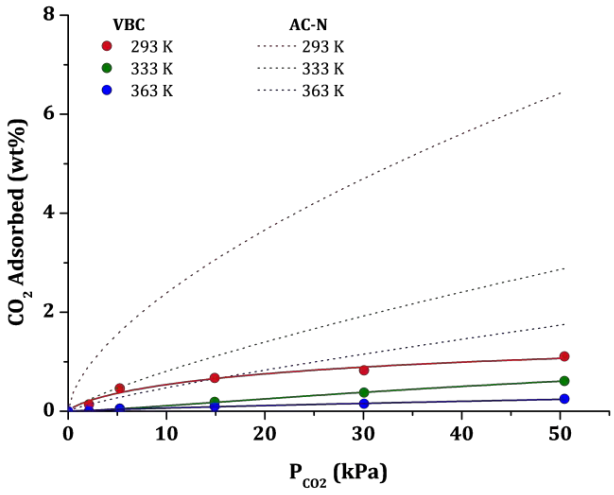

Figure 3-1~ *CO_2 Adsorption Pseudo-isotherms for VBC, taken via PPSA at 293, 333 & 363 K*

From ***Figure 3-2***, the most prominent feature of the CO_2 adsorption pseudo-isotherms obtained for the steam activated VBC derived miACs is that generally they adsorbed an equivalent or greater amount of CO_2 than one of the leading commercial product (AC-N), over all studied temperatures and pressures. This is particularly interesting considering that CO_2 adsorption on miACs is generally attributed to the pore volume of the carbonaceous material; with greater CO_2 adsorption occurring on adsorbents with high micropore volumes compared to those with low micropore volumes [4]. However, based on the pore volumes determined for the AC-N and the VBC derived carbon materials (***Table 2-5***), AC-N might be expected to be a superior CO_2 adsorbent. It seems possible, therefore, that the improved adsorbent properties of the VBC derived carbon materials relative to AC-N (***section 2.3.2***), are the result of other characteristics of these materials.

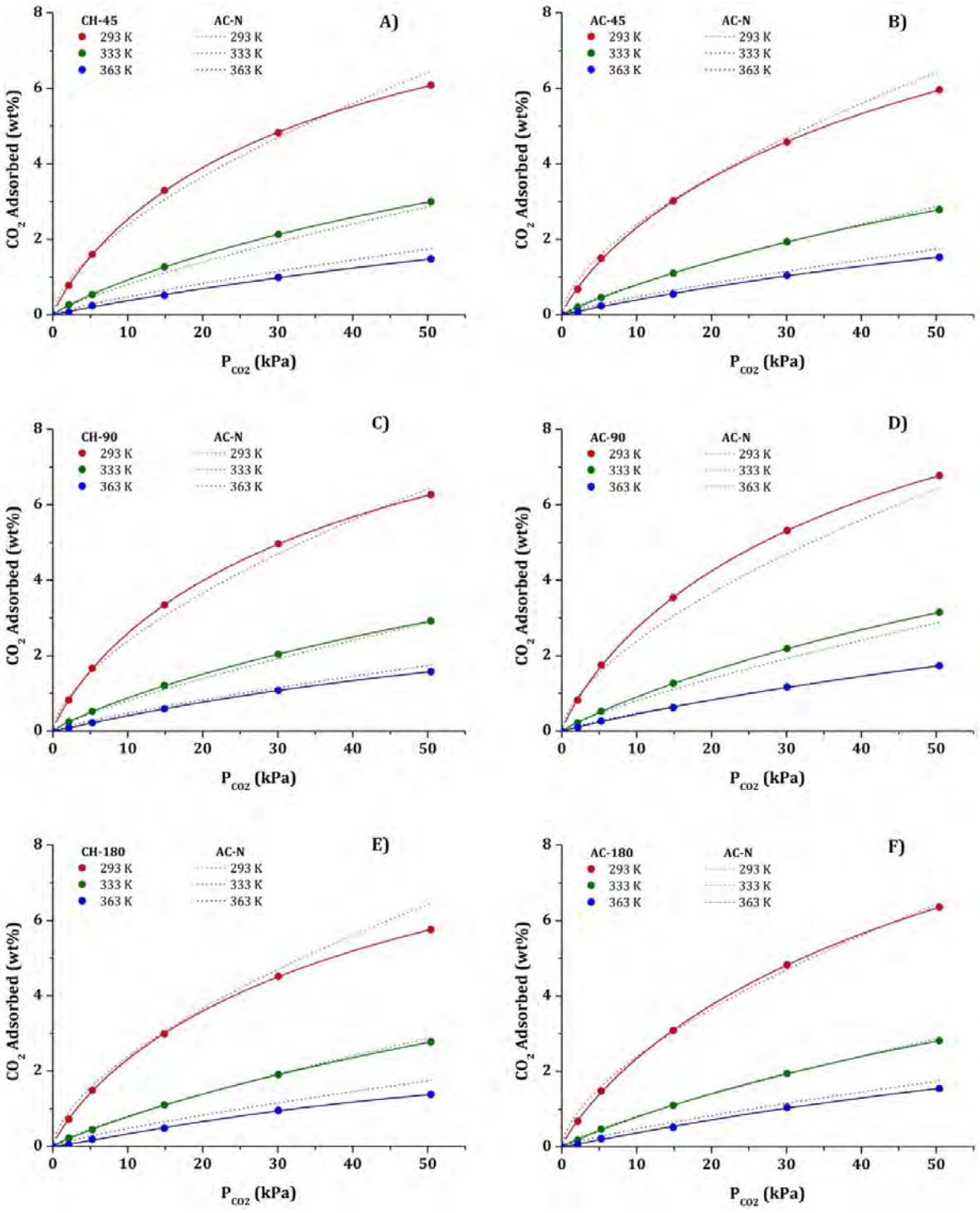

Figure 3-2 *~ CO_2 Adsorption Pseudo-isotherms for Steam Activated Carbons derived from VBC, taken via PPSA at 293, 333 & 363 K. Shown are the Pseudo-isotherms for* ***A)*** *CH-45,* ***B)*** *AC-45,* ***C)*** *CH-90,* ***D)*** *AC-90,* ***E)*** *CH-180, and* ***F)*** *AC-180*

Regarding the pseudo-isotherms obtained for the CH-45/AC-45 pair (***Figure 3-2A*** and ***Figure 3-2B***, respectively), it is interesting to observe that the use of steam during activation has led to a relative decrease in CO_2 uptake with increasing CO_2 partial pressure. This does not correlate

with the increase in the development of the overall pore structure (micro- and mesopore) that was observed (***Table 2-5***). From the XPS and NEXAFS investigations of the surface chemistry of the CH-45/AC-45 pair (***Table 2-2*** and ***Table 2-3***, respectively), the use of steam in the activation process resulted in a significant decrease in the surface concentrations of carbonyl and carboxylic acid groups for AC-45 relative to CH-45, and a corresponding, but relatively small increase in the surface concentration of undifferentiated hydroxyl and ether groups (C-O-R peak, XPS). Moreover, the NEXAFS investigation of the CH-45/AC-45 pair showed there to be little difference in the relative distribution of hydroxyl and ether groups (***Table 2-3***). Theory predicts that higher concentrations of surface carboxylic and hydroxyl groups would enhance the affinity of a carbon surface towards the adsorption of polar gases such as CO_2 [5, 6], which is indeed what was observed. However, even though there was a small increase in surface hydroxyl groups, the overall decrease in surface O for AC-45 relative to that of CH-45 was quite significant. As such the overall reduction in surface polarity seems to have resulted in reduced CO_2 adsorption for AC-45.

The adsorption pseudo-isotherms for CH-90 (***Figure 3-2C***) shows the greatest uptake of CO_2 over the entire CO_2 partial pressure range, at 293 and 363 K of any materials of the CH series. The increase in CO_2 uptake in comparison to that of CH-45 correlates with the increase in both the micro- and mesopore volumes (***Table 2-5***). Conversely, the adsorption pseudo-isotherm obtained for CH-90 at 333 K showed a slight decrease in adsorption relative to CH-45, across the entire CO_2 partial pressure range. This was an interesting result, in that the investigation of the surface chemistry of CH-90 showed only a very minor quantifiable increase in the C-O-R (hydroxyl/ether) peak by XPS (***Table 2-2***), relative to CH-45. Furthermore, the NEXAFS investigation of CH-90 showed it to possess a smaller proportion of hydroxyl to ether groups relative to CH-45 (***Table 2-3***). However, there was a significant decrease in the concentration of carboxylic acids on the surface of CH-90, relative to CH-45 (***Table 2-2***). This could be expected to result in an overall decrease in the affinity for CO_2 by the CH-90 surface over CH-45, as observed.

The adsorption pseudo-isotherms of AC-90 (***Figure 3-2D***) exhibited the greatest CO_2 uptake out of all the carbon materials presented in ***section 3.3.1***. As a result of steam activation, significant increases in both the micro- and mesopore volume was observed for AC-90 relative to CH-90 (***Table 2-5***). The changes in pore structure that occur as a result of steam activation for the CH-90/AC-90 pair can at least partially account for the increased CO_2 adsorption observed, but it is likely that the surface chemistry is also influential. There was only a minor decrease in the surface O concentration of AC-90 relative to CH-90 (XPS, ***Table 2-2***), however, there was a significant change in the distribution of oxygenated functional groups on the surface. This was

observed as a significant decrease in carboxylic acid groups, with an increase in both hydroxyl and ether groups, and a decrease in carbonyl groups. This shift in the distribution of oxygenated functional groups from carboxylic acids to ethers and hydroxyls is also likely to have contributed to the increase in the affinity of the AC-90 surface towards CO_2 relative to that of CH-90 [5, 6]. As such, for AC-90 it can be said that the increased CO_2 adsorption was due to both increases in pore development and the shift in surface chemistry towards a higher CO_2 affinity surface.

The adsorption pseudo-isotherm obtained for the CH-180/AC-180 pair (***Figure 3-2E*** and ***Figure 3-2F*** respectively) showed decreased CO_2 adsorption relative to the other VBC derived carbon materials. In particular, the CO_2 adsorption exhibited by CH-180 was the lowest of all the VBC derived carbon materials, over the entire temperature and CO_2 partial pressure range (***Figure 3-2***). At no temperature or CO_2 partial pressure did the CO_2 uptake of CH-180 ever exceed that of AC-N, however, at 333 K it was nearly identical to AC-N. The differences between the CO_2 adsorption pseudo-isotherms of CH-180 and AC-N diverged more significantly with increasing CO_2 partial pressure (***Figure 3-2E***). Moreover, as there were only minor differences in the micro- and mesopore volume of the CH-90 and CH-180 (***Table 2-5***), the change in pore structure itself, does not account for the significant decreases in the CO_2 uptake observed for CH-180 relative to either CH-90 or AC-N. Therefore some aspect of the surface chemistry of CH-180 must be involved. The surface O concentration of CH-180 was slightly lower than that of CH-90 (XPS, ***Table 2-2***), however this was expressed mostly as a decrease in carbonyl groups. Such a decrease in surface carbonyl group concentration should slightly decrease the overall polarity of the CH-180 surface relative to CH-90, but this would not account for the decrease in CO_2 adsorption observed. Moreover, the NEXAFS comparison of CH-90 and CH-180, showed CH-180 to possess a higher proportion of hydroxyl groups to ethers at the surface relative to CH-90. This might be expected to increase the affinity of the CH-180 surface for CO_2 compared to CH-90. Furthermore, there were no other significant differences in any of the chemical or structural characteristics of CH-180 that were able to explain the observed decrease in CO_2 adsorption of CH-180 relative to CH-90 and AC-N. The difference in CO_2 adsorption from CH-180 relative to CH-90 should be the source of further investigation between the two very similar carbon materials.

Interestingly, AC-180 exhibited lower CO_2 adsorption relative to AC-90 at all temperatures and CO_2 partial pressures. This decrease in adsorption also cannot be accounted for by changes in the pore structure of AC-180 relative to AC-90, as AC-180 possesses both a higher micro- and mesopore volumes relative to AC-90 (***Table 2-5***). In fact, the increase in the mesopore volume from AC-90 to AC-180 was quite extensive (***Table 2-5***). As such the decrease in CO_2 adsorption

must be due to some aspect of the surface chemistry of AC-180 relative to AC-90. The most significant difference between the surface chemistry of AC-180 and any of the VBC derived carbon materials is its low surface O concentration (XPS, ***Table 2-2***). This will have directly affected the polarity of the AC surface, thus decreasing its affinity for CO_2. Moreover, the overall decrease in surface O manifested itself as decreases in all the major oxygenated functional groups (e.g. hydroxyl, ether, carbonyl and carboxylic acid). Therefore, it seems relatively clear that the decrease in CO_2 adsorption of AC-180 relative to AC-90, despite an increase in micropore volume, is due to the substantial decreases in the oxygenated surface functional groups, and in turn the CO_2 affinity of the AC surface.

Overall, the differential-step CO_2 adsorption studies of the VBC derived carbon materials has shown that AC-90 is the best of the VBC derived carbon materials (miAC and CH series) for CO_2 adsorption at all temperatures and CO_2 partial pressures. This was attributed to it possessing the ideal balance between porosity (mostly micropores) and surface oxygen functionality, particularly a high surface hydroxyl concentration resulting in an AC surface with a high affinity for CO_2. The CH series showed a similar result, with a 90 min carbonisation time resulting in a char that exhibited the best CO_2 adsorption within the CH series. It is in part for this reason why the two industrial chars (***section 3.4***) were steam activated for this amount of time.

3.3.2 Multi-cyclic CO_2 Adsorption

The CO_2 multi-cyclic adsorption investigation was undertaken in order to simulate the partial pressure conditions of a VSA system, and to determine the working capacities for CO_2 that could be achieved. Multi-cyclic adsorption was undertaken at 293, 333 and 363 K for the VBC derived carbon materials are presented in ***Figure 3-3A-F***. The details of how the multi-cyclic adsorption measurement were taken are outlined in ***section 6.6.4.2***. Briefly, the system was purged with an Ar/CO_2 mixture (5% CO_2) for one hour prior to analysis. This was then followed by 4 cycles of adsorption with 15% CO_2 for 30 min and desorption with 5% CO_2 for 30 min. The working capacities were calculated using ***equation 6-11*** and were determined at each of the three temperatures (293, 333 and 363 K) for every material are presented in ***Table 3-1***. In addition to calculating the working capacities, the heats of adsorption for the multi-cyclic process were calculated as the average CO_2 heat of adsorption (ΔH_{Ads}) over the four adsorption cycles at 293 K (***section 6.6.4***).

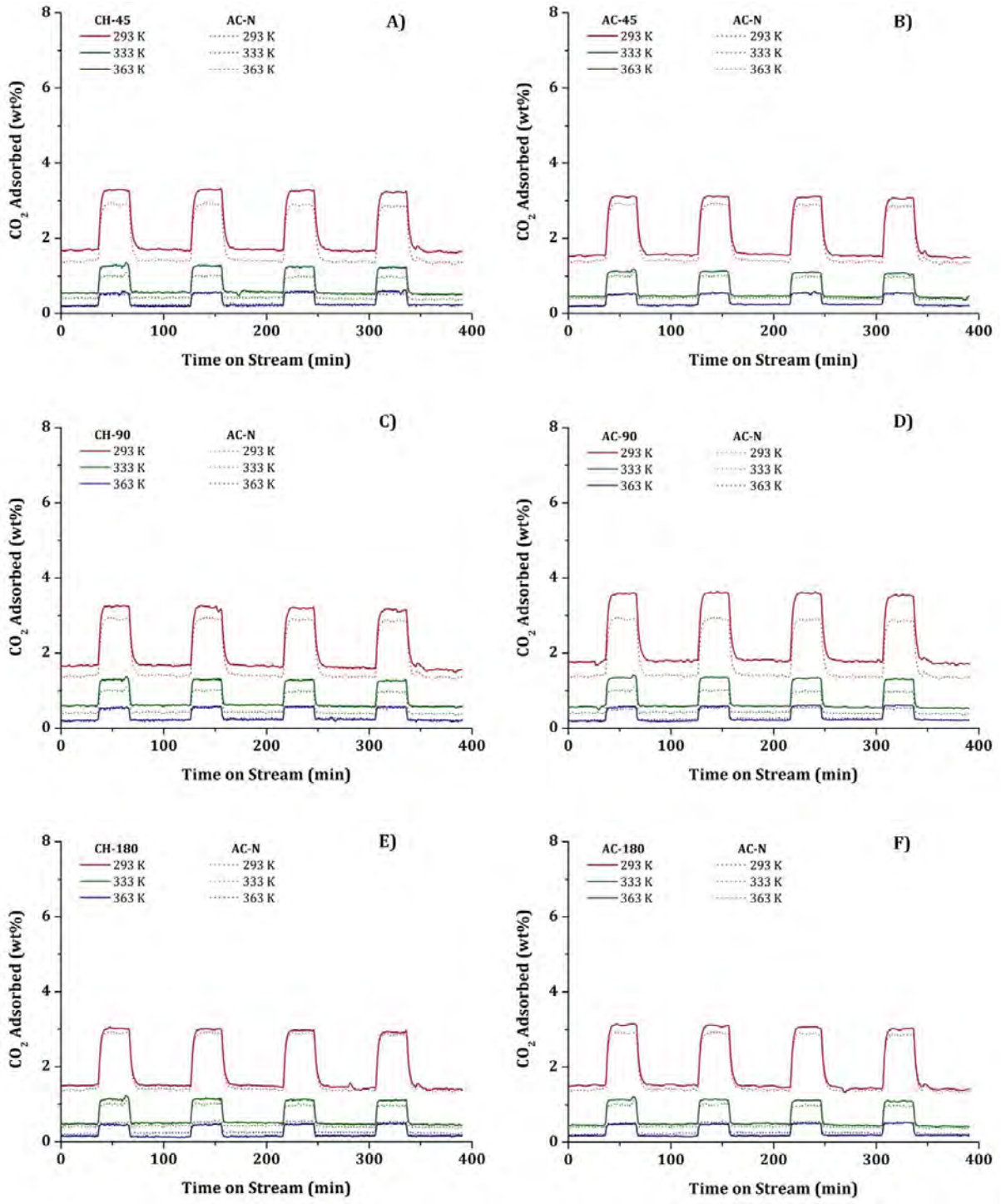

Figure 3-3 *~ CO_2 VSA Simulation for Steam Activated Carbons derived from VBC, taken via PPSA at 293, 333 & 363 K. Shown is the Multi-cyclic Adsorption Data for* ***A)*** *CH-45,* ***B)*** *AC-45,* ***C)*** *CH-90,* ***D)*** *AC-90,* ***E)*** *CH-180, and* ***F)*** *AC-180*

Before delving into any discussion of the results of the multi-cyclic CO_2 adsorption studies of the VBC derived carbon material it is crucial that one significant difference in the way the measurements were done carried out between the multi-cyclic and differential-step adsorption studies is addressed. In order to properly simulate a VSA cycle, it was appropriate to purge the

TGA system with an Ar/CO_2 mixture giving a CO_2 partial pressure of 5 kPa, which is equivalent to the lowest vacuum the proposed VSA system would utilise (for detail refer to section ***6.6.4.2***). As will be seen from the results presented in ***Figure 3-3*** this resulted in an increase in the amount of CO_2 adsorbed at 5 kPa relative to that observed from the differential-step adsorption studies presented in ***Figure 3-2***. Moreover, this increased adsorption that was observed at 5 kPa CO_2 partial pressure from the multi-cyclic adsorption studies also resulting in increases in the amount of CO_2 adsorbed at 15 kPa, as one might expect from incremental-step adsorption studies such as these. This in itself is evidence that true equilibrium had not been achieved in the differential-step adsorption studies at 5 kPa and potentially at 15 kPa. For physisorption systems, equilibrium is generally achieved quite quickly [7], and It is commonly said in adsorption science that 95 % of physisorption occurs within the first two minutes. However, this is only the situation if there are no limitations on mass-transport [8]. Mass-transport limitations arise in carbon materials predominately as a result of small mesopore volumes limiting the rate of gas flow into the larger micropore volume, where the majority of adsorption takes place [9].

From the multi-cyclic CO_2 adsorption studies for CH-45 (***Figure 3-3A***) the amount of CO_2 adsorbed at all temperatures was equal or greater to that of the AC-N. The difference in the amount of CO_2 adsorbed between CH-45 and AC-N were also more prominent with decreasing temperature. This was an interesting result as the amount of CO_2 adsorbed by CH-45 at 5 kPa and 15 kPa CO_2 partial pressure from the differential-step adsorption studies (***section 3.2***) was lower overall, and lower than that of AC-N in many cases. As such it is clear that differences exist between the CO_2 adsorption results from the two studies. Another interesting result of the increased CO_2 adsorption from the multi-cyclic adsorption of CH-45, was that the working capacities determined for CH-45 are significantly higher than for AC-N at all temperatures (***Table 3-1***). Suggesting that not only was the absolute amount of CO_2 adsorbed on CH-45 higher than AC-N, but that the difference in the amount adsorbed at 5 kPa and 15 kPa was also greater.

The CO_2 multi-cyclic adsorption studies for AC-45 (***Figure 3-3B***), exhibited lower CO_2 adsorption relative to CH-45 (***Figure 3-3A***) across the entire temperature range. This is not surprising as a similar result was also apparent from the comparison of the adsorption pseudo-isotherms for the two carbon materials (***Figure 3-2***). In the discussion of the differential-step adsorption studies of the CH-45/AC-45 pair (***section 3.3.1***) this was attributed to the overall decrease in the surface O concentration of AC-45 relative to CH-45, despite an increase in both micro- and mesopore volumes (***Table 2-5***). Furthermore, the amount of CO_2 adsorbed at 5 kPa and 15 kPa CO_2 partial pressure from the multi-cyclic study of AC-45 exceed that observed from the adsorption pseudo-isotherm at the same temperature and CO_2 partial pressure. As was

noted in the opening discussion of this section, the increased adsorption of CO_2 at both 5 kPa and 15 kPa relative to the pseudo-isotherms has been attributed to the pre-treatment of the sample under a CO_2 partial pressure of 5 kPa for 1 h. Another result of the increased CO_2 adsorption from the multi-cyclic studies relative to the differential-step studies, was that not only was the absolute about of CO_2 adsorbed higher than AC-N, but also the working capacities of AC-45 (***Table 3-1***) exceeded those of AC-N at all temperatures tested (293, 333 and 363 K). The heat of adsorption at 293 K for AC-45 (ΔH_{Ads} = 56.0 kJ/mol) was higher than for CH-45 (ΔH_{Ads} = 54.5 kJ/mol), despite AC-45 possessing a lower working capacity at this temperature. This is likely to be associated with the increased surface hydroxyl concentration possessed by AC-45 relative to CH-45 (XPS ***Table 2-2***, and NEXAFS ***Table 2-3***), as this functional group possesses the highest affinity for polar gases [5]. It is also well known that increases in heats of adsorption are strongly associated with increases in micropore volume, on account of the increased number of sites onto which adsorption can occur [9]. As such, the increased heat of adsorption for AC-45 at 293 K relative to CH-45, is likely due to a combination of both surface chemistry and pore structure, despite the lower working capacity exhibited at this temperature.

Table 3-1 ~ *Working Capacities of Physically Activated Coal Derived miACs Determined at 293, 333 and 363 K, and* ΔH_{Ads} *determined at 293 K.*

Sample Name	Working Capacity (wt%)			ΔH_{Ads} (KJ/mol)
	293 K	333 K	363 K	
AC-N	1.46	0.55	0.28	55.3
CH-45	1.61	0.67	0.38	54.5
AC-45	1.54	0.62	0.31	56.0
CH-90	1.52	0.66	0.35	58.0
AC-90	1.78	0.76	0.39	58.7
CH-180	1.50	0.64	0.34	55.9
AC-180	1.60	0.61	0.32	53.3

From the multi-cyclic CO_2 adsorption studies for CH-90 (***Figure 3-3C***) there are clearly observable increases in CO_2 adsorption at both 5 kPa and 15 kPa at all temperatures, relative to that observed from the differential-step adsorption studies (***Figure 3-2C***). It was noted in the opening discussion of this section that some of the increases in CO_2 adsorption at 5 kPa and 15 kPa CO_2 partial pressure were due to equilibrium not being achieved at low CO_2 partial

pressures ≤ 5 kPa) in the differential -step adsorption studies, due to mass-transport limitations. In the multi-cyclic adsorption studies, pre-treatment under a CO_2 gas stream of 5 kPa CO_2 partial pressure for 1 h allowed for equilibrium to be completely achieved at low CO_2 partial pressure. The mass-transport phenomena at low CO_2 partial pressures is compounded by the small mesopore volume of CH-90 (***Table 2-5***), with similar phenomena also being observed for both CH-45 and AC-45. Moreover, it is due to this observed adsorption behaviour at 5 kPa CO_2 partial pressure for CH-90 that explains the low working capacities observed at all temperatures (***Table 3-1***). However, despite exhibiting higher overall CO_2 adsorption at 293 K than either CH-45 or AC-45, the working capacity of CH-90 at 293 K was lower (***Table 3-1***). Furthermore, it exhibited a higher heat of adsorption at 293 K than either CH-45 or AC-45. As there was little overall difference between the surface O concentration of CH-45 and CH-90 (***Table 2-2***), the observed higher heat of adsorption is likely due to the slightly higher micropore volume possessed by CH-90 [9].

The multi-cyclic CO_2 adsorption of AC-90 (***Figure 3-3D***) exhibited the highest adsorption of CO_2 of any of the VBC derived carbon materials, which is consistent with the observations made from the differential-step study in ***section 3.3.1***. The working capacities determined at all temperatures (***Table 3-1***) were significantly higher for AC-90 than any of the VBC derived carbon materials, or AC-N. Moreover, the working capacity of AC-90 at 293 K was 1.78 wt% (***Table 3-1***), by far the largest working capacity of any of the VBC derived carbon material. For example, at 293 K AC-N possessed a working capacity of only 1.46 wt% (***Table 3-1***). It also possessed the highest heat of adsorption (ΔH_{Ads} = 58.7 kJ/mol) for the multi-cyclic adsorption process than any of the other VBC derived carbon materials or AC-N.

The increased CO_2 adsorption of AC-90 relative to the other VBC derived carbon materials and AC-N was commented on in ***section 3.3.1***, where it was attributed to both its favourable surface chemistry and pore structure. Relative to CH-90, AC-90 possessed a significantly higher mesopore volume; a result of the increased pore development that occurs during steam activation (***Table 2-5***). The development of pore structure that occurs during carbonisation is due to the removal of volatile matter from the semi-rigid skeletal carbon structure of the parent carbon. However, during steam activation the removal of volatile matter from the parent carbon occurs but, in addition, gasification of the carbon takes place most rapidly at the outside surface, resulting in slit-shaped pores with wide mouths [10]. It is also for this reason that mass-transport limitations were less pronounced over AC-90, due to its increased mesopore volume despite the increased adsorption time at 5 kPa. Only minor increases in CO_2 adsorption were observed at both 5 kPa and 15 kPa from the multi-cyclic studies of AC-90, relative to the differential-step studies (***Figure 3-3D***). Moreover, AC-90 also exhibited a significant increase in

mesopore volume relative to AC-45 (and CH-45 and CH-90), as a result of further increasing the activation time (***Table 2-5***). In addition to the more favourable pore structure of AC-90, it possessed surface chemistry which endowed its surface with a substantial increase in affinity for CO_2, relative to the other VBC derived carbon materials. Specifically, AC-90 was shown to possess the highest surface concentration of hydroxyl and ether groups of any of the VBC derived carbon materials, and the highest surface concentration of carbonyl and carboxylic acid groups of any of the miACs [5, 6].

Interestingly, the multi-cyclic CO_2 adsorption results (***Figure 3-3E-F***) for the CH-180/AC-180 pair exhibited increased adsorption between 5 kPa and 15 kPa, relative to those from the differential-step adsorption study (***Figure 3-2E-F***). In fact, the multi-cyclic CO_2 adsorption of both CH-180 and AC-180 increased so much as to exceed that of AC-N, which would imply that mass-transport limitations are occurring. This has already been addressed regarding the other VBC derived carbon materials, and has been attributed to equilibrium not be archived at low CO_2 partial pressures ($\leq$ 5 kPa) during the differential -step CO_2 adsorption measurements. However, AC-180 possesses a substantially higher mesopore volume than AC-N, an AC that exhibits no differences in the adsorption between the differential-step and multi-cyclic adsorption studies at either 5 kPa or 15 kPa (and thus no mass-transport limitations). This implies that the mass-transport limitation for the VBC derived carbon materials discussed until this point, may not be due entirely to small mesopore volumes, but may in fact be the result of the inherent interconnectivity of the carbons produced from VBC. A further point of interest regarding the increased multi-cyclic adsorption of CO_2 over AC-180, was that the increases in adsorption were less prominent at higher temperatures. For example the working capacity of AC-180 at 293 K was one of the highest observed for the VBC derived carbon material; whereas, at 363 K it exhibited one of the lowest (***Table 3-1***). Moreover, AC-180 exhibited a heat of adsorption at 293 K (ΔH_{Ads} = 53.3 kJ/mol), that was the lowest of all the VBC derived carbon materials, and lower even than AC-N (ΔH_{Ads} = 55.3 KJ/mol). For the heat of adsorption to be so low when such high adsorption is being exhibited, must mean that some aspect of the interaction between CO_2 and the AC-180 surface is significantly different from that which occurred for the other VBC derived carbon materials. Both the low heat of adsorption in the face of high adsorption, and the decreases in the differences between multi-cyclic and differential-step adsorption; can be explained by differences in the surface chemistry of AC-180 relative to the other carbon materials discussed here. AC-180 possessed the lowest surface O concentration of any of the VBC derived carbon materials, and was the only VBC derived carbon to be lower than AC-N (***Table 3-1***). Furthermore, the concentrations of all the oxygenated surface functional groups were the lowest of all the VBC derived carbon materials. Such a low

surface O concentration will have acted to significantly decrease the surface polarity and hence the affinity of the AC-180 surface for CO_2 [5, 6].

It was clear from the adsorption studies using the VBC derived carbon materials (presented in ***section 3.3***), that AC-90 was the best CO_2 adsorbent of the group and also outperformed the commercial AC-N under all conditions tested. For this reason, a 90 min steam activation time was used for activation of the two industrial chars (CHLR and CHRK). The CO_2 adsorption studies conducted using the industrial chars and their steam activated counterparts are presented in the following section, along with CH-90 and AC-90 for comparison.

3.4 Physically Activated Char Derived Activated Carbons

3.4.1 Differential-step CO_2 Adsorption

The CO_2 adsorption pseudo-isotherms obtained from the differential-step adsorption study for CHLR and CHRK and their respective miACs (AC-CHLR-90 and AC-CHRK-90) are reported in ***Figure 3-4A-D***, with AC-N overlayed as was done in ***section 3.3.1***.

From the differential-step adsorption study for CHLR (***Figure 3-4A***) it can be seen that at all temperatures and CO_2 partial pressures CHLR underperforms relative to AC-N (***Figure 3-2D***). The low CO_2 adsorption behaviour exhibited by CHLR is attributed to the low mesopore volume possessed by CHLR (***Table 2-11***). CHLR did however possess a comparable micropore volume to several of the VBC derived carbon materials (***Table 2-5***), indicating that it did possess the potential for much higher CO_2 adsorption, but due to its low mesopore volume, mass-transport limitations inhibit the timely uptake of CO_2. Interestingly, CHLR possessed the highest surface O content of any of the physically activated carbon materials (**Table 2-8**). Moreover, of this very high surface O content a significant proportion was shown to be due to surface hydroxyl groups (***section 2.3.2***). This high surface hydroxyl group concentration might be expected to result in a carbon surface with a high affinity for CO_2 [5, 6]. However, due to the rate of CO_2 uptake being retarded by mass-transport limitations, adsorption within a reasonable equilibration time would make its use in its present form inefficient for CO_2 capture purposes.

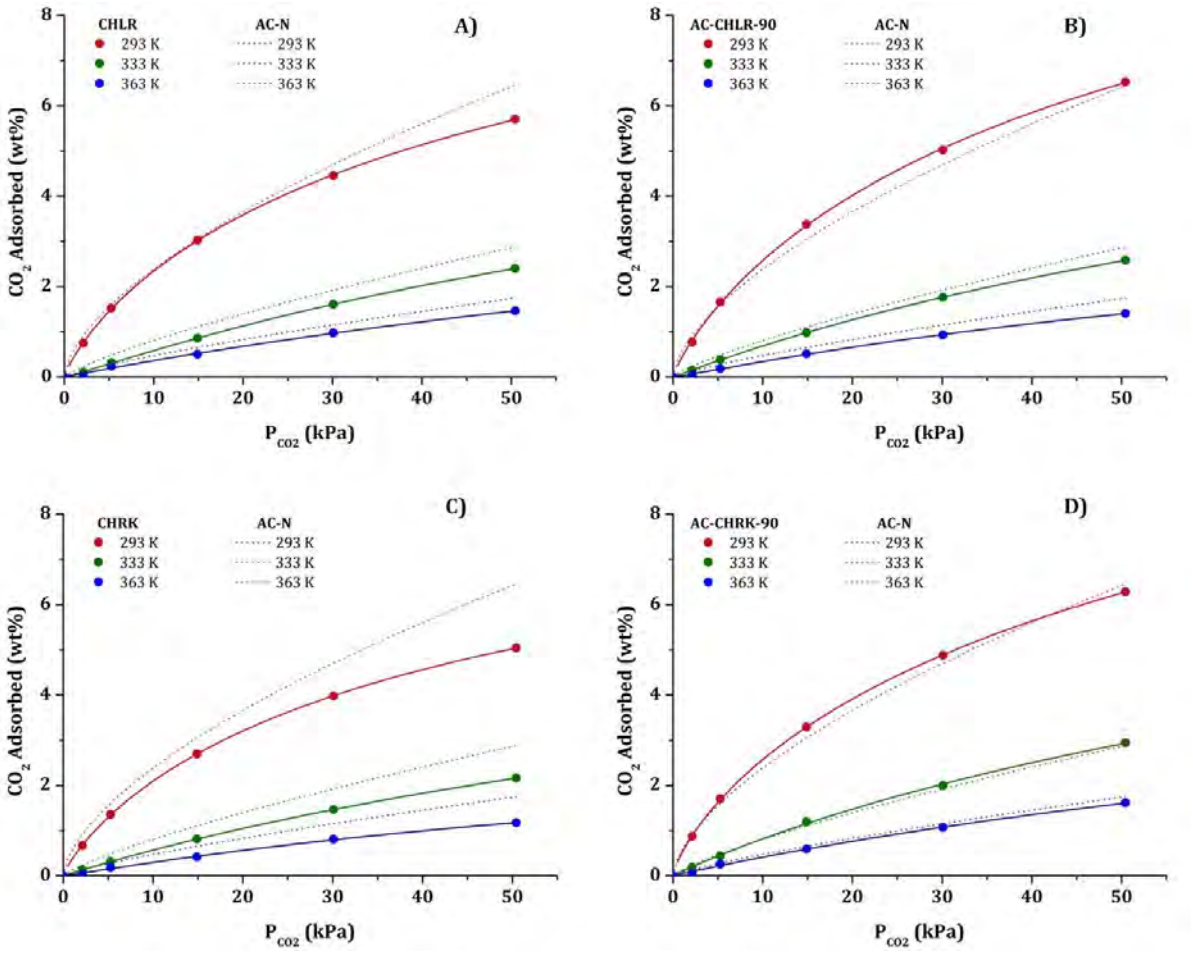

Figure 3-4 *~ CO_2 Adsorption Pseudo-isotherms for Steam Activated CHLR Carbons, taken via PPSA at 293, 333 & 363 K. Shown are the Isotherms for* ***A)*** *CHLR,* ***B)*** *AC-CHLR-90,* ***C)*** *CHLR, and* ***D)*** *AC-CHLR-90*

In ***chapter 2*** (***section 2.4***) the effect of steam activation of CHLR was investigated, resulting in AC-CHLR-90. From the gas physisorption studies the presence of steam was found to have little effect on the development of the pore structure of AC-CHLR-90 relative to CHLR, which was attributed to the unreactive nature of CHLR. The CHLR char was produced industrially via carbonisation of VBC briquettes in a Lurgi-style retort at 1173 K (***section 6.3.2***), where as the steam activation was undertaken at only 1073 K. As such, very little carbon that was still reactive under steam gasification conditions employed. From ***Figure 3-4B***, it can clearly be seen that AC-CHLR-90 exhibits greater CO_2 adsorption than CHLR over the entire CO_2 partial pressure. Interestingly, AC-CHLR-90 possessed essentially the same micropore volume as CHLR (***Table 2-11***), implying that steam activation did not significantly affect the development the micropores. On the other hand, steam activation did increase the mesopore volume of AC-CHLR-90 relative to CHLR (***Table 2-11***). The absolute value of the increase in mesopore volume may seem small, but was in fact more than a doubling of the mesopore volume of CHLR. The actual

effect the change in pore volume had on the CHLR/AC-CHLR-90 may also be understated by these results, as a significant decrease in the total surface O content of AC-CHLR-90 was observed relative to CHLR (***Table 2-8***). Such a significant decrease in surface O might be expected to detrimentally effect the affinity of the carbon surface towards CO_2 [5, 6]. Due to the low mesopore volume of CHLR, timely access to the adsorption sites within the micropores would not have been able to be achieved over the timescale of the differential-step adsorption studies. However, on account of the significant increase in mesopore volume of AC-CHLR-90 relative to CHLR, sites that were previously unable to be accessed could be, and so despite the decrease in surface O concentration, more of these sites are still being made use of for AC-CHLR-90 than for CHLR.

The differential-step CO_2 adsorption study of CHRK (***Figure 3-4C***) exhibited the lowest CO_2 adsorption at all temperature and CO_2 partial pressures, of any carbon material presented in ***section 3.4***. This was to be expected, as CHRK possessed no detectable mesopore volume (***Table 2-11***), and mass-transport to the micropores would be limited [3, 4, 11]. However, CHRK did possess a substantial micropore volume (***Table 2-11***). However, the surface O concentration of CHRK was quite low (***Table 2-8***), and it possessed low concentrations of hydroxyl, ether and carboxylic acid groups. The latter might have also played a role in the low CO_2 adsorption, as the surface chemistry was such that CHRK would have possessed a much lower affinity for CO_2 than other carbon material reported here.

Steam activation of CHRK resulted in an increase in micropore volume equivalent to that observed for the mesopore volume (***Table 2-11***). The resulting increase in both the micro- and the mesopore volumes of AC-CHRK-90 (relative to CHRK, ***Table 2-11***) was reflected in the pseudo-isotherms of the differential-step CO_2 adsorption studies for AC-CHRK-90, shown in ***Figure 3-4E***. The increased adsorption of CO_2 for AC-CHRK-90 relative to CHRK was observed at all temperatures and CO_2 partial pressures. In addition to the increased micro- and mesopore volumes of AC-CHRK-90 relative to CHRK, there was a significant increase in the surface O content (***Table 2-8***). A substantial amount of the increase in surface O concentration was found to be due to hydroxyl groups, with an associated decrease in cyclic aliphatic ethers (hydroxylation) also being observed. This is a good indication that relative to CHRK, AC-CHRK-90 possessed a surface with a higher affinity for CO_2 [5, 6], in addition to larger micro- and mesopore volumes; thus accounting for the significant increases in CO_2 adsorption observed.

Relative to AC-90 (***Figure 3-2D***), both AC-CHLR-90 and AC-CHRK-90 (***Figure 3-4B*** and ***Figure 3-4D***, respectively) exhibited lower CO_2 adsorption at all temperature, especially at CO_2 partial pressures above 5 kPa. This has been predominately attributed to the significantly higher mesopore volume of AC-90, compared to either of the char derived miACs (***Table 2-11***).

However, the effect of differences observed in the surface chemistry of the char derived miACs and AC-90 cannot be discounted. The surface chemistry of AC-90 possessed as much in common with either of the char derived miACs as they did with one another. Specifically, the concentration of surface O for AC-90 was medially placed between that of AC-CHLR-90 and that of AC-CHRK-90 (***Table 2-8***). However, AC-90 possessed a higher proportion of hydroxyl groups to ethers than either of the char derived miACs (***section 2.4.2***). It is more likely that the superior CO_2 adsorption exhibited by AC-90, was principally due to the significantly higher mesopore volume, allowing for the timely adsorption of CO_2.

Overall, the effect of steam activation on the two industrial chars was shown to be favourable, especially in the case of the CHRK/AC-CHRK-90 pair, which exhibited significant increases in CO_2 adsorption as a result of steam activation. However, despite the increased adsorption of CO_2 for the steam activated industrial chars, mass-transport limitations still seem to have impacted the results. The effect of this on the multi-cyclic CO_2 adsorption will be investigated in the following section.

3.4.2 Multi-cyclic CO_2 Adsorption

The multi-cyclic CO_2 adsorption studies of the two industrial chars and the miAC produced from them are presented in ***Figure 3-5A-D***. The working capacities (***equation 6-11***) determined for the adsorption cycles between 5-15 kPa CO_2 partial pressure for both carbons are presented in ***Table 3-2***, along with those of AC-N, CH-90 and AC-90 for reference. The heats of adsorption at 293 K (ΔH_{Ads}) were also calculated from the PPSA data, as outlined in ***section 6.6.4***.

From the multi-cyclic CO_2 adsorption study of CHLR (***Figure 3-5A***) it can be seen that it exhibited the closest adsorption behaviour to AC-N of any of the carbon materials presented in this chapter. However, the working capacities of CHLR were slightly higher than those of AC-N at all temperatures tested (***Table 3-2***). Relative to the adsorption behaviour exhibited from the differential-step adsorption study by CHLR, there is an overall increase in the adsorption of CO_2 at both 5 kPa and 15 kPa. A similar increase in CO_2 adsorption for the multi-cyclic adsorption studies was observed from the multi-cyclic studies of the VBC derived carbon materials (***section 3.3.2***). This was attributed to equilibrium not being achieved within the 20 min step at low CO_2 partial pressures during the differential-step adsorption measurements as a result of mass-transport limitations. The mass-transport limitations are much more significant in the case of CHLR due to its low mesopore volume (***Table 2-11***). This behaviour was observable in the multi-cyclic adsorption studies due to the 1 h pre-treatment of the carbon material under a CO_2 gas stream at 5 kPa CO_2 partial pressure, which was utilised for the PPSA measurements for the

multi-cyclic studies and not in the differential-step adsorption studies. Similar behaviour was observed for the VBC derived carbon materials (***section 3.3***), many of which possessed significantly higher mesopore volumes than CHLR (***Table 2-5***). The effect that the surface chemistry of CHLR had on its adsorption properties was discussed in the previous section, and are equally as applicable here, but cannot account for the increased adsorption relative to the differential-step adsorption studies. That is the high surface O concentration of the CHLR surface might be expected to resulted in a carbon with a high affinity for CO_2 (***Table 2-8***), but this appears to have been limited by the mass-transport phenomena arising from its small mesopore volume.

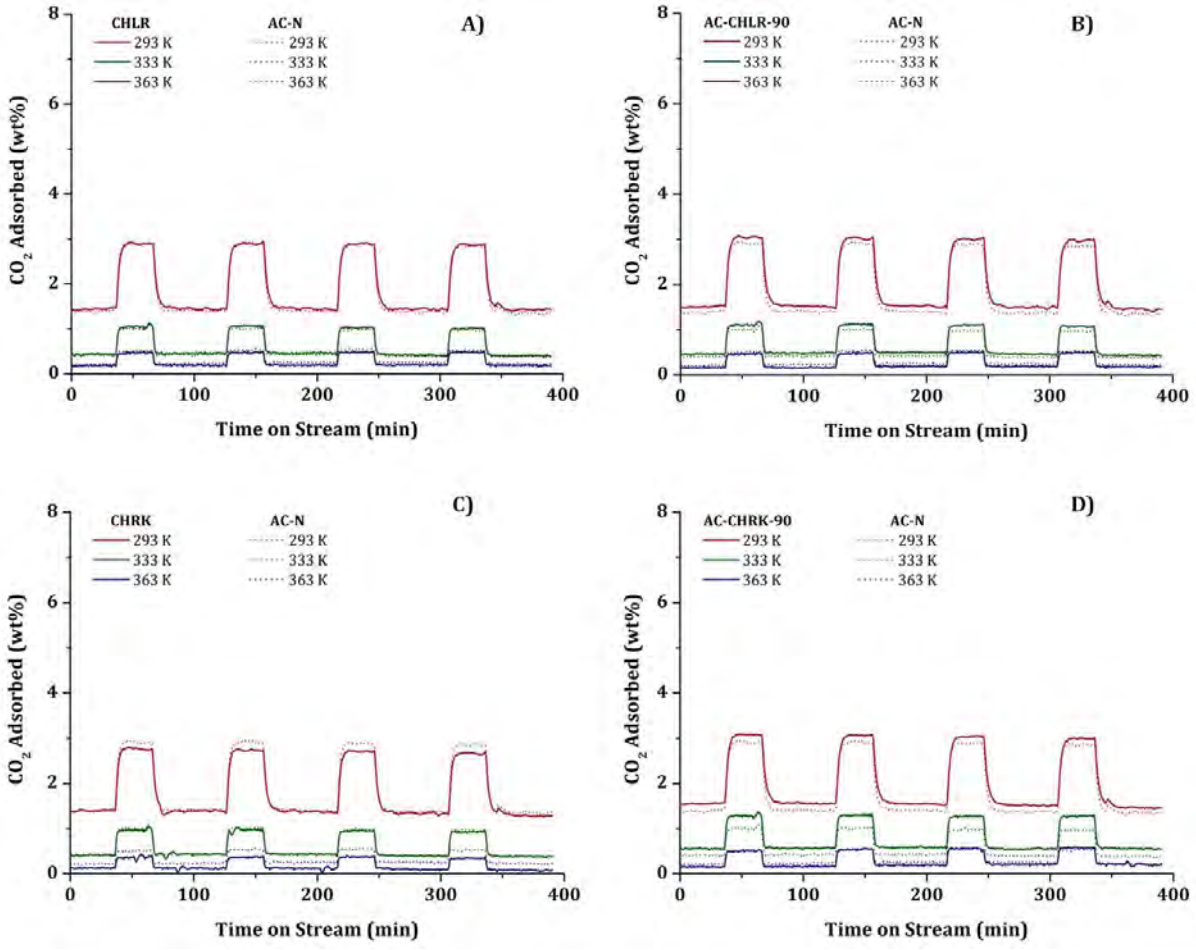

Figure 3-5 *~ CO_2 VSA Simulation for Steam Activated CHLR Carbons, taken via PPSA at 293, 333 & 363 K. Shown are the VSA Studies for* ***A)*** *CHLR, and* ***B)*** *AC-CHLR-90*

The multi-cyclic CO_2 adsorption studies of AC-CHLR-90 (***Figure 3-5B***) showed only minor increases in CO_2 adsorption at both 5 kPa and 15 kPa CO_2 partial pressure, relative to CHLR

parent material at all temperatures (***Figure 3-5A***). This was attributed for the most part to the minor increase in micropore volume of AC-CHLR-90 (only observable from the N_2 data, no detectable change was observed by CO_2 physisorption) relative to CHLR (***Table 2-11***). Furthermore, AC-CHRL-90 possessed a higher mesopore volume to CHLR. This was probably a result of CHLR being somewhat unreactive under the steam activation conditions utilised; because it had been carbonised at a temperature 100 K higher than used in steam activation (1073 K). Furthermore, the carbonisation treatment used to produce CHLR was carried out under flue gas-like conditions, and as such a minor amount of gasification by the CO and CO_2 in the gas stream will have occurred. This resulted in CHLR possessing an enriched surface O concentration. However, it would seem that steam activation of CHLR to produce AC-CHLR-90, resulted in the removal of many of the surface O groups; as characterised by the significant decrease in surface O for AC-CHLR-90 relative to CHLR (XPS, ***Table 2-8***).

Table 3-2 ~ *Working Capacities of Physically Activated Char Derived miACs Determined at 293, 333 and 363 K, and ΔH_{Ads} determined at 293 K.*

Sample Name	Working Capacity (wt%)			ΔH_{ADS} (KJ/mol)
	293 K	333 K	363 K	
AC-N	1.46	0.55	0.28	55.3
CH-90	1.52	0.66	0.35	58.0
AC-90	1.78	0.76	0.39	58.7
CHLR	1.50	0.61	0.30	64.5
AC-CHLR-90	1.55	0.64	0.34	60.7
CHRK	1.39	0.54	0.28	59.8
AC-CHRK-90	1.54	0.68	0.39	59.8

In comparing the amount of CO_2 adsorbed from the differential-step adsorption studies of AC-CHLR-90 relative to the multi-cyclic adsorption studies; it can be seen that there is an overall increase in adsorption at both 5 kPa and 15 kPa for the multi-cyclic studies at all temperatures, which is indicative of mass-transport limitations. These observed changes in the amount of CO_2 adsorption at 5 kPa and 15 kPa from the multi-cyclic studies relative to the differential-step studies are the result of equilibrium not being achieved at low CO_2 partial pressures (≤ 5 kPa) in

the differential-step adsorption studies, which in turn is the result of the small mesopore volume of AC-CHLR-90 (***Table 2-11***). The overall result of the increased adsorption from the multi-cyclic studies of AC-CHLR-90 was that it possessed higher working capacities at all temperatures tested, relative to AC-N. This was interesting, in that like the carbon materials presented in ***section 3.3***, despite mass-transport limitations being apparent, AC-CHLR-90 outperformed AC-N. In order to produce an miAC from CHLR with a more well developed pore structure, a significantly more aggressive steam gasification procedure would be required, at a much higher steam concentration and/or temperature.

The multi-cyclic adsorption studies for CHRK (***Figure 3-5C***) exhibited the lowest CO_2 adsorption at both 5 kPa and 15 kPa of all the carbon materials presented in this chapter (except for VBC), which was consistent with adsorption behaviour observed from the differential-step adsorption studies for CHRK (***Figure 3-4C***). The low CO_2 adsorption behaviour of CHRK can be attributed to the absence of any detectable mesopore volume (***Table 2-11***). Again the results of the multi-cyclic adsorption studies for CHRK indicated an increase in the amount of adsorption of CO_2 relative to that observed from the differential-step adsorption studies under comparable conditions (i.e. temperature and CO_2 partial pressure). Despite the increased CO_2 adsorption from the multi-cyclic studies for CHRK, the working capacities determined were lower than AC-N, except at 363 K where they were equal (***Table 3-2***).

In addition to exhibiting lower adsorption to CHLR at both 5 kPa and 15 kPa, CHRK possessed a much lower heat of adsorption (***Table 3-2***), which can be attributed mostly to the lower surface O concentration of CHRK relative to CHLR. Moreover, CHRK possessed the lowest surface O concentration of any of the carbon materials presented in this chapter (***section 2.4.2***). The low surface O concentration coupled with the non-existent mesopore volume are the main reason behind the low CO_2 adsorption observed over this carbon.

The multi-cyclic CO_2 adsorption of AC-CHRK-90 (***Figure 3-5D***) showed substantially increased CO_2 adsorption relative to CHRK, beyond that which could have been predicted from the differential-step adsorption studies (***Figure 3-4D***). This behaviour is indicative of mass-transport limitation due to the small mesopore volume of AC-CHRK-90 (***Table 2-11***). The mesopore volume of AC-CHRK-90 (***Table 2-11***) is small when compared to the VBC derived carbon materials (***Table 2-5***), but it is still a significant increase in the mesopore volume of AC-CHRK-90 relative to CHRK. From the working capacity determined for AC-CHRK-90 at all temperatures closer evaluation shows that the adsorption between 5 kPa and 15 kPa has increased (***Table 3-2***). Moreover, the working capacities for AC-CHRK-90 at 333 K and 363 K

were equal to or higher than many of the VBC derived carbon materials (***Table 3-1***), as well as CHLR, AC-CHLR-90 and CHRK (***Table 3-2***).

The increase in CO_2 adsorption for AC-CHRK-90 at 293 K relative to CHRK that would be expected from the differential-step studies at 293 K was observed; however, there was no change in the heat of adsorption (***Table 3-2***). There were significant increases in both the micro- and mesopore volume, and in the surface O concentration of AC-CHRK-90 relative to CHRK. As a result of which, there would be an expected increase in the heat of adsorption at 293 K for AC-CHRK-90 relative to CHRK [9]. This observation can be understood on the basis of the increase in mesopore volume, counteracting the increases in micropore volume of surface O concentration.

The working capacities of AC-CHRK-90 (***Table 3-2***) are higher compared to many of the VBC derived carbons at each respective temperature (***Table 3-1***). Compared to the multi-cyclic adsorption of CO_2 exhibited by AC-90 at 293 K (***Table 3-1***), both AC-CHLR-90 and AC-CHRK-90 significantly underperformed. However, at both 333 K and 363 K, AC-CHRK-90 exhibited comparable working capacities to AC-90.

In summary, the differential-step and multi-cyclic adsorption studies of CHLR, CHRK and their respective miACs, showed that steam activation of the chars resulted in significant improvements in CO_2 adsorption behaviour of the miACs relative to the chars from which they were derived. Furthermore, the miAC derived from the steam activation of CHRK (AC-CHRK-90) exhibited superior CO_2 adsorption behaviour not only to AC-CHLR-90, but also many of the VBC derived carbon materials. This CO_2 adsorption behaviour was attributed to the high micropore volume and favourable surface chemistry possessed by AC-CHRK-90.

3.5 Chemically Activated Carbons

The introduction of KOH to the VBC was undertaken via a typical wet impregnation technique, the details of which can be found in ***Section 6.4.4.1***. Briefly, the KOH loading was varied on a mass percentage basis, and the impregnated materials were thermally activated at 1073 K for 60 min. The KOH was removed post-synthetically by washing the ACs with HCl. The differential-step and multi-cyclic CO_2 adsorption studies for the KOH activated miACs that were characterised in the previous chapter (***section 2.5***), and are presented in the following two

sections (***sections 3.5.1*** and ***3.5.2*** respectively). As was the case for the steam activated miACs, the KOH miACs were benchmarked against the AC-N commercial standard.

3.5.1 Differential-step CO_2 Adsorption

The CO_2 adsorption pseudo-isotherms obtained from the differential-step adsorption studies for the KOH activated miACs are presented in ***Figure 3-6A-D***, overlayed with AC-N for comparison.

The CO_2 adsorption behaviour exhibited by the KOH activated miACs was significantly different from that observed from the physically activated carbon materials presented in ***section 3.3*** and ***section 3.4***. This might be expected from the substantial differences that existed between the chemically activated miACs and the physically activated carbon materials (***Table 2-17***). From the differential-step adsorption studies of the KOH activated miACs shown in ***Figure 3-6***, it can be seen that major increases in CO_2 adsorption relative to most of the physically activated carbon materials. In fact, with the exception of AC-K0 (***Figure 3-6A***), which was not impregnated with KOH; all of the KOH activated miACs (AC-K5, AC-K7.5 and AC-K10) exhibited significantly higher CO_2 adsorption than AC-N at all temperatures and CO_2 partial pressures.

From the adsorption pseudo-isotherm of AC-K0 at 363 K (***Figure 3-6A***), it is clearly evident that AC-K0 possesses equivalent adsorption to AC-N across the CO_2 partial pressure range. At 293 K and 333 K, AC-K0 exhibits superior CO_2 adsorption to AC-N across the entire CO_2 partial pressure range. This can be partially attributed to the high micropore volume of AC-K0 (***Table 2-16***), in addition to its higher surface O concentration, relative to AC-N (***Table 2-13***). The surface O concentration was even higher than any of the physically VBC derived carbon materials (***Table 2-3***), although the distribution of oxygenated functional groups was vastly different. Of particular importance were the high surface concentrations of hydroxyl/ether (C-O-R peak) and carboxylic acid groups, as determined by XPS (***Table 2-13***). The NEXAFS investigation of AC-K0 showed that a substantial proportion of the groups responsible for the C-O-R peak from the XPS were due to hydroxyl groups, with the remainder being ethers (***Table 2-14***). The high surface concentration of hydroxyl and carboxylic acid groups might have resulted in the surface of AC-K0 having a high affinity for CO_2 [5, 6].

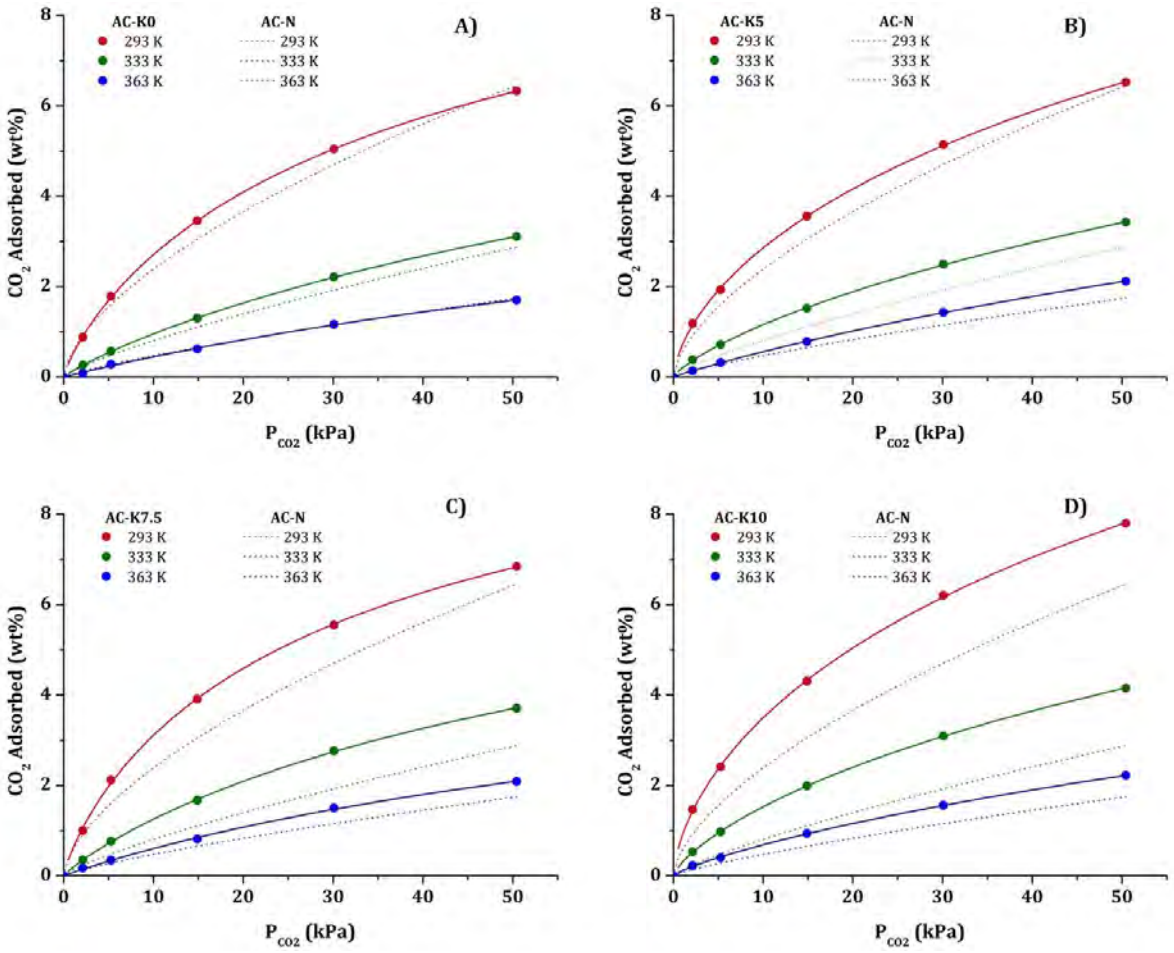

Figure 3-6 ~ *CO_2 Adsorption Pseudo-isotherms for KOH Activated miACs taken via PPSA at 293, 333 & 363 K.* ***A)*** *AC-K0,* ***B)*** *AC-K5,* ***C)*** *AC-K7.5, and* ***D)*** *AC-K10*

For the CO_2 adsorption pseudo-isotherms obtained from the differential-step adsorption studies of AC-K5, this miAC exhibits far superior CO_2 adsorption at all temperatures and CO_2 partial pressures than AC-N. Despite this improvement in CO_2 adsorption behaviour, AC-K5 exhibited no significant difference in the micropore volume relative to AC-K0, and an incredibly small mesopore volume (***Table 2-16***). Improvements in the surface chemistry of AC-K5 were however observed relative to AC-K0, that might increase the affinity of the surface towards CO_2 [5, 6]. Firstly, the total surface O concentration was substantially higher for AC-K5 than AC-K0 (***Table 2-13***). The increase in surface O of AC-K5 relative to AC-K0, manifested in the XPS as a substantial increase in C-O-R groups, and a less significant increase in C=O groups; whilst a decrease in COO-R groups was observed (***Table 2-13***). From the NEXAFS investigation of AC-K5 (***Table 2-14***), there was no significant changes in the distribution of hydroxyl and ether groups. Therefore the overall increase in the C-O-R peak from XPS, coupled with the distribution of hydroxyl and ether groups from NEXAFS, indicate an overall increase in the surface concentration of hydroxyl groups (and ether groups) has occurred on the surface of AC-K5,

relative to AC-K0. Such an increase in hydroxyl groups might be expected due to increase the affinity of the AC-K5 surface for CO_2 [5, 6].

From the differential-step adsorption study of AC-K7.5 (***Figure 3-6C***) it can be seen that increasing the KOH loading from 5-7.5 wt% had significant effects on the CO_2 adsorption behaviour. As was the case of both AC-K0 and AC-K5, the CO_2 adsorption for AC-K7.5 was higher than AC-N, with the most significant increases being present between5 kPa and 30 kPa CO_2 partial pressure. A very significant increase in CO_2 adsorption was also observed across the entire CO_2 partial pressure range was observed for AC-K7.5 at 333 K, whereas at 363 K there were no observable differences between the adsorption of CO_2 for AC-K7.5 or AC-K5. As there was no significant change in the micropore volume of AC-K7.5 relative to AC-K5 (***Table 2-16***), the differences in the surface chemistry of the two miACs must have played a major role in the increase in CO_2 adsorption (***Table 2-13***). The XPS analysis of the KOH activated miACs showed there to be a significant increase in the surface O concentration of AC-K7.5 relative to AC-K5, which was accompanied by an equally significant shift in the distribution of oxygenated surface functional groups (***Table 2-13***). This was primarily observed by XPS as an increase in C-O-R groups that was larger than the increase in surface O itself, along with a significant decrease in C=O groups (***Table 2-13***). Although the NEXAFS investigation of AC-K7.5 and the KOH activated miACs showed some variation in the proportions of certain functional groups, these were relatively minor and had little effect on changing the distribution of hydroxyl and ether groups (***Table 2-14***).

The highest CO_2 adsorption of any carbon material at all temperatures and CO_2 partial pressures presented in this chapter, was observed from the adsorption isotherms of AC-K10 (***Figure 3-6D***). For the other KOH activated miACs (AC-K0, AC-K5 and AC-K7.5) the focus of the discussion of the observed increases in CO_2 adsorption, as a function of KOH loading; whereas, AC-K10 possessed a lower surface O concentration than either AC-K5 or AC-K7.5 (***Table 2-13***). This would indicate that the surface chemistry was not the primary factor behind the significant increase in CO_2 adsorption. Although there was an observed decrease in surface O concentration of AC-K10 relative to the other KOH activated miACs, there was however, a very significant increase in the micropore volume of AC-K10 (***Table 2-16***). The effect of the increased micropore volume can be seen clearly from the pseudo-isotherm at 293 K (***Figure 3-6D***), whereby there is a significant increase in CO_2 adsorption at higher CO_2 partial pressures, not seen for the other KOH activated miACs that all possessed similar micropore volumes. Therefore, despite the significant decrease in the surface O concentration of AC-K10 relative to either AC-K5 or AC-K7.5, the significant increase in micropore volume was more than sufficient to counteract this.

In summary, the adsorption pseudo-isotherms derived from the differential-step adsorption studies of the KOH activated miACs, showed these carbon materials to possess substantially higher CO_2 adsorption relative to the physically active carbons. Moreover, the results of the adsorption pseudo-isotherms of the KOH activated miACs highlighted the delicate balance between surface chemistry and pore structure, and how this affects CO_2 adsorption. Lastly, it is important to make note of the incredibly small mesopore volumes determined for the KOH miACs (***Table 2-16***), although the effect of this was not clear from the adsorption pseudo-isotherms. It is predicted that such small mesopore volumes will result in mass-transport limitations, which will come into play significantly for the multi-cyclic adsorption studies, that will be presented in the following section.

3.5.2 Multi-cyclic CO_2 Adsorption

The multi-cyclic CO_2 adsorption screening was carried out on the KOH miACs between 5-15 kPa CO_2 partial pressure. The multi-cyclic plots were under taken isothermally at 293, 333 and 363 K for miACs at KOH loadings of 0, 5, 7.5 and 10 wt% and are shown in ***Figure 3-7A-D***. The working capacities (***equation 6-11***) calculated from ***Figure 3-7*** are presented in ***Table 3-3***.

From the multi-cyclic adsorption studies of the KOH activated miACs (***Figure 3-7***), it can clearly be seen that these carbon materials outperform AC-N at all temperatures. Moreover, the working capacities were significantly higher than those of AC-N (***Table 3-3***). However, for each miAC the amount adsorbed at 5 kPa and 15 kPa CO_2 partial pressure from the multi-cyclic studies was greater than was observed from the differential-step studies (***Figure 3-6***) at the same temperatures and CO_2 partial pressures. This is due to mass-transport limitations arising from the small mesopore volumes of the KOH activated miACs (***Table 2-16***). This adsorption behaviour is only observable due to equilibrium not being achieved at low CO_2 partial pressures (≤ 5 kPa) in the differential-step adsorption studies (***Figure 3-6***), for which 20 min equilibration times were applied for each step. Furthermore, for the measurements of the multi-cyclic CO_2 adsorption studies, a 1 h pre-treatment under a gas steam at a CO_2 partial pressure of 5 kPa used, ensuring that equilibrium was achieved at 5 kPa partial pressure.

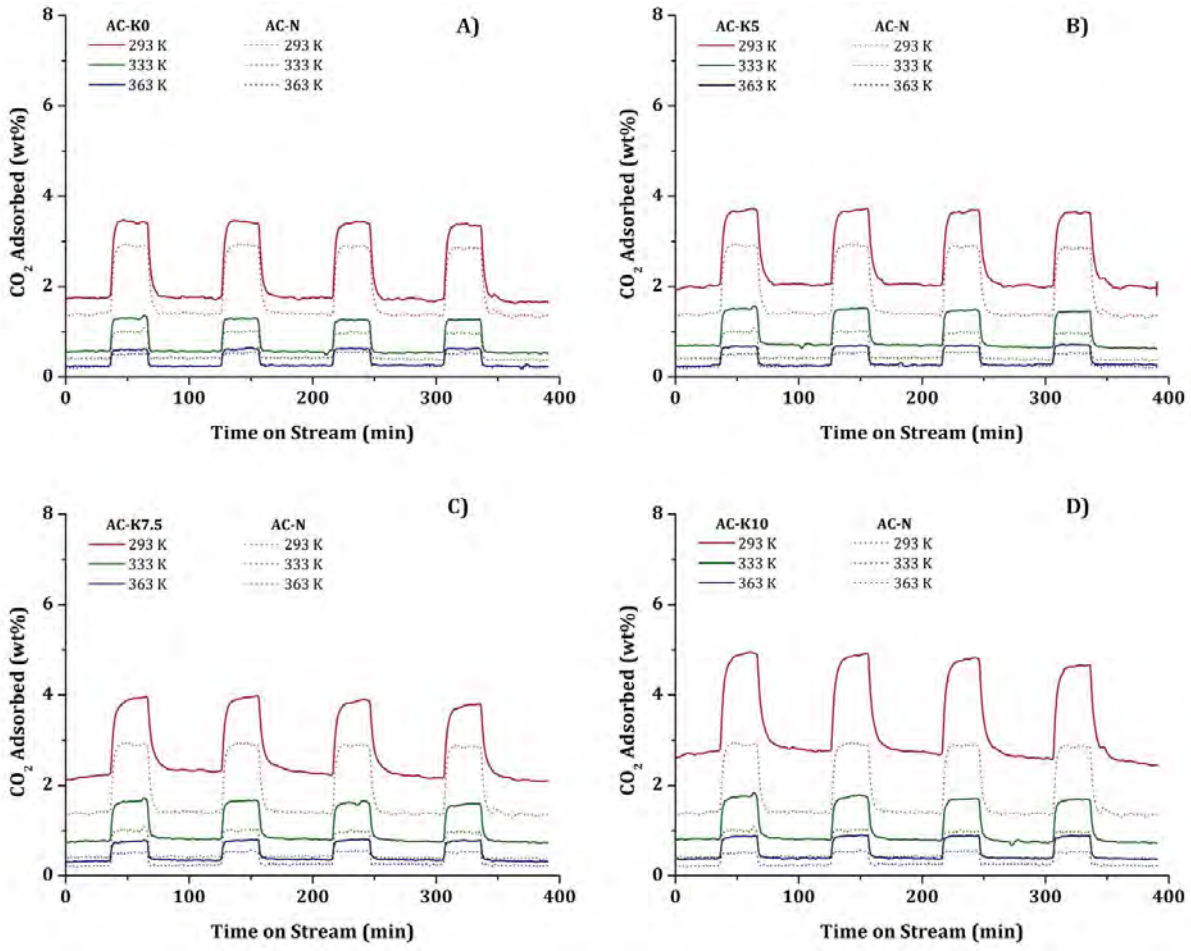

Figure 3-7 ~ *CO_2 VSA Simulation for KOH Activated Carbons, taken via PPSA at 293, 333 & 363 K.* ***A)*** *AC-K0,* ***B)*** *AC-K5,* ***C)*** *AC-K7.5, and* ***D)*** *AC-K10*

From the multi-cyclic CO_2 adsorption studies of AC-K0 (***Figure 3-7A***) some very interesting results were observed. Firstly, at 363 K the amount of CO_2 adsorbed at 5 kPa CO_2 partial pressure was identical to that of AC-N, an observation also made from the differential-step adsorption study (***Figure 3-6A***). However, as has been noted the absolute amount of CO_2 adsorbed at both 5 kPa and 15 kPa was higher in the multi-cyclic studies than was observed from the differential-step studies. This has been attributed to mass-transport limitations arising from the small mesopore volume of AC-K0 and the KOH activated miACs. At 333 K the differences between the adsorption from the differential-step and multi-cyclic studies was much less pronounced for AC-K0 than at 363 K. Although slight, an increase in the adsorption of CO_2 was observed at both 5 kPa and 15 kPa CO_2 partial pressure from the multi-cyclic adsorption study of AC-K0 relative to that of the differential-step adsorption study. For the multi-cyclic adsorption study of AC-K0 at 293 K, proved to exhibit the least variation from the differential-step adsorption study, yet still resulted in a working capacity (***Table 3-3***) higher than all of the physically activated carbon materials, with the exception of AC-90 (***Table 3-1***). Similarly, the

working capacities for AC-K0 at both 333 K and 363 K were higher than the majority of the physically activated carbon materials. The impressive CO_2 adsorption behaviour exhibited by AC-K0, having only undergone carbonisation with no chemical or physical activation; is attributed to its high micropore volume and favourable surface chemistry (***section 3.5.1***). This can in turn be directly attributed to the manner in which it was carbonised, using the secondary quartz reactor, which limited the flow of N_2 through the sample, thus reducing the rate of removal of volatile components within the VBC precursor relative to that of the physically activated carbon materials (***section 6.1***).

The multi-cyclic CO_2 adsorption studies of AC-K5 (***Figure 3-7B***) showed increased adsorption at both 5 kPa and 15 kPa relative to that observed from the differential-step adsorption studies. Again, this has been attributed to equilibrium not being achieved at low CO_2 partial pressures in the differential-step adsorption studies. At both 293 K and 333 K it is clearly evident that there are substantial increases in adsorption at both 5 kPa and 15 kPa CO_2 partial pressure, relative to AC-K0 (***Figure 3-7A***). However, at 363 K the increase in CO_2 adsorption of AC-K5 relative to AC-K0 was limited to 15 kPa CO_2 partial pressure; which is consistent with the observations made from the differential-step adsorption study (***Figure 3-6B***). However, the increase in CO_2 adsorption at 15 kPa CO_2 partial pressure resulted in an increase in the working capacity for AC-K5 at 363 K, relative to that of AC-K0 (***Table 3-3***). Furthermore, as was noted in ***section 3.5.1***, the micropore volume of AC-K5 is essentially the same as AC-K0 (***Table 2-16***). Whilst significant increases in the surface O content of AC-K5 are observed relative to AC-K0, of which increases in the concentration of C-O-R groups (hydroxyl and ether groups) predominated (***Table 2-13***). This reaffirms the contention made in ***section 3.5.1***, pertaining to the differential-step CO_2 adsorption of AC-K5 and AC-K7.5 (***Figure 3-6***) that differences in adsorption behaviour are dominated by changes in the surface chemistry rather than minor changes in pore volume. It is also interesting to note that despite the increase in CO_2 adsorption at 293 K, at both 5 kPa and 15 kPa CO_2 partial pressure observed for AC-K5 relative to AC-K0, the working capacities of the two carbons are essentially the same. Moreover, the value of heat of adsorption for AC-K5 at 293 K (ΔH_{Ads} = 59.1 kJ/mol) increased relative to that of AC-K0 (ΔH_{Ads} = 57.5 kJ/mol), indicative of an increase in the strength of the interaction between the adsorbent and adsorbate [12]. This is further evidence to the argument that the surface functionality of AC-K5 is playing a dominant role in determining the adsorption.

Table 3-3 *~ Working Capacities of KOH Activated miACs Determined at 293, 333 and 363 K, and ΔH_{Ads} determined at 293 K.*

Sample Name	Working Capacity (wt%)			ΔH_{ADS} (KJ/mol)
	293 K	333 K	363 K	
AC-N	1.46	0.55	0.28	55.3
AC-K0	1.66	0.67	0.38	57.5
AC-K5	1.65	0.81	0.43	59.1
AC-K7.5	1.64	0.81	0.46	57.0
AC-K10	2.14	0.93	0.52	56.5

In the multi-cyclic adsorption studies of AC-K7.5 (***Figure 3-7C***), it is evident at all temperatures that the CO_2 adsorption never achieves equilibrium at either 5 kPa or 15 kPa CO_2 partial pressure. This type of adsorption behaviour is indicative of significant retardation in the rate of adsorption, resulting from mass-transport limitations, which can be mostly; accounted for by the small mesopore volume of the KOH activated miACs (***Table 2-16***). This slow adsorption was also observed by AC-K5 at 293 K, but to a smaller extent. Furthermore, the level of adsorption observed for AC-K7.5 at both 5 kPa and 15 kPa CO_2 partial pressure was significantly higher than observed for AC-K5, at all temperatures; which can be attributed to the increases in either the micropore volume (***Table 2-16***) and/or the surface O content (***Table 2-13***). In particular, there was a substantial increase in the concentration of C-O-R groups on the surface of AC-K7.5 relative to AC-K5. Although there was an increase in the surface O concentration of AC-K7.5 relative to AC-K5, the NEXAFS investigation of the AC-K7.5 surface showed only minor variation in the distribution of hydroxyl and ether groups relative to AC-K5. Moreover, the high surface O concentration of AC-K7.5, particularly the high hydroxyl group surface concentration, will have likely resulted in the surface of AC-K7.5 having a much higher affinity for CO_2 than the other KOH activated miACs [5, 6]. Interestingly, despite the increased adsorption of CO_2 at both 5 kPa and 15 kPa for AC-K7.5 relative to AC-K5 at all temperatures, there were no significant increases in the working capacities of AC-K7.5 relative to AC-K5. Moreover, at 293 K, despite exhibiting higher overall adsorption of CO_2 and a similar working capacity (***Table 3-3***), AC-K7.5 possessed a lower heat of adsorption at 293 K (ΔH_{Ads} = 57.0 kJ/mol) than AC-K5 (ΔH_{Ads} = 59.1 kJ/mol). This is seemingly contradictory to what would be expected, as relative to AC-K5, AC-K7.5 possessed essentially the same micropore volume as AC-K5 and a higher surface O concentration, which would be expected to result in an increase in the heat of adsorption. It is proposed that this inconsistency can be ascribed to the fact that at 293 K equilibrium was never truly achieved. In

order to achieve a trend in the average heat of adsorption at 293 K for the multi-cyclic study of AC-K7.5, the achievement of complete equilibria would be required; for these experiments the equipment used for the measurements did not facilitate this.

The multi-cyclic adsorption studies of AC-K10 exhibited the highest CO_2 adsorption of any carbon material presented in this thesis so far (***Figure 3-7D***). This was to be expected from the adsorption pseudo-isotherms present in ***section 3.5.1*** (***Figure 3-6D***). However, again the amount of CO_2 adsorption at 5 kPa and 15 kPa from the multi-cyclic adsorption studies do not match the amount of CO_2 adsorbed at the same CO_2 partial pressures from the differential-step adsorption studies at the equivalent temperature, due to mass-transport limitations (***Table 2-16***). As noted in ***section 3.5.1***, the high CO_2 adsorption behaviour exhibited by AC-K10 can be attributed mostly to its high micropore volume (***Table 2-16***), rather than to aspects of its surface chemistry (***Table 2-13***). The surface O concentration of AC-K10 was substantially lower than that of AC-K7.5 or AC-K5 (XPS, ***Table 2-13***). However, from the NEXAFS analysis for AC-K10, there was no net change in the distribution of hydroxyl groups on the surface of AC-K10 relative to AC-K7.5 (***Table 2-14***). Thus, from the XPS and NEXAFS analyses of the AC-K10 surface, it can be said that the affinity of the AC-K10 surface for CO_2 might have been lower than that of AC-K7.5 [5, 6]. However; due to the significant increase in micropore volume for AC-K10 an overall increase in CO_2 adsorption was observed. AC-K10 exhibited much higher adsorption at both 5 kPa and 15 kPa, relative to AC-K7.5, resulting in the highest working capacities observed at every temperature of any carbon materials reported in ***chapter 3*** (***Table 3-3***). Interestingly, the heat of adsorption for AC-K10 at 293 K was the lowest observed for an of the KOH miACs (ΔH_{Ads} = 56.5 kJ/mol), despite possessing the highest amount of adsorption at this temperature. This can be partially accounted for by the decrease in the concentration C-O-R groups on surface of AC-K10 relative to AC-K7.5, but the surface concentration of C-O-R groups for AC-K10 is still significantly higher than that of AC-K0 (***Table 2-13***). Further complicating the situation is the fact that AC-K10 possesses a significantly higher micropore volume than AC-K0 (***Table 2-16***), which is also known to result in increases in the heat of adsorption [9]. However, as equilibrium was never truly achieved over AC-K10 it is difficult to surmise the actual heat of adsorption at 293 K (also true for AC-K7.5).

Overall, the high capacity of all of the KOH miACs can be attributed to the two most stand-out characteristics of these materials. That is the increased oxygen content of the carbon surface, and the narrow micropore structure of the carbons themselves. The gas physisorption, TEM, Raman spectroscopy and pycnometry data all indicate that the pore structure of these miACs is that of narrow slit-shaped micropores; however, the pores are more abundant than for other

miACs presented here. The details of this will be dealt with at a later stage of this chapter when making a direct comparison between the physically and chemically activated carbon materials.

3.6 CO_2/H_2O Competitive Adsorption

3.6.1 Physically Activated Carbons

As outlined in the experimental section (***section 6.6.4***) all carbon materials that underwent CO_2/H_2O competitive adsorption studies were pre-treated with wet Ar gas for 60 min prior to beginning of the simulated VSA single cycle. As such equilibration of H_2O with the AC had been achieved prior to the start of the CO_2 adsorption analysis. The CO_2 partial pressures employed for simulated VSA cycle were the same as those for the multi-cyclic studies (5-15 kPa). The CO_2/H_2O competitive gas adsorption studies were undertaken at both 363 K and 378 K, as this was the temperature range to be applied to the PEI-AC composite systems; as well as the probable temperature range for a VSA cycle. The simulated single VSA cycle studies for AC-90 under dry and wet gas conditions taken at 363 K and 378 K are presented as ***Figure 3-8***.

From the simulated VSA single cycle study of AC-90 at 363 K under both wet and dry conditions (***Figure 3-8A***), it is clearly evident that the presence of H_2O in the gas stream has little effect on the adsorption of CO_2. There is however, a slight lag in both the adsorption and desorption of CO_2 when H_2O was present in the gas stream. Furthermore, though relatively minor, a decrease in CO_2 adsorption was observed when H_2O was present. Both the lag and decrease in CO_2 adsorption in the presence of H_2O can be attributed to the manner in which the VSA single cycle measurements were taken. Prior to initiating the CO_2 adsorption step of the cycle, the sample was pre-treated under a wet Ar gas stream for 1 h. Hence there will have been pre-adsorbed H_2O, which will have had to be displaced by the incoming CO_2 in order for adsorption to occur. It is apparent that some competitive adsorption was occurring between CO_2 and H_2O, although the degree to which this occurred was limited. This was an interesting result, as one of the major aspects of AC-90 that made it such a good CO_2 adsorbent was its favourable surface chemistry (***section 2.3.2***). The surface hydroxyl and carboxylic acid functional groups that endow the AC-90 surface with a high affinity for CO_2 should also result in the surface having a high affinity for H_2O [6], and this was not observed.

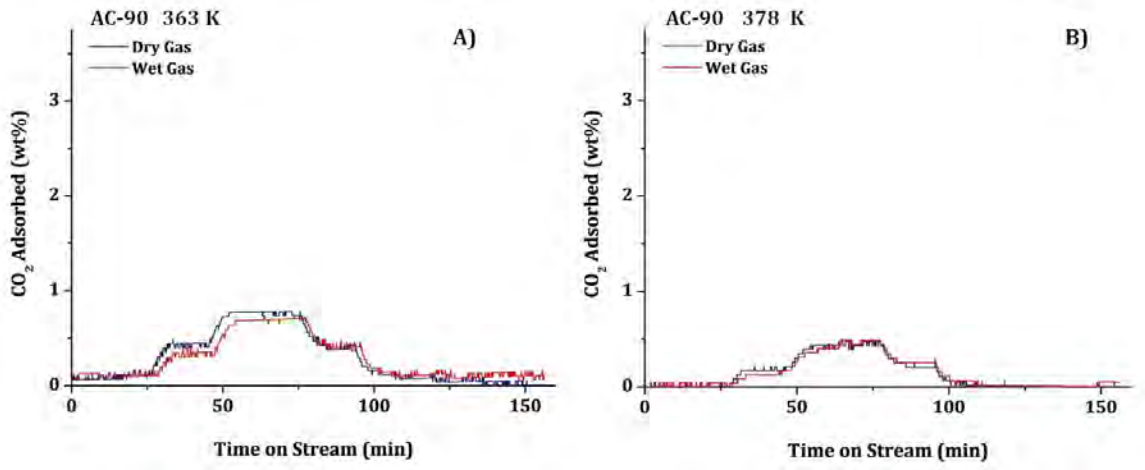

Figure 3-8 *~ CO_2 Wet & Dry Gas Single VSA Cycle for AC-90 taken via PPSA. Shown are the Wet & Dry VSA Studies taken at* ***A)*** *363 K, and* ***B)*** *378 K*

For the VSA single cycle study for AC-90 at 378 K (***Figure 3-8B***) a similar lag was observed under wet gas conditions for both adsorption and desorption. This can again be attributed to competitive adsorption between CO_2 and the pre-adsorbed H_2O. However, unlike the study undertaken at 363 K, at 378 K there was little decrease in the CO_2 adsorption. More importantly, the amount of CO_2 adsorbed in the adsorption step of the VSA cycle. Due to the higher temperature of the measurement, H_2O will be less likely to condense on the AC surface, as the boiling point of H_2O (373 K) is lower than the measurement temperature.

3.6.2 Chemically Activated Carbons

The single VSA cycle CO_2/H_2O competitive adsorption studies for AC-K10 under dry and wet gas conditions taken at 363 K and 378 K are presented as ***Figure 3-9***.

The single VSA cycle study of AC-K10 at 363 K (***Figure 3-9A***), exhibited similar adsorption behaviour to AC-90 (***Figure 3-8A***). However, the overall adsorption of CO_2 at both 5 kPa and 15 kPa CO_2 partial pressure exhibited by AC-K10 was substantially higher than that of AC-90. This is in agreement with the results of both the differential-step and multi-cyclic adsorption studies. Furthermore, the same slight lag in the uptake of CO_2 at both 5 kPa and 15 kPa CO_2 partial pressure were observed in the presence of H_2O, as was observed for AC-90 at 363 K, which has been attributed to the time require for CO_2 to displace the pre-adsorbed H_2O from the AC surface.

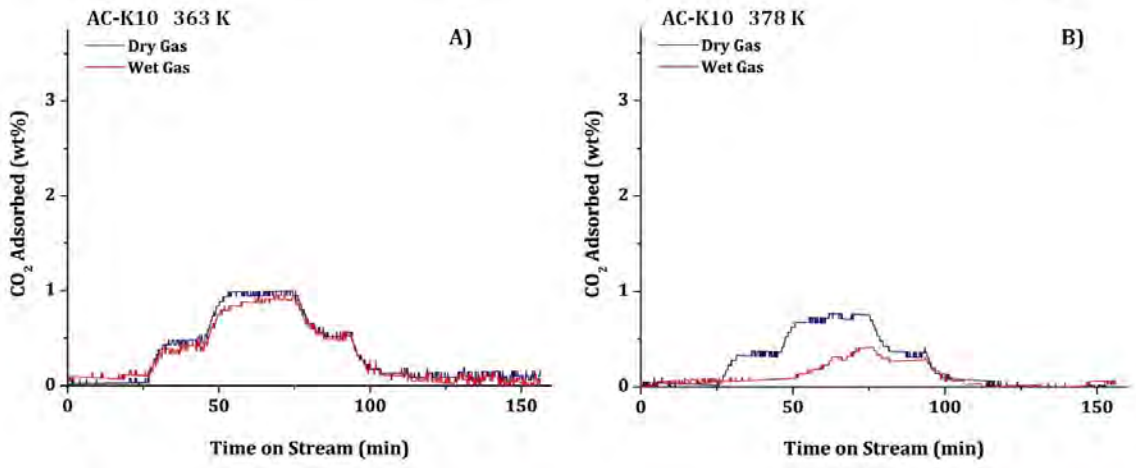

Figure 3-9 *CO_2 Wet & Dry Gas Single VSA Cycle for AC-K10 taken via PPSA. Shown are the Wet & Dry VSA Studies taken at* ***A)*** *363 K, and* ***B)*** *378 K*

The adsorption behaviour observed for AC-K10 (***Figure 3-9B***) under dry gas conditions at 378 K are with the expected results at this temperature, however, under wet conditions at 378 K the amount of CO_2 adsorbed was significantly lower than under dry gas conditions. The decrease in CO_2 adsorption being undeniable evidence of CO_2/H_2O competitive adsorption. This has been attributed to the structure of the pores and the access by water at 363 K and 378 K. At 363 K, the water in the gas stream is not as energetic as at 378 K, it is still below the boiling point of water and as such its access to the pores of AC-K10 being as small and narrow as they are would be limited. At 378 K, the water vapour in the gas stream would be more energetic, and with this extra energy it would be more likely for the water molecules to be able to diffuse into the narrow pores of AC-K10.

Furthermore, under dry gas conditions at both 363 K and 378 K, AC-K10 adsorbed more CO_2 than AC-90 (***Figure 3-8***) under comparable conditions. This result is in itself not surprising as AC-K10 possessed a similar micropore volume to AC-90, whilst AC-K10 possessed a surface with a much higher O concentration than AC-90.

3.7 CO_2 Separation by Microporous Carbons

In order to properly assess the applicability of miACs for CO_2 capture purposes it is helpful to compare the behaviours of both physically (steam or carbonisation) and chemically (KOH) activated carbons. The chemically activated miACs possessed much higher working capacities

and exhibited greater CO_2 uptake than the physically activated carbon materials, across the entire CO_2 partial pressure range and at all tested temperatures. This behaviour was attributed to the differences in both the surface chemistry and chemical and physical structure of the two types of materials.

Differences in the amount of CO_2 adsorbed at 5 kPa and 15 kPa between the differential-step and multi-cyclic adsorption studies were observed for many of the carbon materials presented in this chapter. This was primarily attributed to true equilibrium not being achieved at low CO_2 partial pressures (≤ 5 kPa) in the differential-step adsorption studies. As the equilibration time used in the differential-step adsorption studies was 20 min, which is fully sufficient for other materials, this adsorption behaviour strongly indicates that there are mass-transport limitations at play. This made sense, as many of the carbon materials suffering from such mass-transport limitations possessed small mesopore volumes, which would limit the rate at which diffusion into the micropores could be achieved. In the multi-cyclic adsorption studies, the carbon materials were pre-treated under a CO_2/Ar gas stream at a CO_2 partial pressure of 5 kPa for 1 h, which was found to be sufficient for equilibrium to be achieved.

It was found from the multi-cyclic adsorption studies, that equilibrium was achieved at both 5 kPa and 15 kPa much faster for the physically activated carbon materials, than for the chemically activated miACs. This significant difference in adsorption behaviour of the two classes of carbon materials can be attributed to the differences in the mesopore volume, possessed by each class. For example the chemically activated miACs possessed very small mesopore volumes; and such small mesopore volumes led to significant limitations to the diffusion of gas into and out of the micropores.

The differences in the pore size distributions are the result of the different mechanisms responsible for pore development during activation, for the different methods of activation. Physical activation via steam gasification involves the reaction between the surface of the carbon precursor and the steam. The steam reacts with the opening of the pore, resulting in a pore with a wide mouth and wider initial channel (usually a mesopore). This must occur in order for the steam to access the inner microporosity, which is subsequently developed. In chemical activation however, the activating agent is impregnated into the carbon precursor prior to carbonisation, and so acts from the inside of the carbon particles. As mentioned in ***section 1.7.2*** the exact mechanism of action by alkali metal hydroxides is a source of conjecture amongst researchers, however, all agree that the site of action of the alkali metal hydroxide is within the pores itself.

The reactor configuration may also have played a role in the differences observed. The physically activated carbon materials were produced in a steel mesh reactor that allowed for

unhindered flow of the reactive gas. The activation process used for chemical activation required the use of the quartz reactor, due to the corrosive nature of the KOH towards the steel working tube of the tube furnace. The quartz reactor used had a sintered disc of porosity grade 1 (150-90 μm). The flow of gas through this sintered disc was significantly reduced compared to that of the steel mesh reactor used to produce the physically activated carbon materials. It is thought that this may have further aided in the development of micropores over mesopores through extended slower removal of volatile matter from the carbon precursors. The miACs produced in this way possessed working capacities higher than those produced using the steel mesh reactors.

The affect of the activation process was well exemplified in the case of AC-K0, which exhibited higher working capacities at all temperatures than any of the physically activated carbon materials. AC-K0 was produced using the same reactor configuration as the chemically activated miACs, but no activating agent was used (i.e. carbonisation alone). As such the increased CO_2 adsorption behaviour exhibited by AC-K0 must be the result of the reactor configuration, not a difference in activation mechanism.

From the differential-step adsorption studies the physically activated carbon materials exhibited higher CO_2 adsorption at lower partial pressures than AC-N. Whereas, at CO_2 partial pressures above 5-15 kPa many of these carbon materials exhibited lower CO_2 adsorption than AC-N as CO_2 partial pressures increased. Similarly for the chemically activated carbon materials, the amount of adsorption at low CO_2 partial pressures exceeded that of AC-N. However, as the CO_2 partial pressure was increased, so too did the amount of CO_2 adsorbed relative to AC-N. For the KOH activated carbon materials and AC-90, the high adsorption at higher CO_2 partial pressures was interesting even if not applicable to the VSA post-combustion capture process that was the focus of this thesis. As such these materials may hold wider applications for CO_2 separation from other point sources, such as in natural gas separation of chemical processes.

From the multi-cyclic adsorption studies it was interesting to note that despite the differences in working capacities observed within the series of physically activated carbons, the amount of adsorption at a CO_2 partial pressure of 5 kPa was very similar at each temperature. This was not true for the KOH activated carbon materials. As has been noted, the differences in the amount of CO_2 adsorption were observed between the differential-step and multi-cyclic adsorption studies, due to mass-transport limitations arising from the small mesopore volumes of the carbons in question. This was observable due to a pre-treatment of the carbons at 5 kPa CO_2 partial pressure, done in order to simulate the lowest vacuum applied during a VSA process. This was however, not the only difference in the measurements of differential-step and multi-cyclic adsorption studies. The equilibration time for each step in the differential-step adsorption

measurements was 20 min, whereas that of the multi-cyclic adsorption measurements was 30 min for adsorption and 40 min for desorption. For the physically activated carbon materials this difference in the equilibration time for the 5-15 kPa step had no significant effect. However, for the chemically activated carbon materials it was seen to be much more significant. As the KOH loading of the chemically activated carbon materials increased, it became apparent that equilibrium was not being achieved within either the 30 min adsorption cycle, or the 40 min desorption cycle employed in the measurements of the multi-cyclic adsorption studies. This was clear evidence that the mass-transport limitations of the chemically activated carbon materials would play a major role in determining their suitability for such a multi-cyclic process.

The competitive adsorption studies with wet and dry gas for both AC-90 (***Figure 3-8A***) and AC-K10 (***Figure 3-9A***) showed that at 363 K the presence of water had little effect on the amount of CO_2 adsorbed. Furthermore, for AC-90 at 378 K (***Figure 3-8B***) there were no significant differences in the CO_2 adsorption under wet or dry gas conditions. Conversely, at 378 K, AC-K10 exhibited significant competitive adsorption with water, proving to affect the total amount of CO_2 adsorbed over the timeframe of the adsorption cycle. This was an important result, in that although AC-K10 exhibited much higher CO_2 adsorption to AC-90, its performance under realistic conditions would be adversely affected by the presence of water in the gas stream at temperatures at or around 378 K, whilst AC-90 would not.

3.8 Summary and Conclusions

In summation, it is clear that miACs can be produced from VBC which possess high CO_2 uptake and working capacities over the partial pressure (5-15 kPa) and temperature range (293-363 K) of interest. Importantly, the quantities of CO_2 adsorbed by the miACs produced in this work were close to, and in many cases, greater than the CO_2 adsorbed by the AC-N commercial carbon. As previously stated, this commercial AC was chosen due to its high capacity for CO_2 and wide use in the literature as a CO_2 adsorbent. In particular, two miACs were identified as possessing outstanding CO_2 adsorption properties compared with the commercial standard: the steam activated AC-90, and the KOH activated AC-K10. Both of these materials were then further tested under wet gas conditions to investigate the effect of water in the gas stream, and to identify if any competitive adsorption of CO_2 with H_2O was occurring. For AC-90 carbon the presence of water had little effect at either 363 or 378 K, and any competitive adsorption occurring between CO_2 and H_2O was found to be negligible. For AC-K10, no significant competitive adsorption between CO_2 and H_2O was found at 363 K, but significant effects were

observed at 378 K. This was attributed in part to its increase acidic surface chemistry, as any such groups that would increase CO_2 adsorption would also show great affinity towards H_2O.

An important point to be made regarding the preparation of the miACs by both physical and chemical activation methods, was that in each case the methods used were mild compared to those usually applied in the production of miACs. For the physically activated carbons the amount of steam employed (0.25 cm^3/min) was significantly less than that used in most of the previous studies presented in the literature (5-10 cm^3/min) [13-17]. This is important from a perspective of the economic and industrial viability of such a process, with potential for use of already existing equipment instead of new builds or retro-fitting, thus potentially lowering the capital cost of implementing such a process.

For the chemical activation protocols presented here, utilising KOH as the activating agent significant improvements were achieved on the commonly used pre-existing industrial protocols. Most significant was the large decrease in the quantity of KOH that was required, being only 5-10 wt% that of the VBC, compared to 400-600 wt% commonly employed industrially and in the literature [18-24]. Secondly, by introducing the KOH directly into the coal, rather than into an already produced char, a single-stage process is possible. Again, by having a single reactor instead of two would significantly reduce the capital cost the process, in addition to the running cost of producing such miACs.

3.9 References

1. Ruthven, D.M., *Principles of Adsorption and Adsorption Processes*, D.M. Ruthven, Editor 1984, John Wiley and Sons: New Jersey. p. 29-61.
2. Brunauer, S., *The Adsorption of Gases and Vapors Vol 1: Physical Adsorption*, in *The Adsorption of Gases and Vapors* S. Brunauer, Editor 1943, Oxford University Press: London. p. 3-7.
3. Ruthven, D.M., *Principles of Adsorption and Adsorption Processes*, D.M. Ruthven, Editor 1984, John Wiley and Sons: New Jersey. p. 29.
4. Brunauer, S., *The Adsorption of Gases and Vapors Vol 1: Physical Adsorption*, in *The Adsorption of Gases and Vapors* S. Brunauer, Editor 1943, Oxford University Press: London. p. 317-364.
5. Yang, R.T., *Adsorbents: Fundamentals and Applications*, R.T. Yang, Editor 2003, John Wiley & Sons: New Jersey. p. 79-130.
6. Bandosz, T.J. and C.O. Ania, *Chapter 4 Surface chemistry of activated carbons and its characterization*, in *Interface Science and Technology*, J.B. Teresa, Editor 2006, Elsevier. p. 159-229.
7. Brunauer, S., *The Adsorption of Gases and Vapors Vol 1: Physical Adsorption*, in *The Adsorption of Gases and Vapors* S. Brunauer, Editor 1943, Oxford University Press: London. p. 7-28.
8. Ruthven, D.M., *Principles of Adsorption and Adsorption Processes*, D.M. Ruthven, Editor 1984, John Wiley and Sons: New Jersey. p. 124-165.
9. Bansal, R.C. and M. Goyle, *Activated Carbon Adsorption*, 2005, Taylor & Francis Group: Florida. p. 5.
10. Marsh, H. and F. Rodríguez-Reinoso, *Chapter 5 - Activation Processes (Thermal or Physical)*, in *Activated Carbon*, H.M. Rodríguez-Reinoso, Editor 2006, Elsevier Science Ltd: Oxford. p. 243-321.
11. Ruthven, D.M., *Principles of Adsorption and Adsorption Processes*, D.M. Ruthven, Editor 1984, John Wiley and Sons: New Jersey. p. 125-323.
12. Brunauer, S., *The Adsorption of Gases and Vapors Vol 1: Physical Adsorption*, in *The Adsorption of Gases and Vapors* S. Brunauer, Editor 1943, Oxford University Press: London. p. 180-218.
13. Molina-Sabio, M., et al., *Effect of steam and carbon dioxide activation in the micropore size distribution of activated carbon.* Carbon, 1996. **34**(4): p. 505-509.
14. Martín-Gullón, I., et al., *Steam-activated carbons from a bituminous coal in a continuous multistage fluidized bed pilot plant.* Carbon, 1996. **34**(12): p. 1515-1520.
15. Chattopadhyaya, G., et al., *Preparation and characterization of chars and activated carbons from Saskatchewan lignite.* Fuel Processing Technology, 2006. **87**(11): p. 997-1006.
16. Pokonova, Y.V., *Production of carbon adsorbents from brown coal.* Carbon, 1996. **34**(3): p. 411-415.
17. Sun, J., et al., *Activated carbon produced from an Illinois Basin coal.* Carbon, 1997. **35**(3): p. 341-352.
18. Stavropoulos, G.G., *Precursor materials suitability for super activated carbons production.* Fuel Processing Technology, 2005. **86**(11): p. 1165-1173.
19. Yoshizawa, N., et al., *XRD evaluation of KOH activation process and influence of coal rank.* Fuel, 2002. **81**(13): p. 1717-1722.
20. Lozano-Castelló, D., et al., *Preparation of activated carbons from Spanish anthracite: I. Activation by KOH.* Carbon, 2001. **39**(5): p. 741-749.
21. Önal, Y., et al., *Adsorption kinetics of malachite green onto activated carbon prepared from Tunçbilek lignite.* Journal of Hazardous Materials, 2006. **128**(2-3): p. 150-157.

22. Molina-Sabio, M. and F. Rodríguez-Reinoso, *Role of chemical activation in the development of carbon porosity.* Colloids and Surfaces A: Physicochemical and Engineering Aspects, 2004. **241**(1-3): p. 15-25.
23. Tseng, R.L., et al., *Effects of micropore development on the physicochemical properties of KOH-activated carbons.* Journal of the Chinese Institute of Chemical Engineers, 2008. **39**(1): p. 37-47.
24. Elmouwahidi, A., et al., *Activated carbons from KOH-activation of argan (Argania spinosa) seed shells as supercapacitor electrodes.* Bioresource Technology, 2012. **111**(0): p. 185-190.

4 Synthesis and Characterisation of Mesoporous and Amine Modified Carbons

4.1 Introduction

Polyethylimine (PEI) loaded mesoporous silica materials are promising materials for CO_2 capture [1-5]. These solid adsorbents exploit a reversible chemisorption process involving a reaction between CO_2 and the basic amine groups of PEI to yield a carbamate/carbonate species [6]. Although these CO_2 capture systems have been successful, they suffer from drawbacks associated with the high cost and labour-intensive nature of mesoporous silica production. As such, the objective of the current part of the project was to produce inexpensive mesoporous carbons that could be used as alternative support materials for PEI.

Mesoporous activated carbons (meACs) were prepared by the catalysed steam activation of VBC or AC-90 by lanthanide oxide catalysts (Ln_xO_y, where Ln was Ce or La). These two lanthanide oxides were used due to their reported catalytic properties in promoting oxidative reactions, which has been shown to facilitate mesopore development [7-9]. The CeO_2 and La_2O_3 were used to catalyse partial oxidation reactions of the carbon precursor, and in the process, to aid in the creation or widen the pores of the carbonaceous materials. Both spectroscopic analysis and PXRD were used to confirm that the Ce and La precursors formed oxides in the gasification process.

Post-synthetic catalyst removal was achieved using a novel concentrated H_2SO_4 washing procedure, devised from the refinery process used to remove La and Ce from monazite [10]. The materials were thoroughly characterised before and after catalyst removal in terms of their surface morphology, surface chemistry, microscale structure and chemical composition. Analysis of the surface areas and pore size distributions measured for the materials prior to catalyst removal revealed that the majority of pores in the materials were small (micropores) and were blocked by catalyst. However, after acid washing, the measured pore diameters of the

materials increased into the mesopore range which indicated the removal of the catalyst and unblocking of the pores.

Based on their desirable surface morphologies (e.g. large pore diameter, high surface area, narrow PSD), some of the meACs were selected for PEI impregnation (90% pore filling basis). The PEI-loaded materials were characterised in terms of their surface morphology and chemical composition. Interestingly, the PEI impregnated carbons were not vacuum stable (***section 6.5***), which could limit their applicability to CO_2 separation in a vacuum swing adsorption (VSA) scenario.

4.2 Catalysed Physical Activation

In order to prepare the meACs, the Ln catalyst precursor ($Ce(NO_3)_3.6H_2O$ or $La(NO_3)_3.6H_2O$) was introduced directly into the VBC or the pre-activated AC-90 (steam activated, 90 min, see ***Chapter 2***); this was done on a 3 wt% loading on a metal basis for both Ce and La. The Ln doped carbon materials were then subjected to steam activation for 90 min, in a fixed bed reactor. After activation, the materials were washed with H_2SO_4 (conc.) to remove the catalyst.

Table 4-1 ~ *Nomenclature of CeO_2 and La_2O_3 Catalysed Physically Activated Carbons*

Sample Name	Carbon Precursor	Catalyst	Catalyst Loading (wt%)*	Acid Washed
AC-Ce3-90	VBC	CeO_2	3	No
AC-Ce3-90-AW	VBC	CeO_2	3	Yes
AC-90-Ce3-90	AC-90	CeO_2	3	No
AC-90-Ce3-90-AW	AC-90	CeO_2	3	Yes
AC-La3-90	VBC	La_2O_3	3	No
AC-La3-90-AW	VBC	La_2O_3	3	Yes
AC-90-La3-90	AC-90	La_2O_3	3	No
AC-90-La3-90-AW	AC-90	La_2O_3	3	Yes

* *wt%, on a metal loading basis*

Prior to acid washing the Ln-meACs are referred to as "as produced", as this was the form of the material directly after being produced. After acid washing the Ln-meACs are referred to as acid

washed, and are given the suffix of "-AW" (***Table 4-1***). The production of the VBC derived meACs differ from AC-90 only by the presence of the lanthanide oxide catalyst, and as such will regularly be referred to as a catalysed analogue of AC-90.

In ***Chapters 2*** and ***3***, a commercial miAC (AC-N) was used for benchmarking purposes. In the current chapter, however, AC-90 is used as a reference material because the meACs produced here were either catalysed analogues of AC-90 or were directly prepared from it.

4.3 Ceria Catalysed Physically Activated Carbons

The characterisation results for the cerium oxide (ceria) physically catalysed carbons are presented in this section. The materials were each assessed in terms of their bulk composition, surface chemistry (XPS and NEXAFS) and structural morphology (gas physisorption, Raman spectroscopy, XRD and TEM) in order to gain an understanding of the physio-chemical properties of the materials that effect CO_2 adsorption behaviour under post-combustion VSA conditions (***Chapter 5***) and to also determine candidate materials for use as PEI supports.

4.3.1 Composition of Ceria Catalysed Activated Carbons

The composition of the catalytically and non-catalytically steam activated carbons were investigated using ultimate (Vario MICRO cube, Elementar) and ash analysis (Mettler Toledo, TGA/DSC 1). This was undertaken both prior to and post the acid washing to remove the catalyst, the results of which are presented in ***Table 4-2*** for the ceria catalysed meACs.

From the results in ***Table 4-2***, it can be seen that there is some small variation in the bulk nitrogen and hydrogen content of the Ce-meACs; however, these changes are too small to have significant effect on the physio-chemical or adsorption properties of these materials. On the other hand, the nitrogen and hydrogen content of the two "as produced" Ce-meACs differ significantly. Interestingly, the carbon content of AC-Ce3-90-AW was lower than that of AC-Ce3-90; yet conventional logic would dictate that acid washing to remove the Ce_xO_y should result in enrichment of carbon in the resulting material. From the TEM-EDX of AC-Ce3-90 (***Figure 4-9B***) it can be seen that the Ce is very well distributed throughout the particle being investigated. As such, a likely explanation for the reduction, rather enrichment of carbon in AC-Ce3-90-AW, may be due to partial collapse of the carbon structure. This could potentially result in sections of carbon that formed around Ce_xO_y to have fractured or collapsed upon removal of the Ce_xO_y, and

removed during the washing procedure. Further evidence for this hypothesis may also be observed from the mesopore volumes determined by N_2 physisorption results for the AC-Ce3-90/AC-Ce3-90-AW pair (***Table 4-6***), with a significant decrease in mesopore volume being observed of AC-Ce3-90-AW relative to AC-Ce3-90.

Table 4-2 ~ *Composition of Ceria Catalysed Physically Activated meACs*

Sample	Yield (wt%)	Elemental Analysis (wt%, dafb)				H/C Ratio	Ash (wt%)
		C	H	N	O		
VBC	-	61.4	4.4	0.6	33.5	0.86	0.4
AC-90	43.4	82.2	1.3	0.7	15.7	0.19	6.4
AC-Ce3-90	41.6	81.6	1.1	1.1	16.3	0.16	9.2
AC-Ce3-90-AW	-	78.6	1.5	0.8	19.1	0.23	5.3
AC-90-Ce3-90	33.2	74.5	1.3	0.7	23.5	0.21	11.8
AC-90-Ce3-90-AW	-	84.0	1.6	0.7	13.7	0.23	3.6

It's also interesting to note the significant reduction in ash content as a result of the acid washing; this reduction was so significant as to result in meACs with lower ash content than AC-90. This would indicate that along with Ce_xO_y other inorganic components of the ash were removed.

4.3.2 Surface Chemistry of Ceria Catalysed Activated Carbons

The determination of the surface chemistry of carbon materials is notoriously difficult; no one method alone is able to be used. Instead results from multiple spectroscopic and wet chemical analyses are typically used. Due to issues of reproducibility of many of the wet chemical methods often employed, only spectroscopic investigations have been applied in this study [11].

4.3.2.1 X-ray Photoelectron Spectroscopy (XPS)

An XPS survey scan was performed on each material to establish the presence of C 1s, O 1s, N 1s, and Ce 3d atomic species, for which high-resolution scans were subsequently conducted. In order to determine the concentrations of these elements at the surface, and the distribution of the chemical species associated with them, peak fitting was undertaken. The fitted XPS spectra

obtained for the Ce-meACs are shown in ***Figure 4-1***-***Figure 4-2*** and the derived surface concentrations are reported in ***Table 4-3***, for ease of comparison. Possibly the most important observation to make note of was the C 1s to O 1s peak ratios for the different oxygen functional groups. In the case of the Ce-meACs it is important to note that the C:O ratio of all COO-R peaks were approximately 1.

Acid washing of the Ce-meACs (***Figure 4-1*** and ***Figure 4-2***) resulted in XPS spectra that showed an overall increase in the surface concentration of all oxygen functional groups, despite an overall decrease in surface O content. This would suggest that the acid washing itself had no clearly discernible effects on the surface chemistry other than to remove the ceria cations.

In all cases (both acid washed and non-acid washed) the C:O ratio of the C-O-R peak, was 2, which can only be accounted for by the presence of ether group. A low concentration of hydroxyl groups will have a two-fold effect, firstly it will result in low CO_2 selectively [12, 13], and secondly and it is also likely to mean it will have a lower affinity for the PEI as compared to mesoporous silica materials. The surface of mesoporous silica is covered with hydroxyl groups, that interact with the amine groups of the PEI, binding to the material more strongly. A lack of such groups is likely to result in weak association between PEI and the AC surface.

In ***sections 2.4.2.1*** and ***2.5.2.1***, the XPS results for the steam activated and KOH activated miACs were presented, where it was noted that the reductions observed in the C-C and C=C peaks could be accounted for by the changes in the concentration and distribution of oxygenated functional groups; that is also true of the Ce-meACs.

The XPS analysis of the Ce 3d spectra is much more complicated than those of C 1s or O 1s spectra, owing to the doublets arising from the $3d^{3/2}$ and $3d^{5/2}$ electron spin states (refer to ***section 1.9.2.2***). These two electron states being designated the letters v and u respectively, as is standard nomenclature [14, 15]. Furthermore, certain peaks are typical to one of the two oxidation states of Ce_xO_y, with the v_0, v', u_0 and u' peaks being associated with the Ce(III) oxidation state (i.e. Ce_2O_3) and the v, v'', v''', u, u'' and u''' being associated with the Ce(IV) oxidation state (i.e. CeO_2) [14-18]. The v_0 and u_0 peaks were not observed for the acid washed or "as produced" Ce-meACs. They are both known to be difficult to clearly detect unless the Ce(III) oxidation state is present in significant amounts due to overlapping of peaks [19, 20]. If not present in significant amounts, the v_0 and u_0 peaks are easily hidden under the v and u peaks, making quantification of materials with both Ce (III) and (IV) oxidations states difficult.

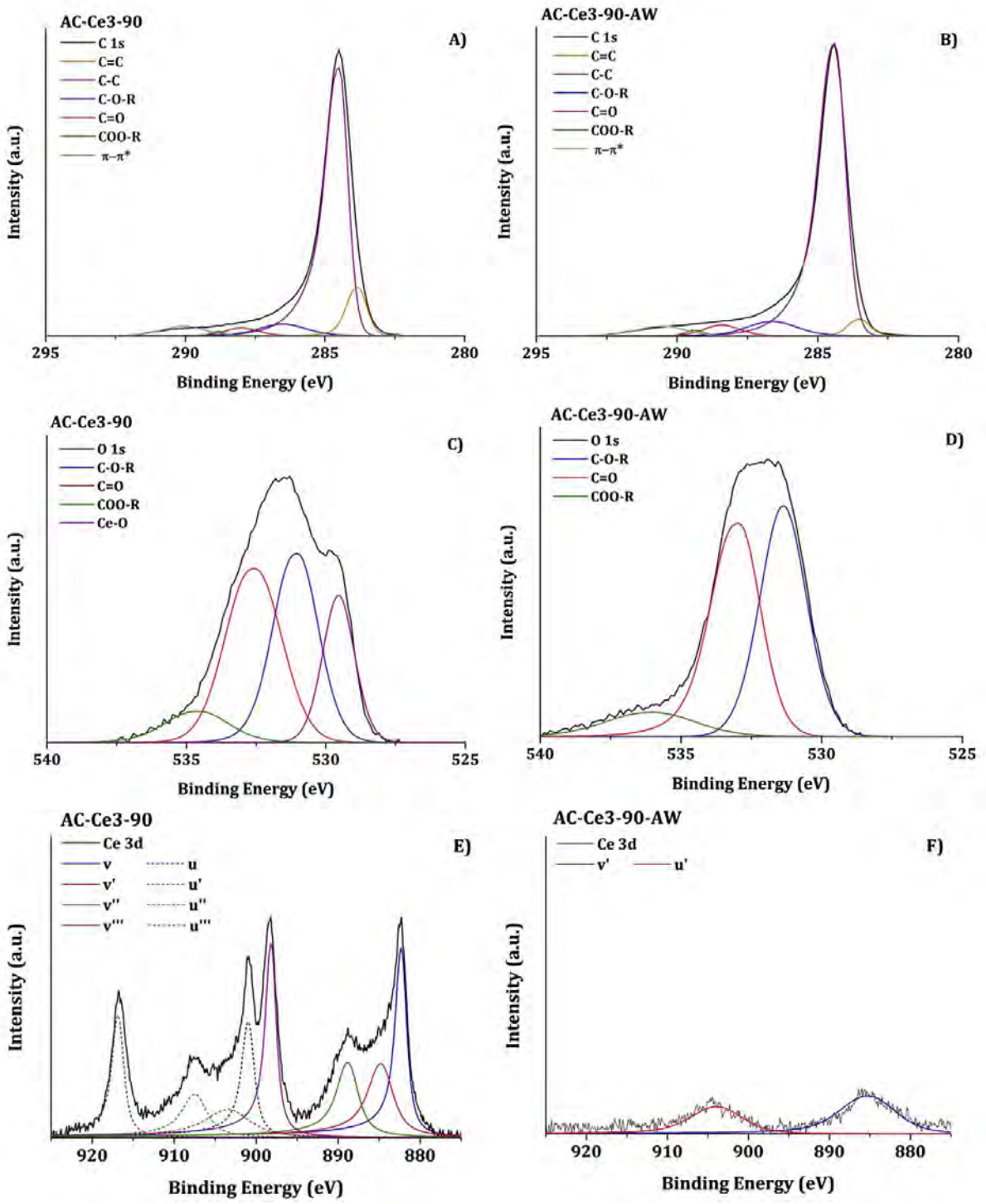

Figure 4-1 *~ High Resolution XPS Spectra of C 1s, O 1s and Ce 3d for AC-Ce3-90 and AC-Ce3-90-AW. Shown are* ***A)*** *C 1s Spectra of AC-Ce3-90,* ***B)*** *C 1s Spectra of AC-Ce3-90-AW,* ***C)*** *O 1s Spectra of AC-Ce3-90,* ***D)*** *O 1s Spectra of AC-Ce3-90-AW,* ***E)*** *Ce 3d Spectra of AC-Ce3-90, and* ***F)*** *Ce 3d Spectra of AC-Ce3-90-AW*

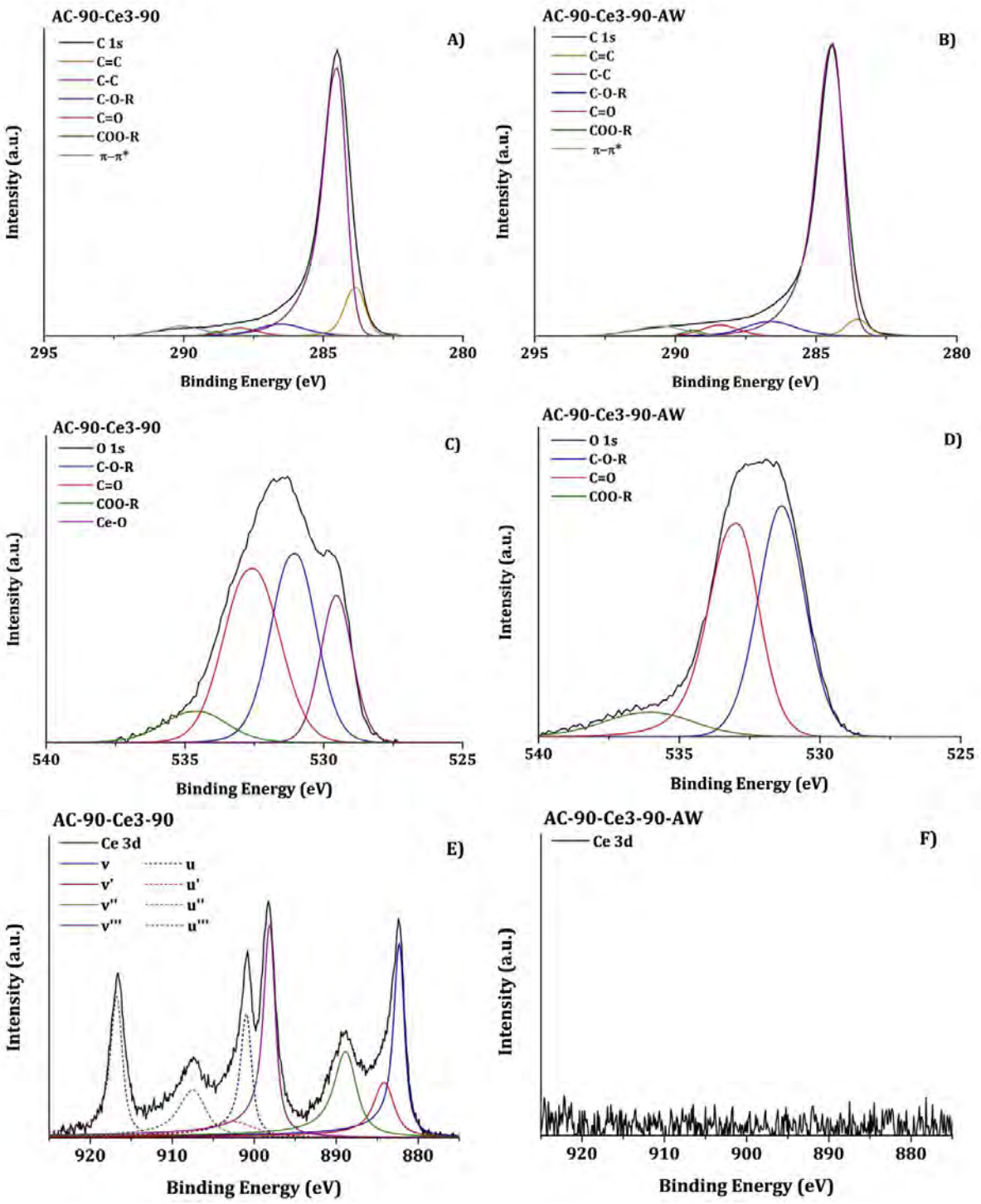

Figure 4-2 ~ *High Resolution XPS Spectra of C 1s, O 1s and Ce 3d for AC-90-Ce3-90 and AC-90-Ce3-90-AW. Shown are* ***A)*** *C 1s Spectra of AC-90-Ce3-90,* ***B)*** *C 1s Spectra of AC-90-Ce3-90-AW,* ***C)*** *O 1s Spectra of AC-90-Ce3-90,* ***D)*** *O 1s Spectra of AC-90-Ce3-90-AW,* ***E)*** *Ce 3d Spectra of AC-90-Ce3-90, and* ***F)*** *Ce 3d Spectra of AC-90-Ce3-90-AW*

Table 4-3 *~ XPS Peak Fitting for AC-Ce3-90, AC-Ce3-90-AW, AC-90-Ce3-90 and AC-90-Ce3-90-AW*

Peak Assignment	Binding Energy (eV)	Surface Concentration (at%)				
		AC-90	AC-Ce3-90	AC-Ce3-90-AW	AC-90-Ce3-90	AC-90-Ce3-90-AW
C 1s	284.0	90.16	91.10	91.66	91.68	93.16
C=C	283.6	6.04	5.17	2.63	9.86	3.09
C-C	284.4	68.28	69.52	74.22	69.81	75.79
C-O-R	286.3	8.48	7.24	8.13	5.19	6.08
C=O	288.3	2.80	2.26	2.07	2.42	3.27
COO-R	289.2	1.56	0.86	1.10	0.52	0.89
π–π*	290.2	3.00	6.06	3.51	3.88	4.02
O 1s	532.0	9.16	7.86	7.60	6.83	6.47
C=O	531.4	2.96	2.08	2.22	2.37	2.91
C-O-R	532.8	4.60	3.48	4.07	2.63	2.98
COO-R	534.7	1.59	0.98	1.09	0.54	0.58
Ce-O	529.7	-	1.32	0.22	1.29	0.00
N 1s	400.0	0.68	0.47	0.63	0.93	0.38
Ce 3d	900.0	-	0.56	0.11	0.56	0.00
v	882.3	-	0.09	0.00	0.09	0.00
v'	884.9	-	0.08	0.07	0.05	0.00
v''	888.9	-	0.07	0.00	0.09	0.00
v'''	898.2	-	0.09	0.00	0.11	0.00
u	901.0	-	0.06	0.00	0.06	0.00
u'	903.5	-	0.05	0.04	0.03	0.00
u''	907.5	-	0.05	0.00	0.06	0.00
u'''	916.9	-	0.06	0.00	0.07	0.00

From the XPS peak fitting of AC-Ce3-90 and AC-90-Ce3-90 (***Figure 4-1E*** and ***Figure 4-2E***, respectively), some of the peaks from both oxidation states are clearly present. However, from a comparison of the Ce 3d spectra of AC-Ce3-90 to AC-Ce3-90-AW (***Figure 4-1***), it can be seen that the acid washing procedure used resulted in the incomplete removal of Ce (III) oxides, due to the presence of *v'* and *u'* peaks in the Ce 3d spectra of AC-Ce3-90-AW. The presence of only the *v'* and *u'* peaks in the Ce 3d spectra of AC-Ce3-90-AW indicates that the Ce remaining is in the form Ce_2O_3 (***section 6.6.2.1***). Furthermore, as the amount of Ce_2O_3 remaining was much less due to the reduction in the *v'* and *u'* peaks, but as the v_0 and u_0 peaks are so small relative to the *v'* and *u'* peaks, it is not surprising that they were unable to be clearly resolved. It is known that the solubility of Ce is lowest for the Ce(III) oxidation state [21], requiring more aggressive acids to solubilise it. This is not the case for Ce in the Ce(IV) oxidation state, which can be solubilised by a wider range of inorganic acids [21]. A similar observation was however not made in the case

of the AC-90-Ce3-90/AC-90-Ce3-90-AW pair, with no Ce peaks being detected on the acid washed sample for either oxidation state. This would indicate more efficient washing of this sample was achieved. From the TEM results of the Ce-meACs (***Figure 4-9***-***Figure 4-12***), it was possible to see that the Ce_xO_y particles were not as well dispersed on AC-90-Ce3-90 as they were on AC-Ce3-90. This would likely result in both Ce oxidation states occurring within the same particles, and thus Ce(III) would be more easily removed along with the Ce(IV).

Overall, two very different pairs of meACs were produced, with equally different surface chemistry. It was also apparent that the effectiveness of the acid washing procedure to remove the Ce_xO_y was dependent on the initial distribution of Ce_xO_y through the material. Furthermore, the acid washing resulted in a clear increase in the surface concentration of C with an associated decrease in surface O concentration.

4.3.2.2 Near Edge X-ray Adsorption Fine Structure (NEXAFS) Spectroscopy

NEXAFS spectroscopy was only undertaken on the AC-Ce3-90-AW and AC-90-Ce3-90-AW meACs due mostly to instrument availability, but also due the fact that these two Ce-meACs were to be used for further study in the production of PEI-AC composites. The peak fitting of the C 1s and O 1s NEXAFS spectra of meACs was the same as that used for the fitting of the NEXAFS spectra of the miACs, described in ***Chapter 6*** (***section 6.6.2.2***). The results of the peak fitting for the NEXAFS spectra for both AC-Ce3-90-AW and AC-90-Ce3-90-AW are shown in ***Table 4-4***, the processed spectra are present in ***Figure 4-3***. The complete fitting for both the C 1s and O 1s spectra can be found in ***Appendix 2 – NEXAFS Spectroscopy Peak Fitting***, for all of the carbon materials investigated.

Making use of the data from ***Table 4-4***, further information pertaining to the identification of certain functional groups that were unable to be fully resolved by XPS was achieved (***Table 4-3***), such as the identification of the carbonyl groups as aldehyde, ketone and even quinone groups. No significant changes in the distribution of carbonyl groups (***C1***, ***C3***, ***O1*** and ***O2, Table 4-4***) were observed from the C 1s and O 1s NEXAFS of AC-Ce3-90-AW relative to AC-90-Ce3-90-AW. However, changes in the absolute concentrations of these groups at the meAC surface exist, but that the relative distribution of these groups to one another to be resolved by the NEXAFS spectra.

It is a well established fact that for carbon materials the C-O-R groups from the XPS analyses are attributed to hydroxyl and/or ether groups, as these cannot be sufficiently resolved by XPS, but can be by NEXAFS spectroscopy. The changes in the C-O-R groups from the XPS analysis of AC-90-Ce3-90-AW, relative to AC-Ce3-90-AW were also observed in both the C 1s and O 1s NEXAFS

for these carbons. This was observed as a decrease in the area of the ***C6*** peaks and increase in the ***O4*** peaks, assigned to hydroxyl groups. There were no discernible differences in the relative proportion of aliphatic or aromatic ether groups for AC-Ce3-90-AW or AC-90-Ce3-90-AW (***C5***, ***C8***, ***O3*** and ***O6***). The overall change in the distribution of hydroxyl and ether groups observed from the NEXAFS is with the change in peak ratios observed from the XPS.

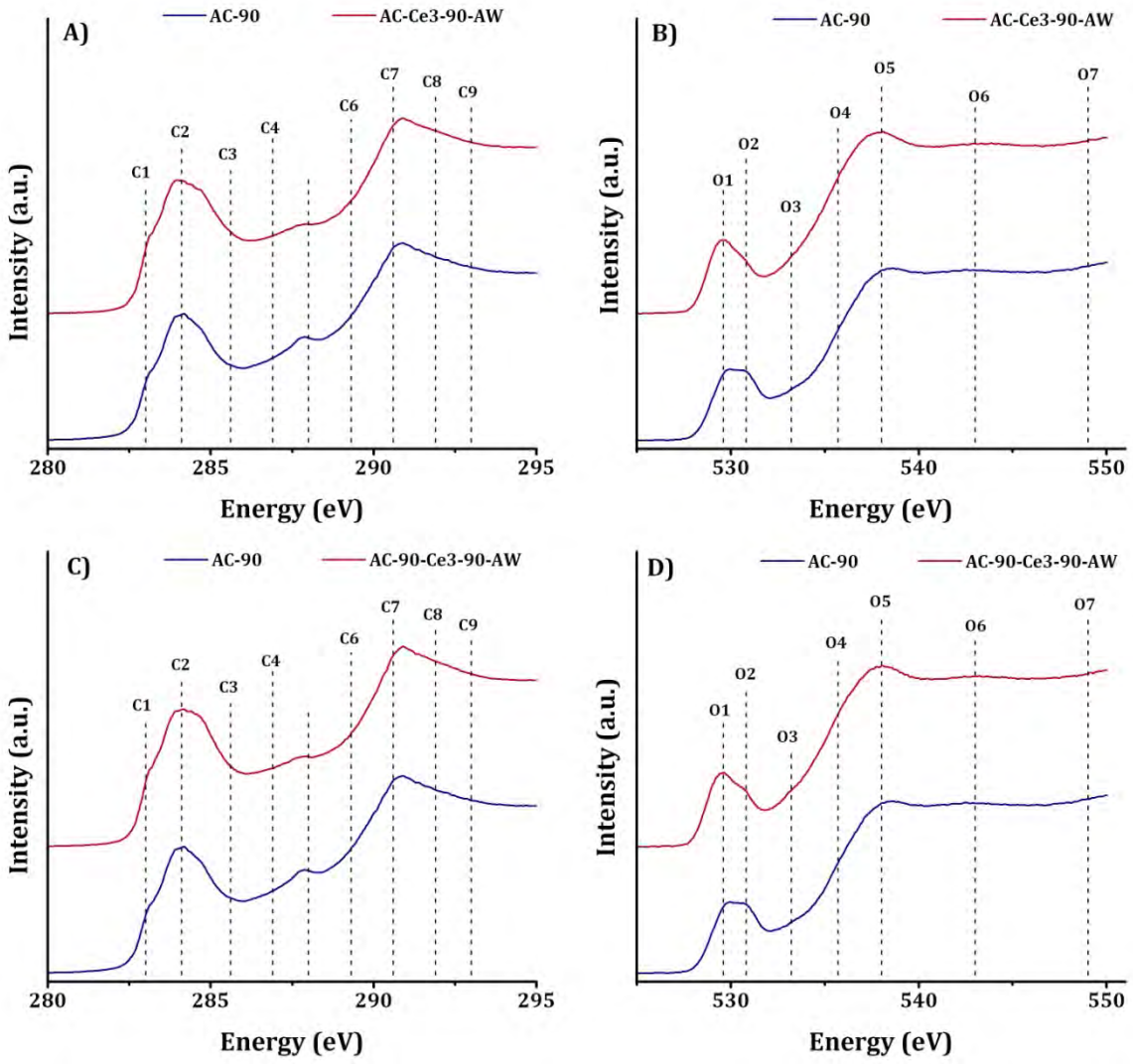

Figure 4-3 ~ *C 1s and O 1s K-edge NEXAFS Spectra of AC-90, AC-Ce3-90-AW & AC-90-Ce3-90-AW. Shown are* ***A)*** *C 1s K Edge NEXAFS Spectra of AC-90 & AC-Ce3-90-AW,* ***B)*** *O 1s K Edge NEXAFS Spectra of AC-90 & AC-Ce3-90-AW,* ***C)*** *C 1s K Edge NEXAFS Spectra of AC-90 & AC-90-Ce3-90-AW,* ***D)*** *O 1s K Edge NEXAFS Spectra of AC-90 & AC-90-Ce3-90-AW*

From the XPS analysis of the Ce-meACs (***Table 4-3***) significant surface concentrations of COO-R groups were found to be present, which are the result of both carboxylic acids and lactones surface groups. Both these groups are known to commonly be present on the surface of ACs

[22], with the former generally being present in higher concentrations than the later [12]. The decrease in the COO-R groups observed from the XPS of AC-90-Ce3-90-AW relative to AC-Ce3-90-AW was observed only as a modest decrease in the ***C4*** peak in the C 1s NEXAFS spectra. The presence of carboxylic acids (and hydroxyls) will potentially have a strong effect on the selectivity of the meACs towards both CO_2 and the amine groups within the PEI polymer [1, 23, 24].

Table 4-4 *~ C 1s & O 1s K Edge NEXAFS Peak Fitting of AC-Ce3-90-AW and AC-90-Ce3-90-AW*

K Edge	Name	Group		Assignment	Photon Energy (eV)	Peak Area %		
						AC-90	AC-Ce3-90-AW	AC-90-Ce3-90-AW
C 1s	C1	C=O	π*	Carbonyl substituted aromatic carbon (quinone)	283.0	1.1	1.9	1.8
	C2	C-C C=C	π*	Aromatic carbon, or aliphatic substituted aromatic carbon	284.1	31.3	30.5	30.7
	C3	C-OH C=O	π*	Phenol or ketone substituted aromatic carbon	285.6	8.5	15.5	16.2
	C4	COOH COO	π*	Carboxylic acid substituted aliphatic carbon (lactone)	286.9	11.2	8.4	7.5
	C5	C-O-C	π*	Cyclic ether carbon	288.0	13.3	7.7	8.4
	C6	C-OH C=O	π*	Aldhyde or hydroxyl substituted aliphatic carbon	289.3	10.5	13.2	11.9
	C7	COOH	σ*	Carboxylic acid substituted aromatic carbon	290.6	15.2	10.5	11.0
	C8	C-O-C	σ*	Cyclic ether carbon	291.9	6.4	10.6	10.6
	C9	C-C C=C	σ*	Aromatic carbon (long range order)	293.0	2.5	1.6	1.9
O 1s	O1	C=O	π*	Aliphatic (linear or cyclic) aldehyde oxygen	529.6	6.4	14.6	13.6
	O2	C=O	π*	ketonic oxygen	530.8	16.5	4.6	4.5
	O3	C-O-C	π*	Aliphatic cyclic ether	532.7	16.4	10.1	9.2
	O4	C-OH	π*	Hydroxyl oxygen (alcohol)	535.7	24.6	50.4	52.9
	O5	C-OH C=O	σ*	Hydroxyl or carbonyl oxygen of carboxylic acid	538.0	17.0	9.8	9.7
	O6	C-O-C	σ*	Aromatic cyclic ether	543.0	14.7	3.0	2.8
	O7	C-OH	σ*	Phenolic oxygen	549.8	4.5	7.6	7.3

There was no significant difference between the ***C2*** or ***C9*** peaks of the C 1s NEXAFS spectra of either AC-Ce3-90-AW or AC-90-Ce3-90-AW, indicating that the two meACs possessed a similar amount of surface aromaticity/degree of long range order.

Compared to AC-90, both AC-Ce3-90-AW and AC-90-Ce3-90-AW show significant decreases in both C 1s (***C5***) and O 1s (***O3*** and ***O6***) ether peaks (***Table 4-4***). Similar decreases were not observation for the C-O-R peak from the XPS of the Ce-meACs compared to AC-90(***Table 4-3***). This can be accounted for by the significant increase in phenols (***C3*** and ***O7***). Whilst this resulted in no quantifiable change in the C-O-R XPS peak, a significant shift in the distribution of groups is observed. This shift in the distribution of functional groups is likely due to the aggressive acid washing procedure used to remove the CeO_2 phase. It is expected that the increase in surface hydroxyl groups should increase the affinity of the surface of the meACs for the PEI relative to the miACs, as is the case with the hydroxyl rich surface of mesoporous silica materials [23].

The shift in the distribution of surface functional groups of the acid washed Ce-meACs showed an overall decrease in the ***C4***, ***C7*** and ***C5*** carboxylic acid peaks, and an increase in the ***C2*** and ***O4*** hydroxyl group peaks relative to AC-90. The overall effect of which is predicted to increase the affinity of the AC surface for both CO_2 and PEI, which is in agreement with the increase in C-O-R groups observed as an effect of acid washing by XPS of the Ce-meACs.

4.3.3 Structure of Ceria Catalysed Activated Carbons

Gas physisorption methods were primarily employed in order to determine the structure of the catalysed physically activated meACs; however, transmission electron microscopy (TEM), x-ray diffraction (XRD) and Raman spectroscopy were also employed.

4.3.3.1 Chemical Structure of Ceria Catalysed Activated Carbons

4.3.3.1.1 Raman Spectroscopy

Raman spectroscopy of the Ce catalysed physically activated meACs was undertaken both before and after the H_2SO_4 washing to remove the catalyst. Spectral collection was done in the same manner as for the miACs, which is outlined in ***chapter 6*** (***section 6.6.3.1.1***). No adjustments to the energy range was required as the Raman scattering of Ce_xO_y occurs at much lower range as carbon [25, 26], and therefore would not cause any interference with the Raman active signals from carbon. The same data treatment involving baseline correction, normalisation and multiple peak fitting was undertaken for all spectra. As with the multiple

peak fitting of the miACs close attention was paid to the ***S***, ***D*** and ***A*** peaks. The Raman spectra for the Ce catalysed physically activated meACs are presented in ***Figure 4-4***. The spectral deconvolution and peak fitting was carried out as per that reported by Sadezky *et al* [27], and are presented in ***Table 1-4***.

Treatment of carbon materials with concentrated H_2SO_4 in order to remove the CeO_2 is also known to remove some of the outer carbon layers along with CeO_2 [28, 29]. As such, it is expected that differences in the chemical structure of the Ce-meACs will arise as a result of acid washing.

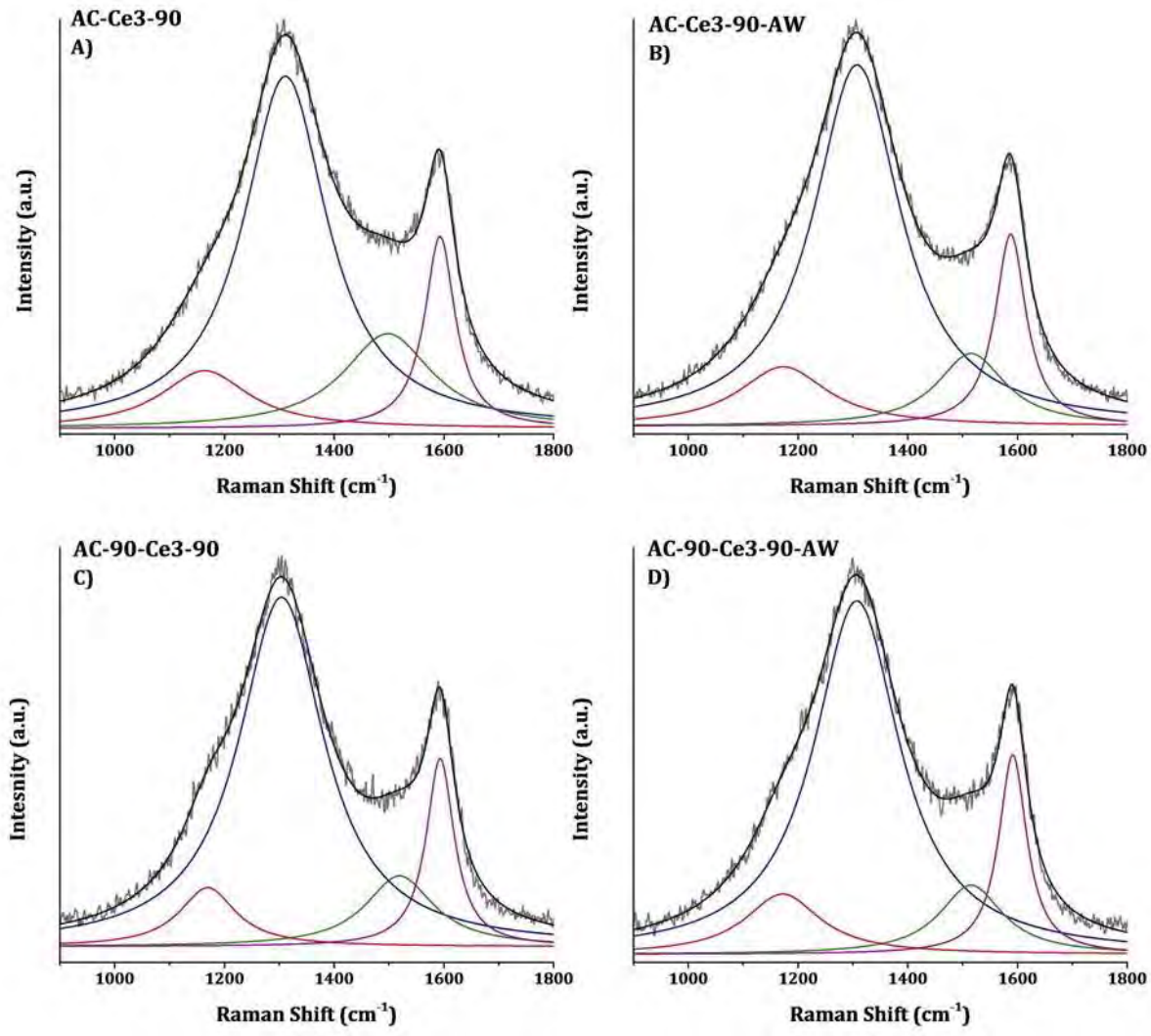

Figure 4-4 ~ *Raman Spectra of Ceria Catalysed Physically ACs. Shown are the peaks for the (—) Normalised Data, (—) Sum of Deconvoluted Peaks, (—) S band, (—) D band, (—) A band, (—) G band,* ***A)*** *AC-Ce3-90,* ***B)*** *AC-Ce3-90-AW,* ***C)*** *AC-90-Ce3-90, and* ***D)*** *AC-90-Ce3-90-AW*

From the Raman spectra of AC-Ce3-90 and AC-90-Ce3-90, it can be seen that the area of the ***S*** peak of AC-90-Ce3-90 is much smaller than that of AC-Ce3-90. There was also a significant difference in the area of the ***D*** peak for AC-Ce3-90 and AC-90-Ce3-90. However, the combined area of the ***S*** and ***D*** peaks of AC-90-Ce3-90 show it to possess a greater amount of disordered graphitic carbon relative to that observed for AC-Ce3-90. This agrees well with the differences observed in the peak area of the ***A*** peak for both Ce-meACs (***Table 4-5***). The area of the ***A*** peak observed for AC-90-Ce3-90 (***Figure 4-4C***) was significantly lower than that of AC-Ce3-90 (***Figure 4-4A***), despite possessing the same Ce loading. This would indicate that ACs produced from AC-90 possessed a lower amount of amorphous carbon. Whether this is the result of AC-90-Ce3-90 having gone through a second activation step will require further study.

For both the AC-Ce3-90/AC-Ce3-90-AW and AC-90-Ce3-90/ AC-90-Ce3-90-AW pairs, the area of the ***S*** peak increased after acid washing. Thus as the ***S*** peak area increases, there are a greater number of hetero-atoms (H, N and O, not Ce) bound to the edges of the graphene sheets, as a result of oxidation of the carbon by the H_2SO_4.

The changes in area of the ***D*** peak as a result of acid washing were different for AC-Ce3-90 and AC-90-Ce3-90. The area of the ***D*** peak of AC-Ce3-90-AW was significantly higher than that of AC-Ce3-90. The combined increases in the area of the ***S*** and ***D*** peaks upon acid washing of AC-Ce3-90 are equal to the decrease observed in the area of the ***A*** peak.

Table 4-5 ~ *Raman Peak Fitting for CeO_2 Catalysed Physically Activated Carbons*

Sample Name	Peak Area			
	S	D	A	G
	Disordered Graphitic Lattice*	Disordered Graphitic Lattice†	Amorphous Carbon	Ideal Graphitic Lattice
AC-90	11.7	62.4	12.7	13.0
AC-Ce3-90	10.4	60.2	17.3	12.0
AC-Ce3-90-AW	11.1	65.9	10.4	12.4
AC-90-Ce3-90	7.7	68.8	11.2	12.2
AC-90-Ce3-90-AW	10.1	67.5	9.8	12.5

* *Heteroatoms Bond to Graphene Layer Edges*

† *Graphene Layer Edges*

The area of the ***A*** peak also changed upon acid washing of both AC-Ce3-90 and AC-90-Ce3-90, with the peak decreasing as a result of acid washing. This would indicate that there has been an

overall decrease in amorphous carbon as a result of acid washing. Interestingly though, there was little variation in the area of the ***G*** peak as a function of which starting material was used, or whether or not acid washing had taken place. As such the increase in ordered carbon has manifested as an increase in disordered graphitic carbon. This statement may seem counterintuitive, but the so called "disordered graphitic carbon" possesses a much higher degree of order than amorphous carbon.

Relative to the Raman spectra of AC-90 (***Figure 2-8D***), the Ce-meACs, both "as produced" and acid washed exhibited a slightly lower amount of ideal graphitic carbon. A much higher degree of similarity was observed overall between AC-90 and the AC-Ce3-90/AC-Ce3-90-AW pair, which was a "catalysed analogue" of AC-90, differing in the way it was produced only by the presence of CeO_2. This is particularly true in respect of the ***S*** and ***D*** peak areas, with a great deal more variation being observed for the area of the ***A*** peak of the AC-Ce3-90/AC-Ce3-90-AW pair relative to AC-90, than to one another. These observations are consistent with what would be expected from a catalysed analogue of AC-90.

The combined peak areas of the ***S*** and ***D*** peaks for the AC-90 derived Ce-meACs showed more similarity to AC-90 than the VBC derived Ce-meACs, in that there was less variation. However, the combined peak areas of the ***S*** and ***D*** peaks of the AC-90-Ce3-90/AC-90-Ce3-90-AW pair was slightly higher than AC-90, whilst the area of the ***A*** peak for both AC-90-Ce3-90 and AC-90-Ce3-90-AW were slightly lower. This suggests that undergoing a second round of steam activation has resulted in a slight increase in the order within the chemical structure of the carbon, with amorphous carbon being possibly restructured into disordered graphitic carbon.

The overall changes in chemical structure that were observed by Raman spectroscopy for both the VBC and AC-90 derived Ce-meACs showed two quite different types of carbons, with significantly different carbon chemical structures. Those derived from VBC were CeO_2 catalysed analogues of AC-90, and exhibited many similarities with it. The Ce-meACs derived from AC-90 itself, exhibited a lower amount of amorphous carbon, with an associated increase in disordered graphitic carbon, which suggests that a second round of steam activation in resulted in a increase in the order within the chemical structure of the carbon within the AC-90-Ce3-90/AC-90-Ce3-90-AW pair. The observed differences between the two carbon types may be attributed to the second round of steam activation, but may also be influenced by the degree of dispersion of CeO_2 throughout the material. From the TEM images of AC-Ce3-90 (***Figure 4-9***), CeO_2 is shown to be highly dispersed, whilst the TEM images of AC-90-Ce3-90 (***Figure 4-11***) show the CeO_2 to be badly dispersed; being located predominately within the pore structure.

4.3.3.1.2 Powder X-Ray Diffraction (PXRD)

The x-ray diffraction pattern (XRD) patterns of the Ce-meACs were taken prior to and subsequent to acid washing. A pure ceria (CeO_2) standard was run as a reference, this is shown below in ***Figure 4-5***, the diffraction pattern for the Ce-meACs are presented in ***Figure 4-6***.

The characteristic Ce peaks observed from the XRD patterns of the CeO_2 (***Figure 4-5***) reference material were only observed to be present in AC-Ce3-90 (***Figure 4-6A***), and not for AC-90-Ce3-90 (***Figure 4-6B***). Only very slight indication of any of the characteristic CeO_2 peaks (***Figure 4-5***) were detected for the XRD patterns of the AC-90-Ce3-90 (***Figure 4-6B***). This is likely due to the presence of the majority of the CeO_2 being within the pore structure where it cannot diffract significant quantities of x-rays. For AC-90-Ce3-90 it is due to the Ce being poorly distributed, being present predominately within the pores; which can be clearly observed from the TEM images of AC-90-Ce3-90 (***Figure 4-11***). Overall the characteristic CeO_2 peaks observed are in line with those observed for similar AC-CeO_2 composite materials reported by Shen *et al* [7, 8].

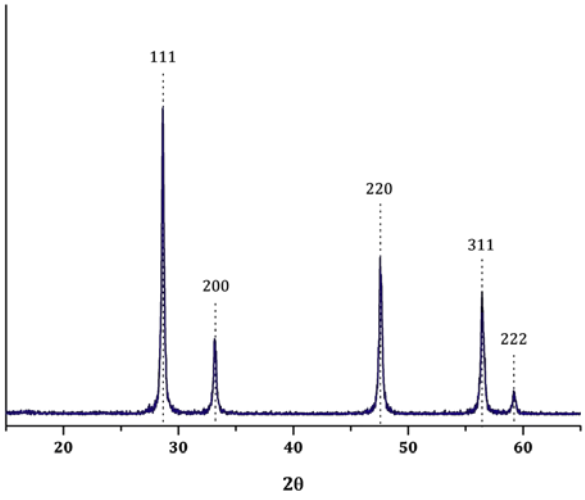

Figure 4-5 ~ *X-ray Diffraction Pattern of the Ceria Standard*

Furthermore, in all cases the XRD patterns of the acid washed meACs were very similar to that of the AC-90 benchmark. This would indicate that the acid washing resulted in a high level of ceria removal from the meACs. The main peaks observed for the AC phase were the ***002*** and ***10*** (overlapping ***100*** and ***101*** reflections) peaks, which are typical of the diffraction pattern of amorphous carbons [7, 30-35]. The ***002*** reflection arises from the diffraction by parallel graphitic domains, and slight increases are observed in the intensity of this peak for the acid washed meACs, relative to AC-90. This can be a strong indication of the presence of micropores, that in ACs can exist between parallel graphene sheets [30]. The presence of the ***10*** reflection

indicates the presence of lateral order within the graphitic domains [31, 35]. Furthermore, as was noted in ***section 2.3.3.1.2*** for AC-90, a third peak can be observed in the carbon phase at 27 2θ°. This peak is assigned to amorphous metal oxides (MO), such as those present within the ash of coal [33]. Of interest however, is the observation of this peak in the diffraction pattern of AC-90-Ce3-90, indicating that the Ce_xO_y may be somewhat amorphous.

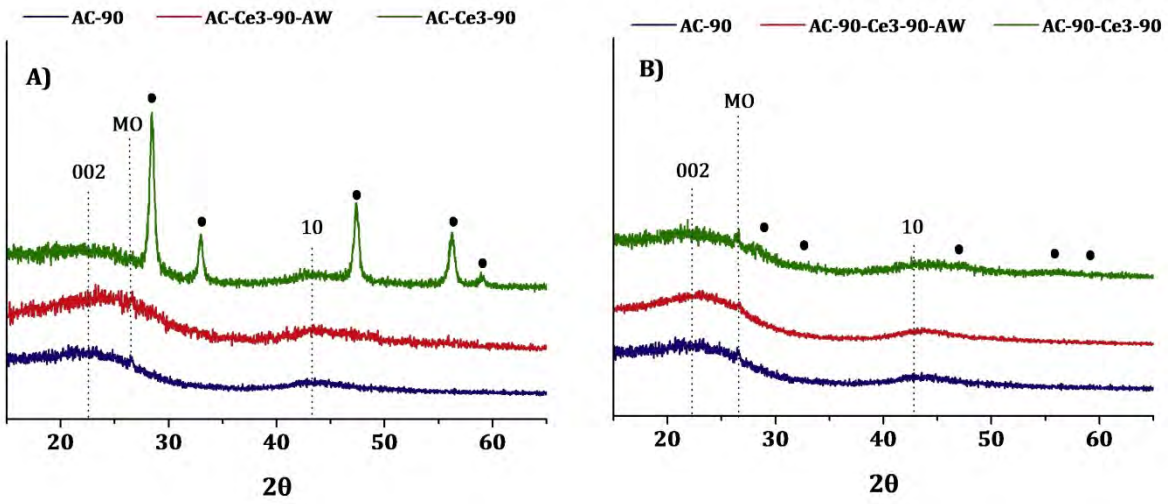

Figure 4-6 *~ X-ray Diffraction Patterns of the Acid Washed and "as produced" Ceria Catalysed Steam Activated Carbons. Shown are the XRD Patterns Highlighting the 002, 10 and MO Peaks for the AC Phase and the Peaks for the CeO_2 Phase (●) for* ***A)*** *AC-Ce3-90 & AC-Ce3-90-AW, and* ***B)*** *AC-90-Ce3-90 & AC-90-Ce3-90-AW*

It is also of interest to note that the peaks typical of a CeO_2 diffraction pattern were not as clear for AC-90-Ce3-90 (***Figure 4-6B***) as they were for AC-Ce-90 (***Figure 4-6A***). This may indicate the activation after impregnation into VBC results in larger Ce_xO_y particles, whilst impregnation and activation into AC-90 results in finer particles of Ce_xO_y being formed. However, the TEM of these two Ce-meACs shows there is no significant difference in the sizes or distribution of sizes of the CeO_2 particles between to the two Ce-meACs. It is also likely that the CeO_2 phase in AC-90-Ce3-90 formed an amorphous phase, evidence of which can be seen by the presence of the MO peak in the diffraction pattern of AC-90-Ce3-90 but not AC-Ce3-90 (***Figure 4-6***). In the work of Shen *et al* a well defined XRD pattern for CeO_2 was not observed until temperatures of 1143 K [7]. In this work the Ce was introduced into preformed ACs, not the AC precursor; as such as the VBC underwent pyrolysis and oxidation the $(Ce(NO_3)_3.6H_2O$ salts will have more easily been oxidised to Ce_xO_y than when AC was used as the carbon precursor.

In summary, despite observing clearly distinct AC and CeO_2 diffraction patterns, once the Ce-meACs had been acid washed, no CeO_2 phase was observed, leaving only a typical AC diffraction pattern, essentially indistinguishable from AC-90.

4.3.3.2 Physical Structure of Ceria Catalysed Activated Carbons

4.3.3.2.1 Gas physisorption

The surface area and porosity of each AC was determined from the adsorption isotherms of N_2 and CO_2 at 77 and 273 K, respectively. The details outlining the analysis conditions used to obtain the isotherms by the adsorption of the aforementioned gases onto the physically activated Ce-meACs can be found in ***section 6.6.3.2.1***, in addition to the models and equations used for data analysis. The surface morphology of the CeO_2 was determined before and after catalyst removal, and are presented in ***Table 4-6***.

CO_2 Physisorption

The CO_2 adsorption isotherms taken at 273 K for the Ce-meACs were carried out on a TriStar II 3020 instruments (Micromeritics), over a relative pressure range of 0-0.03. The CO_2 isotherms for AC-Ce3-90, AC-Ce3-90-AW, AC-90-Ce3-90 and AC-90-Ce3-90-AW are presented in ***Figure 4-7.*** The surface areas and micropore volumes calculated using the DR equation (***equation 6-1***) presented in ***Table 4-6***, along with the BET surface areas, micropore volumes (calculated using the DR equation for both CO_2 and N_2), the mesopore volumes (BJH) determined from N_2 physisorption and true density values determined by He displacement.

There was an observed decrease in micropore volume for the acid washed Ce-meACs relative to their "as produced" counterparts (***Table 4-6***). This is primarily the result of removal of the CeO_2 phase, thus widening the diameter of the micropores, in some cases to mesopores. The pore expansion observed upon acid washing was not due to a change in the carbon pore structure itself, but to removal of the Ce_xO_y coating the walls of the pores. Furthermore, the PSD of CeO_2 is generally quite broad, possessing both micro- and mesopores. As such some of the reduction in micropore volume may be due to the removal of CeO_2 and the microporosity inherent within it.

Furthermore, the micropore volumes determined from the CO_2 physisorption data for the Ce-meACs show that the AC-Ce3-90/AC-Ce3-90-AW pair possessed lower micropore volumes relative to AC-90. On the other hand the micropore volumes of the AC-90-Ce3-90/AC-90-Ce3-90-AW pair were both higher than AC-90, showing no change as a result of acid washing. This

observation is as would be expected as the latter pair had undergone a second round of steam activation.

Table 4-6 *~ Surface Area, Pore Volume & True Density of CeO_2 Catalysed Physically Activated meACs*

Sample Name	Surface Area (m^2/g)		Pore Volume (cm^3/g)				True Density (g/cm^3)
	CO_2	N_2	CO_2	N_2			
	DR	BET	V_{micro}	V_{micro}	V_{meso}	V_{total}	
VBC	148	-	0.05	-	-	-	1.40
AC-90	696	397	0.23	0.20	0.13	0.24	1.90
AC-Ce3-90	614	450	0.20	0.23	0.16	0.32	1.92
AC-Ce3-90-AW	616	300	0.20	0.17	0.07	0.19	1.77
AC-90-Ce3-90	792	458	0.26	0.24	0.16	0.35	2.03
AC-90-Ce3-90-AW	707	418	0.23	0.22	0.16	0.31	1.82

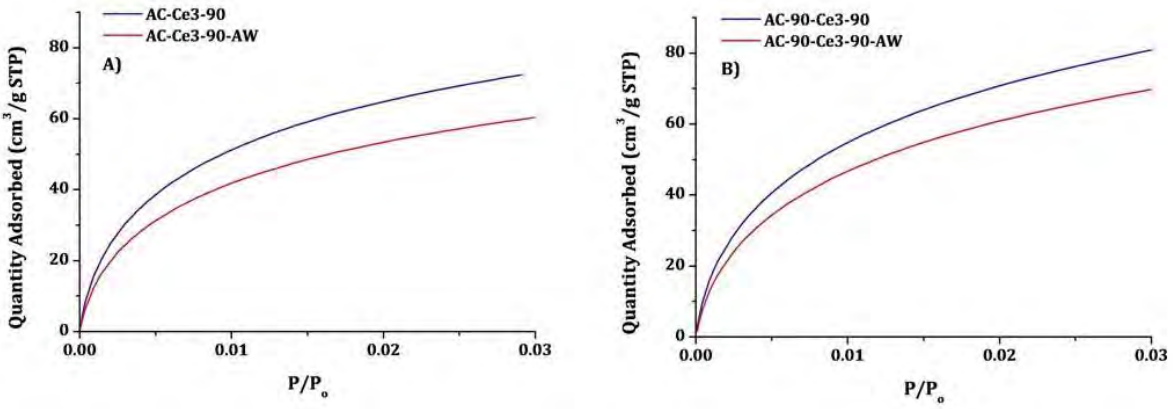

Figure 4-7 *~ CO_2 Adsorption Isotherms taken at 273 K for the CeO_2 Physically Activated Carbons*

N_2 Physisorption

The N_2 adsorption-desorption isotherms taken at 77 K for the Ce meACs and their acid washed counterparts were taken over a P/P_0 range of 0-0.99 on an ASAP 2020 HP instrument (Micromeritics), from which PSDs were determined using the BJH method; which are shown in ***Figure 4-8***. The BET surface areas and mesopore volumes (BJH) are given in ***Table 4-6***, along

with the micropore volumes calculated using the DR equation for both CO_2 and N_2 physisorption (***equation 6-1***).

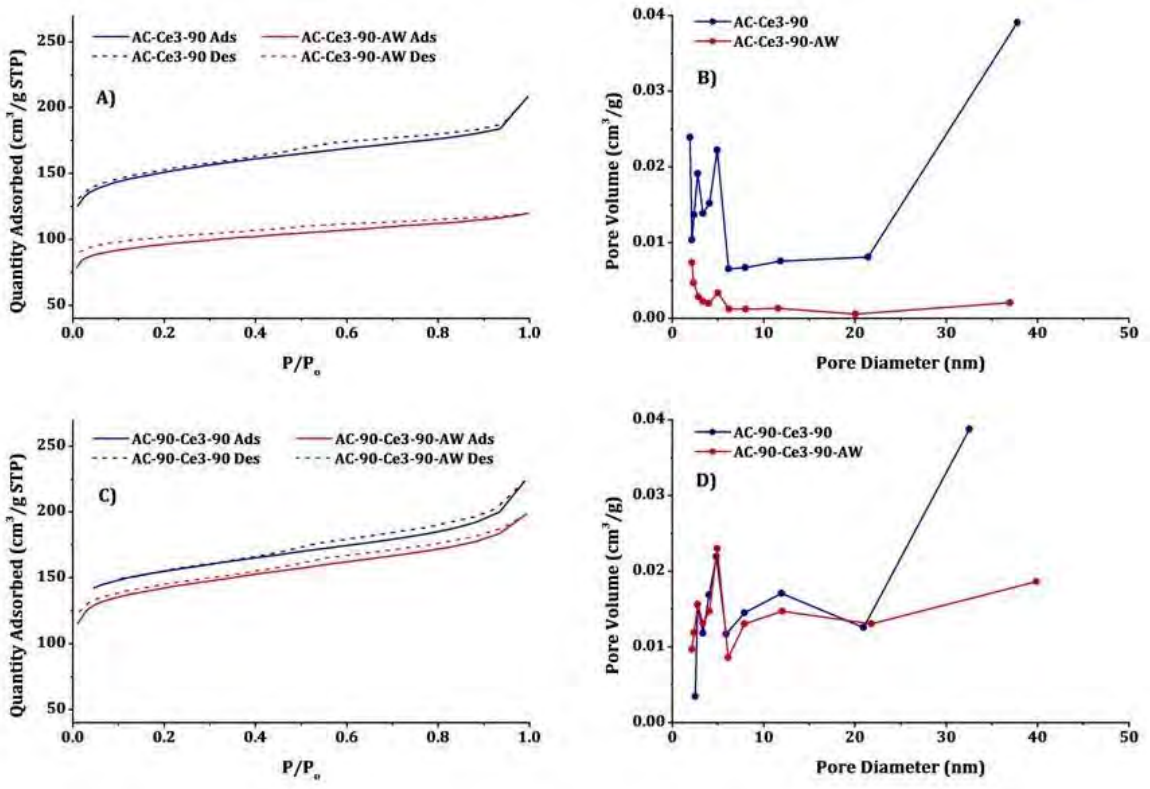

Figure 4-8 *~ N_2 Adsorption Isotherms and PSDs taken at 77 K for the CeO_2 Loaded Physically Activated Carbons. Shown are* ***A)*** *Isotherms for AC-Ce3-90 & AC-Ce3-90-AW,* ***B)*** *PSDs for AC-Ce3-90 & AC-Ce3-90-AW,* ***C)*** *Isotherms for AC-90-Ce3-90 & AC-90-Ce3-90-AW, and* ***D)*** *PSDs for AC-90-Ce3-90 & AC-90-Ce3-90-AW*

The N_2 adsorption isotherms for the Ce-meACs all exhibit standard type ***IV*** isotherms with type ***H4*** hysteresis loops. Prior to the acid washing both the Ce-meACs exhibited isotherms that exhibited complete closure of the hysteresis loop, where as those which were acid washed possess isotherms with hysteresis loops that never fully achieve closure. In ***chapter 2*** for the microporous carbon materials this was attributed to low pressure hysteresis (LPH), that can arise due to incomplete equilibrium being achieved during the measurement of the adsorption branch of the isotherm (a common problem for microporous materials)[36-38]. The type ***H4*** hysteresis loops are indicative of materials that possess a mixture of both micro- and mesopores (e.g. a broad PSD).

The micropore volumes determined for the Ce-meACs (***Table 4-6***) by applying the DR equation to the micropore region of the N_2 physisorption data tell a slightly different story to the micropore volumes determined from the CO_2 physisorption data. The differences between the

two data sets can be attributed to have arisen from three potential sources. Firstly, the N_2 physisorption data obtained at 77 K was not obtained to relative pressures as low as was done for the CO_2 physisorption measurements obtained at 273 K (***section 6.6.3.2.1***). As such the shape of the adsorption isotherms for the N_2 and CO_2 physisorption data sets will differ slightly. Secondly, the entire purpose of applying the DR equation to the N_2 physisorption data, was to obtain micropore data that would not be potentially compromised by interactions between the adsorbate and the surface chemistry of the adsorbate. The investigations of the surface chemistry of the meACs (***section 4.3.2***) indicated the presence of several functional groups that may significantly affect the adsorption of CO_2, which is as applicable to the adsorption at 273 K as it would be at 293-378 K. Such complications should not arise from the interactions of N_2 with the meAC surface, and thus discrepancies between the two data sets may imply such effects are at play. Finally, some of the ACs presented in this thesis may possess micropores with very small diameters (i.e. ultramicropores and supermicropores [39]), such that the adsorption of N_2 at 77 K into the inner depths of the micropores by N_2 molecules is not possible.

For the N_2 physisorption of both AC-Ce3-90 and AC-90-Ce3-90, it is interesting to note the strong similarities between the two samples, despite them having been produced from two different precursors. Moreover, it can be seen from ***Table 4-6*** that both these meACs possess near identical mesopore volumes. The similarity between these materials strongly deviates upon acid washing, with AC-Ce3-90-AW possessing a lower mesopore volume than AC-90. Since the Ce 3d XPS spectra of AC-Ce3-90-AW indicated the retention of some of the Ce on the surface, this may explain in part the reduction in pore volume, as pore blockage may have persisted. Conversely the Ce 3d XPS spectra of AC-90-Ce3-90-AW show no significant amount of Ce remaining on the surface as a result of the acid washing. Since the precursor used to produce AC-90-Ce3-90 was AC-90, which already had well developed porosity, it is likely that the second stage of activation will have enabled the development of a greater mesopore volume, regardless of the presence of any CeO_2 phase.

Overall, due to the development of the acid washing procedure, it was able to be determined, that a significant degree of the mesoporous character of the "as produced" Ce-meACs was actually due to the porous nature of the Ce_xO_y. In previous works published in the literature (most notably those of Shen *et al* [8, 40] and Yoshizawa *et al* [41, 42]), the Ce_xO_y was not removed from the Ce-meACs. As such certain aspects of the Ce-meAC morphology was never investigated, such as the amount of the porosity measured that was due to the Ce_xO_y and not the AC. Here it has been shown that supposed improvements in pore volume were likely to be owing to that which is inherent in the Ce_xO_y in addition to that of the AC. Although increases in

the mesopore volume of the Ce-meACs (produced here) were achieved relative to AC-90, this was not as extensive as had been sought.

4.3.3.2.2 Transmission Electron Microscopy (TEM)

The physical structure of several of the Ce-meACs were futher investigated using TEM. The TEM micrographs along with the EDX elemental mapping of C, O and Ce for AC-Ce3-90, AC-Ce3-90-AW, AC-90-Ce3-90 and AC-90-Ce3-90-AW are shown in ***Figure 4-9***-***Figure 4-12***, respectively. For each material imaging and mapping of 3-4 particles was undertaken, with the most representative being presented here, as was the case for the miACs in ***Chapter 2***.

From the TEM micrograph of AC-Ce3-90 (***Figure 4-9***) showed a significant number of Ce_xO_y particles dispersed throughout the dense amorphous carbon phase. The Ce_xO_y particles were able to be clearly differentiated from the carbon phase by their distinct particle edges, spreading out in 3 dimensions, as compared to the graphitic carbon phases possessing striations. The elemental mapping of AC-Ce3-90 shows the Ce phase to be highly dispersed throughout the entire particle mapped, chosen for its excellent representation of the majority of particles investigated.

From the TEM micrograph of AC-Ce3-90-AW (***Figure 4-10***) it can be seen that the structure of the carbon is very similar to that of AC-Ce3-90 (***Figure 4-9***). Furthermore, AC-Ce3-90-AW possessed significant amounts of amorphous carbon with no well defined graphitic carbon being observed; although, some alignment of the carbon structure can be observed on the outer edges of the particle. The acid washing resulted in a material with substantially reduced Ce_xO_y, as is evident from the elemental mapping shown in ***Figure 4-10E***. Overall, TEM has shown AC-Ce3-90-AW to possess no distinct structure features, which is in good agreement with the Raman spectroscopy results (***Table 4-5***).

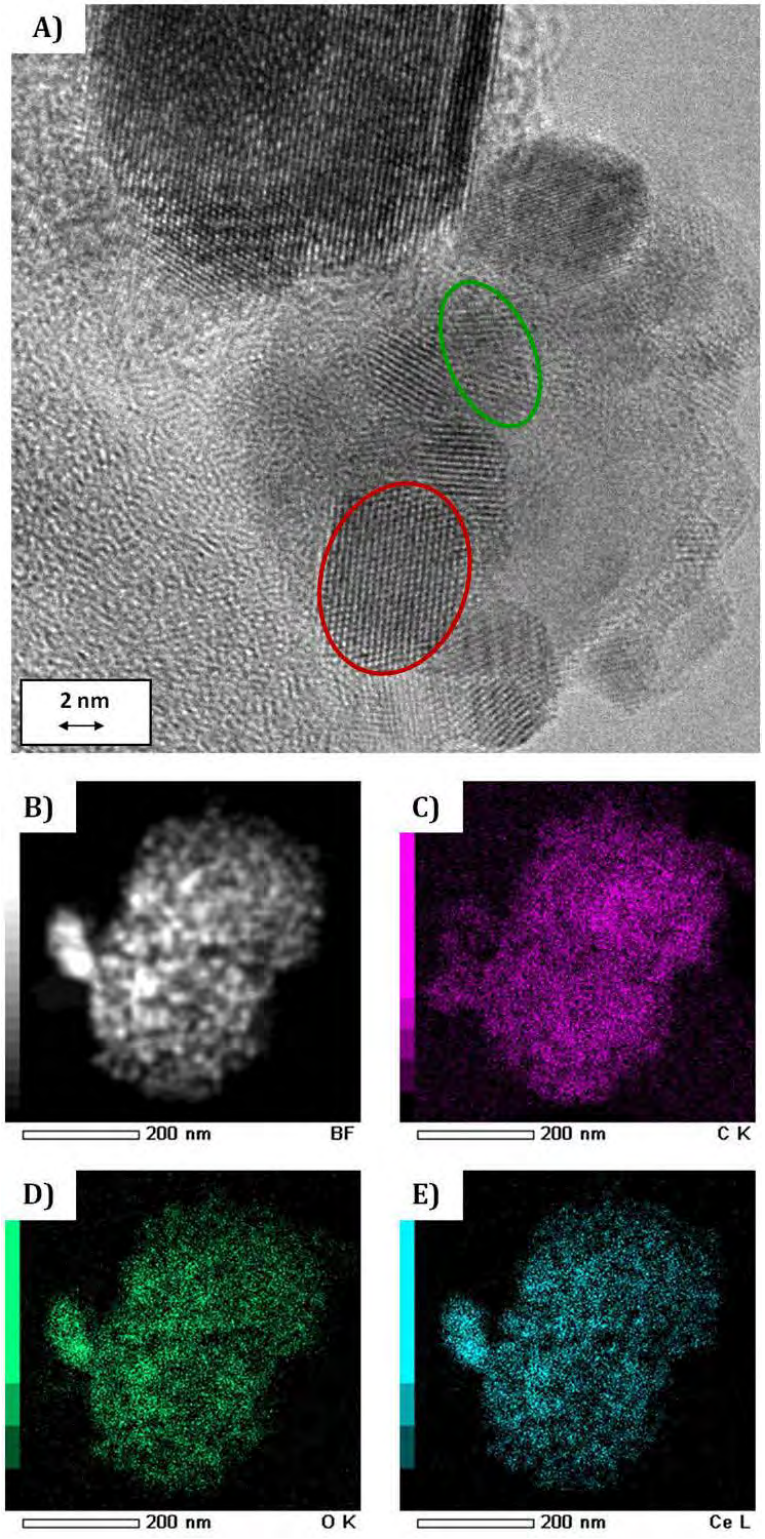

Figure 4-9 *~ Transmission Electron Micrograph and Elemental Mapping of Ce Catalysed Physically Activated meAC AC-Ce-90. Shown is* ***A)*** *High Magnification Electron Micrograph, CeO_2 particle circled (◯), lattice fringes of graphitic domain (◯),* ***B)*** *Bright Field Image of Mapped Particle,* ***C)*** *EDX Mapping of the C K-edge,* ***D)*** *EDX Mapping of the O K-edge, and* ***E)*** *EDX Mapping of the Ce L-edge*

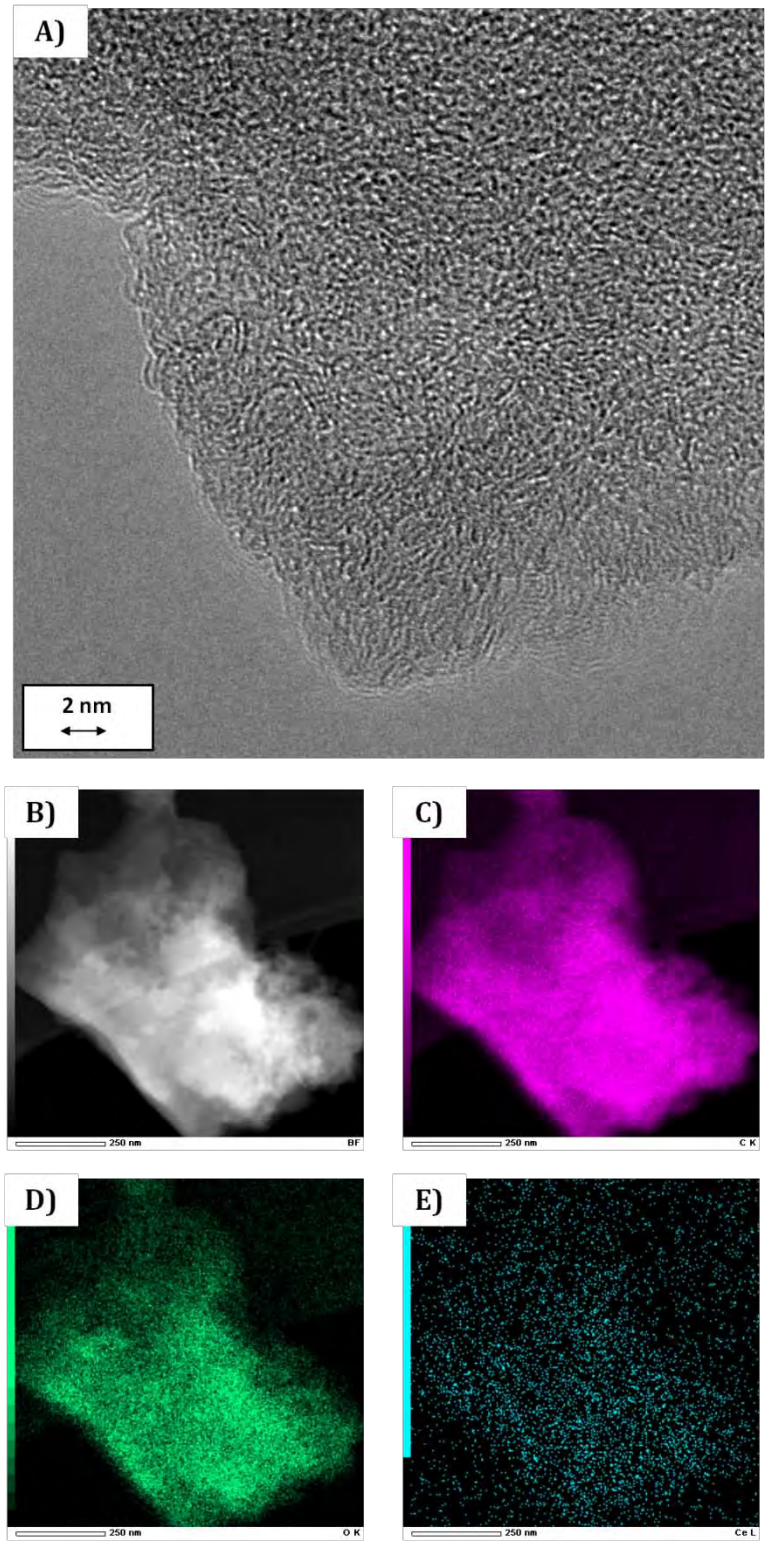

Figure 4-10 ~ *Transmission Electron Micrograph and Elemental Mapping of Ce Catalysed Physically Activated meAC AC-Ce-90-AW. Shown is* ***A)*** *High Magnification Electron Micrograph,* ***B)*** *Bright Field Image of Mapped Particle,* ***C)*** *EDX Mapping of the C K-edge,* ***D)*** *EDX Mapping of the O K-edge, and* ***E)*** *EDX Mapping of the Ce L-edge*

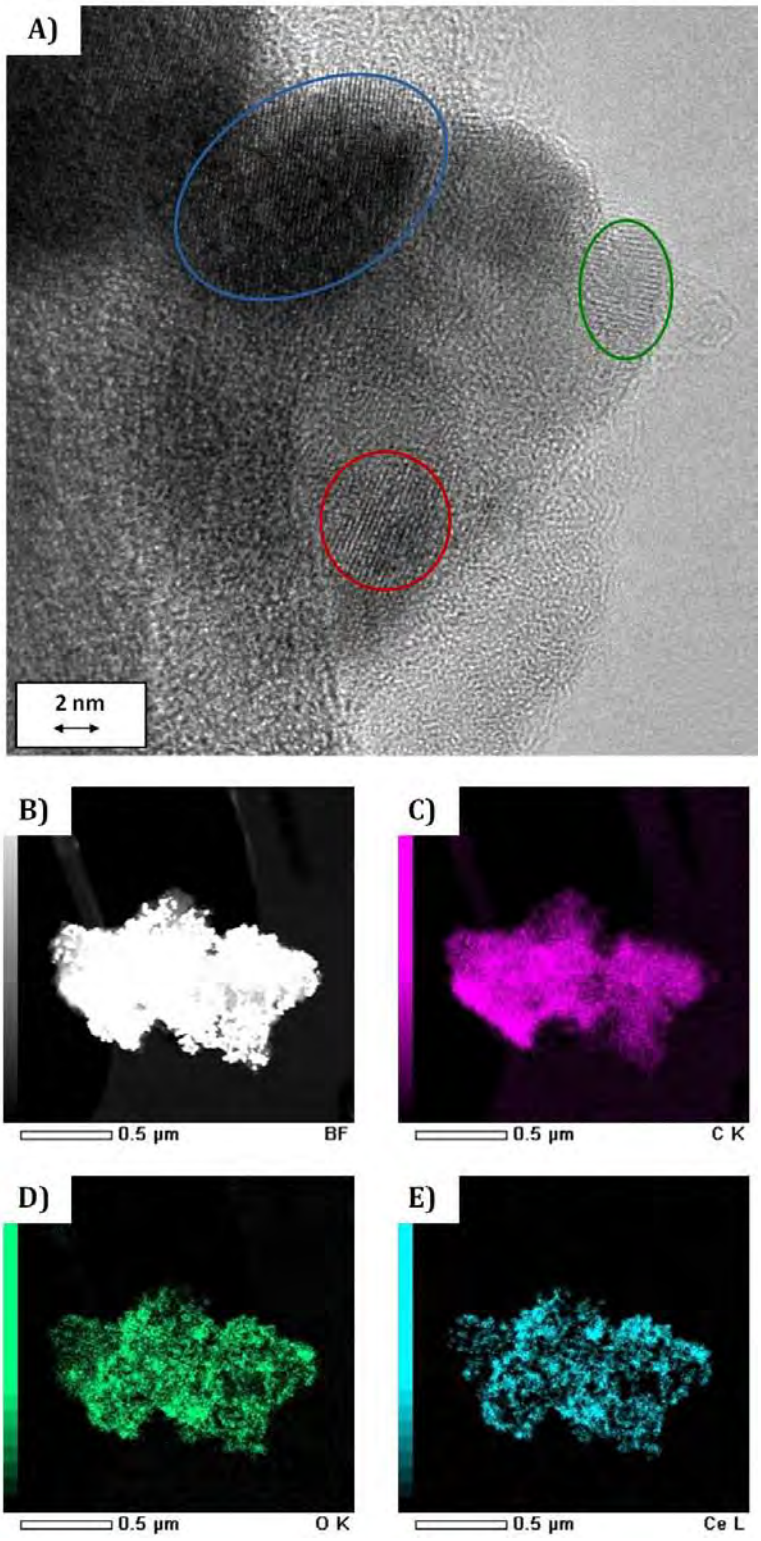

Figure 4-11 *~ Transmission Electron Micrograph and Elemental Mapping of Ce Catalysed Physically Activated meAC AC-90-Ce-90. Shown is* ***A)*** *High Magnification Electron Micrograph, CeO_2 particles (◯, ◯, ◯),* ***B)*** *Bright Field Image of Mapped Particle,* ***C)*** *EDX Mapping of the C K-edge,* ***D)*** *EDX Mapping of the O K-edge, and* ***E)*** *EDX Mapping of the Ce L-edge*

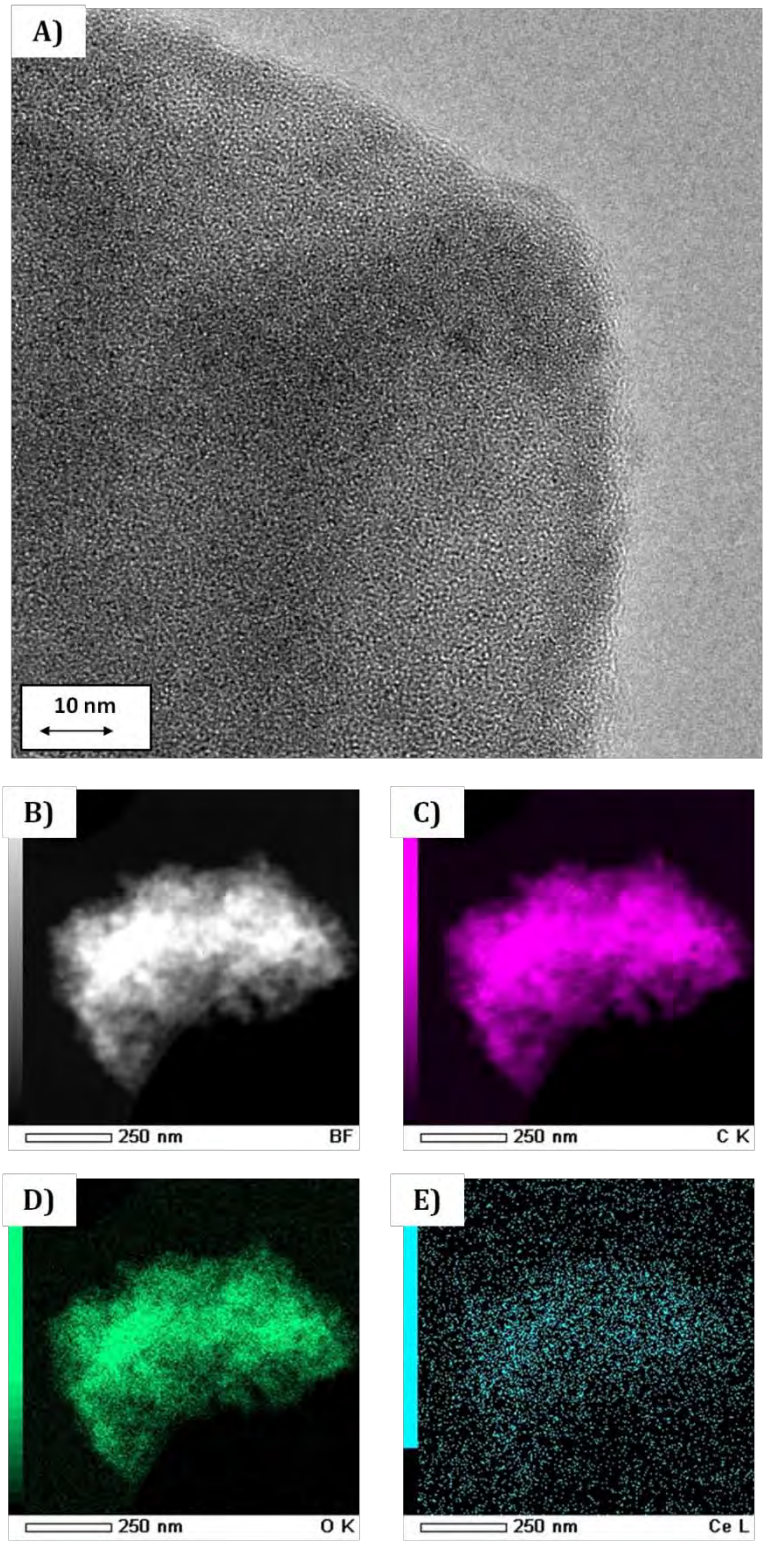

Figure 4-12 ~ *Transmission Electron Micrograph and Elemental Mapping of Ce Catalysed Physically Activated meAC AC-90-Ce-90-AW. Shown is* ***A)*** *High Magnification Electron Micrograph,* ***B)*** *Bright Field Image of Mapped Particle,* ***C)*** *EDX Mapping of the C K-edge,* ***D)*** *EDX Mapping of the O K-edge, and* ***E)*** *EDX Mapping of the Ce L-edge*

The TEM micrograph of AC-90-Ce3-90 (***Figure 4-11***) showed it to possess similar morphology to AC-Ce3-90 (***Figure 4-9***), despite having been produced by a different activated method. Particles of Ce_xO_y are clearly visible from the distinct layer edges of their crystallites, these particles were not well dispersed throughout the amorphous carbon. Unlike for AC-Ce3-90 (***Figure 4-9***), the distribution of Ce_xO_y was clearly concentrated within the pore structure of the material. This is consistent with what would be expected to be observed, as the AC-90 precursor of AC-90-Ce3-90 possessed a very well developed pore structure, unlike the VBC precursor of AC-Ce3-90. The structure of the carbon within AC-90-Ce3-90 was similar to that observed for AC-Ce3-90 and AC-Ce3-90-AW (***Figure 4-9*** and ***Figure 4-10***, respectively), with no well defined graphitic carbon; being predominately amorphous in nature. However, some alignment of the carbon structure was observed around the edges of the particles. The lack of a well defined carbon structure in the case of AC-90-Ce3-90 is in good agreement with the Raman spectroscopy results, where the major types of carbon was that of disordered graphitic and amorphous carbons (***Table 4-5***).

From the TEM micrograph of AC-90-Ce3-90-AW (***Figure 4-12***) it can be seen that the effect of acid washing on morphology was minor, other than to act in the removal of the Ce_xO_y particles. No well defined graphitic phases were observed within the carbon itself, which is consistent with the results of the Raman spectroscopy that the major carbon types were disordered graphitic and amorphous (***Table 4-5***). From the elemental mapping of Ce on the chosen particle only a slightly higher signal was obtained for this particle than for the background. This was in good agreement with the XPS and XRD results obtained for the AC-90-Ce3-90/AC-90-Ce3-90-AW pair (***Figure 4-6*** and ***Table 4-3***, respectively), where significant reduction in the amount of Ce_xO_y was observed. Furthermore, no significant graphitic carbon phase of any consequence was observed for any particles investigated.

Overall, few structural features were observed in the carbon structure, as was apparent from the TEM investigation of the miACs. This became more clearly evident upon acid washing, as there were no well defined graphitic domains observed, which is assumed to be a result of the acid washing itself, with the CeO_2 phase having been removed.

4.3.4 Summary

The production of meACs using ceria catalysed physical activation was achieved by two different activation protocols. The protocol used in the production of the AC-Ce3-90/AC-Ce3-90-AW pair involved the use of VBC as the carbon precursor, making it, in many respects a

catalysed analogue of AC-90; whereas, the AC-90-Ce3-90/AC-90-Ce3-90-AW pair were produced using AC-90 as the carbon precursor. This resulted in two distinctly different types of ACs being produced. Compositionally, AC-90-Ce3-90 (***Table 4-2***) possessed a lower bulk carbon content relative to AC-Ce3-90, which, when it is considered that AC-90-Ce3-90 had undergone two rounds of steam activation, this might be expected. The most significant differences in composition of the Ce-meACs that were observed were in the bulk oxygen concentrations, being the result of the two different methods used to produce the two different types of Ce-meACs. Furthermore, it is apparent that a significant amount of inorganic matter has been removed as part of the acid washing procedure, used to remove Ce_xO_y. In fact the ash content of AC-Ce3-90-AW and AC-90-Ce3-90-AW were lower than that of AC-90, which would suggest that some of the inorganic material present within the coal was removed in addition to the Ce_xO_y.

From the investigation of the surface chemistry small overall differences were observed in the amount of surface C and O, relative to AC-90 (XPS, ***Table 4-3***). Only minor overall differences in the C or O surface concentration were observed as a function of which procedure was used to prepare the Ce-meACs. For both the AC-Ce3-90/AC-Ce3-90-AW and AC-90-Ce3-90/AC-90-Ce3-90-AW pairs, XPS showed the acid washing to result in a slight increase in surface C, with an associated decrease in surface O. The decrease in surface O that was observed as a result of acid washing, was in part due to the removal of O in the form of Ce_xO_y (Ce-O peak, XPS). This was however, further complicated by the fact that some surface O will have been shielded from detection by Ce-O, and some surface O associated with surface functional groups appears to have been removed or introduced via reactions with the H_2SO_4 used in the acid washing. Further to the changes in surface C and O, were the changes in the distribution of surface functional groups, which required the use of both XPS and NEXAFS to fully understand.

XPS showed that for both the VBC and AC-90 derived Ce-meACs, acid washing resulted in increases in the surface concentration of the three major oxygenated surface functionalities (C-O-R, C=O and C-OOR, ***Table 4-3***). The AC-90 derived Ce-meACs exhibited lower amount of C-O-R, C=O and C-OOR groups, relative to the VBC derived Ce-meACs. Further investigation of the surface of the acid washed Ce-meACs showed the distribution of C-O-R groups detected by XPS to be predominately due to surface hydroxyl groups. In fact the proportion of hydroxyl groups on the surface of AC-Ce3-90-AW and AC-90-Ce3-90-AW were close to twice that present on the surface of AC-90 (***Table 4-4***). Furthermore, NEXAFS showed the proportion of carboxylic acids and ethers of the acid washed Ce-meACs were significantly lower than observed for AC-90, and that the distribution of carbonyl groups relative to AC-90 were shifted towards aldehydes over ketones. As such the polarity of the surface of the acid washed Ce-meACs will be significantly higher than that of AC-90, and this could potentially increase the affinity of the AC surface for

both CO_2 and PEI [12, 13]. Moreover, there were no clearly discernible correlations between the changes in the bulk and surface compositions.

From the Raman spectroscopy of the Ce-meACs (***Table 4-5***) there was a small but distinct difference between the areas of the ***G*** peak for the Ce-meACs relative to AC-90. Furthermore, regardless of production method or whether or not acid washing had taken place, there was no significant change in the area of the ***G*** peak for any of the Ce-meACs. This would suggest that the Ce-meACs possessed a slightly lower amount of carbon in the ideal graphitic form, but that the way in which Ce_xO_y was introduced and the precursor carbon affected this. There was a very clear relationship between amorphous carbon (***A*** peak) and disordered graphitic lattice carbon (***S*** and ***D*** peaks). Specifically, acid washing of the Ce-meACs resulted in a decrease in the area of the ***A*** peak and an increase in the area of the ***S*** peak. There was also a decrease in the ***D*** peak, but relative to the increase in the ***S*** peak this was minor and an overall increase in disordered graphitic lattice carbon (***S*** and ***D***) was observed as a result of acid washing.

The XRD investigation of the Ce-meACs revealed two broad peaks being assigned to the ***002*** and ***10*** reflections, typical of the diffraction pattern of amorphous carbons (***Figure 4-6***). Furthermore, the XRD pattern of AC-Ce3-90 (***Figure 4-6A***) clearly exhibited the typical Ce diffraction peaks of CeO_2 (***Figure 4-5***), whereas, AC-90-Ce3-90 (***Figure 4-6B***) exhibited very weak reflections of the main peaks. This was attributed to the Ce_xO_y being located predominately within the pore structure of the material, where it would be unable to be detected; or to the structure of the Ce_xO_y itself. This difference between the dispersion of the VBC and AC-90 derived Ce-meACs was confirmed by TEM-EDX mapping (***Figure 4-9***-***Figure 4-12***). Moreover, the XRD analysis of the Ce-meACs also reviled that upon acid washing, none of the signature peaks of CeO_2 remained present. Alternatively, the Ce_xO_y phase formed under the activation conditions may be somewhat amorphous, which is consistent with the observed XRD results and those of Shen *et al* [7]. In the work of Shen *et al* [7], it was shown that a clear XRD pattern for CeO_2 was not observed until an activation temperature of 1143 K; whereas the activation temperature used here was 1073 K.

The significant differences in the chemical structure of both the VBC and AC-90 derived Ce-meACs were further seen in the gas physisorption results (***Table 4-6***). From the N_2 physisorption results it was seen that both the "as produced" and acid washed Ce-meACs exhibited type ***IV*** isotherms with ***H4*** type hysteresis loops (***Figure 4-8***), typical of materials possessing both micro- and mesopores [43]. The CO_2 physisorption showed all the Ce-meACs to exhibit type ***I*** isotherms (***Figure 4-7***), typical for the adsorption of non-condensable gases in materials possessing micropores [43].

The N_2 physisorption data (***Table 4-6***) showed the acid washing of the Ce-meACs to result in decreases in the micropore volume and surface area. In the case of the AC-Ce3-90/AC-Ce3-90-AW pair, the decrease in pore volume that arose from acid washing extended beyond just the micropore volume, to significant decreases in the mesopore volume. The extent of this was such that AC-Ce3-90-AW possessed a lower mesopore volume than AC-90, of which it was a catalysed analogue. The significant decrease in the micro- and mesopore volumes of AC-Ce3-90-AW relative to AC-Ce3-90, may in fact be due to the high degree of dispersion of the Ce_xO_y, as this was not observed for the AC-90-Ce3-90/AC-90-Ce3-90-AW pair. The TEM-EDX mapping of AC-Ce3-90 (***Figure 4-9***) showed Ce to be very well dispersed, relative to that of AC-90-Ce3-90 (***Figure 4-11***). The TEM-EDX mapping of Ce for AC-90-Ce3-90 showed it to be mostly located within the pore structure of the Ce-meAC particles. It is proposed that removal of the well dispersed Ce_xO_y of AC-Ce3-90 could likely result in pore collapse of micro- or mesopores, which would be less likely to occur in the case of the less well dispersed AC-90-Ce3-90 material.

Furthermore, the decrease in the micropore volume that resulted from acid washing of AC-Ce3-90, was only observed from the N_2 physisorption data, whereas the CO_2 physisorption data showed no such decrease (***Table 4-6***). However, a direct comparison of the pore structure from the CO_2 and N_2 physisorption data of the "as produced" and acid washed Ce-meACs was complicated by the fact that Ce_xO_y itself possesses a wide PSD [7, 26, 44-46]. As such, it is difficult to say with absolute certainty what proportion of the micro- and mesopore volume of the "as produced" Ce-meACs was due to Ce_xO_y and what was in fact due to the AC.

Other than the Ce_xO_y structural features observed from the TEM micrographs of the Ce-meACs, no significant graphitic domains were observed, for either the "as produced" or acid washed Ce-meACs (***Figure 4-9***-***Figure 4-12***). Some alignment of the carbon structure was observed, but none that could be termed a well defined graphitic domain as were observed for the miACs in ***chapter 2***.

To conclude, the use of Ce_xO_y as a catalyst in the physical activation of VBC and VBC derived ACs with the purpose of producing ACs that possessed predominately mesopore character was reasonably unsuccessful. Although the mesopore character of the "as produced" Ce-meACs was promising, upon acid washing the some of the desired mesopore character was also removed along with the Ce_xO_y phase. This is however an important step, as previous investigations along similar lines from the literature, such as those of Shen *et al* [8, 40]; never investigated this aspect of the meACs produced. Regardless, the two acid washed Ce-meACs (AC-Ce3-90-AW and AC-90-Ce3-90-AW) were subsequently chosen to be impregnated with PEI as support materials.

4.4 Lanthana Catalysed Physically Activated Carbons

Lanthanum oxide (lanthana) was also used as a catalyst for the development of mesopores in ACs. The La_2O_3 was introduced into the carbon precursor is the same manner as for Ce_xO_y (***section 4.3***), as a nitrate salt ($La(NO_3)_3.6H_2O$). In the opening discussion of this chapter, it was noted that both Ln oxides (Ln_xO_y, where Ln is La or Ce) were introduced into either VBC or AC-90 prior to steam activation, at a loading of 3 wt% on a metal loading basis. After steam activation, La_2O_3 was removed by washing with concentrated H_2SO_4 using the same protocol as was used for acid washing of the Ce-meACs. The nomenclature used for naming the La-meACs was the same as the Ce-meACs, and is outlined in ***section 4.2*** (***Table 4-1***).

4.4.1 Composition of Lanthana Catalysed Activated Carbons

The composition of the catalytically and non-catalytically steam activated carbons for the lanthana catalysed meACs were investigated using elemental (Vario MICRO cube, Elementar) and ash analysis (Mettler Toledo, TGA/DSC 1). This was undertaken both prior to and subsequent to the acid washing to remove the lanthana catalyst, the results of which are presented in ***Table 4-7***, compared to AC-90 for benchmarking.

Table 4-7 *~ Composition of La_2O_3 Catalysed Steam Activated meACs*

Sample	Yield (wt%)	Elemental Analysis (wt%, dafb)				H/C Ratio	Ash (wt%)
		C	H	N	O		
VBC	-	61.4	4.4	0.6	33.5	0.86	0.4
AC-90	43.4	82.2	1.3	0.7	15.7	0.19	6.4
AC-La3-90	42.5	74.7	1.4	0.8	23.1	0.22	9.1
AC-La3-90-AW	-	87.8	1.5	1.0	9.7	0.20	0.9
AC-90-La3-90	31.5	82.9	1.1	0.8	15.1	0.16	8.2
AC-90-La3-90-AW	-	85.5	1.7	0.8	12.0	0.23	0.3

There is little change in either the nitrogen or hydrogen content for the La-meACs, regardless of activation process or whether or not they had been acid washed. Interestingly the level of ash observed after acid washing for both the AC-La3-90 and AC-90-La3-90 decreased remarkably to < 1 wt%. Such a significant decrease in the ash content was not observed for the Ce-meAC

series, implying that the acid washing protocol was much more efficient for the solubilisation of La_2O_3 than it was at solubilising CeO_2 (***Table 4-2***).

Another interesting result was the significant decrease in the bulk oxygen content of AC-La3-90-AW compared to its unwashed counterpart AC-La3-90 (ΔO_{bulk} = 13 wt%). This was not observed for the acid washing of AC-90-La3-90 (forming AC-90-La3-90-AW), despite an even more significant degree of ash reduction as a result of the acid washing (ΔO_{bulk} = 3 wt%). This would indicate that the oxygen incorporated into the AC-90 (used as the precursor of AC-90-La3-90) was much more stable against the acid washing than the oxygen incorporated into the AC-La3-90 by using VBC as the precursor.

A great deal of variation was observed in the bulk content of the La-meACs relative to AC-90, as a function of both the carbon precursor and acid washing. Decreases in the O content were observed as a result of acid washing, with profound decreases in the bulk ash content, to level close to VBC itself. That is the say that not only was the La_2O_3 phase removed, but the majority of the ash from the produced material as well.

4.4.2 Surface Chemistry of Lanthana Catalysed Activated Carbons

4.4.2.1 X-ray Photoelectron Spectroscopy (XPS)

The XPS analyses of the La-meACs were carried out in an analogous manner to the Ce-meACs. The high resolution XPS spectra for the C 1s, O 1s and La 3d are presented in ***Figure 4-13*** for the AC-La3-90/AC-La3-90-AW pair, and ***Figure 4-14*** for the AC-90-La3-90/AC-90-La3-90-AW pair. The tabulated peak fitting data is shown in ***Table 4-8***, with peak assignments being made as per the nomenclature outlined in ***section 6.6.2.1***.

Firstly it should be noted that the XPS results show that for both AC-La3-90 (***Figure 4-13***) and AC-90-La3-90 (***Figure 4-14***) that the acid washing removed all detectable La_2O_3 on the surface (***Table 4-8***). This agrees well with the compositional results (***Table 4-7***), showing significantly reduced ash content, implying that remaining ash is free of La_2O_3; or that the La_2O_3 that remains is not located on the surface but deep within the pore structure (***section 6.6.2.1***).

Interestingly both La-meACs showed an increase in the peak area of the carbonyl peak and a decrease in that of the C-O-R peak as a result of the acid washing. The shift in both peak areas correlated well to one another, suggesting a possible relationship between to two group types. Under the highly acid conditions of the acid removal ether formation is possible, through a hemiacetal intermediate [47]; further study would however be required to confirm both the relationship and mechanisms involved. Moreover, for the acid washed La-meACs the C 1s to O

1s ratio of the ether/hydroxyl peaks possess a 2:1 ratio, this in itself is indicative of the presence of ether groups.

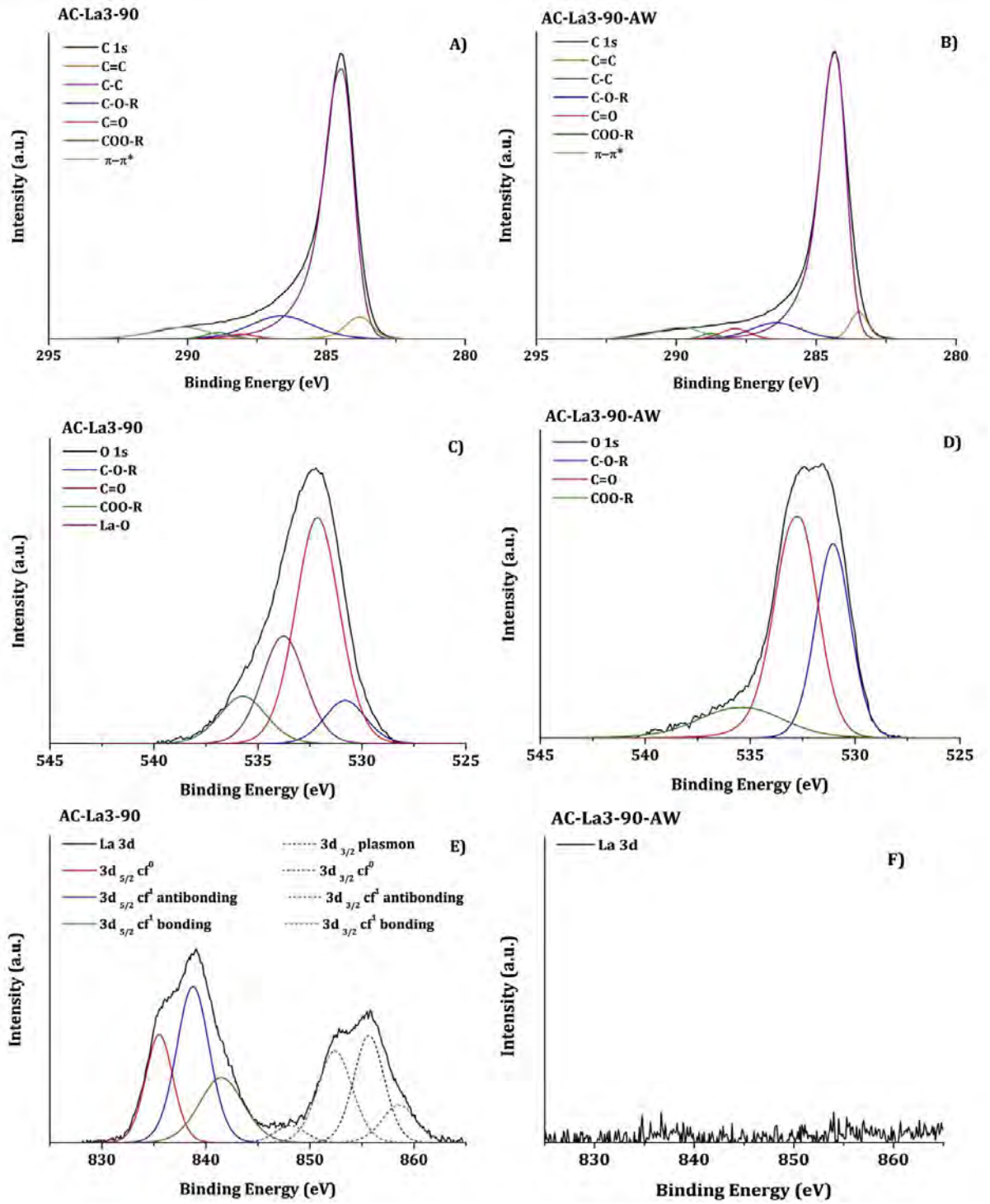

Figure 4-13 ~ *High Resolution XPS Spectra of C 1s, O 1s and La 3d for AC-La3-90 and AC-La3-90-AW. Shown are* ***A)*** *C 1s Spectra of AC-La3-90,* ***B)*** *C 1s Spectra of AC-La3-90-AW,* ***C)*** *O 1s Spectra of AC-La3-90,* ***D)*** *O 1s Spectra of AC-La3-90-AW,* ***E)*** *La 3d Spectra of AC-La3-90, and* ***F)*** *La 3d Spectra of AC-90-La3-90-AW*

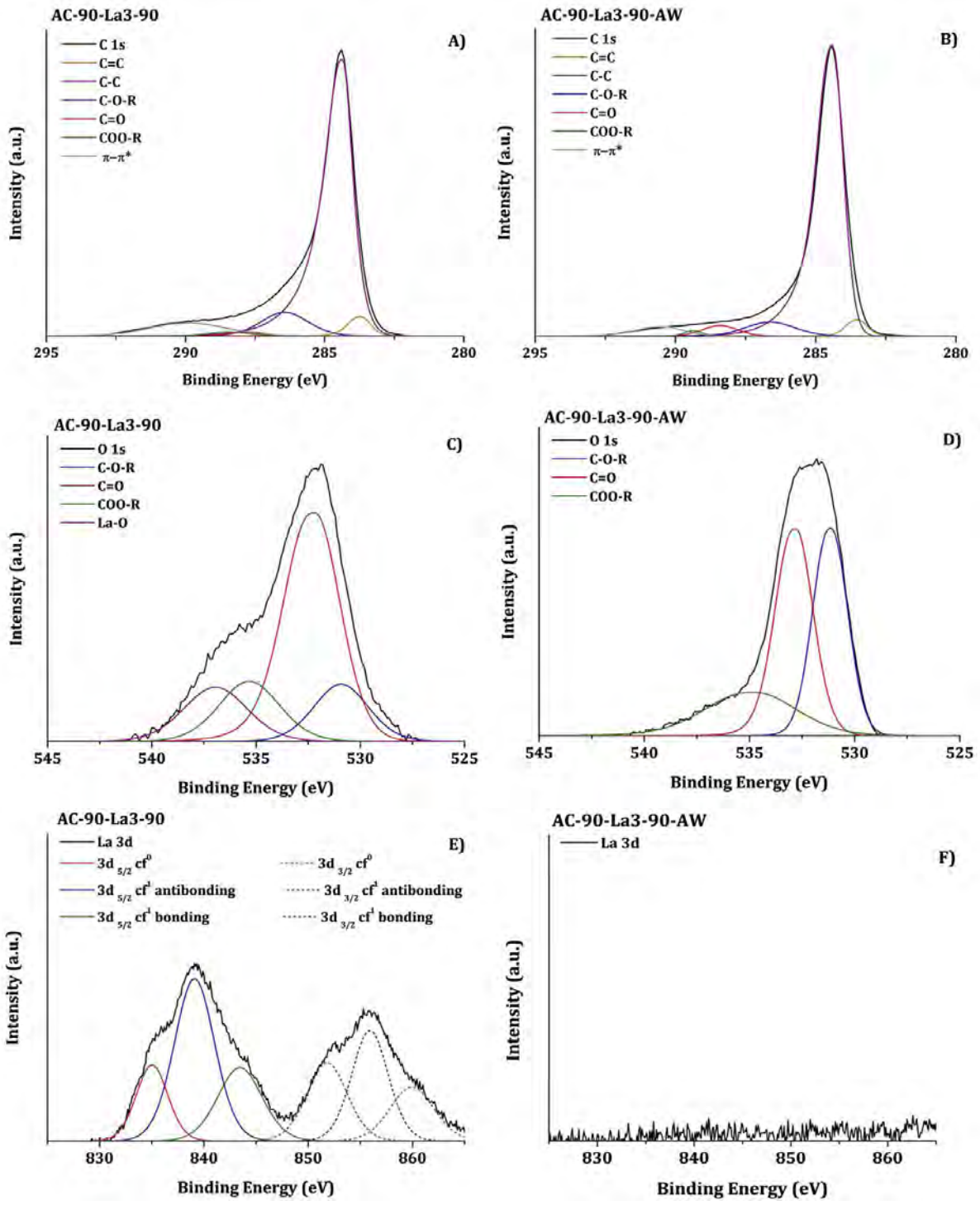

Figure 4-14 ~ *High Resolution XPS Spectra of C 1s, O 1s and La 3d for AC-90-La3-90 and AC-90-La3-90-AW. Shown are* ***A)*** *C 1s Spectra of AC-90-La3-90,* ***B)*** *C 1s Spectra of AC-90-La3-90-AW,* ***C)*** *O 1s Spectra of AC-90-La3-90,* ***D)*** *O 1s Spectra of AC-90-La3-90-AW,* ***E)*** *La 3d Spectra of AC-90-La3-90, and* ***F)*** *La 3d of AC-90-La3-90-AW*

Table 4-8 *~ XPS Peak Fitting for La_2O_3 Catalysed Physically Activated Carbons*

Peak Assignment	Binding Energy (eV)	Surface Concentration (at%)				
		AC-90	AC-La3-90	AC-La3-90-AW	AC-90-La3-90	AC-90-La3-90-AW
C 1s	284.0	90.16	88.01	92.90	90.65	92.93
C=C	283.6	6.04	4.37	4.16	3.37	2.33
C-C	284.4	68.28	66.18	73.38	69.18	76.58
C-O-R	286.3	8.48	10.39	7.07	8.32	5.69
C=O	288.3	2.80	0.98	2.56	1.05	2.54
COO-R	289.2	1.56	1.21	0.93	1.24	1.57
π-π^*	290.2	3.00	4.87	4.79	7.48	4.22
O 1s	532.0	9.16	9.84	6.71	7.52	6.87
C=O	531.4	2.96	0.94	2.39	1.01	2.58
C-O-R	532.8	4.60	5.27	3.43	4.22	2.87
COO-R	534.7	1.59	1.17	0.90	1.18	1.43
La-O	529.7	-	2.46	0.00	1.11	0.00
N 1s	400.0	0.68	0.65	0.39	1.06	0.20
La 3d	853.0	-	1.50	0.00	0.77	0.00
$3d_{5/2}$ cf^0	835.5	-	0.23	0.00	0.09	0.00
$3d_{5/2}$ cf^1 antibonding	838.8	-	0.40	0.00	0.23	0.00
$3d_{5/2}$ cf^1 bonding	841.5	-	0.22	0.00	0.12	0.00
$3d_{3/2}$ cf^0	852.4	-	0.25	0.00	0.11	0.00
$3d_{3/2}$ cf^1 antibonding	855.7	-	0.26	0.00	0.14	0.00
$3d_{3/2}$ cf^1 bonding	858.6	-	0.10	0.00	0.08	0.00
$3d_{3/2}$ plasmon	848.1	-	0.04	0.00	0.00	0.00

As has been previously noted for most of the ACs presented in this thesis, for the La-meACs the C 1s to O 1s ratio of the peak areas of the COO-R peak is approximately 1:1; which would suggest that anhydrides are possibly present in addition to surface carboxylic acid groups.

All in all the acid washing of the La-meACs resulted in an increase in the surface C concentration and a decrease in the surface O, as would be expected from the removal of the La_2O_3 phase, exposing more of the AC surface in the process.

4.4.2.2 Near Edge X-ray Absorption Fine Structure (NEXAFS) Spectroscopy

Both oxygen and carbon K-edge NEXAFS spectra of the acid washed La catalysed physically ACs were taken on the soft x-ray (SXR) beamline at the Australian Synchrotron (AS), Victoria, Australia. As was the case for the Ce-meACs, only the acid washed La-meACs were studied by NEXAFS spectroscopy due to constraints on the beam time available. The details under which all spectra were collected and processed can be found in ***section 6.6.2.2*** and the NEXAFS spectra are presented in ***Figure 4-15*** and the results of the peak fitting of both C 1s and O 1s spectra are reported in ***Table 4-9***. The complete fitting for both the C 1s and O 1s spectra can be found in ***Appendix 2 – NEXAFS Spectroscopy Peak Fitting***, for all of the carbon materials investigated.

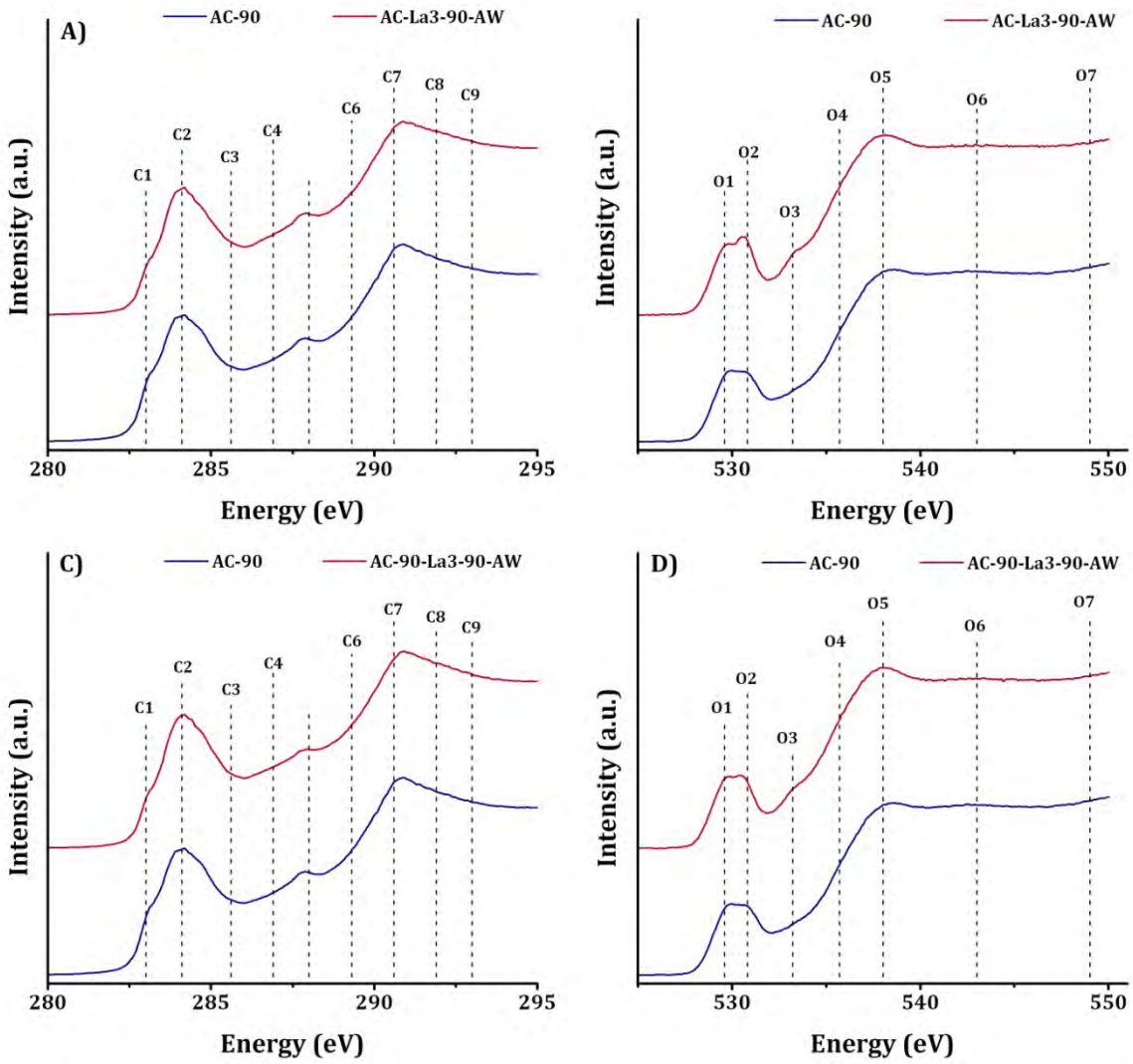

Figure 4-15 ~ *C 1s and O 1s K-edge NEXAFS Spectra of AC-90, AC-La3-90-AW & AC-90-La3-90-AW. Shown are* ***A)*** *C 1s K Edge NEXAFS Spectra of AC-90 & AC-La3-90-AW,* ***B)*** *O 1s K Edge NEXAFS Spectra of AC-90 & AC-La3-90-AW,* ***C)*** *C 1s K Edge NEXAFS Spectra of AC-90 & AC-90-La3-90-AW,* ***D)*** *O 1s K Edge NEXAFS Spectra of AC-90 & AC-90-La3-90-AW*

Table 4-9 *~ C 1s & O 1s K Edge NEXAFS Peak Fitting of AC-La3-90-AW & AC-90-La3-90-AW*

K Edge	Name	Group		Assignment	Photon Energy (eV)	Peak Area %		
						AC-90	AC-La3-90-AW	AC-90-La3-90-AW
C 1s	C1	C=O	π*	Carbonyl substituted aromatic carbon (quinone)	283.0	1.1	1.5	1.4
	C2	C-C C=C	π*	Aromatic carbon, or aliphatic substituted aromatic carbon	284.1	31.3	27.7	28.5
	C3	C-OH C=O	π*	Phenol or ketone substituted aromatic carbon	285.6	8.5	14.1	14.3
	C4	COOH COO	π*	Carboxylic acid substituted aliphatic carbon (lactone)	286.9	11.2	8.8	8.8
	C5	C-O-C	π*	Cyclic ether carbon	288.0	13.3	9.3	8.7
	C6	C-OH C=O	π*	Aldhyde or hydroxyl substituted aliphatic carbon	289.3	10.5	15.2	15.9
	C7	COOH	σ*	Carboxylic acid substituted aromatic carbon	290.6	15.2	10.8	10.8
	C8	C-O-C	σ*	Cyclic ether carbon	291.9	6.4	10.0	10.4
	C9	C-C C=C	σ*	Aromatic carbon (long range order)	293.0	2.5	2.5	2.4
O 1s	O1	C=O	π*	Aliphatic (linear or cyclic) aldehyde oxygen	529.6	6.4	8.8	7.9
	O2	C=O	π*	ketonic oxygen	530.8	16.5	8.1	8.5
	O3	C-O-C	π*	Aliphatic cyclic ether	532.7	16.4	6.4	5.7
	O4	C-OH	π*	Hydroxyl oxygen (alcohol)	535.7	24.6	39.6	39.0
	O5	C-OH C=O	σ*	Hydroxyl or carbonyl oxygen of carboxylic acid	538.0	17.0	8.5	10.9
	O6	C-O-C	σ*	Aromatic cyclic ether	543.0	14.7	2.5	2.0
	O7	C-OH	σ*	Phenolic oxygen	549.8	4.5	26.1	26.1

From the peak fitting of the C 1s and O 1s NEXAFS spectra (***Figure 4-15***) of AC-La3-90-AW and AC-90-La3-90-AW in ***Table 4-9***, a very minor increase can be seen in the ***C2*** peak of AC-90-La3-90-AW relative to AC-La3-90-AW. Furthermore, no change of any consequence was observed for the ***C9*** peak, meaning that, in addition to the similarities in the aromatic nature of the carbon surface, the long range order of these carbons also possessed a great deal of similarity.

The decrease observed in the comparison of the XPS analysis (***Table 4-8***) of AC-90-La3-90-AW to AC-La3-90-AW with respect to the C-O-R peak was mirrored in both the C 1s and O 1s

NEXAFS of the two La meACs. This was expressed as a decrease in both the ***C5*** and ***O3*** peaks, assigned to aliphatic ethers.

Furthermore, the increases in the COO-R peak seen from the XPS analysis of AC-90-La3-90-AW as compared to that of AC-La3-90-AW was also detected in the O 1s NEXAFS spectra (***O5***) of the two carbons, but not in the C 1s NEXAFS spectra (***C4*** or ***C7***). It is difficult to gain further insight as to the nature of this change, as no respective change in the C 1s NEXAFS was observed, nor have any similar observations been reported in the literature. As such further identification of these groups as carboxylic acids or lactones was not pursued.

As was the case for the Ce-meACs (***section 4.3.2.2***), the ether peaks from the C 1s (***C5***) and O 1s (***O3*** and ***O6***) NEXAFS showed a significant decrease, with a consequent increase C 1s (***C3*** and ***C6***) and O 1s (***O4*** and ***O7***) in hydroxyl peaks. The shift towards a surface with a higher concentration of hydroxyl groups should increase the affinity of the AC surface for PEI, particularly at higher temperatures [23].

To summarise the NEXAFS spectroscopy was successfully used to expand on the investigation of the surface chemistry by XPS, allowing for further identification of the C=O, C-O-R and COO-R groups. These were found to be due to ketones, aldehydes, ethers, hydroxyls and carboxylic acids, with a much higher proportion of hydroxyl groups than was observed for the miACs, which is expected to increase the affinity of the surface for both CO_2 and PEI.

4.4.3 Structure of Lanthana Catalysed Activated Carbons

Similarly to the Ce-meACs, gas physisorption, transmission electron microscopy (TEM), x-ray diffraction (XRD) and Raman spectroscopy were also employed to characterise the structural features of the La-meACs.

4.4.3.1 Chemical Structure of Lanthana Catalysed Activated Carbons

4.4.3.1.1 Raman Spectroscopy

The Raman spectra for the La-meACs were collected, processed and analysed in the same manner used for the Ce-meACs (***section 4.3.3.1.1***). The deconvoluted, peak-fitted spectra are shown in ***Figure 4-16*** and the corresponding peak data are presented in ***Table 4-10***.

The acid washing of AC-La3-90 (resulting in AC-La3-90-AW) resulted in similar changes to the meAC as was observed for the AC-Ce3-90/AC-Ce3-90 pair (***Table 4-5***). That is to say that although differences were observed between the peak area of the ***S*** and ***D*** peaks, there was no

significant change in the combined area of the ***S*** and ***D*** peaks. This was the result of the removal of the La_2O_3 phase, thus exposing both the graphene layer edges (***D*** peak) and the hetero-atoms bound to it (***S*** peak). Additionally acid attack on the graphene layer edges will have acted to induce new chemical functionality, resulting in an increase in the ***S*** peak area. Furthermore, the removal of the La_2O_3 from the AC-La3-90 also resulted in an increase in the amount of graphitic layers (***G*** peak) previously covered by the La_2O_3.

The decrease in the amorphous phase (***A*** peak) observed from the acid washing of the AC-La3-90 was not due to an actual decrease in the amorphous carbon on the surface, but to the increase in other groups, previously covered by the La_2O_3 phase.

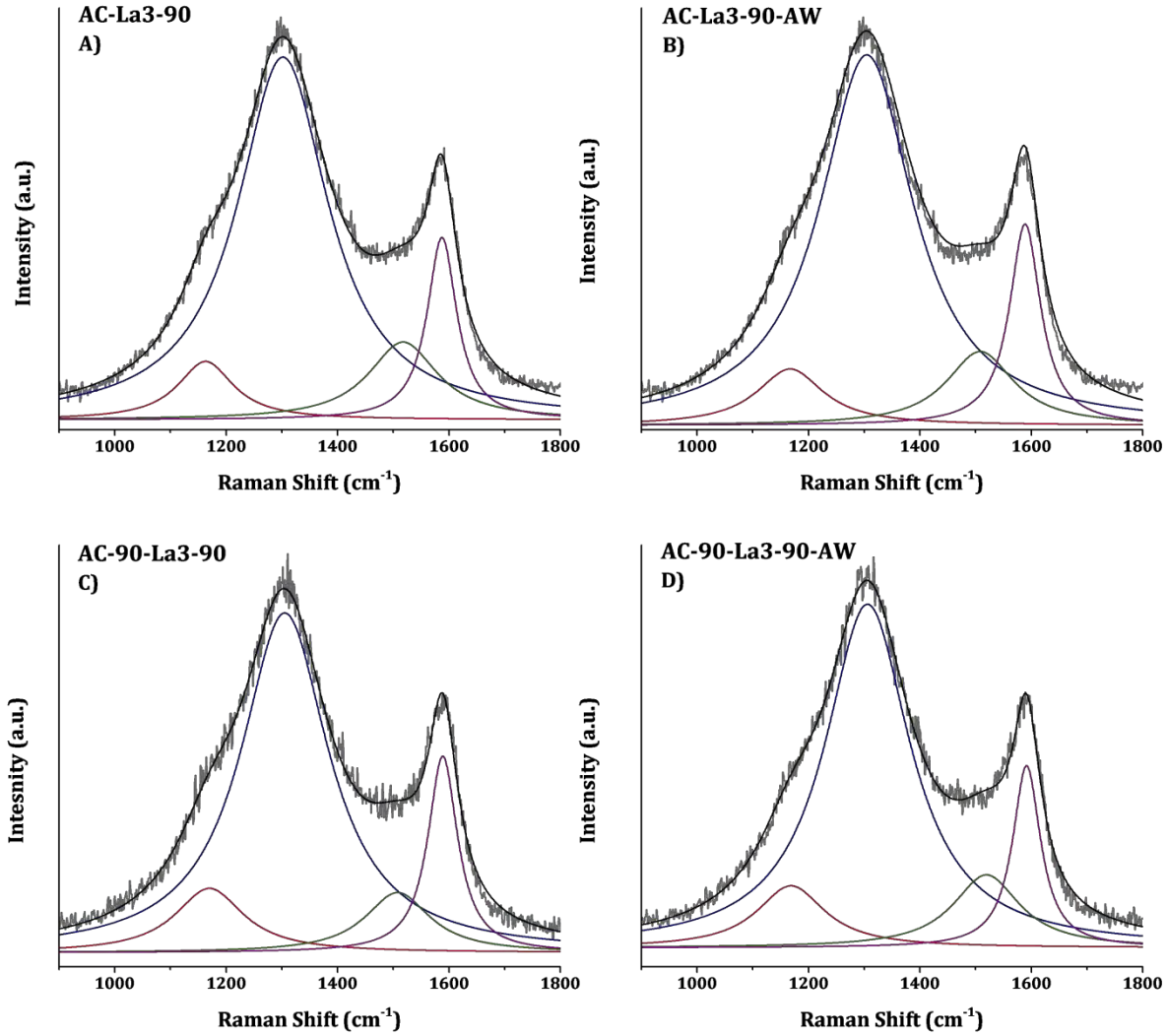

Figure 4-16 *~ Raman Spectra of Lanthanum (3 wt% La) Catalysed Physically ACs. Shown are the peaks for the (—) Normalised Data, (—) Sum of Deconvoluted Peaks, (—) S band, (—) D band, (—) A band, (—) G band,* ***A)*** *AC-La3-90,* ***B)*** *AC-La3-90-AW,* ***C)*** *AC-90-La3-90, and* ***D)*** *AC-90-La3-90-AW*

Interestingly the changes that were observed as a result of acid washing of the AC-90-La3-90, were opposite to those observed from the acid washing of AC-La3-90 (***Table 4-10***). This does despite first appearances make sense. From the XPS peak fitting for AC-90-La3-90 (***Table 4-8***) it could be seen that the surface concentration of La was half that of AC-La3-90. As half the amount of La (in the form of La_2O_3) was present on AC-90-La3-90 than on AC-La3-90, only half the amount of La_2O_3 was present on the surface to react with the H_2SO_4. This being the case, more of the meAC surface reacted with the H_2SO_4 and thus more of the meAC surface will have been degraded. The degradation of the surface will have occurred via acid attack of the graphene layer edges, both ordered and disordered alike (i.e. reduction in the area of the ***S***, ***D*** and ***G*** peaks).

The overall changes in the order of the carbon chemical structure that were detectable by Raman spectroscopy for the La-meACs were relatively small both as a function of starting material and a function of acid washing.

Table 4-10 ~ *Raman Peak Fitting Data for Lanthana Catalysed Physically Activated Carbons*

Sample Name	Peak Area			
	S	D	A	G
	Disordered Graphitic Lattice*	Disordered Graphitic Lattice†	Amorphous Carbon	Ideal Graphitic Lattice
AC-90	11.7	62.4	12.7	13.0
AC-La3-90	6.9	70.0	11.5	11.4
AC-La3-90-AW	7.6	69.6	10.1	12.6
AC-90-La3-90	10.1	67.6	8.9	13.2
AC-90-La3-90-AW	9.7	67.2	11.2	11.7

* *Heteroatoms Bound to Graphene Layer Edges*

† *Graphene Layer Edges*

4.4.3.1.2 Powder X-Ray Diffraction (PXRD)

The x-ray diffraction (XRD) pattern of the La-meACs we taken prior to and subsequent to acid washing. Due to the separate nature of the different catalysts used for mesopore development, the spectra have been separated on this basis. A Lanthanum reference was run that was produced from the same La precursor as was used in the La-meACs, treated under the same thermal and oxidative conditions as the La-meACs (***section 6.6.3.1.2***), this is shown below in

Figure 4-17, with the XRD spectra of the La-meACs are presented in ***Figure 4-18***, overlayed with that of AC-90 for benchmarking purposes.

The La reference material showed incomplete oxidation to La_2O_3, with a $La(OH)_3$ phase also being present (***Figure 4-17***). Interestingly, the XRD pattern of AC-La3-90 (***Figure 4-18A***) exhibits reflections that correlate with the La_2O_3 diffraction pattern only; whilst AC-90-La3-90 (***Figure 4-18B***) exhibits reflections correlating to both the La_2O_3 and $La(OH)_3$ diffraction patterns. This would indicate that AC-La3-90 possesses only a La_2O_3 phase, whilst AC-90-La3-90 possesses both a La_2O_3 and $La(OH)_3$ phase. From the XPS of AC-90-La3-90 (***Table 4-8***) there was no evidence of an $La(OH)_3$ phase, which may only indicate that the $La(OH)_3$ phase identified by XRD was not present at the surface of AC-90-La3-90 in sufficient quantities to be detected by XPS. Furthermore, for AC-90-La3-90 the peaks were much broader than observed for AC-La3-90, which strongly indicates that the La_2O_3 and $La(OH)_3$ phases were more amorphous than the La_2O_3 phase of AC-La3-90. The situation becomes more complicated where both La_2O_3 and $La(OH)_3$ phases are present, as many of the reflections observed in the diffraction pattern of each overlap with one another [48].

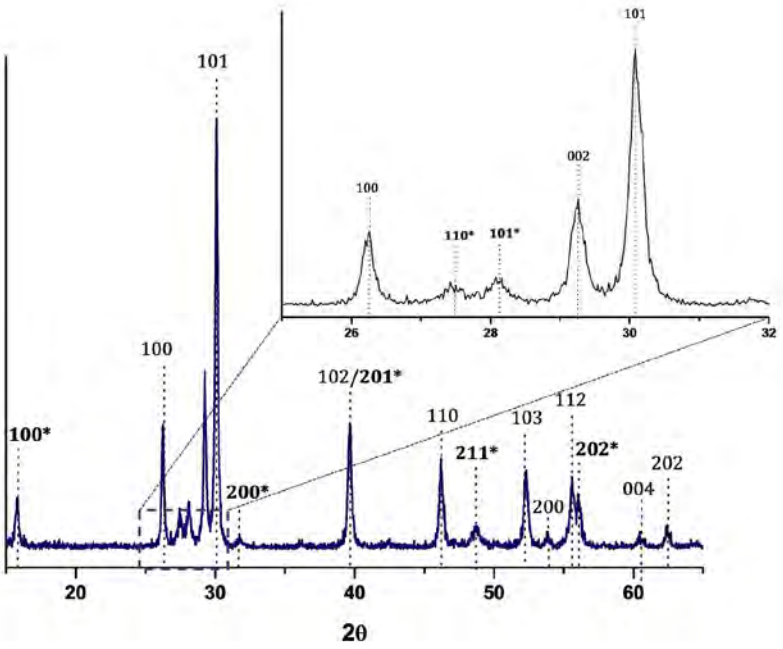

Figure 4-17 ~ *X-ray Diffraction Pattern of the Lanthanum Reference, shown the both La_2O_3 and $La(OH)_3$ phases. The $La(OH)_3$ phase diffraction pattern is denoted by * after the peak assignment*

The XRD pattern of both the acid washed La-meACs were very similar AC-90, with no peaks other that those observed in the AC-90 are present. This does not necessarily indicate complete

removal of the La_2O_3 and $La(OH)_3$ phases from the meAC, but it does suggest a high degree of its removal, in agreement with the XPS data for the acid washed La-meACs (***Table 4-8***). This was also the case for the Ce-meACs, with two major broad peaks being observed for the carbon phase of the La-meACs was attributed to the ***002*** and ***10*** reflections (24° and 43° 2θ, respectively). The ***002*** reflection indicating well structured graphitic domains, with the ***10*** peak (***100*** and ***101*** overlapping peaks) due to lateral order within the graphitic domains [30-35]. There was no observable change in the intensity of the ***10*** reflection of the acid washed La-meACs relative to AC-90, however, small increases in the intensity of the ***002*** reflection were observed, possibly suggesting some small increase in the number of graphitic domains in the acid washed La-meACs. Additionally, a peak was present at 27 2θ°, denoted as the ***MO*** peak, arising from the diffraction of x-rays by amorphous metal oxides. This peak has been observed in the diffraction pattern of most ACs produced in this thesis, and is particularly prominent in the diffraction pattern of AC-90.

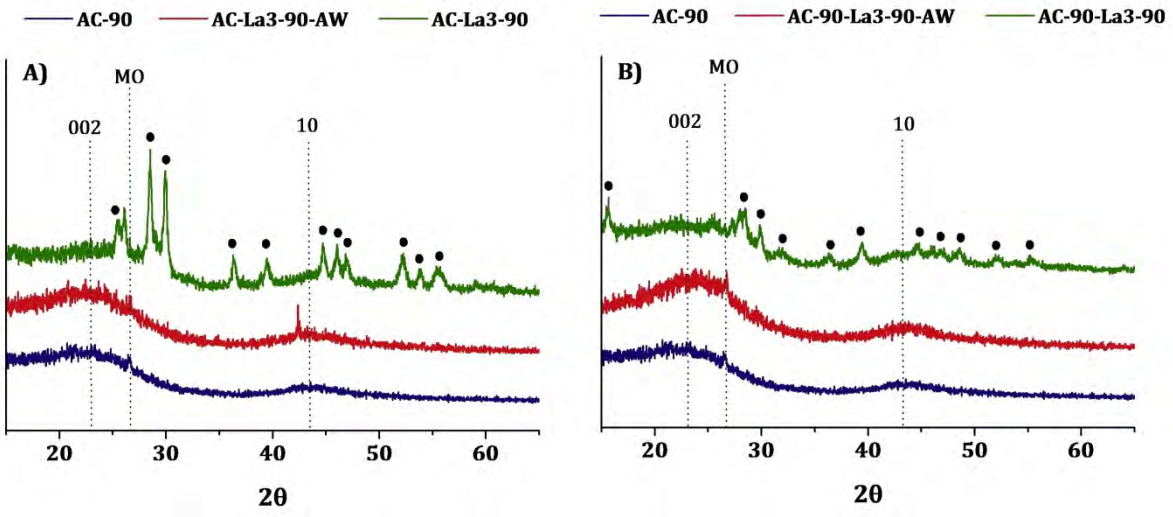

Figure 4-18 ~ *X-ray Diffraction Pattern of La_2O_3 Catalysed Physically Activated Carbons. Shown are the XRD Patterns Highlighting the 002, 10 and MO Peaks for the AC Phase and the Peaks for the $La_2O_3/La(OH)_3$ Phases (●) for* ***A)*** *AC-90, AC-La3-90 and AC-La3-90-AW, and* ***B)*** *AC-90, AC-90-La3-90 and AC-90-La3-90-AW*

In summation there are clearly defined AC and $La_2O_3/La(OH)_3$ phases present in the La-meAC composite materials. However, once acid washing had been undertaken, no identifiable La_2O_3 or $La(OH)_3$ phases were detected, leaving on an AC phase with an XRD pattern that was essentially identical to AC-90.

4.4.3.2 Physical Structure of Lanthana Catalysed Activated Carbons

4.4.3.2.1 Gas Physisorption

The surface area and porosity of each AC was determined from the adsorption isotherms of N_2 and CO_2 at 77 and 273 K respectively. The details outlining the analysis conditions used to obtain the isotherms by the adsorption of the aforementioned gases onto the physically activated meACs can be found in ***section 6.6.3.2.1***, in addition to the models and equations used for data analysis. The surface morphology of the La-meACs before and after catalyst removal are shown in ***Table 4-11***.

CO_2 Physisorption

The CO_2 adsorption isotherms taken at 273 K for the La-meACs were carried out on a TriStar II 3020 instruments (Micromeritics), over a relative pressure range of 0-0.03. The CO_2 isotherms for AC-La3-90, AC-La3-90-AW, AC-90-La3-90 and AC-90-La3-90-AW are presented in ***Figure 4-19***. The DR-derived surface areas and micropore volumes calculated (***equation 6-1***) from these isotherms are given in ***Table 4-11***.

Table 4-11 ~ *Surface Morphology of La_2O_3 Catalysed Steam Activated meACs*

Sample Name	Surface Area (m^2/g)		Pore Volume (cm^3/g)				True Density (g/cm^3)
	CO_2	N_2	CO_2	N_2			
	DR	BET	V_{micro}	V_{micro}	V_{meso}	V_{total}	
VBC	148	-	0.05	-	-	-	1.40
AC-90	696	397	0.23	0.20	0.13	0.24	1.90
AC-La3-90	634	426	0.21	0.23	0.14	0.31	2.05
AC-La3-90-AW	664	329	0.22	0.18	0.09	0.24	1.83
AC-90-La3-90	727	545	0.24	0.29	0.24	0.40	2.04
AC-90-La3-90-AW	666	396	0.22	0.21	0.14	0.30	1.75

From the CO_2 physisorption study of the AC-La3-90/AC-La3-90-AW pair (***Figure 4-19A***) it can be seen that both the meACs possess similar micropore volumes, both to each other and to AC-90 (***Table 4-11***). This indicates that either the La_2O_3 phase possessed very little microporosity, or that the micropore volume of the acid washed meAC was remarkably similar to that of the "as

produced" La-meAC. Moreover, the CO_2 isotherms for both AC-La3-90 and AC-La3-90-AW were quite similar across the whole relative pressure range tested (***Figure 4-19A***).

The effect that acid washing had on the La-meACs was much more pronounced from the CO_2 isotherms of the AC-90-La3-90/AC-90-La3-90-AW pair (***Figure 4-19B***) than it was for the AC-La3-90/AC-La3-90-AW pair (***Figure 4-19A***). However, the observed differences in the CO_2 isotherms were predominately at higher relative pressures ($P/P_o > 0.01$), as such much less significant differences were observed in micropore volumes determined (***Table 4-11***). Moreover, the small degree of variation in the micropore volumes calculated for the AC-90-La3-90/AC-90-La3-90-AW pair was strong evidence that the La_2O_3 phase present within these La-meACs possessed few micropores. This was in good agreement with the CO_2 physisorption results for the AC-La3-90/AC-La3-90-AW pair, with little change in the micropore volume as a result of acid washing to remove the La_2O_3 phase.

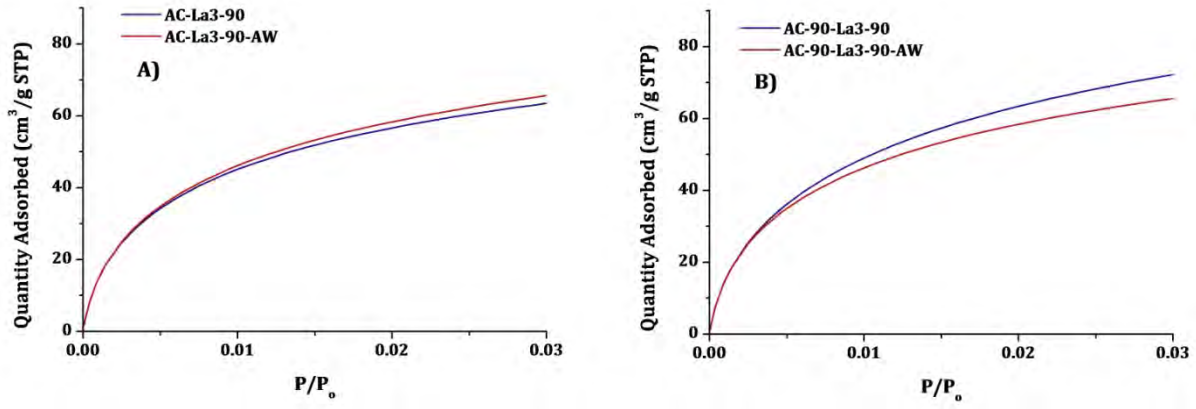

Figure 4-19 ~ *CO_2 Adsorption Isotherms taken at 273 K for the La_2O_3 Physically Activated Carbons. Shown are the isotherms for* ***A)*** *AC-La3-90 and AC-La3-90-AW, and* ***B)*** *AC-90-La3-90 and AC-90-La3-90-AW*

It is also important to keep in mind that as AC-90-La3-90 (and AC-90-La3-90-AW) were produced using AC-90 as the parent carbon, which itself possessed a much more well developed pore structure, which would have allowed for a greater dispersion of the La_2O_3 phase across both the micro- and mesopore region. As such pore blockage would be less likely to occur than in the VBC derived AC-La3-90 and AC-La3-90-AW, as the VBC parent carbon possessed no discernible well developed pore structure.

N_2 Physisorption

The N_2 adsorption-desorption isotherms taken at 77 K for the La-meACs and their acid washed counterparts were taken over a P/P_0 range of 0-0.95, from which PSDs were determined using the BJH method are shown in ***Figure 4-20***. The BET surface areas and mesopore volumes being given in ***Table 4-11***, along with the limiting micropore volumes calculated using the DR equation (***section 6.6.3.2.1***).

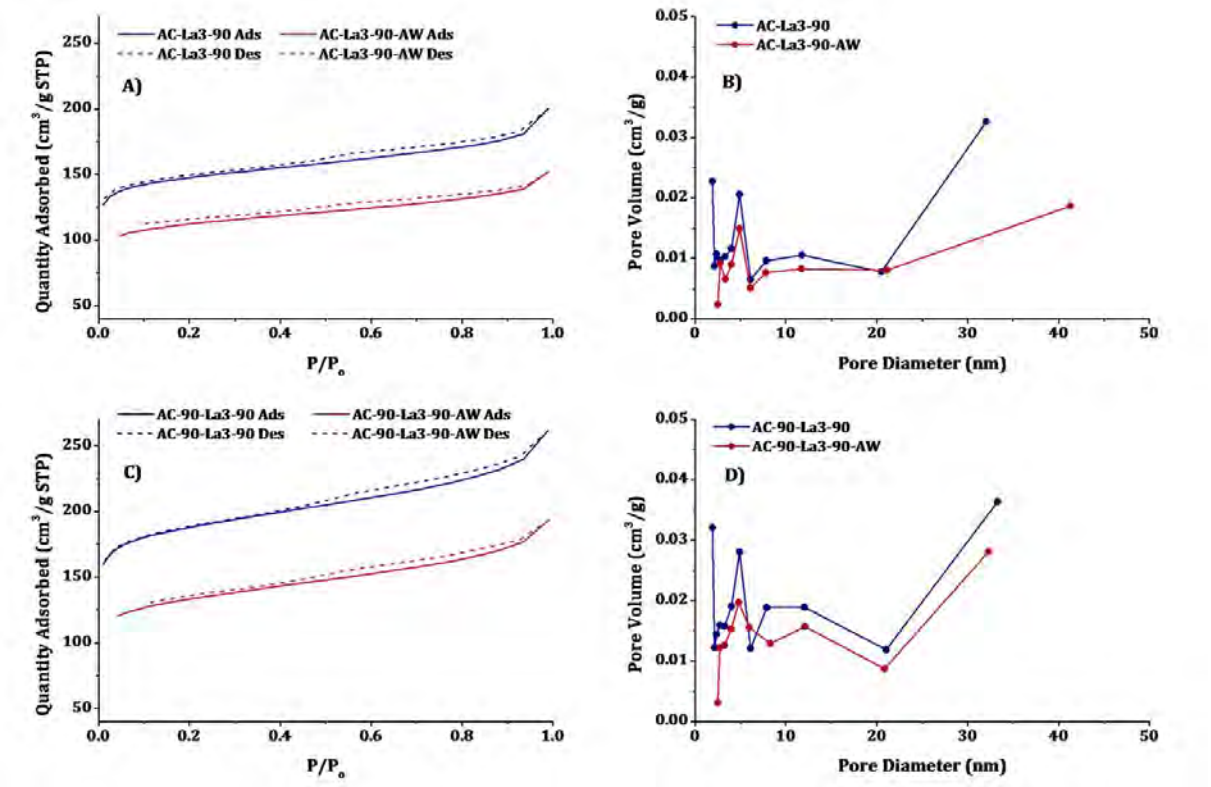

Figure 4-20 ***~*** *N_2 Adsorption Isotherms PSDs at 77 K for La Catalysed Steam Activated meACs. Shown are the* ***A)*** *Isotherms for AC-La3-90 and AC-La3-90-AW,* ***B)*** *PSDs for AC-La3-90 and AC-La3-90-AW,* ***C)*** *Isotherms for AC-90-La3-90 and AC-90-La3-90-AW, and* ***D)*** *PSDs for AC-90-La3-90 and AC-90-La3-90-AW*

Discrepancies were observed between the CO_2 and N_2 physisorption data obtained for the La-meACs with respect to the micropore volumes determined from the physisorption data, similarly to that observed for the Ce-meACs. This can again be the result of one or all of the three main potential phenomena that can cause such discrepancies to arise. Briefly, this can be caused by interactions between the surface of the AC with CO_2 due to aspects of the surface chemistry that do not affect the adsorption of N_2; by the differences in the relative pressure ranges investigated for each adsorbate; or by steric hindrances of N_2 by micropores with very

small pore diameters (i.e. ultramicropores and supermicropores [39]). Regardless of the discrepancies between the results from the two adsorbates, it is clear that overall the La-meACs possessed larger micropore volumes compared to their analogous Ce-meACs (AC-Ce3-90/AC-Ce3-90-AW and AC-90-Ce3-90/AC-90-Ce3-90-AW).

The N_2 isotherms of the La-meACs exhibited type ***IV*** isotherms with ***H4*** hysteresis loops, which is consistent with similar observations made for the Ce-meACs (***Figure 4-8***). The hysteresis loops of the AC-La3-90 and AC-90-La3-90 isotherms achieved complete closure, which was also observed for the "as produced" Ce-meACs. Conversely, the acid washed La-meACs never fully achieved closure of their hysteresis loops, again this was also observed for the acid washed Ce-meACs. In the case of the Ce-meACs this adsorption behaviour was attributed to LPH, resulting from equilibrium not being achieved between the adsorbate and adsorbent over the micropore region [36-38].

Furthermore, the effect that acid washing had on the N_2 adsorption and mesopore volumes, was to significantly reduce both. This implies that a high proportion of the mesoporosity in the "as produced" samples was due to the La_2O_3 phase itself, as mentioned in the CO_2 adsorption section. It should also be noted that the total pore volume (combined micro- and mesopore volumes) were the largest of all ACs presented in this thesis.

The PSDs of the La-meACs are a continuum; as such there was no clear distinction between micro- and mesopore regions. For AC-La3-90 and AC-90-La3-90 as the PSDs approached the lower pore diameters a clear increase was observed in micropore volume. For both the acid washed La-meACs the pore volume increased less at smaller pore diameters than was observed for the "as produced" La-meACs. This was due to low relative pressures not being able to be obtained for the acid washed La-meACs compared to that achieved for the "as produced" La-meACs. Furthermore, the increase in pore volume with increasing pore diameter for AC-La3-90 was not mirrored for AC-La3-90-AW. However, for the AC-90-La3-90/AC-90-La3-90-AW pair, an increase in pore volume was observed with increasing pore diameter for both ACs. As previously mentioned this has been mostly attributed to the removal of the La_2O_3 phase, which possessed its own inherent porosity in addition to taking up pore volume prior to its removal.

In short, the use of La_2O_3 as a catalyst in the physical activation of VBC in an analogous manner to AC-90 was unsuccessful, resulting in an AC with less developed micro- and mesopore volumes. The La-meACs did possess a higher ratio of micro- to mesopore volume than AC-90, however, the total mesopore volumes were only slightly higher for both the "as produced" and acid washed La-meACs than AC-90 (***Table 4-11***).

4.4.3.2.2 Transmission Electron Microscopy (TEM)

In order to observe futher details of the physical structure of the La-meACs, TEM was undertaken on the La-meACs and their acid washed countparts. This was carried out on an JEOL 2100F FEGTEM microscope in addition to elemental mapping of C, O and La by EDX. The micrographs and mapping for AC-La3-90, AC-La3-90-AW, AC-90-La3-90 and AC-90-La3-90-AW are presented in ***Figure 4-21***-***Figure 4-24***, respectively.

The TEM micrograph of AC-La3-90 (***Figure 4-21A***) showed it to be significantly amorphous, interlaced with La_2O_3 particles. The La_2O_3 particles were clearly differentiated by the striated structure of the particles, as compared to the CeO_2 particles, that possessed a more of mesh-like architecture. From the La L edge elemental mapping of AC-La3-90, it can be seen that the La is well dispersed throughout the particle being investigated. Moreover, the La_2O_3 particles can be seen to be concentrated within the particle as bright areas, which are presumably located within the pore structure of the La-meAC particle (***Figure 4-21B***). Additionally, the bright areas observed from the La 3d mapping of AC-La3-90 have analogous areas in the O K edge mapping of AC-La3-90 (***Figure 4-21C***). These analogous areas between the mapping of the O K edge and La L edge are a strong indication of the presence of La_xO_y, most likely present as La_2O_3.

Acid washing of AC-La3-90 resulted in a meAC (AC-La3-90-AW) that showed little visual signs of a La_2O_3 phase (TEM micrograph, ***Figure 4-22***). The highly amorphous structure exhibited by AC-La3-90-AW possessed no ordered graphitic domains, nor La_2O_3 crystallites. However, the elemental mapping of AC-La3-90-AW showed that some La still remained (***Figure 4-22E***). The amount of La remaining was small, as can be seen by the intensity of La for the particle relative to that of the background (***Figure 4-22E***). The background intensity of La shown for AC-La3-90-AW (***Figure 4-22E***) is significantly higher than observed for AC-La3-90 (***Figure 4-21E***). Despite the lack of observable graphitic domains, some ordering of the graphitic layer edges was observed around the edges of the meAC particles.

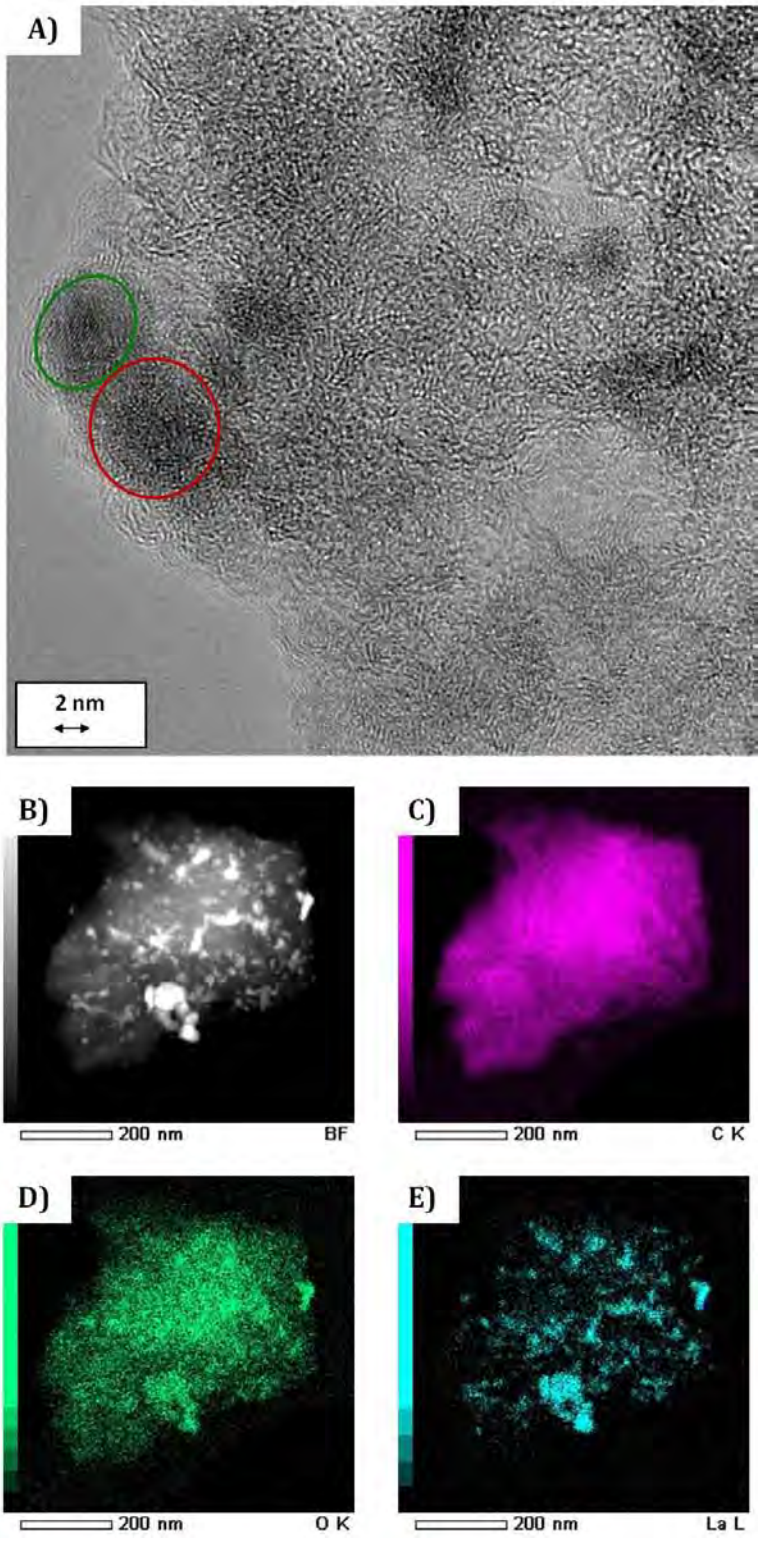

Figure 4-21 *~ Transmission Electron Micrograph and Elemental Mapping of La Catalysed Physically Activated meAC AC-La3-90. Shown is* ***A)*** *High Magnification Electron Micrograph, La_2O_3 particles (○ , ○),* ***B)*** *Bright Field Image of Mapped Particle,* ***C)*** *EDX Mapping of the C K-edge,* ***D)*** *EDX Mapping of the O K-edge, and* ***E)*** *EDX Mapping of the La L-edge*

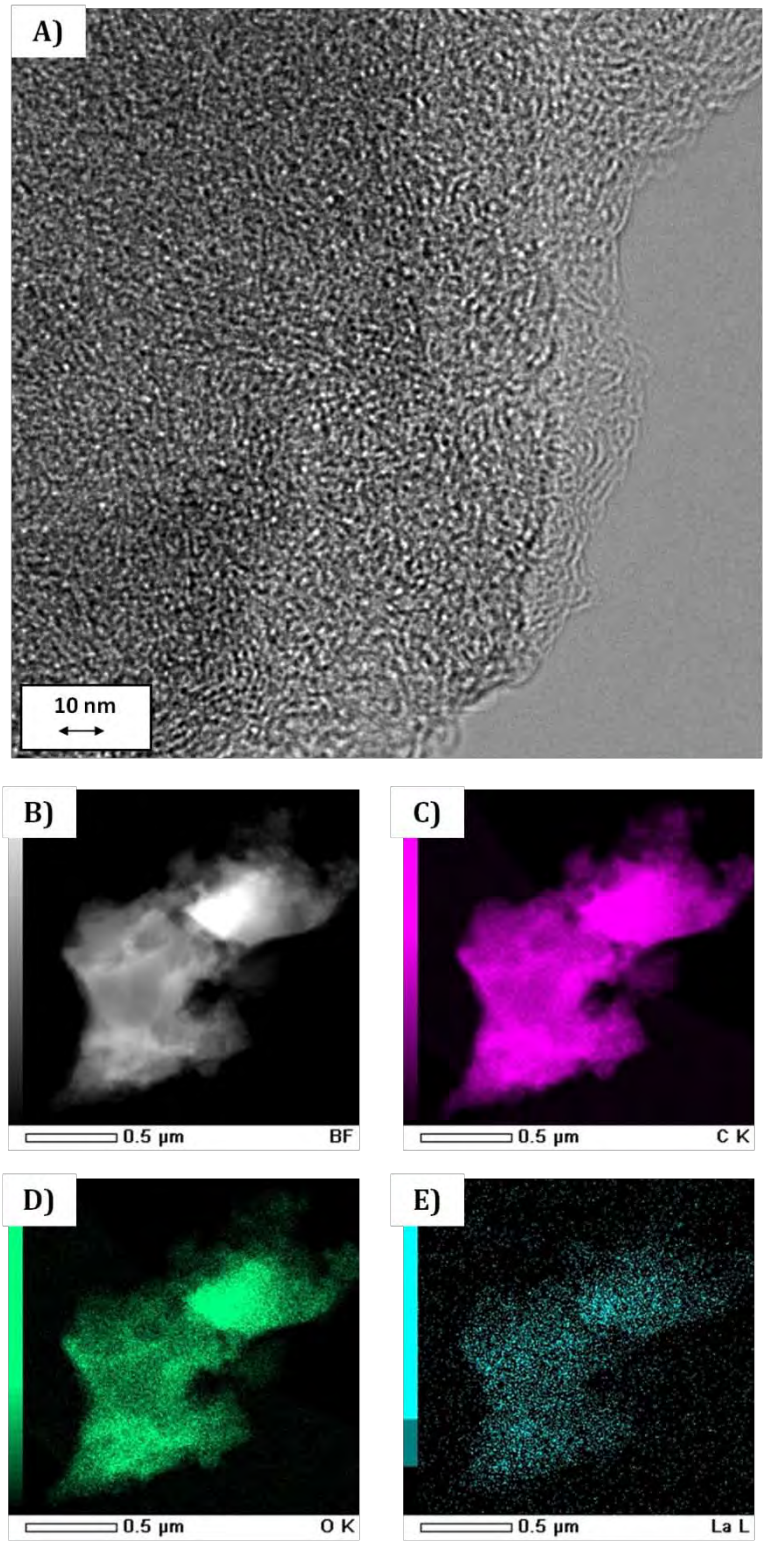

Figure 4-22 ~ *Transmission Electron Micrograph and Elemental Mapping of La Catalysed Physically Activated meAC AC-La3-90-AW. Shown is* ***A)*** *High Magnification Electron Micrograph,* ***B)*** *Bright Field Image of Mapped Particle,* ***C)*** *EDX Mapping of the C K-edge,* ***D)*** *EDX Mapping of the O K-edge, and* ***E)*** *EDX Mapping of the La L-edge*

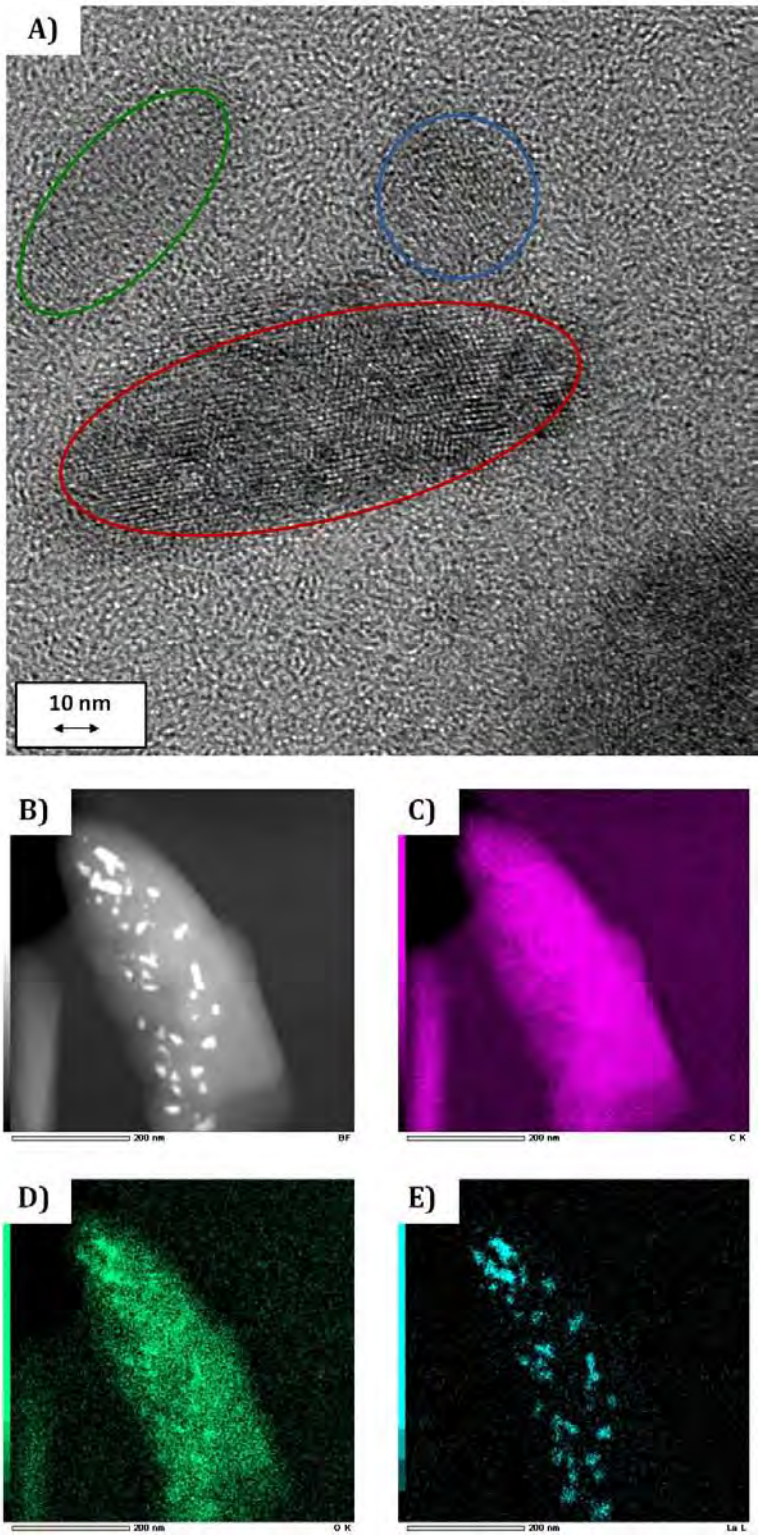

Figure 4-23 *~ Transmission Electron Micrograph and Elemental Mapping of La Catalysed Physically Activated meAC AC-90-La3-90. Shown is* ***A)*** *High Magnification Electron Micrograph, La_2O_3 particles (◯,◯,◯),* ***B)*** *Bright Field Image of Mapped Particle,* ***C)*** *EDX Mapping of the C K-edge,* ***D)*** *EDX Mapping of the O K-edge, and* ***E)*** *EDX Mapping of the La L-edge*

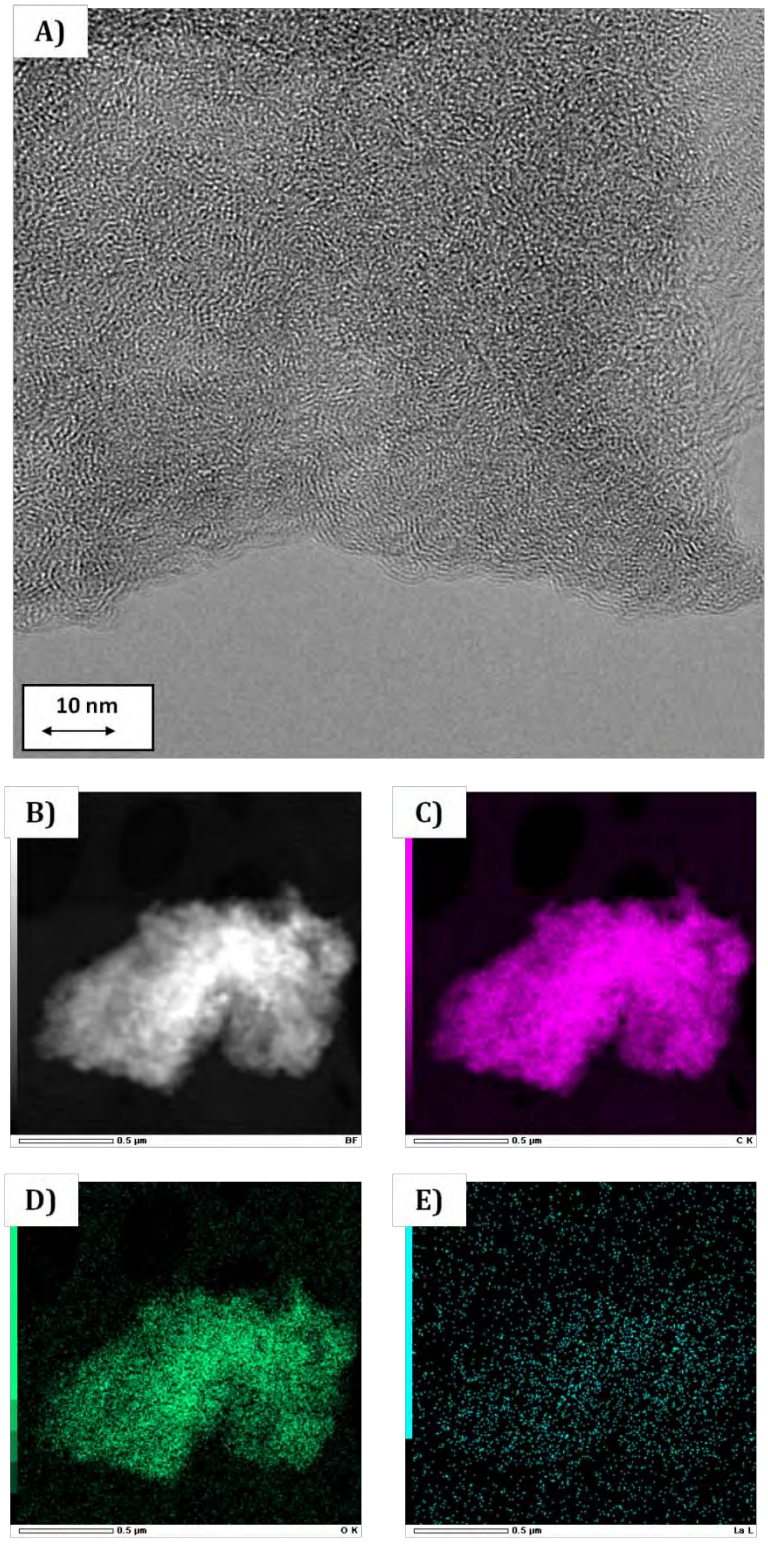

Figure 4-24 ~ *Transmission Electron Micrograph and Elemental Mapping of La Catalysed Physically Activated meAC AC-90-La3-90-AW. Shown is* ***A)*** *High Magnification Electron Micrograph,* ***B)*** *Bright Field Image of Mapped Particle,* ***C)*** *EDX Mapping of the C K-edge,* ***D)*** *EDX Mapping of the O K-edge, and* ***E)*** *EDX Mapping of the La L-edge*

The TEM micrograph of AC-90-La3-90 (***Figure 4-23***) shows a meAC with much greater La density than that of AC-La3-90, the distribution of La_2O_3 particles is less diffuse and the particles more strongly entrenched into the meAC structure. Upon mapping AC-90-La3-90 it can be seen that the La_2O_3 is much more concentrated within the particle structure. This was also observed from the TEM analysis of AC-90-Ce3-90 (***Figure 4-11***), in both cases this is attributed to the fact that the precursor was an AC, not the VBC and as such had already had a well defined pore structure into which the metal salts could be impregnated. As was also observed for AC-La3-90 (***Figure 4-21***), the TEM of AC-90-La3-90 showed strong concentrations of La_2O_3 particles from the bright field image in ***Figure 4-23B***. Moreover, the bright spots observed in ***Figure 4-23B*** correlate well to concentrations of particles in the O K and La L edge mapping (***Figure 4-23C*** and ***Figure 4-23D***, respectively).

The TEM micrograph of AC-90-La3-90-AW showed good similarity to its unwashed counterpart (AC-90-La3-90, ***Figure 4-23***) in that it possessed a condensed highly amorphous carbon phase, with no visible signs of graphitic domains. Furthermore, the mapping of AC-90-La3-90-AW revealed an ever weaker signal for La that was observed for AC-La3-90-AW (***Figure 4-22***), indicating a higher degree of removal of the La_2O_3 phase.

Overall, the TEM investigation of the La-meACs showed meACs with no significant well structured carbon domains. Of the few structural features that were observed for the La-meACs, most were due to the La_2O_3 phase and not the carbon itself. This is particularly apparent for the acid washed meACs, with no clearly observable structural features whatsoever.

4.4.4 Summary

For the "as produced" (non-acid washed) La-meACs derived from both VBC and AC-90 (AC-La3-90 and AC-90-La3-90, respectively) exhibited substantial differences in the yield of La-meAC produced. A lower yield was obtained for AC-90-La3-90 compared to AC-La3-90 is of little surprise, as the same result was obtained for the Ce-meACs, being attributed to the reactive nature of AC-90, having already had most of the volatile matter already removed. The bulk C content of AC-90-La3-90 was higher than AC-La3-90 by 8.2 wt%, whilst the bulk O of AC-90-La3-90 is lower than that of AC-La3-90 by 8.0 wt%. For both the "as produced" La-meACs, acid washing resulted in an increase in the bulk C and massive decrease in the ash content. Along with the increases in the bulk C content of AC-90-La3-90 relative to AC-La3-90, there was an increase in the surface concentration of C of AC-90-La3-90, relative to AC-La3-90. Although the overall surface O concentration was observed to decrease as a result of acid washing, this was predominately due to the removal of the La_2O_3 phase from the surface of the La-meACs (XPS,

Table 4-8). Furthermore, the C-O-R groups were determined by XPS to by the most prominent functional group on the surface of both the "as produced" and acid washed La-meACs. Further investigation of the C-O-R groups observed from the XPS analysis of the La-meACs by NEXAFS spectroscopy (***Table 4-9***), elucidated that the groups assigned to the C-O-R groups were predominately due to hydroxyl groups. The increase in the distribution of hydroxyl groups as determined by NEXAFS spectroscopy for the La-meACs relative to AC-90 showed there was significant increase in the ***C3***, ***C6***, ***O4*** and ***O7*** peaks, all of which are assigned to hydroxyl groups (***Table 4-9***), as was the case with the NEXAFS investigation of the Ce-meACs (***Table 4-4***) relative to AC-90. In addition to the changes observed for the C-O-R groups as a result of the acid washing of the La-meACs, there were significant increases in the surface concentration of C=O groups (XPS, ***Table 4-8***). Further investigation by NEXAFS spectroscopy as to the distribution of functional groups assigned to the C=O group from XPS, found that there was a relatively even distribution of ketones and aldehydes (***O1*** and ***O2*** peaks, ***Table 4-9***).

The Raman spectroscopy of the La-meACs (***Table 4-10***) showed that AC-90-La3-90 possessed 30% higher peak area for the ***S*** peak and a 3% lower peak area of the ***D*** peak, relative to AC-La3-90. For AC-90-La3-90 there was also a decrease in the peak area of the ***A*** peak, with an associated increase in the peak area of the ***G*** peak relative to AC-La3-90, suggesting an overall increase in the order of the chemical structure of the carbon as a result of using AC-90 as the parent carbon over VBC. It may seem somewhat irrelevant to point out the changes in the chemical structure of the "as produced" La-meACs, rather than for the acid washed La-meACs. However, despite the changes in bulk and surface C as a result of acid washing, there were no significant changes in the chemical structure of either La-meAC as a result of acid washing, at least not from the Raman spectroscopy. Moreover, as was the case with the Ce-meACs (***Figure 4-6***), the XRD patterns of the La-meACs (***Figure 4-18***) showed that the only major difference between the "as produced" and acid washed La-meACs was the lack of any distinguishable diffraction pattern for an La_2O_3/$La(OH)_3$ phases. Other than the evidence from the bulk and surface composition, and XRD patterns suggesting significant removal of the La_2O_3/$La(OH)_3$ phases, TEM also strongly suggested this to be the case (***Figure 4-21-Figure 4-24***). This was both observable from the TEM images themselves as well as the EDX elemental mapping for the La 3d edge (***Figure 4-21-Figure 4-24***). Although an $La(OH)_3$ phase was observed for AC-90-La3-90, this phase is unlikely to interact with the CO_2 during the adsorption studies as no evidence of this phase was observed by XPS and as such it is not present in sufficient amounts at the surface to interact with CO_2. The observation of an $La(OH)_3$ phase is indicative of incomplete oxidation of the La precursor salt, and as this was only observed for AC-90-La3-90; which from the TEM was shown to possess a highly segregated La_2O_3 phase. As AC-La3-90 possessed a well distributed La_2O_3 phase with no evidence of a $La(OH)_3$ phase, which would indicate that the

presence of an $La(OH)_3$ phase in AC-90-La3-90 was due to incomplete oxidation of the La salt at the centre of the La_2O_3 phase.

In addition to higher bulk and surface C for AC-90-La3-90 relative to AC-La3-90, higher volumes for micro- and mesopores were also observed (ΔV_{micro} = 0.05 cm^3/g and ΔV_{meso} = 0.10 cm^3/g). The differences in pore volume between AC-La3-90 and AC-90-La3-90 became much more substantial upon acid washing, and thus removal of the La_2O_3 phase from the meAC (***Table 4-11***). AC-La3-90-AW possessed a slightly higher micropore volume than AC-La3-90 (ΔV_{micro} = 0.01 cm^3/g), as a result of acid washing. Whereas the mesopore volume of AC-La3-90-AW had decreased by a third, compared to AC-La3-90 (ΔV_{meso} = 0.03 cm^3/g). The changes in pore volume for AC-90-La3-90-AW as a result of the acid washing were significantly greater than those observed for the AC-La3-90/AC-La3-90-AW pair. The decreases in pore volume for both sets of La-meACs as a result of the acid washing has been attributed to a loss in pore volume possessed by the La_2O_3 phase, and to an actual decrease in the pore volume of the meACs themselves. This was also the case for the Ce-meACs, however, in the case of the La-meACs acid washing also resulted in considerable decrease in the ash content of the meACs. This could potentially have resulted in some of the pore structure having also collapsed, as the ash could have been well ingrained into the carbon structure.

The use of La_2O_3 in the catalysed physical activation of VBC and AC-90 resulted in meACs that possessed a higher ratio of mesopores to micropores, but were inferior in many respects to AC-90. The surface chemistry was shown to potentially possess similar attributes that could make them well suited for PEI impregnation, however, due to the lower than desired mesopore volumes their usefulness as support materials may show to outweigh any advantages. How these meACs fare in the separation of CO_2 from flue gas stream will be the focus of the following chapter (***chapter 5***), as both acid washed meACs and as supports for PEI impregnation.

4.5 Amine Modified Activated Carbons

Amine-modification of solid adsorbents has been shown to significantly increase the selectivity of adsorbents towards CO_2. However, many mesoporous adsorbents commonly used (e.g. SBA-15, MCM-41) are likely to be costly to produce on a large scale. As such the use of coal derived ACs with a reasonable degree of mesoporosity may enable such amine-modified adsorbents to be more industrially viable.

Unlike their silica analogues, the meACs produced in this work possess significantly lower mesopore volumes. This has been attributed to the semi-rigid structure of brown coal, and an

inability to truly drive the formation of mesopores without over gasifying the parent material to produce something akin to fly ash.

Several ACs produced in this work (AC-90, AC-Ce3-90-AW, AC-90-Ce3-90-AW, AC-La3-90-AW and AC-90-La3-90-AW) were identified as potential candidates to be used as supports for impregnation with an amine-based polymer, PEI.

4.5.1 Amine-modification of Activated Carbons

The full details of the modification procedure used can be found in ***section 6.5***. Briefly, the ACs selected for impregnation with PEI (AC-90, AC-Ce3-90-AW, AC-90-Ce3-90-AW, AC-La3-90-AW and AC-90-La3-90-AW) were dispersed in methanol (MeOH), then mixed with a PEI-MeOH solution via sonication at ambient temperature for 2 h. The MeOH was then removed via rotary evaporation and the PEI-AC composites dried in a vacuum oven at 333 K for 48 h to remove any volatile low molecular weight PEI. The PEI loading was done on a 90% pore volume basis, and the samples were given the suffix 90PEI-R prior to the vacuum treatment and 90PEI-VT after the vacuum treatment.

4.5.2 Composition of Amine Modified Activated Carbons

The compositions of the PEI-AC materials are presented in ***Table 4-12***. Both the elemental and ash contents were determined using the same methods used elsewhere in this thesis (CHN and TGA respectively). In addition to the elemental composition and ash content of these materials, those of their non-modified counterparts are also presented in ***Table 4-12***. The most important feature of ***Table 4-12***, is the nitrogen content of the PEI loaded ACs and their non-modified counter parts. Particular attention should also be focused on the second column of nitrogen data for the PEI-AC composites. This value is the "adjusted nitrogen" (N*), which takes into account the nitrogen already present in the parent AC (prior to PEI impregnation). This is calculated by subtracting the nitrogen present in the support carbon from the PEI-AC, such that only the nitrogen introduced as a result of the PEI impregnation is determined. The importance of this value will become apparent later (***section 5.6.2***), as it allows for the *"amine efficiency"* to be determined according to ***equation 6-10*** (***section 6.6.4***).

The most important thing to make note of regarding the compositional results of the PEI-AC composites and their supports (***Table 4-12***) are the changes in the nitrogen (both absolute and adjusted) and hydrogen content. Both nitrogen and hydrogen significantly increased with PEI loading, however, the true indication of the increase in nitrogen as a result of PEI impregnation

is also shown in ***Table 4-12*** as the "adjusted nitrogen" concentration. Furthermore, as the nitrogen and hydrogen content had increased through the impregnation of PEI, consequent decreases in carbon, oxygen and ash contents would be expected. This is indeed what is observed, however, no actual change in the elemental composition of the support carbons has actually occurred. It is also interesting to note the difference in bulk N between AC-90-90PEI-R and AC-90-90PEI-VT, which indicates the degree of PEI loss that has occurred as a result of the vacuum treatment used to remove the low molecular weight PEI.

Table 4-12 ~ *Composition of Amine Modified & Non-modified Activated Carbons*

Sample Name	Elemental Analysis (wt%, dafb)					H:C Ratio	Ash (wt%)
	C	H	N	N*	O_{diff}		
VBC	61.4	4.4	**0.6**	-	33.5	**0.86**	0.4
AC-90	82.2	1.3	**0.7**	-	15.7	0.19	6.4
AC-90-90PEI-R	74.1	4.2	**8.1**	**7.4**	13.4	0.68	3.6
AC-90-90PEI-VT	77.5	3.3	**6.9**	**6.1**	12.3	0.51	3.6
AC-Ce3-90-AW	78.6	1.5	**0.8**	-	19.1	0.23	5.3
AC-Ce3-90-90PEI-VT	77.0	3.1	**5.5**	**4.7**	14.4	0.49	1.5
AC-La3-90-AW	87.8	1.5	**1.0**	-	9.7	0.20	0.9
AC-La3-90-90PEI-VT	80.7	3.6	**7.0**	**6.1**	8.7	0.54	0.5
AC-90-Ce3-90-AW	84.0	1.6	**0.7**	-	13.7	0.23	3.6
AC-90-Ce3-90-90PEI-VT	76.7	4.3	**8.9**	**8.2**	10.1	0.67	1.1
AC-90-La3-90-AW	85.5	1.7	**0.8**	-	12.0	0.23	0.3
AC-90-La3-90-90PEI-VT	79.1	4.0	**7.9**	**7.1**	9.0	0.60	0.0

** Adjusted nitrogen, the nitrogen present within the PEI only*

4.5.3 Structure of Amine Modified Activated Carbons

Due to concerns with the vacuum stability of the PEI loaded ACs, no electron microscopy studies were undertaken to determine their surface morphology. Furthermore, as impregnation with PEI would have had no effect on the AC structure, Raman spectroscopy was not carried out on

the PEI-AC composites. With the above considerations taken into account, gas physisorption was the only technique used for elucidation of the structure of the PEI loaded ACs.

4.5.3.1 Physical Structure of Amine Modified Activated Carbons

4.5.3.1.1 Gas Physisorption

In addition to the above mentioned complications with structure analysis methods only N_2 physisorption was undertaken in order to determine the pore structure of the PEI loaded ACs. The use of CO_2 was avoided as even at 273 K, some chemisorption would inevitably occur, greatly skewing the results. The results for the N_2 physisorption over PEI-AC composite materials at 77 K are presented in and the mesopore and total pore volumes derived from these presented in ***Table 4-13***.

Table 4-13 ~ *Surface Area & Pore Volume of PEI-AC Composites & Their Carbon Supports*

Sample Name	Surface Area (m^2/g)		Pore Volume (cm^3/g)		
	DR_{CO2}	BET_{N2}	V_{micro}	V_{meso}	V_{total}
VBC	148	-	0.05	-	-
AC-90	646	397	0.21	0.13	0.24
AC-90-90PEI-R	-	0.3	-	0.00	0.00
AC-90-90PEI-VT	-	0.3	-	0.00	0.00
AC-Ce3-90-AW	570	300	0.18	0.07	0.19
AC-Ce3-90-90PEI-VT	-	0.2	-	0.00	0.00
AC-La3-90-AW	655	329	0.21	0.09	0.24
AC-La3-90-90PEI-VT	-	0.0	-	0.00	0.00
AC-90-Ce3-90-AW	702	418	0.23	0.16	0.31
AC-90-Ce3-90-90PEI-VT	-	1.1	-	0.00	0.00
AC-90-La3-90-AW	657	396	0.21	0.14	0.30
AC-90-La3-90-90PEI-VT	-	1.2	-	0.00	0.00

The pore morphology of the carbon supports were presented earlier in this chapter, but are presented here again in ***Table 4-13*** for the purpose of comparison. From ***Table 4-13*** it can be seen that upon the introduction of PEI to the carbon support, that both the surface area and pore volume become substantially reduced. Essentially there is no surface area or pore volume remaining in the resulting PEI-AC composites. Since the carbon supports were impregnated with PEI on a 90% pore filling basis, this is in line with expectations.

4.6 Chapter Summary and Closing Remarks

In this chapter it was shown that ACs possessing desirable pore characteristics were able to be produced from VBC and AC-90. This was accomplished through the use of lanthanide (Ln) oxides (Ln_xO_y, where Ln is Ce and La) to catalyse the partial oxidation reactions responsible for pore development. Furthermore, methods were developed for the removal of the lanthanide oxides, without severe degradation to the structure of the carbons themselves, something that has never been reported in the literature [8, 40]. In the closing discussion to this chapter, the primary focus will be on the comparison of the physicochemical characteristics of the acid washed CeO_2 and La_2O_3 catalysed physically activated meACs derived from both VBC and AC-90.

Almost all of the acid washed Ln-meACs possessed a bulk C content several percent higher than AC-90, with the sole exception being AC-Ce3-90-AW (***Table 4-14***). On the other hand the bulk O content of the acid washed meACs varied over a range (ΔO_{bulk} =9.5-19.5 wt%) relative to that of AC-90 (O_{bulk} = 15.7 wt%). Interestingly the H/C ratio of the acid washed Ce-meACs (~0.23) show no significant level of variation as a function of which carbon precursor was used. Whilst AC-90-La3-90-AW also possessed a H/C ratio of 0.23, AC-La3-90-AW only possessed a H/C ratio of 0.20 (***Table 4-14***). The surface chemistry of the Ln-meACs showed them to possess surface O concentrations that were lower than AC-90. The decrease in surface O content of the meACs relative to AC-90 by XPS (***Table 4-14***), were attributed to decreases in all major oxygenated functional groups on the AC surface (C=O, C-O-R and COO-R).

The most prominent decreases in the oxygenated functional groups detected by XPS were observed for the C-O-R groups. Interestingly from the NEXAFS spectroscopy investigation of these groups for the Ln-meACs, there was a significant shift in the distribution of both ether and hydroxyl groups relative to that observed for AC-90 (***Table 4-4*** and ***Table 4-9*** for the Ce-meACs and La-meACs, respectively). As such there may have been little overall change in the hydroxyl group content, and thus the decrease in the C-O-R groups from the XPS of these meACs can be mostly attributed to decreases in the ether content of the meAC surface, relative to AC-90. This

potential lack of a change in the hydroxyl group content should act to maintain the strong affinity of the meAC surface to both CO_2 and PEI that was also possessed by AC-90 [12, 13].

Table 4-14 *~ Characterisation Summary Table for meACs and PEI-AC Composites*

Sample	Bulk Composition							Surface Composition			Structural Morphology						
	Elemental Analysis (wt%, daf)					H/C Ratio	Ash (wt%)	Contentration (at%)			Surface Area (m^2/g)		Pore Volume (cm^3/g)				True Density (g/cm^3)
	C	H	N	N*	O_{diff}			C	O	N	DR	BET	V_{micro} CO_2	V_{micro} N_2	V_{meso}	V_{total}	
VCB	61.4	4.4	0.6	-	33.5	0.86	0.4	-	-	-	148	-	0.05		-	-	1.40
AC-90	82.2	1.3	0.7	-	15.7	0.19	6.4	90.2	9.2	0.7	696	397	0.23	0.20	0.13	0.24	1.90
AC-Ce3-90	81.6	1.1	1.1	-	16.3	0.16	9.2	91.1	7.9	0.5	614	450	0.20	0.23	0.16	0.32	1.92
AC-Ce3-90-AW	78.6	1.5	0.8	-	19.1	0.23	5.3	91.7	7.6	0.6	616	300	0.20	0.17	0.07	0.19	1.77
AC-90-Ce3-90	74.5	1.3	0.7	-	23.5	0.21	11.8	91.7	6.8	0.9	792	458	0.26	0.24	0.16	0.35	2.03
AC-90-Ce3-90-AW	84.0	1.6	0.7	-	13.7	0.23	3.6	93.2	6.5	0.4	707	418	0.23	0.22	0.16	0.31	1.82
AC-La3-90	74.7	1.4	0.8	-	23.1	0.22	9.1	88.0	9.8	0.7	634	426	0.21	0.23	0.14	0.31	2.05
AC-La3-90-AW	87.8	1.5	1.0	-	9.7	0.20	0.9	92.9	6.7	0.4	664	329	0.22	0.18	0.09	0.24	1.83
AC-90-La3-90	82.9	1.1	0.8	-	15.1	0.16	8.2	90.7	7.5	1.1	727	545	0.24	0.29	0.24	0.40	2.04
AC-90-La3-90-AW	85.5	1.7	0.8	-	12.0	0.23	0.3	92.9	6.9	0.2	666	396	0.22	0.21	0.14	0.30	1.75
AC-90-90PEI-R	74.1	4.2	8.1	7.4	13.4	0.68	3.6	-	-	-	-	0.3	-	-	0.00	0.00	-
AC-90-90PEI-VT	77.5	3.3	6.9	6.1	12.3	0.51	3.6	-	-	-	-	0.3	-	-	0.00	0.00	-
AC-Ce3-90-90PEI-VT	77.0	3.1	5.5	4.7	14.4	0.49	1.5	-	-	-	-	0.2	-	-	0.00	0.00	-
AC-90-Ce3-90-90PEI-VT	76.7	4.3	8.9	8.2	10.1	0.67	1.1	-	-	-	-	1.1	-	-	0.00	0.00	-
AC-La3-90-90PEI-VT	80.7	3.6	7.0	6.1	8.7	0.54	0.5	-	-	-	-	0.0	-	-	0.00	0.00	-
AC-90-La3-90-90PEI-VT	79.1	4.0	7.9	7.1	9.0	0.60	0.0	-	-	-	-	1.2	-	-	0.00	0.00	-

** Adjusted nitrogen, the nitrogen present within the PEI only*

The decreases in the COO-R peaks showed from the XPS of the Ln-meACs relative to AC-90, was also mirrored in the NEXAFS spectroscopy investigation by decreases in the ***C7*** and ***O5*** peaks (***Table 4-4*** and ***Table 4-9***). This could result from conversion of the carboxylic acid groups to anhydrides, a commonly known reaction to occur between H_2SO_4 and carboxylic acids [49].

For the C=O peaks observed from the XPS investigation of the Ln-meACs there is a great deal of variation in the quantification across both series, although never exceeding the quantity present for AC-90 (***Table 4-8***). From the NEXAFS investigation of AC-90 the distribution of aldehyde and ketone groups (***O1*** and ***O2***, respectively) was shown to favour a higher concentration of ketones on the surface. Conversely in the case of the two 3 wt% loaded Ce-meACs. As these groups exert

the most minor effect on the affinity of the AC surface towards both CO_2 and PEI, the changes in their distribution are not expected to exert any effect of major significance.

The variation in the chemical structure of the Ln-meACs as determined by Raman spectroscopy relative to one another were relatively minor, with the VBC derived La-meACs showing a similar pattern of change in chemical structure as was observed for both the Ce-meACs. On the other hand, the AC-90-La3-90/AC-90-La3-90-AW pair exhibited little change in the amount of disordered graphitic carbon (***S*** and ***D***), whilst exhibiting a decrease in ideal graphitic carbon (***G***) and an increase in amorphous carbon (***A***). This was in with the changes in the chemical structure of the other Ln-meACs as a result of acid washing, being predominately a decrease in amorphous carbon, with an associated increase in disordered graphitic carbon; and no overall change in ideal graphitic carbon. The observed changes in the ***S***, ***D*** and ***A*** peaks from the Raman spectroscopy of the Ln-meACs relative to AC-90, indicate an overall increase in the level of order within the carbon structure of the Ln-meACs relative to AC-90 (***Table 4-5*** and ***Table 4-10***). Similarly, the XRD investigation of the Ln-meACs relative to AC-90 showed only very minor differences, with the meACs possessing slightly elevated ***002*** peaks (***Figure 4-6*** and ***Figure 4-18***), assigned to parallel graphitic domains. The slight increase in the ***002*** peak from XRD is in good agreement with the small increases in the area of the ***D*** peak observed from the Raman spectroscopy of the same meACs. As such, the changes observed in both the Raman spectroscopy and XRD showed an overall increase in the chemical structure of the carbons within the meACs relative to AC-90, as an increase in graphitic domains within the Ln-meACs. Despite the clear results indicating changes in the chemical structure of the acid washed Ln-meACs from Raman spectroscopy and XRD relative to AC-90, no clear visual observations of changes of this type were made from the TEM investigation of these meACs relative to AC-90 (***Figure 4-9-Figure 4-12*** and ***Figure 4-21-Figure 4-24*** for the Ce-meACs and La-meACs, respectively).

The pore structure of the meACs was investigated by gas physisorption using both CO_2 and N_2 gases as adsorbates (refer to ***section 6.6.3.2.1*** for details), the results of which are presented in the ***Table 4-14***. From ***Table 4-14***, it can clearly be seen that the amount of both CO_2 and N_2 physisorbed over the AC-90 derived Ln-meACs was significantly higher than that observed for the VBC derived meACs. Moreover, the increased adsorption of the AC-90 derived Ln-meACs was higher than the VBC derived Ln-meACs regardless of which lanthanide oxide was used as catalyst. This makes a great deal of sense, as the AC-90 derived Ln-meACs had undergone two rounds of activation and, as such, would be expected to possess and more well developed pore structure.

The changes in the CO_2 physisorption from the acid washing of the VBC derived Ln-meACs were relatively minor (***Table 4-14***), and the changes in the micropore volumes determined using this method also showed little variation with acid washing. More substantial changes were observed as a result of acid washing in the N_2 physisorption data of the VBC derived meACs. These changes took on the form of significant decreases in both the micro- and mesopore volumes determined. The decreases in the micropore volume were quite significant, but were substantially smaller than the decreases observed in the mesopore volumes as a result of acid washing. From the TEM-EDX mapping of the "as produced" Ln-meACs the distribution of both lanthanide oxides was shown to be low for the AC-90 derived materials, whilst the lanthanide oxides were shown to be well distributed for both the VBC derived materials (***Figure 4-9-Figure 4-12*** and ***Figure 4-21-Figure 4-24*** for the Ce-meACs and La-meACs, respectively). As such, it can be expected that the removal of the well distributed lanthanide oxides could likely result in some degradation of the pore structure. Furthermore, as is the case for all the "as produced" Ln-meACs, the lanthanide oxide phase will itself exhibit significant porosity, possessing a wide PSD [7, 26, 44-46].

Unlike the VBC derived Ln-meACs, there were quite significant differences between the AC-90 derived meACs depending on which lanthanide oxide was used as the catalyst (***Table 4-14***). For both the AC-90 derived Ln-meACs significant decrease in CO_2 physisorption was observed (relative to AC-90), as such reductions in the surface area and micropore volumes calculated from it were also observed. From the N_2 physisorption data there were almost insignificant decreases in both micro- and mesopore volumes of the AC-90-Ce3-90/AC-90-Ce3-90-AW pair as a result of acid washing. On the other hand the N_2 physisorption data of the AC-90-La3-90/AC-90-La3-90-AW pair indicated that acid washing had a significant affect both the micro- and mesopore volumes (***Table 4-14***). However, both the micro- and mesopore volumes of AC-90-La3-90 determined by N_2 physisorption were the highest for any meAC reported. Even with the significant decreases in pore volume observed, AC-90-La3-90-AW still possessed micro- and mesopore volumes similar to AC-La3-90-AW.

On the basis of the favourable surface chemistry and pore structure of the acid washed Ln-meACs, these Ln-meACs were chosen for further study as carbon supports of PEI. Furthermore, the use of these Ln-meACs allowed for the effect of parent carbon on the capability of the support materials to also be investigated, as well as the effect of which lanthanide oxide was used.

As was noted earlier in this chapter, the loading of PEI into the Ln-meACs was done on a 90 vol%, on a pore loading basis. This was confirmed to have been successful from the substantial decreases in the surface area and pore volume of the PEI-AC composites relative to their AC

supports as determined by N_2 physisorption (***Table 4-14***). Furthermore, substantial increases in the bulk N and H content of the PEI-AC composites were observed relative to their respective Ln-meAC supports, from the CHN analysis of their bulk composition (***Table 4-14***).

In closing ACs were able to be produced with favourable pore structure and surface chemistry for use as supports for PEI. Several of these were chosen for further study and impregnated with PEI on a 90 vol% on a pore filling basis, which was shown to be seemingly successful. In the following chapter (***Chapter 5***) all the lanthanide oxide catalysed physically activated meACs, their acid washed counterparts and the PEI-AC composites were tested for their ability to separate CO_2 from simulated flue gas mixtures using PPSA in the same manner as was conducted in ***Chapter 3***, and outlined in ***section 6.6.4*** of ***Chapter 6***.

4.7 References

1. Gregory, P.K., et al., *Silica/Polyethyleneimine Composite Adsorbent S-PEI for CO_2 Capture by Vacuum Swing Adsorption (VSA)*, in *Recent Advances in Post-Combustion CO_2 Capture Chemistry*2012, American Chemical Society. p. 177-205.
2. Subagyono, D.J.N., et al., *CO2 adsorption by amine modified siliceous mesostructured cellular foam (MCF) in humidified gas.* Microporous and Mesoporous Materials, 2014. **186**: p. 84-93.
3. Yan, X., et al., *Amine-modified mesocellular silica foams for CO2 capture.* Chemical Engineering Journal, 2011. **168**(2): p. 918-924.
4. Gargiulo, N., et al., *Preparation and characterization of polyethylenimine-modified mesoporous silicas as CO_2 sorbents*, in *Studies in Surface Science and Catalysis*2007, Elsevier. p. 1938-1943.
5. Son, W.-J., J.-S. Choi, and W.-S. Ahn, *Adsorptive removal of carbon dioxide using polyethyleneimine-loaded mesoporous silica materials.* Microporous and Mesoporous Materials, 2008. **113**(1-3): p. 31-40.
6. Knowles, G.P., et al., *Amine-functionalised mesoporous silicas as CO_2 adsorbents*, in *Studies in Surface Science and Catalysis*2005, Elsevier. p. 887-896.
7. Shen, W., et al., *Preparation of mesoporous carbon from commercial activated carbon with steam activation in the presence of cerium oxide.* Journal of Colloid and Interface Science, 2003. **264**(2): p. 467-473.
8. Shen, W., et al., *The effect of temperature on the mesopore development in commercial activated carbon by steam activation in the presence of yttrium and cerium oxides.* Colloids and Surfaces A: Physicochemical and Engineering Aspects, 2003. **229**(1-3): p. 55-61.
9. Tamai, H., et al., *Extremely large mesoporous carbon fibers synthesized by the addition of rare earth metal complexes and their unique adsorption behaviors.* Advanced Materials, 1997. **9**(1): p. 55-58.
10. Sastri, V.S., et al., *Introduction*, in *Modern Aspects of Rare Earths and Their Complexes*2003, Elsevier: Amsterdam. p. 1-72.
11. Goertzen, S.L., et al., *Standardization of the Boehm titration. Part I. CO2 expulsion and endpoint determination.* Carbon, 2010. **48**(4): p. 1252-1261.
12. Yang, R.T., *Adsorbents: Fundamentals and Applications*, R.T. Yang, Editor 2003, John Wiley & Sons: New Jersey. p. 79-130.
13. Bandosz, T.J. and C.O. Ania, *Chapter 4 Surface chemistry of activated carbons and its characterization*, in *Interface Science and Technology*, J.B. Teresa, Editor 2006, Elsevier. p. 159-229.
14. Burroughs, P., et al., *Satellite structure in the X-ray photoelectron spectra of some binary and mixed oxides of lanthanum and cerium.* Journal of the Chemical Society, Dalton Transactions, 1976(17): p. 1686-1698.
15. Bêche, E., et al., *Ce 3d XPS investigation of cerium oxides and mixed cerium oxide (CexTiyOz).* Surface and Interface Analysis, 2008. **40**(3-4): p. 264-267.
16. Zhang, F., et al., *Cerium oxidation state in ceria nanoparticles studied with X-ray photoelectron spectroscopy and absorption near edge spectroscopy.* Surface Science, 2004. **563**(1–3): p. 74-82.
17. Răduţoiu, N. and C.M. Teodorescu, *Satellites in Ce 3d X-ray photoelectron spectroscopy of ceria.* Digest Journal of Nanomaterials and Biostructures, 2013. **8**(4): p. 1535-1549.
18. Pfau, A. and K.D. Schierbaum, *The electronic structure of stoichiometric and reduced CeO2 surfaces: an XPS, UPS and HREELS study.* Surface Science, 1994. **321**(1–2): p. 71-80.
19. Holgado, J.P., R. Alvarez, and G. Munuera, *Study of CeO2 XPS spectra by factor analysis: reduction of CeO2.* Applied Surface Science, 2000. **161**(3–4): p. 301-315.
20. Paparazzo, E., *On the curve-fitting of XPS Ce(3d) spectra of cerium oxides.* Materials Research Bulletin, 2011. **46**(2): p. 323-326.

21. Zhao, J., et al., *Extraction and separation of cerium(IV) from nitric acid solutions containing thorium(IV) and rare earths(III) by DEHEHP.* Journal of Alloys and Compounds, 2004. **374**(1–2): p. 438-441.
22. Bansal, R.C., *Activated Carbon and Its Surface Structure*, in *Activated Carbon Adsorption*2005, CRC Press. p. 1-65.
23. Ma, X., X. Wang, and C. Song, *"Molecular Basket" Sorbents for Separation of CO2 and H2S from Various Gas Streams.* Journal of the American Chemical Society, 2009. **131**(16): p. 5777-5783.
24. Choi, S., J.H. Drese, and C.W. Jones, *Adsorbent materials for carbon dioxide capture from large anthropogenic point sources.* ChemSusChem, 2009. **2**(9): p. 796-854.
25. Long, R.Q., Y.P. Huang, and H.L. Wan, *Surface Oxygen Species Over Cerium Oxide and Their Reactivities with Methane and Ethane by Means ofin situConfocal Microprobe Raman Spectroscopy.* Journal of Raman Spectroscopy, 1997. **28**(1): p. 29-32.
26. Li, S., et al., *Preparation and characterization of three-dimensional ordered macroporous rare earth oxide—CeO2.* Journal of Porous Materials, 2007. **15**(5): p. 589-592.
27. Sadezky, A., et al., *Raman microspectroscopy of soot and related carbonaceous materials: Spectral analysis and structural information.* Carbon, 2005. **43**(8): p. 1731-1742.
28. Gomez-Serrano, V., M. Acedo-Ramos, and A.J. Lopez-Peinado, *Study and Characterisation of Activated Carbon Treated with H2SO4 Solutions.* Journal of Chemical Technology & Biotechnology, 1997. **68**(1): p. 82-88.
29. Gómez-Serrano, V., et al., *Regeneration of activated carbon after contact with sulfuric acid solution.* Journal of Chemical Technology & Biotechnology, 2000. **75**(9): p. 835-839.
30. Bratek, W., et al., *Characteristics of activated carbon prepared from waste PET by carbon dioxide activation.* Journal of Analytical and Applied Pyrolysis, 2013. **100**(0): p. 192-198.
31. Li, Z.Q., et al., *X-ray diffraction patterns of graphite and turbostratic carbon.* Carbon, 2007. **45**(8): p. 1686-1695.
32. Yoshizawa, N., et al., *XRD evaluation of KOH activation process and influence of coal rank.* Fuel, 2002. **81**(13): p. 1717-1722.
33. Skodras, G., et al., *Production of special activated carbon from lignite for environmental purposes.* Fuel Processing Technology, 2002. **77-78**: p. 75-87.
34. Liu, L., et al., *Effect of preparation conditions on the properties of a coal-derived activated carbon honeycomb monolith.* Carbon, 2007. **45**(14): p. 2836-2842.
35. Byrne, C.E. and D.C. Nagle, *Carbonized wood monoliths—Characterization.* Carbon, 1997. **35**(2): p. 267-273.
36. Silvestre-Albero, A.M., et al., *Low-Pressure Hysteresis in Adsorption: An Artifact?* The Journal of Physical Chemistry C, 2012. **116**(31): p. 16652-16655.
37. Silvestre-Albero, J., et al., *High-Resolution N2 Adsorption Isotherms at 77.4 K: Critical Effect of the He Used During Calibration.* The Journal of Physical Chemistry C, 2013. **117**(33): p. 16885-16889.
38. Silvestre-Albero, J., et al., *Physical characterization of activated carbons with narrow microporosity by nitrogen (77.4 K), carbon dioxide (273 K) and argon (87.3 K) adsorption in combination with immersion calorimetry.* Carbon, 2012. **50**(9): p. 3128-3133.
39. Amarasekera, G., M.J. Scarlett, and D.E. Mainwaring, *High-resolution adsorption isotherms of microporous solids.* Journal of Physical Chemistry, 1996. **100**(18): p. 7580-7585.
40. Shen, W., et al., *Preparation of mesoporous activated carbon fiber by steam activation in the presence of cerium oxide and its adsorption of congo red and vitamin B12 from solution.* Journal of Materials Science, 2004. **39**(14): p. 4693-4696.
41. Yoshizawa, N., et al., *XRD evaluation of CO2 activation process of coal- and coconut shell-based carbons.* Fuel, 2000. **79**(12): p. 1461-1466.
42. Yoshizawa, N., et al., *Coal-Based Activated Carbons Prepared with Organometallics and Their Mesoporous Structure.* Energy & Fuels, 1997. **11**(2): p. 327-330.
43. Lowell, S., et al., *Characterization of Porous Solids and Powders: Surface Area, Pore Size and Density*, B. Scarlett, Editor 2004, Springer: Dordrecht. p. p. 13.

44. Thundathil, M.A., et al., *High surface-area ceria aerogel.* Journal of the American Ceramic Society, 2004. **87**(8): p. 1442-1445.
45. Ramos-Fernández, E., et al., *The effect of the cerium precursor and the carbon surface chemistry on the dispersion of ceria on activated carbon.* Journal of Materials Science, 2008. **43**(5): p. 1525-1531.
46. Kamimura, Y., M. Shimomura, and A. Endo, *Simple template-free synthesis of high surface area mesoporous ceria and its new use as a potential adsorbent for carbon dioxide capture.* Journal of Colloid and Interface Science, 2014. **436**: p. 52-62.
47. McMurry, J., *Organic Chemistry*, 2004, Brooks/Cole: CA,USA. p. 703.
48. Aghazadeh, M., et al., *La2O3 nanoplates prepared by heat-treatment of electrochemically grown La(OH)3 nanocapsules from nitrate medium.* Journal of the Electrochemical Society, 2011. **158**(12): p. E136-E141.
49. Welch, C.M. and H.A. Smith, *Reactions of Carboxylic Acids in Sulfuric Acid.* Journal of the American Chemical Society, 1953. **75**(6): p. 1412-1415.

5 Gas Separation by Mesoporous and Amine Modified Carbons

5.1 Introduction

In ***Chapter 4***, mesoporous ACs (meACs) were produced by the lanthanide oxide (Ln_xO_y, where Ln is Ce or La) catalysed physical activation of VBC and AC-90 (a VBC derived AC). Several of these materials were found to have desirable or interesting characteristics that warranted further investigation for their potential to become supports for PEI. The meACs were produced by one of two methods that differed with respect to the stage at which the catalyst precursor was introduced to the carbon precursor (see ***Table 5-1***). In the first method, catalyst precursors were directly impregnated into VBC prior to steam activation (90 min). In the second method, catalysts precursors were impregnated into the already steam activated AC-90, and were subjected to another 90 min round of steam activation. In essence, the materials produced using the first method were the "catalysed analogues" of AC-90, while materials produced using the second method employed AC-90 as the parent material. Therefore in the current chapter, AC-90 is used as the benchmark for comparison of the Ln-meAC materials. The catalysts used for mesopore development were removed post-synthetically by concentrated sulphuric acid (H_2SO_4). The results presented in the following sections relate to the Ln-meACs before (as produced) and after acid washing (acid washed).

The primary aim of the current chapter is to establish a basic understanding of the CO_2 adsorption behaviour of the meACs, for use in studying the adsorption properties of the PEI-AC composite materials. For reference, ***Table 5-1*** provides a summary of the meACs presented in ***Chapter 4*** that are considered in this chapter (***section 5.3*** and ***section 5.4***). In ***Chapter 1*** (***section 1.7.3***) it was reported for PEI-SiO_2 composites, that increases in CO_2 adsorption were observed in the presence of H_2O. Similar behaviour was expected using the PEI-AC composites characterised in ***Chapter 4*** (AC-Ce3-90-90PEI, AC-90-Ce3-90-90PEI, AC-La3-90-90PEI and AC-90-La3-90-90PEI). A secondary aim of the research presented in this chapter is to assess the

changes in CO_2 adsorption behaviour brought about by loading the meACs with PEI. In particular, single cycle adsorption studies, under both wet and dry gas conditions, were undertaken in order to look for evidence of carbonate formation and subsequently increased CO_2 capacity under humid gas conditions.

Table 5-1 *~ Index of Mesoporous Activated Carbons Studies in this Chapter*

Sample Name	Carbon Precursor	Catalyst	Catalyst Loading (wt%)*	Acid Washed
AC-Ce3-90	VBC	CeO_2	3	No
AC-Ce3-90-AW	VBC	CeO_2	3	Yes
AC-90-Ce3-90	AC-90	CeO_2	3	No
AC-90-Ce3-90-AW	AC-90	CeO_2	3	Yes
AC-La3-90	VBC	La_2O_3	3	No
AC-La3-90-AW	VBC	La_2O_3	3	Yes
AC-90-La3-90	AC-90	La_2O_3	3	No
AC-90-La3-90-AW	AC-90	La_2O_3	3	Yes

* *wt%, on a metal loading basis*

5.2 Partial Pressure Swing Adsorption (PPSA)

Having fully characterised and developed a good understanding of the Ln_xO_y catalysed physically activated carbons presented in ***Chapter 4***, the following sections assess the CO_2 adsorption properties of the materials. Adsorption isotherms are used to understand the adsorption behaviour of the meACs as a function of increasing CO_2 partial pressure; whereas the multi-cyclic studies were undertaken in order to determine the working capacity (***equation 6-11***) at different temperatures under the same CO_2 partial pressure conditions of a VSA cycle, and to also determine the stability of the adsorption over multiple cycles. As the meACs were themselves not intended to be adsorbents, but rather as supports for PEI, competitive adsorption studies in the presence of wet gas where not investigated for them.

5.3 Ceria Catalysed Physically Activated Carbons

5.3.1 Differential-step CO_2 Adsorption

In this section, adsorption pseudo-isotherms constructed from differential-step CO_2 dosing experiments performed at 293, 333 and 363 K, for the Ce catalysed physically activated carbons are presented and discussed. The pseudo-isotherms obtained for AC-Ce3-90, AC-Ce3-90-AW, AC-90-Ce3-90 and AC-90-Ce3-90-AW are shown in ***Figure 5-1A-D***, respectively. In all cases, the pseudo-isotherms obtained for AC-90 under equivalent analytical conditions are presented as a reference, since the meACs presented here were either "catalysed analogues" of AC-90 (e.g. AC-Ce3-90) or were directly prepared from it (e.g. AC-90-Ce3-90).

From the adsorption pseudo-isotherms of AC-Ce3-90 (***Figure 5-1A***) is can be observed that at CO_2 partial pressures less than 5 kPa; at all temperatures, that AC-Ce3-90 possessed similar adsorption behaviour to AC-90, of which it is a "catalysed analogue". At CO_2 partial pressures greater than 15 kPa AC-Ce3-90 exhibits similar adsorption behaviour to AC-90 at 333 K and 363 K, but significant deviation from AC-90 is observed at 293 K. This behaviour might normally be attributed to the similar pore overall micropore volume of AC-Ce3-90 to that of AC-90 (***Table 4-6***). However, from the literature several investigations have shown that, even at ambient temperature CeO_2 exhibits an affinity for CO_2, and thus may also explain the obscured CO_2 adsorption results [1-4]. In recent works by Kamimura *et al.* it was observed that CO_2 adsorption over mesoporous CeO_2 in the presence of water resulted in the formation of carbonates [1, 2]. The surface chemistry of AC-Ce3-90 differs significantly to that of AC-90 (XPS, ***Table 4-3***), specifically with respect to the content and distribution of surface O groups. However, this is to be expected due to the presence of the surface Ce-O phase on AC-Ce3-90, not present on the surface of AC-90. These differences in the distribution of surface O groups could also partially account for the slightly decreased adsorption observed. To fully understand the effect of Ce_xO_y on the affinity of the Ce-meACs for CO_2, would require detailed adsorption studies of CO_2 over Ce_xO_y under the same conditions applied here, but this was beyond the scope of this project. It was difficult to make a direct comparison between the CO_2 adsorption results of the "as produced" and the acid washed Ce-meACs due to the obscuring effects of CeO_2. It is also possible that at least some of the observed decrease in CO_2 adsorption that occurred as a result of the acid washing procedure was due to removal of the CeO_2 phase and its innate capacity for CO_2 [1-4].

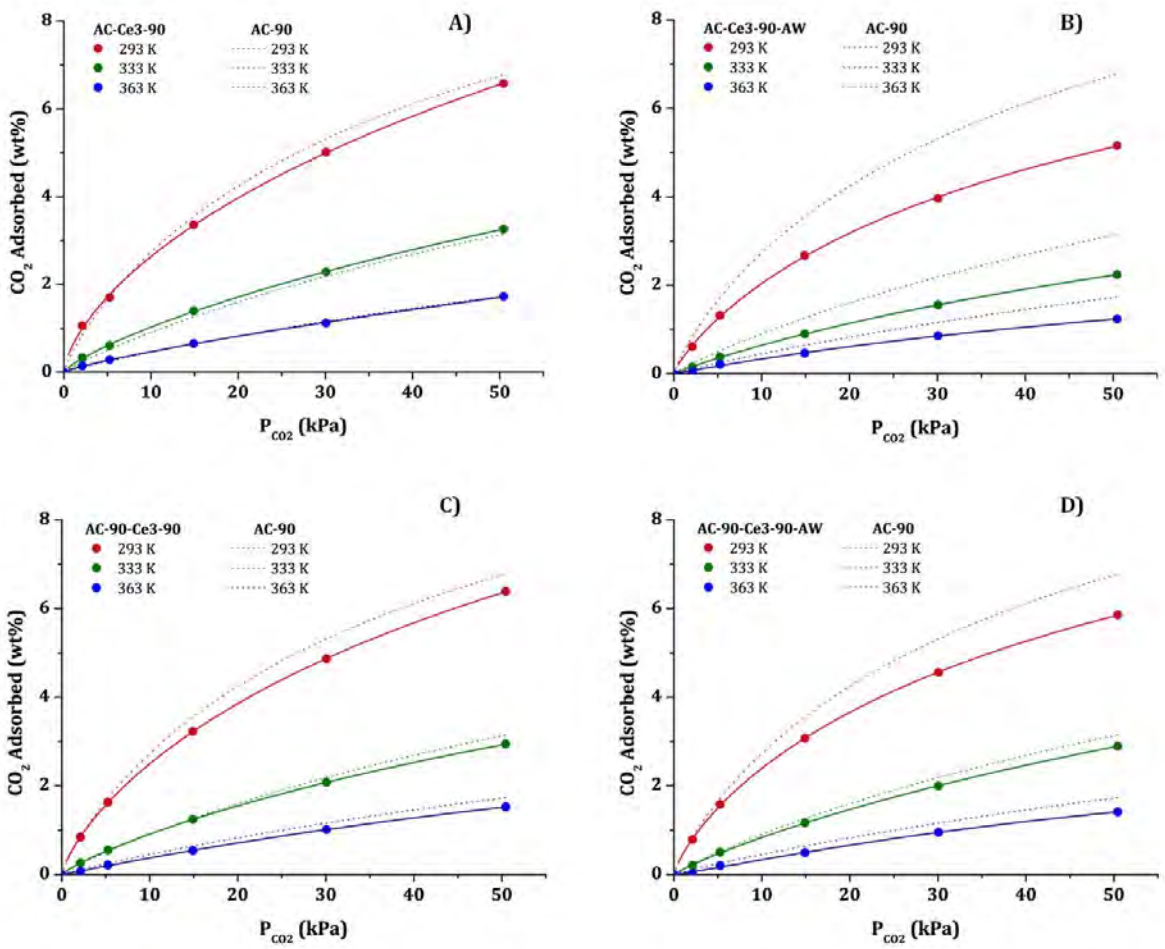

Figure 5-1 ~ *CO_2 Adsorption Pseudo-Isotherms for CeO_2 Catalysed Physically Activated Carbons, taken via PPSA at 293, 333 & 363 K. Shown are **A)** AC-Ce3-90, **B)** AC-Ce3-90-AW, **C)** AC-90-Ce3-90, and **D)** AC-90-Ce3-90-AW*

The most significant feature of the adsorption pseudo-isotherms of AC-Ce3-90-AW (***Figure 5-1B***) are the significant decreases in CO_2 adsorption at all temperatures and CO_2 partial pressures, relative to AC-Ce3-90. This can be associated with the decrease in both the micro- and mesopore volume resulting from the removal of the Ce_xO_y and its inherent porosity (***Table 4-6***). A small increase was observed in the surface concentration of C=O, C-O-R and COO-R groups for AC-Ce3-90-AW relative to AC-Ce3-90, which might be expected to result in an increase in the CO_2 affinity of the AC surface (XPS, ***Table 4-3*** and NEXAFS, ***Table 4-4***) [5, 6]. As substantial amounts of Ce-O were removed from the surface, the adsorption sites that were blocked by CeO_2 became available for adsorption; this would probably account for the increases in surface C=O, C-O-R and COO-R groups. However, relative to AC-Ce3-90, a decrease in CO_2 adsorption has been observed. This is attributed to the decrease in micropore volume, which, in this case is clearly more important than the increase in the concentration in surface O groups (***Table 4-6***). Relative to AC-90, AC-Ce3-90-AW possesses lower surface concentrations of C=O,

C-O-R and COO-R groups (***Table 4-6***), in addition to possessing lower micro- and mesopore volumes; both of which will have acted to decrease the adsorption of CO_2 for AC-Ce3-90-AW relative to AC-90.

The adsorption pseudo-isotherms for AC-90-Ce3-90 (***Figure 5-1C***) at all temperatures were similar to those obtained for AC-Ce3-90. This is not entirely surprising, as both Ce-meACs possess similar pore volumes (***Table 4-6***) and surface chemistry (XPS, ***Table 4-3***). The differences in the differential-step adsorption behaviour of AC-90-Ce3-90 relative to AC-90 can be better explained in terms of the pore structure of the ACs. This was due to complications arising from directly attributing adsorption phenomena to aspects of the surface chemistry on account of the surface Ce_xO_y phase. On the basis of the N_2 physisorption data, there is little difference in the pore structure of AC-90-Ce3-90 and AC-Ce3-90. However, on the basis of the CO_2 physisorption data AC-90-Ce3-90 possesses a larger micropore volume than either AC-Ce3-90 or AC-90, yet it exhibits lower CO_2 adsorption than either AC. The surface Ce-O phase of AC-90-Ce3-90 may mask the detection of surface functional groups by x-rays used for XPS. For these similar samples (since both contain Ce) the differences in surface chemistry may be used to explain the differences observed in the differential-step adsorption of AC-Ce3-90 and AC-90-Ce3-90. The surface concentration of the Ce-O phase on AC-90-Ce3-90 was twice that observed on the surface of AC-Ce3-90. Therefore, more potential adsorption sites may have been inaccessible on the surface of AC-90-Ce3-90 than for AC-Ce3-90, on account of a greater amount of CeO_2 covering the surface.

The adsorption pseudo-isotherm for AC-90-Ce3-90-AW (***Figure 5-1D***) at 293 K significantly deviated from that of AC-90-Ce3-90 (***Figure 5-1C***) under the same conditions. The acid washed sample exhibited lower CO_2 adsorption relative to AC-90-Ce3-90, which can predominately be attributed to decreases in its micropore volume as a result of acid washing. The changes in the surface chemistry of AC-90-Ce3-90-AW relative to AC-90-Ce3-90 were similar to those observed by acid washing for the AC-Ce3-90/AC-Ce3-90-AW pair. In both cases the changes in surface chemistry were predominately the result of removing the surface Ce_xO_y phase. The concentration of C-O-R groups on the surface of AC-90-Ce3-90-AW was significantly lower than AC-90 (XPS, ***Table 4-3***), whilst the NEXAFS analysis (***Table 4-4***) showed a significant shift in the distribution of hydroxyl and ether groups. AC-90-Ce3-90-AW possessed a much higher proportion of hydroxyl groups to ether groups, relative to those observed on the surface of AC-90. As hydroxyl groups have a greater affinity for CO_2 than ethers, this might be expected to increase the affinity of the meAC surface towards polar gases, such as CO_2 [5, 6]. The difference in the distribution of C-O-R groups on the surface of AC-90-Ce3-90-AW relative to AC-90 was clearly more significant for CO_2 adsorption than the similar shift in the distribution of ether and

hydroxyl groups observed for AC-Ce3-90-AW relative to AC-90. Moreover, the effect that acid washing of AC-90-Ce3-90 had on the resulting decrease in micropore volume, was much smaller than in the case of the AC-Ce3-90/AC-Ce3-90-AW pair (***Table 4-6***). This is with the higher adsorption of CO_2 over AC-90-Ce3-90-AW relative to AC-Ce3-90-AW. As was noted for AC-Ce3-90, the decrease in CO_2 adsorption observed could be partially accounted for by the removal of the CeO_2; which has been shown to possesses CO_2 adsorption properties in the literature [1-4].

5.3.2 Multi-cyclic CO_2 Adsorption

The CO_2 adsorption behaviour of the CeO_2 catalysed physically activated carbon materials were also examined under multi-cyclic conditions, cycling between CO_2 partial pressures of 5-15 kPa, at 293, 333, and 363 K. This was undertaken in order to investigate the adsorption behaviour under CO_2 partial pressure conditions proposed for use in a VSA process [7]. ***Figure 5-2A-D*** shows the results obtained from the multi-cyclic studies using AC-Ce3-90, AC-Ce3-90-AW, AC-90-Ce3-90 and AC-90-Ce3-90-AW, respectively. As was the case for the isothermal studies of the Ce catalysed physically activated carbons, AC-90 was used as a reference material under equivalent conditions. The working capacities calculated (***equation 6-11***) from ***Figure 5-2*** and are presented in ***Table 5-2***.

Unlike the multi-cyclic dosing studies presented in ***chapter 3*** (***section 3.3.2***, ***section 3.4.2*** and ***section 3.5.2***), heats of adsorption were not calculated for any of the materials presented here in ***chapter 5***. The main reason for this was due to instrumentation issues which arose at the time of the measurements; also, it was not further pursued as the purpose of the meACs was not so much to use them as physisorbents, but rather as supports for PEI.

The working capacities for AC-Ce3-90 (***Table 5-2***) calculated from the multi-cyclic adsorption studies (***Figure 5-2A***) were in the higher range obtained out of all meACs at each temperature. From the N_2 physisorption data AC-Ce3-90 exhibited higher micro- and mesopore volumes than AC-90; however from the CO_2 physisorption data of AC-Ce3-90 it was shown to possess a lower micropore volume to AC-90 (***Table 4-6***). This situation is likely due to interactions between CO_2 and the surface functionality of AC-90, whilst many of the strongly binding functional groups that may be present on the surface of AC-Ce3-90 are inaccessible due to the surface Ce-O phase.

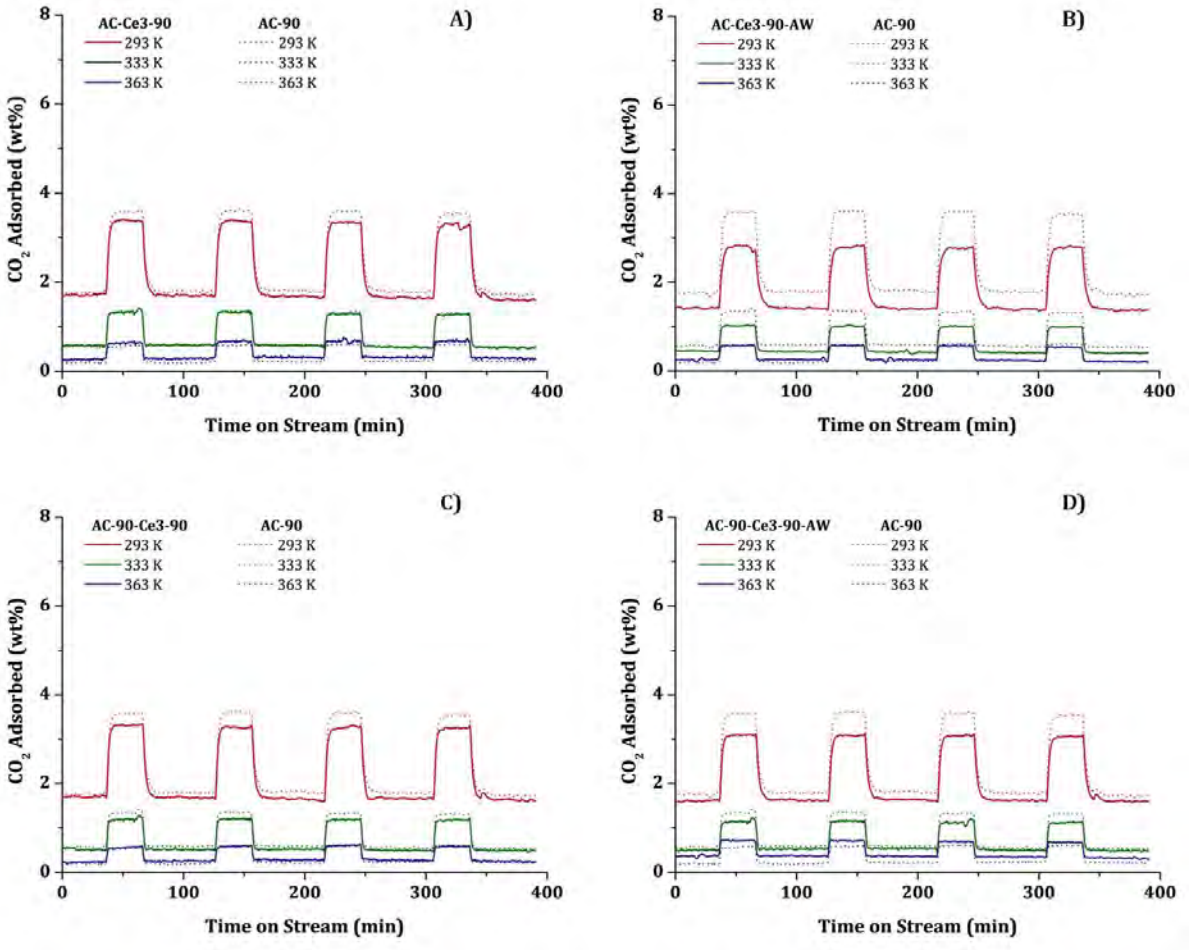

Figure 5-2 ~ *VSA Simulations for CeO_2 Catalysed Physically Activated Carbons, taken via PPSA at 293, 333 & 363 K. Shown are* ***A)*** *AC-Ce3-90,* ***B)*** *AC-Ce3-90-AW,* ***C)*** *AC-90-Ce3-90, and* ***D)*** *AC-90-Ce3-90-AW*

Acid washing AC-Ce3-90 to produce AC-Ce3-90-AW resulted in a significant decrease in the multi-cyclic adsorption observed for AC-Ce3-90-AW at all temperatures (***Figure 5-2B***). This is likely due to both the decrease in the micro- and mesopore volume of AC-Ce3-90-AW relative to AC-Ce3-90 (***Table 4-6***), and the changes in surface chemistry of AC-Ce3-90-AW relative to both AC-Ce3-90 and AC-90. Although the working capacities determined (***Table 5-2***) from the multi-cyclic studies of AC-Ce3-90-AW (***Figure 5-2B***) are not significantly different from those calculated from the differential-step adsorption studies (***Figure 5-1B***), the total amount of CO_2 adsorbed at both 5 kPa and 15 kPa was greater under the multi-cyclic adsorption conditions. This finding is attributed to the pre-dosing protocol used in the multi-cyclic experiments (refer ***section 6.6.4.2***), which permits a greater amount of CO_2 to equilibrate on the sample prior to commencement of the cycling (refer ***section 6.6.4.1***). Of the changes in the surface chemistry of AC-Ce3-90-AW that were observed from the XPS (***Table 4-3***) relative to AC-90, the decrease in the C-O-R groups was the most significant. Not only was a decrease observed from the XPS of the C-O-R groups, but a very significant shift in the distribution of these groups was observed

from the NEXAFS analysis (***Table 4-4***). This was addressed in ***section 5.3.1***, accounting for the decrease in CO_2 adsorption from the differential-step dosing, used to construct the adsorption pseudo-isotherms. The changes in the distribution of ether and hydroxyl groups were expressed as an increase in hydroxyl groups, with an associated decrease in ether groups, on the surface of AC-Ce3-90-AW relative to AC-90. The overall effect of the increase in the proportion of hydroxyl groups would be to increase the affinity of the meAC surface towards polar gases like CO_2 [5, 6], and tentatively to offset the decreases in micropore volume that occurred as a result of the acid washing used to remove CeO_2. Moreover, as previously noted (***section 5.3.1***) the adsorption results of the Ce-meACs could be obscured by the fact that CeO_2 itself exhibits an affinity for CO_2. As such, the degree to which the decrease in CO_2 adsorption was due to the removal of the CeO_2 phase and its inherent porosity is confounded by the CO_2 adsorption properties of CeO_2 itself, making a direct comparison difficult [1-4].

Table 5-2 ~ *Working Capacities of CeO_2 Catalysed Physically Activated Carbons*

Sample Name	Working Capacity (wt%)		
	293 K	333 K	363 K
AC-N	1.46	0.55	0.28
AC-90	1.78	0.76	0.39
AC-Ce3-90	1.66	0.71	0.41
AC-Ce3-90-AW	1.41	0.59	0.33
AC-90-Ce3-90	1.67	0.71	0.35
AC-90-Ce3-90-AW	1.52	0.66	0.33

The results of the multi-cyclic adsorption studies over AC-90-Ce3-90 (***Figure 5-2C***) were very similar to those of AC-Ce3-90 (***Figure 5-2A***), as was also the case for the adsorption isotherms for both meACs (***Figure 5-2A*** and ***Figure 5-2C***, for AC-Ce3-90 and AC-90-Ce3-90, respectively). Furthermore the pore structure and surface chemistry of both meACs are very similar, as such the underlying aspects affecting the adsorption are similar, and will not be discussed any further here (to avoid repetition).

The effect of acid washing AC-90-Ce3-90 to produce AC-90-Ce3-90-AW (***Table 5-2***) resulted in reduced multi-cyclic CO_2 adsorption relative to AC-90-Ce3-90 at both 293 K and 333 K, with an increase in adsorption at 363 K. This is likely due to the decrease in the micropore volume of

AC-90-Ce3-90-AW relative to AC-90-Ce3-90, as observed from both the N_2 and CO_2 physisorption data (***Table 4-6***). At 363 K the increase in adsorption relative to both AC-90-Ce3-90 and AC-90 was greater at 5 kPa than at 15 kPa, and as such even though the total amount of adsorption at both CO_2 partial pressures was greater for AC-90-Ce3-90-AW than for AC-90, the working capacity of AC-90 at 363 K is higher than for AC-90-Ce3-90-AW (***Table 5-2***). This can be associated with a significant decrease in the surface concentration of C-O-R groups that were observed for AC-90-Ce3-90-AW, relative to both AC-90 and AC-90-Ce3-90 (***Table 4-3***). Furthermore, the NEXAFS analysis of AC-90-Ce3-90-AW (***Table 4-4***), showed a significant decrease in ether groups relative to AC-90. Associated with the decrease in ether groups was an increase in hydroxyls, known to strongly increase the affinity of the AC surface for CO_2 (***section 4.3.2***) [5, 6]. Again however, directly tying adsorption properties to the "as produced" Ce-meACs is difficult due to the confounding effects of the Ce-O phase. It has been shown that both AC and CeO_2 possess unique adsorption properties [1-4], so it is also for this reason that the surface chemistry and adsorption properties of the acid washed meACs can be more meaningfully compared to AC-90.

In the end however, the main purpose of producing the meACs were to screen for those appropriate for use as supports for PEI impregnation, and as such the adsorption properties of the meACs were required more for bench marking purposes, than as a screening tool.

5.4 Lanthana Catalysed Physically Activated Carbons

5.4.1 Differential-step CO_2 Adsorption

The differential-step adsorption studies for the La_2O_3 catalysed physically activated carbons were measured over a CO_2 partial pressure range of 0-50 kPa, at 293, 333 and 363 K from which adsorption pseudo-isotherms were constructed. The pseudo-isotherms for AC-La3-90, AC-La3-90-AW, AC-90-La3-90 and AC-90-La3-90-AW are shown in ***Figure 5-3A-D***, respectively. Furthermore, as was the case for the pseudo-isotherms for the Ce catalysed physically activated carbons from ***section 5.3.1***, AC-90 was used as a point of reference for the adsorption at all CO_2 partial pressures and temperatures.

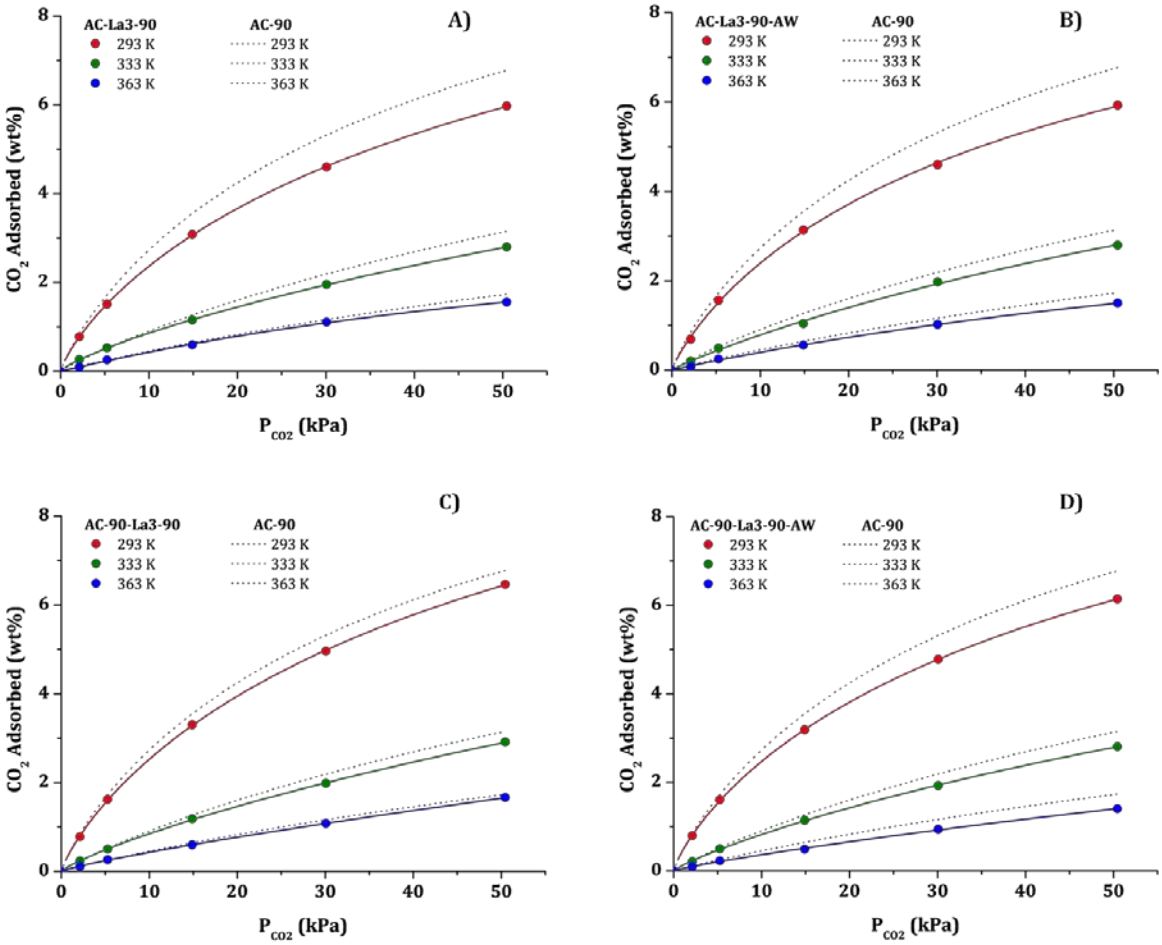

Figure 5-3 ~ *CO_2 Adsorption Pseudo-Isotherms for La_2O_3 Catalysed Physically Activated Carbons, taken via PPSA at 293, 333 & 363 K. Shown are* ***A)*** *AC-La3-90,* ***B)*** *AC-La3-90-AW,* ***C)*** *AC-90-La3-90, and* ***D)*** *AC-90-La3-90-AW*

In ***section 5.3.1*** it was noted that tying the changes in CO_2 adsorption to removal of the CeO_2 phase is obscured by the changes in pore structure and the inherent affinity that CeO_2 has for CO_2 resulting from the CeO_2 phase. Research has also been conducted into the use of La_2O_3 for the post-synthetic modification of MCM-41 for CO_2 capture purposes by Shen *et al.* [8], where improvements were observed in CO_2 adsorption by the introduction of La_2O_3 onto the MCM-41 surface. As such the CO_2 adsorption results for the La-meACs are confounded by the affinity that La_2O_3 has for CO_2 and the increased pore volume that results from La_2O_3 being present.

With respect to the CO_2 adsorption pseudo-isotherms obtained for AC-La3-90 and AC-La3-90-AW (***Figure 5-3A*** and ***Figure 5-3B*** respectively), it is interesting to note that there is little observable difference in the amount of CO_2 adsorption over the entire CO_2 partial pressure range at any temperature. This has been attributed to the almost negligible change in micropore volume observed as a function of acid washing. Furthermore, the mesopore volume decreased

as a result of the acid washing (***Table 4-11***). It is this decrease in micropore volume relative to AC-90 that has been attributed to the decrease in CO_2 adsorption at all temperatures and CO_2 partial pressure, relative to AC-90.

Although there was a significant decrease in the mesopore volume of AC-La3-90-AW relative to AC-La3-90 (***Table 4-11***), there is an almost negligible change in micropore volume. At all temperatures and CO_2 partial pressures there were very few differences between the adsorption over the two carbons (***Figure 5-3A-B***). At the same time there was a significant decrease in surface O groups (***Table 4-8***), that was predominately the result of the La_2O_3 phase removal. The changes in surface O functionality were expressed as two major shifts in the XPS and NEXAFS spectroscopies. The first from the XPS analysis (***Table 4-8***), being a threefold increase in carbonyl group concentration on the surface of AC-La3-90-AW, relative to AC-La3-90. The second major change in surface chemistry as a result of acid washing was a decrease in the concentration of C-O-R groups, relative to AC-La3-90 (XPS, ***Table 4-8***). The decrease in the concentration of C-O-R groups of AC-La3-90-AW relative to AC-La3-90 resulted in a value that was also significantly lower than AC-90. In addition to the lower concentration of C-O-R groups exhibited by AC-La3-90-AW relative to AC-90 there was also a shift in the distribution of ether and hydroxyl groups. This shift took the form of an increase in hydroxyl groups, with an associated decrease in ether groups (***Table 4-9***). As such, despite the lower overall concentration of C-O-R groups, the increase in hydroxyl groups will have acted to increase the affinity of the AC-La3-90-AW surface for CO_2, slightly offsetting the decreased micropore volume relative to AC-90 (***Table 4-11***). A similar result was also observed for the Ce-meACs presented in ***section 5.3***.

The adsorption pseudo-isotherms for AC-90-La3-90 (***Figure 5-3C***) showed increased CO_2 adsorption compared to AC-La3-90 and AC-La3-90-AW, but lower adsorption than AC-90 under the same conditions. This could be attributed to the higher micropore volume that AC-90-La3-90 possesses relative to AC-90 (***Table 4-11***). However, on this basis the CO_2 adsorption over AC-90-La3-90 might be expected to exceed that of AC-90. As this was not the case, some aspect of the surface chemistry must also be at play. The total surface O content of AC-90-La3-90 is less than AC-90 (***Table 4-8***), yet much of the surface O present on AC-90-La3-90 is due to the presence of La_2O_3. This slight shift in surface O functionality along with the difference in CO_2 affinity of La_2O_3 compared to the AC surface may be able to account for the differences in CO_2 adsorption observed [8]. This is especially true when one takes into account that the most significant change in O functionality between AC-90-La3-90 and AC-90 was the change in C=O groups (***Table 4-8***).

Acid washing of AC-90-La3-90 led to significant decreases in both micro- and mesopore volumes of the resulting AC-90-La3-90-AW material (***Table 4-11***), yet only minor decreases in CO_2 adsorption were observed as a function of either temperature or CO_2 partial pressure in the pseudo-isotherms of AC-90-La3-90-AW relative to AC-90-La3-90 (***Figure 5-3C-D***). This is likely due to the presence of the La_2O_3 phase on the surface of AC-90-La3-90 making adsorption sites on the AC surface unavailable to take part in adsorption processes, thus obscuring the adsorption results of the two materials. Moreover, relative to either AC-90-La3-90 or AC-90, AC-90-La3-90-AW possesses a significantly lower surface O concentration. XPS of AC-90-La3-90-AW revealed that it possessed the lowest C-O-R concentration of the La-meAC series. Further investigation of this material by NEXAFS spectroscopy revealed that the relative proportion of hydroxyls increased and ethers decreased, relative to AC-90 (unfortunately, NEXAFS was not undertaken for AC-90-La3-90). As has been noted several times for both the Ce- and La-meACs, the decrease in ether groups and increase in hydroxyl groups that result from the acid washing to remove the lanthanide oxide phase, results in an increase in the affinity of the meAC surface for CO_2 [5, 6]. The reduction in CO_2 adsorption for AC-90-La3-90-AW relative to AC-90-La3-90 may also be the result of the loss of CO_2 capacity inherent in the La_2O_3 itself [8].

The intended end purpose of these meACs is as supports for PEI impregnation. As such the adsorption behaviour is needed only in order to develop a basic understanding of the adsorption behaviour of the support. This will allow us to understand the effects that the use of PEI impregnation has actually had on the CO_2 adsorption for the PEI-AC composite materials.

5.4.2 Multi-cyclic CO_2 Adsorption

The multi-cyclic CO_2 adsorption behaviour of the La_2O_3 catalysed physically activated carbons were examined at 293 K, 333 K and 363 K under CO_2 partial pressures of 5-15 kPa in order to simulate the CO_2 partial pressure conditions proposed for use in a VSA process. For the La catalysed physically activated carbons these are presented as ***Figure 5-4A-D*** for AC-La3-90, AC-La3-90-AW, AC-90-La3-90 and AC-90-La3-90-AW, respectively. The working capacities (***equation 6-11***) determined from the multi-cyclic studies in ***Figure 5-4*** are presented in ***Table 5-3***. Again, the results obtained for AC-90 under equivalent analytical conditions are presented as a reference.

The working capacities (***Table 5-3***) derived from the multi-cyclic studies of AC-La3-90 (***Figure 5-4A***), are remarkably similar to those predicted from the adsorption pseudo-isotherms of AC-La3-90 (***Figure 5-3A***). The differences observed between the adsorption pseudo-isotherms and multi-cyclic studies of the miACs in ***Chapter 3*** were attributed to the pre-treatment under an

Ar/CO_2 gas stream at 5 kPa CO_2 partial pressure. As such, it is clear that mass-transport limitations were not encountered for AC-La3-90.

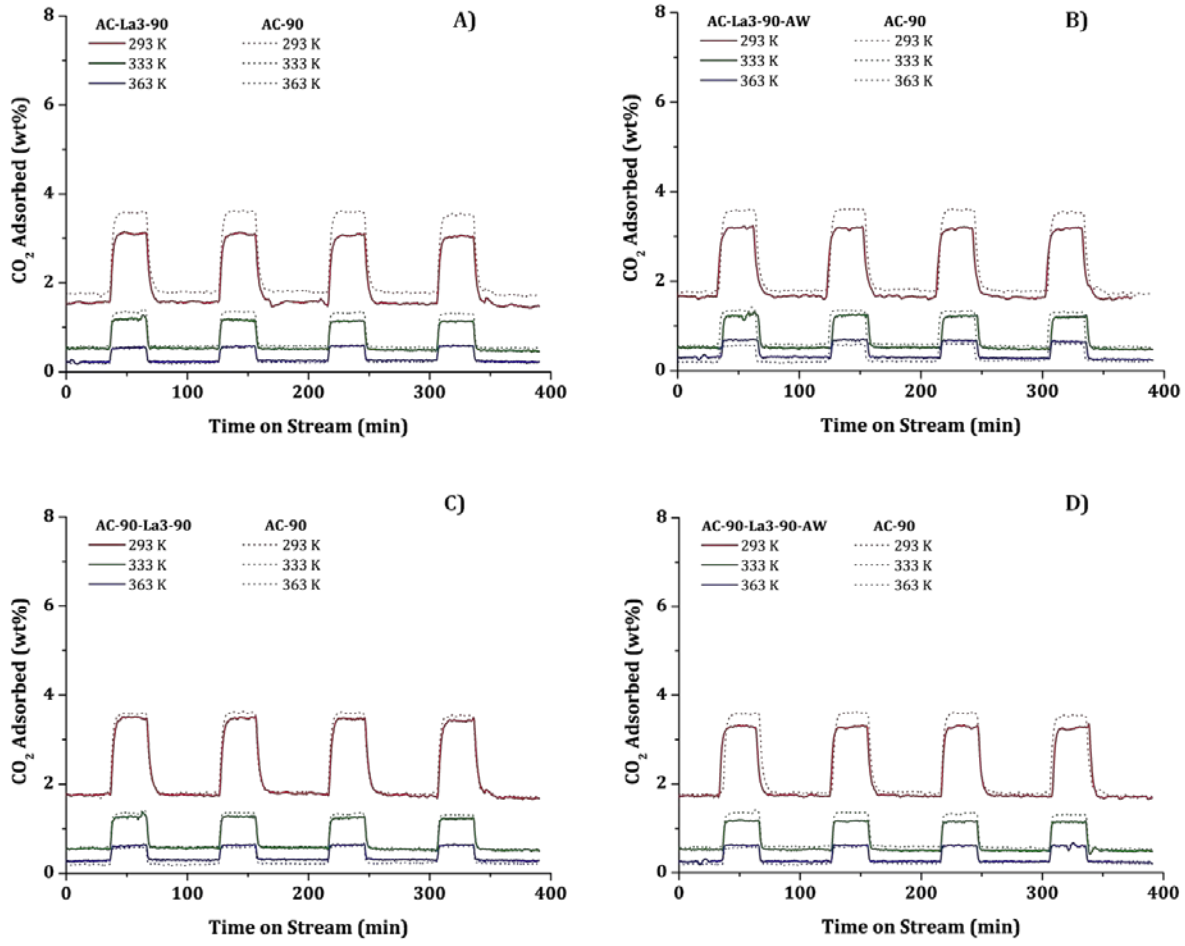

Figure 5-4 *~ VSA Simulations for La Catalysed Physically Activated Carbons, taken via PPSA at 293, 333 & 363 K. Shown are* ***A)*** *AC-La3-90,* ***B)*** *AC-La3-90-AW,* ***C)*** *AC-90-La3-90, and* ***D)*** *AC-90-La3-90-AW*

Upon acid washing of AC-La3-90 (resulting in AC-La3-90-AW, ***Figure 5-4***), slightly different adsorption behaviour was observed for the multi-cyclic adsorption studies. The working capacities and the predicted adsorption between 5 kPa and 15 kPa CO_2 partial pressure from the differential-step measurements, differ to those actually calculated from the multi-cyclic adsorption studies (***Table 5-3***). Slightly increased CO_2 adsorption was observed at both 5 kPa and 15 kPa, which is indicative of mass-transport limitations. The mass-transport limitations encountered can be attributed to the decrease in mesopore volume resulting from the acid washing. Moreover, at 333 K and 363 K the working capacities of AC-La3-90-AW were actually higher than AC-La3-90, an observation that was not made for the acid washed Ce activated

meACs (***section 5.3.2***, ***Table 5-2***). This result was interesting, as the N_2 physisorption results showed that the acid washing resulting in decreases to both the micro- and mesopore volumes (***Table 4-11***). These changes in pore volume can account for discrepancies between the differential-step and multi-cyclic dosing studies, but not the increased working capacities at 333 K and 363 K. Furthermore, the only aspect of the changes in surface chemistry that can account for the adsorption results observed at 363 K and 378 K is the fact that the La_2O_3 will likely possess a lower affinity for CO_2 than the AC surface. As such, removal of the La_2O_3 phase will have increased the AC surface available to interact with CO_2 during the adsorption studies. In fact the working capacities of AC-La3-90-AW were higher above 293 K than any of the other La catalysed physically activated carbon (***Table 5-3***). The working capacities at the higher temperatures and were the closest of any meAC to those of AC-90 (***Table 5-3***), despite having a smaller micropore and larger mesopore volume in comparison (***Table 4-11***).

Table 5-3 ~ *Working Capacities for La_2O_3 Catalysed Physically Activated Carbon*

Sample Name	Working Capacity (wt%)		
	293 K	333 K	363 K
AC-N	1.46	0.55	0.28
AC-90	1.78	0.76	0.39
AC-La3-90	1.51	0.60	0.34
AC-La3-90-AW	1.51	0.76	0.37
AC-90-La3-90	1.74	0.72	0.36
AC-90-La3-90-AW	1.55	0.67	0.36

The multi-cyclic adsorption studies of AC-90-La3-90 were the closest overall to that of AC-90. In particular at 293 K, with a working capacity was almost equal to that of AC-90 under the same conditions, the closest of any AC at this temperature (***Table 5-3***). As was noted for AC-La3-90, the high mesopore volume of AC-90-La3-90 (***Table 4-11***) is linked with its higher working capacities that can be predicted from its adsorption pseudo-isotherms (***Figure 5-3C***), on account of unrestricted mass-transport. Furthermore, AC-90-La3-90 possessed one of the highest surface concentrations of both COO-R and C-O-R groups (XPS, ***Table 4-8***) of any AC

presented in this thesis (with the sole exception of AC-90). Throughout this thesis it has been stated several times that the C-O-R peak in XPS is assigned to both hydroxyl and ether groups, whilst the COO-R groups are assigned to both carboxylic acid and lactone groups. Moreover, it is well documented that hydroxyl and carboxylic acid groups exhibit the greatest effect the affinity of the surface for polar gases [5, 6]. As such the changes in these strongly binding surface groups and the micropore volume appear to account for the high working capacities observed across the entire temperature range for any AC other than AC-90.

The effects of acid washing on AC-90-La3-90 are the most prominent reported in this thesis. The decreases in both micro- and mesopore volume of AC-90-La3-90-AW relative to AC-90-La3-90 were the most substantial observed (***Table 4-11***). It is however, interesting to note that despite a significant decrease in micropore volume, an accompanying decrease in the working capacity was not observed. This is contrary to many of the arguments made to correlate changes in working capacity and CO_2 uptake for many carbons reported throughout this thesis. However, the decrease in mesopore volume of AC-90-La3-90-AW relative to AC-90-La3-90 that was observed was more significant than that which was observed for the micropore volume. The working capacity of AC-90-La3-90-AW at 293 K is lower than that of AC-90-La3-90, but higher than either of the AC-La3-90 carbons at the same temperature (***Table 5-3***). From the XPS of AC-90-La3-90-AW (***Table 4-8***) the surface concentrations of C=O and COO-R groups show remarkably strong similarity to those of AC-90. Furthermore, the concentration of C-O-R on the surface of AC-90-La3-90-AW are half those of AC-90. As the C-O-R peak has assigned to both hydroxyl and ether groups a change in the surface concentration in only one of these groups may significantly change the overall signal of this peak as detected by XPS. Like AC-La3-90-AW, both C 1s and O 1s NEXAFS spectroscopy was undertaken on AC-90-La3-90-AW (***Figure 4-15*** and ***Table 4-9***). Relative to AC-90, there was a significant decrease in ether content with an associated increase in both hydroxyl and phenol groups (***Table 4-9***). As hydroxyl groups are one of the groups that most strongly increase the affinity of an AC surface towards CO_2 [5, 6], this increase will have had the effect of slightly offsetting the decrease in micropore volume as a result of the acid washing procedure. Moreover, as noted several times throughout this chapter, the intended end use of AC-90-La3-90-AW was as a support for PEI impregnation.

5.5 CO_2 Separation by Mesoporous Carbons

In ***chapter 4*** mesoporous ACs were produced using lanthanide oxides (in the form Ln_xO_y, where Ln was Ce or La) as catalysts for the development of mesopores during the preparation of steam activated carbons. Characterisation of these materials showed that upon removal of the lanthanide oxide a significant degree of the mesopore character was also removed, as well as significant changes to the surface chemistry relative to both their "as produced" counterparts and AC-90 (***Table 4-14***). The CO_2 adsorption properties of the lanthanide oxide catalysed meACs were tested in order to create an understanding of the baseline adsorption for use in evaluating the PEI-ACs.

The pseudo-isotherms of the "as produced" Ce-meACs exhibited similar CO_2 adsorption behaviour to AC-90 at all temperatures and CO_2 partial pressures (***Figure 5-1***). These results were attributed to the similarities between the pore volumes of the "as produced" Ce-meACs to AC-90, and potentially the high affinity of CO_2 for CeO_2 [1-3]. Washing of the "as produced" Ce-meACs resulted in significant decreases in CO_2 adsorption, the difference between the "as produced" and acid washed Ce-meACs increasing with CO_2 partial pressure at each temperature.

The differences in multi-cyclic adsorption (***Figure 5-2***) between the Ce-meACs and AC-90 were similar to those observed from the pseudo-isotherms (***Figure 5-1***), although minor differences in the absolute amount of CO_2 adsorbed were observed. The minor increases were predominately observed at 5 kPa CO_2 partial pressure, and were due to the increased equilibration time at this partial pressure, prior to the actual cyclic measurements taking place. However, these differences were far less significant than those encountered for the miACs (***chapter 3***).

Attributing differences in CO_2 adsorption between the "as produced" and acid washed Ce-meACs was difficult due to the effects of acid washing on the AC surface itself, as well as the high affinity of CeO_2 for CO_2 [1-3]. From the XPS analysis of the Ce-meACs (***Table 4-3***) it was shown that relative to AC-90 the acid washed Ce-meACs possessed lower overall surface concentrations of C-O-R groups. Further investigation of the surface chemistry of the acid washed Ce-meACs using NEXAFS spectroscopy (***Table 4-4***) showed that even though the absolute amount of C-O-R groups was reduced, that the proportion of hydroxyl groups present was higher, and as such no net reduction in hydroxyl groups was likely. As hydroxyl groups are the groups with the highest affinity for CO_2, significant reductions in adsorption would not be expected, which agrees with what was observed.

The pore volumes determined from the N_2 physisorption data of AC-Ce3-90 were higher than those determined for AC-90 (***Table 4-6***). Upon acid washing of AC-Ce3-90, significant decreases

in pore volume were observed. This was attributed to the removal of porous and highly amorphous Ce_xO_y that was well distributed (TEM, ***section 4.3.3.2.2***). Despite the significant decreases in pore volume observed by acid washing AC-Ce3-90, acid washing of AC-90-Ce3-90 resulted in only a minor decrease in micropore volume, and no detectable change in the mesopore volume. This was due in part to the highly crystalline nature of the Ce_xO_y phase of AC-90-Ce3-90 relative to that of AC-Ce3-90 (refer to XRD patterns in **figure4-6**), and as crystalline phases are generally possess significantly less porous character, the lack of change in pore volume makes sense. Furthermore, the distribution of Ce_xO_y was better for AC-Ce-90 than AC-90-Ce3-90 (TEM, ***section 4.3.3.2.2***), and if the Ce_xO_y was less porous as well as the particles segregated (as was the case for AC-90-Ce3-90) this might explain the lack of change in pore volume observed (***Table 4-6***).

The pseudo-isotherms of the "as produced" La-meACs exhibited similar but slightly lower CO_2 adsorption to AC-90 at all temperatures and CO_2 partial pressures (***Figure 5-3***), despite both possessing micro- and mesopore volumes that exceeded AC-90. This was attributed to the lower affinity for CO_2 that La_2O_3 possesses relative to CeO_2, in accordance with the observations from the literature [1-3, 8]. For both the La-meACs acid washing resulted in only minor reductions in CO_2 adsorption relative to their "as produced" counterparts, regardless of temperature or CO_2 partial pressure. This was interesting as acid washing resulted in significant reductions in both the micro- and the mesopore volumes for both La-meAC pairs.

The multi-cyclic adsorption studies of the La-meACs (***Figure 5-4***) showed slight increases in adsorption at 5 kPa CO_2 partial pressure relative to the CO_2 adsorption observed under the same conditions from the pseudo-isotherms (***Figure 5-3***). However, in the case of AC-90-La3-90 increased CO_2 adsorption was observed at both 5 kPa and 15 kPa CO_2 partial pressures, the result for this particular La-meAC makes a great deal of sense, on account of it possessing the highest micro- and mesopore volume of any carbon produced throughout this project (***Table 4-14***).

The effect of the surface chemistry of the "as produced" La-meACs (***section 4.4.2***) on their CO_2 adsorption properties was not able to be made without a substantial study of CO_2 adsorption on La_2O_3, which was beyond the scope of this project. However, determining the affects of the surface chemistry on the CO_2 adsorption properties of the acid washed La-meACs was possible, using both XPS and NEXAFS spectroscopies. From the XPS analysis of the acid washed La-meACs there is a clear and significant decrease in all three major oxygenated functional group (C=O, C-O-R and COO-R), relative to both AC-90 and their "as produced" counterparts (***Table 4-8***). The NEXAFS spectroscopy of the acid washed La-meACs showed that despite the decrease in C-O-R groups relative to AC-90 (XPS) that a significant increase in the proportion of surface hydroxyl

groups relative to AC-90 was observed. Therefore, despite the decrease overall in C-O-R groups (hydroxyl and ether groups) a significant amount of hydroxyl groups were still present at the surface of the acid washed La-meACs. Thus as there was no significant difference in the surface hydroxyl group content of the acid washed La-meACs relative to AC-90, the surface of the acid washed La-meACs will possess a significant affinity for CO_2.

The pore volumes of the "as produced" La-meACs were larger than AC-90, especially in the case of AC-90-La3-90 (***Table 4-11***). However, significant difference existed between both the micro- and mesopore volumes of AC-90-La3-90 and AC-La3-90, yet much less significant differences were observed from the differential-step and multi-cyclic adsorption studies.

Interestingly, both the "as produced" Ce-meACs exhibited quite similar working capacities at all temperatures, while the La-meACs showed a significant degree of variation (***Table 5-4***). On the basis of the N_2 physisorption data both "as produced" Ce-meACs possessed similar micro- and mesopore volumes, whereas the "as produced" La-meACs did not. AC-90-La3-90 possessed the highest micro- and mesopore volume of any AC produced in this work, it also possessed higher working capacities to AC-La3-90 and both the Ce-meACs at all temperatures.

A similar decrease in pore volume was observed for AC-Ce3-90-AW and AC-La3-90-AW relative to their "as produced" counterparts (AC-Ce3-90 and AC-La3-90, respectively), as a result of acid washing (***Table 4-14***). However, from the adsorption pseudo-isotherms the decrease in CO_2 adsorption observed for AC-Ce3-90-AW relative to AC-Ce3-90 (***Figure 5-1A-B***) was much more substantial than decrease in CO_2 adsorption observed for AC-La3-90-AW relative to AC-La3-90 (***Figure 5-3A-B***). On a similar note significant decreases were observed in both the micro- and mesopore volumes of the AC-90 derived meACs as a result of acid washing, with a larger decrease in pore volume for the AC-90-La3-90/AC-90-La3-90-AW pair than the AC-90-Ce3-90/AC-90-Ce3-90-AW pair (***Table 4-14***), but a larger decrease in CO_2 adsorption was observed for the AC-90-Ce3-90/AC-90-Ce3-90-AW pair (***Figure 5-1C-D***). The reason for this observed difference between the Ce- and La-meACs can be attributed to the different affinity that each lanthanide oxide possesses for CO_2. Of the few studies in the literature, the evidence suggests that CeO_2 has a higher affinity for CO_2 than La_2O_3 [1-4, 8].

The effects of acid washing on the CO_2 adsorption properties were most easily observed from the working capacities, as this property could be quantified. The working capacities of both the Ce- and La-meACs are summarised in ***Table 5-4***, from which is can be seen that although there is great deal of similarity in the working capacities of the "as produced" Ce-meACs after acid washing these similarities cease, whereas significant differences exist between the working capacities of the "as produced" La-meACs, but after acid washing the magnitude of these differences is significantly less. Furthermore, the differences between the working capacities of

both the "as produced" and acid washed meACs become significantly smaller as the adsorption temperature increases (***Table 5-4***).

Table 5-4 ~ *Working Capacities for meACs*

Sample Name	Working Capacity (wt%)		
	293 K	333 K	363 K
AC-90	1.78	0.76	0.39
AC-Ce3-90	1.66	0.71	0.41
AC-Ce3-90-AW	1.41	0.59	0.33
AC-90-Ce3-90	1.67	0.71	0.35
AC-90-Ce3-90-AW	1.52	0.66	0.33
AC-La3-90	1.51	0.60	0.34
AC-La3-90-AW	1.51	0.76	0.37
AC-90-La3-90	1.74	0.72	0.36
AC-90-La3-90-AW	1.55	0.67	0.36

Overall, the use of Ce and La oxides as catalysts for the preferential development of mesopores in coal derived AC via steam activation was partially successful, as was shown in ***chapter 4***. The CO_2 adsorption studies of the meACs showed them to exhibit lower CO_2 adsorption than AC-90 at all temperatures, regardless of which lanthanide oxides was used. From the adsorption studies of the "as produced" Ln-meACs good baseline adsorption data was able to be elucidated for use in the adsorption studies of the PEI-AC composite materials, allowing for the adsorption resulting from the PEI itself to be determined.

5.6 Adsorption Studies Using PEI-AC Composites

In the following sections, the CO_2 adsorption behaviour of the PEI impregnated materials are studied in order to determine whether PEI incorporation improves the CO_2 capacity of the carbons. Single cycle studies under both wet and dry gas were undertaken in the same manner as ***Chapter 3***, however, here the purpose is to look for evidence of carbamate and bicarbonate formation, rather than competitive physisorption.

Furthermore, for the PEI-ACs as the amount of amine groups are known from the "adjusted nitrogen" content of the materials; which allows for how efficiently the amine groups are by the amount of CO_2 they adsorb.

5.6.1 Differential-step CO_2 Adsorption

In this section, adsorption pseudo-isotherms constructed from differential-step CO_2 dosing experiments performed at 363 K and 378 K, are presented and discussed. The rationale for using these temperatures compared to those used in other sections of this work is due to the slow diffusion of CO_2 through PEI at temperatures below 363 K, due to its viscosity [9]. Moreover, from adsorption studies previously undertaken [7], it has been shown that the optimal operating temperature for PEI towards CO_2 adsorption is 378 K. In these experiments, the non-modified parent carbon was used as a reference for all adsorption pseudo-isotherms, instead of AC-N or AC-90.

The CO_2 adsorption pseudo-isotherms at 363 K and 378 K for the "as produced" and vacuum treated PEI loaded AC-90 (AC-90-90PEI-R and AC-90-90PEI-VT, respectively) are presented in ***Figure 5-5A-B***, along with AC-Ce3-90-AW and AC-90-Ce3-90-AW and their PEI loaded counterparts (***Figure 5-5C-F***). From ***Figure 5-5A-B***, the effect that vacuum treatment had on the CO_2 adsorption of the PEI-AC composites can be seen. Furthermore, the amine efficiencies (a measure of the efficiency CO_2 adsorption per amine group, ***section 6.6.4***) derived from ***Figure 5-5A-F*** (***equation 6-10***), are presented in ***Table 5-5***. The adsorption pseudo-isotherms obtained for the La catalysed physically activated carbons AC-La3-90-AW and AC-90-La3-90-AW and their PEI loaded counterparts (AC-La3-90-AW and AC-90-La3-90-AW) are presented in ***Figure 5-6A-D***, with the amine efficiencies (***equation 6-10***) given in ***Table 5-5***.

The adsorption pseudo-isotherms of AC-90-90PEI-R (***Figure 5-5A***) showed the highest adsorption of any adsorbent material presented in this thesis. Specifically, the adsorption at 363 K, was higher than that observed for any other adsorbent, even at 293 K. At 363 K the most significant increases were observed between 2.5 kPa and 15 kPa CO_2 partial pressure, indicating strong uptake. This bodes well for the use of AC-90-90PEI-R in a VSA process, with the cycle being between 5 kPa and 15 kPa CO_2 partial pressure. Furthermore, the adsorption at 378 K was higher than any other AC tested at this temperature. Moreover, it possessed higher adsorption at 378 K than AC-90 at any temperature (and most other physisorbents). Not only did AC-90-90PEI-R exhibit the highest adsorption of CO_2 at both 363 K and 378 K, but it also exhibited the highest amine efficiencies (***Table 5-5***) over the entire CO_2 partial pressure range. This means

that AC-90-90PEI-R used the PEI impregnated into its pore structure better than any other PEI-AC, as will be seen in the following discussion.

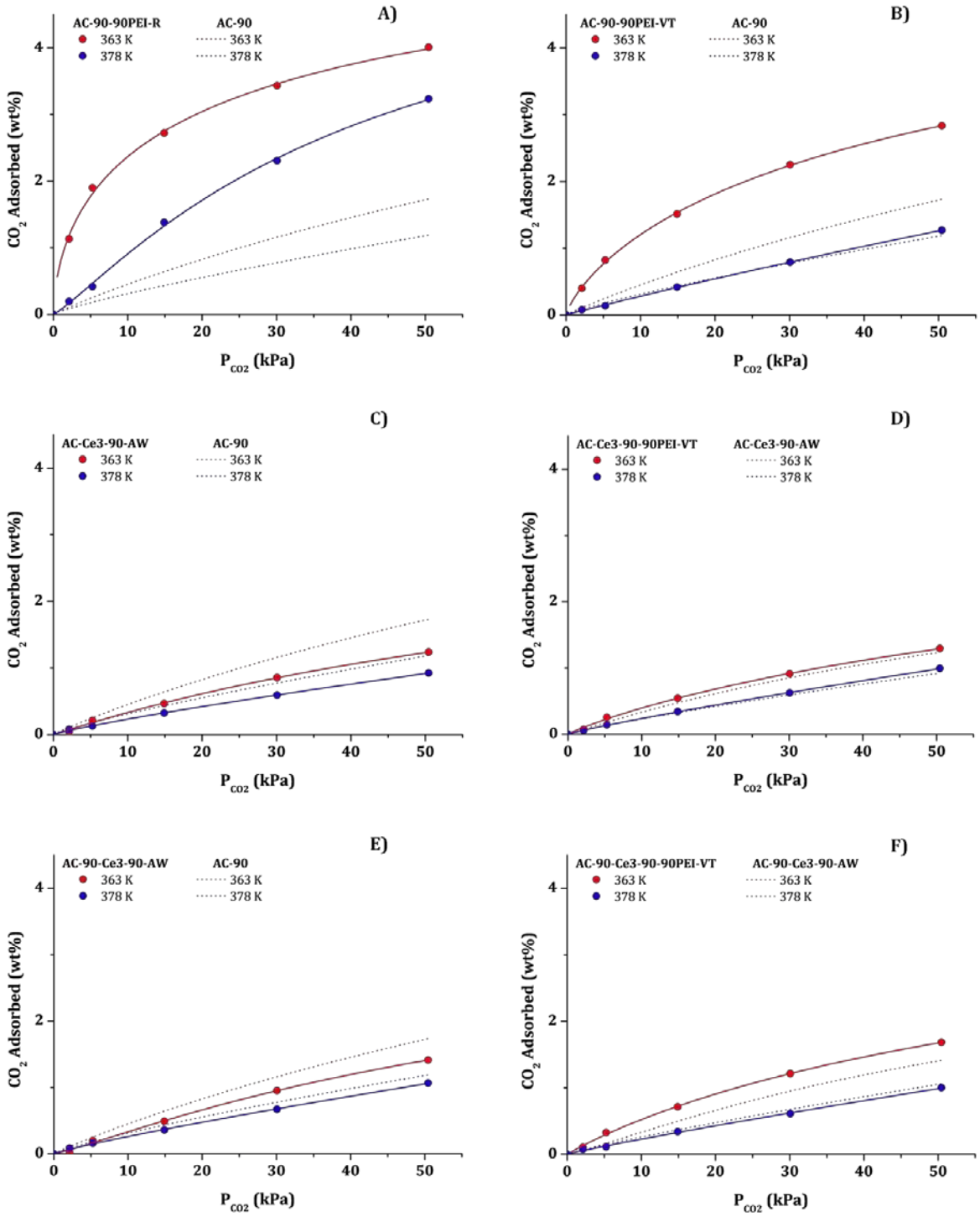

Figure 5-5 ~ *CO_2 Adsorption Pseudo-Isotherms for PEI Loaded CeO_2 Catalysed Physically Activated Carbons, taken via PPSA at 333 & 363 K. Shown are **A)** AC-90-90PEI-R, **B)** AC-90-90PEI-VT, **C)** AC-Ce3-90-AW, **D)** AC-Ce3-90-90PEI-VT, **E)** AC-90-Ce3-90-AW, and **F)** AC-90-Ce3-90-90PEI-VT*

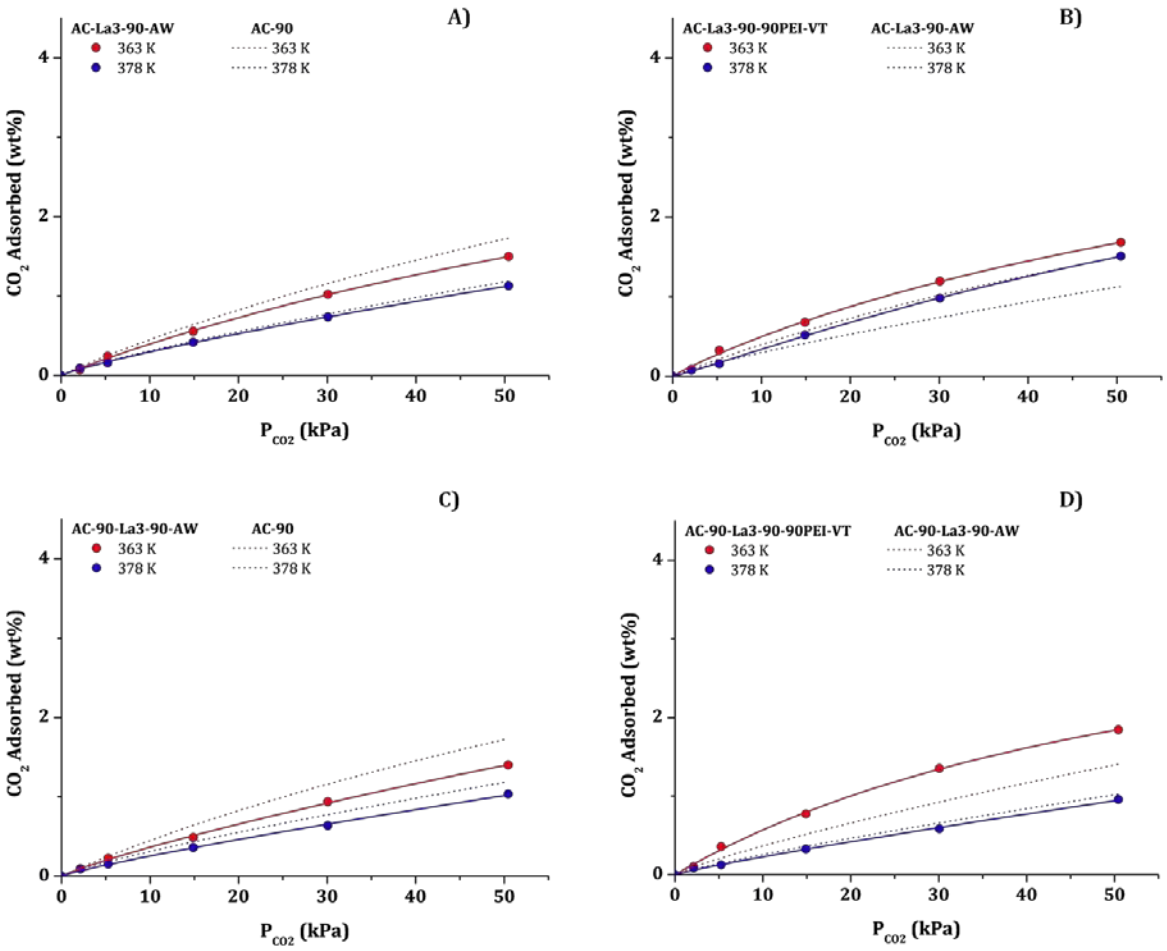

Figure 5-6 *~ CO_2 Adsorption Pseudo-Isotherms for PEI Loaded La_2O_3 Catalysed Physically Activated Carbons, taken via PPSA at 333 & 363 K. Shown are* ***A)*** *AC-La3-90-AW,* ***B)*** *AC-La3-90-90PEI-VT,* ***C)*** *AC-90-La3-90-AW, and* ***D)*** *AC-90-La3-90-90PEI-VT*

The vacuum treatment of AC-90-90PEI-R (leading to AC-90-90PEI-VT) used to remove low molecular weight volatile PEI (see ***section 6.5***), resulted in significant decreases in adsorption at both 363 K and 378 K for the adsorption pseudo-isotherms of AC-90-90PEI-VT (***Figure 5-5B***). As the low molecular weight PEI was removed, it appears that the higher molecular weight PEI may have been drawn deeper into the pore structure of the AC support, increasing the number of interactions between the PEI and AC. The surface of AC-90 is known to possess a high surface concentration of hydroxyl groups, that will potentially form hydrogen bonds with the amine groups of PEI [10]. In addition to hydrogen bonding (weak interactions) between the PEI and AC surface, there are potentially much stronger interactions (electrostatic) between the amine groups and the acidic groups (e.g. carboxylic acids and phenols) of the AC surface. The electrostatic interactions were able to form through the protonation of the amines by the acid AC surface moieties (e.g. carboxylic acids and phenols). Moreover, the pores of the ACs employed here possessed closed, slit shaped pores (***section 2.3.3.2.1***, ***section 4.3.3.2.1***, and

section 4.4.3.2.1); it is therefore conceivable that any CO_2 that was adsorbed to the PEI deep within this structure would have significant difficulty diffusing out. Further evidence supporting the increased number of interactions between the amines and AC surface can be seen from the amine efficiencies of AC-90-90PEI-VT relative to AC-90-90PEI-R (***Table 5-5***). From the amine efficiencies across the partial pressure range it is clear that there was a significant decrease in the efficiency of the amine groups of the PEI within AC-90-90PEI-VT relative to AC-90-90PEI-R. The amine efficiency is a good measure of how effective the amine groups within the PEI of a sample are, as it excludes the effects of the loss in PEI on adsorption, resulting from the vacuum treatment. Therefore, the decrease in amine efficiency observed for AC-90-90PEI-VT relative to AC-90-90PEI-R would result from an increase in the number of amine groups interacting with the AC surface, resulting from being drawn deeper into the AC pore structure, making them unavailable for CO_2 adsorption.

Table 5-5 ~ *Amine Efficiencies of PEI Loaded miACs and meACs*

Sample Name		Amine Efficiency (mol CO_2/mol N)				
		CO_2 Partial Pressure (kPa)				
		2.13	5.27	14.89	30.09	50.45
AC-90-90PEI-R	363 K	0.049	0.082	0.118	0.148	0.173
	378 K	0.008	0.018	0.060	0.100	0.140
AC-90-90PEI-VT	363 K	0.021	0.043	0.079	0.117	0.147
	378 K	0.002	0.006	0.020	0.041	0.067
AC-Ce3-90-90PEI-VT	363 K	0.005	0.018	0.037	0.062	0.089
	378 K	0.004	0.010	0.023	0.043	0.068
AC-90-Ce3-90-90PEI-VT	363 K	0.004	0.013	0.028	0.047	0.066
	378 K	0.003	0.004	0.013	0.024	0.039
AC-La3-90-90PEI-VT	363 K	0.005	0.017	0.036	0.063	0.089
	378 K	0.004	0.008	0.027	0.052	0.079
AC-90-La3-90-90PEI-VT	363 K	0.005	0.016	0.035	0.061	0.083
	378 K	0.004	0.006	0.015	0.026	0.043

The incorporation of PEI into the pore structure of AC-Ce3-90-AW resulted in little overall increase in CO_2 adsorption over the entire CO_2 partial pressure range of the differential-step adsorption studies of AC-Ce3-90-90PEI-VT (***Figure 5-5C-D***). At 363 K AC-Ce3-90-90PEI-VT exhibited only minor increases in CO_2 uptake relative to the AC-Ce3-90-AW, and at 378 K almost

no discernible differences were apparent until a CO_2 partial pressure greater than 15 kPa; after which only relatively minor increases in adsorption were observed. This is due to the PEI being drawn deep into the pore structure of AC-Ce3-90-AW, which possesses a higher concentration of hydroxyl and phenol groups than AC-90, and these groups may interact with the amines within the PEI, making them unavailable to take part in CO_2 adsorption. As has already been noted, the hydroxyl groups are likely to form weak interactions with the amines (hydrogen bonds), whilst the phenol and carboxylic acid groups may form strong interactions with the amines (electrostatic). As the CO_2 adsorption was lower than would be expected from a PEI loaded material it is of little surprise that the amine efficiency of AC-Ce3-90-90PEI-VT was also low across the entire CO_2 partial pressure range (***Table 5-5***). This was particularly apparent when compared to the amine efficiencies of AC-90-90PEI-R (***Table 5-5)***. Due to the effect that the vacuum treatment had on AC-90-90PEI-VT, it is proposed that a similar effect has occurred for other PEI-ACs as a result of the vacuum treatment. The proposed effects of the vacuum treatment would be accentuated in the case of AC-Ce3-90-90PEI-VT as the concentration of phenol groups on the surface of AC-Ce3-90-AW were significantly higher than for AC-90 (***Table 4-4***). This might result in a greater amount of amine groups within the PEI being made unavailable for CO_2 adsorption due to the formation of electrostatic interactions, which also agrees with the low amine efficiencies observed (***Table 5-5***). Furthermore, the AC-Ce3-90-AW support had the smallest mesopore volume of any carbon supports used to produce PEI-ACs composites, which may also have been a factor, as less PEI could be impregnated into the support.

The adsorption pseudo-isotherms of AC-90-Ce3-90-90PEI-VT (***Figure 5-5E***) exhibited interesting adsorption behaviour relative to its support (AC-90-Ce3-90-AW). At 363 K AC-90-Ce3-90-AW-90PEI-VT exhibited significantly higher adsorption compared to AC-90-Ce3-90-AW, whereas, at 378 K the adsorption of CO_2 was lower. The pore volumes of AC-90-Ce3-90-AW were greater than AC-Ce3-90-AW (***Table 4-6***) and, with this, the PEI loading of AC-90-Ce3-90-90PEI-VT was greater than that of AC-Ce3-90-90PEI-VT on a mass loading basis. As was also noted for AC-Ce3-90-90PEI-VT, the high surface concentration of phenol groups will have resulted in few amines from the PEI being available to take part in adsorption due to the electrostatic interactions between the amines and phenol groups (as well as hydrogen bonding between hydroxyl and amine groups) of the AC-Ce3-90-AW surface. At 378 K the diffusion of CO_2 through the PEI will have been faster than at 363 K, however, the reverse carbamation reaction will also have been occurring at an increased rate (***Figure 1-5***). This is similar to the increase in the rate of desorption with increasing temperature observed for physisorption systems [11].

The pseudo-isotherms of AC-La3-90-90PEI-VT exhibited elevated CO_2 adsorption relative to AC-La3-90-AW at both 363 K and 378 K (***Figure 5-6B***). Furthermore, relative to the CeO_2 catalysed counterpart of AC-La3-90-90PEI-VT (AC-Ce3-90-90PEI-VT, ***Figure 5-5D***) it possessed significantly higher CO_2 adsorption at both 363 K and 378 K. Although AC-La3-90-AW and AC-Ce3-90-AW possessed similar micro- and mesopore volumes, the surface hydroxyl concentration of AC-La3-90-AW was lower than AC-Ce3-90-AW. It is suggested that this resulted in fewer amine groups within AC-La3-90-90PEI-VT being available for CO_2 adsorption because of interactions with the hydroxyl, carboxylic acid and phenol groups of the AC surface. Another reason for the increased CO_2 adsorption over AC-La3-90-90PEI-VT compared to AC-Ce3-90-90PEI-VT can be attributed to the overall higher loading of PEI. Though both were loaded on a 90% pore filling basis, AC-La3-90-AW possessed a higher total volume than AC-Ce3-90-AW (***Table 4-13***), and as such was loaded with more PEI overall (elemental analysis, ***Table 4-12***). It was also noted for the Ce-meAC supported PEI-ACs that the significantly lower CO_2 adsorption relative to the AC-90 supported PEI-ACs was due to the substantially higher surface phenol concentration; that could form electrostatic interactions with the amine groups.

The adsorption pseudo-isotherms of AC-90-La3-90-90PEI-VT (***Figure 5-6C***) exhibited remarkably similar adsorption behaviour to AC-90-Ce3-90-90PEI-VT (***Figure 5-5E***). However, the increased CO_2 adsorption at 363 K for AC-90-La3-90-90PEI-VT relative to its support was greater than observed for AC-90-Ce3-90-90PEI-VT, on account of the lower concentration of hydroxyl groups on the surface of AC-90-La3-90-AW (***Table 4-8*** and ***Table 4-9***) compared to AC-90-Ce3-90-AW (***Table 4-3*** and ***Table 4-4***). The lower surface hydroxyl group concentration of AC-90-La3-90-AW relative to AC-90-Ce3-90-AW will have allowed for fewer amine groups within AC-90-La3-90-90PEI-VT to hydrogen bond to the AC-90-La3-90-AW surface, thus making them available for CO_2 adsorption. Although the adsorption behaviour of AC-90-La3-90-90PEI-VT and AC-90-Ce3-90-90PEI-VT were similar, the amine efficiencies of AC-90-La3-90-90PEI-VT at 363 K and 378 K were higher (***Table 5-5***). Even though the total adsorption was similar over both PEI-ACs, the total PEI loading of AC-90-La3-90-90PEI-VT was lower (elemental analysis, ***Table 4-12***). Therefore, it can be said that AC-90-La3-90-90PEI-VT used the PEI in its pore structure more effectively than AC-90-Ce3-90-90PEI-VT (***Table 5-5***).

5.6.2 Multi-cyclic CO_2 Adsorption

The CO_2 adsorption behaviour of the PEI-loaded carbon materials produced by Ln_xO_y catalysed physical activation were also examined under multi-cyclic conditions, cycling between CO_2 partial pressures of 5 kPa and 15 kPa, at 363 K and 378 K. This was undertaken in order to

investigate the adsorption behaviour of the materials under the CO_2 partial pressure conditions proposed for use in a VSA process and thus their application to such a system. The multi-cyclic studies at 363 K and 378 K for AC-90-90PEI-R, AC-90-90PEI-VT, AC-Ce3-90-AW, AC-Ce3-90-90PEI-VT, AC-90-Ce3-90-AW and AC-90-Ce3-90-90PEI-VT are presented in ***Figure 5-7A-F***, whilst those for AC-La3-90-AW, AC-La3-90-90PEI-VT, AC-90-La3-90-AW and AC-90-La3-90-90PEI-VT at 363 K and 378 K are shown in ***Figure 5-8A-D***. Finally, from the multi-cyclic adsorption studies, working capacities (***equation 6-11***) were derived for each PEI-AC composite, the results of which are presented in ***Table 5-6***.

The multi-cyclic study for AC-90 at 363 K was presented as ***Figure 3-3D*** in ***section 3.3.2***. It is interesting to note that upon increasing the temperature from 363 K to 378 K (reference plots in ***Figure 5-7*** and ***Figure 5-8***). There was no apparent change in the adsorption at 5 kPa CO_2 partial pressure, and only relatively minor decreases at 15 kPa. Additionally, the working capacity at 378 K for AC-90 was one of the highest values obtained at that temperature for either the ACs or PEI-AC composite (***Table 5-6***).

From the multi-cyclic studies of AC-90-90PEI-R (***Figure 5-7A***) similar increases in CO_2 adsorption are observed at 363 K relative to AC-90, as were apparent from the differential-step adsorption studies (***Figure 5-5A***). Furthermore, the adsorption exhibited by AC-90-90PEI-R at 15 kPa CO_2 partial pressure never achieves equilibrium, implying that if a longer cycle was employed, then substantially more CO_2 would be expected to be adsorbed. At 378 K increased CO_2 adsorption is also observed relative to the AC-90 support, in addition to much faster diffusion of gas through the PEI, with equilibrium being achieved within the timeframe of the adsorption cycle. Although the diffusion of gas through the PEI has increased with the increase in temperature to 378 K, the amount adsorbed is significantly less than observed at 363 K. Moreover, as there is a progressive upward drift in the mass signal at 5 kPa CO_2 partial pressure with successive cycles it is safe to say that incomplete desorption is also occurring. This is an important factor in regards to the long term stability or applicability of the adsorbent in an industrial setting.

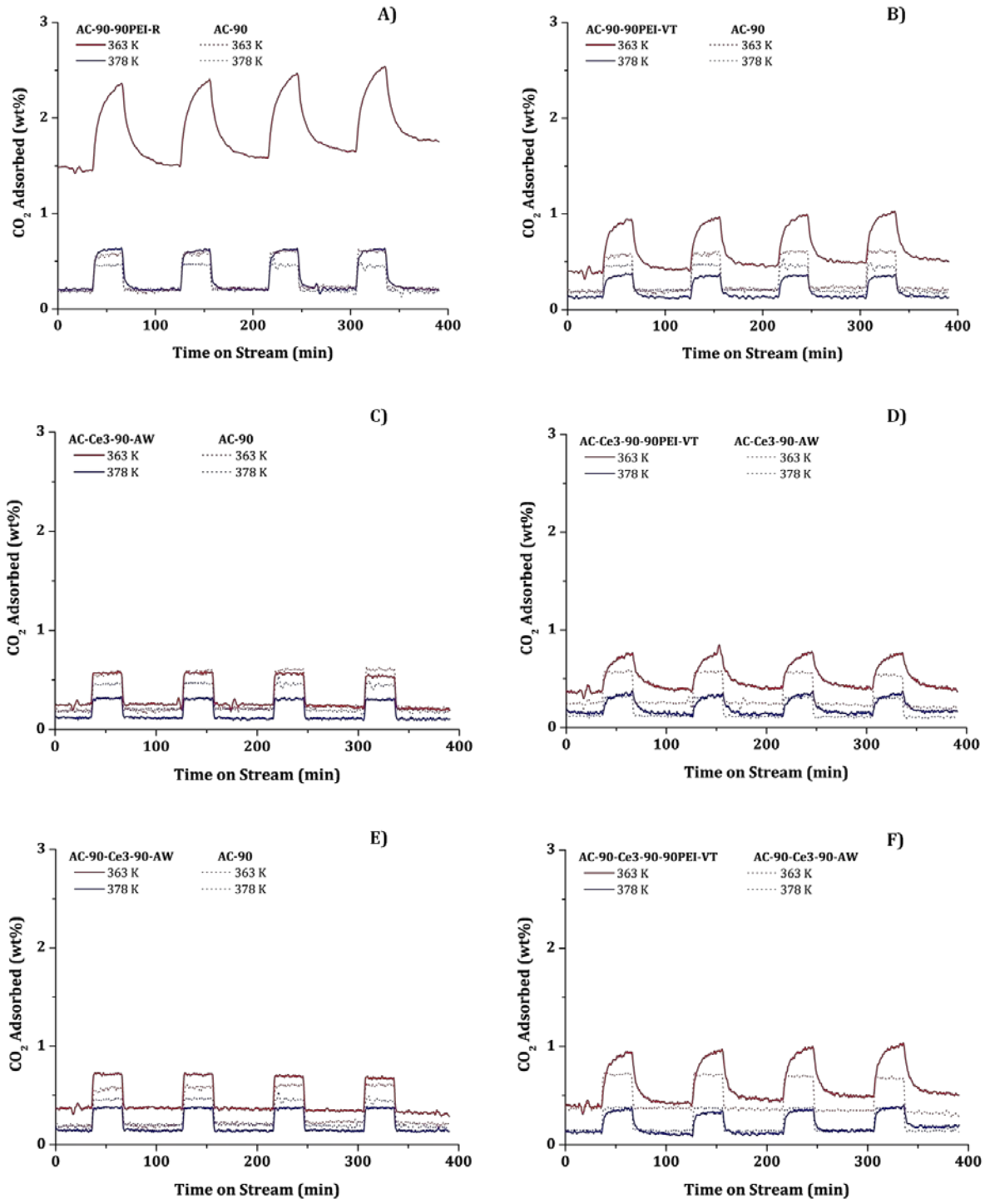

Figure 5-7 ~ *VSA Simulations for PEI Loaded Physically Activated Carbons, taken via PPSA at 333 & 363 K. Shown are* ***A)*** *AC-90-90PEI-R,* ***B)*** *AC-90-90PEI-VT,* ***C)*** *AC-Ce3-90-AW,* ***D)*** *AC-Ce3-90-90PEI-VT,* ***E)*** *AC-90-Ce3-90-AW, and* ***F)*** *AC-90-Ce3-90-90PEI-VT*

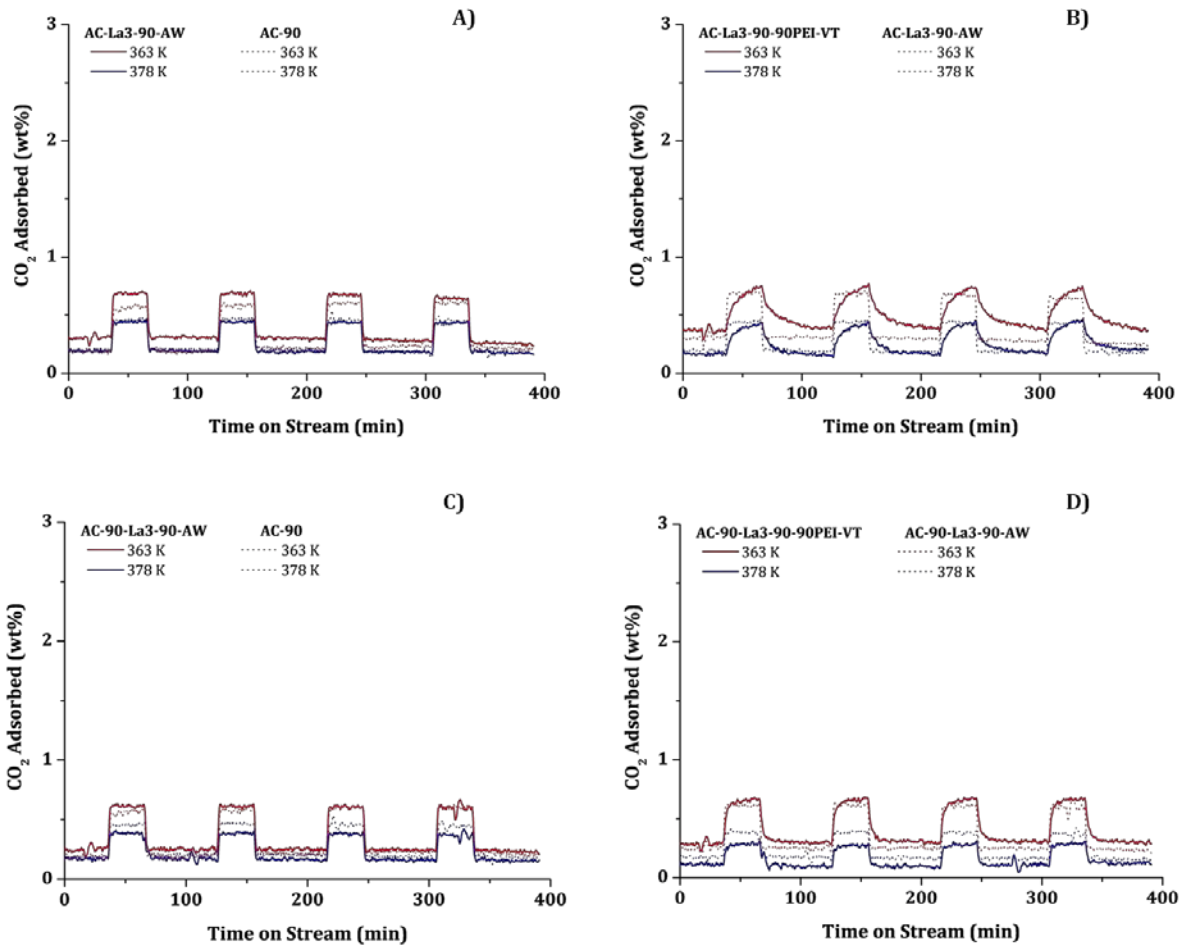

Figure 5-8 ~ *VSA Simulations for PEI Loaded Physically Activated Carbons, taken via PPSA at 333 & 363 K. Shown are* ***A)*** *AC-La3-90-AW,* ***B)*** *AC-La3-90-90PEI-VT,* ***C)*** *AC-90-La3-90-AW, and* ***D)*** *AC-90-La3-90-90PEI-VT*

The decrease in CO_2 adsorption at 363 K observed from the pseudo-isotherms of AC-90-90PEI-VT relative to AC-90-90PEI-R (***Figure 5-5B*** and ***Figure 5-5A***, respectively) were also mirrored in the multi-cyclic adsorption studies (***Figure 5-7A-B***). However, equilibrium is still not achieved at a CO_2 partial pressure of 15 kPa. This reduction can in part be attributed to the decrease in PEI of AC-90-90PEI-VT relative to AC-90-90PEI-R as a result of the vacuum treatment (25 wt%, ***Table 4-12***), but also the proposed migration of PEI deeper into the pores, as noted in ***section 5.6.1*** may be a factor. Relative to the working capacity of AC-90-90PEI-R at 363 K, that of AC-90-90PEI-VT was 60% lower as a result of the vacuum treatment, which is far beyond that which might be expected from the removal of low molecular weight PEI (***Table 4-12***). At 378 K the multi-cyclic adsorption of AC-90-90PEI-VT was lower relative to both AC-90-90PEI-R and the AC-90 support. Equilibrium was achieved within the timeframe of the adsorption cycle, although this was still much slower compared to AC-90. The working capacity at 378 K for AC-90-90PEI-VT was slightly lower than that observed for AC-90 (***Table 5-6***).

However, the selectivity of CO_2 adsorption from a mixed gas stream by the PEI-ACs should be better than for AC-90.

Table 5-6 ~ *Working Capacity of PEI-AC Composites at 363 & 378 K*

Sample Name	Working Capacity (wt%)	
	363 K	378 K
AC-90	0.39	0.27
AC-90-90PEI-R	0.86	0.44
AC-90-90PEI-VT	0.51	0.25
AC-Ce3-90-AW	0.33	0.21
AC-Ce3-90-90PEI-VT	0.40	0.22
AC-La3-90-AW	0.37	0.25
AC-La3-90-90PEI-VT	0.37	0.29
AC-90-Ce3-90-AW	0.33	0.23
AC-90-Ce3-90-90PEI-VT	0.51	0.25
AC-90-La3-90-AW	0.36	0.23
AC-90-La3-90-90PEI-VT	0.39	0.20

The multi-cyclic adsorption over AC-Ce3-90-90PEI-VT (***Figure 5-7D***) at 363 K exhibited typical adsorption behaviour to that observed at 363 K for the other PEI-ACs presented thus far. That is to say relatively high adsorption was observed at a CO_2 partial pressure of 15 kPa, but equilibrium was never achieved within the timeframe of the adsorption cycle. Furthermore, equilibrium was not achieved during the desorption part of the cycle either. Hence when the successive adsorption cycle started, some of the CO_2 from the previous adsorption cycle was still present. As such there was a gradual drift in the mass signal over the course of the multi-cyclic adsorption studies, this behaviour being attributed to slow mass transport through the bulk PEI phase at 363 K. This phenomenon is still evident at 378 K, even though the adsorption/desorption rates are faster than at 363 K. However, unlike the multi-cyclic studies of the PEI an impregnated AC-90 material, for AC-Ce3-90-90PEI-VT at 378 K equilibrium was never fully achieved within the timeframe of the adsorption cycle. The working capacity of AC-Ce3-90-90PEI-VT (***Table 5-6***) at 363 K was significantly higher than that of the AC-Ce3-90-AW

support. Conversely, at 378 K there was no apparent difference in the working capacity of AC-Ce3-90PEI-VT relative to the AC-Ce3-90-AW support.

The multi-cyclic adsorption study for AC-La3-90-90PEI-VT (***Figure 5-8B***) at 363 K was higher than that observed for the AC-La3-90-AW support under the same conditions. The working capacity (***Table 5-6***) at 363 K was essentially identical for both AC-La3-90-90PEI-VT and AC-La3-90-AW. AC-La3-90-90PEI-VT exhibited higher overall adsorption, but the difference between the amounts adsorbed at 5 kPa and 15 kPa CO_2 partial pressure was not significantly different to these for AC-La3-90-AW. Furthermore, it is of interest to note that at both 363 K and 378 K, that equilibrium was not achieved within the timeframe of the adsorption cycle. The observation of this at 378 K was also made for AC-Ce3-90-90PEI-VT, but to a lesser extent (***Figure 5-7D***). Thus, mass-transport limitations through the PEI bulk phase are still apparent even at 378 K. Compared to AC-90 and AC-Ce3-90-AW, AC-La3-90-AW possesses larger meso- and total pore volumes (***Table 4-13***), as such there is a larger amount of bulk PEI phase within the large pores.

The second highest adsorption was observed at 15 kPa CO_2 partial pressure (second only to AC-90-90PEI-R, ***Figure 5-7A***) from the multi-cyclic adsorption study of AC-90-Ce3-90-90PEI-VT (***Figure 5-7E***) at 363 K. The working capacities at both 363 K and 378 K were essentially identical to those of AC-90-90PEI-VT (***Table 5-6***). However, the nitrogen content of AC-90-Ce3-90-90PEI-VT was higher than for AC-90-90PEI-VT (***Table 4-12***), and as such the amine efficiency of AC-90-Ce3-90-90PEI-VT was poorer when this was taken into account (refer to amine efficiencies in ***Table 5-5***). Furthermore, as was the case for all the PEI-ACs presented thus far, equilibrium was not achieved over the timeframe of the cycle.

The multi-cyclic adsorption studies of AC-90-La3-90-90PEI-VT (***Figure 5-8D***) exhibited adsorption behaviour at 363 and 378 K that showed the achievement of equilibrium at both 5 kPa and 15 kPa CO_2 partial pressure. Although at both temperatures equilibrium was achieved within the timeframe of the adsorption cycle, the working capacities of AC-90-La3-90-90PEI-VT (***Table 5-6***) were in the lower range of those presented in ***Table 5-6***. However, as the adsorption kinetics were significantly faster than the other PEI-ACs in particular at 363 K, this would potentially allow for shorter cycles to be run, at a lower temperature.

5.6.3 CO_2/H_2O Adsorption

The adsorption of CO_2 in the presence of H_2O; such as is actually encountered in post-combustion flue gas streams have to this point been confined to competitive adsorption on physisorbents (e.g. activated carbons and chars). For the PEI-AC composite materials the effect of H_2O on the PEI itself (i.e. steam stripping, adsorption kinetics, etc) and carbonate formation are of interest (refer to ***Figure 1-5***). As such a similar method to that used in ***sections 3.6*** was utilised (refer to ***section 6.6.4.3*** for full details), but for an altogether different purpose (to study chemisorption). The single cycle measurements under both wet and dry gas conditions at 363 K and 378 K are presented for AC-90, AC-90-90PEI-R and AC-90-90PEI-VT in ***Figure 5-9A-F***, for AC-Ce3-90-90PEI-VT and AC-90-Ce3-90-90PEI-VT as ***Figure 5-10A-D***, and for AC-La3-90-90PEI-VT and AC-90-La3-90-90PEI-VT as ***Figure 5-11A-D***.

From the wet vs. dry single cycle gas adsorption study for AC-90-90PEI-R (***Figure 5-9C***) at 363 K, it can clearly be seen that the presence of H_2O increases the adsorption of CO_2, presumably through carbonate formation [12-15]. Furthermore, at 363 K under dry gas conditions complete desorption was not observed by the end of the desorption phase of the cycle, which may be due to the formation of urea compounds [7, 16, 17]. It has been well documented that CO_2 adsorption over PEI composite materials under wet gas conditions both inhibits the formation of urea compounds and promotes the formation of carbonates [7]. This may explain why complete desorption was observed at 363 K under wet gas conditions, as the urea formation would be inhibited by the presence of H_2O. Moreover, under both wet and dry gas conditions equilibrium is not achieved, as was noted in ***section 5.6.2***. At 378 K the adsorption under dry gas conditions for AC-90-90PEI-R (***Figure 5-9D***) did achieve equilibrium, whilst this was not the case under wet gas conditions. Furthermore, under wet gas conditions a significant increase in the level of adsorption was observed at 15 kPa CO_2 partial pressure. As equilibration was not achieved at 15 kPa CO_2 partial pressure under wet gas conditions it is proposed that over a longer time scale that significantly more CO_2 would be adsorbed, which is also applicable to the adsorption at 363 K under wet gas conditions.

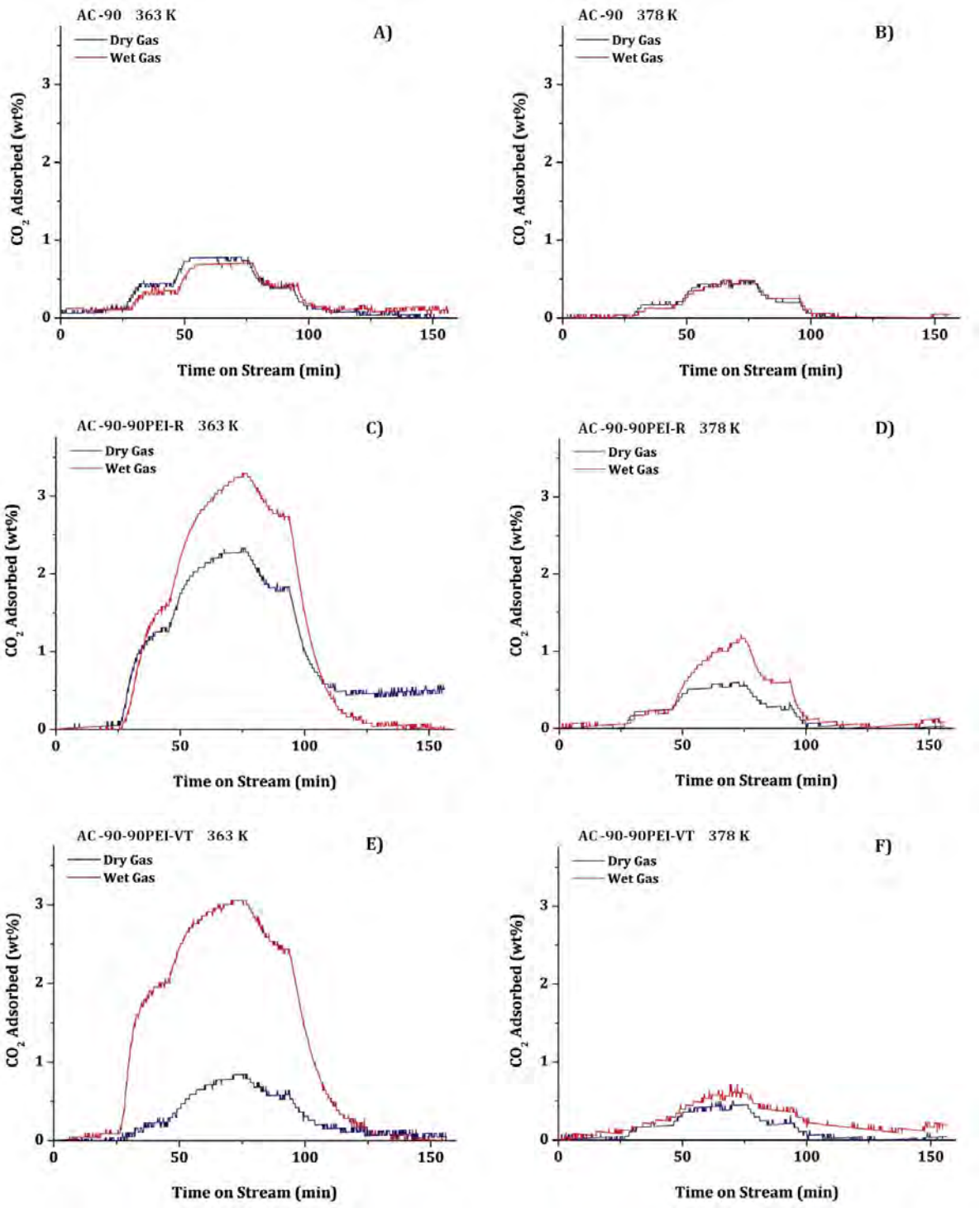

Figure 5-9 *~ Single Cycle Wet & Dry Gas Adsorption for PEI Loaded AC-90 at 363 & 378 K. Shown are the Plots for* ***A)*** *AC-90 at 363 K,* ***B)*** *AC-90 at 378 K,* ***C)*** *AC-90-90PEI-R at 363 K,* ***D)*** *AC-90-90PEI-R at 378 K,* ***E)*** *AC-90-90PEI-VT at 363 K, and* ***F)*** *AC-90-90PEI-VT at 378 K*

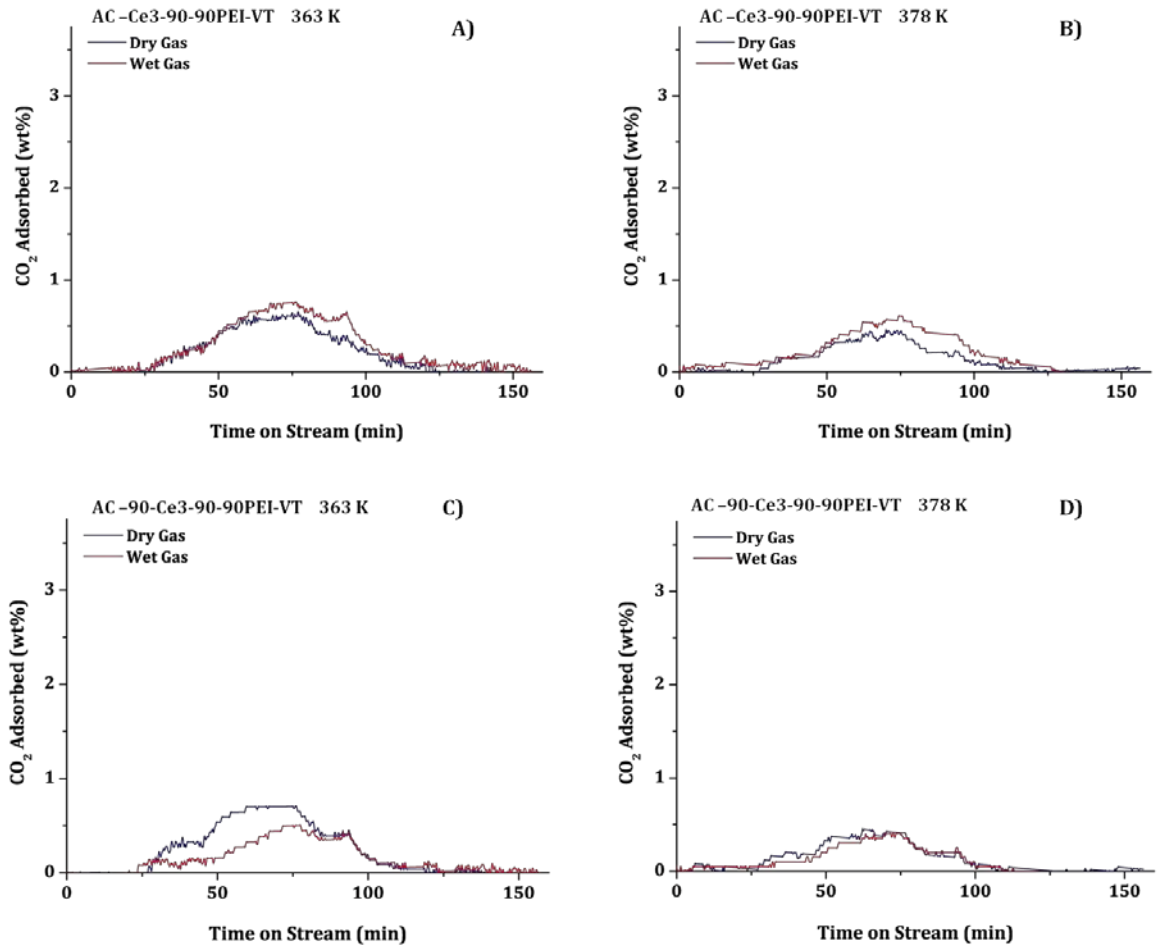

Figure 5-10 *~ Single Cycle Wet & Dry Gas Adsorption for PEI Loaded CeO_2 Catalysed Physically Activated Carbons at 363 & 378 K. Shown are the Plots for* ***A)*** *AC-Ce3-90-90PEI-VT at 363 K,* ***B)*** *AC-Ce3-90-90PEI-VT at 378 K,* ***C)*** *AC-90-Ce3-90-90PEI-VT at 363 K, and* ***D)*** *AC-90-Ce3-90-90PEI-VT at 378 K*

The amount of CO_2 adsorbed by AC-90-90PEI-VT under dry gas conditions at 363 K (***Figure 5-9E***) was significantly lower than that observed for AC-90-90PEI-R (***Figure 5-9C***) under the same conditions. This was with the observed CO_2 adsorption behaviour of both PEI-ACs determined in the multi-cyclic adsorption studies (***Figure 5-7***), which exceeded the decrease expected by simply reducing the number of amine sites upon vacuum treatment (***Table 4-12***). This behaviour can likely be attributed to PEI being drawn deeper into the pore structure of the AC-90 support, thereby increasing the number of interactions between PEI and the AC-90 surface and concurrently rendering these amine sites inaccessible/unavailable for CO_2 adsorption (as proposed earlier in this section).

While complete CO_2 desorption was observed for AC-90-90PEI-VT, it was not for AC-90-90PEI-R. The incomplete desorption under dry gas conditions at 363 K for AC-90-90PEI-R could be attributed to significant urea formation. Conversely, complete desorption was observed for AC-90-90PEI-VT, which would suggest that urea formation was minimal; which is likely to result

from the vacuum treatment used to remove the low molecular weight PEI. Two potential situations could explain why the vacuum treatment resulted in a reduction in urea formation. Firstly, the low molecular weight PEI would be more likely to react with CO_2 due to its greater mobility within the bulk PEI phase. Secondly, the increased number of interactions between PEI and the AC-90 surface which arose from PEI being drawn deeper into the AC pore structure, resulted in fewer amine sites being available for CO_2 adsorption could also foreseeably lead to a decrease in the proportion of urea formed. Both situations are plausible and it is likely that both occur simultaneously.

At 363 K under wet gas conditions, AC-90-90PEI-VT exhibited substantially higher CO_2 adsorption than it did under dry gas conditions, and was almost comparable to that exhibited by AC-90-90PEI-R under similar conditions (***Figure 5-9C***). It is proposed that whilst achieving equilibrium with the wet Ar gas stream prior to analysis at 363 K, many of the weaker interactions (hydrogen bonds) between the amine and the AC-90 surface hydroxyl were disrupted by H_2O, which would be more likely to occur at 363 K due to the presence of condensed H_2O. From the single cycle, differential-step and multi-cyclic adsorption studies of AC-90-90PEI-VT at 378 K, it was clear that under dry gas conditions the amount of CO_2 adsorbed varied little to that observed for AC-90 itself. However, under wet gas conditions at 378 K, there was a small but noticeable increase in CO_2 adsorption. At 378 K (i.e. above the boiling point of water), the interactions between the PEI and AC-90 surface would have been better maintained, thereby limiting the number of amine sites available to take part in CO_2 adsorption.

The Ln-meACs supported PEI-ACs displayed significantly lower CO_2 adsorption than the AC-90 supported PEI-ACs from the differential-step (***section 5.6.1***) and multi-cyclic (***section 5.6.2***) adsorption studies, with similarly reduced CO_2 adsorption being observed for the single cycle studies (***Figure 5-10*** and ***Figure 5-11***). This has been attributed to a higher number of strong interactions between the PEI amines and the acidic functionality (e.g. carboxylic acids and phenols) of the Ln-meACs as compared to AC-90. However, on the basis of the bulk N content and pore volumes of the supports, the Ln-meAC supported PEI materials should have exhibited a similar amount of CO_2 adsorption as the PEI-loaded AC-90 materials. This finding indicated that fewer amines in the PEI of the Ln-meAC supported materials were available to take part in adsorption processes, which corresponded to the low amine efficiencies determined for these materials (***Table 5-5***). In many cases the rate of CO_2 adsorption was slower under wet gas conditions than dry gas conditions, which is likely due to the formation of condensed H_2O at 363 K, which would compete for space with CO_2. The Ln-meAC supports possessed more surface acid groups than AC-90, which may have given rise to strong electrostatic interactions with the

amines, which H_2O would not have been likely to disrupt. As such the H_2O will have been competing for amine sites with CO_2. However, it was only for AC-90-Ce3-90-90PEI-VT under wet gas conditions at 363 K, that the actual amount of CO_2 adsorbed was significantly affected by the presence of H_2O.

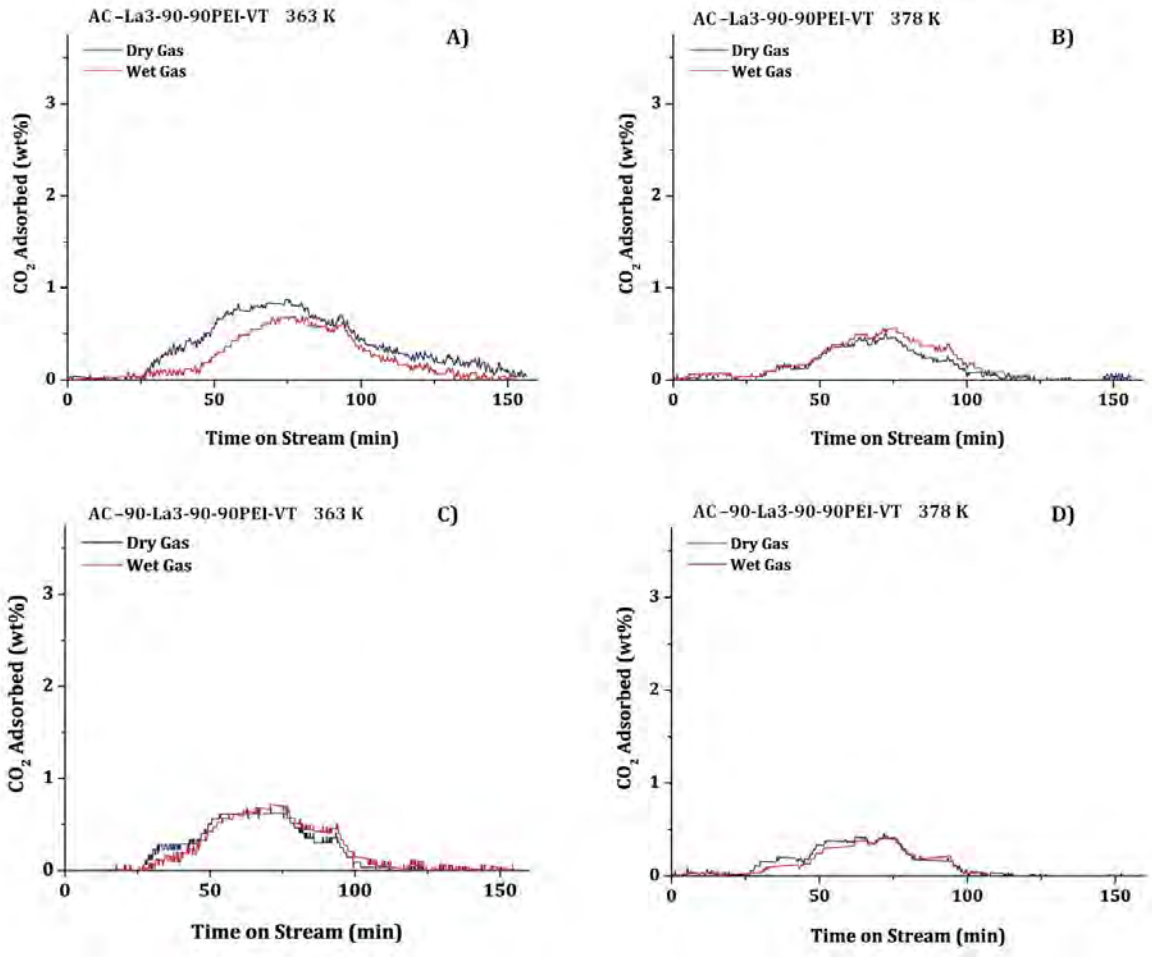

Figure 5-11 *~ Single Cycle Wet & Dry Gas Adsorption for PEI Loaded La_2O_3 Catalysed Physically Activated Carbons at 363 & 378 K. Shown are the Plots for* ***A)*** *AC-La3-90-90PEI-VT at 363 K,* ***B)*** *AC-La3-90-90PEI-VT at 378 K,* ***C)*** *AC-90-La3-90-90PEI-VT at 363 K, and* ***D)*** *AC-90-La3-90-90PEI-VT at 378 K*

The adsorption of CO_2 under dry gas conditions for the single cycle adsorption studies of the Ln-meAC supported PEI-ACs showed comparable levels of adsorption to that observed from the differential-step and multi-cyclic adsorption studies, which was also the case at 363 K under dry gas conditions. However, the reduced rate of CO_2 adsorption observed under wet gas conditions at 363 K for the Ln-meAC supported PEI-ACs was not as prolific at 378 K, which can be primarily attributed to condensed H_2O being unlikely to form at this temperature. In fact at 378 K under wet gas conditions for AC-Ce-90-90PEI-VT and AC-La3-90-90PEI-VT no observable

reduction in the rate of CO_2 adsorption was observed, and small but noticeable increases in the amount of CO_2 adsorbed were observed.

Overall, the AC-90 supported PEI-ACs showed the most promise, but they still exhibited several drawbacks. While AC-90-90PEI-R exhibited superior CO_2 adsorption in wet conditions, in dry conditions irreversible adsorption occurred due to the formation of ureas in the low molecular weight PEI species. This also brought into question the vacuum stability of AC-90-90PEI-R in the vacuum conditions the materials would be exposed to during a VSA process. Vacuum treatment of AC-90-90PEI-VT to remove the chemically unstable low molecular weight PEI resulted in significant decreases in CO_2 capacity due to the PEI being drawn deeper into the pore structure of the AC-90 support. Even more significant decreases in CO_2 adsorption were observed for the Ln-meACs. It was proposed that when PEI is drawn deeper into the pores of the support upon vacuum treatment, stronger and more numerous interactions occur between PEI and the AC support which reduces the number available amine sites for CO_2 adsorption.

5.7 Summary and Conclusions

In summation, the meACs and PEI-ACs produced in ***chapter 4*** were examined for their ability to separate CO_2 from flue gas streams under conditions aimed at simulating the temperature and partial pressure conditions of a practical VSA system. Reductions were observed in the pore volume of the Ln_xO_y catalysed physically activated ACs as a result the acid washing procedure used for the post-synthetic removal of the lanthanide oxide catalysts. This was attributed to the removal of the inherent porosity of the amorphous Ln_xO_y phase itself.

In this chapter it was shown from the CO_2 adsorption pseudo-isotherms that the Ln-meACs exhibited equal or lower CO_2 adsorption than AC-90 at all temperatures and CO_2 partial pressures. The multi-cyclic adsorption studies of the "as produced" Ln-meACs showed similar adsorption behaviour in the differential-step adsorption studies, however, two of the acid washed Ln-meACs (AC-Ce3-90-AW and AC-La3-90-AW) showed some signs of mass-transport limitations. Both of these Ln-meACs were derived directly from VBC and possessed low mesopore volumes which accounted for this adsorption behaviour.

Impregnation of AC-90 with PEI resulted in a PEI-AC composite that exhibited significantly increased CO_2 adsorption relative to AC-90, at all temperatures and CO_2 partial pressures. The effect that the post-synthetic vacuum treatment had on the CO_2 adsorption properties of the PEI-AC composites was to significantly reduce the amount of CO_2 adsorbed, as could be clearly observed from both the adsorption studies of AC-90-90PEI-VT relative to AC-90-90PEI-R. This

was attributed to an increase in the interactions between the PEI and the AC surface, which arose from the vacuum treatment; with the end result being a decrease in amine groups available for adsorption. These interactions were stronger and more numerous for the Ln-meACs supported PEI-ACs, and was in part the reason why similar or reduced adsorption was observed under wet gas conditions relative to dry conditions. Although further study of these types of PEI-AC composite materials may be warranted, the evidence of vacuum instability suggests they are not suitable for application of CO_2 directly from post-combustion flue gas streams.

5.8 References

1. Kamimura, Y. and A. Endo, *CO2 adsorption performance of mesoporous ceria with co-adsorbed water.* Chemistry Letters, 2015. **44**(11): p. 1494-1496.
2. Kamimura, Y., M. Shimomura, and A. Endo, *Simple template-free synthesis of high surface area mesoporous ceria and its new use as a potential adsorbent for carbon dioxide capture.* Journal of Colloid and Interface Science, 2014. **436**: p. 52-62.
3. Li, C., et al., *Carbon monoxide and carbon dioxide adsorption on cerium oxide studied by Fourier-transform infrared spectroscopy. Part 1.-Formation of carbonate species on dehydroxylated CeO2, at room temperature.* Journal of the Chemical Society, Faraday Transactions 1: Physical Chemistry in Condensed Phases, 1989. **85**(4): p. 929-943.
4. Li, C., et al., *Adsorption of carbon monoxide and carbon dioxide on cerium oxide studied by Fourier-transform infrared spectroscopy. Part 2.-Formation of formate species on partially reduced CeO2 at room temperature.* Journal of the Chemical Society, Faraday Transactions 1: Physical Chemistry in Condensed Phases, 1989. **85**(6): p. 1451-1461.
5. Yang, R.T., *Adsorbents: Fundamentals and Applications*, R.T. Yang, Editor 2003, John Wiley & Sons: New Jersey. p. 79-130.
6. Bandosz, T.J. and C.O. Ania, *Chapter 4 Surface chemistry of activated carbons and its characterization*, in *Interface Science and Technology*, J.B. Teresa, Editor 2006, Elsevier. p. 159-229.
7. Gregory, P.K., et al., *Silica/Polyethyleneimine Composite Adsorbent S-PEI for CO_2 Capture by Vacuum Swing Adsorption (VSA)*, in *Recent Advances in Post-Combustion CO_2 Capture Chemistry*2012, American Chemical Society. p. 177-205.
8. Shen, S.C., X. Chen, and S. Kawi, *CO2 Adsorption over Si-MCM-41 Materials Having Basic Sites Created by Postmodification with La2O3.* Langmuir, 2004. **20**(21): p. 9130-9137.
9. Qi, G., et al., *High efficiency nanocomposite sorbents for CO2 capture based on amine-functionalized mesoporous capsules.* Energy and Environmental Science, 2011. **4**(2): p. 444-452.
10. Hicks, J.C. and C.W. Jones, *Controlling the density of amine sites on silica surfaces using benzyl spacers.* Langmuir, 2006. **22**(6): p. 2676-2681.
11. Brunauer, S., *The Adsorption of Gases and Vapors Vol 1: Physical Adsorption*, in *The Adsorption of Gases and Vapors* S. Brunauer, Editor 1943, Oxford University Press: London. p. 9.
12. Knowles, G.P., S.W. Delaney, and A.L. Chaffee, *Diethylenetriamine[propyl(silyl)]-functionalized (DT) mesoporous silicas as CO_2 adsorbents.* Industrial and Engineering Chemistry Research, 2006. **45**(8): p. 2626-2633.
13. Choi, S., et al., *Application of amine-tethered solid sorbents for direct CO2 capture from the ambient air.* Environmental Science and Technology, 2011. **45**(6): p. 2420-2427.
14. Knowles, G.P., et al., *Amine-functionalised mesoporous silicas as CO_2 adsorbents*, in *Studies in Surface Science and Catalysis*2005, Elsevier. p. 887-896.
15. Drese, J.H., et al., *Synthesis-structure-property relationships for Hyperbranched aminosilica CO_2 adsorbents.* Advanced Functional Materials, 2009. **19**(23): p. 3821-3832.
16. Pinto, M.L., et al., *Adsorption and activation of CO2 by amine-modified nanoporous materials studied by solid-state NMR and 13CO2 adsorption.* Chemistry of Materials, 2011. **23**(6): p. 1387-1395.
17. Drage, T.C., et al., *Thermal stability of polyethylenimine based carbon dioxide adsorbents and its influence on selection of regeneration strategies.* Microporous and Mesoporous Materials, 2008. **116**(1–3): p. 504-512.

6 Experimental

6.1 Introduction

Many of the concepts regarding the production of activated carbons (ACs) from coal and the methods used to characterise these materials were introduced in ***Chapter 1***. In the current chapter these concepts are expanded upon, and further details of the various production and characterisation techniques are given.

Several series of ACs were produced from Victorian brown coal (VBC) or coal derived chars, and are separated here based upon the activation method used (i.e. physical activation, chemical activation or catalysed physical activation) and the targeted pore size (i.e. micropores or mesopores). In ***section 6.6***, the analytical procedures are separated into subsections based upon the characterisation of bulk composition, surface chemistry and physical and chemical structure.

6.2 Fixed Bed Reactor Development

In a previous PhD project in the Chaffee group [1], a fixed bed reactor system was developed for the steam activation of different AC precursors. This system was, however, found to be inadequate for the current project and numerous modifications and improvements were made over the course of the project.

The fixed bed reactor is comprised of a vertically mounted 3 temperature zone tube furnace [1]. A schematic of this system in its current incarnation is shown in ***Figure 6-1A***. Each heating zone is controlled independently by a separate temperature controller (BrainChild, BTC-9100). The

temperature at the centre of the respective heating zone is fed back via a K-type thermocouple situated within the steel reactor at the appropriate position within the heating zone. A peristaltic pump (Gilson, Minipuls 3) was used to deliver water to the steel reactor. At the top of the reactor was a bed of alumina beads was positioned in order to ensure complete vaporization of the incoming water.

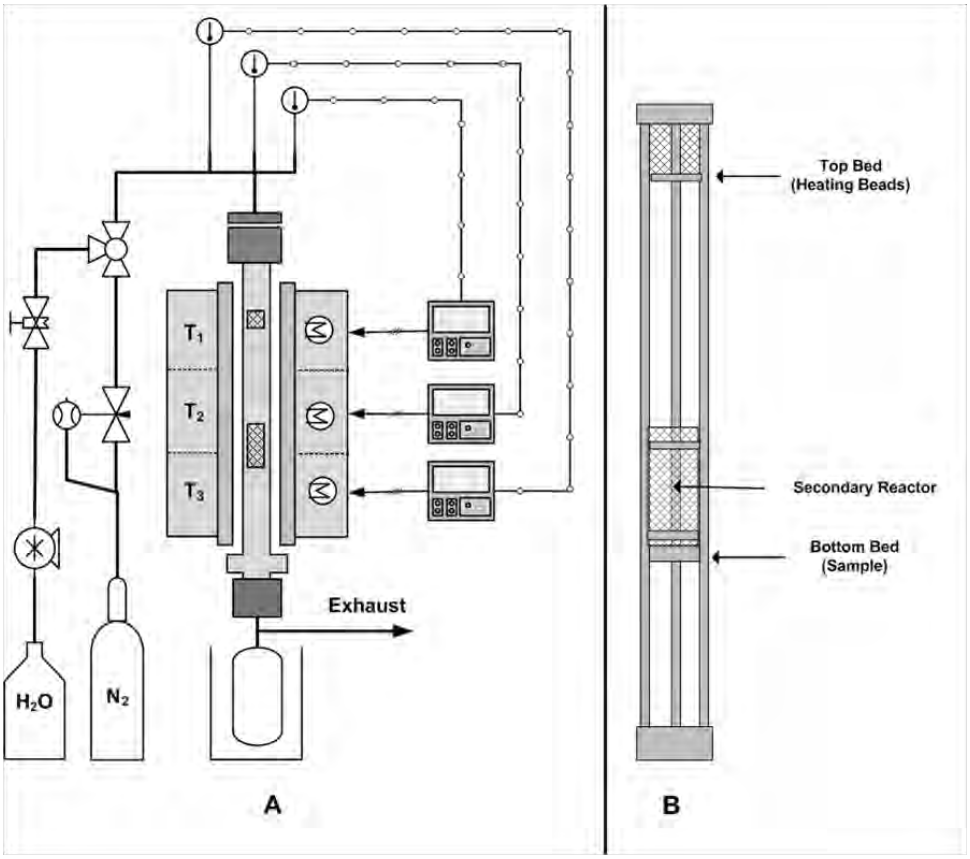

Figure 6-1 *~ Steam Activation/Pyrolysis System,* ***A)*** *Fixed Bed Reactor,* ***B)*** *Internal Sample Holder Assembly*

Previous work using the original system focused solely on the steam activation of AC precursors. Due to the requirement for KOH activation through pyrolysis and the corrosive nature of KOH on steel, a quartz reactor was needed. To enable the system to quickly and easily switch between steam and KOH activation the internal assembly was redesigned. The new internal assembly is shown in ***Figure 6-1B***, contained a removable secondary reactor. Two removable secondary reactors were subsequently constructed, one from fine steel mesh (316SS), the other from quartz. The quartz reactor was composed of a quartz tube, with a sintered quartz frit at the base (porosity grade 1).

6.3 Carbon Precursors and Reference Materials

6.3.1 Victorian Brown Coal Briquettes

Victorian brown coal (VBC) briquettes (58mm × 43mm × 40mm) were obtained from Energy Brix Pty Ltd, care of Australian Char Pty Ltd (AusChar). The nominal composition of these briquettes was 80% Loy Yang coal and 20% Yallourn East coal (see ***Appendix 1 – Parent Material Data Sheets*** for further details).

6.3.2 Industrial Brown Coal Chars

Two industrial chars were used in this project, both produced and supplied by Australian Char Pty Ltd (AusChar), produced from the same VBC briquettes used in the production of activated carbons. One a run of production char produced in a Lurgi style retort at 1173 K (CHLR), the other was an experimental char produced in a rotary kiln at 973 K (CHRK).

6.3.3 Norit R2030 CO2

A commercially available activated carbon, Norit R2030 CO2 (referred to as AC-N), is used as a reference material throughout this thesis as it is marketed as having an extremely high CO_2 capacity [2, 3]. AC-N is produced from extruded peat using by steam activation at 1223 K [4, 5], the product brochure for Norit R2030 CO2 can be found in ***Appendix 1 – Parent Material Data Sheets*** (***section 8.1.2***).

6.4 Production of Activated Carbons

6.4.1 Coal Preparation and Pre-treatment

In order to use the briquetted VBC and industrial chars they had to be reduced to a workable particle size. To this end, the briquettes were milled using two different jaw crushers and a fraction taken in the particle size range of 1-4 mm diameter. Unless otherwise stated the particles in this size range (1-4 mm) were used to prepare all ACs. The briquetting process resulted in reducing the moisture content of the coal from ~60 wt% to 11-13 wt%, no additional drying of the coal was carried out.

6.4.2 Steam Activation

The steam activation process was carried out in the same fixed bed reactor used for carbonisation. A known mass sample (8-12 g) was placed into a steel mesh flow through reactor (secondary reactor), and subsequently into the steel reactor (primary reactor). Once the primary reactor was sealed, the fixed bed system was purged for 30 min with N_2 gas at a flow rate of 3 dm^3/min. The cold trap was cooled down prior to initiating the temperature ramp via the use of an ice bath.

For the temperature ramp, the controller operating the top heating zone was set to 823 K to ensure the water pumped into the system was sufficiently vaporized. The middle and bottom zones were both set to 1073 K. The ramp rate employed for all three controllers was 10 K/min. Once the temperature had been reached, 30 min was allowed for thermal equilibration to be achieved.

Upon thermal equilibration, the water pump was turned on for 45, 90 or 180 min at a flow rate of 0.25 cm^3/min (0.47 RPM). Once the gasification was complete, the pump was switched off. The steam was allowed to pass through the system for a further 5 min, before all three temperature controllers were set to 273 K and the system was allowed to cool at a rate no greater than 10 K/min. The resulting material was weighed in order to determine the yield. A small fraction of the material was put aside as an "as produced" reference and stored in a desiccator. The remaining material was crushed in a small ball mill and sieved to obtain particles of < 250 μm diameter. The ground material was then dried at 378 K under N_2 for 24 h to remove any moisture adsorbed during the milling process.

6.4.3 Carbonisation

Carbonisation, otherwise known as thermal activation, was carried out in a similar manner as the steam activation protocol. The same fixed bed reactor system was used, with slight alterations to the internal set-up. For instance the secondary reactor used was composed of quartz, but was of the same dimensions as the steel mesh reactors. The bed of the second reactor was a quartz sintered disc of porosity 1. The same temperatures, gas flows and venting protocols were employed as in the steam activation, however for carbonisation the reaction time of set to 60 min. Although no steam was used, the alumina heating beads were still present. The same post-production protocols were applied for the carbonised carbons as were observed for the steam activated ones.

6.4.4 Catalyst Impregnation of Coal and Activated Carbons

The impregnation of catalysts in the form of KOH or lanthanide salts was carried out using typical wet impregnation methods, using water as the solvent.

6.4.4.1 Catalyst Impregnation and Activation

The appropriate amount of coal/AC (5-10 g) and catalyst were weighed out into a crystallizing dish, to which 300 cm^3 deionised water was added. The AC/coal-catalyst dispersion was stirred for 12 h at ambient temperature, and then heated to 343 K until a slurry had formed, the slurry was left to air dry under laminar air flow for several days. The resulting material was then activated as described in ***section 6.4.3*** for the chemically activated miACs using KOH; for the catalysed physically activated meACs using lanthanide catalysts the details of the steam activation procedure are outlined in ***section 6.4.2***.

6.4.4.2 Post-synthetic Catalyst Removal by Acid Washing

6.4.4.2.1 HCl Acid Wash

For the post-synthetic removal of the KOH catalysts from the ACs, the milled ACs was treated with 0.1 M HCl. According to the following general procedure HCl (250 cm^3) was dispensed into a conical flask containing the 3 g of the AC sample, and the suspension stirred for 1 h. The AC was isolated by vacuum filtration and dried under N_2 at 378 K. A second round of acid washing was then carried out followed by sequential washing with hot, then cold deionised water followed by filtration and drying under N_2 at 378 K.

6.4.4.2.2 H_2SO_4 Acid Wash

The only acid capable of removing all the metal oxides used as catalysts was sulphuric acid [6]. Into a 500 cm^3 3-neck round bottom flask 2-3 g of the milled catalyst impregnated AC was dispersed into 50 cm^3 of deionised water. To the necks of the round bottom flask a Liebig condenser, dropping funnel and N_2 supply were fitted. The round bottom flask was initially immersed in an ice bath to control the heat of dissolution of the H_2SO_4 when being added to the AC-water dispersion. Using the dropping funnel, 150 cm^3 of concentrated sulphuric acid was slowly added drop wise to the AC-water dispersion, under N_2 flow. Once all the acid had been added, the mixture was stirred for 30 min to allow complete dissolution. The round bottom flask was removed from the ice bath, and the mixture stirred at ambient temperature for 3 h. The AC

was then recovered by vacuum filtration and washed with cold deionised water followed by filtration and subsequent drying under N_2 at 378 K.

6.5 Amine Modification of Activated Carbons

The polymer used in all cases was polyethyleneimine (PEI), with an average molecular weight (M_w) of 1200 g/mol, obtained from Sigma-Aldrich Australia. The impregnation method used was based on that of Arenilla *et al* [7], and Xu *et al* [8]. All impregnations were undertaken on a pore filling basis, not a weight percent basis as has been commonly described in the literature [8, 9]. Briefly, the desired mass of PEI was dissolved into 15 g of methanol (MeOH), and sonicated for 20 min to allow complete dissolution. Simultaneously 3-5 g of the appropriate AC was added to 100 g MeOH and sonicated for 20 min. The AC-MeOH dispersion was then added to the PEI-MeOH solution, the resulting slurry was stirred for a further 120 min [10], then dried at 343 K under reduced pressure (93.3 kPa) for 16 h.

6.6 Instrumental Characterisation

Several different methods of instrumental analysis were used for full characterisation of the carbon materials produced in this thesis. The characterisation of the carbon materials is separated into three sections based on the aspect of the materials they cover, these are:

- Bulk composition
- Surface chemistry
- Material structure
    - Chemical structure
    - Physical structure

For each of the two major classes of carbon materials produced either the industrial carbon Norit R2030 CO2 (AC-N) or the steam activated VBC derived miAC AC-90, were used as benchmark materials for comparison. The AC-N carbon was used as the benchmark for all miACs, whilst AC-90 was used for all meACs. In all cases, the characterisations were performed using either material obtained from a single synthetic batch, or a composite sample comprising a mixture of several synthetic batches. Furthermore, in all cases the material used for characterisation was the same as that used in the adsorption testing.

6.6.1 Composition of Carbonaceous Materials

6.6.1.1 Elemental Analysis

Elemental analysis was carried out in order to determine the carbon, nitrogen and hydrogen content of the samples directly, with the oxygen content being determined by difference, once the ash had been taken into account (determined via proximate analysis). A Vario MICRO cube (Elementar), and was done using protocols typical for coal and coke analysis. Briefly, a mass of the carbon material (particle size <250 μm) previously dried at 378 K overnight under an N_2 atmosphere, in the range 5-7 mg was dispensed into the tin pan and placed into the auto sampler, with 4 replicates being taken for each sample. The samples were then combusted at 1223 K using the oxygen jet injection capability of the instrument. The error in the measured values was ±0.1 wt%.

6.6.1.2 Ash Analysis

Ash analysis was undertaken by combusting 5 mg of the sample in a thermogravimetric analyser (TGA, Mettler Toledo), at 1173 K under 100 % air. All samples were run in duplicate and weighed both before and after the analysis and correlated with the thermograph obtained. Similarly to the elemental analysis the level of error in the final values was ±0.1 wt%.

6.6.2 Determination of Surface Chemistry

6.6.2.1 X-ray Photoelectron Spectroscopy (XPS)

XPS was performed on a Kratos Axis HSi X-ray photoelectron spectrometer fitted with an electrostatic charge neutraliser and magnetic focusing lens. The excitation source used was an Al Kα with a monochromatic energy of 1486.7 eV. Each spectrum was the accumulation of 6 scans, each with a pass energy of 160 eV and dwell time of 0.1 sec, with the charge neutraliser on.

High resolution spectra were taken for the C 1s, O 1s, N 1s, K 2p, Ce 3d and La 3d regions depending on the AC being investigated. Peak fitting was applied to all high resolution spectra using the CasaXPS software (version 2.3.16), except for the N 1s and K 2p regions due to the low surface concentration of these elements. The errors in the XPS values are ± 0.2 at%.

Table 6-1 ~ *XPS Peak Assignments for C 1s, O 1s, N 1s, K 2p, Ce 3d and La 3d High Resolution Spectra*

Peak Assignment			Binding Energy (eV)	Ref.
C 1s		**Carbon 1s**	**284.0**	[11]
C=C		Aromatic Carbon	283.6	[12-14]
C-C		Graphitic Carbon	284.4	[12-14]
C-O-R		Ether or Hydroxyl	286.3	[12-14]
C=O		Carbonyl	288.3	[12-14]
COO-R		Carboxylic Acid or Lactone	289.2	[12-14]
π-π*		Plasmon	290.2	[12-14]
O 1s		**Oxygen 1s**	**532.0**	[11]
Ce-O		Cerium Oxide	529.7	[15-17]
La-O		Lanthanum Oxide	529.7	[15]
C=O		Carbonyl	531.4	[12-16, 18]
C-O-R		Ether or Hydroxyl	532.8	[12, 15, 16, 18]
COO-R		Carboxylic Acid or Lactone	534.7	[12, 14, 16, 18]
N 1s		**Nitrogen 1s**	**400.0**	[11]
K 2p		**Potassium 2p**	**293.9**	[11]
Ce 3d		**Cerium 3d**	**900.0**	[11]
v	Ce $3d^5/_2$	Ce $3d^9$ $4f^2$ final state for Ce(IV)	882.3	[17, 19]
v'	Ce $3d^5/_2$	Ce $3d^9$ $4f^1$ final state for Ce(III)	884.9	[17, 19]
v''	Ce $3d^5/_2$	Ce $3d^9$ $4f^1$ final state for Ce(IV)	888.9	[17, 19]
v'''	Ce $3d^5/_2$	Ce $3d^9$ $4f^0$ final state for Ce(IV)	898.2	[17, 19]
u	Ce $3d^3/_2$	Ce $3d^9$ $4f^2$ final state for Ce(IV)	901.0	[17, 19]
u'	Ce $3d^3/_2$	Ce $3d^9$ $4f^1$ final state for Ce(III)	903.5	[17, 19]
u''	Ce $3d^3/_2$	Ce $3d^9$ $4f^1$ final state for Ce(IV)	907.5	[17, 19]
u'''	Ce $3d^3/_2$	Ce $3d^9$ $4f^0$ final state for Ce(IV)	916.9	[17, 19]
La 3d		**Lanthanum 3d**	**853.0**	[11]
$3d_{5/2}$ cf^1	La $3d^5/_2$	La $3d^9$ $4f^1$ bonding final state	835.5	[19, 20]
$3d_{5/2}$ cf^{1*}	La $3d^5/_2$	La $3d^9$ $4f^1$ anti-bonding final state	838.8	[19, 20]
$3d_{5/2}$ cf^o	La $3d^5/_2$	La $3d^9$ $4f^0$ final state	841.5	[19, 20]
$3d_{3/2}$ cf^1	La $3d^3/_2$	La $3d^9$ $4f^1$ bonding final state	852.4	[19, 20]
$3d_{3/2}$ cf^{1*}	La $3d^3/_2$	La $3d^9$ $4f^1$ anti-bonding final state	855.7	[19, 20]
$3d_{3/2}$ cf^o	La $3d^3/_2$	La $3d^9$ $4f^0$ final state	858.6	[19, 20]
$3d_{3/2}$ Plasmon		Plasmon	848.1	[19, 20]

The background correction for all the high resolution C 1s, O 1s, N 1s and K 2p were done using Shirley type backgrounds [21]. The peak fitting for the C 1s and O 1s peaks were done using "Gaussian-Lorentzian" peak fitting with 30% Gaussian character, with asymmetry being applied to the C-C, C=C and π-π^* peaks within the high resolution C 1s spectra. The main functional

groups being investigated for those commonly present on an AC surface, being C-C, C=C, C=O, COO-R and C-O-R groups (***Table 6-1***).

The Ce 3d and La 3d spectra were peak fitted using Donaich-Sunjic type peak fitting, with controlled asymmetry parameters and a reduced Shirley type background, appropriate for lanthanides [21]. The peak assignments and nomenclature used followed the protocol of Burroughs *et al*, the first to describe them; and has since become the standard nomenclature [19, 22-25]. The fitting for both the Ce 3d and La 3d spectra involved fitting a duplicated series of peaks for the $^{3}/_{2}$ and $^{5}/_{2}$ electron spin states, which was fit at a ratio of 5:2 (1.5) for the $^{5}/_{2}$ to $^{3}/_{2}$ spin states, respectively [17]. Each peak in the Ce 3d and La 3d spectra describe excitations of individual electrons from the 3d to 4f orbitals [17, 19].

6.6.2.2 Near Edge X-Ray Fine Structure (NEXAFS) Spectroscopy

NEXAFS measurements were undertaken at the Australian Synchrotron (AS) on the Soft X-Ray (SXR) beamline. Both carbon and oxygen k-edge NEXAFS spectra were taken on all samples, using two detectors, a drain current detector and a microchannel plate (MCP) detector. The first detector set-up was using the drain current and total fluorescence yield (TFY) detectors. The second detector set-up used a partial electron yield (PEY) detector with the flood gun switched on to control charging of the samples.

The C 1s NEXAFS spectra were taken over a photon energy range of 275-330 eV, whilst the O 1s NEXAFS spectra were taken over a photon energy range of 520-570 eV. The energy steps used were 0.1 eV and the dwell time of each reading was 0.5 sec.

Carbon and oxygen NEXAFS spectra were obtained at three designated positions. Data processing and fitting were undertaken on the averaged spectrum. The method employed for peak fitting was a method in common use for both carbon and oxygen NEXAFS spectra [26-29]. It involves fitting the pre- and post-edge to normalise the edge step followed by use of an error function or inverse tangent baseline to fit the end step prior to actual peak fitting. Here the Athena program, part of the Demeter package (version 0.9.21 [30]) was used. The normalised, baseline corrected spectra were then deconvoluted and peak fitted against peaks of known position from the literature for both C 1s and O 1s NEXAFS, as outlined in ***Table 6-2***. An example of this process as it was undertaken for AC-90 is reported below in ***Figure 6-2A-B***, for the C 1s and O 1s NEXAFS spectra respectively.

It is important to note that while XPS is quantifiable, NEXAFS is semi-quantifiable at best. The power of NEXAFS lies within its ability to identify functional groups or oxidation states within a material, which are unable to be differentiated by XPS. Its use here was to gain further

information as to the nature and identity of the three oxygenated functional groups identified by XPS, namely the C=O, C-O-R and COO-R.

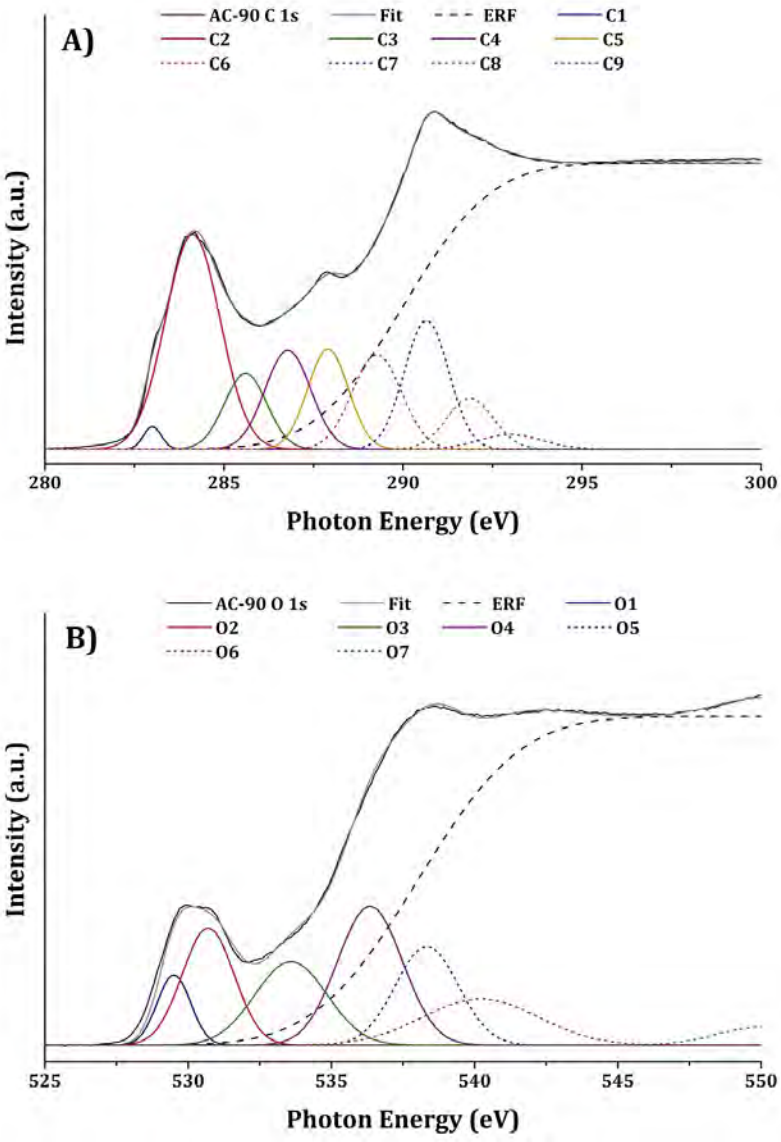

Figure 6-2 *~ C 1s and O 1s NEXAFS, Example of Peak Fitting for AC-90. Shown are* ***A)*** *C 1s peak fitting for AC-90, and* ***B)*** *O 1s peak fitting for AC-90. The peak assignments shown are done as outlined in* ***Table 6-2****.*

Table 6-2 ~ *C 1s and O 1s NEXAFS Peak Assignments*

K Edge	Name	Group		Photon Energy (eV)	Assignment	Ref.
C 1s	**C1**	C=O	**π***	283.0	Carbonyl substituted aromatic carbon (quinone)	[26, 31, 32]
	C2	C-C C=C	**π***	284.1	Aromatic carbon, or aliphatic substituted aromatic carbon	[26, 28, 33]
	C3	C-OH C=O	**π***	285.6	Phenolic or ketonic carbon	[26, 27]
	C4	C-OH COOH COO C=O	**π***	286.9	Carboxylic acid or lactone carbon	[27, 28, 31, 32, 34]
	C5	C-O-C	**π***	288.0	Cyclic ether carbon	[27, 33]
	C6	C-OH C=O	**π***	289.3	Aldehyde or hydroxyl substituted aliphatic carbon	[27, 28, 32, 33]
	C7	C-OH COOH COO C=O	**σ***	290.6	Carboxylic acid or lactone carbon	[26, 27, 33, 34]
	C8	C-O-C	**σ***	291.9	Cyclic ether carbon	[26, 32, 35]
	C9	C-C C=C	**σ***	293.0	Aromatic carbon (long range order)	[27, 28, 33]
O 1s	**O1**	C=O	**π***	529.6	Aliphatic (linear or cyclic) aldehyde oxygen	[27, 36, 37]
	O2	C=O	**π***	530.8	Carbonyl oxygen (ketonic or carboxylic acid)	[33, 36-38]
	O3	C-O-C	**π***	532.7	Aliphatic cyclic ether	[27, 33, 36, 37]
	O4	C-OH	**π***	535.7	Hydroxyl oxygen (alcohol)	[27, 33, 36, 37]
	O5	C-OH C=O	**σ***	538.0	Hydroxyl or carbonyl oxygen of carboxylic acid	[27, 33, 37]
	O6	C-O-C	**σ***	543.0	Aromatic cyclic ether	[27, 33, 37, 38]
	O7	C-OH	**σ***	549.8	Phenolic oxygen	[27]

6.6.3 Structural Characterisation

6.6.3.1 Characterisation of the Chemical Structure of Carbons

6.6.3.1.1 Raman Spectroscopy

Raman spectroscopy was undertaken on a Renishaw Invia confocal micro-Raman system, taking measurements over the wavenumber range of 400-2000 cm^{-1}, with an Ar ion laser at a wavelength of 514.5 nm, with spectral resolution of 4 cm^{-1}, with each spectra being the average of 10 scans. This was undertaken over several areas of the sample until three concordant results were obtained.

Due to differences in the signal intensity for the spectra of the different carbon materials, all spectra had to be normalised, this and the peak fitting were undertaken using OriginPro 8 (OriginLab). The normalisation technique used is that commonly employed when confocal Raman systems are employed, whereby the spectra were normalised (weight normalisation) against the major peak centred at 1275-1350 cm^{-1} (**D** peak) and baseline correction was done prior to peak identification.

The peak fitting was carried out using OriginPro 8 and the built-in multiple peak fitting function of the software. This was done using known information about the most common peaks to be observed in the spectra of similar ACs, as outlined in ***Table 6-3*** [39-43]. Attempts to fit any number of peaks other than 4, whether more or less, was inefficient and unable to provide good fits to the data (***Figure 6-3***).

Table 6-3 ~ *Raman Peak Assignments*

Peak Name	Peak Assignment	Raman Shift (cm^{-1})	Ref.
S	Disordered Graphitic Lattice*	1150-1250	[39-42]
D	Disorder Graphitic Lattice†	1275-1350	[39-42, 44]
A	Amorphous Carbon	1475-1525	[39, 41, 42]
G	Ideal Graphitic Lattice	1575-1625	[39-42, 44]

** Hetro-atoms bound to graphene layer edges*

† Graphene layer edges

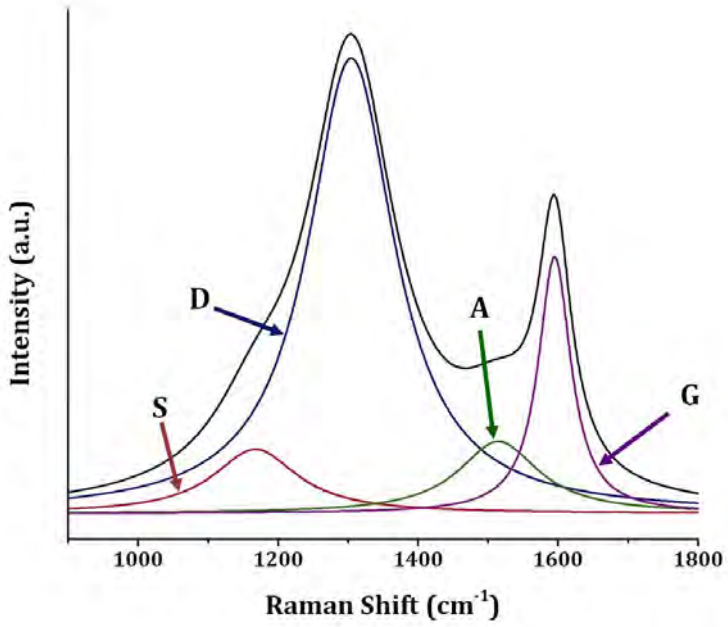

Figure 6-3 ~ *Example of Raman Peak Fitting Against Known Peaks from* ***Table 6-3***

6.6.3.1.2 Powder X-ray Diffraction (XRD)

The powder X-ray diffraction data were collected using a Bruker Axis D8 Focus powder diffractometer with Cu Kα radiation (1.54 Å), over a 2θ range of 5-80°, at a scan rate of 1 deg°/min using a step size of 0.02 deg°. Two major peaks were observed, being assigned to the **002** and **10** (overlapping **100** and **101** reflections) reflections at 24° 2θ and 43° 2θ, respectively [45]. The **002** peak is assigned to reflections of atoms in parallel graphene sheets, whilst the **10** peak is known to arise from lateral order within graphitic domains [45]. In some cases a third peak was also observable at 27° 2θ, known from the literature to be the results of amorphous metal oxides (**MO**) present in the ash (e.g. SiO_2, K_2O, Na_2O or Al_2O_3) [46].

For the Ln_xO_y catalysed physically activated carbons, CeO_2 and La_2O_3 standards were prepared under the same conditions as their respective Ln-meACs (***section 6.4.2***). The reference peaks used for the Ln_xO_y standards were checked against the TOPAS database. This enabled confirmation of a CeO_2 for the Ce-meACs, and both La_2O_3 and $La(OH)_3$ phase for the La-meACs.

6.6.3.2 Characterisation of the Physical Structure of Carbons

6.6.3.2.1 Gas Physisorption and Displacement

Due to the wide pore size distribution (PSD) of ACs several adsorbates (N_2, CO_2 & Ar) were employed in order to accurately characterise the surface structure of all ACs and related materials. The primary instrument used for all surface area and porosity determination was the TriStar II 3020 (Micromeritics), equipped with 1 and 10 torr pressure transducers, with the errors in the measurements being ±0.005 % for the isotherm data obtained on this instrument. This was used to obtain accurate physisorption data in the micro- and mesopore regions using CO_2 and N_2 at 273 and 77 K respectively.

Additionally high resolution adsorption isotherms were obtained using an ASAP 2020 HP system (Micromeritics), which was equipped with 0.1, 1 and 10 torr pressure transducers, allowing for greater resolution at lower partial pressures. Between the three transducers the error in the measurements was ±0.0005 %. The adsorbates used were N_2 and Ar, with physisorption being undertaken at 77 and 87 K, respectively. Furthermore, the ASAP 2020 HP used was equipped with a cryostat, making it possible to run cryogen free and for extended periods of time. The cryostat attachment was capable of temperatures in the range of 25-300 K. High resolution isotherms were only obtained for AC-N, AC-90 and AC-K10, as these miACs warranted further investigation due to their high adsorption of CO_2 during PPSA investigations.

The equilibration times between the two instruments varied, for the TriStar II 3020 the equilibration time used was 30 sec, whilst that used for the ASAP 2020 HP was 45 sec. The difference in equilibration time for the ASAP 2020 HP was due to the higher resolution able to be achieved with this instrument, which could be further improved by a longer equilibration time. Regardless of equilibration time for either instrument, 10 consecutive measurements had to be obtained within 0.05% error of each other.

CO_2 Physisorption

Only adsorption of CO_2 was carried out at 273 K, which is typically done; as at this temperature CO_2 is a non-condensing adsorbate. This was done over a P/P_o range of 0.0001-0.030 (0.01-101.3 kPa), and the surface area and pore volume of the micropore region were calculated using the Dubinin-Radushkevich (DR) ***equation 6-1***[47]:

$$W = W_0 exp[-(A/\beta E_o)]^2 \qquad \textbf{6-1}$$

where W is the volumes of adsorbate, W_0 is the limiting micropore volume, E_0 is energy of adsorption of a standard vapour (usually benzene), β is the affinity coefficient for the polarisability of the adsorbate and A is the adsorption potential, as defined by Polanyi (***equation 6-2***)[47]:

$$A = RT \ln\left(\frac{P_0}{P}\right) \qquad \textbf{6-2}$$

where P is the adsorbate pressure, P_0 is the partial pressure, T is the temperature, and R the universal gas constant.

It is important to note that the value for the cross-sectional surface area of a CO_2 molecule used in the calculations of the DR equation was 21 nm^2, not the theoretical value often used of 17.6 nm^2 [48]**.** Using the theoretical value for the cross-sectional area of 17.6 nm^2 grossly underestimates the surface area and pore volume attributed to micropores. The cross-sectional area value of 21 nm^2 is the most commonly used and is based on experimental evidence, which is why it was used here. Furthermore, the DR equation was applied to the CO_2 adsorption data across the entire P/P_o range tested (i.e. 0.001-0.03).

N_2 Physisorption

Full adsorption-desorption isotherms were determined using N_2 at 77 K, over a P/P_o range of 0.0005-0.9950 (0.05-101.3 kPa), using 45 sec equilibration times. High resolution studies used an initial doses of 10 cm^3/STP were used with the data being recorded, until the first relative pressure point of 0.0005 was reached. The specific surface area was calculated using the Brunauer, Emmet and Teller (BET) ***equation 6-3*** [49]:

$$\frac{1}{W[P/P_o - 1]} = \frac{1}{W_m C} + \frac{C-1}{W_m C}\left(\frac{P}{P_o}\right) \qquad \textbf{6-3}$$

where W_m is the weight adsorbed for monolayer formation, and C is the BET constant, expressed in ***equation 6-4*** [49]**:**

$$C = e^{(q_1 - q_L)/RT} \qquad \textbf{6-4}$$

where q_1 is the heat of adsorption for the first layer, and q_L is the heat of liquefaction of gas beyond the monolayer, R the universal gas constant, T the absolute temperature, and e Euler's number.

The PSD pertaining to the mesopore region was constructed by applying the Barrett-Joyner-Halenda (BJH) method to the desorption arm of the N_2 isotherms [50]. The PSD pertaining to the micropore region was undertaken by applying the Horvath-Kawazoe (HK) method to the adsorption arm of the N_2 isotherms [51], outlined in ***equation 6-5***:

$$\ln\frac{P}{P_o} = \frac{K}{RT} \times \alpha \times \beta \qquad \textbf{6-5}$$

where P is the adsorbate pressure, P_0 is the partial pressure, T is the temperature, K is Avogadro's number, σ the gas solid separation at zero interaction energy, and R the universal gas constant. And value of α is defined by ***equation 6-6***:

$$\alpha = \frac{IP \times 10^{23}\, JA/Jcm^4}{\sigma^4 \times (L - 2 \times d_o)} \qquad \textbf{6-6}$$

and the value of β is defined by ***equation 6-7***:

$$\beta = \left[\frac{\sigma^4}{3 \times (L \times d_o)^3} - \frac{\sigma^{10}}{9 \times (L - d_o)^9} - \frac{\sigma^4}{3 \times d_o^3} + \frac{\sigma^{10}}{9 \times d_o^9}\right] \qquad \textbf{6-7}$$

where σ is defined by ***equation 6-8*** and d_o defined by ***equation 6-9***:

$$\sigma = \frac{Z_S + Z_A}{2} \qquad \textbf{6-8}$$

$$d_o = \frac{D_A + D_S(A)}{2} \qquad \textbf{6-9}$$

where Z_S is the sample equilibrium diameter at zero interaction energy, Z_A is the zero interaction energy diameter, L is the pore width and IP the interaction parameter.

Furthermore, DR micropore volumes were also calculated for the ACs by applying the ***equation 6-1*** to the N_2 physisorption data, using the same fitting conditions as was used for CO_2.

Ar Physisorption

Ar adsorption was only undertaken for samples AC-N, AC-90 and AC-K10, as high resolution isotherms at 87 K, using the ASAP 2020 HP instrument, with the cryostat attachment. The relative pressure range over which the isotherms were collected was 0.0005-0.9950 (0.05-101.3 kPa), using 45 sec equilibration times. Initial doses of 10 cm^3/STP were used with the data being recorded, until the first relative pressure point of 0.0005 was reached.
The surface area from this data was calculated using the BET equation (***equation* 6-3*)***[49] over a relative pressure range of 0.06-0.20, that typically employed when Ar is the molecular probe. As was the case for the N_2 isotherms, the PSD for the micro- and mesopore regions were obtained by applying the HK (***equation 6-5***) and BJH methods respectively [50, 51].

True Density by Gas Displacement

The true density of all ACs, starting materials and standards were determined using helium pycnometry. The instrument used was an AccuPyc II 1340 (Micromeritics), with a 10 cm^3 cell, and a 1 cm^3 insert was employed. Prior to analysis all materials were milled to a particle size of < 250 μm, using a small ball mill with an agate ball and capsule (Specamill, Specac). The instrument was controlled via a computer interface and a standard protocol was used for all analyses. The protocol involved 99 purges, 20 cycles with a run precision of 0.5 %; which resulted in most analyses only requiring 5-10 cycles for concordant results to be achieved.

6.6.3.2.2 Transmission Electron Microscopy

All micrographs, elemental mapping and EDX profiles were collected at the Monash Centre for Electron Microscopy (MCEM) by Dr. Jamileh Taghavimoghaddam. Transmission electron microscopy (TEM) and high resolution transmission electron microscopy (HRTEM) micrographs were collected using a JEOL 2100F FEGTEM equipped with a Gatan UltraScan 1000 (2K×2K) CCD camera at an accelerating voltage of 200 kV.

Scanning transmission electron microscopy (STEM) was also carried out using also a JEOL 2100F FEGTEM microscope equipped with a high angular annular dark field (HAADF) detector (camera length 10 cm and 0.2 nm probe) to collect elemental mapping profiles. A 50 mm JEOL Si(Li) electron dispersive X-ray (EDX) detector was used for elemental mapping

Multiple images of different particles within each sample were analysed, with the micrographs of the most representative particle being presented in this work.

6.6.4 Assessment of Gas Separation

The capability of the ACs to adsorb CO_2 was investigated using partial pressure swing adsorption (PPSA) on a thermogravimetric analyser equipped with differential thermal analysis (TGA-DTA). The TGA used was a Setaram 1600 model equipped with several mass flow controllers run through a gas manifold. Initially the gas flow over the sample (20-25 mg, <250 µm particle size) was 100 %v/v Ar, at 70 cm^3/min. Prior to initiating the measurements the sample was heated to 423 K and held for 10 min in order to remove any pre-adsorbed molecules, such as H_2O or CO_2. As the CO_2 gas was introduced, the Ar gas was equally reduced, thus maintaining a constant flow throughout the system. This was done in one of three separate dosing modes (***Figure 6-4***):

1. *Differential-step dosing*
2. *Multi-cyclic dosing*
3. *Single-cycle dosing*

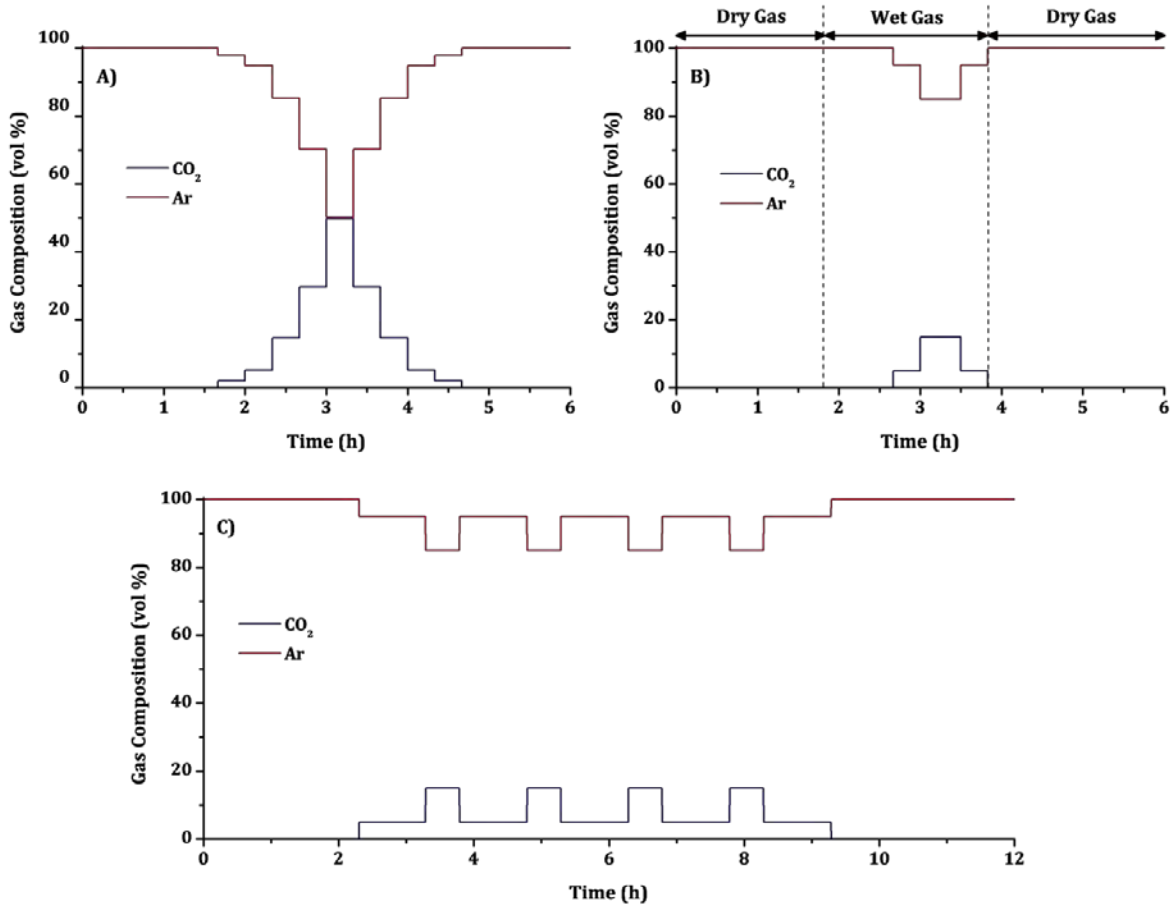

Figure 6-4 *~ Partial Pressure Swing Adsorption (PPSA) Gas Programs,* ***A)*** *Differential-step CO_2 Adsorption-Desorption,* ***B)*** *Wet Gas Single Cycle Simulation of VSA,* ***C)*** *Multi-cyclic Simulation of VSA*

6.6.4.1 Differential-step dosing

The CO_2 increments used in the differential-step dosing method were 2.13, 5.27, 14.89, 30.09 and 50.45 kPa CO_2 partial pressure, shown in ***Figure 6-4A***. The Ar flow through the system was simultaneously decreased by a volume equivalent to each CO_2 partial pressure increment. The equilibration time for each step was 20 min, at the conclusion of the adsorption program the reverse of that program was run in order to obtain the desorption arm of the pseudo-isotherm.
Amine efficiencies allow for the determination of the efficiency with which the amine groups are adsorbing CO_2. This is only applicable to amine-modified adsorbents, and is calculated using ***equation 6-10*** [52, 53]:

$$\eta_{NH3} = \frac{Ads_{CO2}}{n(N)} \qquad \textbf{6-10}$$

where η_{NH3} is the amine efficiencies, Ads_{CO2} is the adsorbed CO_2 in moles, and n(N) is the number of moles of nitrogen present in the sample.

6.6.4.2 Multi-cyclic dosing

For the multi-cyclic dosing method the CO_2 partial pressures used for the cycle were 5.27-14.89 kPa, shown in ***Figure 6-4c***. One major difference between the differential-step and multi-cyclic dosing method was that the sample was pre-dosed with CO_2 at a partial pressure of 5 kPa for an hour prior to initiating the cycling. The main purpose of this method was to simulate the CO_2 partial pressure conditions of a vacuum swing adsorption (VSA) cycle. During a VSA cycle, the baseline partial pressure of CO_2 in the gas stream would be ~5 kPa. As such the samples were allowed 30 min to achieve equilibrium with this level of CO_2 in order to achieve adsorption behaviour closer to that of a true VSA system. From this the "working capacity" can be determined, which is done so according to ***equation 6-11***:

$$Cw_{temp} = Ads_2 - Ads_1 \qquad \textbf{6-11}$$

where Cw_{temp} is the working capacity at a particular temperature (in Kelvin), Ads_1 is the level of adsorption at 5 kPa, and Ads_2 is the adsorption at 15 kPa. This calculation was carried out separately for each of the four cycles and an average value taken.

The heats of adsorption for the adsorption step of the cycle (i.e. between 5-15 kPa CO_2 partial pressure) were calculated for each cycle and averaged. This was done by determining the enthalpy of the adsorption step; derived from the differential thermal analysis (DTA) data, expressed as heat flow. The enthalpy change (kilojoules, kJ) of the adsorption step was then correlated to the CO_2 adsorbed (moles), determined from the thermogravimetric data (thus giving values in kJ/mol). This was only undertaken for the measurements at 293 K, as the heat flow data was insufficient at higher temperatures, which is common for physisorption systems.
Both the working capacities and heats of adsorption values presented are the average values of four cycles, with the values from all cycles falling within the first standard deviation of the mean value for both working capacities and heats of adsorption.

6.6.4.3 Single-cycle dosing

The single-cycle dosing method was undertaken in a similar manner to the multi-cyclic dosing, as shown in ***Figure 6-4b***, the CO_2 partial pressure range used for the cycle was 5.27-14.89 kPa, and an hour pre-dose at the same partial pressure was also undertaken. The main difference, other than the fact that a single cycle was run, was that the measurement for each sample at the temperatures of interest (363 and 378 K) was done two-fold, one under dry gas conditions (equivalent to a single cycle of the multi-cyclic work) and another measurement was taken under wet gas conditions. The wetting of the gas was achieved by passing the gas through a gas washing bottle filled with deionised water at 303 K. The overall effect of wetting the gas in this way gave it a 2 % (v/v) H_2O content, giving a H_2O partial pressure of the gas stream of 2.12 kPa. It is also important to note that both Ar and CO_2 were treated in this way, such that regardless of the CO_2 partial pressure the overall H_2O content of the gas stream was 2 % (v/v).

6.7 References

1. Delaney, S.W., *Electrically Regenerable Carbon Adsorbents for CO_2 Capture*, in *Faculty of Science, School of Chemistry*2009, Monash University: Melbourne.
2. Dantas, T.L.P., et al., *Adsorption of carbon dioxide onto activated carbon and nitrogen-enriched activated carbon: Surface changes, equilibrium, and modeling of fixed-bed adsorption.* Separation Science and Technology, 2010. **45**(1): p. 73-84.
3. Dantas, T.L.P., et al., *Carbon dioxide–nitrogen separation through adsorption on activated carbon in a fixed bed.* Chemical Engineering Journal, 2011. **169**(1–3): p. 11-19.
4. Bagreev, A. and T.J. Bandosz, *H2S adsorption/oxidation on unmodified activated carbons: importance of prehumidification.* Carbon, 2001. **39**(15): p. 2303-2311.
5. García, S., et al., *Breakthrough adsorption study of a commercial activated carbon for pre-combustion CO2 capture.* Chemical Engineering Journal, 2011. **171**(2): p. 549-556.
6. Sastri, V.S., et al., *Introduction*, in *Modern Aspects of Rare Earths and Their Complexes*2003, Elsevier: Amsterdam. p. 1-72.
7. Arenillas, A., et al., *CO_2 capture using some fly ash-derived carbon materials.* Fuel, 2005. **84**(17): p. 2204-2210.
8. Xu, X., et al., *Preparation and characterization of novel CO_2 "molecular basket" adsorbents based on polymer-modified mesoporous molecular sieve MCM-41.* Microporous and Mesoporous Materials, 2003. **62**(1-2): p. 29-45.
9. Basaldella, E.I., et al., *Amine modified, micro-mesoporous matrices for CO2 retention: effect of occluded templates on performance*, in *Studies in Surface Science and Catalysis*2008, Elsevier. p. 619-622.
10. Subagyono, D.J.N., et al., *PEI modified mesocellular siliceous foam: A novel sorbent for CO_2.* Energy Procedia, 2011. **4**(0): p. 839-843.
11. *X-ray Data Booklet*, ed. A.C. Thompson and D. Vaughan2001: Lawrence Berkeley National Laboratory, University of California.
12. Biniak, S., et al., *The characterization of activated carbons with oxygen and nitrogen surface groups.* Carbon, 1997. **35**(12): p. 1799-1810.
13. Puziy, A.M., et al., *XPS and NMR studies of phosphoric acid activated carbons.* Carbon, 2008. **46**(15): p. 2113-2123.
14. Nowicki, P., R. Pietrzak, and H. Wachowska, *X-ray photoelectron spectroscopy study of nitrogen-enriched active carbons obtained by ammoxidation and chemical activation of brown and bituminous coals.* Energy and Fuels, 2010. **24**(2): p. 1197-1206.
15. Starck, J., et al., *The influence of demineralisation and ammoxidation on the adsorption properties of an activated carbon prepared from a Polish lignite.* Carbon, 2006. **44**(12): p. 2549-2557.
16. Shen, W., et al., *Preparation of mesoporous carbon from commercial activated carbon with steam activation in the presence of cerium oxide.* Journal of Colloid and Interface Science, 2003. **264**(2): p. 467-473.
17. Bêche, E., et al., *Ce 3d XPS investigation of cerium oxides and mixed cerium oxide (CexTiyOz).* Surface and Interface Analysis, 2008. **40**(3-4): p. 264-267.
18. Desimoni, E., et al., *XPS determination of oxygen-containing functional groups on carbon-fibre surfaces and the cleaning of these surfaces.* Surface and Interface Analysis, 1990. **15**(10): p. 627-634.
19. Burroughs, P., et al., *Satellite structure in the X-ray photoelectron spectra of some binary and mixed oxides of lanthanum and cerium.* Journal of the Chemical Society, Dalton Transactions, 1976(17): p. 1686-1698.
20. Sunding, M.F., et al., *XPS characterisation of in situ treated lanthanum oxide and hydroxide using tailored charge referencing and peak fitting procedures.* Journal of Electron Spectroscopy and Related Phenomena, 2011. **184**(7): p. 399-409.
21. Fairley, N., *CasaXPS Manual 2.3.15 (Orange Book)*, 2009, Acolyte Science.

22. Holgado, J.P., R. Alvarez, and G. Munuera, *Study of CeO2 XPS spectra by factor analysis: reduction of CeO2.* Applied Surface Science, 2000. **161**(3–4): p. 301-315.
23. Paparazzo, E., *On the curve-fitting of XPS Ce(3d) spectra of cerium oxides.* Materials Research Bulletin, 2011. **46**(2): p. 323-326.
24. Pfau, A. and K.D. Schierbaum, *The electronic structure of stoichiometric and reduced CeO2 surfaces: an XPS, UPS and HREELS study.* Surface Science, 1994. **321**(1–2): p. 71-80.
25. Răduţoiu, N. and C.M. Teodorescu, *Satellites in Ce 3d X-ray photoelectron spectroscopy of ceria.* Digest Journal of Nanomaterials and Biostructures, 2013. **8**(4): p. 1535-1549.
26. Singh, B., et al., *NEXAFS and XPS characterisation of carbon functional groups of fresh and aged biochars.* Organic Geochemistry, 2014. **77**(0): p. 1-10.
27. Ganguly, A., et al., *Probing the Thermal Deoxygenation of Graphene Oxide Using High-Resolution In Situ X-ray-Based Spectroscopies.* The Journal of Physical Chemistry C, 2011. **115**(34): p. 17009-17019.
28. Hunt, A., et al., *Epoxide Speciation and Functional Group Distribution in Graphene Oxide Paper-Like Materials.* Advanced Functional Materials, 2012. **22**(18): p. 3950-3957.
29. Tanaka, M., et al., *Oxygen K-edge X-ray absorption near edge structures (XANES) of sublimated films of amino acids.* Journal of Synchrotron Radiation, 2001. **8**(2): p. 1009-1011.
30. Ravel, B. and M. Newville, *ATHENA, ARTEMIS, HEPHAESTUS: data analysis for X-ray absorption spectroscopy using IFEFFIT.* Journal of Synchrotron Radiation, 2005. **12**(4): p. 537-541.
31. Heymann, K., et al., *C 1s K-edge near edge X-ray absorption fine structure (NEXAFS) spectroscopy for characterizing functional group chemistry of black carbon.* Organic Geochemistry, 2011. **42**(9): p. 1055-1064.
32. Wan, J., T. Tyliszczak, and T.K. Tokunaga, *Organic carbon distribution, speciation, and elemental correlations within soil microaggregates: Applications of STXM and NEXAFS spectroscopy.* Geochimica et Cosmochimica Acta, 2007. **71**(22): p. 5439-5449.
33. Liang, X., et al., *X-ray absorption spectroscopy study on the thermal and hydrazine reduction of graphene oxide.* Journal of Electron Spectroscopy and Related Phenomena, 2014. **196**(0): p. 89-93.
34. Jeong, H.K., et al., *X-ray absorption spectroscopy of graphite oxide.* EPL, 2008. **82**(6).
35. Kuznetsova, A., et al., *Oxygen-Containing Functional Groups on Single-Wall Carbon Nanotubes: NEXAFS and Vibrational Spectroscopic Studies.* Journal of the American Chemical Society, 2001. **123**(43): p. 10699-10704.
36. Takashiro, J.I., et al., *Heat treatment effect on the electronic and magnetic structures of nanographene sheets investigated through electron spectroscopy and conductance measurements.* Physical Chemistry Chemical Physics, 2014. **16**(16): p. 7280-7289.
37. Takashiro, J.-i., et al., *Preferential oxidation-induced etching of zigzag edges in nanographene.* Physical Chemistry Chemical Physics, 2014. **16**(39): p. 21363-21371.
38. De Jesus, L.R., et al., *Inside and Outside: X-ray Absorption Spectroscopy Mapping of Chemical Domains in Graphene Oxide.* The Journal of Physical Chemistry Letters, 2013. **4**(18): p. 3144-3151.
39. Sadezky, A., et al., *Raman microspectroscopy of soot and related carbonaceous materials: Spectral analysis and structural information.* Carbon, 2005. **43**(8): p. 1731-1742.
40. Li, X., J.-i. Hayashi, and C.-Z. Li, *Volatilisation and catalytic effects of alkali and alkaline earth metallic species during the pyrolysis and gasification of Victorian brown coal. Part VII. Raman spectroscopic study on the changes in char structure during the catalytic gasification in air.* Fuel, 2006. **85**(10–11): p. 1509-1517.
41. Shimodaira, N. and A. Masui, *Raman spectroscopic investigations of activated carbon materials.* Journal of Applied Physics, 2002. **92**(2): p. 902-909.
42. Wesełucha-Birczyńska, A., K. Babeł, and K. Jurewicz, *Carbonaceous materials for hydrogen storage investigated by 2D Raman correlation spectroscopy.* Vibrational Spectroscopy, 2012. **60**(0): p. 206-211.

43. Zhang, S., et al., *Effects of volatile-char interactions on the evolution of char structure during the gasification of Victorian brown coal in steam.* Fuel, 2011. **90**(4): p. 1529-1535.
44. Cuesta, A., et al., *Raman microprobe studies on carbon materials.* Carbon, 1994. **32**(8): p. 1523-1532.
45. Bratek, W., et al., *Characteristics of activated carbon prepared from waste PET by carbon dioxide activation.* Journal of Analytical and Applied Pyrolysis, 2013. **100**(0): p. 192-198.
46. Skodras, G., et al., *Production of special activated carbon from lignite for environmental purposes.* Fuel Processing Technology, 2002. **77-78**: p. 75-87.
47. Dubinin, M.M., *The potential theory of adsorption of gases and vapors for adsorbents with energetically nonuniform surfaces.* Chemical Reviews, 1960. **60**(2): p. 235-241.
48. Lowell, S., et al., *Characterization of Porous Solids and Powders: Surface Area, Pore Size and Density*, B. Scarlett, Editor 2004, Springer: Dordrecht. p. p. 92.
49. Brunauer, S., P.H. Emmett, and E. Teller, *Adsorption of gases in multimolecular layers.* Journal of the American Chemical Society, 1938. **60**(2): p. 309-319.
50. Barrett, E.P., L.G. Joyner, and P.P. Halenda, *The Determination of Pore Volume and Area Distributions in Porous Substances. I. Computations from Nitrogen Isotherms.* Journal of the American Chemical Society, 1951. **73**(1): p. 373-380.
51. Horvath, G. and K. Kawazoe, *METHOD FOR THE CALCULATION OF EFFECTIVE PORE SIZE DISTRIBUTION IN MOLECULAR SIEVE CARBON.* Journal of Chemical Engineering of Japan, 1983. **16**(6): p. 470-475.
52. Knowles, G.P., et al., *Amine-functionalised mesoporous silicas as CO_2 adsorbents*, in *Studies in Surface Science and Catalysis*2005, Elsevier. p. 887-896.
53. Knowles, G.P. and A.L. Chaffee, *Aminopropyl-Functionalized Silica CO_2 Adsorbents via Sonochemical Methods.* Journal of Chemistry, 2016. **2016**.

7 Concluding Remarks and Future Directions

7.1 Concluding Remarks

This thesis was based on the premise that excellent carbon adsorbents could be prepared from Victorian Brown Coal (VBC). Detailed methods were established and described for the preparation of microporous and mesoporous carbons and post-synthetic amine modified carbon composites. The resulting materials were systematically assessed for their gas separation performance and applicability as adsorbents for CO_2 capture from post-combustion flue gas streams.

Overall, the studies showed that the pore size and volume could be modulated using different pre-treatment and carbonisation/activation conditions (i.e activation time, presence/absence of steam, activation agent, catalyst). Intensive characterisation of the prepared materials, particularly in terms of their surface chemistry, enabled the identification and elucidation of the distribution of important surface functional groups (hydroxyl, carboxylic acids) that contribute significantly to the CO_2 adsorption behaviour of VBC derived carbons under various conditions.

In this chapter an overall summary of the work produced in this thesis is presented, and the outstanding adsorbent materials are highlighted. This is followed by a section outlining recommendations for future research efforts regarding these materials.

7.1.1 Microporous Carbon Adsorbents

7.1.1.1 Physically Activated Coal Derived Carbon Adsorbents

The carbonisation/activation of VBC to produce the CH and miAC series of materials caused an increase in bulk C and a decrease in both bulk O and H relative to VBC. Although there was no clear relationship between the bulk compositions of either the CH or miAC materials as a

function of carbonisation/activation time, clear differences were observed when steam was used during activation. Steam resulted in higher bulk O and lower bulk C materials, which is with oxidation of the carbon precursor.

XPS showed that the surface O decreased as a result of steam activation relative to materials prepared in the absence of steam. There was also a substantial shift in the distribution of oxygenated functional groups, with C-O-R groups becoming most prominent at the surface, while both C=O and COO-R species decreased. Further investigation of the surface chemistry of the CH and miAC materials by NEXAFS spectroscopy revealed that the C-O-R groups detected by XPS arose from hydroxyl and ether groups, with a higher proportion of the former being present in all cases. It was noted that the proportion of hydroxyl groups on the surface of CH-90 and AC-90 was the lowest of their respective series, but they also possessed the highest surface concentration of C-O-R groups, as determined by XPS. The overall effect of this may have been to increase the affinity of the carbon surface of these materials towards CO_2, as hydroxyl groups are well known for having the highest affinity for CO_2 of any functional groups on carbon surfaces.

The Raman spectra obtained for the CH and miAC materials revealed that they were mostly composed of disordered graphitic carbon, with amorphous and ideal graphitic carbon making up the remainder. XRD analysis further indicated that the carbon materials were composed of parallel but disordered graphene sheets, which is in good agreement with what is known about coal derived carbon materials. Evidence of aligned graphene layer edges was found in the TEM micrographs obtained for the CH and miAC materials. Dispersed amongst the graphene layer edges were highly ordered graphitic domains, which accounted for the ideal graphitic carbon observed from the Raman spectroscopy. The gas physisorption studies for the CH and miACs revealed both series of materials to possess both micropores and mesopores, with the miACs possessing significantly greater mesopore volume on account of the greater pore development. The N_2 adsorption isotherms for both the CH and miACs were ***type IV*** with ***H4*** hysteresis loops, with the hysteresis loops exhibiting incomplete closure. Incomplete closure of hysteresis loops in carbon materials is often due to LPH which is a strong indication of materials that possesses slit shaped pores with little mesopore character.

From the CO_2 adsorption pseudo-isotherms of the CH series of materials, it was seen that at 333 K and 363 K, a similar amount of CO_2 was adsorbed to that of AC-N (the commercial carbon chosen as a benchmark) between CO_2 partial pressures of 5-30 kPa. Significant increases in CO_2 adsorption were observed when steam was used for carbonisation/activation times of 90 and 180 min (relative to the corresponding CH analogue), whereas a decrease in CO_2 adsorption was observed for a carbonisation/activation time of 45 min. The highest CO_2 adsorption was

observed for AC-90 on account of its high surface hydroxyl concentration and high micro- and mesopore volumes. Although AC-180 possessed higher micro- and mesopore volumes than AC-90, it also possessed a significantly lower surface concentration of hydroxyl groups. This clearly highlights the important role of surface chemistry in the adsorption properties of these carbon materials, a factor that is often overlooked. Of the CH and miAC series the carbon material with the highest performance as a CO_2 adsorbent was AC-90. It is for this reason that AC-90 was chosen for further investigation of its adsorption properties under wet gas conditions. Although there was a minor lag in the adsorption of CO_2 in the presence of H_2O, the amount of CO_2 adsorbed was not significantly affected by the presence of H_2O at the temperatures tested, and as such no competitive adsorption was observed. This bodes well for the applicability of AC-90 as an adsorbent for CO_2 from post-combustion flue gas streams.

7.1.1.2 Physically Activated Char Derived Carbon Adsorbents

The char derived miACs were produced in quite high yield, which can be attributed to the fact that the chars had previously been carbonised, removing much of the volatile matter that would be removed during carbonisation/activation of VBC. Steam activation of the char derived miACs, resulted in a decrease in bulk O relative to the chars.

There were significant differences in the surface chemistry of the CHLR and CHRK chars as determined by XPS, which extended to the miACs produced from them. The differences in surface chemistry were mostly confined to the distribution of surface O functionality, which can be attributed to the different processes by which the two chars were produced. More specifically, the overall surface O concentration of CHLR was significantly higher than AC-90, much of which was due to the higher surface concentration of C-O-R groups. Further investigation of CHLR by NEXAFS showed the C-O-R groups observed by XPS to be due to both hydroxyl and ether groups, with a higher proportion arising from hydroxyl groups. Steam activation of CHLR resulted in a significant decrease in surface O, which was observed by a change in the distribution of C-O-R and C=O groups, with both groups decreasing in concentration to be well below that of AC-90. In addition to the decrease in C-O-R groups, NEXAFS showed that relative to CHLR, AC-CHLR-90 possessed a much lower proportion of hydroxyl groups relative to ethers. CHRK also possessed a lower surface O concentration than CHLR, particularly with respect to the concentration of C-O-R groups, that NEXAFS revealed to be due to both hydroxyl and ether groups. Steam activation of CHRK resulted in a significant increase in the surface O concentration, mostly in the form of C-O-R groups. The surface concentration of C-O-R groups that AC-CHRK-90 possessed was the highest of any of the

physically activated carbon materials, which NEXAFS revealed to be predominately due to hydroxyl groups, with some ether groups.

The investigation of the chemical structure of the chars and char derived miACs yielded similar overall results by XRD and Raman spectroscopy as the VBC derived carbon materials. Gas physisorption studies using CHLR showed that it possessed well developed microporosity, with little detectable mesoporosity. From the N_2 physisorption of CHLR the isotherms obtained were ***type IV*** with ***H4*** hysteresis loops, however, the hysteresis loops exhibited no signs of closure, which indicates significant LPH is occurring, arising from equilibrium within the small pores not being achieved. Steam activation of CHLR resulted in only minor increases in the development of either micro- or mesopores, and although complete closure of the hysteresis loops was not observed, the shapes were much more defined.

The investigation of the pore structure of CHRK by gas physisorption revealed reasonable microporosity by CO_2 physisorption, but by N_2 physisorption no significant microporosity and no detectable mesoporosity. Steam activation of CHRK resulted in only minor micro- or mesopore development. ***Type IV*** N_2 isotherms with ***H4*** hysteresis loops were obtained, which are typical of carbons. The hysteresis loop from the N_2 isotherm of CHRK showed no signs of closure, but steam activation of CHRK resulted in some development in the shape of the hysteresis loop, arising from a minor increase in mesopore volume.

From the CO_2 adsorption pseudo-isotherms obtained for CHLR and CHRK, it was clear that at no temperature or CO_2 partial pressure tested did the amount of CO_2 adsorbed exceed that of AC-N, and in many cases it was significantly lower. This was mainly attributed to the negligible mesopore volumes of these chars and the mass-transport limitations that would be likely to result under the test conditions. Only minor increases in CO_2 adsorption were observed as a result of the steam activation of the chars, which is in good agreement with the small increases in pore development which occurred as a result of steam activation of the chars. The increased CO_2 adsorption observed over the steam activated chars was greater for AC-CHRK-90 than for AC-CHLR-90, on account of its more favourable surface chemistry (high surface hydroxyl concentration), as both steam activated chars possessed similar pore structures. The amount of CO_2 adsorbed from the multi-cyclic studies was greater than that observed from the differential-step adsorption studies, due to mass-transport limitations under the test conditions in the latter case. The mass-transport limitations arise due to the incredibly small mesopore volumes present in the chars and miACs derived from them, which limits the rate at which gas can diffuse through these materials. Although some interesting adsorption results were obtained for the steam activated chars, their CO_2 adsorption capacities were insufficient to warrant further investigation by H_2O competitive adsorption studies.

7.1.1.3 Chemically Activated Coal Derived Carbon Adsorbents

There was a strong linear relationship between the composition of the KOH activated miACs and the KOH loading used for their preparation. The KOH miACs exhibited the lowest bulk C concentration of any of the miACs, which was attributed to their high bulk O concentration. As the KOH loading increased the bulk O and the ash content of the carbons increased, the bulk C content decreased. This can be mostly attributed to the mechanism by which KOH activates the VBC parent carbon. One of the most accepted mechanisms of activation of carbon materials by KOH is based on the transfer of oxygen from KOH to the carbon.

The surface chemistry of the KOH activated miACs differed to that of the physically activated miACs. The KOH-miACs exhibited particularly high surface O concentrations, much of which was due to an increase in C-O-R groups. This was not just a result of the chemical activation mechanism, but also the reactor type and configuration used. The quartz reactor used in the chemical activation process possessed a sintered quartz frit which hindered both the flow of gas through the KOH-VBC samples and the removal of volatile matter by the inert carrier gas. By retaining much of the volatile matter in the VBC sample during carbonisation a greater number of small micropores were formed. This also allowed more of the oxygen to be retained than in the physical activation process. This was well exemplified by the high surface O concentration of AC-K0 (produced using the quartz reactor without KOH) compared to many of the physically activated VBC derived miACs. Much of the elevated surface O content of the KOH miACs was due to increases in C-O-R groups, which NEXAFS showed to be due to both hydroxyl and ether groups. Interestingly, the proportion of hydroxyl groups was significantly higher than for the physically activated miACs.

The chemical structure of the KOH miACs was similar in many respects to the other miACs. The Raman spectroscopy of the KOH miACs revealed the familiar result of the major type of carbon present being disordered graphitic carbon, with lesser contributions made by amorphous and ideal graphitic carbon. However, for the KOH miAC a decrease in the amount of ideal graphitic carbon was observed, which was confirmed by TEM. There was a greater amount of order to the disordered graphitic layer edges observed by TEM, which increased with KOH loading. Although an increase in the alignment was observed, this was not to the extent of well defined graphitic domains being formed. From the XRD patterns obtained for the KOH miACs, an increase in the intensity of the **100/101** reflection was observed with KOH loading, which suggests that the lateral order of the parallel graphitic domains is increasing with KOH loading. The gas physisorption studies of the KOH miACs revealed significant micropore volumes with essentially undetectable mesoporosity. Even when using high resolution N_2 and Ar physisorption (at 77 K and 87 K, respectively) it was still not possible to obtain useful mesopore

data, which in itself strongly indicate that the KOH miACs have pore diameters too small to allow the diffusion of N_2 or Ar.

The CO_2 adsorption pseudo-isotherms of the KOH miACs exhibited equal or greater CO_2 adsorption at all temperatures and CO_2 partial pressures than AC-N, regardless of KOH loading. However, with increasing KOH loading CO_2 adsorption did significantly increase, particularly between CO_2 partial pressures of 5-30 kPa. When the KOH loading reached 10 wt%, the CO_2 adsorption continued to increase with CO_2 partial pressure over the entire range tested. The high CO_2 adsorption results observed for the KOH activated miACs can be directly attributed to their high micropore volumes and surface O concentrations relative to the physically activated miACs. From the multi-cyclic adsorption studies for the KOH miACs the amount of CO_2 adsorbed at 5 kPa and 15 kPa was significantly greater than from the differential-step studies. This was again attributed to mass-transport limitations that arose because of the almost negligible mesoporosity that the KOH activated miACs possessed. In the multi-cyclic adsorption studies the samples were treated at 5 kPa for extended periods of time prior to the cyclic measurements, which allowed for true equilibrium to be achieved at 5 kPa.

Although all of the KOH activated miACs performed extremely well as CO_2 adsorbents AC-K10 was the best of the series. As such it was chosen for further investigation of its adsorption properties by wet gas adsorption. At both 363 K and 378 K AC-K10 exhibited competitive adsorption behaviour between CO_2 and H_2O, which probably limits its applicability to industrial scale carbon capture, as H_2O is present in flue gas streams. Regardless of this fact, due to the substantial CO_2 capacity of AC-K10, further investigation of this material is strongly advised.

7.1.2 Mesoporous Carbon Adsorbents

In general the composition of the lanthanide (Ln) oxide catalysed physically activated mesoporous carbons (Ln-meACs, where Ln is either Ce or La) were quite typical of carbon materials derived from coal, possessing predominately C and O as the major components, with minor contributions from H and N. The “as produced” Ln-meACs possessed much higher ash contents than the miACs, but this was significantly reduced upon acid washing. In fact for the La-meACs acid washing reduced the ash content to far lower values than the other carbon materials produced in this thesis.

The investigation of the carbon surface chemistry of the Ln-meACs was obscured by the presence of the surface Ln_xO_y phase. As such only direct comparison of the acid washed Ln-meACs could be made to AC-90. It was also for this reason that only the acid washed Ln-meACs were further investigated by NEXAFS spectroscopy. From the comparison of the Ce and La 3d

spectra of the "as produced" and acid washed Ln-meACs it was clear that a significant amount of the Ln_xO_y surface phase was removed by the acid washing procedure, on account of the significant reduction in all peaks in the Ln 3d spectra. Furthermore, investigation of the acid washed Ln-meAC surface chemistry by XPS showed them to possess much lower concentrations of C=O, C-O-R and COO-R groups relative to AC-90. However, NEXAFS of these Ln-meACs revealed that they possessed a significantly higher proportion of hydroxyl groups relative to ethers; the two groups attributed to the C-O-R peak in XPS. Furthermore, the amount of phenolic groups on the surface of the Ln-meACs were substantially higher than was observed for AC-90. This will have had a significant effect on the affinity for CO_2 of the acid washed Ln-meACs, despite the overall decrease in surface O relative to AC-90 observed by XPS.

The investigation of the chemical structure of the Ln-meACs yielded very similar results to the other physically activated ACs. Raman spectroscopy showed the major type of carbon present to be disordered graphitic carbon, with minor contributions from amorphous and ideal graphitic carbon; and XRD showed the familiar two broad peaks typical of amorphous carbon, suggesting the presence of some parallel graphitic domains and some degree of lateral structure. The TEM micrographs of the Ln-meACs confirmed the observations of both XRD and Raman spectroscopy, showing alignment of the graphene layer edges interspersed with well defined graphitic domains. These observations are typical of coal derived carbon materials, composed of disordered but parallel graphene sheets. The gas physisorption investigations of the Ln-meACs revealed that although the "as produced" Ln-meACs exhibited significant micro- and mesopore volumes, acid washing proved that much of this pore volume was in fact due to the porosity inherent within the Ln_xO_y itself.

The CO_2 adsorption pseudo-isotherms of the acid washed Ln-meACs exhibited significantly lower CO_2 adsorption relative to AC-90, which could be directly attributed to the overall lower surface O concentration of the acid washed Ln-meACs relative to AC-90. The lower overall surface O concentration of the acid washed Ln-meACs was mainly due to lower concentrations of C-O-R and COO-R groups. NEXAFS showed that compared to AC-90, the Ln-meACs possessed higher concentrations of phenolic groups and higher proportions of hydroxyl groups relative to ethers. The latter will have had the overall effect of slightly increasing the surface concentration of hydroxyl groups of the acid washed Ln-meACs relative to AC-90, resulting in an increase in CO_2 affinity. From the multi-cyclic adsorption studies of the acid washed Ln-meACs it could be seen that the amount of CO_2 adsorbed by AC-Ce3-90-AW and AC-La3-90-AW at both 5 kPa and 15 kPa from the multi-cyclic studies were slightly greater than were observed at the same CO_2 partial pressure from the differential-step adsorption studies. This was due to mass-transport limitations that arose due to the small mesopore volume of AC-Ce3-90-AW and AC-La3-90-AW.

No evidence of mass-transport limitations was observed from the multi-cyclic adsorption studies over AC-90-Ce3-90-AW or AC-90-La3-90-AW, with the same amount of CO_2 being observed at 5 kPa and 15 kPa from both the multi-cyclic and differential-step adsorption studies. Despite the lower than desired mesopore volumes of the acid washed Ln-meACs they were still investigated as supports for PEI.

7.1.3 Amine Modified Activated Carbons Adsorbents

The characterisation of the PEI-ACs was limited to the use of elemental analysis and gas physisorption, as any other form of characterisation would not yield useful information.

PEI impregnation of the AC resulted in significant increases in the bulk H and N content, the degree of which was a good indication of the degree of success of the impregnation procedure. Furthermore, as the bulk N content of the support materials was known, the "adjusted nitrogen" content could be determined, which allowed for the amount of N in the sample that was due to the PEI alone to be determined. This was of particular importance for determining the "amine efficiency", which allowed assessment of how efficiently the amine groups were performing at a particular temperature and CO_2 partial pressure. N_2 physisorption at 77 K allowed the degree to which the pores had been filled by PEI to be determined. In all cases the pore volume was barely within the detectable range, a good indication that the pores had essentially been filled with PEI.

The adsorption pseudo-isotherms for the PEI-ACs at 363 K revealed that the amine modified materials exhibited greater CO_2 adsorption relative to the corresponding carbon supports. This was especially true for the PEI impregnated AC-90 materials (AC-90-90PEI-R and AC-90-90PEI-VT), which exhibited higher CO_2 adsorption at 293 K than most of the non-modified carbon materials presented in this thesis. At 378 K, AC-90-90PEI-R also exhibited exceptionally high CO_2 adsorption over the entire CO_2 partial pressure range. These findings were supported by the high amine efficiencies determined for AC-90-90PEI-R at both 363 and 378 K. Unfortunately, all the other PEI-ACs exhibited equivalent or lesser adsorption than the corresponding carbon supports at 378 K. For the Ln-meAC supported PEI-ACs it was proposed that the lower than expected CO_2 adsorption could possibly be attributed to the high concentration of phenolic surface moieties, which may have formed strong interactions (electrostatic) with the amines of PEI. Furthermore, if the PEI had been drawn deeper into the pore structure of the Ln-meAC supports, then the interactions between the PEI and AC support would have increased. Such associations would result in a decrease in the number of amine sites

available to take part in CO_2 adsorption; a phenomenon that was apparent from the low amine efficiencies determined for the Ln-meAC supported PEI-ACs.

Higher CO_2 adsorption was observed in the multi-cyclic adsorption studies than in the differential-step adsorption studies due to pre-dosing at 5 kPa prior to the cyclic measurements. This behaviour was attributed to the slow diffusion of CO_2 through PEI, which in several cases led to equilibrium not being achieved over the adsorption cycle. The wet gas investigations of the Ln-meAC supported PEI-ACs showed decreased CO_2 adsorption in the presence of H_2O, relative to dry gas conditions. However, excellent CO_2 adsorption was observed over AC-90-90PEI-R and AC-90-90PEI-VT, with significant increases in CO_2 capacity being observed in wet gas conditions compared to dry conditions; strongly indicating the formation of bicarbonates. It was proposed that since fewer strong electrostatic interactions existed between PEI and AC-90, H_2O was able to disrupt hydrogen bonding, making more amine sites available to take part in adsorption and form bicarbonates. This was particularly prominent for AC-90-90PEI-R, and it is believed that with further study this material may hold significant promise as a CO_2 adsorbent.

7.1.4 Overall Conclusions

The work presented in this thesis demonstrates that VBC holds great promise for use in the production of carbon adsorbents for CCS from post-combustion flue gas. This was due to the unique composition of VBC, which allowed for carbon materials with superior surface chemistry to be produced by simple methods, which are potentially economically viable. Several outstanding adsorbents were identified over the course of this project, which include: AC-90 from the steam activated miAC series, AC-K10 from the KOH activated miAC series, and AC-90-90PEI-R from the PEI-AC composites. These materials are strongly recommended for further investigation, as outlined below.

Of the physically activated carbon materials, AC-90 held the most potential as a CO_2 adsorbent. It outperformed the benchmark (AC-N) under all conditions tested, despite AC-90 possessing significantly lower pore volume than AC-N. The superior adsorption behaviour of AC-90 was attributed to the favourable distribution of surface functional groups, which also allowed for preferential adsorption of CO_2 even in the presence of H_2O; a major component of flue gas. There were particularly high concentrations of polar functional groups such as hydroxyls and carboxylic acids on the surface of AC-90 relative to AC-N. Furthermore, the amount of steam required to produce AC-90 was lower than is commonly reported. This may enable for cost reduction in the production of AC-90 to other ACs, and is one of the many reasons that this AC should be investigated further.

All of the KOH activated miACs exhibited excellent CO_2 adsorption behaviour, especially AC-K10. From the differential-step and multi-cyclic adsorption studies, AC-K10 clearly outperformed AC-N to a greater extent than any of the other miACs. However, H_2O competitively adsorbed to AC-K10 which may limit the direct application of this material in the separation of CO_2 from flue gas streams. Importantly, the methods used to produce the KOH activated miACs are cheaper than those used to produce other chemically activated ACs because KOH was directly impregnated into the VBC precursor instead of a pre-produced char, and significantly lower amounts of KOH were required (10 wt%) than those traditionally employed (400-600 wt%). As such, capital costs could be reduced by using lower grade steel to construct the reactor. Operating costs would be reduced because of the reduced amount of KOH used in production. Also corrosive waste would be minimised which would have environmental benefits and reduce the safety risks associated with handling the materials.

Ln_xO_y was used to promote the development of mesoporosity in physically activated carbons by catalysing partial oxidation reactions that occur during VBC gasification. The study of the Ln-meACs undertaken here enabled the elucidation of important details relating to the catalytic activity of Ln_xO_y during pore development. Most importantly, it was discovered that the apparent increases in the mesopore volumes reported in the literature for other Ln-meACs, in fact arose from the innate porosity of Ln_xO_y. In this work, an acid washing method was developed to remove the Ln_xO_y, which had never been reported in previous studies. It was observed that the pore volumes of the acid washed Ln-meACs were substantially lower than the non-acid washed analogues in previous reports. It is believed that the semi-rigid carbon structure of VBC prevents the production of materials with the extent of mesoporosity desired here. Although it may be possible to generate more highly mesoporous materials from VBC using more severe conditions (e.g. alkali hydroxide coal digestion and extensive gasification), these approaches are likely to be less attractive from an economic perspective.

The acid washed Ln-meACs and AC-90 were then investigated as support materials for PEI. The CO_2 adsorption exhibited by AC-90-90PEI-R under all conditions was significantly greater than for other carbon materials produced in this thesis. However, the vacuum treatment used to remove low molecular weight PEI from the composites was detrimental. Vacuum treatment drew PEI deeper into the close ended, slit-shaped pores of the support and led to an increased number of interactions between the amines of the PEI and the AC surface. Thus, it appears that fewer amine sites were available for CO_2 adsorption. These effects were more pronounced for the Ln-meACs which possessed significantly higher proportions of phenolic groups on their surface that could result in strong electrostatic interactions forming between PEI and the Ln-meACs. AC-90-90PEI-R exhibited significantly increased CO_2 adsorption in wet gas conditions,

which supported the formation of bicarbonate species. Therefore, of all of the PEI-ACs only AC-90-90PEI-R exhibited any promise for carbon capture applications. However, further work is still required to develop a full understanding the applicability of AC-90-90PEI-R to carbon capture.

7.2 Future Directions

The next major step to be taken towards evaluating the applicability of the carbon materials produced here to industrial scale CCS processes are to undertake breakthrough adsorption studies with more realistic gas mixtures. These must firstly be undertaken at the lab scale on the carbons in the powdered form, before larger scale quantities are investigated at the bench scale.

The first breakthrough studies that will be required to be undertaken are on N_2/CO_2 mixtures, in order to establish the selectivity of the adsorbents towards CO_2. Once the baseline selectivity of the adsorbents towards CO_2 has been established, competitive adsorption studies with H_2O, the third major component of flue gas will be required. The competitive H_2O/CO_2 studies that were undertaken in this work were limited by the TGA system used to 2 %(v/v) of H_2O in the gas stream, where as in a real flue gas stream the concentration of H_2O is closer to 15 %(v/v). The seemingly negligible effect that H_2O had on CO_2 adsorption at 2 %(v/v) may very well not be the case at 15 %(v/v) H_2O. Moreover, the effects of SO_x and NO_x on the adsorption of will need to be investigated for all adsorbents marked for further investigation. Competitive adsorption studies with SO_x and NO_x will be required for AC-90 and AC-K10 due to the presence of these compounds in flue gas, which will not irreversibly affect the ACs, but may compete for adsorption sites. In the case of the PEI-AC composites the situation is much more complicated, as SO_x and NO_x can potentially irreversibly bind to the amine moieties, essentially deactivating the amine site [1-3], and so more in depth studies may be required.

The second type of breakthrough studies to be undertaken on the carbon adsorbents are on the bench scale, using the adsorbent in pelletised form. Obviously, this will first require fabrication studies to be undertaken in order to ascertain the most appropriate fabrication process and determine the effects this will have on CO_2 adsorption of the adsorbents. Most importantly the behaviour of the adsorbent pellets on gas flow through a fixed bed system, minimising the void volume of the column in addition to the diffusion of gas through the pellets themselves. It is proposed here that the primary binder to be investigated for use in pelletisation studies for AC-90 and AC-K10 should be the tar produced from the production of these adsorbents. In the case of the PEI-AC composites the PEI itself could act as a binder. Vacuum treatment prior to pelletisation should probably be avoided, but post-synthetic vacuum treatment might be

appropriate. Further down the track bench scale studies utilising larger quantities of materials will be required, as part of the pelletisation study itself, which will feed important information into a techno-economic viability study.

Regarding the wider use of the carbon adsorbents beyond their use in post-combustion flue gas streams using a VSA system, two applications have been identified outside of the scope dealt with in this research. Firstly, the AC-90 and AC-K10 adsorbents may have potential use in electrothermal swing adsorption (ESA) from flue gas streams; secondly, these carbon materials may be useful as adsorbents for the separation of CO_2 from natural gas. The use of ACs for gas separation by ESA has been looked at previously [4, 5], and requires that the carbons possess electrical conductivity and are able to be fabricated into monoliths. Both these characteristics can be achieved, but will require studies of reasonable length and detail in order to achieve these goals. Furthermore, the use of ACs for natural gas separation have also been studied in the past [6-9], even using VBC derived ACs [10]. Single gas and breakthrough adsorption studies will be the first step in determining the applicability of the ACs produced here for natural gas separation.

7.3 References

1. Xu, X., et al., *Adsorption separation of carbon dioxide from flue gas of natural gas-fired boiler by a novel nanoporous "molecular basket" adsorbent.* Fuel Processing Technology, 2005. **86**(14–15): p. 1457-1472.
2. Khatri, R.A., et al., *Thermal and chemical stability of regenerable solid amine sorbent for CO_2 capture.* Energy and Fuels, 2006. **20**(4): p. 1514-1520.
3. Choi, S., J.H. Drese, and C.W. Jones, *Adsorbent materials for carbon dioxide capture from large anthropogenic point sources.* ChemSusChem, 2009. **2**(9): p. 796-854.
4. Grande, C.A. and A.E. Rodrigues, *Electric Swing Adsorption for CO_2 removal from flue gases.* International Journal of Greenhouse Gas Control, 2008. **2**(2): p. 194-202.
5. Moon, S.H. and J.W. Shim, *A novel process for CO_2/CH_4 gas separation on activated carbon fibers-electric swing adsorption.* Journal of Colloid and Interface Science, 2006. **298**(2): p. 523-528.
6. Azevedo, D.C.S., et al., *Microporous activated carbon prepared from coconut shells using chemical activation with zinc chloride.* Microporous and Mesoporous Materials, 2007. **100**(1-3): p. 361-364.
7. Bastos-Neto, M., et al., *Effects of textural and surface characteristics of microporous activated carbons on the methane adsorption capacity at high pressures.* Applied Surface Science, 2007. **253**(13): p. 5721-5725.
8. Biloé, S., V. Goetz, and A. Guillot, *Optimal design of an activated carbon for an adsorbed natural gas storage system.* Carbon, 2002. **40**(8): p. 1295-1308.
9. Sun, J., et al., *Natural gas storage with activated carbon from a bituminous coal.* Gas Separation & Purification, 1996. **10**(2): p. 91-96.
10. Chaffee, A.L. and A.G. Pandolfo. *Coal Derived Carbons for Methane Storage*. in *Proceedings - 4th Australia Coal Science Conference, Brisbane*. 1990.

8 Appendices

8.1 Appendix 1 – Parent Material Data Sheets

8.1.1 Victorian Brown Coal Briquettes

ENERGY BRIX AUSTRALIA

TYPICAL COMPOSITION & PROPERTIES

VICTORIAN BROWN COAL BRIQUETTES

ENERGY BRIX AUSTRALIA CORPORATION PTY LTD ACN 074 736 833

This typical briquette composition and properties is based on briquette production from a mixture of 80% Loy Yang Coal and 20% Yallourn Eastfield Coal. The ash yield of the 2 coal types used for briquette production has been assumed to be 0.7% to 1.5% dry basis (db) for Loy Yang Coal and 1.8% to 2.5% dry basis (db) for Yallourn Eastfield Coal. The moisture content of the briquettes is controlled by Energy Brix during its production process and is assumed to be between 10% to 13%.

TYPICAL DIMENSIONS		
	Type I "L" Industrial 43mm Victoria Briquettes	**Type II** "3-piece" Household 86mm Victoria Briquettes
Size (approx.)	58mm x 43mm x 40mm	86mm x 62mm x 40mm
Weight (approx.)	90g	230g
Bulk Density	0.75 tonne/m³	0.75 tonne/m³

TYPICAL ANALYSIS				
	COMPONENT		**PREDICTED RANGES**	
			As Fired	**Dry Basis**
Proximate	Fixed Carbon	(%)	42 to 46	48 to 52
	Volatile Matter	(%)	41 to 44	47 to 50
	Moisture	(%)	10 to 13	-
	Ash	(%)	0.8 to 1.5	0.9 to 1.7
Ultimate	Carbon	(%)		67 to 70
	Hydrogen	(%)		4.7 to 5.1
	Nitrogen	(%)		0.53 to 0.66
	Total Sulphur	(%)		0.29 to 0.42
	Oxygen	(%)		22.8 to 27.0
Energy	Gross	(MJ/kg)	22.6 to 24.3	26.0 to 27.0
		(Btu/lb)	9,716 to 10,447	11,178 to 11,608
		Kcal/kg	5,398 to 5,804	6,210 to 6,449
	Net	(MJ/kg)	21.5 to 23.2	
		(Btu/lb)	9,243 to 9,974	
		Kcal/kg	5,135 to 5,541	

Based on predicted Loy Yang and Yallourn Eastfield Coal as at February 2002

ENERGY BRIX AUSTRALIA

TYPICAL COMPOSITION & PROPERTIES

VICTORIAN BROWN COAL BRIQUETTE ASH

ENERGY BRIX AUSTRALIA CORPORATION PTY LTD ACN 074 736 833

ANALYSIS OF ASH CONSTITUENTS		
Ash Constituents (Laboratory Furnace Ash)	**Predicted Minimum Value (% db)**	**Predicted Maximum Value (% db)**
Silica	1.0	50
Alumina	1.0	25
Titanium oxide	0.1	2.0
Iron oxide	10	20
Calcium oxide	5	10
Magnesium oxide	10	15
Sodium oxide	5	15
Potassium oxide	0.1	1.5
Sulphur trioxide*	10	40

Briquette ash analysis varies depending upon the combustion method (laboratory muffle furnace, domestic heater or industrial boiler).

* The sulphur trioxide values in furnace/fly ash produced from these briquettes may be lower than the predicted furnace ash values reported here; hence, concentration of other oxides would also increase proportionally.

OTHER PROPERTIES	
Ash Fusion Temperature	> 1250°C (reducing atmosphere)
Hardgrove Index	40 – 45
Compressive Strength (kg/cm^3)	160 – 200
Briquette Particle Density (g/cm^3)	1.118 – 1.240

Based on predicted Loy Yang and Yallourn Eastfield Coal as at February 2002

8.1.2 Norit R2030 CO2

Norit Digital Library

Norit Electronic Version

Datasheet

Gas & Air

Norit R 2030

Norit R2030 is a steam activated extruded carbon with a particle diameter of 3 mm. The established activity of Norit R2030 is ideal to remove low concentrations of contaminants from gas flows. The superior mechanical hardness in combination with the extruded particle shape result in a low pressure drop over the filter. Norit R2030 is used in gas phase applications dealing with low concentrations (in general 1 – 200 ppm) requiring high removal efficiencies. For high contaminant concentrations this type of carbon should not be used. For this, alternatives are available.

SPECIFICATIONS

Butane adsorption at p/p_0 = 0.1	**min. 13**	**g/100 g**
Butane adsorption at p/p_0 = 0.1	**max. 18**	**g/100 g**
Moisture (as packed)	**max. 5**	**mass-%**

GENERAL CHARACTERISTICS

Butane adsorption at p/p_0 = 0.1	16	g/100 g
Total surface area (B.E.T.)	800	m^2/g
Apparent density	520	kg/m^3
Ball-pan hardness	99.9	-
Abrasion index	10	mg/min
Particle size > 2.36 mm	99	mass-%
Moisture (as packed)	1	mass-%
Ignition temperature, above	450	°C

Document No.
R2030

Product / Application
Extruded activated carbon

Version
15 August 2011

Norit Nederland BV
Nijverheidsweg-Noord 72
3812 PM Amersfoort
P.O. Box 105
3800 AC Amersfoort
The Netherlands

T: +31 33 46 48 911
F: +31 33 46 17 429
E: sales@norit.com
I: www.norit-ac.com

MGMT. SYS. RvA C 030 BSI REGISTERED
FM 26618

Norit Activated Carbon
leading in purification

NOTES

1 All analyses based on Norit Standard Test Methods (NSTM)
2 Specifications are guaranteed values based on lot to lot quality control, as covered by Norit's ISO 9001 certification.
3 General characteristics reflect average values of product quality.
4 Detailed information on **pressure drop characteristics** in air can be found in Technical Bulletin TB 136: Pressure drop characteristics of Norit extruded activated carbon grades.

PACKAGING

Norit R 2030 is available in:
- Polyethylene bags of 25 kg, 44 bags per pallet, stretch wrapped on 115 x115 cm pallets (1100 kg net weight per pallet)
- Bulk bags of 2 x 500 kg net weight on a pallet, shrink wrapped

Product availabilities depend on the type of packaging.

Caution: For health and safety related aspects please refer to the Material Safety Datasheet (MSDS), which is available on request.

Notes: Any product quality information including specifications given was valid at the time of issuance of the publication. However, we maintain a policy of continuous development and reserve the right to amend any product quality aspects without notice. All data and suggestions regarding the use of our products are believed to be reliable and given in good faith. However, they are given without guarantee, as the use of our products is beyond our control, and are not to be construed as recommendation or instigation to violate any existing patent.

This datasheet is generated in an electronic way and is meant to be used only for the purpose of convenience. In case of divergencies between this datasheet and the original datasheet available at Norit's headoffice, the original datasheet prevails. Customer should notify Norit immediately of this divergence.

This datasheet (Issue 15 August 2011) replaces previous issues.

Norit Activated Carbon
leading in purification

8.2 Appendix 2 – NEXAFS Spectroscopy Peak Fitting

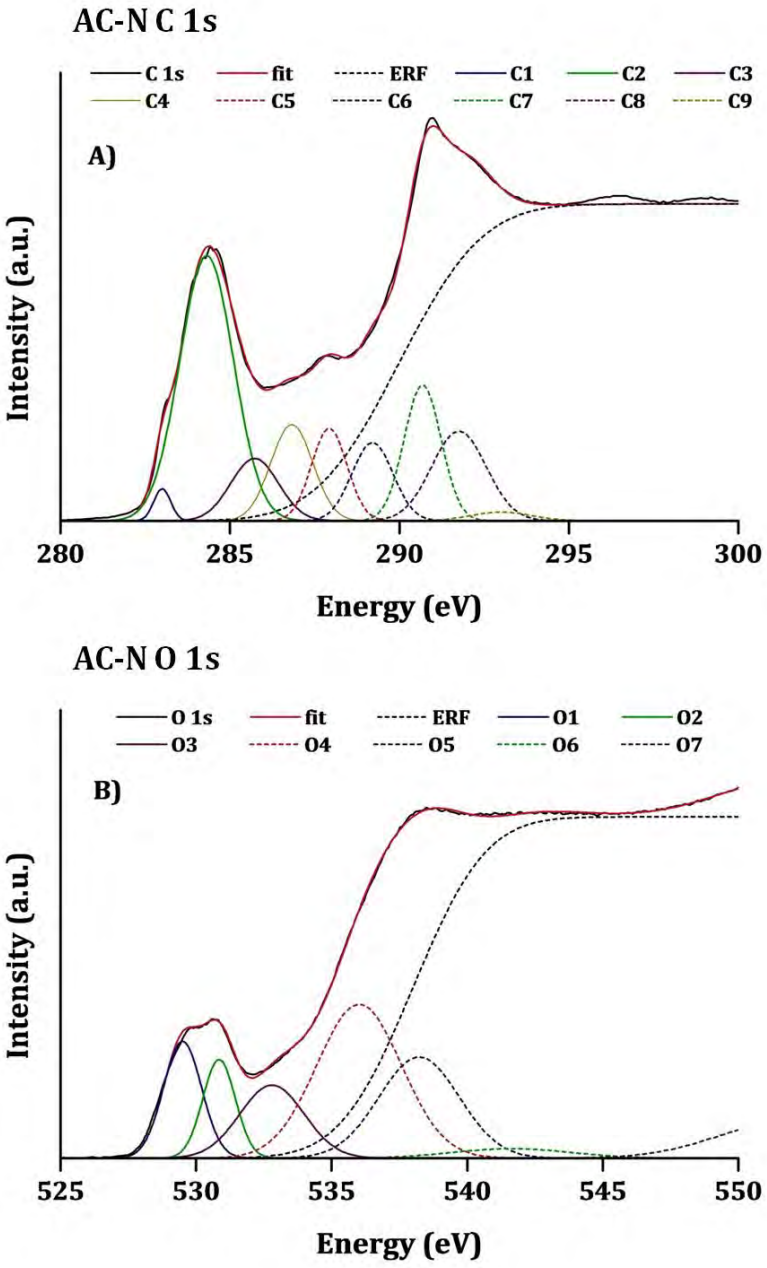

Figure 8-1 *~ C 1s and O 1s NEXAFS Spectra for AC-N, with Complete Peak Fitting. Shown are* ***A)*** *C 1s NEXAFS Spectrum for AC-N,* ***B)*** *O 1s NEXAFS Spectrum for AC-N*

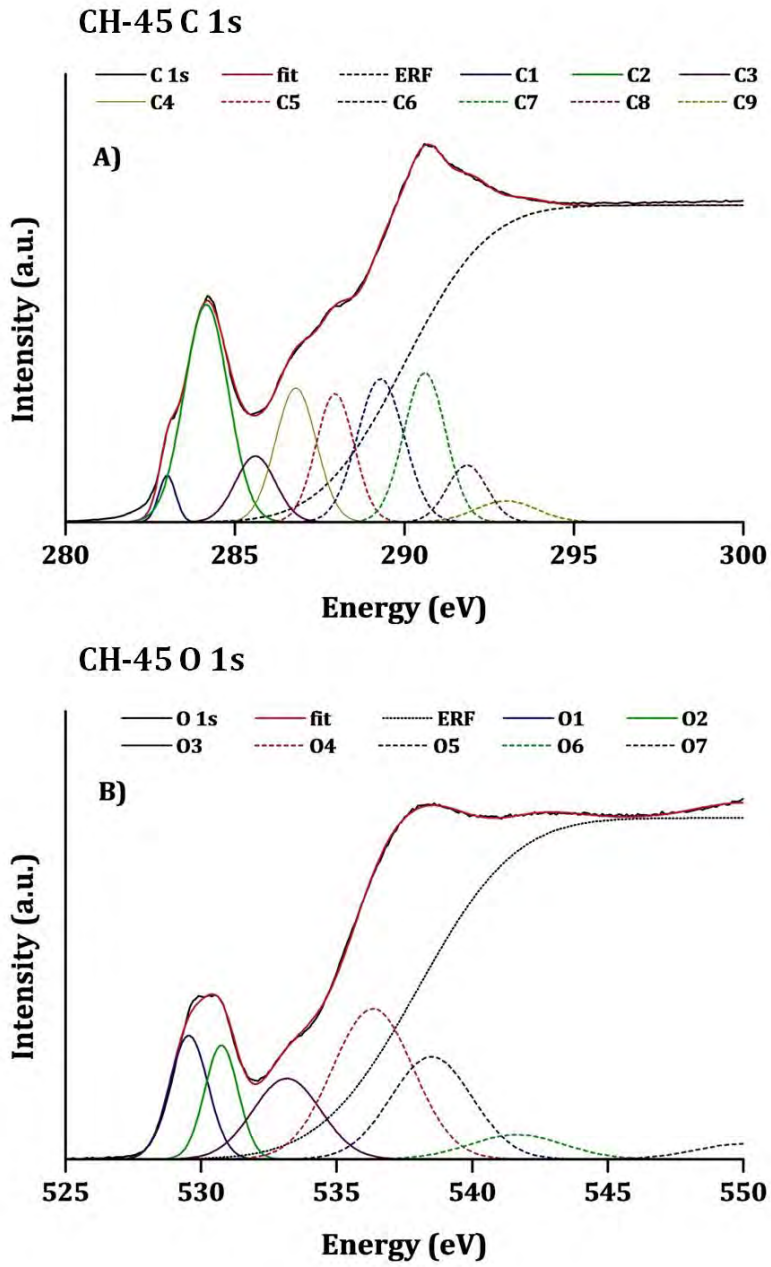

Figure 8-2 *~ C 1s and O 1s NEXAFS Spectra for CH-45, with Complete Peak Fitting. Shown are* ***A)*** *C 1s NEXAFS Spectrum for CH-45,* ***B)*** *O 1s NEXAFS Spectrum for CH-45*

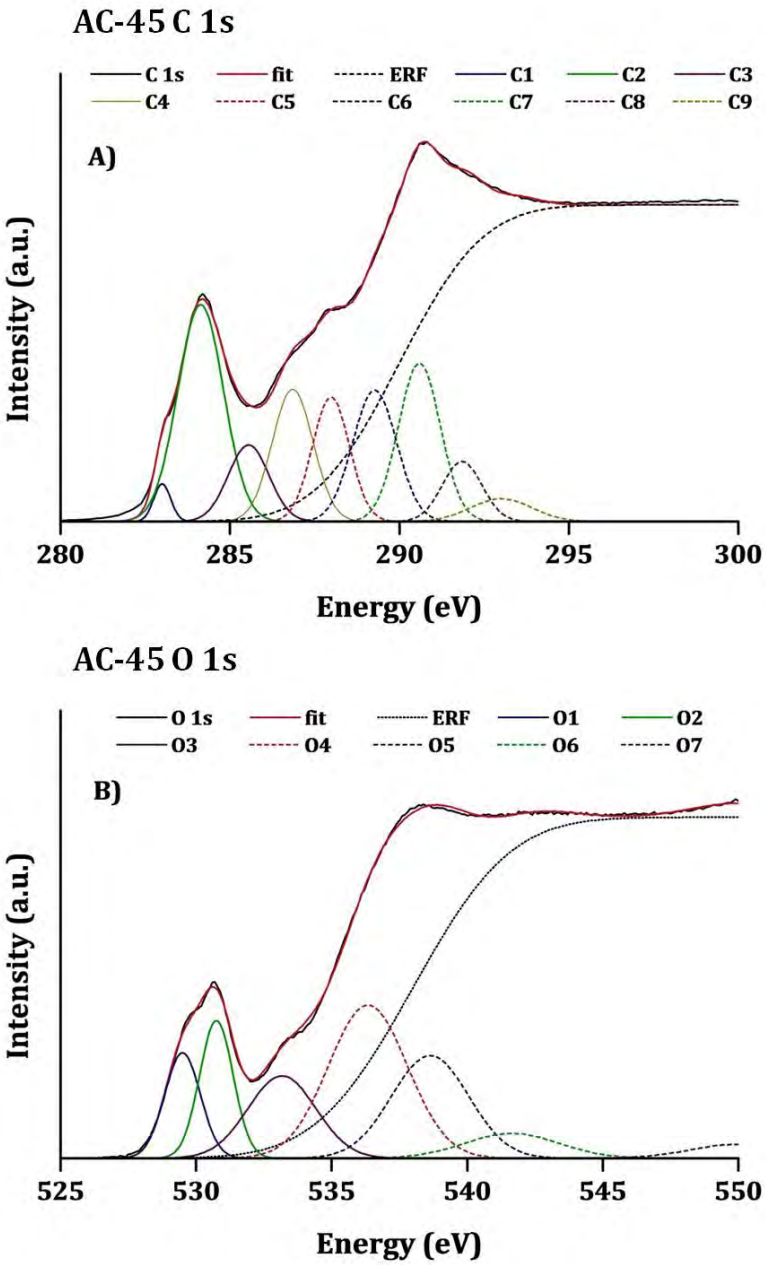

Figure 8-3 *~ C 1s and O 1s NEXAFS Spectra for AC-45, with Complete Peak Fitting. Shown are* ***A)*** *C 1s NEXAFS Spectrum for AC-45,* ***B)*** *O 1s NEXAFS Spectrum for AC-45*

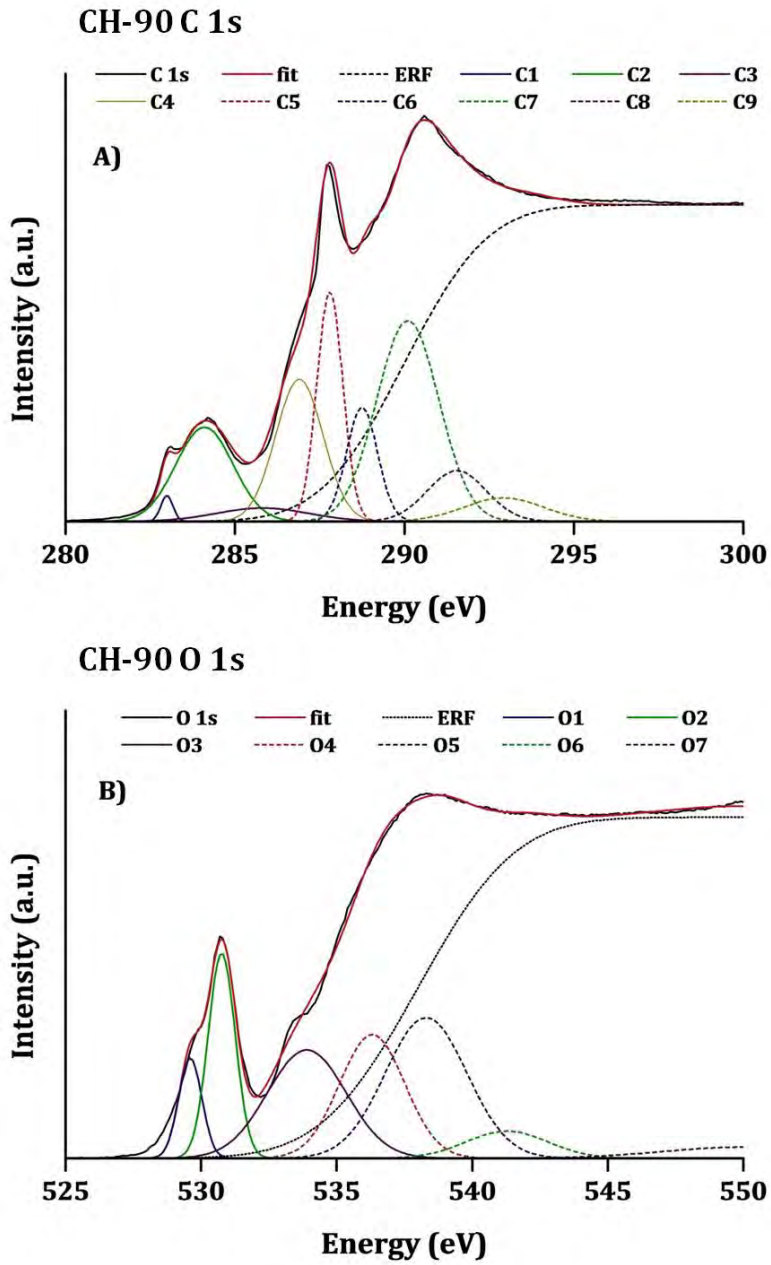

Figure 8-4 *~ C 1s and O 1s NEXAFS Spectra for CH-90, with Complete Peak Fitting. Shown are* ***A)*** *C 1s NEXAFS Spectrum for CH-90,* ***B)*** *O 1s NEXAFS Spectrum for CH-90*

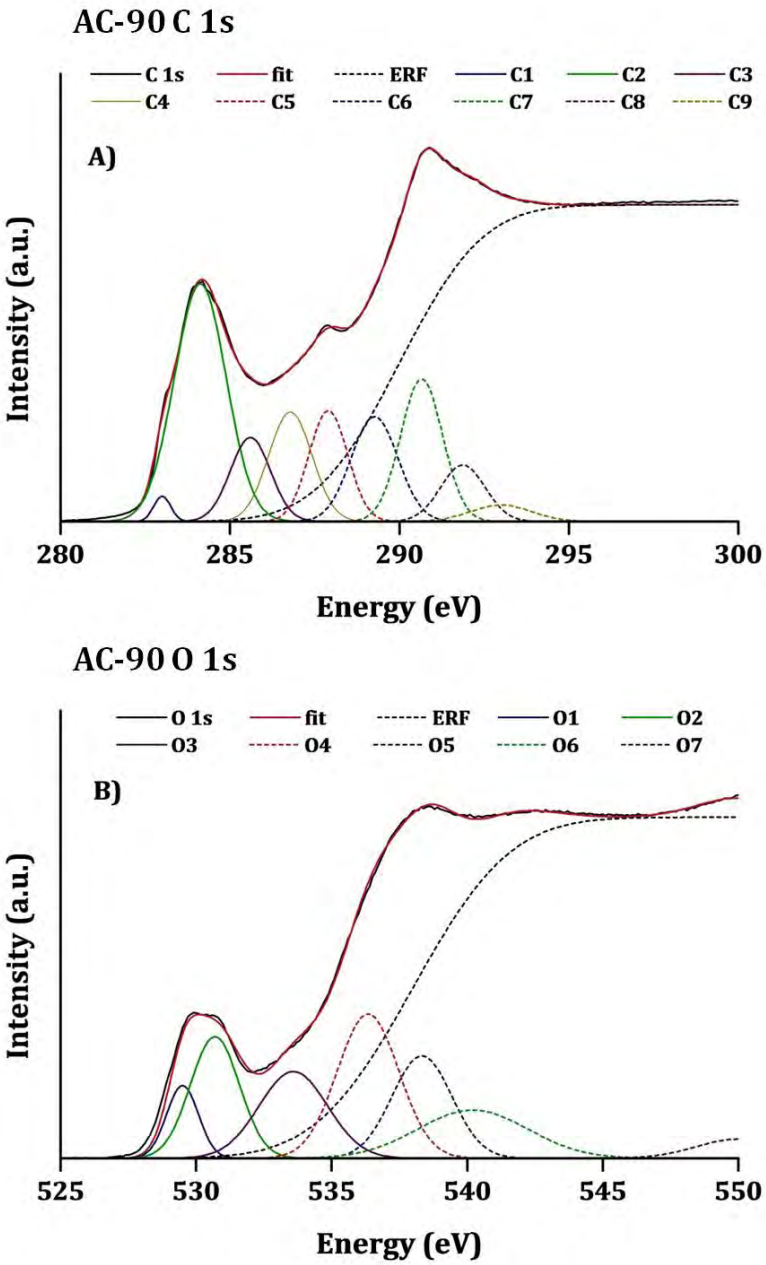

Figure 8-5 *~ C 1s and O 1s NEXAFS Spectra for AC-90, with Complete Peak Fitting. Shown are* ***A)*** *C 1s NEXAFS Spectrum for AC-90,* ***B)*** *O 1s NEXAFS Spectrum for AC-90*

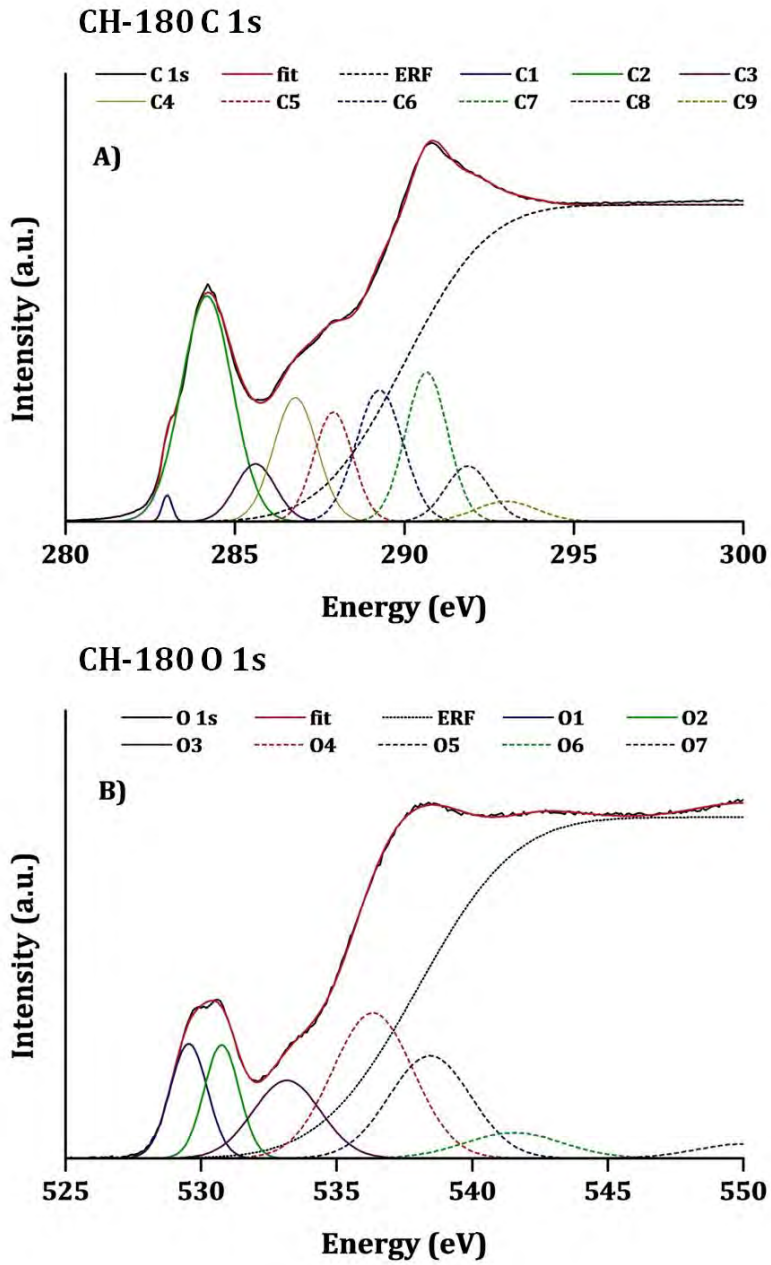

Figure 8-6 *~ C 1s and O 1s NEXAFS Spectra for CH-180, with Complete Peak Fitting. Shown are* ***A)*** *C 1s NEXAFS Spectrum for CH-180,* ***B)*** *O 1s NEXAFS Spectrum for CH-180*

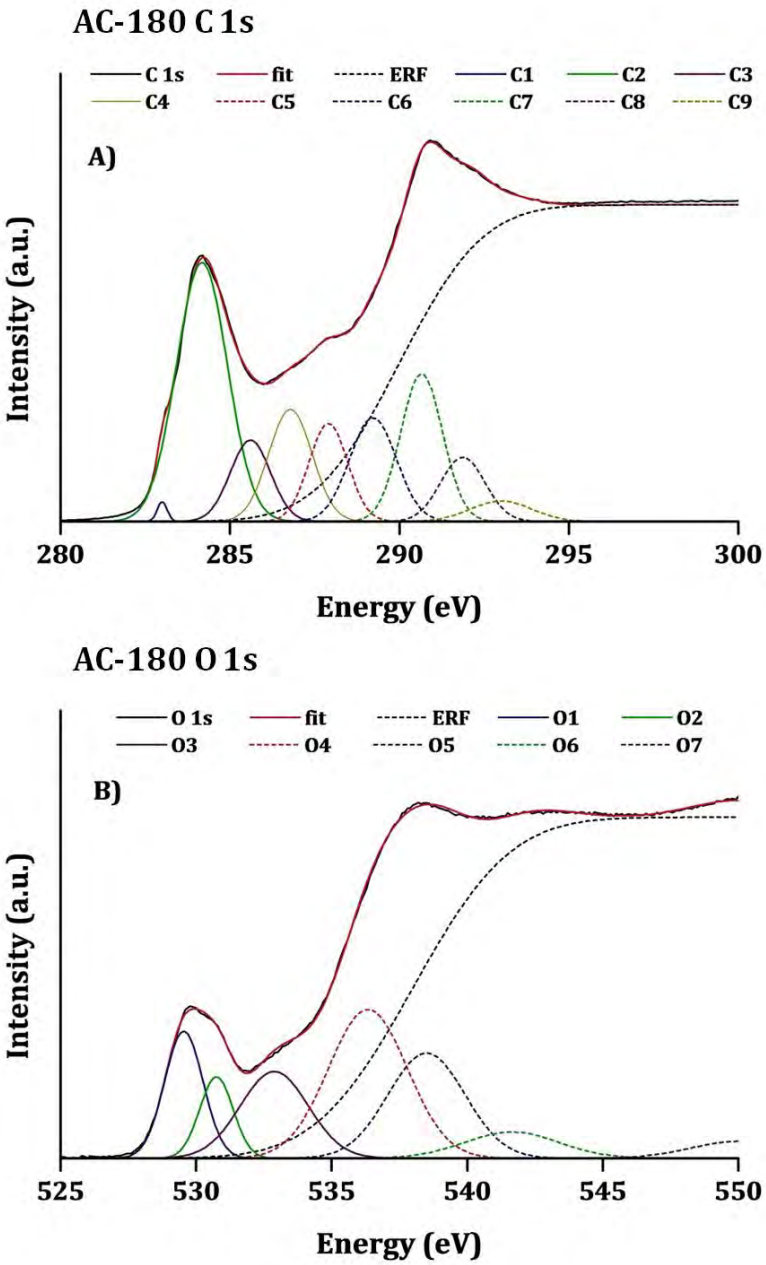

Figure 8-7 *~ C 1s and O 1s NEXAFS Spectra for AC-180, with Complete Peak Fitting. Shown are* ***A)*** *C 1s NEXAFS Spectrum for AC-180,* ***B)*** *O 1s NEXAFS Spectrum for AC-180*

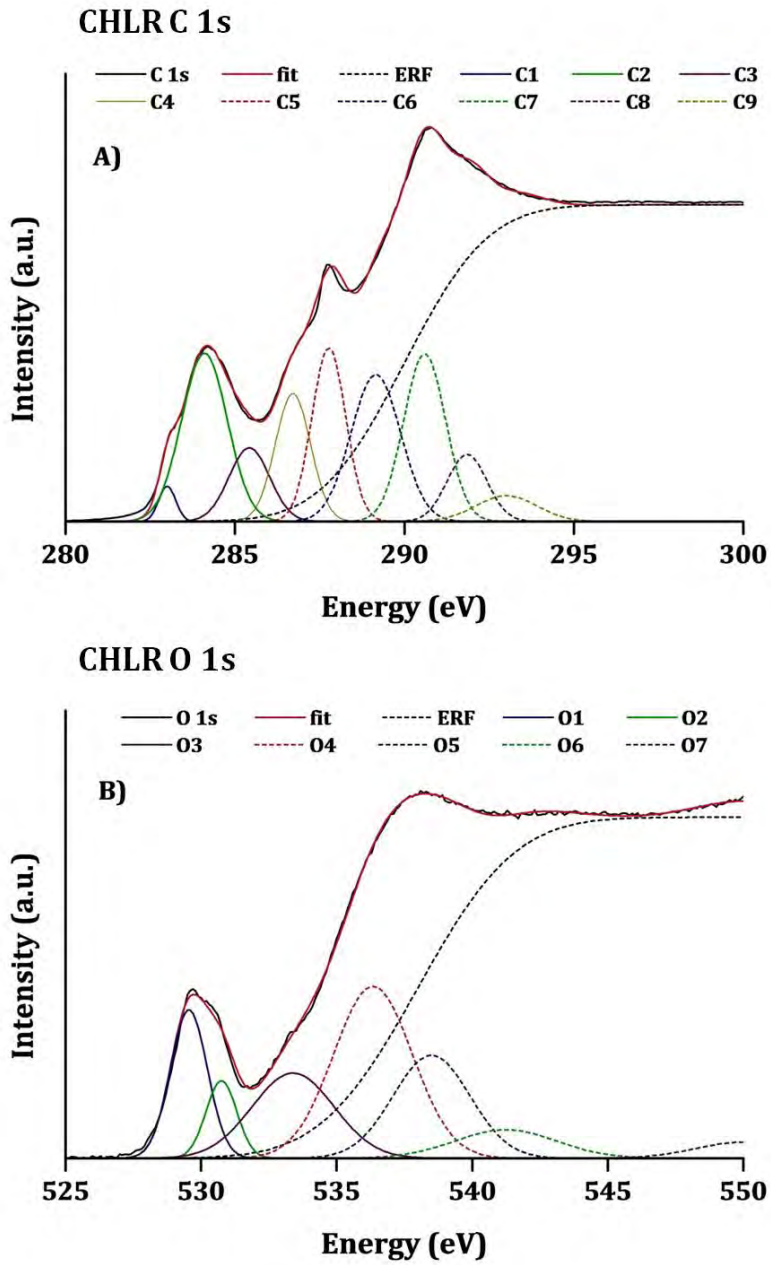

Figure 8-8 *~ C 1s and O 1s NEXAFS Spectra for CHLR, with Complete Peak Fitting. Shown are* ***A)*** *C 1s NEXAFS Spectrum for CHLR,* ***B)*** *O 1s NEXAFS Spectrum for CHLR*

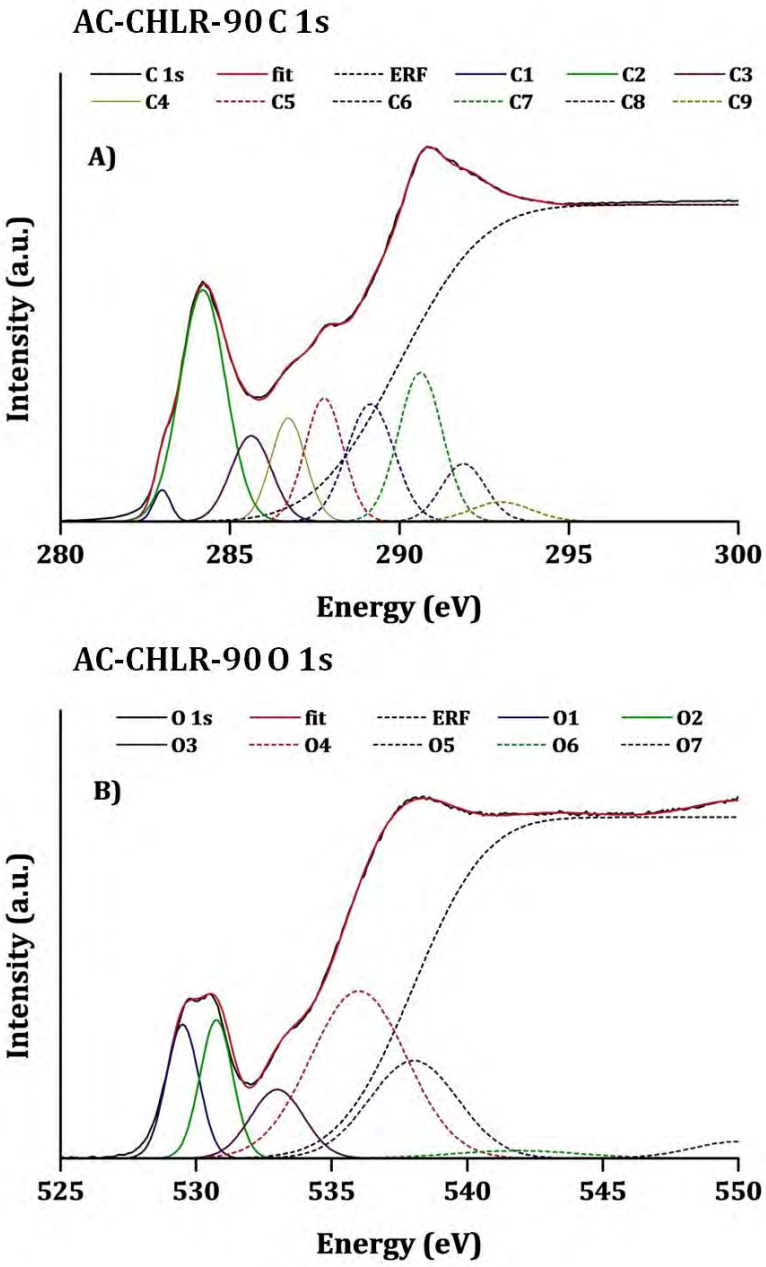

Figure 8-9 *~ C 1s and O 1s NEXAFS Spectra for AC-CHLR-90, with Complete Peak Fitting. Shown are* ***A)*** *C 1s NEXAFS Spectrum for AC-CHLR-90,* ***B)*** *O 1s NEXAFS Spectrum for AC-CHLR-90*

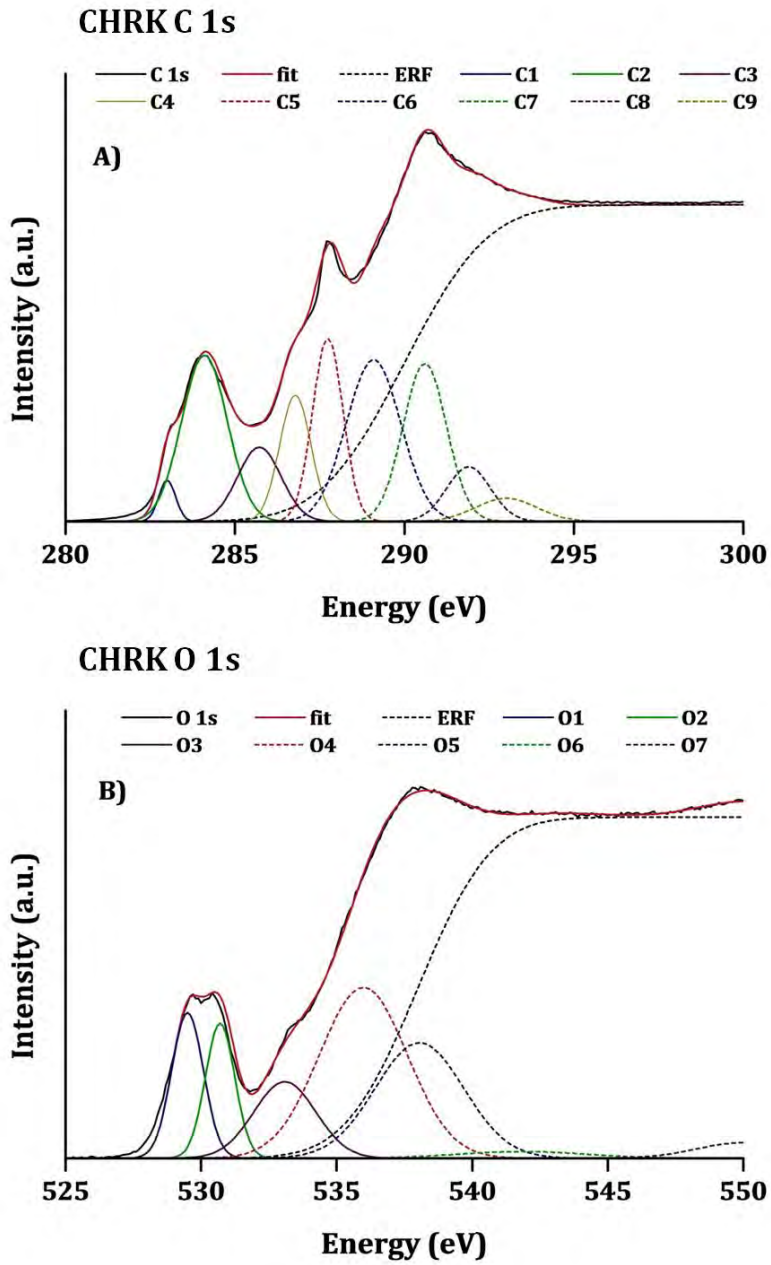

Figure 8-10 *~ C 1s and O 1s NEXAFS Spectra for CHRK, with Complete Peak Fitting. Shown are* ***A)*** *C 1s NEXAFS Spectrum for CHRK,* ***B)*** *O 1s NEXAFS Spectrum for CHRK*

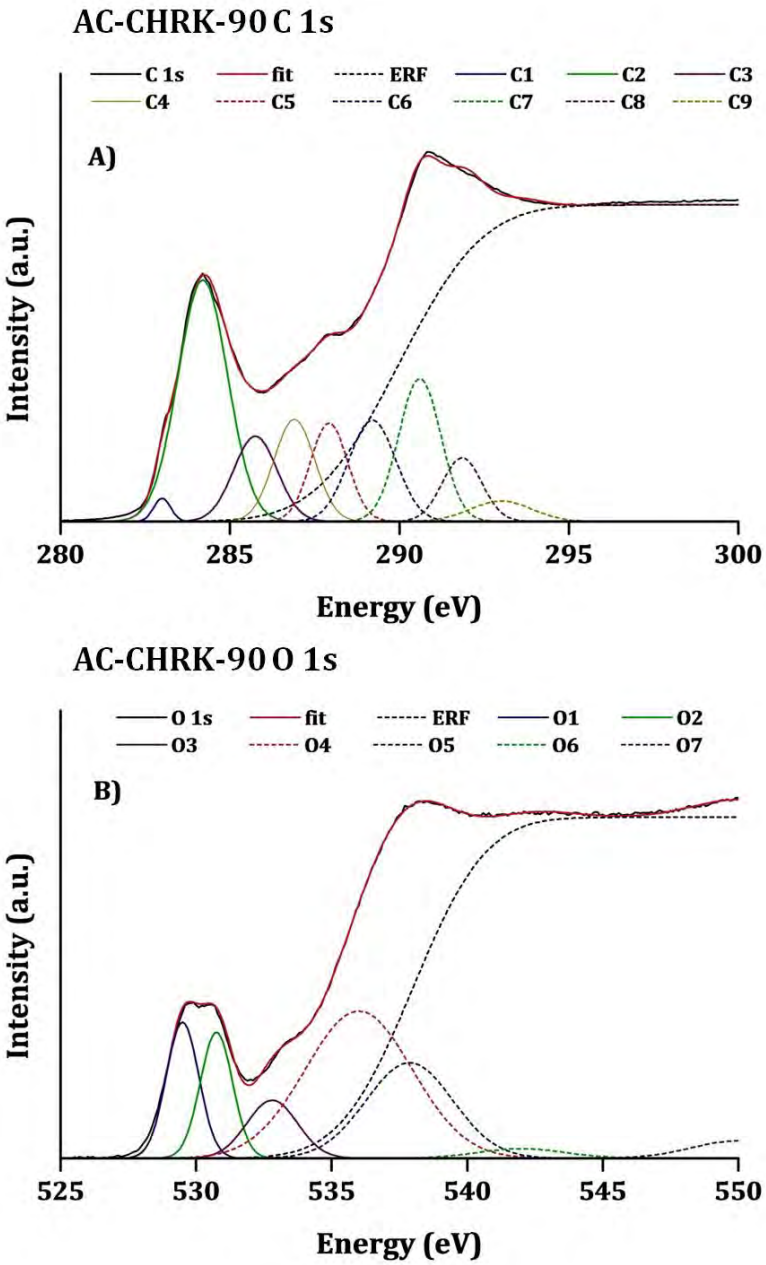

Figure 8-11 *~ C 1s and O 1s NEXAFS Spectra for AC-CHLR-90, with Complete Peak Fitting. Shown are* ***A)*** *C 1s NEXAFS Spectrum for AC-CHLR-90,* ***B)*** *O 1s NEXAFS Spectrum for AC-CHLR-90*

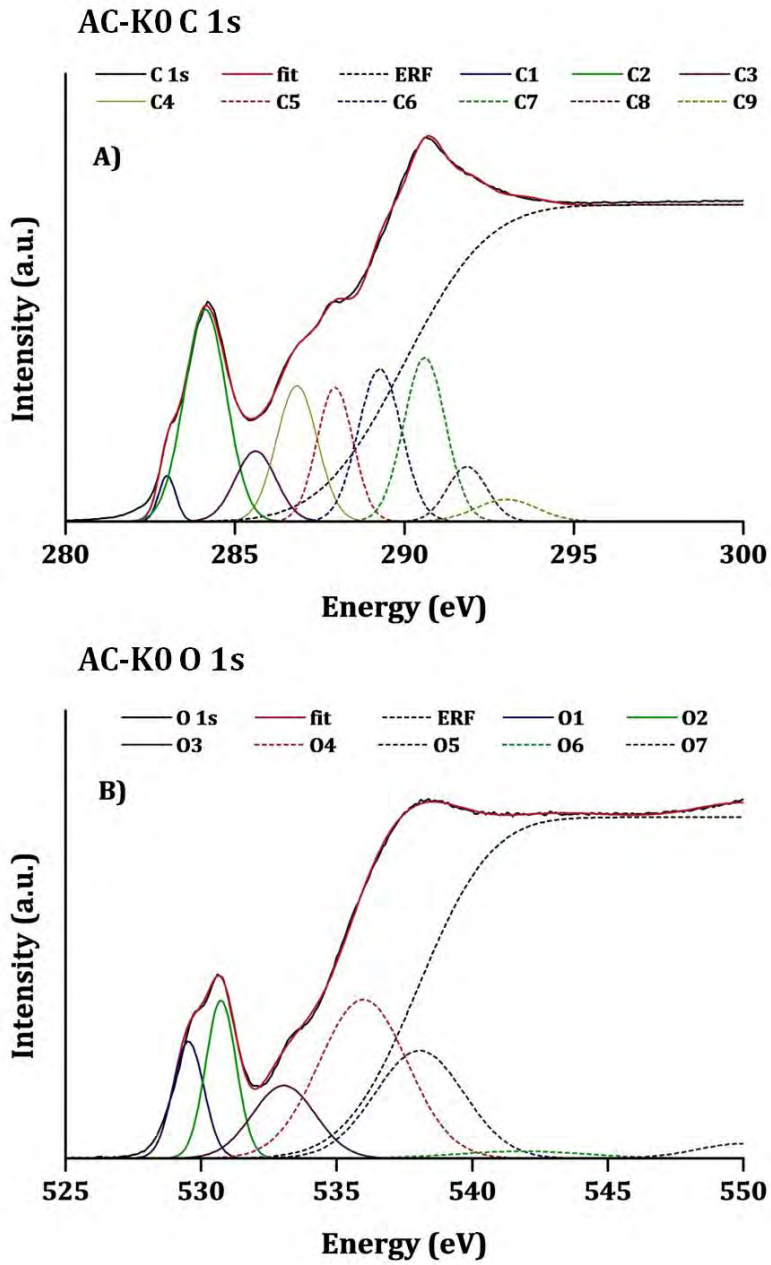

Figure 8-12 *~ C 1s and O 1s NEXAFS Spectra for AC-K0, with Complete Peak Fitting. Shown are* ***A)*** *C 1s NEXAFS Spectrum for AC-K0,* ***B)*** *O 1s NEXAFS Spectrum for AC-K0*

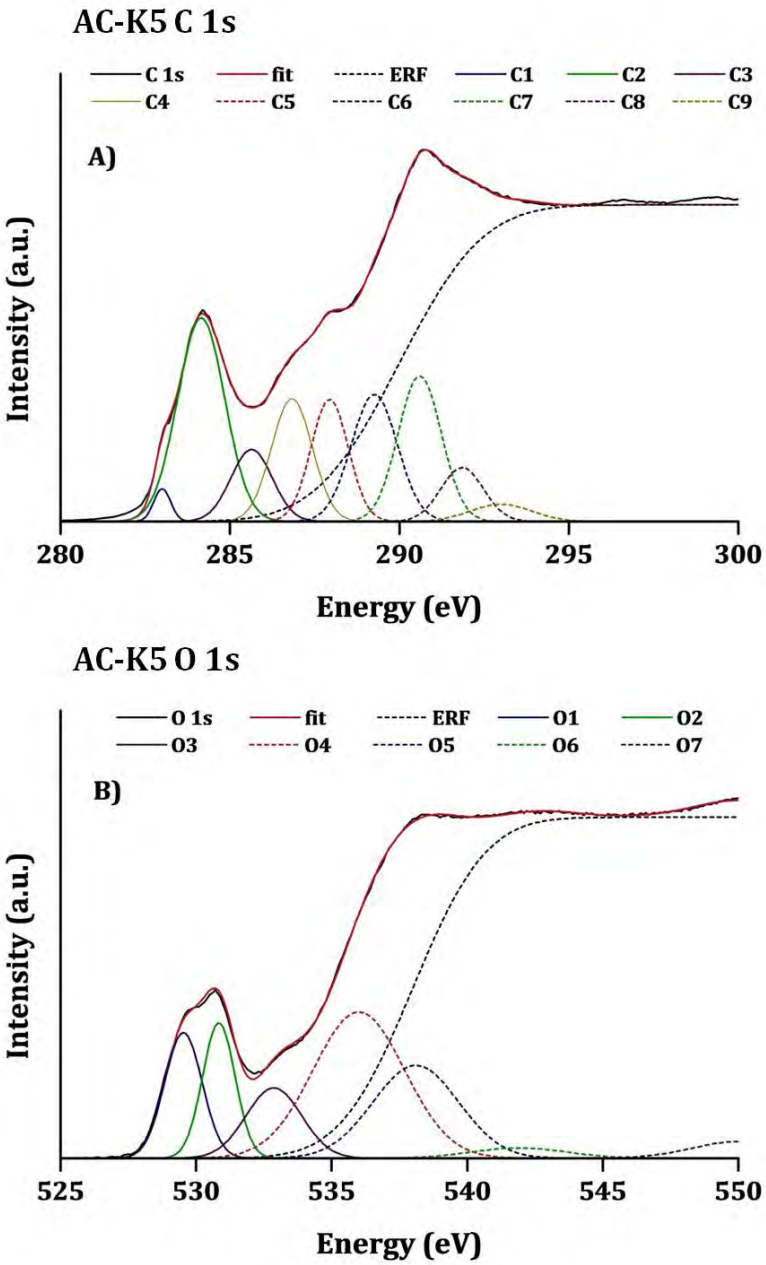

Figure 8-13 *~ C 1s and O 1s NEXAFS Spectra for AC-K5, with Complete Peak Fitting. Shown are* ***A)*** *C 1s NEXAFS Spectrum for AC-K5,* ***B)*** *O 1s NEXAFS Spectrum for AC-K5*

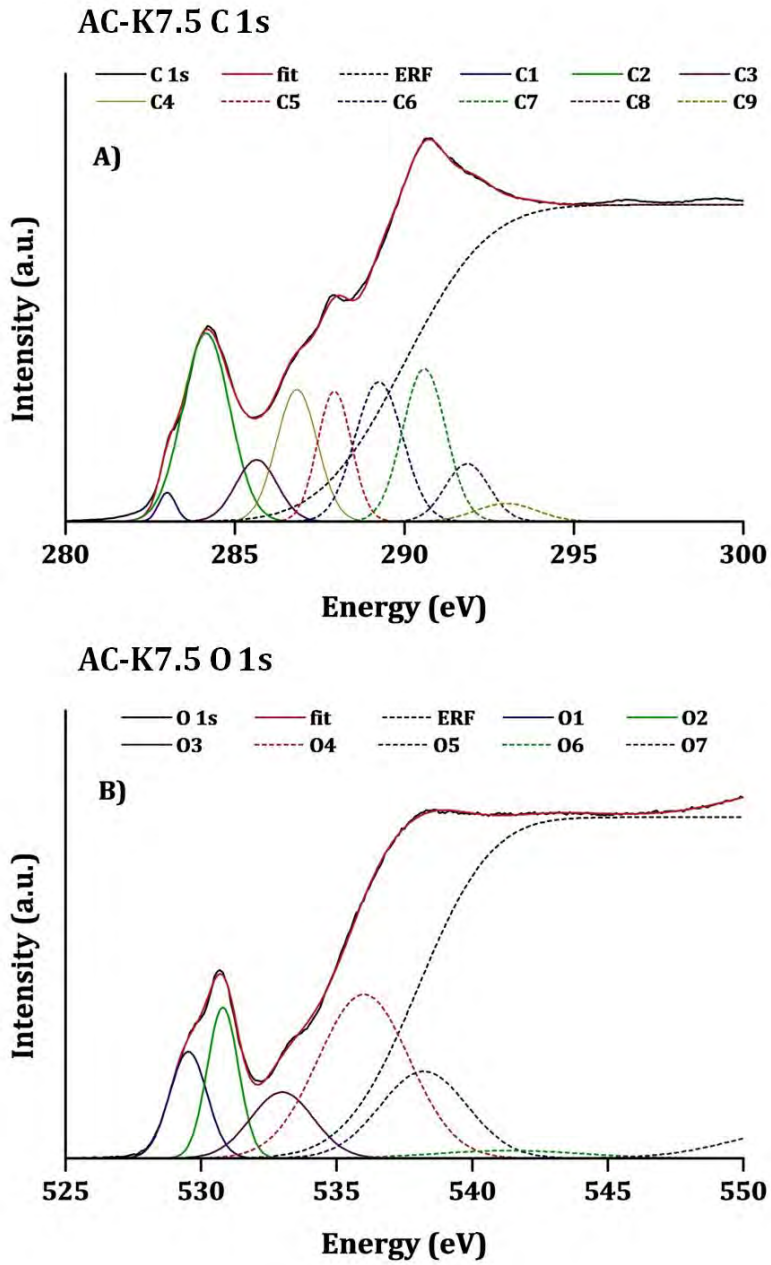

Figure 8-14 *~ C 1s and O 1s NEXAFS Spectra for AC-K7.5, with Complete Peak Fitting. Shown are* ***A)*** *C 1s NEXAFS Spectrum for AC-K7.5,* ***B)*** *O 1s NEXAFS Spectrum for AC-K7.5*

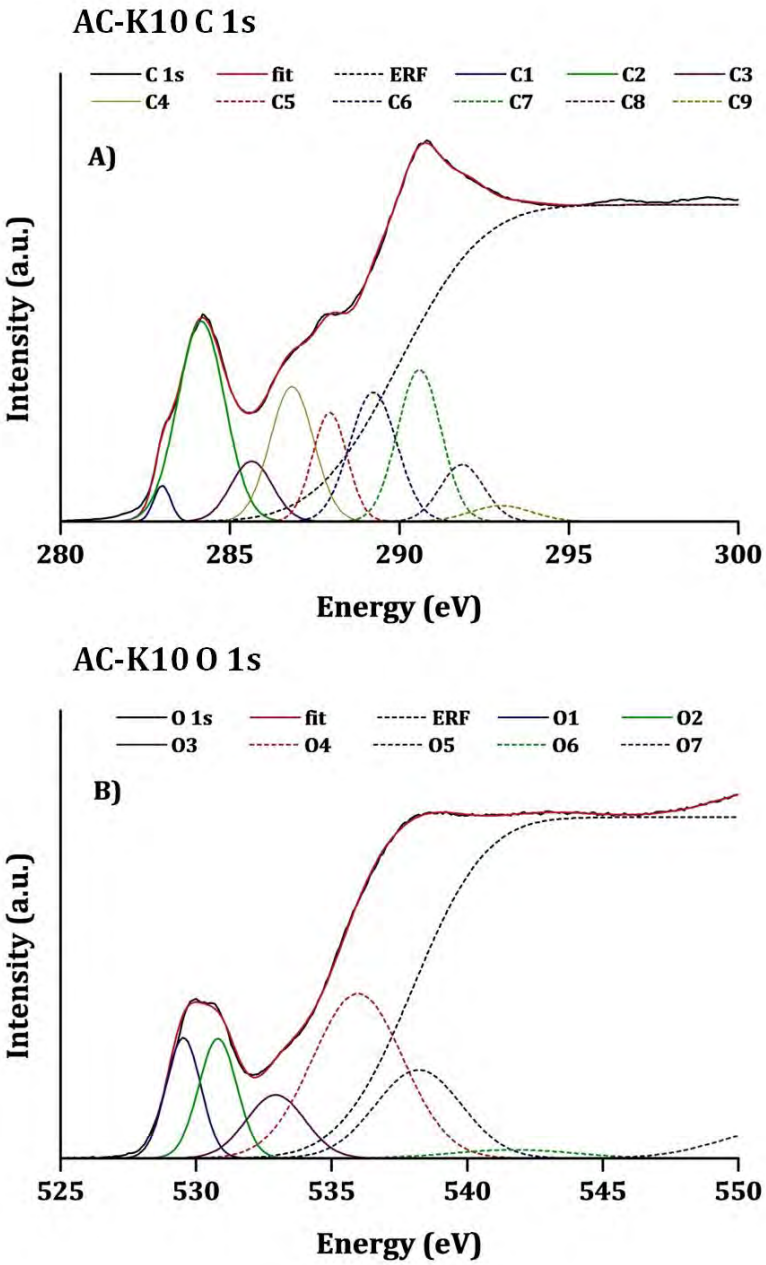

Figure 8-15 *~ C 1s and O 1s NEXAFS Spectra for AC-K10, with Complete Peak Fitting. Shown are* ***A)*** *C 1s NEXAFS Spectrum for AC-K10,* ***B)*** *O 1s NEXAFS Spectrum for AC-K10*

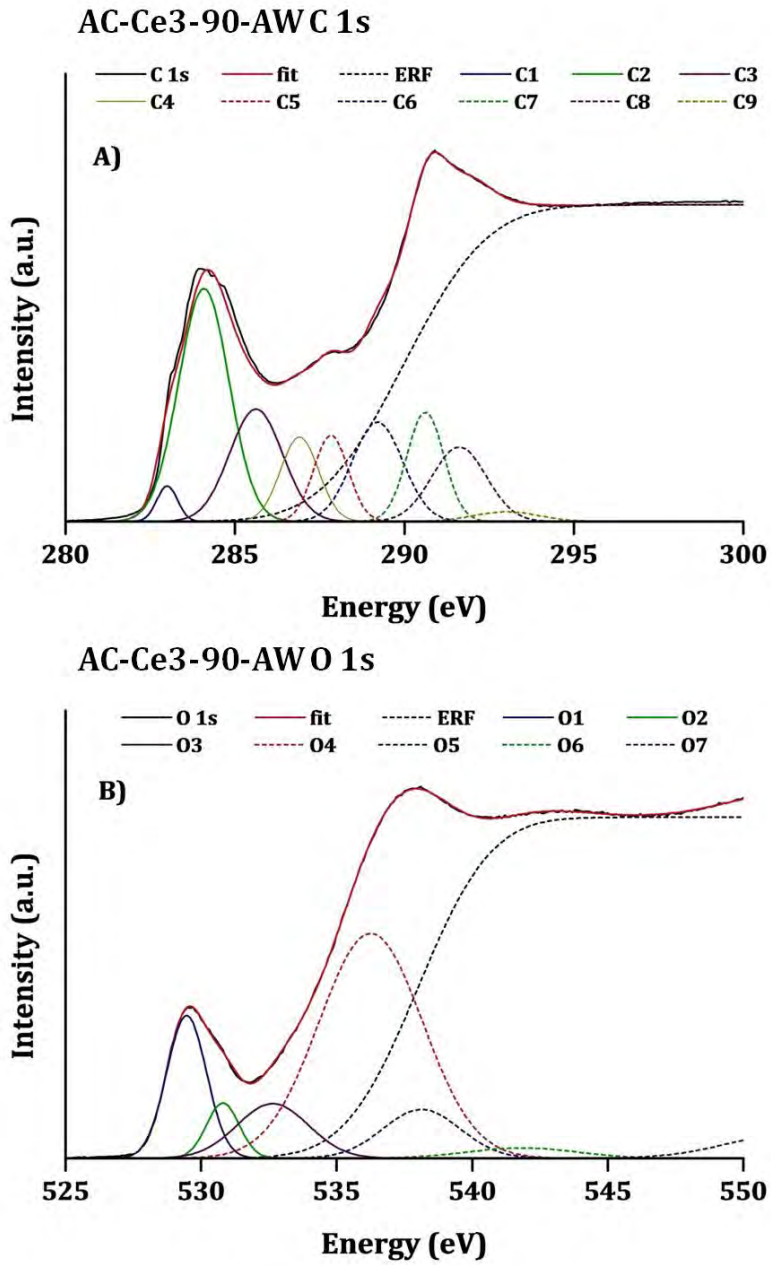

Figure 8-16 *~ C 1s and O 1s NEXAFS Spectra for AC-Ce3-90-AW, with Complete Peak Fitting. Shown are* ***A)*** *C 1s NEXAFS Spectrum for AC-Ce3-90-AW,* ***B)*** *O 1s NEXAFS Spectrum for AC-Ce3-90-AW*

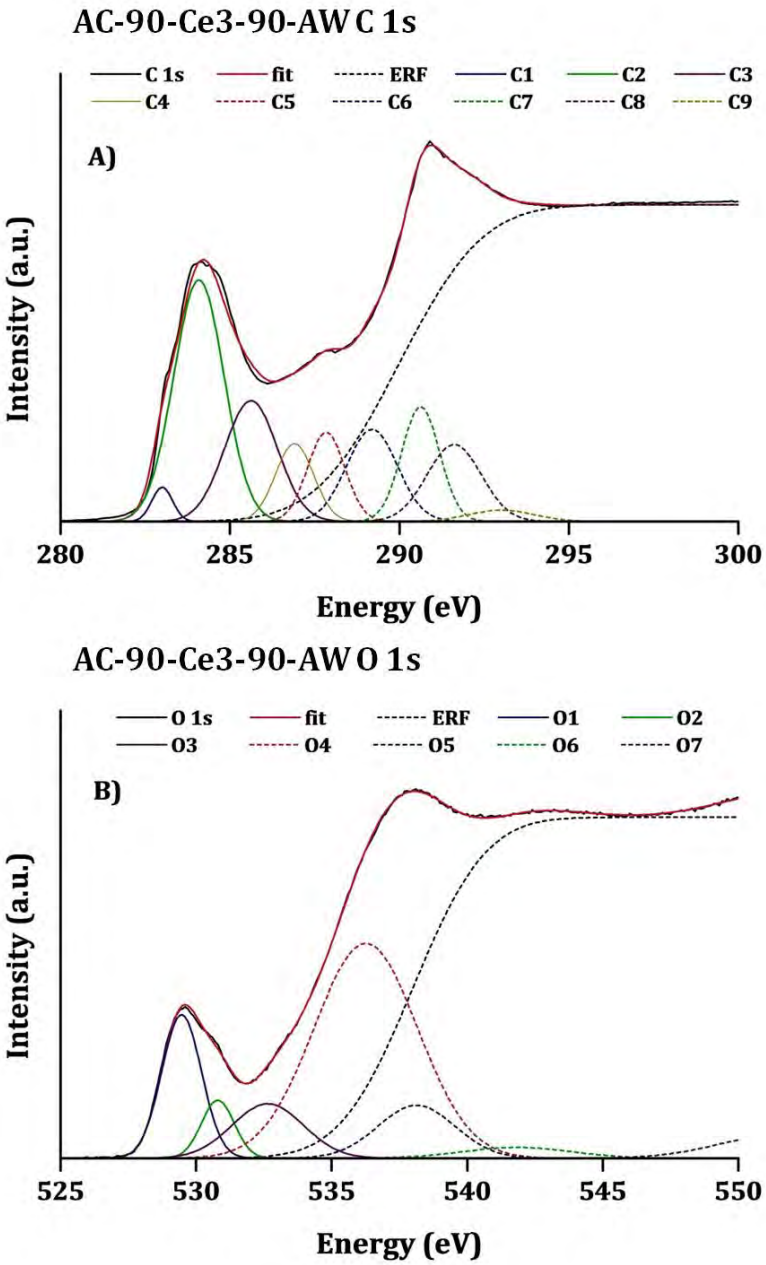

Figure 8-17 *~ C 1s and O 1s NEXAFS Spectra for AC-90-Ce3-90-AW, with Complete Peak Fitting. Shown are* ***A)*** *C 1s NEXAFS Spectrum for AC-90-Ce3-90-AW,* ***B)*** *O 1s NEXAFS Spectrum for AC-90-Ce3-90-AW*

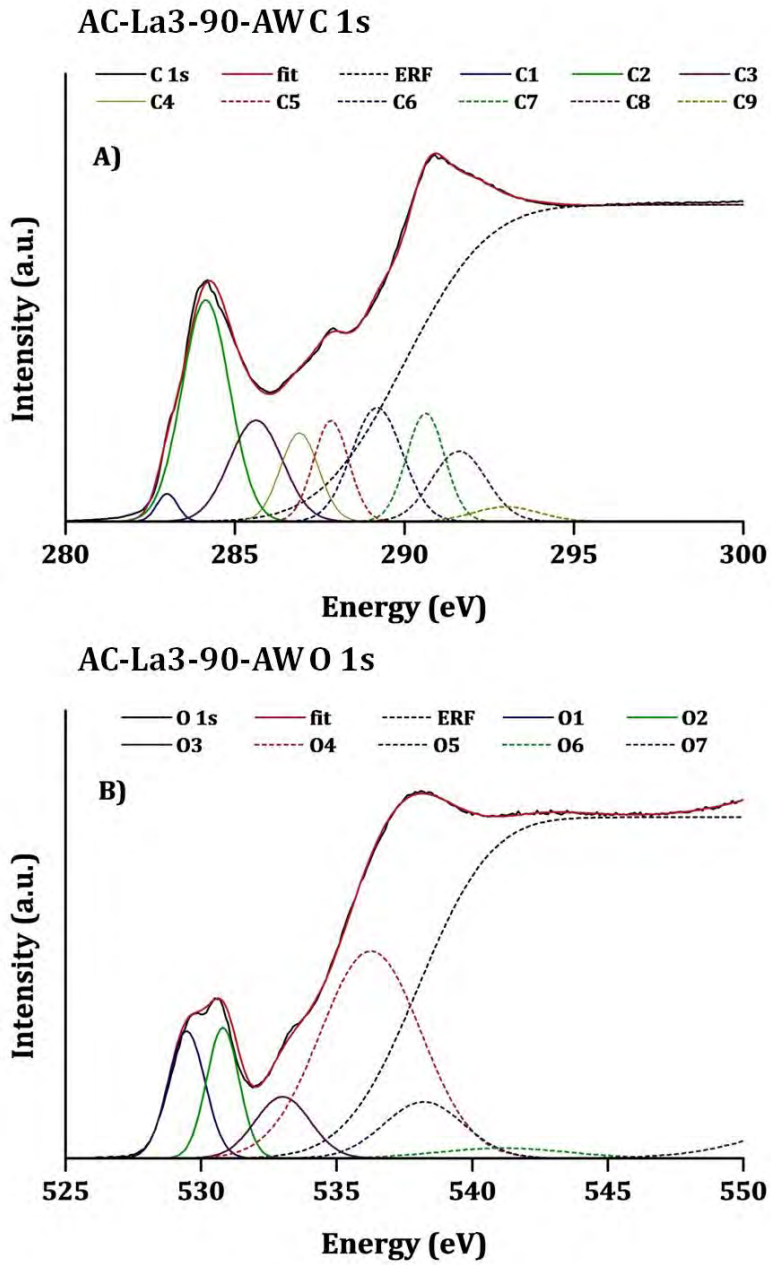

Figure 8-18 *~ C 1s and O 1s NEXAFS Spectra for AC-La3-90-AW, with Complete Peak Fitting. Shown are* ***A)*** *C 1s NEXAFS Spectrum for AC-La3-90-AW,* ***B)*** *O 1s NEXAFS Spectrum for AC-La3-90-AW*

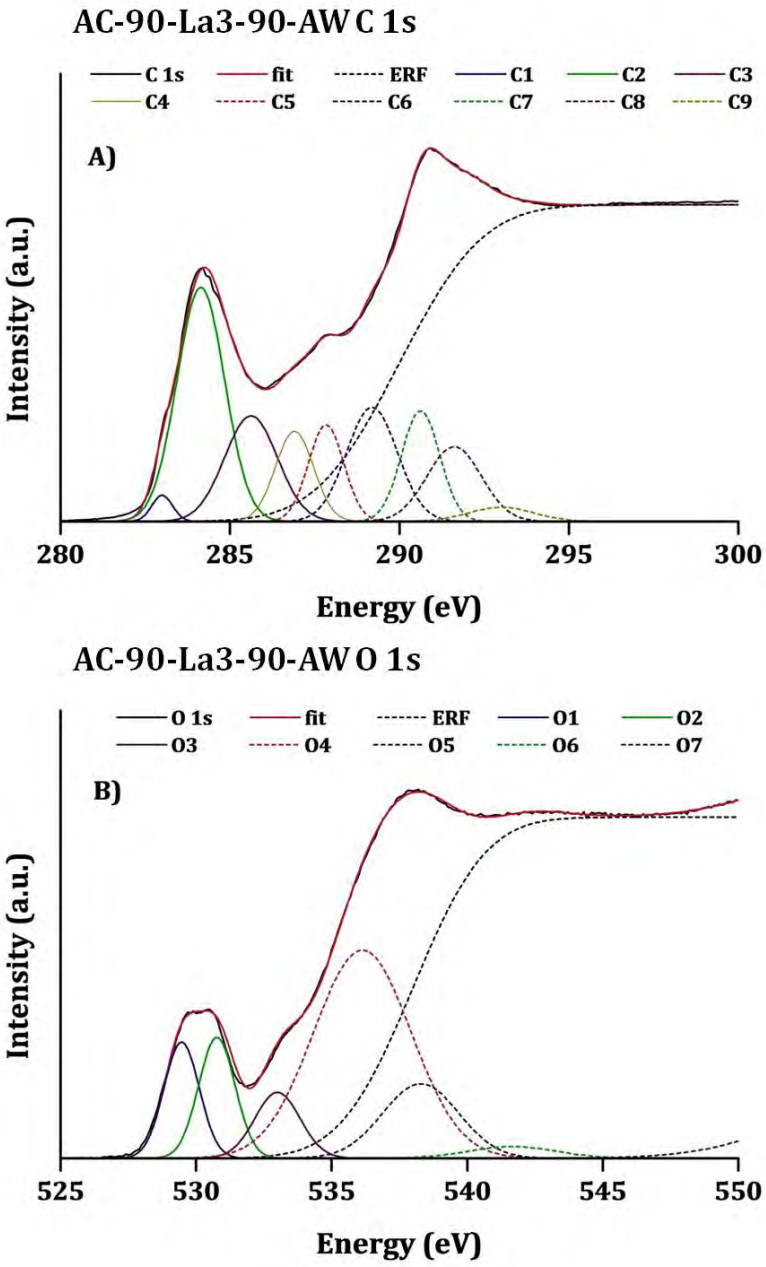

Figure 8-19 *~ C 1s and O 1s NEXAFS Spectra for AC-90-La3-90-AW, with Complete Peak Fitting. Shown are* ***A)*** *C 1s NEXAFS Spectrum for AC-90-La3-90-AW,* ***B)*** *O 1s NEXAFS Spectrum for AC-90-La3-90-AW*